INSTITUTE FOR APPLIED PROBLEMS IN MECHANICS AND MATHEMATICS
NATIONAL ACADEMY OF SCIENCES OF UKRAINE

As a manuscript

PETRUK Oleh Leonidovych

UDK 524.354:524.1-6

ACCELERATION OF COSMIC RAYS IN SHELL SUPERNOVA REMNANTS (ПРИСКОРЕННЯ КОСМІЧНИХ ПРОМЕНІВ В ОБОЛОНКОВИХ ЗАЛИШКАХ НАДНОВИХ ЗІР)

01.03.02 – astrophysics, radioastronomy

Thesis for scientific degree of
doctor in physics and mathematics

Lviv – 2010

CONTENTS

LIST OF ABBREVIATIONS

1-D – one-dimensional

3-D – three-dimensional

BSNRs – Bilateral SNRs

CMB – Cosmic Microwave Backgraund

CR, CRs – Cosmic Ray, Cosmic Rays

HESS – High Energy Stereoscopic System

IC – Inverse-Compton

ISM – Interstellar Medium

ISMF – Interstellar Magnetic Field

LoS – Line of Sight

MF – Magnetic Field

MHD – Magneto-Hydro Dynamics

PoS – Plane of Sky

PDS – Pressure-Driven Snowplow

SNR, SNRs – Supernova Remnant, Supernova Remnants

TXC – Thermal X-ray Composite

index "s" – value immediately after the shock

index "o" – value before the shock

index "$\parallel$" – value at the parallel shock

index "$\perp$" – value at the perpendicular shock

Reference times for evolution of the strong shock (Sect. 2.2)

$t_{\rm sag}$ "sag" time [121], radiative cooling begins to affect the temperature distribution downstream of the shock;

$t_{\rm dyn}$ "dynamics-affected" time [121], the temperature of a fluid element shocked after this time decreases faster due to radiation than due to expansion;

$t_{\rm tr}$ "transition" time [90], estimation of the time when the deviations from Sedov solutions are prominent; Sedov solution may be approximately used till this time;

$\Delta t_{\rm cool}$ "cooling" time [119, 120, 206], a shocked fluid element cools during this time;

$t_{\rm s}$ "shock" time [119, 120], moment when the shock encountered given fluid element;

t_1 moment when the shock encountered the fluid element which cools first [119, 120];

$t_{\rm c}$ sum of $t_{\rm s} + \Delta t_{\rm cool}$;

$t_{\rm cool}$ "SNR cooling" time [119,120,122], the minimum of $t_{\rm c}$, i.e. the age of SNR when the first cooled element appears;

$t_{\rm sf}$ "shell-formation" time [119, 120, 122], approximately after this time the shock may be described by the radiative PDS model;

$t_{\rm low}$ moment during the adiabatic stage when the radiative losses of the decelerating shock wave reach their minimum value;

$t_{\rm hi}$ moment when the radiative losses of the decelerating shock wave reach their maximum value [89, 269];

$t_{\rm i}$ "intersection" time [65], moment when two functions – adiabatic $R(t)$ and radiative $R_{\rm sh}(t)$ intersect;

$t_{\rm max}$ moment during the radiative stage when the function $m(\tau)$ reaches its maximum [65];

$\tilde{t}$ timescale;

τ dimensionless time, $\tau = t/\tilde{t}$.

INTRODUCTION

Thesis is devoted to development of methods for modeling of evolution of strong nonrelativistic shocks in nonuniform media and fields, kinetics of charged relativistic particles in its vicinity, applications of the methods to calculation of nonthermal emission of the shell-type supernova remnants and comparison with observations.

Actuality of the work. Do SNRs are main sources of Galactic CRs? This question remains to be one of most intriguing in high-energy astrophysics.

Almost 100 years ago, on August 7, 1912, V. Hess has conducted most successful experiment revealing increase of radioactivity with height and explained it by the assumption about "a radiation of very great penetrating power" which enters the atmosphere from space. Hess was awarded the Nobel Prize in 1936 for this discovery.

It was long thought that the phenomenon is of the electromagnetic origin (photons) and therefore was given the name "Cosmic Radiation", which later evolved to "Cosmic Rays". During the decade from 1927 (geomagnetic effect) to 1937 (east-west effect), a wide variety of experimental investigations demonstrated that cosmic rays are affected by the Earth's magnetic field, thus they are charged particles.

From the 1930s to the 1950s, before the man-made particle accelerators reached very high energies, CRs served as a source of particles for high energy physics, and led to discovery of subatomic particles including the positron and muon. Although these applications continue, the main focus of CR research has been directed towards astrophysical investigations of where cosmic rays originate, how they get accelerated to such high velocities, what role they play in the dynamics of the Galaxy, and what their composition tells us about matter from outside the solar system.

It is common belief that CRs with energies smaller than the knee, or even up to 10^{17} eV, are produced in our Galaxy. Though CRs are accelerated in different types of sources (OB stars, pulsars etc.), common belief is that no other objects in Galaxy

can be responsible for the most of galactic CRs except of SNRs.

CRs with energies $\leq 3 \times 10^{15}\,\mathrm{eV}$ in ISMF of order $3\,\mu\mathrm{G}$, considerably affects propagation of such charged particles deviating them from directions to the sources. Therefore, one cannot observe CRs from SNRs directly. The only possibility to study them is to consider different kind of emission resulted from interactions of accelerated particles with magnetic and photon fields or other particles.

Studies of CRs is closely related to radio-astronomy. Since 1950, radio-observations give important evidences about electronic component of CRs throughout of the Universe. Over the last decade, methods for space observations of high-energy radiation (X-rays and γ-rays) have achieved considerable development. Present data from satellites and ground-based experiments in high-energy astrophysics allows us to test theories of particle acceleration by the strong shock waves. Therefore, sources of nonthermal radiation, in particular supernova remnants, are intensively studied. Their emission carries information about physics of strong shocks, motion and emission of cosmic rays (high-energy charged particles), properties of magnetic field. They are an important and unique experimental "platform" for studies of the interaction of plasma and relativistic particles. SNRs are one of the main objects for observations of modern space- and ground-based telescopes in many parts of the electromagnetic spectrum, from radio to hard gamma-ray bands (see, for example the Roadmap for Astroparticle Physics in Europe [339]).

X-ray observations of SNRs are of particular importance for understanding the microphysics occurring in the vicinity of the shocks. Maximum of the thermal radiation of SNRs are in the X-ray range. However, high spatial and spectral resolution of modern X-ray telescopes allows us to detect and analyze nonthermal X-ray component, which is a consequence of synchrotron radiation of relativistic electrons. Discovery of the nonthermal component in X-ray spectrum of supernova remnant in 1995 [215] grow new interest to study these objects. This nonthermal component give evidence about acceleration of electronic components of CRs on the fronts of shock waves of SNRs to energies $\sim 30 \div 300$ TeV [184, 312]. Electrons with such energies should also radiate in the γ-ray range (through inverse-Compton effect and

nonthermal bremsstrahlung). Conclusions about the proton component of CRs can be inferred only through the observation of γ-photons that arise from decay of pions, generated by collisions of protons accelerated to relativistic velocities with the target protons. Thus, tools for observations are developed actively. Most prominent success is reached in the very-high energy γ-ray band. The first γ-ray map of SNR, obtained in 2004 with the system of Cherenkov telescopes HESS, open an era of the visual gamma astronomy. Since then, the observations gave maps of a number of SNRs. These results, along with X-ray and radio observations, provide direct evidence that cosmic rays are really accelerated in SNRs to energies of order of 100 TeV. However, while the spectral properties of radiation of relativistic particles in SNRs are studied enough, the rest of observational data, namely the properties of the surface brightness distributions, remains almost unused because of the complexity of the theoretical and numerical modeling.

Observations and theoretical analysis of nonthermal emission from SNRs allows one to explore physical processes which may not be experimentally studied on Earth; it helps in understanding the problem of origin of galactic CRs. SNRs are among priority targets for observations with space X-ray and γ-ray observatories Chandra, XMM-Newton, Integral, Fermi, as well as ground-based experiments with observations of Cherenkov light from atmosphere after impact with very-high energy γ-photons (with energies in range $0.1 - 100$ TeV): HESS, MAGIC, VERITAS and other. At present, nonthermal X-ray emission is detected in few dozens of shell-like SNRs, out of 274 known [172]. Since 2004, TeV γ-rays is observed from about twenty SNRs [158]. Gamma-observatory Fermi launched in 2008 has detected γ-rays from many sources, in particular from SNRs [24].

Every year, few hundred papers dealing with different aspects of galactic CR origin and SNRs appear. Theoretical results, obtained mainly in the last 10 years, are reviewed in [79, 98, 131, 136, 226, 306, 348]. Development of theoretical studies and observations of SNRs reveals new phenomena which happens around strong nonrelativistic shocks propagating in ISM. These phenomena are related to motion in ISM with gradients of density and magnetic field, with injection of thermal particles

and their further acceleration till highly relativistic energies by strong shocks and their interaction with ISMF.

These are the reasons for rapidly developing field of exploration of nonthermal emission from SNRs.

Relations to the scientific programs, plans and projects. The work was carried out in the Institute for Applied Problems in Mechanics and Mathematics NAS of Ukraine in the frames of the scientific projects "Розвиток диференціально-геометричних методів дослідження рівнянь математичної і теоретичної фізики" (state registration number 0102U000451), "Диференціально-топологічні та геометричні аспекти теорії динамічних систем, рівнянь математичної фізики, теорії фундаментальних взаємодій" (state registration number 0106U000593), "Дослідження некласичних крайових задач для рівнянь із частинними похідними та руху часток у неоднорідних середовищах і полях" (0105U000929), "Розробка моделей Всесвіту з космологічними полями, моделей темної енергії, дослідження впливу темної енергії на еволюцію Всесвіту" (0109U003207), "Дослідження природи джерел космічних променів надвисоких енергій" (0103U006381), as well as in projects carried out in the Astronomical Observatory of Lviv National University: "Визначення фізичних параметрів змінних зір, газопилових туманностей, зоряних скупчень, галактик та квазарів" (0105U002240), "Спостереження, статистичний аналіз та моделювання фізичних процесів галактичних та позагалактичних джерел випромінювання" (0107U002061), "Дослідження змінних зір, залишків наднових та галактичних зоряних скупчень на основі наземних та космічних телескопів" (0110U001384).

The purpose and objectives of the study. The purpose of the study is development of magneto-hydrodynamical models of SNRs evolving in ISM with different types on nununiformities of density and magnetic field, development of new analytical methods of solution of systems of nonlinear differential equations in partial derivatives which describe evolution of the strong shocks, motion and radiation of relativistic charged particles around these shocks, calculation of nonthermal emission

of SNRs in different energy ranges, comparison of models with modern observations.

The main objectives of the study are:

1. to investigate evolution of SNR from time when condition of adiabaticity becomes to be invalid;
2. to develop an approximate analytical methods for dynamics of shock and flow in the spatially nonuniform plasma after the end of adiabatic era;
3. to develop an analytical method for description of electron injection which allow us to obtain the momentum distribution of injected electrons;
4. to describe evolution of the energy spectrum of accelerated electrons downstream of the shock which evolve in nonuniform ISM and nonuniform ISMF;
5. to construct an analytical approximation for calculation of the γ-ray emissivity of electrons due to inverse-Compton process;
6. to model and investigate properties of the surface brightness distribution of adiabatic SNRs in uniform ISM and uniform ISMF due to leptonic emission in radio, X-ray and γ-ray bands; reveal the main factors determining the morphology of SNRs;
7. to reveal reasons for assymetries in surface brightness distribution of SNRs through modeling their evolution in nonuniform ISM and nonuniform ISMF;
8. to develop methods for analysis of observed maps of SNRs in radio, X-ray and γ-ray ranges on example of a certain SNR, with the use of data from modern space- and ground-based experiments.
9. to make statistical analysis of characteristics and radio emission of SNRs in our Galaxy and neighboring galaxies with goal in mind to test models of acceleration of charged particles in strong shocks.

Object of research – cosmic rays and shock waves in the shell-like supernova remnants.

Subject of investigation – MHD properties of the strong nonrelativistic shocks in nonuniform media and fields, properties of acceleration of charged particles in these shocks, nonthermal emission of accelerated particles.

Methods of research. Development of approximate analytical and numerical methods of solution of systems of differential equations in partial derivatives which describes dynamics of strong nonrelativistic shocks in nonuniform media and fields and kinetics of charged particles in its vicinity. Application of methods to theoretical modeling of the nonthermal emission of SNRs, in particular to synthesis of their surface brightness distributions. Observations and analysis of integral and spatially resolved characteristics of nonthermal emission of SNRs, comparison with models.

Scientific novelty of results.

1. A model-independent method to synthesize the inverse Compton gamma-ray image of SNR starting from its the radio (or hard X-ray) map and using results of the spatially resolved X-ray spectral analysis is developed for the first time. The method is applied to SN 1006. Synthesized IC gamma-ray images of SN 1006 is in a agreement with observations that may be considered as an evidence that the γ-ray emission of SN 1006 is leptonic in origin.
2. A new method for determination of the three-dimensional orientation of ISMF around SNR from its radio map is developed for the first time. Method is applied to SN 1006 that allows us to determine orientation of ambient MF around this SNR.
3. Maps of surface brightness of spherical SNR in the γ-ray band are modeled for the first time, as well as radio, X-ray and γ-ray maps of SNRs in nonuniform ISM or nonuniform ISMF. Properties of the γ-ray maps are analyzed for the first time and influence of ISM and ISMF nonuniformities on the leptonic images of SNRs in different bands are revealed.
4. A new model of morphological class of SNRs - thermal X-ray composites – are proposed. It bases on the idea about the SNR evolution in ISM the a nonuniform density distribution with the length-scale smaller than 10 parsec. Model suggests that thermal X-ray composites might be prospective sources of hadronic γ-rays.
5. Approximate analytical formulae for the azimuthal and radial profiles of the synchrotron radio and X-ray as well as the inverse-Compton γ-ray brightness

of adiabatic SNRs in uniform ISM/ISMF are derived for the first time. Factors which determine patterns of surface brightness distribution are revealed.

6. It is shown, for the first time, that, in the common scenario of SNR evolution, it is necessary to consider an additional phase between the end of adiabatic and the beginning of radiative stages with duration comparable with duration of the adiabatic stage. Approximate analytical methods for hydrodynamic description of post-adiabatic and radiative shocks and flow are developed.
7. A new analysis of radio and X-ray observations of SN 1006 is presented. The experimental data (the broadband spectrum surface brightness distributions in different bands, spatially-resolved spectral analysis), are used to put constraints on SNR and properties of leptonic component of CRs and MF in this SNR, to determine its three-dimensional orientation and other properties.
8. It is shown for the first time that $\Sigma - D$ relationship cannot represent evolutionary track of a "typical" SNR but reflects evolution of many SNRs in very different ambient conditions; that models prescribing constant efficiencies for both magnetic field amplification and electron acceleration are rejected by the data; that cumulative distribution of SNRs with size is not related to law of shock motion but to densities of ISM where SNRs are evolved.

Practical significance of results. Model of thermal X-ray composites suggests to consider them as prospective sources of hadronic γ-rays.

Hydrodynamic models of the post-adiabatic and radiative SNRs allow for simulations of old SNRs and their emission, in particular for study of decrease of the radio emission that is important for understanding the $\Sigma - D$ relationship.

Methodology to track changes in energy spectrum of accelerated electrons, downstream of the shock in nonuniform ISM and ISMF, and approximation for their inverse-Compton emission opens the possibility to synthesize maps of SNRs in nonuniform ISM and/or nonuniform IMSF.

Synthesized maps provide understanding of the reasons which determine patterns of surface brightness and their assymetries of different types. This facilitates devel-

opment of methods for analysis of observed SNR maps in oder to put constraints on properties of CRs and MF in these objects.

Proposed methods for determinations of properties of CRs and MF in SNRs are theoretical basis for analysis of observations. In the present work, they are applied to SN 1006, but may be used in other SNRs as well. It is primarily about a method to predict IC γ-ray maps of SNRs, a method to determine aspect angle of ISMF from radio map, a method to obtain "pure" thermal image of SNR from X-ray data.

Results may be used for development of theory of charged particles interactions with magnetic field and plasma, they may be extended to relativistic shocks, may be used in studies of other astrophysical objects with strong shocks (solar flares, active galactic nuclei, gamma-ray bursts).

Personal contribution of the author. Papers [15, 16, 271–278, 280] are done without coauthors. In papers, published in co-authorship, author of the thesis has:

- in [8, 9, 72]: participated in the setting up the objectives, participated in development of models, conducted numerical modeling, participated in analysis of results and writing the papers;
- in [65]: investigated branches of solutions and their properties, participated in writing the paper;
- in [17, 18, 279]: set up the objectives, developed the method, provided general advising;
- in [66]: set up the objectives, prepared samples, participated in discussion on statistical methods;
- in [250, 281, 283, 284]: participated in analysis of results and writing the papers as well as set up the objectives and developed the methods in [281, 283, 284], set up the principle for spatially-resolved spectroscopy in [250], conducted calculations in [281, 283, 284];
- in [264, 265, 282, 285]: set up the objectives, developed the model in the part related to behavior of relativistic electrons and their emission, participated in testing the methods, participated in analysis of results and writing the papers.

Presentations of results. Results obtained in the thesis were presented on a number of conferences and seminars:

- 35th COSPAR Scientific Assembly (Paris, France, 2004);
- 37th COSPAR Scientific Assembly (Montreal, Canada, 2008);
- 38th COSPAR Scientific Assembly (Bremen, Germany, 2010);
- Annual International Conference "Relativistic Astrophysics, Gravitation and Cosmology" (Kyiv, 2003-2010);
- International conference "Astrophysics and Cosmology after Gamov" (Odesa, 2004, 2009);
- Scientific conference in memory of B.Babiy "Selected issues in astronomy and astrophysics" (Lviv, 2002, 2006, 2008);
- International Conference "The X-ray Universe" (Granada, Spain, 2008);
- International mathematical conference "New approaches to solution of differential equations" in memory of V.Skorobohatko (Drohobych, 2001, 2004, 2007);
- Endpoints and Interactions: A Workshop On the Future of Supernova Remnant Research (Honolulu, Hawaii, 2007);
- IAU XXVIth General Assembly (Joint Discussion 1: Cosmic Particle Acceleration, - Prague, Czech Republic, 2006);
- International Conference "New Century in X-ray Astronomy" (Yokohama, Japan, 2001);
- International School of Cosmic Ray Astrophysics (Erice, Sicilia, Italy, 2000);
- scientific seminars in the department for theory of functions and differential equations in Institute for Applied Problems in Mechanics and Mathematics NAS of Ukraine (2000-2010), in Astronomical observatory in Lviv National University (2000-2010), Astronomical observatory in Kyiv National University (2000-2010), Main Astronomical observatory of NAS of Ukraine (2010), Astronomical observatory in Jagellonian University (Krakow, Poland, 2006, 2007, 2009), Astrophysical Observatory (Florence, Italy, 2003, 2004, 2006), Astronomical Observatory

(Palermo, Italy, 2006, 2008) of Italian National Institute for Astrophysics.

Publications. Main results of the present thesis are published in 2000-2010, in 27 papers in scientific journals [8, 9, 17, 18, 65, 66, 72, 250, 264, 265, 271–274, 276–285] and proceedings [15, 16, 275], as well as in 29 abstracts.

CHAPTER 1

COSMIC RAYS AND SUPERNOVA REMNANTS

1.1. Cosmic rays: history and general insight

Cosmic rays are relativistic charged particles of the cosmic origin. The history of its discovery and investigations is described in a number of sources, e.g. [4, 118, 135].

After the discovery of radioactivity by H. Becquerel in 1896, it was generally believed that atmospheric electricity (ionization of the air) was caused only by radiation from radioactive elements in the ground or the radioactive gases (isotopes of radon) they produce. Almost 100 years ago, on August 7, 1912, V. Hess has conducted most successful experiment revealing increase of radioactivity with height, up to 5350 m above the sea level. He has concluded in his paper from 1912 that "the results of my observation are best explained by the assumption that a radiation of very great penetrating power enters our atmosphere from above". In fact, V.Hess was not the first[1] who stated such idea and there were objections against it even after a number of his experiments in 1911-1913. Nevertheless, 1912 is now accepted as the date of discovery of cosmic rays (CRs). Hess was awarded the Nobel Prize in 1936 for this discovery.

It was long thought that the phenomenon is of the electromagnetic origin (photons) and therefore was given the name "Cosmic Radiation", which later evolved to "Cosmic Rays". During the decade from 1927 (geomagnetic effect) to 1937 (east-west effect), a wide variety of experimental investigations demonstrated that cosmic rays are affected by the Earth's magnetic field, thus they are charged particles.

In the following decade, a number of experiments carried by balloons to near the top of the atmosphere showed the composition of CRs, namely, that the primary

[1] C. Wilson has suggested such hypothesis in 1901, however, he rejected it later.

cosmic particles are mostly protons with some ($\sim 10\%$) helium nuclei (alpha particles) and a small fractions of heavier nuclei ($\sim 1\%$), electrons ($\sim 1\%$), positrons and antiprotons. These are general numbers; the exact composition of cosmic rays depends on the energy of particles. At present, it is known that the common heavier elements (such as carbon, oxygen, magnesium, silicon, and iron) are present in CRs in about the same relative abundances as in the solar system; there are, however, some important differences in elemental and isotopic composition that provide information on the origin and history of galactic cosmic rays. For example there is a significant overabundance of the rare elements Li, Be and B produced when heavier cosmic rays such as C, N, and O fragment into lighter nuclei during collisions with the interstellar gas.

From the 1930s to the 1950s, before the man-made particle accelerators reached very high energies, CRs served as a source of particles for high energy physics, and led to discovery of subatomic particles including the positron and muon. Although these applications continue, the main focus of CR research has been directed towards astrophysical investigations of where cosmic rays originate, how they get accelerated to such high velocities, what role they play in the dynamics of the Galaxy, and what their composition tells us about matter from outside the solar system. There are a number of monographs devoted to astrophysics of cosmic rays, e.g. [1,2,161,233,326].

CR studies are closely related to radio astronomy and high-energy astrophysics. In the beginning of 1950, the radio-astronomy provided important evidences about electronic component of CRs throughout of the Universe. Since then, the synchrotron radiation from relativistic electrons is also observed in other parts of electromagnetic spectrum, up to X-rays and γ-rays. Development of γ-ray astronomy is also of the great importance for CR studies. In particular, there is a hope that γ-radiation from cosmic sources will give firm evidences about acceleration of the proton component of CRs in various astrophysical environments. Relativistic protons and electrons are reason of diffuse γ-ray background; the former as consequence of the neutral pion decays [182], the later due to inverse-Compton process [149] or non-thermal bremsstrahlung [198].

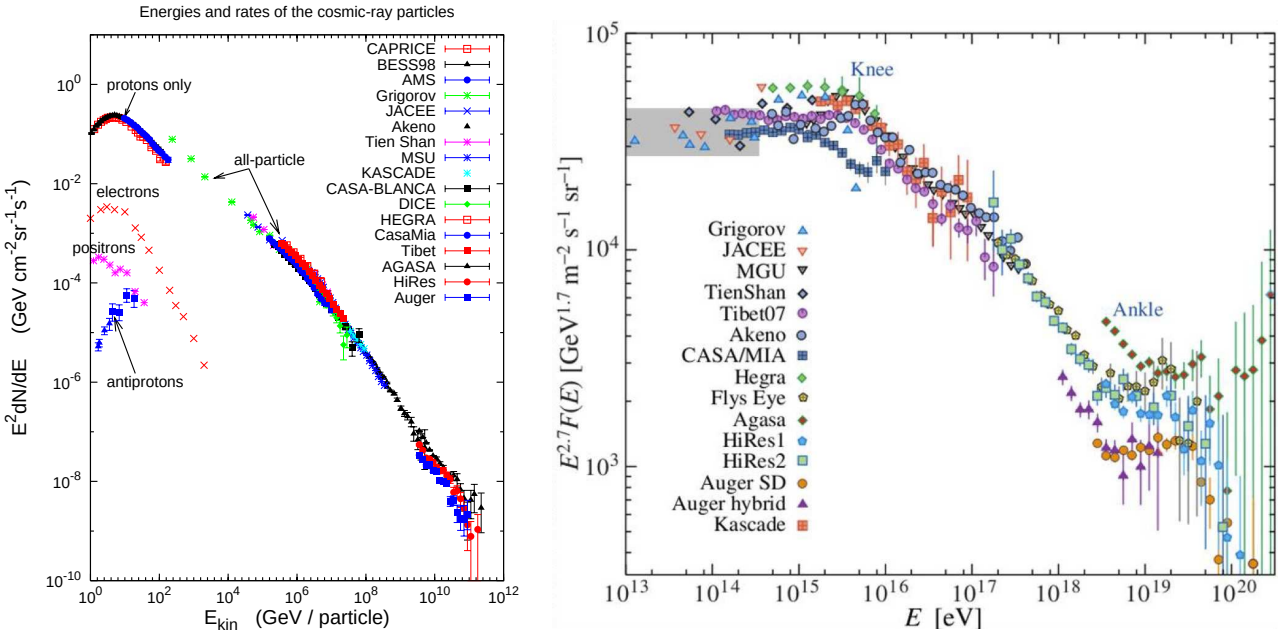

Figure 1.1. Energy spectrum of cosmic rays: left [163], right [179]. The "knee" and the "ankle" are clearly visible on the right where the spectrum has been multiplied by a power $E^{2.7}$ in order to visually enhance the structure in the spectrum.

The energy spectrum of CRs extends from few hundred MeV to 300 EeV; it has in general the power-law shape with some features related to change of the slope (Fig. 1.1). Solar system affects the CR spectrum below energy $E = 10\,\mathrm{MeV}$; solar wind prevent us from knowing anything about interstellar CRs with energies lower than 300 MeV. Differential proton energy spectrum in the energy range $10^{10}\,\mathrm{eV} \leq E \leq 3 \times 10^{15}\,\mathrm{eV}$ is [88]

$$N(E) = 8.7 \times 10^{-2} \left(\frac{E}{1\,\mathrm{TeV}}\right)^{-2.73} \frac{\text{particles}}{\mathrm{m^2\ s\ st\ TeV}} .$$

Integral intensity of CRs in the same energy range is well represented by [4]

$$I(>E) = 1 \left(\frac{E}{1\,\mathrm{GeV}}\right)^{-1.7} \frac{\text{particles}}{\mathrm{cm^2\ s\ st}} = 300 \left(\frac{E}{1\,\mathrm{TeV}}\right)^{-1.7} \frac{\text{particles}}{\mathrm{m^2\ hour\ st}} ,$$

while in $3 \times 10^{15}\,\mathrm{eV} \leq E \leq 10^{18}\,\mathrm{eV}$ it is

$$I(>E) = 3 \times 10^{-10} \left(\frac{E}{1\,\mathrm{PeV}}\right)^{-2.0} \frac{\text{particles}}{\mathrm{cm^2\ s\ st}} = 100 \left(\frac{E}{1\,\mathrm{PeV}}\right)^{-2.0} \frac{\text{particles}}{\mathrm{m^2\ year\ st}} .$$

Spectrum above $E = 10^{18}\,\mathrm{eV}$ represents ultra-high energy CRs (UHECRs); they should be extragalactic in origin since magnetic field of the Galaxy is small to allow for confinement of such particles. The highest energy cosmic rays measured to date have had more than 10^{20} eV, that is equivalent to the kinetic energy of a

baseball traveling at approximately 150 km/s. It was expected that the CR spectrum should suffer from GZK cut-off (around 5×10^{19} eV for protons [176, 374]) resulted from interactions of CRs with CMB radiation (e.g. [1, 262]); a feature is confirmed recently by the Pierre Auger Observatory [25]. Ultra-high energy CRs are quite rare. Intensities for particles with $E \geq 10^{18}$ eV is 60 particles per km^2 per year per steradian; while it is just about 1 particle per km^2 per century per steradian for $E \simeq 10^{20}$ eV.

Around the "knee" at $E = 3 \times 10^{15}$ eV, the spectral index of the differential spectrum E^{-s} changes from $s = 2.7$ to $s = 3.1$; the last value is valid up to the "ankle" at $E = 3 \times 10^{18}$ eV where it turns to $s = 2.7$ again. Electrons have a spectrum similar to that of protons below 10 GeV, and steeper, $s = 3.3$, above (Fig. 1.1). The observed slope of the CR spectrum $s = 2.7$ generally agrees with the index $s = 2$ predicted by the acceleration theory (e.g. [294]). Source spectrum ($s \simeq 2$) steepens (to $s \simeq 2.7$) due to dependence of the diffusion coefficient on energy $D \propto E^{\delta}$, so that if the produced spectrum was $N \propto E^{-s}$, the observed spectrum becomes $N_{\rm obs} \propto E^{-s-\delta}$; the particle escape from Galaxy (most energetical particles escapes easier) also makes contribution to change of the spectrum slope from a source to the observer; also, the chemical abundance, in some energy range, varies with E. In addition, one of the effects predicted by the non-linear acceleration theory, may also affect the general slope of the observed CR spectrum. Namely, the the theory predicts concave shape of CRs, i.e. with index s variable with energy: $s = s + \delta s(E)$, where δs decreases monotonically from $\delta s \leq 0.2$ for very low energies to $\delta s \geq -0.5$ for energies close to $E_{\rm max}$ (e.g. [74]). There are some observational hints about such behavior [309]; however, there is still no definitive evidence of such a general upturn in the cosmic-ray spectrum.

It is common belief that CRs with energies smaller than the knee, or even up to 10^{17} eV, are produced in our Galaxy. Heavy elements are progressively dominating one another in the energy range 3×10^{15} eV $\leq E \leq 10^{17}$ eV (Fig. 1.2 [81]; see also [163, 190]). Similar situation may happen in the UHECR range [26].

There is no significant anisotropy of cosmic rays at any energy, even at the highest

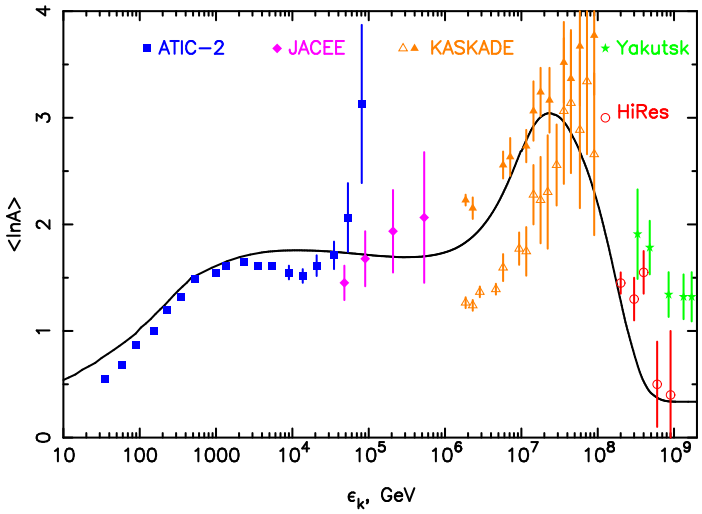

Figure 1.2. Mean logarithm of the CR nucleus atomic number as a function of particle kinetic energy [81].

energies, beyond the GZK cutoff, where galactic and intergalactic MF is almost inefficient in deviation of UHECRs from direction to sources. However, it seems that observational data reveal some correlations of UHECRs with AGNs (e.g. [27]).

Under equilibrium condition, one can expect that energy density of CRs have to be of the order of the energy density of interstellar magnetic field, namely,

$$\omega_{\rm cr} \sim \omega_{\rm mf} = B^2/8\pi \sim 10^{-12}\,{\rm erg/cm^3},$$

for typical strength $B = 5\,\mu$G. The energy density of interstellar gas is of the same order, $\omega_{\rm g} = 3nkT/2 \sim 10^{-12}\,{\rm erg/cm^3}$, for $n = 1\,{\rm cm^{-3}}$ and $T = 10^4\,{\rm K}$. Thus, CRs (having very small number density, $n_{\rm cr} \sim 10^{-10}\,{\rm cm^{-3}}$) are important dynamical and energetical factor for ISM. They also cause prominent kinetic and MHD effects; in particular, streaming instability of CRs leads to increase of MF strength in ISM and, to higher extent, in the CR sources (see e.g. [19] and references therein).

Let us assume that CRs are everywhere in our Galaxy including halo with characteristic scale $h \sim 10\,{\rm kpc}$ [4]. Then CRs occupy volume $V_{\rm cr} \sim 4\pi h^3/3 = 10^{68}\,{\rm cm^3}$. The total energy in CRs is therefore $W_{\rm cr} \sim \omega_{\rm cr} V_{\rm cr} \sim 10^{56}\,{\rm erg}$. The characteristic time-scale for CR propagation in the Galaxy is $T_{\rm cr} \sim 3 \times 10^8\,{\rm years}$ [4]. Thus, luminosity of CR sources in our Galaxy should be $L_{\rm cr} \sim W_{\rm cr}/T_{\rm cr} \sim 3 \times 10^{40}\,{\rm erg/s}$.

In 1934, Baade and Zwicky suggested that the main sources of CRs in the Galaxy are supernovae [58,59]; Shklovskii wrote that "ionized interstellar atoms are acceler-

ated in the moving magnetic fields connected with an expanding [supernova remnant] nebula" [332]. Really, an energy $E_{\rm sn} \sim 10^{50} - 10^{51}$ erg is deposited in each supernova explosion which happens every $t_{\rm sn} \sim 30$ years. An average power from supernovae is thus $L_{\rm sn} \sim E_{\rm sn}/t_{\rm sn} \sim 10^{41} - 10^{42}$ erg/s. If CRs take up to $\sim 10\%$ of SN kinetic energy then supernovae can provide necessary power $L_{\rm cr}$ of CR in Galaxy ([4], see also [2, 88, 189]).

Of course, the above estimates are rather general and even firm confirmations about acceleration of CRs in certain SNR may not be directly extended to all SNRs. In particular, the particle acceleration process is strongly dependent on the environment in which the supernova explodes [88]. For instance, we can expect that the blast wave of a SN-type Ia has a larger Mach number than that of a type II SN, mainly because of the lower temperature of the ordinary ISM compared with that of the material around a massive star with powerful winds. For the same reason we can expect the gas density to be lower for type-II SNe. While type-II SNe are more frequent than type Ia, it is probably more difficult to observe hadronic emission in γ-rays from these objects because of the lower gas density.

Nevertheless, though CRs are accelerated in other sources as well (OB stars or pulsars, the latter are probably responsible for CR positrons [31]), common belief is that no other objects in Galaxy can be responsible for the most of galactic CRs [130].

1.2. Supernova remnants as sources of cosmic rays

Strong collisionless shocks are present in various astrophysical objects, and under a wide range of conditions. These shocks effectively ionize and heat the gas and are also believed to accelerate a fraction of particles up to very high energies. Really, shock waves running through a magnetic and ionized gas accelerate charged particles, as we know from theory and in situ observations in the solar wind, and this forms the basis of almost all theories of CRs; in particular, of production of galactic CRs by forward shocks in SNRs. However, except of the electronic component of CRs,

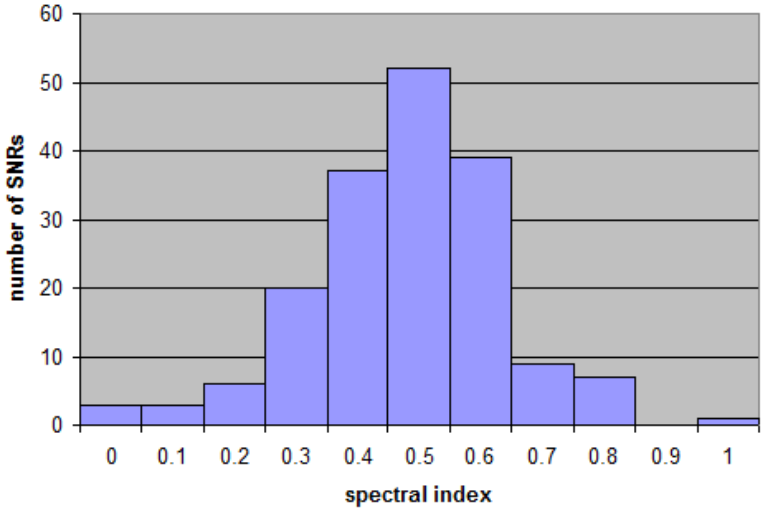

Figure 1.3. Spectral index for SNRs in our Galaxy (data are taken from Green's catalogue [172]).

we still have no unambiguous proof for that.

The mechanism believed to be responsible for acceleration of charged particles in SNR is diffusive shock acceleration (for review see, e.g. [86, 128, 202]): such particles are repeatedly scattered off by magnetic turbulence on both sides of an SNR shock front, gaining speed as a result of the difference in the plasma velocities on either side of the shock. The greater the velocity difference, the greater the energy gained by the particle per shock crossing; the larger the magnetic field (and turbulence), the higher the particle crossing frequency; the larger time allowed for such cycles, the higher the energy attained.

A well-known result of this process, for the test particles (i.e. those which do not make any influence on the system), is its power-law energy distribution with index s dependent only on the shock compression ratio: $N(E) \propto E^{-s}$, $s = (\sigma+2)/(\sigma-1)$ where $\sigma = \rho_{\rm s}/\rho_{\rm o}$ is the shock compression ratio (equal to 4 for strong shocks and $\gamma = 5/3$). The prediction is thus $s = 2$ which, for electrons, implies a synchrotron spectral index $\alpha = (s-1)/2 = 0.5$; that is generally in agreement with observed spectra in Galactic SNRs (Fig. 1.3).

With the diffusive shock acceleration mechanism, SNRs provide not only the spectral index s close to the expected one, not only enough energy budget (Sect. 1.1), but also necessary elemental composition of CRs. The elemental composition of the accelerated particles should be that of the gas swept up by the outer shock. Different

ions enter the shock at the same speed, and the Fermi acceleration forms a power-law momentum spectrum starting from this initial velocity: the result is that the different types of accelerated particle should have the same proportions as in the gas if measured at the same velocity or Lorentz factor. This is almost as observed, — a reasonable indirect evidence about the shock injection and acceleration [190]. Some further, in the context of the non-linear theory of acceleration, considerations for the contribution of nuclei to the all-particle spectrum observed at Earth have recently been carried out in [81, 101, 296].

SNRs is also able to provide $E_{\max}$ at about the knee region, as observed, for different species. Initially, Lagage and Cesarsky [220] demonstrated that the diffusive shock acceleration can give maximum energies near $E = Z \times 10^{13}\,\mathrm{eV}$ where Z is a charge. Hillas [189], based on the Bell & Lucek [70] theory of MF amplification, found with a "toy model" for spectrum generation, that SNRs is able to generate spectra with sharp cut-off at $E = Z \times 2 \times 10^{15}\,\mathrm{eV}$. Much more detailed studies [242, 293] put the maximum energies of CRs from SNRs near the observed knee, as well.

CRs with energies $\leq 3 \times 10^{15}\,\mathrm{eV}$ in ISMF of order $3\,\mu\mathrm{G}$, considerably affects propagation of such charged particles deviating them from directions to the sources. Therefore, one cannot observe CRs from SNRs directly. The only possibility to study them is to consider different kind of emission resulted from interactions of accelerated particles with magnetic and photon fields or other particles.

The first radio source to be identified as a previously unknown SNR was Cassiopea A; an idea of Shklovskii from 1953 [332], who also suggested that synchrotron radiation was the mechanism for producing radio emission, based on the observed power-law spectrum $S_\nu \propto \nu^{-\alpha}$, with $\alpha \approx 0.8$ for Cas A. Since then, radio telescopes have drawn attention to SNRs as principal sources of GeV electrons, through their synchrotron radiation.

It was found that synchrotron emission in SNRs may also be responsible for some of X-rays. An idea dated back to 1981 [308], was confirmed by ASCA observations of SN 1006 in 1995 [215]. Hard X-ray images of supernova remnants, by XMM and especially Chandra, have also revealed many details about electrons accelerated to

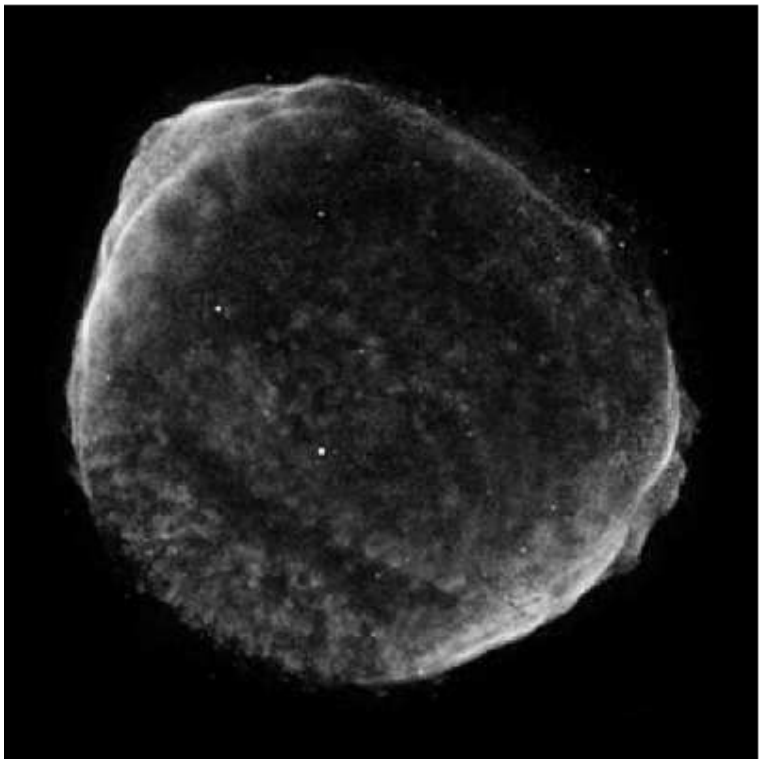

Figure 1.4. Chandra X-ray image of SN 1006 (taken from [190]). Hard X-ray band shows emission of electrons accelerated to $E \sim E_{\max}$.

energies 10 – 100 TeV. Fig. 1.4 shows an extremely narrow smooth shell of synchrotron X-ray radiation at the outer edge of SN 1006. Such radiation were detected in other SNRs, including Cas A, Tycho, Kepler etc.

If nonthermal X-ray emission is, like radio, synchrotron in nature then one would expect that synchrotron radiation should reveal itself in the intermediate photon ranges, too. Such a proof was derived on example of Cas A. Namely, observations show that, in this SNR, the image [164] and polarization [204] of the infrared emission is the same as in radio.

γ-ray emission from SNRs is one of the key components in investigation of the processes around strong nonrelativistic shocks, namely, dynamics and structure of the shock itself, magnetic field behavior, and microphysics of charged particles including their injection and acceleration. Observations in this energy domain demonstrate that charged particles are really accelerated in SNRs up to the highest energies observed in galactic cosmic rays. Quite important evidence about CR acceleration in SNRs has been presented in 2004 when the first map of SNR (RX J1713.7-3946) in γ-rays was published (Fig. 1.5 [44]). In the recent years, there are dozens of SNRs

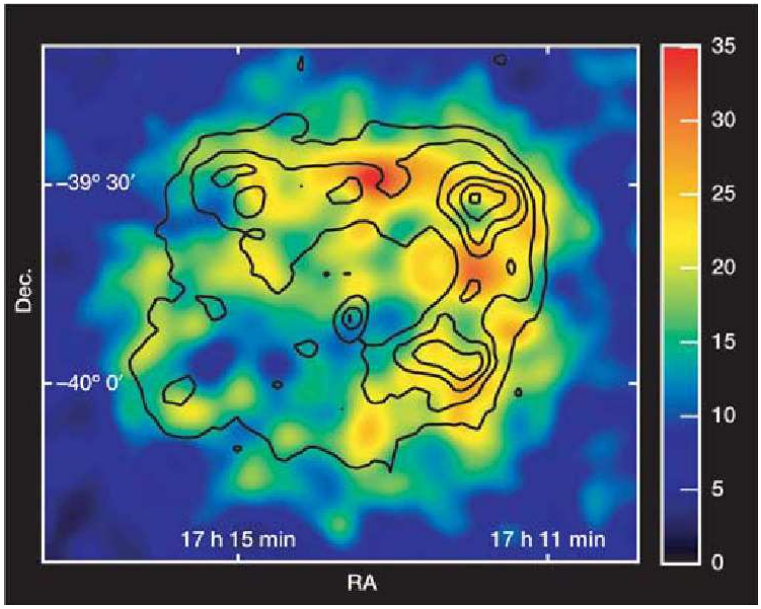

Figure 1.5. HESS TeV γ-ray image of RX J1713.7–3946 [44]. The linear colour scale is in units of counts. The superimposed (linearly spaced) contours show the X-ray surface brightness as seen by ASCA in the 1–3 keV range for comparison (the angular resolution of ASCA is comparable to that of HESS which enables direct comparison of the two images).

observed in γ-rays.

With energy spectrum of CRs, predicted by the diffusive shock acceleration theory, the broad-band (from radio to TeV γ-rays) nonthermal spectrum of SNRs (i.e. radiation of CRs) may well be explained.

1.3. Observations of SNRs in modern astrophysical missions

Populations of relativistic ions and electrons can produce observable continuum radiation through four mechanisms, one hadronic and three leptonic (Fig. 1.6; see e.g. review [306] or monographs [2, 3, 32, 326]). The hadronic mechanism is the inelastic scattering of CR protons on thermal nuclei, producing pions. The charged pions decay to electrons and positrons, making a (probably) negligible contribution to the relativistic lepton pool, but the neutral pions decay to γ-rays of comparable energy. The spectrum slope of emitted photons should be that of the ions that produce them. The three leptonic processes are synchrotron emission, as well as nonthermal bremsstrahlung, with the same spectrum as that of the nonthermal electrons, and inverse-Compton (IC) upscattering of photons from any significant

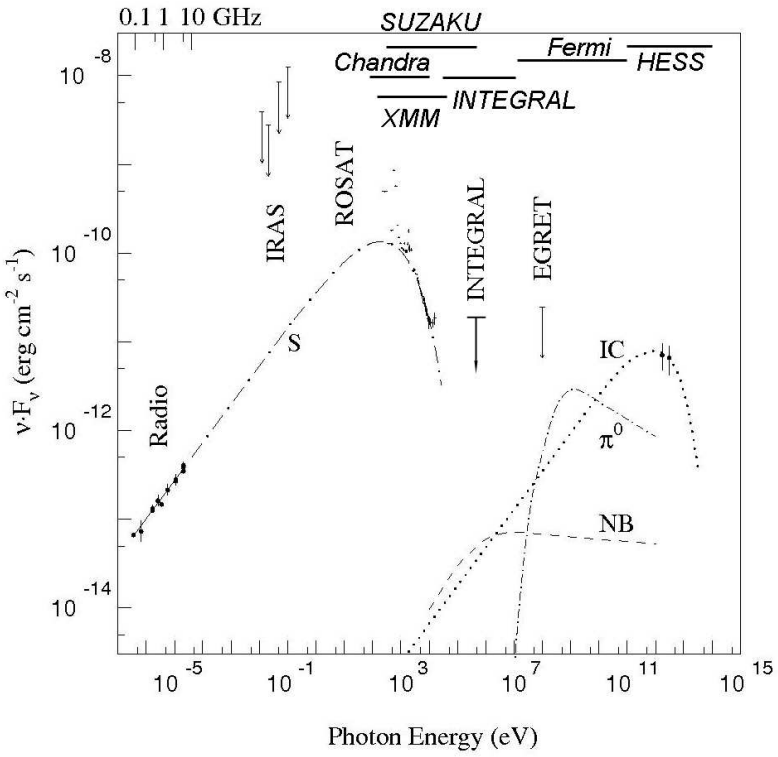

Figure 1.6. Emission process in SNR on example of some model of SN 1006 [53] (S - synchrotron, IC - inverse-Compton, NB - nonthermal bremsstrahlung, π^o - neutral pion decays from pp interactions). Photon bands where modern X-ray and γ-ray missions work are shown at the top.

ambient radiation. In practice, this is likely to be primarily the CMB, though in some cases, IC from UV/optical/IR photons may be competitive. The slope of the spectrum will be the same as that of the synchrotron emission. While the synchrotron process is clearly operating, it is not clear which of the other processes might be responsible for emission from any particular object.

It is important that γ-rays from the decay of secondary pions is the only "window" to "see" protons accelerated by shock in SNRs. Present experimental technics (systems of Cherenkov telescopes: HESS, MAGIC, VERITAS and others) are able to detect fluxes from such a process in a number of sources. However, even though protons are by a factor of about 100 more abundant than electrons in CRs at energies near 1 GeV, we cannot yet prove directly that supernova shocks provide the acceleration of protons. Really, in TeV photon band, γ-rays of the hadronic origin are in competition with γ-ray from inverse-Compton process (and probably with nonthermal bremsstrahlung) which is leptonic in origin, that leaves inconclusive hypothesis about SNRs as sources of CR protons.

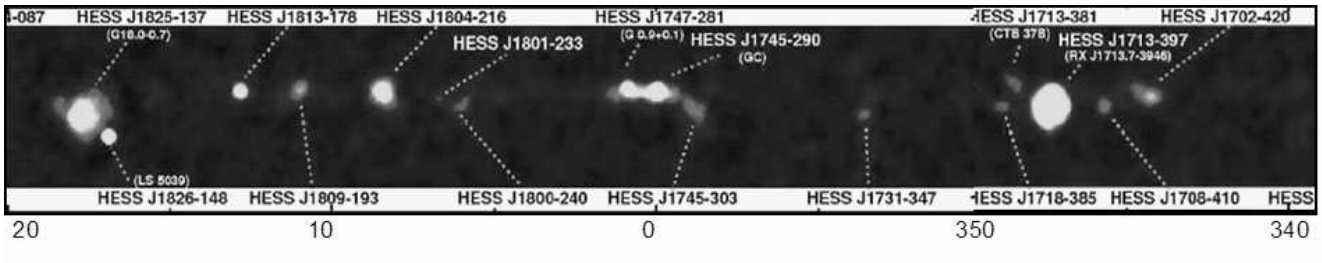

Figure 1.7. Region of the galactic center, as from data of HESS (in γ-rays with energy > 0.3 TeV, galactic coordinates). Most of sources are SNRs.

The best evidence for ion acceleration is the spectral feature resulting from the minimum photon energy from a created pion nearly at rest, about 70 MeV. However, detailed calculations (e.g. [67]) show that this feature may not be highly distinct in a real object.

Detecting the neutrinos accompanying proton-proton interactions would provide incontrovertible evidence for CR acceleration in the sources.

History of γ-ray observations of SNRs may be found in [33, 102, 158, 306]. Since many years, the only γ-ray fluxes were known for a number of cosmic sources. Essential step in γ-ray astrophysics was done in 2003-2004 when the system of Cherenkov telescopes HESS has done first observations. HESS sky survey [37] reveals most sources which are bright in TeV γ-rays (Fig. 1.7).

Ground-based experiments HESS [185], MAGIC, VERITAS as well as the space observatory Fermi [151] allow one, for the first time, to analyze images of cosmic objects in γ-rays. SNRs are always between priority targets in such experiments. At present, there are less than 20 SNRs with known TeV γ-ray images; they include SN 1006 [28] (Fig. 1.8), RX J1713.7-3946 [45, 46], Vela Jr. [36, 38], RCW86 [42], G12.8-0.0, Kepler, Tycho, IC443 [50], W28 [39], CTB 37B [41], G0.9+0.1 [34], MSH 15-52 [35], Kes 75, HESS J1731-347, HESS J1813-178 [95], CTB 37A [40]. Pulsar-wind nebulae could be the origin of γ-rays in G0.9+0.1 and MSH 15-52 while the particles accelerated at the forward shock of SNRs are likely to be responsible for emission in the other SNRs. It is interesting that some SNRs were discovered in TeV γ-rays and only after that were confirmed in radio and other bands (HESS J1813-178, HESS J1731-347).

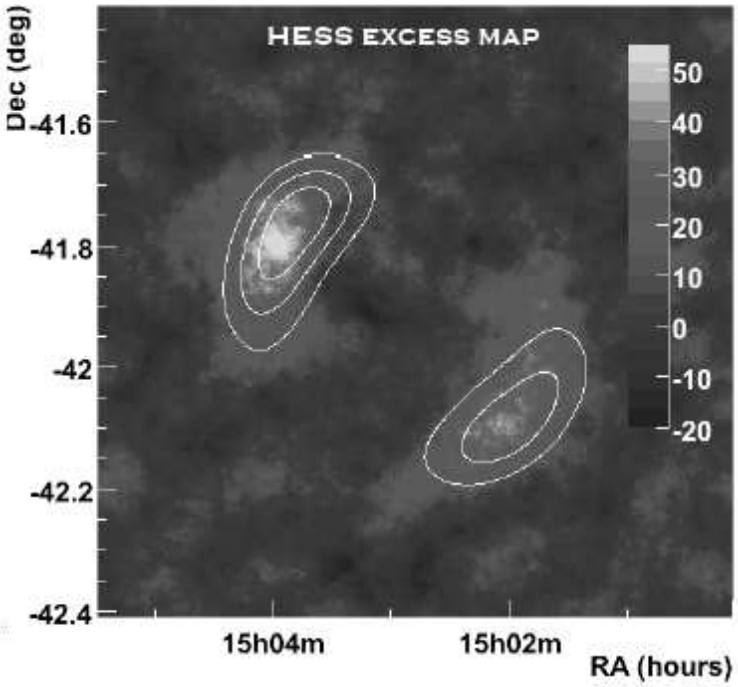

Figure 1.8. HESS image of SN 1006 [28].

GeV γ-rays, the last electro-magnetic window, are observed since 2008 when the Fermi γ-ray space telescope was launched. Till now, Fermi observatory has detected 7 SNRs, namely, young and historical SNRs: Cas A, RXJ 1713.7-3946; intermediate age ($\sim 10^4\,\mathrm{yr}$) SNRs: IC443; middle-aged ($\geq 3\times 10^4\,\mathrm{yr}$) SNRs: W51C, W44, W28, G349.7+0.2 (these likely interact with molecular clouds).

There are 274 Galactic SNRs [172] known from their radio emission. Thus, there are less than 10% of SNRs detected in γ-rays. For comparison, 60-70% of SNRs are visible in X-rays; mostly through thermal X-ray emission of the plasma heated to $T\sim 10^7\,\mathrm{K}$ on the shock. About 20 SNRs has non-negligible nonthermal X-ray emission.

The featureless X-ray spectrum of the remnant of SN 1006 above 1 keV was first attributed in 1981 to synchrotron radiation from the shock-accelerated electrons [308]. X-ray synchrotron radiation arises from electrons with energies $\sim 10-100\,\mathrm{TeV}$ [184, 312]; it represents the rolling off of the spectrum due to some process limiting the maximum energy of electrons [302]. The extreme thinness of the hard X-ray rims is consistent with the very short radiative cooling lifetime of such extremely relativistic electrons in magnetic fields with strength $\sim 10-100\,\mu\mathrm{G}$.

There are now four known Galactic remnants whose soft X-ray spectrum is dom-

inated by synchrotron X-rays: in addition to SN 1006, G1.9+0.3 [313]; G347.3-0.5 (also known as GX J1713.7-3946) [335]; and G266.2-1.2, "Vela Jr." [56, 336]. Synchrotron X-ray emission contributes to the spectrum of several more Galactic remnants (reviewed in [306]). In historical (or quasi-historical) remnants RCW 86 (probably SN of 185 year), Tycho (SN 1572), Kepler (SN 1604), and Cas A (SN $\sim$1680), "thin rims" of featureless X-ray emission lie at the edges of the remnants, and are presumed to indicate the outer blast wave. It appears that synchrotron X-ray emission from the blast wave is a common feature in young SNRs, less than a few thousand years old.

Spatial and spectral resolution of modern X-ray missions (XMM [372] and Chandra [111]) allow for very detailed information on SNRs, including spectra, images and even spatially resolved spectroscopy, that gives big advantage for studies of CR acceleration in these objects.

One of the recent achievements in SNR studies is discovery of the youngest SNR, G1.9+0.3, with synchrotron emission dominating in X-rays. It is a remnant of about 100 years old, as it follows from expansion between radio observations made in 1985 and X-ray Chandra observations in 2007 [313]. This SNR is the only object which cover gap in evolution from radio supernovae (few years) [366] to young historical SNRs (few hundred years) [340]. This discovery opens a new possibility to understand the very early development of a SNR from supernova and the physics of the very fast shock.

It is necessary to emphasize that the broad-band analysis of the spectra from SNRs is useful to set constraints on model parameters but it still leaves open the nature of VHE γ-ray flux either as leptonic or as hadronic in origin. An example is presented on Fig. 1.9 where the observed spectrum of SN 1006 is shown fitted either with the inverse-Compton emission or with γ-rays from the pp collisions, or in the mixed model [28]. Since analysis of the spectrum may not give preference to a certain emission mechanism, it is necessary to make wider use of observational data. In particular, the spatial distribution of radio, X-ray and γ-ray emission is an additional important channel of experimental information.

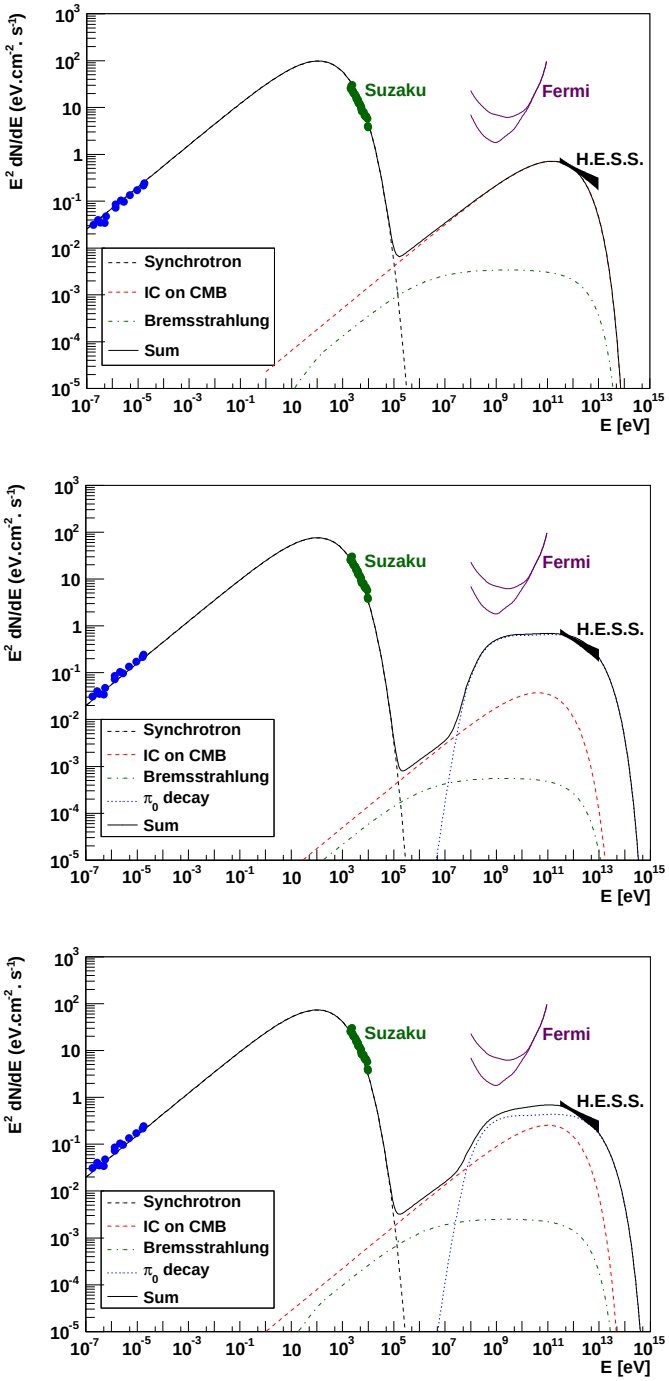

Figure 1.9. Broad-band spectra of SN 1006 for three alternative models of TeV γ-ray emission: leptonic (top), hadronic (middle) and mixed (bottom) [28]. The Fermi/LAT sensitivity for one year is shown for Galactic (upper) and extragalactic (lower) background. The latter is more representative given that SN 1006 is 14° north of the Galactic plane.

Main achievements of observers in the field of emission of CRs in SNRs are presented in reviews [49, 57, 60, 92, 100, 125, 192, 306, 324, 357–359, 364, 367].

1.4. Progress and problems in studies of cosmic rays in SNRs

1.4.1. Maximum energy. The maximum energy to which particles can be accelerated depends on the limiting mechanism: $E_{\max}$ may be limited by the geometrical size of the object (if gyro-radius of a particle is larger then it may leave the region of acceleration), by the age of acceleration engine, by escape due to absence of the MHD waves of the lengths required for further acceleration and by the radiative losses [73, 303]. Some of these mechanisms are similar for different kinds of CRs, some other operates with only a given species (e.g. synchrotron and inverse-Compton radiative losses limit energy of electrons only). Observed X-ray spectrum allows one to suggest a method to put limitation on $E_{\max}$ for electrons from X-ray spectrum [184, 312]. Respective algorithm is implemented in the code XSPEC developed for the X-ray spectrum analysis. The basic ideas are the following [307].

Let a diffusion coefficient κ scale with particle energy. Then the particle mean free path is a multiple η of its gyroradius $r_{\rm g}$: $\lambda_{\rm mfp} = \eta r_{\rm g} = \eta E/eB$ for ultra-relativistic particles, since $r_{\rm g} = \gamma mc^2/eB$ (cgs units). Then the "Bohm limit" in which the mean free path is a gyroradius is $\eta = 1$. For weak turbulence, one expects $\eta \geq 1$. For a remnant of age t with shock speed V, with surroundings containing MHD scattering waves only up to a wavelength $\lambda_{\max}$, the maximum energies scale as

$$E_{\max}(\text{age}) \;\propto\; t\,V^2\,B\,\eta^{-1} \tag{1.1}$$

$$E_{\max}(\text{escape}) \;\propto\; \lambda_{\max}\,B \tag{1.2}$$

$$E_{\max}(\text{loss}) \;\propto\; V\,B^{-1/2}\,\eta^{-1/2} \tag{1.3}$$

In all cases, for $V \geq 1000$ km s^{-1} and ages above a few hundred years, maximum energies of 10 – 100 TeV are easily obtainable.

The diffusion coefficient may be anisotropic; in particular, diffusion along and across magnetic-field lines is likely to take place at different rates, with effects on the acceleration time τ to some energy. If the shock velocity makes an angle $\Theta_{\rm o}$ with the mean upstream magnetic field, one can parameterize this effect with $R_J(\Theta_{\rm o}, \eta, r) = \tau(\Theta_{\rm o})/\tau(\Theta_{\rm o} = 0)$. Let values be scaled to typical values for young SNRs: $V_{8.5} =$

$V/3000$ km s^{-1}; $t_3 = t/1000$ yr; $B_{10} = B/10$ μG; and $\lambda_{17} = \lambda_{\max}/10^{17}$ cm. The frequencies at which electrons with energy $E_{\max}$ emit their peak power for each limiting mechanism are then

$$h\nu_{\rm roll}({\rm age}) \sim 0.4\, V_{8.5}^4\, t_3^2\, B_{10}^3\, (\eta R_J)^{-2} \text{ keV} \quad (1.4)$$

$$h\nu_{\rm roll}({\rm esc}) \sim 2\, B_{10}^3\, \lambda_{17}^2 \text{ keV} \quad (1.5)$$

$$h\nu_{\rm roll}({\rm loss}) \sim 2\, V_{8.5}^2\, (\eta R_J)^{-1} \text{ keV}. \quad (1.6)$$

In a given object, and in a given location, the lowest value of $E_{\max}$ will be the operative value. Thus if one can determine the mechanism causing the spectral cutoff, its value constrains considerably more physical parameters than the simple observation of a radio power-law spectrum.

We adopt such an approach in Sect. 5.4.

1.4.2. Injection. Even if "acceleration efficiency", i.e. fraction of kinetic energy of the flow transmitted to CRs, is prominent, the accelerated particles represent only $< 10^{-3}$ of all particles. The fraction of number density of particles participating in the acceleration process is called "injection efficiency"; it is unknown a priori, neither from theoretical nor observational considerations. The injection problem consists in understanding of how particles are "injected", i.e. how they become involved into the acceleration process.

A self-consistent treatment of injection and acceleration must include a model of particle-wave interactions in the plasma. A few physical models proposed for the proton and electron injection are reviewed in [146, 240].

As to electrons, their scattering is suggested to be due to some ion-generated instabilities [96], whistler waves [228] or lower-hybrid waves from ions [227]. These models mainly address the plasma microphysics; while only Bykov & Uvarov [96], to our knowledge, are able to model the formation of the post-shock electron distribution. Both injection and thermalisation of electrons happen in vicinity of the shock front, presumably by the same scattering centers; thus, they may affect one another. In Sect. 3.1 we suggest a simplified approach for electron injection, which allows us to relate the injection efficiency to the level of electron-proton equilibration.

Another important effect is eventual dependence of the injection on the shock obliquity (an angle between the ambient MF and the shock normal). Simple considerations demonstrate ambiguity of expectations. At large angles, the injection would be suppressed allowing the of acceleration at the quasi-parallel shocks only: particles guided by the field will be constrained to move along the front and the re-crossing process could never start. However, the acceleration efficiency is typically larger at the quasi-perpendicular shocks (particles with large enough gyro-radius may re-cross the shock during gyration); such effect might help also injection - an opposite behavior. Thus, in the absence of a theory for oblique shocks, we can only assume some eventual dependences for injection efficiency, e.g. const for isotropic injection, $\propto \cos^2 \Theta_o$ for quasi-parallel and $\propto \sin^2 \Theta_o$ for quasi-perpendicular one [157].

The problem of injection, hard enough for protons and electrons, is even harder for nuclei especially for those that may result from sputtering of dust grains [139].

1.4.3. Efficient acceleration. There are a number of effects which may also be considered as indirect evidences about acceleration of protons and ions by SNR shocks. Namely, if the acceleration is rather effective (i.e. when CR protons takes considerable fraction of kinetic energy from the system), one would expect some deviation of the processes from the test-particle theory of acceleration. That results in a number of effects, namely,

- the temperature at the forward shock should be depressed [197],
- efficient CR acceleration changes the structure of the shock front,
- and makes plasma more compressible that leads to lower adiabatic index and to increased shock compression factor,
- the physical separation between the forward shock and the "contact discontinuity" (or reverse shock) should be reduced [371],
- the pressure gradient of CR should lead to concave shape of the energy spectrum (steeper at small energies and flatter, up to $E^{-3/2}$ at very-high energies), instead of the power-law one predicted by the test-particle theory [87, 309],

- the instability originated from the CR flow should lead to grow of some turbulence modes, i.e. to MF amplification in the pre-shock region [71],
- such grow of MF should cause the "blinking" X-ray spots (rapid rise and fall of the spots indicate that electrons are being accelerated to near-light speed in the presence of strong magnetic fields) [270, 353] (though another explanation exists: such "twinkling" may be due to fluctuations of highly turbulent MF even if the strength of the mean magnetic field is lower [99]),
- such grow of MF should be reason for quite thin X-ray rims [76] (an alternative explanation of the thin rims: disappearance of MF downstream due to wave damping [289]),
- larger MF and turbulence should result in higher $E_{\max}$ [268],
- charge exchange with neutrals in the shock precursor may lead to broader narrow Balmer line than in the absence of CR induced precursor [183] (so called Balmer dominated shocks; see Sect. 3.2 in review [88] and references therein),
- radial structure of the shock front upstream (observed in X-rays) seems to confirm back-reaction of particles and MF amplification, at least locally in SN 1006 [258] (however an alternative explanation, involving acceleration at perpendicular shocks and magnetic field amplification due to turbulent eddies downstream of the shock [165], may still be possible).

Such effects of non-linear acceleration (i.e. when back-reaction of accelerated particles on the system is included into consideration; see review [240]) are intensively studied both theoretically and experimentally.

Actually, even the test-particle diffusive shock acceleration theory supposes that accelerated particles are responsible for the production of the magnetic field structures on which they may scatter [69, 220].

At present, the non-linear theory has a number of difficulties. Let us note just two of them.

It is not clear which role the amplified field can play in terms of scattering particles up to the knee energy since the unstable waves are produced at wavelengths much

shorter than the Larmor radius of the particles generating them [88]. Non linear effects in wave evolution can lead however to transporting energy towards longer wavelengths, though it is not clear whether this process is fast enough to occur within the precursor and thereby lead to efficient particle scattering, essence of the acceleration process.

One of another difficulty is related to particle diffusion. The concavity of the CR energy spectrum (steeper at small energies and flatter, up to $E^{-3/2}$ at very-high energies) yields an effective $s \leq 2$ at high-energies. CR spectrum generated at the source $N \propto E^{-s}$ transforms to the observed spectrum $N_{\rm obs} \propto E^{-s-\delta}$ for energy-dependent diffusion coefficient $D(E) \propto E^{-\delta}$. In the two main models [294], $\delta = 0.6$ (clear diffusion) or $\delta = 0.34$ (diffusion with re-acceleration). The first one almost agrees with the production spectrum in SNRs ($s \simeq 2$) though it should result in excessive observed anisotropy [295]. A possible solution of this contradiction may consist in relatively large velocities of scattering centers responsible for particle acceleration, that may be a consequence of MF amplification [101,295]; this leads to steepening of the particle spectrum ($s \geq 2$) as needed. However, if so, the non-linear theory predicts smaller MF and lower acceleration efficiency [101].

1.4.4. Magnetic field. Emission of the accelerated charged particles in SNRs keeps information about magnetic field.

MF strength. Since the intensity of synchrotron radiation from a power-law distribution of electrons $N(E) = KE^{-s}$ scales as $\nu^{-\alpha} K B^{\alpha+1}$, radio synchrotron fluxes only give roughly the product of the energy densities in magnetic field and electrons.

The ratio of synchrotron and γ-ray fluxes may be used to put limitations on MF strength [117,362], under assumption that γ-ray flux is due to inverse-Compton process (in fact, such estimate yields lower limit on the strength because at least a part of the γ-flux may be of different origin).

Very thin X-ray rims in a number of young SNRs are used to estimate the strength of the post-shock magnetic field (e.g. [76]). Locally, in the thinnest filaments, the strength derived is of order hundred micro Gauss, much above the value of a typical

interstellar field compressed by the forward shock. Such strong field is believed to be driven by effective amplification of the initial interstellar field in the shock cosmic-ray precursor. However, there are other suggestions explaining so thin rims. Namely, synchrotron emission may quickly disappear downstream due to disappearance of radiating electrons (large radiative losses due to large MF, scenario described above) or due to MF disappearance as a consequence of some wave damping [289].

MF orientation within SNRs. Magnetic-field orientations can be derived from radio polarization directions. A uniform synchrotron source with spectral index 0.5 has a polarized fraction of about 70%, but very few remnants show values above 40% [307]. Young SNRs have much lower values, typically of order 10% – 15% ([311] and references therein), implying that their magnetic fields are primarily disordered. The ordered components, however, tend to be radial. In older remnants, magnetic-field orientations are typically confused, but it is fairly common to see a tangential orientation, which one would expect if a high-compression radiative shock compresses upstream magnetic field, increasing the tangential component by a factor of the large compression ratio [307].

MF orientation around SNRs. It is generally unknown how MF is oriented in places of SNR locations, though, it could be expected that, typically, MF have to be oriented along the Galactic plane. In fact, Gaensler [159] has measured an angle between the symmetry axis in 17 'clearly' bilateral SNRs and the Galactic plane. Axes are more or less aligned with the Galactic plane in 12 SNRs (angle $< 30^{\rm o}$), 2 SNRs have angle $\approx 45^{\rm o}$ and 3 SNRs are almost perpendicular ($> 60^{\rm o}$). In Sect. 5.3, a method to determine the MF orientation around an SNR is proposed.

1.4.5. Radiative shocks, ISM/ISMF nonuniformities. The role of radiative losses, which is negligible till the end of adiabatic phase of SNR evolution, becomes more and more prominent with time. They are so important in old SNRs, that they essentially modify the dynamics of such SNRs. One of the consequence of radiative channel of the shock energy dissipation is the increased compression factor of the shock that results in creation of the thin radiative shell. Such compression

affects also MF. Being almost unimportant in the shock dynamics till the end of adiabatic stage, the energy density of MF increases further on, with increasing the compression of the plasma on the shock. Thus, MF becomes to be an important factor in the shock dynamics. All these factors should affect the injection and acceleration of CRs as well. Such picture is of the special importance in the case of SNR-cloud interaction: the shock front moving into dense medium cools rather quickly. There are a number of old SNRs with observed γ-ray emission (W28, W49B, W51C etc.) which reveal also signs of interaction with clouds. Interpretation of such observations requires understanding of magneto-hydrodynamics of such post-adiabatic and radiative shock as well as CR acceleration process in its vicinity.

Such task is closely related to the shock motion in the non-uniform media. In addition, most of SNRs reveal assymetries in surface brightness distribution, deviation from sphericity; these effects being different in different photon bands in the same object. Thus large-scale (the scale larger than the SNR radius) nonuniformities of ISM and/or ISMF naturally happen. Effects of non-uniform media and fields on CRs and MF in SNRs should be studied [203].

1.5. Conclusions and outline of the present work

SNRs are one of important class of objects for astroparticle physics. Outline of modern problems and tasks in studies of CRs in SNRs are given in [68, 130, 203, 304, 339, 360]. Main questions in such studies may be summarized as follows.

- How efficiently is shock kinetic energy converted to CR energy? What is the maximum particle energy?
- Do SNRs accelerate protons (p/e ratio; similar to that observed at Earth or not)? Can we find direct evidence for the acceleration of protons/ions in SNRs?
- What is the nature of γ-ray emission in SNRs (electrons/protons)?
- How effective are non-linear effects in diffusive shock acceleration? How can we observe them? Do they affect thermal emission?

- Is the magnetic field amplified in SNRs? What does it depend on? Is it widely-present or rather rare and local effect?
- How do particles start acceleration? Injection problem.
- How do injection, acceleration, MF compression/amplification depend on the shock obliquity and strength?
- What is the role of ISMF/ISM nonuniformities?
- Can and how old (post-adiabatic and radiative) shocks inject and accelerate charged particles, what is the behavior of MF around them?

Results of the present thesis give some answers to the above questions. We determine the process responsible for limitation of the electron maximum energy in SN 1006. We suggest a model-independent test (γ-ray image from radio and X-ray data) as an argument for leptonic origin of TeV γ-ray emission of this SNR. Though our work are devoted greatly to investigation of the formation of SNR images in different bands and, therefore, we are bounded by the test-particle theory (at present, the non-linear approaches operate with initially quasi-parallel shocks), we pay attention to some of nonlinear effects. Namely, we found high MF in SN 1006, but only locally, in the thinnest filament at the rim; our approximate analytical formulae for azimuthal and radial profiles of surface brightness are ready to account for the non-linear effects if necessary; possible effects from the back reaction of particles on our results are analyzed where appropriate. We show how statistical analysis of SNR samples allows to discard a model of non-linear acceleration which predicts constant efficiencies in MF amplification and acceleration. A new approach to describe electron injection is proposed. Hydrodynamic descriptions of the post-adiabatic and radiative stages of SNR evolution are developed. It is determined how nonthermal images of SNRs may be used to put constraints on physics of CR and MF. In particular, it is shown how the dependences on the shock obliquity and velocity modify maps of SNRs. The influence of the large-scale nonuniformities of ISM/ISMF on the appearance of SNRs is studied.

CHAPTER 2

DYNAMICS OF THE SHELL-TYPE SNRS IN NON-UNIFORM MEDIUM

There are three phases in a common scenario of SNR evolution: free expansion (when the ambient medium does not affect the shock motion), adiabatic (when the shell decelerates in the medium but the energy of thermal emission of the shocked plasma is negligible comparing to the kinetic energy of the shock) and radiative (when radiative losses of plasma become prominent factor in modification of the shock dynamics).

There are analytical and numerical solutions which describe to model the shock and the flow during free expansion and adiabatic stages: [21,110]. Influence of radiative losses on the flow dynamics in the further evolution of SNR were studied only numerically [90,109,114,147,148,241]. Analytical solutions for motion of the radiative shock front [89,247,263,266], as it is shown in Sect. 2.4 (see also [269]), cannot be used for description of real SNRs because SNRs do not reach these theoretical approximants, dissipating in ISM well in advance.

Another important factor influencing SNRs is nonuniformity of media (e.g. [203]); most of SNRs are not spherical in shape and have assymetries in surface brightness distribution.

One of our previous works was devoted to a new analytical method for hydrodynamical modeling of adiabatic SNR in nonuniform ISM [195]. The method allows us to suggest a new interpretation for thermal X-ray composites, a morphological class of SNRs. In the present chapter, the approach developed in [195] is extended to description of SNR after the end of adiabatic era.

Thus, in Sect 2.1, we consider model of TXC as adiabatic SNR in a medium with nonuniform density distribution; such SNRs may be prominent sources of gamma-

ray emission from protons accelerated by the shock (this is considered in more details in Sect 3.4). Then we present methods for hydrodynamic description of SNR evolution from the time when deviation from condition of adiabaticity becomes to be prominent. Namely, Sect 2.2 considers evolution of SNR in details and the need is demonstrated to introduce a new transition phase after the end of the adiabatic and before beginning of the radiative one. It is shown that the duration of this phase is comparable to the duration of the adiabatic stage. Approximate analytical method for hydrodynamic modeling the shock and the flow during this new stage is presented in Sect 2.3, for the case of uniform ISM. Analytical solutions for motion of radiative shock in uniform ISM are presented in Sect 2.4; they are extended to nonuniform ISM with the power-low density variation in our work [15] and to motion of shock under a force from gas with non-zero mass in [16]. Sect 2.5 presents an approximate analytical method for hydrodynamic description of the flow downstream of the radiative shock, in case of nonuniform ISM. These methods allow one to study nonthermal emission from cosmic rays in SNRs after the end of adiabatic era.

Results presented in this chapter are published in [8, 9, 15, 16, 65, 272, 273, 277].

2.1. Thermal X-ray composites as adiabatic SNRs in nonuniform ISM

2.1.1. Thermal X-ray composites as morphological class of SNRs. Observations show that supernova remnants (SNRs) have anisotropic distributions of surface brightness [330,368]. There are four morphological classes of SNRs: shell-like, Crab-like (or plerionic), composite and thermal X-ray composites (or mixed-morphology, or centrally-influenced) [203,316]. In the past decade interest to TXCs has risen (e.g. [122, 203, 331, 344]). TXCs are SNRs with the centrally concentrated thermal X-ray and the limb brightened radio morphologies. Remnants W44, W28, 3C 400.2, Kes 27, 3C 391, CTB 1, MSH 11-61A and others represent a mixed-morphology class [316].

Two physical models have been presented so far to explain TXC (see [316] for review). One of them is an enhanced interior X-ray emission from the evaporated material of numerous swept-up clouds which increases density in the central region of SNR. This model is frequently used; sometimes its application is intrinsically inconsistent, e.g., as in MSH 11-61A where evaporation timescales exceed the age of SNR 50-100 times [203]. In the second model, shock temperature is small due to essential cooling; very soft emission of the shell is absorbed by ISM and only the interior region remains visible; thermal conduction may level temperature profiles and increase the central density altering the interior structure [122].

The mentioned models are used to obtain the centrally-filled morphology within the framework of one-dimensional (1-D) hydrodynamic approaches. When we proceed to 2-D or 3-D models, we note that a simple projection effect may cause the shell-like SNR to fall into another morphology class, namely, centrally-influenced [195]. The main feature of such SNR is the thermal X-rays emitted from swept-up gas and peaked in the internal part of the projection. Therefore, getting beyond one dimension, we obtain a new possibility to explain the nature of TXC. Such a possibility is considered in this section.

2.1.2. Observed properties of thermal X-ray composites. It is proved [316] that mixed-morphology SNRs create a separate morphological class because their properties distinguish these remnants from others. Having analysed X-ray data on a number of such SNRs, the authors found their two prominent morphological distinctions: a) the X-ray emission is thermal, the distribution of X-ray surface brightness is centrally-peaked or amorphous and fills the area within the radio shell and may reveal weak evidence of an X-ray shell, b) the emission arises primarily from the swept-up ISM material, not from the ejecta.

It is emphasized [316] that, besides similar morphology, the sample of SNRs also has similar physical properties. Namely, a) the same or higher central density comparing with the edge, b) complex interior optical nebulosity, as in W28 and probably in 3C 400.2 [231]; c) higher emission measure $\int n_e^2 dl$ (n_e is the electron number den-

sity, l is the length inside SNR) in the central region, as e.g. in 3C 391 [315]; d) X-ray surface brightness in the central region (with radial coordinate $r < 0.2R_{\rm p},\ R_{\rm p}$ is the average radius of the projection), in general, exceeds the brightness near the edge ($r > 0.6R_{\rm p}$) in 2-5 times, e) temperature profiles are close to uniform. As to the latter property, it should be noted that the temperature may decrease towards the centre, as in 3C 391 [315]; no strong evidence of increasing the temperature towards the centre has been found for all TXCs, but [122] note that spectral hardness in W44 is greater in the centre, so the temperature might be higher in this region. A possible variation of temperature may be within factor 2, as in the case of W44 [122, 317]) or in W28 [231].

7 objects from the list of 11 TXCs reveal observational evidence of an interaction with molecular clouds [316]. Thus, ambient media in the regions of their localization are nonuniform and cause nonspherisity of SNRs. Observational evidence of cloud localization just on the line of sight for some of these SNRs also exists (e.g., [317]).

2.1.3. Modelling a thermal X-ray composite. The Sedov [21] model does not give a centrally-concentrated morphology due to geometrical properties of self-similar solutions. The solutions are 1-D and give a specific internal profile of the flow gas density: most of the mass is concentrated near the shock front. These factors and cumulation of the emission along the line of sight cause a shell-like morphology. If we consider a more complicated nonuniform ISM, we get beyond one dimension and need to consider additional parameters responsible for nonuniformity of the medium and orientation of a 3-D object.

Projection effects may essentially change the morphology of SNRs [195]. Densities over the surface of a nonspherical SNR may essentially differ in various regions. If the ambient density distribution provides a high density in one of the regions across the shell of SNR and is high enough to exceed the internal column density near the edge of the projection, we will see a centrally-filled projection of a really shell-like SNR. Such density distribution may be ensured e.g. by a molecular cloud located near the object.

What is a really shell-like 3-D SNR? We suggest that such a remnant has internal density profiles similar to those in the Sedov solutions. Thus, we separate a shell-like SNR (as an intrinsic property of a 3-D object) from its limb brightened projection (as a morphological property of the projection). Let us call shell-like SNRs with centrally-filled projections "projected composites".

Hydrodynamic models. For simplicity, let us consider the case of a 2-D SNR and the characteristics of SNR and the surrounding medium which could be possible on smoothed boundaries of molecular clouds. Thus, SNR evolves in the ambient medium with hydrogen number density n distributed according to

$$n(\tilde{r}) = n_{\rm ic} + n_c \exp(-\tilde{r}/h), \tag{2.1}$$

where $n_{\rm ic}$ is the density of the intercloud medium, the second term represents the density distribution into the boundary region and the cloud, h is the scale-hight, $\tilde{r}$ is the distance. Let us take the explosion site to be at point $\tilde{r}_o$ where $n(\tilde{r}_o) = 2n_{\rm ic}$. Other parameters are assumed to be $n_{\rm ic} = 0.1$ cm^{-3}, $n_c = 100$ cm^{-3}. The energy of the supernova explosion is $E_o = 1 \cdot 10^{51}$ erg. We consider three basic evolutionary cases of SNR models which cover practically the whole adiabatic phase (models *a*-*c*, Table 2.1[1]) and then we vary parameter h in intermediate model *b* (models *d*-*f*, Table 2.1), in order to see how the gradient of the ambient density affects X-ray characteristics of objects.

Emission models. The gas density n and temperature T distributions inside the volume of a nonspherical SNR are obtained with the approximate analytic method of Hnatyk & Petruk [195]. The equilibrium thermal X-ray emissivities are taken from the Raymond & Smit [301] model. The model for radio emission of nonspherical SNR is described later in our work. In short, it generalizes the model of Reynolds [303] developed for uniform ISM. Namely, the distribution of magnetic field over the shock depends on the shock obliquity: the radial component $B_\parallel$ is not modified by the shock: $B_{\parallel,\rm s}/B^o_{\parallel,\rm s} = 1$; the tangential component $B_\perp$ rises at the

[1]The denser part of the shell in model *c* just enters the radiative phase since this part has $\lg(T_{\rm s}, {\rm K}) = 5.6$ and the transition temperature for the Sedov blast wave is $\lg(T_{\rm s}, {\rm K}) = 5.8$ [90].

Table 2.1
Parameters of SNR models. t is the age of the SNR, R and V are the radius and velocity of the shock front, $T_{\rm s}$ and $n_{\rm s}$ are the temperature and number density of the swept-up gas right behind the shock. $R_{\rm max}$, $R_{\rm min}$ ($V_{\rm max}$, $V_{\rm min}$) are the maximum and minimum shock radii (shock velocities) of nonspherical SNR. Analogously, $T_{\rm s,\,max}$, $T_{\rm s,\,min}$ ($n_{\rm s,\,max}$, $n_{\rm s,\,min}$) are maximum and minimum temperatures (number densities) of the gas flow right behind the shock. $L_{\rm x}^{>0.1\ {\rm keV}}$ is the thermal X-ray luminosity (for photon energy > 0.1 keV) and α is the spectral index (at photon energy 5 keV) of the thermal X-ray emission from the whole SNR. $T_{\rm ef}$ is the effective temperature of a nonspherical SNR defined in [195] as $T_{\rm ef} \propto M^{-1}$, where M is the swept-up mass. The contrasts in the distribution of X-ray surface brightness $\lg(S_{\rm c}/S_{\rm max,\,2})$ and spectral index $\alpha_{0.95}/\alpha_{\rm c}$ are presented for the case of $\delta = 90^{\rm o}$. Subscript "c" corresponds to the center of the projection, $\alpha_{0.95}$ is the value of the index at $0.95R_{\rm p}$, $R_{\rm p}$ is the radius of the projection.

Parameter	Model					
	a	*b*	*c*	*d*	*e*	*f*
h, pc	2.5	2.5	2.5	5	10	40
t, 10^3 yrs	1.0	6.8	17.7	6.8	6.8	6.8
$\lg T_{\rm ef}$, K	8	7	6.5	7	7	7
M, $M_\odot$	9.5	94	280	98	95	94
$R_{\rm max}/R_{\rm min}$	1.4	1.8	2.1	1.4	1.2	1.1
$V_{\rm max}/V_{\rm min}$	1.9	2.8	3.1	1.9	1.5	1.1
$T_{\rm s,\,max}/T_{\rm s,\,min}$	3.5	7.9	9.8	3.7	2.2	1.2
$n_{\rm s,\,max}/n_{\rm s,\,min}$	9.5	45	84	11	3.9	1.4
$\lg L_{\rm x}^{>0.1\ {\rm keV}}$	34.1	36.7	37.3	36.4	36.2	36.1
$\alpha^{5\ {\rm keV}}$	0.98	3.2	3.1	3.9	4.1	4.2
$\lg(S_{\rm c}/S_{\rm max,\,2})$	0.43	2.1	2.3	0.72	-0.10	-0.54
$\alpha_{0.95}/\alpha_{\rm c}$	1.6	1.8	3.6	1.3	1.2	1.3

shock by the factor of $\rho_{\rm s}/\rho_{\rm s}^o = \sigma$; no turbulent amplification of the magnetic field is assumed. Inside the non-spherical SNR, MF strength is found from Eqs. (D.4)-(D.5) in Appendix D, with known distribution of n. The ISMF is assumed to be uniform. Evolution of energy distribution of relativistic electrons is described in Sect. 3.2. Maximum energy of electrons and efficiency of injection, for simplicity, are assumed to be constant over the surface of SNR.

Radio morphology depends on aspect angle $\phi_{\rm o}$ between the line of sight and the ambient magnetic field [303], also on the inclination angle δ between the density gradient and the plane of the sky and, in a complex 3-D case, on the third angle between the density gradient and the magnetic field.

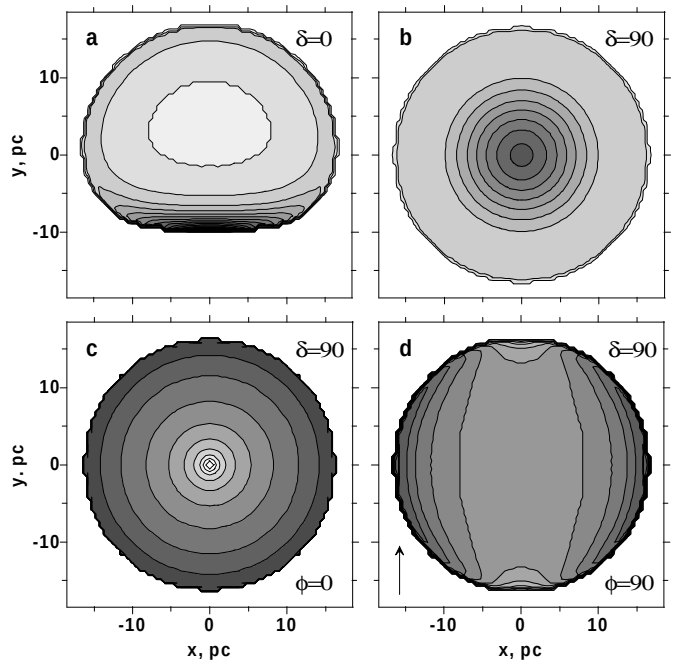

Figure 2.1. a-d. Logarithmic distributions of thermal X-ray surface brightness S in erg s^{-1} cm^{-2} st^{-1} for photon energy $\varepsilon > 0.1$ keV (**a, b**), and radio surface brightness S_ν at some frequency in relative units (**c, d**). The SNR model is b, power $s = 2$. Angles δ and ϕ_o are shown in the figure. **a, b**: $\lg S_{\max} = -3.1$, $\Delta \lg S = 0.3$. **c**: $\Delta \lg S_\nu = 0.3$. **d**: $\Delta \lg S_\nu = 0.15$. The darker colour represents a higher intensity. The arrow indicates a magnetic field orientation.

2.1.4. Theoretical properties of "projected composites". Fig. 2.1a-b demonstrates the influence of the projection on a thermal X-ray morphology of SNR. The X-ray brightness maximum which located near the shock front in the projection with $\delta = 0^o$ (Fig. 2.1a) moves towards the centre of the projection with the increase of δ from 0^o to 90^o (Fig. 2.1b). Radio images (Fig. 2.1c-d) show that the radio limb-brightened morphology clearly appears at $\phi = 0^o$, i. e. if both the density gradient and the magnetic field are nearly aligned.

Variation of the magnetic field orientation changes the radio morphology from shell-like to barrel-like [159, 212]. Contrast $\lg(S_{\nu,\max}/S_{\nu,\min})$ in the radio surface brightness decreases with increasing ϕ_o, from 2.7 ($\phi_o = 0^o$) to 1.8 ($\phi_o = 90^o$). Such behaviour of the radio morphology may be used for testing orientation of the magnetic field.

Thus, we found that the morphological properties of the projected composites match the basic features of the TXC class: centrally-peaked distribution of the thermal X-ray surface brightness is within the area of the radio shell; emission arises

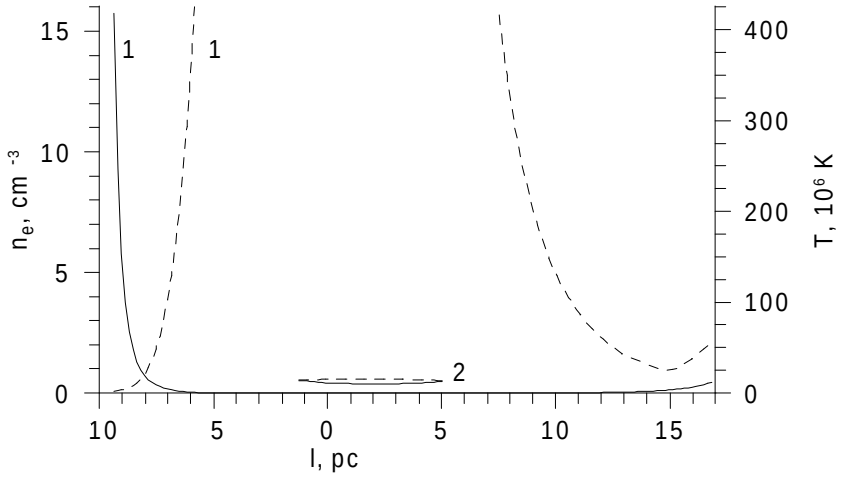

Figure 2.2. Distribution of density (solid curves) and temperature (dashed curves) along the line of sight inside SNR (model b, $\delta = 90^{\rm o}$): 1 – at the center of the projection, 2 – at $0.95R_{\rm p}$. Emission measure $\int n_e^2 dl = 74$ cm^{-6}pc at the center and $\int n_e^2 dl = 1.1$ cm^{-6}pc at $0.95R_{\rm p}$.

from the swept-up ISM material.

Let us consider physical properties of TXCs. a) The column number density increases from the edge towards the centre of the projection (e.g., for model b from $10^{18.9}$ cm^{-2} to $10^{19.4}$ cm^{-2}). b) The diffuse optical nebulosity over the internal region of the projection may naturally take place in such a model. c) Emission measure $\int n_e^2 dl$ (n_e is the electron number density, l is the length within SNR) is the highest in the X-ray peak because both n_e and l are maximum there (Fig. 2.2).

As Fig. 2.3 demonstrates, the distribution of X-ray surface brightness has strong maximum $S_{\rm c}$ around the centre and a weaker shell with second maximum $S_{\rm max,\,2}$ just behind the forward shock. It is essential that such a morphology takes place in different X-ray bands (lines b, 1, 2). The contrasts $S_{\rm c}/S_{\rm max,\,2}$ in X-ray surface brightness depend on the photon energy band and may lie within a wide range: in our models from 3 to 200 for $\varepsilon > 0.1$ keV (Table 2.1). The ratios of X-ray luminosity $\int S(r) 2\pi r dr$ of central region $R < 0.2R_{\rm p}$ to the luminosity beyond $R > 0.6R_{\rm p}$ are 0.16, 5.2 and 16 in models a, b and c, respectively. Thus, observational property d of TXCs takes place just at the adiabatic stage.

Surface distribution of spectral index $\alpha = \partial \ln P_{\rm c}/\partial \ln \varepsilon$, of the thermal X-ray emission where $P_{\rm c}$ is the continuum emissivity and ε is the photon energy, gives us profiles of effective temperature T of the column of emitting gas ($\alpha \propto T^{-1}$, if the

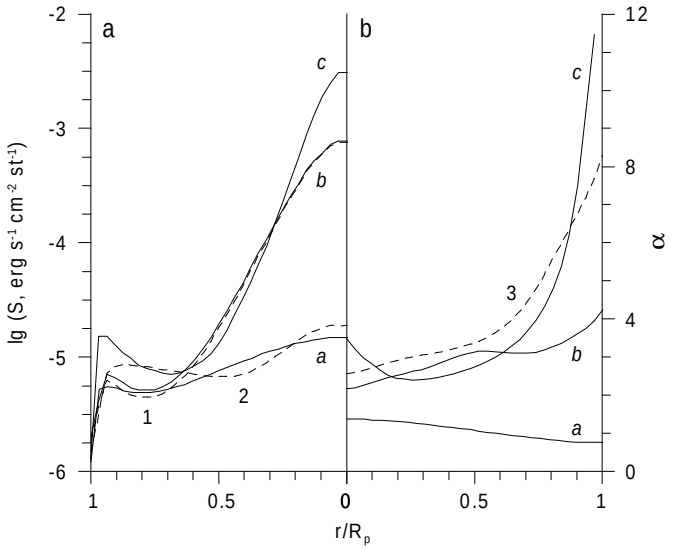

Figure 2.3. a and b. Evolution of the distribution of thermal X-ray surface brightness (**a**) and spectral index (**b**). Solid curves are labelled with the model codes according to Table 2.1; they represent $\lg S$ in band $\varepsilon > 0.1$ keV and α at 5 keV. Dashed lines represent model b in other bands: 1 – S in $\varepsilon = 0.1 - 2.4$ keV, 2 – S in $\varepsilon > 4.5$ keV (multiplied by 10^2), 3 – α at 10 keV. Radii are normalized to unity.

Gaunt factor is assumed to be constant). Fig. 2.3 shows that the temperature may either increase or decrease towards the centre. Decreasing takes place early in the adiabatic phase. Variation of the spectral index lies within factors 1.6 to 3.6 at the adiabatic stage (Table 2.1); the contrast in the spectral index distribution increases with age. Such values correspond to the possible range of temperature variation over the projection of thermal X-ray composites.

In order to reveal the dependence of the distributions of S and α on the ISM density gradient, a number of models with different h were calculated (Fig. 2.4 and Table 2.1). The surface brightness distribution has a stronger peak for a stronger gradient. With increasing h, the outer shell becomes more prominent in the projection. Only a scale-height of order $h < 10$ pc can cause projected composites. A less strong gradient of the ambient density makes effective temperature T more uniformly distributed in the internal part of the projection.

Projection model versus other models. Distinctions of the previous physical models for TXC from the projection model are noted below. 1) The model with strong cooling can be used within the frame of the radiative model of SNR; the presented model describes TXCs as SNRs in the adiabatic phase of their evolution.

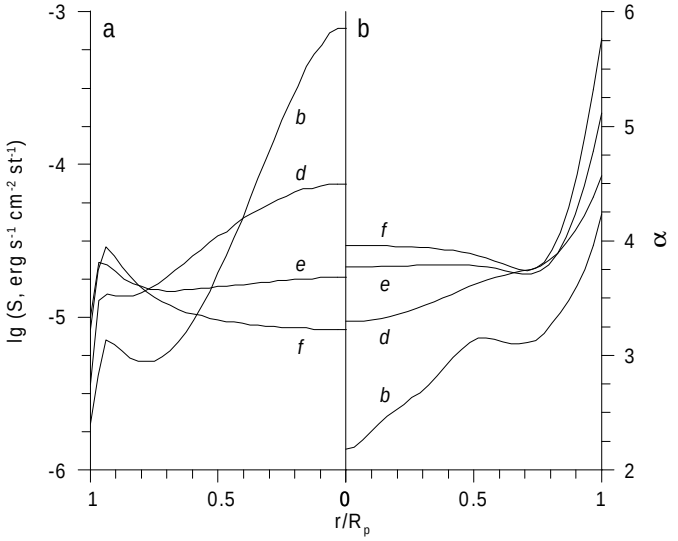

Figure 2.4. a and b. Influence of h on the distribution of thermal X-ray surface brightness ($\lg S^{>0.1\ \mathrm{keV}}$) (**a**) and spectral index ($\alpha^{5\ \mathrm{keV}}$) (**b**). Curves are labelled with the model codes according to Table 2.1. Radii are normalized to unity.

2) In comparison with the projection model, the spectrum of the central region in the model with thermal conduction is softer due to reducing the temperature [203]. 3) The models with thermal conduction or evaporation increase the density in the internal part of SNR. The projection model does not require such modification of internal density distribution; the density profiles in this model are similar to those in the Sedov [21] solution. 4) A small-scale inhomogeneous ISM is required for the model with evaporation. Projected composites are a consequence of large-scale nonuniformity of the ISM with the scale-height of order < 10 pc. 5) Other possibilities of creating a centrally-filled morphology, such as differential absorption or emission from ejecta, modify the spectra of the object and may be determined from observations.

2.2. Post-adibatic stage in evolution of SNRs

Physical processes accompanying the evolution of SNRs is a complex system. It is almost impossible to account for all of them in a single model of SNR. Therefore, the whole evolution of SNR from a supernova explosion until the mixing of a very old object with the interstellar matter is divided on a number of the model phases

(e.g. [14,22,370]): the free-expansion, adiabatic and radiative stages. There are some physical processes important during a given stage, some others could be neglected. Such an approach allows for simplification of description of SNR evolution during each phase.

The role of radiative losses, which is negligible in the adiabatic phase of SNR evolution, becomes more and more promiment with time. They are so important in old SNRs, that they essentially modify the dynamics of such SNRs. Theoretical systematization of timescales and the role of different physical process in cooling of adiabatic SNR was first reviewed by Cox [121]. The transition to the radiative stage was studied numerically, by following the history of the shocked flow, in [90, 109, 114, 148, 154, 241]. The analytical treatments for dynamics of the shock front are of great importance as well, it is treated in [65, 89, 247, 263, 266, 269].

The physical processes in the radiative blast wave, namely, quick cooling of an incoming flow and formation of the thin dense cold shell which moves due to the pressure of internal gas makes the so called "pressure-driven snowplow" (PDS) model within the "thin-layer" approximation to be adequate for description of this stage of SNR evolution [10, 85, 266].

The PDS model was introduced by McKee & Ostriker; their *analytical solution* [247, 266], widely used for the description of evolution of the radiative shell, gives a power-law dependence for the shock radius $R \propto t^m$ with constant m (which equals to 2/7 for the uniform medium). However, *numerical studies* cited above give a bit different value of the deceleration parameter m (defined as $m = d\ln R/d\ln t$), namely ≈ 0.33 [90,109]. We shall show analytically in Sect. 2.4 that the evolution of the radiative shell is, in fact, given by variable m and that the discrepancy between the analytical and numerical results is only apparent. Namely, the usage of McKee & Ostriker analytical solution assumes that SNR has already reached the asymptotic power-law regime with constant value of $m = 2/7$. The time needed to reach this asymptotic regime is however long compared to the SNR age.

It is common for an approximate theoretical description of SNR evolution to simply switch from the adiabatic solution to the PDS radiative one at some moment

of time. However, we point out below the result visible also in previous calculations, namely, the need for an intermediate transition phase between the adiabatic and radiative stages, with duration comparable to SNR age it has at the time when radiative losses of gas begin to be prominent. Thus, the radiative era which begins after the end of the adiabatic one, have to be divided on two phases: the transition (or post-adiabatic) phase, when the radiative losses become to modify dynamics and to lead to the formation of the thin radiative shell, and the radiative PDS stage when the shell is already created and one can apply the PDS analytic solution [65, 269].

2.2.1. Transition of the adiabatic SNR to the radiative phase.

Definitions of different reference times. Let us consider the spherical shock motion in the medium with the power-law density variation $\rho_{\rm o}(R) = AR^{-\omega}$, where A and ω are constant. The dynamics of the adiabatic shock in such a medium is given by Sedov solutions [21] where the shock velocity $V \propto R^{-(3-\omega)/2}$ and $R \propto t^{2/(5-\omega)}$.

Moving through medium, the shock decelerates if the ambient density distribution increases or does not quickly decrease ($\omega < 3$). The shock temperature $T_{\rm s} \propto V^2$ decreases with time as well. Starting from some age $t_{\rm low}$ when $T_{\rm s} = T_{\rm low} \sim 3\times10^7\,{\rm K}$, which corresponds to the minimum of the cooling function $\Lambda(T)$, the radiative losses of shocked plasma are more and more prominent with falling of T (Fig. 2.5). The maximum in the energy losses is when the shock temperature $T_{\rm s} = T_{\rm hi} \sim 2\times10^5\,{\rm K}$, the corresponding Sedov time (i.e. calculated under the assumption that the shock is adiabatic up to this time) is $t_{\rm hi}$.

There is a number of reference times in between $t_{\rm low}$ and $t_{\rm hi}$ [90, 119, 121]. Once a parcel of gas is shocked its temperature changes due to expansion and cooling $\dot{T}_{\rm a} = \dot{T}_{\rm a,exp} + \dot{T}_{\rm a,rad}$, where the dot marks the time derivative. One may define the "dynamics-affected" time $t_{\rm dyn}$ by the equation

$$\dot{T}_{\rm a,exp}(t_{\rm dyn}) = \dot{T}_{\rm a,rad}(t_{\rm dyn}). \tag{2.2}$$

If a fluid element is shocked after this time, its temperature decreases faster due to radiation than as a consequence of expansion. At other time $t_{\rm sag}$, the radiative

cooling begins to affect the temperature distribution inside the shock. When the rate of change of the shock temperature $\dot{T}_{\rm s}$ begin to be less than $\dot{T}_{\rm a}$, the temperature downstream of the shock will sag rather than rise. Thus the equation for $t_{\rm sag}$ is

$$\dot{T}_{\rm s}(t_{\rm sag}) = \dot{T}_{\rm a}(t_{\rm sag}). \tag{2.3}$$

Radiative losses cause the faster – comparing to the adiabatic phase – deceleration of the forward shock. This faster deceleration begins to be prominent around the "transition age" $t_{\rm tr}$ when the shock pressure decrease due to the radiative losses becomes to be effective. Then, the shocked gas radiates away its energy rather quickly, cools till the temperature $T \sim 10^4$ K and forms a dense shell. The formation of the shell is completed around the "time of shell formation" $t_{\rm sf}$ which is larger than $t_{\rm tr}$; the latter which marks the end of adiabatic era. After $t_{\rm sf}$ the thermal energy of all swept-up gas is rapidly radiated and the thin dense shell expansion is caused by the thermal pressure of the interior.

The time $t_{\rm low}$ is given by the equation

$$T_{\rm s}(t_{\rm low}) = T_{\rm low}. \tag{2.4}$$

A similar equation defines the time $t_{\rm hi}$

$$T_{\rm s}(t_{\rm hi}) = T_{\rm hi}, \tag{2.5}$$

which was suggested to be a measure of $t_{\rm tr}$ [89,269]. However, as we shall demonstrate later, the post-shock temperature of plasma at $t_{\rm tr}$ is of order $10^6\,{\rm K} > T_{\rm hi}$ and $t_{\rm hi}$ is larger than $t_{\rm tr}$ in about 3.5 times (Sect. 2.2.2). Therefore, it is not correct to calculate the "highest-losses" SNR age with the shock motion law valid during the adiabatic era.

A simple approach to locate $t_{\rm tr}$ bases on the comparison of the radiative losses with the initial thermal energy of the shocked fluid [90]. A shocked fluid element cools during the cooling time $\Delta t_{\rm cool} \propto \epsilon(T_{\rm s}, \rho_{\rm s})/\Lambda(T_{\rm s}, \rho_{\rm s})$, where $\epsilon = (\gamma - 1)^{-1}\rho_{\rm s} k T_{\rm s}/\mu m_{\rm p}$ is its initial thermal energy density, γ is the adiabatic index, μ the mean mass per particle in terms of $m_{\rm p}$. During the adiabatic phase the cooling time is larger

than SNR age t. The radiative losses may be expected to modify dynamics when the cooling time $\Delta t_{\rm cool} \leq t$. In such approach the transition time is a solution of equation

$$t_{\rm tr} = \Delta t_{\rm cool}(t_{\rm tr}). \tag{2.6}$$

Let us assume that the cooling function $\Lambda \propto n^2 T^{-\beta}$ with $\beta > 0$ and n is the hydrogen number density, then $\Delta t_{\rm cool} \propto n_{\rm o}^{-1} T_{\rm s}^{1+\beta} \propto t^{-6(1+\beta)/5}$ with the use of Sedov solutions for uniform medium. For the shock running in the power-law density distribution, the upstream hydrogen number density and the post-shock temperature at time t is

$$n_{\rm o} \propto t^{-2\omega/(5-\omega)}, \qquad T_{\rm s} \propto t^{-2(3-\omega)/(5-\omega)}. \tag{2.7}$$

Therefore $\Delta t_{\rm cool} \propto t^{-\eta}$ with $\eta = (2(3-\omega)(1+\beta) - 2\omega)/(5-\omega))$ for such density distribution. For $\beta = 1/2$ the index η is the same as found in [154].

The way to estimate the time of the shell formation $t_{\rm sf}$ was suggested in [119,120]. If an element of gas was shocked at time $t_{\rm s}$ then the age of SNR will be $t_{\rm c} = t_{\rm s} + \Delta t_{\rm cool}(t_{\rm s})$ when it cools down. The minimum of the function $t_{\rm c}(t_{\rm s})$ has the meaning of SNR age when the first element of gas cools and is called "SNR cooling time" $t_{\rm cool}$. Let t_1 be the time when the shock encountered the fluid element which cools first. If so, $t_{\rm c} = t_1(t_{\rm s}/t_1) + \Delta t_{\rm cool}(t_1)(t_{\rm s}/t_1)^{-\eta}$. Setting $dt_{\rm c}/dt_{\rm s}|_{t_{\rm s}=t_1} = 0$ one obtain that

$$t_{\rm cool} = (1+\eta)\Delta t_{\rm cool}(t_1), \tag{2.8}$$

$$\frac{t_{\rm cool}}{t_1} = \frac{1+\eta}{\eta}, \tag{2.9}$$

The cooling time $t_{\rm cool} > t_1$ by the definition, therefore it must be that $\eta > 0$. This is the case for

$$\omega < 3(1+\beta)/(2+\beta); \tag{2.10}$$

that is $\omega < 2$ (9/5) for $\beta = 1$ (1/2). The equation

$$t_1 = \eta \Delta t_{\rm cool}(t_1) \tag{2.11}$$

is more suitable for practical use than (2.8). If the medium is uniform then $t_{\rm cool} = 17t_1/12$ for $\beta = 1$ and $t_{\rm cool} = 14t_1/9$ for $\beta = 1/2$.

The "SNR cooling time" $t_{\rm cool} = \min(t_{\rm c})$ was initially suggested to be taken as the time of the shell formation. Numerical experiments for shock in the uniform medium suggest that $t_{\rm sf}$ is a bit higher (of order 10%) than $t_{\rm cool}$ [122] and the reason of this could be that the compression of the shell is also effective after cooling of the first element and takes additional time.

Another point is that the solution for adiabatic shock used in (2.7) might not formally be applicable there because $t_1 > t_{\rm tr}$ (see Eq. (2.40)). We believe however that the level of accuracy in estimation of $t_{\rm tr}$, the small difference between $t_{\rm tr}$ and t_1 (about 30% in the case of uniform medium, Sect. 2.2.2) as well as close values of $t_{\rm cool}$ and $t_{\rm sf}$ allow one to use the Sedov solution in (2.7) and to assume $t_{\rm sf} \approx t_{\rm cool}$.

We would like to note once more that the transition time $t_{\rm tr}$ is an approximate estimation on the end of the adiabatic stage and beginning of the radiative era, while the time of the shell formation $t_{\rm sf}$ marks the time when one can start to use the PDS model where hot gas pushes the cold dense shell. The structure of the flow re-structurises and the shell forms during the transition phase given by the time interval $(t_{\rm tr}, t_{\rm sf})$. We shall demonstrate later that the ratio $t_{\rm sf}/t_{\rm tr}$ with $t_{\rm tr}$ given by (2.6) and $t_{\rm sf}$ by (2.9) is always larger than unity (see Eq. (2.39)) and that the transition phase is not short as it is generally assumed.

One more time, namely the "intersection time" $t_{\rm i} \in (t_{\rm tr}, t_{\rm sf})$ was introduced in [65], as a time when two functions – the adiabatic dependence $R = R(t)$ (valid before $t_{\rm tr}$) and the PDS dependence $R_{\rm sh} = R_{\rm sh}(t)$ (valid after $t_{\rm sf}$) – intersect being extrapolated into the transition phase. This intersection time could be useful in some tasks when the level of accuracy is such that one may sharply switch from the adiabatic solution to the radiative one without consideration of the transition phase.

Cooling time. The expression

$$\Delta t_{\rm cool} = \frac{\epsilon(T_{\rm s}, \rho_{\rm s})}{\Lambda(T_{\rm s}, \rho_{\rm s})} \tag{2.12}$$

used in [90] to calculate the cooling time, equates the energy losses $\Lambda \Delta t_{\rm cool}$ with initial thermal energy density $\epsilon_{\rm s}$ of a fluid element under condition that the density and temperature of this element are constant. More detailed model should account

for the density and temperature history during $\Delta t_{\rm cool}$. Namely the above equation should be replaced with a differential one:

$$d\epsilon/dt = -\Lambda(T, \rho). \tag{2.13}$$

The total internal energy $U = \epsilon V$ of gas within the volume V changes as $dU = TdS - PdV$ where S is entropy and P is pressure. The evolution of the thermal energy per unit mass $E = \epsilon/\rho$ is therefore

$$\frac{\partial E}{\partial t} - \frac{P}{\rho^2}\left(\frac{\partial \rho}{\partial t}\right) = T\frac{\partial s}{\partial t} \tag{2.14}$$

where $s = (3k/2m_{\rm p}\mu)\ln(P/\rho^{\gamma})$ is the entropy per unit mass. So, Eq. (2.13) becomes

$$T\frac{\partial s}{\partial t} = -\frac{\Lambda(T, \rho)}{\rho}, \tag{2.15}$$

here the temperature T, density ρ, pressure P, energy E are functions of Lagrangian coordinate a and time t.

As it follows from (2.15) and the definition of s, the time $\Delta t_{\rm cool}$ may be also defined as a time taken for the adiabat P/ρ^{γ} to fall to zero. Kahn [206] have found an interesting result. Namely, if

$$\beta = \frac{2-\gamma}{\gamma - 1} \tag{2.16}$$

(that is $\beta = 1/2$ for $\gamma = 5/3$) then one can derive $\Delta t_{\rm cool}$ from (2.15) independently of the density and temperature history:

$$\Delta t_{\rm cool}^{\rm Kahn} = \frac{\epsilon(T_{\rm s}, \rho_{\rm s})}{(\beta+1)\Lambda(T_{\rm s}, \rho_{\rm s})}. \tag{2.17}$$

It can be checked that the same solution may be obtained from (2.14)-(2.15) for any β if one assume that the gas is not doing work during $\Delta t_{\rm cool}$ that is equivalent to putting $\partial\rho/\partial t = 0$ in (2.14). However, the density of fluid is not expected to be constant. In such situation one should solve the full set of the hydrodynamic equations which can be performed only numerically, while we are interested in a rather simple analytical estimation on cooling time for a general β. Therefore it is more suitable to use the estimation (2.12) for the cooling time which follows just from comparison of the radiative losses with the initial energy. We shall see later that such approach describe the shock dynamics rather well.

Equations for the reference times. Let us write equations for $t_{\rm tr}$ and $t_{\rm sf}$ for shock in nonuniform medium. We assume hereafter $\beta = 1$. Note that all the rest formulae can easily be modified if one uses β which coincides with a value given by (2.16); namely, as it follows from comparison of (2.17) and (2.12), $\mathcal{T}$ in (2.18) have to be simply divided by $\beta + 1$.

If the cooling function for a fluid is approximately $\Lambda = CT^{-\beta} n_e n_H$, where C is a constant, then (2.12) yields

$$\Delta t_{\rm cool} = \mathcal{T} \frac{T_{\rm s}^{1+\beta}}{n_{\rm o}(R)} \quad \text{where} \quad \mathcal{T} = \frac{k\mu_e}{C\mu(\gamma+1)}, \tag{2.18}$$

μ_e is the mean mass of particle per one electron in terms of the proton mass (i.e. $\rho = \mu_e n_e m_{\rm p} = \mu n m_{\rm p}$). The transition time $t_{\rm tr}$ is a solution of equation (2.6):

$$t_{\rm tr} = \mathcal{T} \frac{T_s(t_{\rm tr})^{1+\beta}}{n_{\rm o}(R(t_{\rm tr}))}, \tag{2.19}$$

where the dependencies $T_{\rm s}(t)$, $R(t)$ are those valid on the adiabatic phase. The time t_1 can be estimated from (2.11):

$$t_1 = \eta \mathcal{T} \frac{T_s\,(t_1)^{1+\beta}}{n_{\rm o}\,(R(t_1))}. \tag{2.20}$$

Now the SNR cooling time $t_{\rm cool}$ and the time of the shell formation $t_{\rm sf} \approx t_{\rm cool}$ is given by (2.9). The estimations for the transition and the shell formation times are somewhat different in the literature because of different ways used to find the cooling time $\Delta t_{\rm cool}$ and to approximate the cooling function $\Lambda(T)$.

For the adiabatic shock the rate of change of the shock temperature is

$$\dot{T}_{\rm s} = -\frac{2(3-\omega)}{5-\omega} \frac{T_{\rm s}}{t}. \tag{2.21}$$

Close to the shock, the fluid temperature in Sedov solution [21] is approximately

$$\frac{T(a)}{T_{\rm s}} \approx \left(\frac{a}{R}\right)^{-\kappa(\gamma,\omega)}, \tag{2.22}$$

where a is Lagrangian coordinate. The value of κ is given by

$$\kappa = \left(-\frac{a}{T(a)} \frac{\partial T(a)}{\partial a} \right)_{a=R}. \tag{2.23}$$

where $T(a)$ is the profile from Sedov solutions. It is $\kappa = 1 - 3\omega/4$ for $\gamma = 5/3$ (see Appendix A). Now we may find that the temperature in a given fluid element a changes due to expansion as

$$\dot{T}_{\rm a,exp} \approx -\frac{2(3-\omega-\kappa)}{5-\omega}\frac{T(a)}{t}. \tag{2.24}$$

The rate $\dot{T}_{\rm a,rad}$ due to cooling follows from $dE/dt = -\Lambda/\rho$:

$$\dot{T}_{\rm a,rad} = -\frac{\gamma-1}{\gamma+1}\mathcal{T}^{-1} n_{\rm H}(a) T(a)^{-\beta}. \tag{2.25}$$

Now we have to compare the above rates at the time $t_{\rm s}$, i.e. at the time when the parcel of fluid was shocked. The coordinate $a = R(t_{\rm s})$ by the definition. Thus Eq. (2.2) rewrites:

$$t_{\rm dyn} = \frac{2(3-\omega-\kappa)}{5-\omega}\Delta t_{\rm cool}(t_{\rm dyn}). \tag{2.26}$$

Similarly, the equation for $t_{\rm sag}$ follows from (2.3):

$$t_{\rm sag} = \frac{2\kappa}{5-\omega}\Delta t_{\rm cool}(t_{\rm sag}). \tag{2.27}$$

As one can see, the most of reference times are given by the equations of the form

$$t_* = K\Delta t_{\rm cool}(t_*), \tag{2.28}$$

where t_* is a given reference time and K is corresponding constant. It may be shown that the solution of such equation may be found as

$$t_* = K^{1/(1+\eta)} t_{\rm tr}. \tag{2.29}$$

The Sedov radius of the shock at this time is $R_* = K^{2/((5-\omega)(1+\eta))} R_{\rm tr}$.

The cooling function. There are two choices of β in the literature, namely 1 and 1/2. The first case is used for *nonequilibrium* cooling model [345] where the cooling function for plasma with solar abundance may be approximated as [90]

$$\Lambda = 10^{-16} n_e n_H T^{-1} \text{ erg cm}^{-3} \text{ s}^{-1}. \tag{2.30}$$

This approximation is valid for range of temperatures $T = (0.2-5)\times 10^6\,\text{K}$ which is important for description of transition into the radiative phase. Another possibility

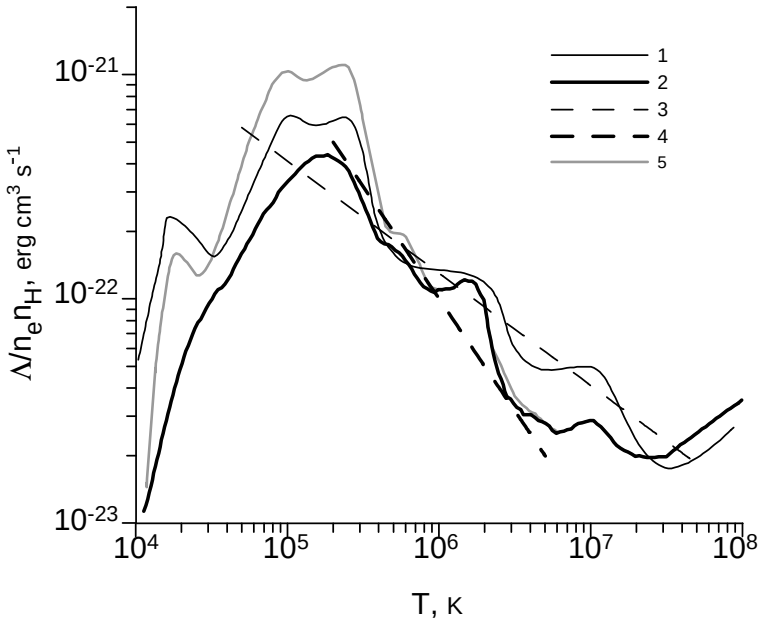

Figure 2.5. Equilibrium (line 1) [300] and nonequilibrium (line 2) [345] cooling functions, used in the literature to study the transition of SNRs into the radiative phase, and approximations (2.31) (line 3) and (2.30) (line 4). The equilibrium cooling function from [345] is also shown for comparison (line 5).

is to use the *equilibrium* cooling model as it was done in [119, 122, 154, 206, 235]. In this case the approximate proportionality $\Lambda \propto T^{-1/2}$ is a reasonable one, e.g. for results on the cooling of the collisional equilibrium plasma from [300,338]; the actual approximation

$$\Lambda = 1.3 \times 10^{-19} n_e n_H T^{-1/2} \text{ erg cm}^{-3} \text{ s}^{-1} \tag{2.31}$$

is written for plasma with almost the same abundance as above and is valid for $T = (0.05 - 50) \times 10^6$ K [206].

Different cooling functions are compared with their approximations on Fig. 2.5. At lower temperatures, the nonequilibrium cooling is less effective in energy losses than the equilibrium one (compare lines 2 and 5). This is because the cooling rate for temperatures higher than $\sim 3 \times 10^7$ K is mostly due to free-free emission while below this temperature the cooling is mostly due to the line emission from heavy elements (most heavy elements are completely ionized above $\sim 3 \times 10^7$ K). Under nonequilibrium ionization conditions the ions are underionized because electrons are much colder than ions and thus there is less emission from ions [154, 180] (see also Fig. 18 in [345]).

2.2.2. Reference times and properties of the transition phase.

Shock in a uniform ISM. Let us compare the sequence of different reference times with numerical calculations [90] of transition of the adiabatic shock into the radiative era, on example of the shock motion in the uniform ambient medium. Let us consider the same parameters as in [90], namely $\gamma = 5/3$, $\beta = 1$, the same abundance ($\mu = 0.619$, $\mu_{\rm e} = 1.18$, $\mu_{\rm H} = 1.43$) as well as assume $t_{\rm sf} = t_{\rm cool}$ and use (2.12) for calculation of $\Delta t_{\rm cool}$.

If shock wave moves in the uniform medium, then – with the use of Eq. (2.19) – the transition time is

$$t_{\rm tr} = 2.84 \times 10^4 E_{51}^{4/17} n_{\rm o}^{-9/17}\,{\rm yr} \tag{2.32}$$

where $E_{51} = E_{\rm SN}/(10^{51}\,{\rm erg})$. The gas element which first cools (at $t_{\rm cool}$) was shocked at t_1 which follows from Eq. (2.20):

$$t_1 = 3.67 \times 10^4 E_{51}^{4/17} n_{\rm o}^{-9/17}\,{\rm yr}. \tag{2.33}$$

The time of the shell formation is given by Eq. (2.9):

$$t_{\rm sf} = 5.20 \times 10^4 E_{51}^{4/17} n_{\rm o}^{-9/17}\,{\rm yr}, \tag{2.34}$$

so that $t_{\rm sf}/t_{\rm tr} = 1.83$. The time when the radiative losses of the shocked gas reach their minimum is (2.4):

$$t_{\rm low} = 1.60 \times 10^3 T_{\rm 3e7}^{-5/6} E_{51}^{1/3} n_{\rm o}^{-1/3}\,{\rm yr} \tag{2.35}$$

where $T_{\rm 3e7} = T_{\rm low}/(3 \times 10^7\,{\rm K})$. Under assumption that radiative losses does not change the shock dynamics till $t_{\rm hi}$, with the use of Sedov solutions for the shock motion, one has from Eq. (2.5) that

$$t_{\rm hi} = 1.04 \times 10^5 T_{\rm 2e5}^{-5/6} E_{51}^{1/3} n_{\rm o}^{-1/3}\,{\rm yr} \tag{2.36}$$

where $T_{\rm 2e5} = T_{\rm hi}/(2 \times 10^5\,{\rm K})$. The fluid temperature drops faster due to cooling than due to expansion from time

$$t_{\rm dyn} = 2.66 \times 10^4 E_{51}^{4/17} n_{\rm o}^{-9/17}\,{\rm yr}. \tag{2.37}$$

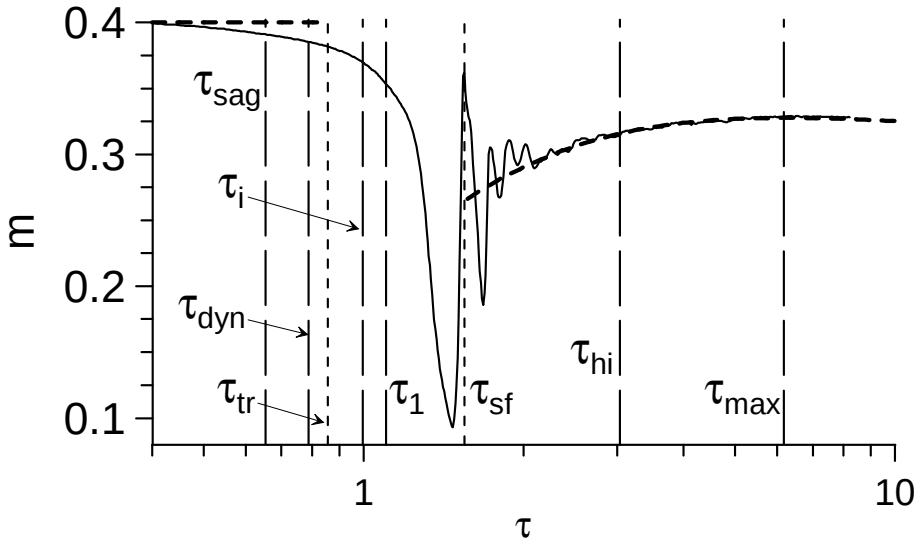

Figure 2.6. The evolution of the deceleration parameter m and different reference times for the shock motion in the uniform medium. Solid line – numerical calculations [90], thick dashed lines – Sedov solution (till $\tau_{\rm tr}$) and analytical solution from Sect. 2.4 (after $\tau_{\rm sf}$). The dimensionless reference times are $\tau_{\rm sag} = 0.654$, $\tau_{\rm dyn} = 0.802$, $\tau_{\rm tr} = 0.855$, $\tau_{\rm i} = 1.01$, $\tau_1 = 1.10$, $\tau_{\rm sf} = 1.57$, $\tau_{\rm low} = 0.047$, $\tau_{\rm hi} = 3.03$. The function $m(\tau)$ reaches his maximum at the radiative phase at $\tau_{\rm max} = 6.18$ (Sect. 2.4).

The time when one may expect to have the temperature decrease downstream close to the shock is

$$t_{\rm sag} = 2.17 \times 10^4 E_{51}^{4/17} n_{\rm o}^{-9/17} \,{\rm yr}. \tag{2.38}$$

The Sedov solutions give at time $t_{\rm tr}$ the shock radius $R_{\rm tr} = 19 E_{51}^{5/17} n_{\rm o}^{-7/17}\,{\rm pc}$, the shock velocity $V_{\rm tr} = 260\ E_{51}^{1/17} n_{\rm o}^{2/17}\,{\rm km/s}$, the post-shock temperature $T_{\rm tr} = 0.95 \cdot 10^6\ E_{51}^{2/17} n_{\rm o}^{4/17}\,{\rm K}$ and the swept up mass $M_{\rm tot}(t_{\rm tr}) = 10^3\ E_{51}^{15/17} n_{\rm o}^{-4/17}\,{\rm M}_\odot$.

The above reference times are shown on Fig. 2.6 together with evolution of the deceleration parameter $m(\tau)$ calculated numerically [90]. The analytical solutions for the adiabatic [21] and the radiative shock (Sect. 2.4) are also shown. Numerical result is found for supernova energy $E_{\rm SN} = 10^{51}\,{\rm erg}$ and interstellar hydrogen number density $n_{\rm o} = 0.84\,{\rm cm}^{-3}$. With these values, the times are $t_{\rm sag} = 2.4 \times 10^4\,{\rm yr}$, $t_{\rm dyn} = 2.9 \times 10^4\,{\rm yr}$, $t_{\rm tr} = 3.1 \times 10^4\,{\rm yr}$, $t_1 = 4.0 \times 10^4\,{\rm yr}$, $t_{\rm sf} = 5.7 \times 10^4\,{\rm yr}$, $t_{\rm low} = 1.7 \times 10^3\,{\rm yr}$, $t_{\rm hi} = 1.1 \times 10^5\,{\rm yr}$; the intersection time is $t_{\rm i} = 3.6 \times 10^4\,{\rm yr}$ [65]. The function $m(\tau)$ reaches his maximum during the radiative stage at $t_{\rm max} = 2.3 \times 10^5\,{\rm yr}$ (Sect. 2.4). Results on Fig. 2.6 are presented in terms of the dimensionless time $\tau = t/\tilde{t}$ because the analytical solutions allow for scaling (numerical results for various input parameters differs by oscillation transient only; see e.g. Fig. 8 in [90]).

The dimensional scale for time determined from fitting of analytical and numerical results is $\tilde{t} = 3.6 \times 10^4\,\mathrm{yr}$ (Sect. 2.4).

It is apparent from Fig. 2.6 that the transition time $t_{\rm tr}$ is a reasonable estimation for the end of the adiabatic stage while $t_{\rm sf}$ could be the time when one can start to use the radiative solutions (Sect. 2.4) coming from the PDS model of McKee & Ostriker [247]. The duration of the intermediate transition phase is $(\tau_{\rm sf}-\tau_{\rm tr})/\tau_{\rm tr} = 0.83$ times the age of SNR at the end of the adiabatic stage, i.e. almost the same as duration of the adiabatic stage itself. This means that there is a strong need for a theoretical model which describe evolution of SNR in this phase.

For estimation of reference times, a number of authors [114,119,120,122,154] keep a bit different approach from that used above, namely they use the approximation of the equilibrium cooling function with $\beta = 1/2$ and the Kahn solution for cooling time (2.17). Let us compare the results of this approach with those obtained above. The evolution of the deceleration parameter in the refereed approach is presented in [114]. There is also the same definition of the time of the shell formation $t_{\rm sf} = t_{\rm cool}$. The estimation is $t_{\rm sf,C} = 4.31\times10^4 E_{51}^{3/14} n_{\rm o}^{-4/7}\,\mathrm{yr}$ for their abundance and the cooling function (2.31). For the parameters used in the numerical calculations $E_{51} = 0.931$ and $n_{\rm o} = 0.1\,\mathrm{cm}^{-3}$ the time is $t_{\rm sf,C} = 1.58 \times 10^5\,\mathrm{yr}$ while with the use of our Eq. (2.34) we obtain $t_{\rm sf} = 1.73 \times 10^5\,\mathrm{yr}$. The both estimations are close. Analytical solutions shows that, before $t_{\rm tr}$ and after $t_{\rm sf}$, the evolution of dynamic parameters of the shock can be expressed in a dimensionless form, i.e. independently of E_{51} and $n_{\rm o}$. The behavior of the shock velocity depends however on these parameters during the transition phase; the difference is in the frequency of oscillations (Fig. 8 in [90]). Nevertheless, as one can see from this figure, the strong deceleration of the shock right after $t_{\rm tr}$ up to the first minimum is almost the same for different parameters, i.e. can also be scaled. We use this property in order to find the scale factor $\tilde{t}$ for calculations being done in [114]. Namely, the fit of curve $m(\tau)$ from [114] to that of [90] (within the time interval from $t_{\rm tr}$ to the first minimum) gives $\tilde{t}_{\rm C} = 1.05 \times 10^5\,\mathrm{yr}$. The both calculations of the transition to the radiative stage agree rather well as it may be seen on Fig. 2.7. The dimensionless times for results

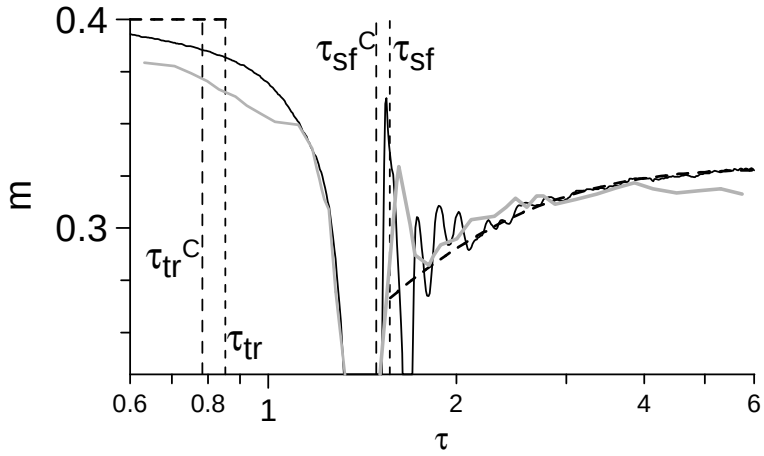

Figure 2.7. Numerical calculation of evolution of the deceleration parameter m from [90] (thin black line) and from [114] (thick gray line). The transition and shell formation times from [114] are marked by "C".

in [114] are: the shell formation time $\tau_{\rm sf,C} = t_{\rm sf,C}/\tilde{t}_{\rm C} = 1.51$ and the transition time (as it is follows from (2.39)) $\tau_{\rm tr,C} = \tau_{\rm sf,C}/1.92 = 0.785$. Fig. 2.7 shows that the both approaches for localization of the limits of the transition phase – with the use of the nonequilibrium-ionization cooling function (2.30) and the simple estimation for $\Delta t_{\rm cool}$ (2.12) [90] or with the equilibrium cooling function (2.31) together with Kahn solution for $\Delta t_{\rm cool}$ (2.17) [114] – give almost the same estimations.

Shock in a medium with a power-law density variation. Let us now consider the shock motion in the ambient medium with the power-law density variation $\rho^o(R) = AR^{-\omega}$. With the use of (2.19), (2.20), (2.9), (2.7) and the definition $t_{\rm sf} = t_{\rm cool}$ one can show that the duration of the transition phase is given by

$$\frac{t_{\rm sf}}{t_{\rm tr}} = \frac{t_{\rm cool}}{t_{\rm tr}} = \frac{1+\eta}{\eta^{\eta/(1+\eta)}} \ . \tag{2.39}$$

The shell formation time is always larger than the transition time $t_{\rm tr}$, provided by the fact that $\eta > 0$. The ratio

$$\frac{t_1}{t_{\rm tr}} = \eta^{1/(1+\eta)} \tag{2.40}$$

is also always larger than unity. Note that these relations do not depend on abundance and γ. The ratios between all other times may be found from (2.29).

The consequence of times is $t_{\rm dyn} < t_{\rm tr} < t_1 < t_{\rm sf}$ (Fig. 2.8) in nonuniform medium with increasing density. The time t_1 may be smaller than $t_{\rm tr}$ and $t_{\rm dyn}$ for the decreasing density medium. The sag time $t_{\rm sag} < t_{\rm tr}$ for $\omega > -6$ only.

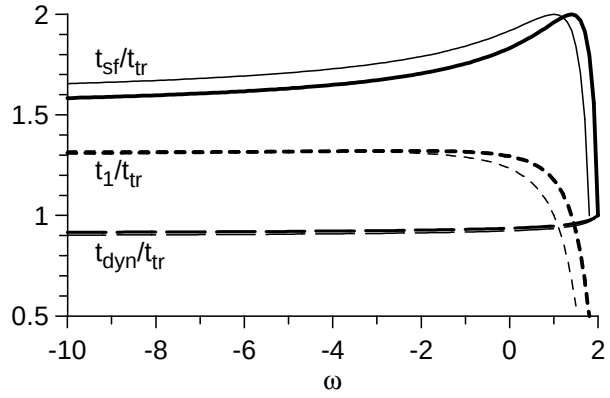

Figure 2.8. The ratios of times for $\beta = 1$ (thick lines) and $\beta = 1/2$ (thin lines) as it is obtained from (2.39) and (2.40).

Fig. 2.8 shows the two ratios (2.39) and (2.40) as a functions of ω for two values of β. Namely, the ratios $t_1/t_{\rm tr} \approx 1.3$ and $t_{\rm sf}/t_{\rm tr} \approx 1.6 \div 1.8$ are almost the same for shock in the medium with increasing density ($\omega \leq 0$). Therefore, in case of a uniform medium and a medium with increasing density, *there is a need of introduction of transition phase with duration more than a half of SNR age at the beginning of this phase*, $t_{\rm tr}$. The transition time $t_{\rm tr}$ and therefore the transition phase $t_{\rm sf} - t_{\rm tr} \propto t_{\rm tr}$ are less for higher density and lower initial energy:

$$t_{\rm tr} \propto E_{51}^{(2+2\beta+\omega)/\delta} A^{-(7+2\beta)/\delta} \tag{2.41}$$

where $\delta = 11+6\beta-\omega(5+2\beta)$. Such dependence on density is also visible in numerical calculations (Fig. 8 in [90]). The dependence of $t_{\rm tr}$ on density an explosion energy is stronger for higher ω because the powers in (2.41) increase with ω.

Medium with decreasing density. It seems that the formulae (2.39) and (2.40) suggest for the case of decreasing density that the PDS radiative stage can even begin right after the end of adiabatic stage: $t_{\rm sf}/t_{\rm tr} \to 0$ with $\omega \to 3(1+\beta)/(2+\beta)$. Another result, already stated in [154], also follows: there will be no radiative shell formation for $\omega \geq 3(1+\beta)/(2+\beta)$. In order to understand the reasons of such behavior let us consider more details.

What is the coordinate a_1 of the element which cools first? This element was shocked at $t_1 = \eta^{1/(1+\eta)} t_{\rm tr}$. The Sedov radius at this time is

$$R(t_1) = a_1 = \eta^{2/((5-\omega)(1+\eta))} R_{\rm tr}, \tag{2.42}$$

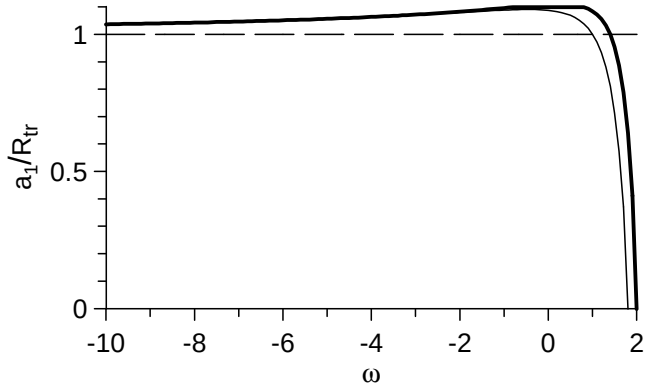

Figure 2.9. The ratio $a_1/R_{\rm tr}$ and $a_{\rm dyn}/R_{\rm tr}$ for $\beta = 1$ (thick lines) and $\beta = 1/2$ (thin lines).

thus the coordinate $a_1 > R_{\rm tr}$ if $\omega < 1.4$ ($\beta = 1$) as it is shown on Fig. 2.9. The ratio $a_1/R_{\rm tr}$ is close to unity and is almost the same for such ω, i.e. the fluid we are interested in will be shocked soon after $t_{\rm tr}$. However, if $\omega > 1.4$ then $a_1 \to 0$ quickly with increasing of ω from 1.4 to 2, i.e. the element which cools first is already inside the shock and may be in a very deep interior. The situation looks like that there could not be any "radiative shell" in a common sense.

It is clear that the trend $t_{\rm sf}/t_{\rm tr} \to 0$ does not mean that radiative processes in the shock develop quickly for $\omega > 1.4$. The transition and the shell formation times correspond to different processes: $t_{\rm tr}$ comes from comparison of the initial thermal energy density of the shocked fluid with radiative losses though $t_{\rm sf} = t_{\rm cool}$ is a time when the first cooled element appears. The two mentioned processes have place in vicinity of the shock if ambient medium is uniform or with increasing density. Numerical results suggest that they may be used for approximate estimates of the limits of the transition phase in such media. However these two process are separated in space for media with decreasing density. It could be, that one (or both) of the times $t_{\rm tr}$ and $t_{\rm sf}$ may not be suitable to mark stages of SNR in medium with decreasing density.

The hydrodynamical properties of the shock in media with $\omega > 0$ seem to cause a trend to absence of the radiative phase in a common sense. The cooling of shock moving in the medium with decreasing density differs from a commonly accepted scenario of the "thin dense shell" formation and should be studied in more details in the future.

2.3. Approximate analytical method for full hydrodynamical description of the post-adiabatic shock

In this subsection, an analytical approach to the description of the post-adiabatic stage in the SNR evolution is developed. We start from Sedov solutions for the adiabatic stage and conclude with the formation of a cool shell when the next, radiative PDS, stage begins. We consider the propagation of the shock, formation of the shell and distribution of hydrodynamical parameters of hot gas flows inside this shell.

2.3.1. Flow parameters at the end of the adiabatic stage. The hydrodynamical parameters of adiabatic SNRs in uniform media (or in the media where the matter is distributed according to power law) are determined by Sedov solutions [21]. The approximate analytical method for the description of the adiabatic stage in the media with a large-scale density gradient was developed in our study [195]. The method is based on the sector approximation and on the simultaneous use of the Lagrangian and Eulerian variables for the description of the plasma flow. Here we use the same method to describe the transition stage, with the flow parameters at the end of the adiabatic stage taken as initial data. Let us restrict ourselves to the uniform density distribution in the interstellar medium $\rho_{\rm ISM} = \rho_{\rm o} = \text{const}$. According to Sedov solutions [21], the radius R and velocity V of the shock generated by the supernova with energy $E_{\rm sn}$ are the following functions of time t:

$$R(t) = \left(\frac{E_{\rm sn}}{\alpha_A \rho_o}\right)^{1/5} t^{2/5} \tag{2.43}$$

$$V(t) = 2/5 \left(\frac{E_{\rm sn}}{\alpha_A \rho_o}\right)^{1/5} t^{-3/5} \tag{2.44}$$

where α_A is the self-similar constant. Based on our approximation [195] for the relationship between the Eulerian coordinate $r(a,t)$ and the Lagrangian coordinate a ($0 \le r(a,t) \le R$), we derive the following expressions for the gas velocity $v(a,t)$,

pressure $P(a,t)$, density $\rho(a,t)$, and temperature $T(a,t)$ in the SNR interior:

$$v(a,t) = \frac{\partial r(a,t)}{\partial t}, \tag{2.45}$$

$$P(a,t) = P(R,t)\left[\frac{\rho^0(a)}{\rho^0(R)}\right]^{1-\gamma}\left[\frac{V(a)}{V(R)}\right]^2\left[\frac{\rho(a,t)}{\rho(R,t)}\right]^{\gamma}, \tag{2.46}$$

$$\rho(a,t) = \rho^0(a)\left(\frac{a}{r(a,t)}\right)^N\left(\frac{\partial r(a,t)}{\partial a}\right)^{-1}, \tag{2.47}$$

$$T(a,t) = \frac{\mu P(a,t)}{R_{\rm g}\rho(a,t)}. \tag{2.48}$$

Eqs. (2.43)-(2.48) describe the evolution of the adiabatic SNR until some moment $t_{\rm tr}$ when the role of radiative losses become efficient for the flow dynamics.

2.3.2. The thin shell formation and dynamics during the post-adiabatic stage. Numerical simulations [90, 114] and analytical estimates (Sect. 2.2) demonstrate that deviations from self-similarity appears around time $t_{\rm tr}$.

Radiation losses cause the thermal energy of gas elements to decrease as the gas continues to radiate. A high pressure of adjacent elements and the interaction of the system of shocks moving in opposite directions result in an increase in the density of radiative layers, and thus they intensify the radiation from the gas. Such a positive feedback leads to the rapid formation of a cool dense shell in the neighborhood of the shock front. The velocity of this shell is somewhat smaller than the hot-gas velocity at the inner boundary of the shell. The shell mass grows due to the hot SNR gas which is cooled down by the reverse shock after hitting the inner boundary of the shell as well as due to swept up gas of ISM. The transition stage ends at time $t_{\rm sf}$. Then the hot gas inside the volume limited by the cooled shell forces the shell to expand. The shell isothermally swept the interstellar gas up during this expansion. The classical radiative stage begins.

We describe the transition process as follows. In time of the beginning of the transition phase $t_{\rm tr}$, the first cold fluid element appears with temperature of ISM $T_{\rm sh} = T_{\rm ISM} = 10^4\,{\rm K}$. The pressure of gas in the cold shell $P_{\rm sh}$ is equal to dynamical pressure of ISM $P_{\rm dyn} = \rho_{\rm ISM}V_{\rm sh}^2$ at its outer boundary and dynamical pressure of

hot gas at its internal boundary $\rho_{\rm sw}(v_{\rm sw}-V_{\rm sh})^2$, therefore, we obtain for the shell velocity

$$V_{\rm sh}^2=\frac{\gamma+1}{\gamma-1}\left(\frac{2}{\gamma+1}V(t_{\rm tr})-V_{\rm sh}\right)^2 \tag{2.49}$$

or

$$V_{\rm sh}=\frac{1}{2}V(t_{\rm tr})=const \tag{2.50}$$

for $\gamma=5/3$. Since the external dynamic pressure and the internal dynamic pressure almost does not change, the shell velocity remains almost constant (2.50) all over the transition stage.

The transition stage comes to an end when the typical time of the hot-gas cooling by the reverse shock at the shell's inner boundary becomes greater than the SNR age. Since then, hot gas is no longer transferred to the shell. The numerical simulations [90] show that, at the beginning of the transition stage, the width Δr of the gas layer to be cooled can constitute up to 5 percent of the shock radius at $t_{\rm tr}$: $\Delta r=\alpha R_{\rm tr}$, $\alpha=0.05$.

Parameter α is the only free parameter in our model. The corresponding width of the cool layer in the Lagrangian coordinates is $\Delta a=((\gamma+1)/(\gamma-1))\Delta r$. The duration of the transition stage is taken equal to the time Δt required for the farthest hot gas element to overtake the shell (this element is initially located at the distance Δr from the shock front), moving with the typical gas velocity $v_{\rm sw}=2/(\gamma+1)V$ (gas velocity with respect to the shock is $v_{\rm sw}-V_{\rm sh}$):

$$\Delta t=t_{\rm sf}-t_{\rm tr}=\alpha R/(v_{\rm sw}-V_{\rm sh})\sim 10\alpha t_{\rm tr}. \tag{2.51}$$

When the formation of the shell is finished (at the beginning of the radiative stage), its radius is

$$R_{\rm sf}=R_{\rm tr}+V_{\rm sh}\Delta t=R_{\rm tr}(1+2\alpha). \tag{2.52}$$

The dimensionless deceleration parameter $m=V_{\rm sh}t/R_{\rm sh}$, which equals to $m_{\rm ad}=0.4$ during adiabatic phase, at $t_{\rm tr}$ drops to $m_{\rm tr}=V_{\rm sh}t_{\rm tr}/R_{\rm tr}=0.5m_{\rm ad}=0.2$; then it increases almost linearly during the post-adiabatic stage and equals to $m_{\rm sf}=m_{\rm tr}(1+0.4(\alpha/0.05))$ at the end of this stage.

2.3.3. The hot gas inside the shell. We have already noted that the distinctive feature of the transition stage is the transfer of appreciable amounts of hot gas to the cool gas of the shell. At the beginning of the transition stage, the hot gas is described by Sedov solutions (2.46)-(2.48) in which the velocity of each gas element decreases after this element passes through the shock front. The radiative cooling of the layers adjacent to the shock front and the corresponding pressure drop lead to the reorganization of the hot gas flow, which attains additional acceleration. Hence we can assume, to a quite good approximation, that the velocity of every hot gas element is constant all over the transition stage: $v(a,t) = v(a,t_{\rm tr})$. Those gas elements which had time to overtake the shell during the transition stage are expected to join the shell. Therefore, for the transition stage we have

$$\begin{aligned} &v(a,t) = v(a,t_{\rm tr}), \quad 0 < a < a_{\rm c}(t) \\ &v(a,t) = V_{\rm sh}, \qquad\quad a_{\rm c}(t) < a < R_{\rm tr} \end{aligned} \tag{2.53}$$

where Lagrangian coordinate $a_{\rm c}(t)$ of the cooling fluid element, is determined from the condition that this element overtakes the shell at the moment t:

$$R_{\rm tr} - r(a_{\rm c}, t_{\rm tr}) = (v(a_{\rm c}, t_{\rm tr}) - V_{\rm sh})(t - t_{\rm tr}). \tag{2.54}$$

At the end of the transition stage, the coordinate $a_{\rm c}(t_{\rm sf}) = a_{\rm c,min}$ is found from the relation $r(a_{\rm c,min}, t_{\rm tr}) = r_{\rm min} = (1-\alpha)R_{\rm tr}$. By using equation (2.54) for the farthest cool gas element with the Eulerian coordinate $r_{\rm min}$, we can estimate more accurately the duration of the transition stage:

$$\Delta t = t_{\rm sf} - t_{\rm tr} = \frac{\alpha R_{\rm tr}}{(v(r_{\rm min}, t_{\rm tr}) - V_{\rm sh})}. \tag{2.55}$$

Let us calculate some parameters of the hot gas inside the shell. For some moment t, $t_{\rm tr} < t < t_{\rm sf}$, the velocity of the hot gas with $0 < a < a_{\rm c}(t)$ is determined by formula (2.54). So, for the Eulerian coordinate $r(a,t)$ we obtain

$$\begin{aligned} &r(a,t) = r(a,t_{\rm tr}) + v(a,t_{\rm tr})(t - t_{\rm tr}), \quad 0 < a < a_{\rm c}(t) \\ &r(a,t) = R_{\rm sh}, \qquad\qquad\qquad\qquad\quad a_{\rm c}(t) < a < R_{\rm tr}. \end{aligned} \tag{2.56}$$

The density distribution $\rho(a,t)$ is found from the continuity condition:

$$\rho(a,t_{\rm tr}) r(a,t_{\rm tr})^2 dr(a,t_{\rm tr}) = \rho(a,t) r(a,t)^2 dr(a,t). \tag{2.57}$$

It can be rewritten as

$$\rho(a,t) = \rho(a,t_{\rm tr}) \left(\frac{r(a,t_{\rm tr})}{r(a,t)}\right)^2 \frac{dr(a,t_{\rm tr})}{dr(a,t)}. \tag{2.58}$$

By taking into account that

$$dr(a,t) = dr(a,t_{\rm tr}) + \left(\frac{\partial v}{\partial r}\right)_{\rm t=t_{tr}} dr(a,t_{\rm tr})(t-t_{\rm tr}), \tag{2.59}$$

Eq. (2.58) may be re-written as

$$\rho(a,t) = \rho(a,t_{\rm tr}) \left(\frac{r(a,t_{\rm tr})}{r(a,t)}\right)^2 \left(1 + \left(\frac{\partial v}{\partial r}\right)_{\rm t=t_{tr}} (t-t_{\rm tr})\right)^{-1}. \tag{2.60}$$

For the distributions of the pressure and temperature of the hot gas, we obtain the relations

$$P(a,t) = P(a,t_{\rm tr}) \left(\frac{\rho(a,t)}{\rho(a,t_{\rm tr})}\right)^{\gamma}, \tag{2.61}$$

$$T(a,t) = \frac{\mu P(a,t)}{R_{\rm g}\rho(a,t)}. \tag{2.62}$$

Equations (2.53), (2.56), (2.60-2.62) provide a complete description of distribution of the hot gas inside the shell.

Thus, we suppose that, during the transition stage, every hot gas element moves with the velocity it had at the moment $t_{\rm tr}$. If there were no cool shell, the hot gas would occupy $0 < a < R_{\rm tr}$ in the Lagrangian and $0 < r < R_{\rm out}(t) = R_{\rm tr} + v_{\rm sw}(t_{\rm tr})(t-t_{\rm tr})$ in Eulerian coordinates, where $v_{\rm sw}(t) = (3/4)V(t)$ is the gas velocity immediately behind the shock. The cool shell, whose velocity $V_{\rm sh}$ is smaller than the hot-gas velocity, entrains those hot gas elements (layers) which overtake it during the transition stage. These are the layers with the Lagrangian coordinate lying in the range $a_{\rm c}(t_{\rm sf}) < a < R_{\rm tr}$. At the same time, the layers with $0 < a < a_{\rm c}(t)$ experience no influence of the shell at any moment from the range $t_{\rm tr} < t < t_{\rm sf}$. Sedov hot-gas velocity depends almost linearly on the Eulerian coordinate:

$$\frac{v(r,t)}{v_{\rm sw}(t)} = \frac{r}{R(t)} \tag{2.63}$$

Let us take into account the relation $\partial v/\partial r_{\rm (t=t_{tr})} = v_{\rm sw}(t_{\rm tr})/R_{\rm tr}$ in the equation (2.60) for the gas density. In the framework of this approximation, the hot-gas

parameters at the transition stage are described as

$$v(r,t) = v_{\rm sw}(t_{\rm tr}) \left(\frac{r}{R_{\rm out}(t)} \right) \tag{2.64}$$

$$r(a,t) = r(a,t_{\rm tr}) \left(\frac{R_{\rm out}(t)}{R_{\rm tr}} \right) \tag{2.65}$$

$$\rho(a,t) = \rho(a,t_{\rm tr}) \left(\frac{R_{\rm tr}}{R_{\rm out}(t)} \right)^3 \tag{2.66}$$

$$P(a,t) = P(a,t_{\rm tr}) \left(\frac{R_{\rm tr}}{R_{\rm out}(t)} \right)^{3\gamma} \tag{2.67}$$

$$T(a,t) = T(a,t_{\rm tr}) \left(\frac{R_{\rm tr}}{R_{\rm out}(t)} \right)^{3(\gamma-1)} \tag{2.68}$$

Thus, we adopted the approximation in which the hot gas freely expands during the transition stage and in which the gas velocity distribution is almost linear at the beginning. It allowed us to construct a simple analytical model for the homologic expansion of the hot gas. The resulting flow parameters are the power-law functions of time.

2.3.4. The cold gas of the shell. The shell mass $M_{\rm sh}(t) = M_{\rm sh,in}(t) + M_{\rm sh,out}(t)$ grows starting from the moment $t_{\rm tr}$ when the first cold element appears at the distance $R_{\rm tr}$. The mass of the interstellar gas swept up by the shell is

$$M_{\rm sh,out}(t) = 4\pi \int_{\rm R_{tr}}^{R_{\rm sh}} \rho_o a^2 da \tag{2.69}$$

and the mass of the cooled hot gas which was transferred to the shell is

$$M_{\rm sh,in}(t) = 4\pi \int_{\rm a_c(t)}^{R_{\rm tr}} \rho_o a^2 da \tag{2.70}$$

The temperature of the cool gas in the shell is equal to the initial temperature of the interstellar gas:

$$T_{\rm sh}(t) = T_{\rm ism} = 10^4 K \tag{2.71}$$

The cool-gas pressure is determined by the dynamic pressure of the interstellar gas:

$$P_{\rm sh} = P_{\rm dyn} = \rho_{\rm ISM} V_{\rm sh}^2, \tag{2.72}$$

Next, we use the equation of state

$$P_{\rm sh} = \left(\frac{R_{\rm gas}}{\mu}\right) \rho_{\rm sh} T_{\rm sh} = c_{\rm iso}^2 \rho_{\rm sh} \tag{2.73}$$

to calculate the cool-gas density:

$$\rho_{\rm sh} = \rho_{\rm ISM} \left(\frac{V_{\rm sh}}{c_{\rm iso}}\right)^2 = \rho_{\rm ISM} \mathcal{M}_{\rm iso}^2 \tag{2.74}$$

Here $c_{\rm iso} = T_{\rm sh} R_g/\mu$ is the isothermal sound velocity in ISM and $\mathcal{M}_{\rm iso}$ is the isothermal Mach number of the cool shell. The gas compression in the shell is

$$\rho_{\rm sh}/\rho_{\rm ISM} = 170 V_{\rm sh,2}^2 T_{\rm ISM,4}^{-1}, \tag{2.75}$$

where $V_{\rm sh,2}$ is the shell velocity in units 100 km/s and $T_{\rm ISM,4}$ is the shell temperature in 10^4 K. The shell thickness is

$$\Delta_{\rm sh}(t) = \frac{M_{\rm sh}(t)}{4\pi R_{\rm sh}^2 \rho_{\rm sh}} \sim \frac{R_{\rm sh}}{3M_{\rm iso}} \tag{2.76}$$

It is much smaller than the shell radius.

2.3.5. Flow parameters at the end of the transition stage. The transition stage ends at the moment $t_{\rm sf}$ when the hot gas inside the shell ceases to cool down and to enrich the shell. It is the moment when the radiative stage begins. The corresponding mass of the shell and the corresponding thermal energy and kinetic energy of the hot gas are

$$M_{\rm hot} = \frac{4}{3}\pi {R_{\rm tr}}^3 \rho_{\rm ISM} - M_{\rm sh,in}(t_{\rm sf}) \tag{2.77}$$

$$W_{\rm th,hot} = \frac{4\pi}{\gamma - 1} \int_0^{a_{\rm c}(t_{\rm sf})} P(a, t_{\rm sf}) a^2 da \tag{2.78}$$

$$W_{\rm kin,hot} = 2\pi \int_0^{a_{\rm c}(t_{\rm sf})} \rho(a, t_{\rm sf}) v^2(a, t_{\rm sf}) a^2 da \tag{2.79}$$

The hydrodynamical model of the transition stage becomes inadequate when the hot gas ceases to cool down. In this case the traditional thin-layer model is more appropriate. The rest of the hot gas inside the shell expands adiabatically and push the shell, whose mass grows due to ambient gas which is swept up by the shell [85, 266]. High temperature and large velocity of sound in the hot gas are believed

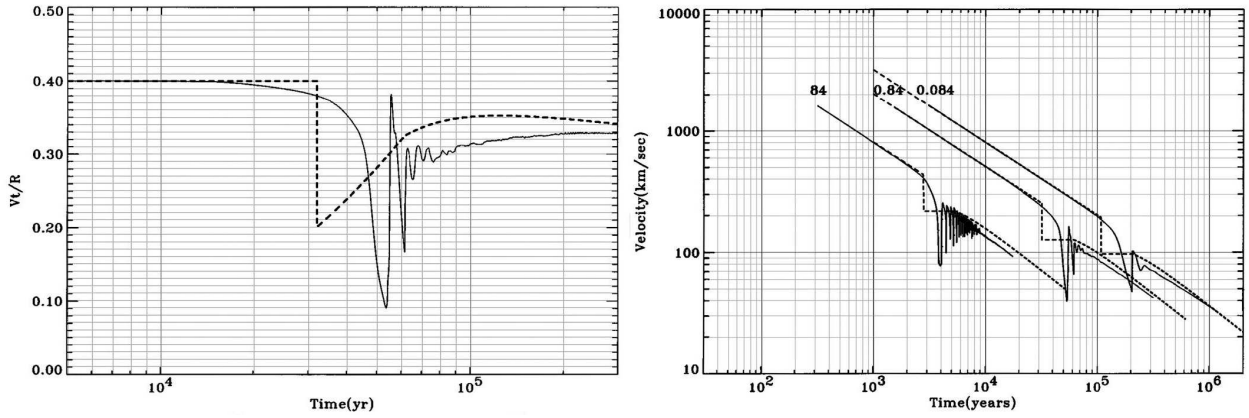

Figure 2.10. Evolution of the (a) deceleration parameter $m = Vt/R$ and (b) shock front velocity V for SNR (the explosion energy is 10^{51} erg) during the adiabatic, transition and radiative stages: dashed lines – our method, solid lines – numerical simulations from [90]. Numbers near the lines show ISM number densities.

to be the factors which are responsible for making the pressure uniform over the whole volume of the hot gas and for the gas expansion with a minor role of kinetic energy. The thin-layer condition is satisfied when the majority of the kinetic energy is transformed into thermal energy.

For simplicity we assume that these processes are instantaneous and that they take place at the moment $t_{\rm sf}$ of the transition to the radiative stage. In other words, we postulate that at the beginning of the radiative stage the thermal energy of the hot gas is equal to the sum of the thermal energy and kinetic energy of the hot gas at the end of the transition stage:

$$W_{\rm hot}(t = t_{\rm sf}) = W_{\rm th,hot} + W_{\rm kin,hot} \tag{2.80}$$

Then the average hot-gas pressure is

$$P_{\rm in}(t_{\rm sf}) = \frac{3(\gamma - 1)W_{\rm hot}(t_{\rm sf})}{4\pi {R_{\rm sh}}^3(t_{\rm sf})} \tag{2.81}$$

The method to describe the shell and the flow dynamics during the radiative stage is described in Sects. 2.4 and 2.5.

2.3.6. Accuracy of the method. We compared our model with the numerical simulations from [90, 114, 331]. Our approximate analytical treatment fits the results of numerical simulations with a sufficiently high accuracy (Figs. 2.10-2.12). So, our approach may be used to model the evolution of point explosion during the post-adiabatic stage.

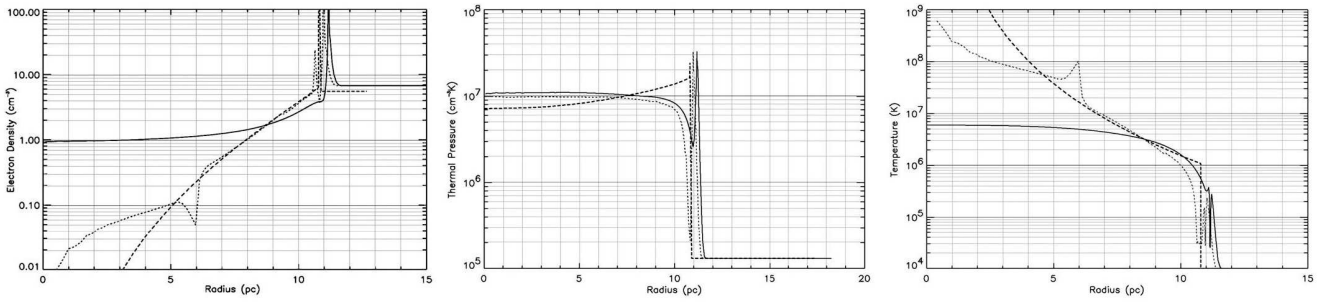

Figure 2.11. Radial distributions of (a) density, (b) pressure and (c) temperature inside SNR at the transition stage ($E_{\rm sn} = 10^{51}$ erg, $n_{\rm H} = 5.6\,{\rm cm}^{-3}$, $t = 20000\,{\rm yr}$): dashed lines – our method, dotted lines – numerical simulations from [331], solid lines – numerical simulations from [331] for the case of a significant heat conduction.

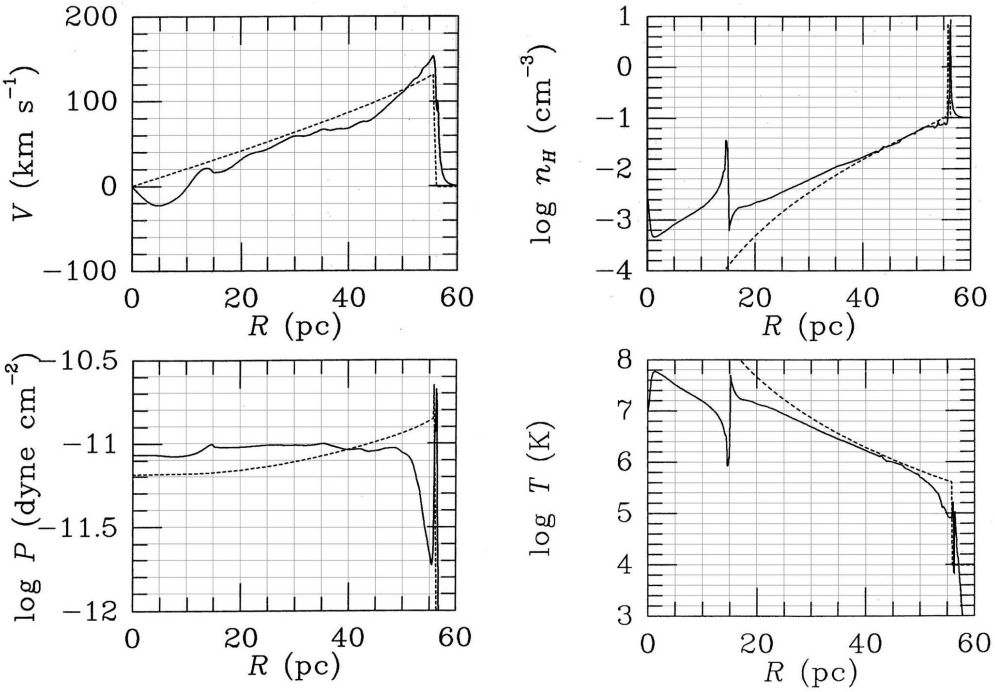

Figure 2.12. Radial distributions of (a) velocity, (b) density, (c) pressure and (d) temperature for SNR at the end of the transition stage ($E_{\rm sn} = 0.931 \cdot 10^{51}$ erg, $n_{\rm H} = 0.1\,{\rm cm}^{-3}$, $t = 170000\,{\rm yr}$): dashed lines – our method, solid lines – numerical simulations from [114].

2.4. Analytical solutions for dynamics of the radiative shock front

The adiabatic phase of SNR evolution (in a uniform and homogeneous medium) is well described by the Sedov [21] analytic solution, which reproduces both the SNR radial evolution and its inner structure. This exact solution has been made possible by the fact that during this phase the SNR evolution is self-similar. This is no longer the case when radiative losses become important, and therefore no exact analytic solution is known for the late SNR evolution.

Approximated solutions in the adiabatic regime and beyond may be also obtained using a "thin-shell" model (see e.g. [10, 266]). This approach assumes that the whole mass (and therefore kinetic energy) of SNR is located in a rather thin shell just behind the outer shock; while the inner region is filled with a very hot and rarefied gas, of negligible total mass, but containing most of the SNR internal energy.

For the adiabatic phase this approximation is only moderately accurate (see e.g. [10]). In fact, according to the Sedov solution the gas density vanishes in the inner regions while its pressure keeps finite; however, the outer layer containing most of the mass is geometrically rather thick. On the other hand, numerical works (e.g. [90, 147]) trace the formation of a much thinner shell in the radiative phase, therefore indicating that a thin-shell approximation should be far more accurate in describing the late evolution.

Oort [263] presented a first thin-shell approach to a radiative SNR expansion. By assuming momentum conservation in the shell, he found the SNR radius to evolve as $R \propto t^{1/4}$. This solution, also known as "momentum-conserving snowplow", assumes that cooling is extremely efficient everywhere (and therefore that the interior pressure vanishes). However, numerical models (e.g. [109]) show that, even in the radiative phase, the gas in the central regions becomes so rarefied that its cooling time still keeps considerably longer than the SNR age. This led McKee & Ostriker [247] to introduce a "pressure-driven snowplow" model, in which a fossil pressure in the hot interior has a substantial dynamical effect on the outer shell: in this case the radial evolution is $R \propto t^{2/7}$ (for adiabatic index $\gamma = 5/3$).

Even though the "pressure-driven snowplow" formula gets closer than the "momentum-conserving snowplow" one to the numerical results, some discrepancy still remains. For instance, by defining the "deceleration parameter" as $m = d \log R / d \log t$, numerical models obtain an asymptotic value ranging from 0.31 [109] to 0.33 [90]. These values are significantly different from the analytic value, 2/7 (namely 0.286), and various authors have discussed the origin of such discrepancy. Cioffi et al. [114] ascribe it to a "memory" of the previous Sedov phase, leading to an actual internal pressure larger than that derived from the analytic model. Blondin et al. [90], in-

stead, attribute this discrepancy to the influence of the reverse shock, which moves towards the center raising the thermal energy, thus leading to a milder deceleration.

Other authors have estimated analytically the radial evolution under more general conditions than those given above.

Ostriker & McKee [266] have shown that, for a general γ as well as a power-law ambient density profile ($\rho_{\rm a}(r) \propto r^{-\omega}$), $m = 1/(4-\omega)$ for a "momentum-conserving snowplow", while $m = 2/(2+3\gamma-\omega)$ for a "pressure-driven snowplow".

Liang & Keilty [229] have considered the case in which only a (constant) fraction ϵ of the kinetic energy of the incoming flow is radiated in the outer shock. For $\gamma = 5/3$, m is found to decrease quasi-linearly with ϵ, from 2/5 for the adiabatic case ($\epsilon = 0$) to 2/7 for the fully radiative case ($\epsilon = 1$); and a value of ϵ of about 0.8 (0.6) is required in order to obtain $m = 0.31$ (0.33), as indicated by the numerical models. However, while $\epsilon < 1$ may be appropriate to describe gamma-ray burst afterglows [116], SNR radiative shocks should be described as fully radiative ones (namely with ϵ very close to unity).

The effect of cooling in the hot interior on the deceleration parameter has been studied by Gaffet [160], with the following results. Adiabaticity holds throughout most of the volume occupied by the hot gas, while cooling occurs only near the boundary with the radiative shell, giving as effect a net mass transfer from the hot interior to the shell. Assuming that the gas in the hot interior follows a cooling law $\Lambda \propto T^{-c}$, this section discusses different regimes for different choices of γ and c, showing that the asymptotic value of m must be in the range between the values 1/4 (Oort limit) and $2/(2+3\gamma)$ (McKee and Ostriker limit).

When $c > (2/3)(5\gamma-8)/(3-2\gamma)$ ($c > -2/3$ for $\gamma = 5/3$) the asymptotic value of m is 1/4. This is the case for cooling functions typical of the SNR regime, where $c > 0$ and is usually taken in the range from 0.5 (e.g. [114]) to 1.0 [90]. Therefore, according to this result, after the commonly known radiative phase there could be a very late evolutive phase, in which radiative losses of hot interior become to be prominent and the SNR evolves as "momentum-conserving snowplow". However, as it may be derived from numerical results, in a typical SNR, radiative cooling of the

hot interior is negligible until very late times. Therefore the onset of the "momentum-conserving snowplow" regime should occur only near the end of a SNR lifetime, or not to occur at all.

A common limitation of all above-mentioned analytical models is that the radial evolution of the radiative shock has been approximated by a power-law behaviour $R \propto t^m$ (with constant m). This allows a simplified treatment of radiative SNR evolution; however, it is natural to expect that a power-law expansion occurs only at late times (i.e. at large R values), after the transition from adiabatic to radiative expansion has been completed.

In this subsection we show: 1) that the quoted difference between the numerical and asymptotic analytic value is just a consequence of the fact that the time needed to reach the asymptotic power-law regime is long compared with the age of the SNR; 2) that the SNR radial evolution during that phase is adequately described by a thin-shell model; 3) that a general analytic solution of this problem exists.

2.4.1. Equations and solutions for a general adiabatic index. Let us consider a fully radiative shock expanding into a uniform medium and neglect the cooling of the hot interior. In the thin-shell approximation, mass, momentum, and central pressure evolution are described by the following set of equations:

$$\frac{dM}{dt} = 4\pi\rho_{\rm a}R^2\dot{R}, \tag{2.82}$$

$$\frac{d(M\dot{R})}{dt} = 4\pi P R^2, \tag{2.83}$$

$$\frac{dP}{dt} = -3\gamma P\frac{\dot{R}}{R}, \tag{2.84}$$

where R and $\dot{R}$ are respectively shock radius and velocity, M is the mass of the radiative shell, P is the pressure of the (adiabatically evolving) inner region, γ is the adiabatic coefficient, and $\rho_{\rm a}$ is the (constant) density of the ambient medium.

The above equations can be reduced to a single one:

$$\ddot{R} + \frac{3\dot{R}^2}{R} = \frac{3P_{\rm o}R_{\rm o}^{3\gamma}}{\rho_{\rm a}}R^{-3\gamma-1}, \tag{2.85}$$

where the quantities $R_{\rm o}$ and $P_{\rm o}$ indicate respectively the SNR radius and the pressure

of the hot cavity at a reference time ($t_{\rm o}$), that can be arbitrarily chosen.

In order to solve analytically Eq. (2.85) for a general value of γ (with the condition $1 < \gamma < 2$) let us first define the quantity:

$$K = \frac{2}{2-\gamma}\frac{PR^{3\gamma}}{\rho_{\rm a}}. \tag{2.86}$$

K is constant in time, and therefore it can be evaluated in terms of quantities at the time $t_{\rm o}$. By using the substitution $w(R) = \dot{R}^2$, Eq. (2.85) trasforms into:

$$\frac{dw}{dR} + 6\frac{w}{R} = 3(2-\gamma)KR^{-3\gamma-1}, \tag{2.87}$$

that is a linear differential equation and can then be easily integrated. Its general solution is:

$$w = K(R^{-3\gamma} - HR^{-6}), \tag{2.88}$$

where the constant H is, at any time, equal to:

$$H = R^{3(2-\gamma)}\left(1 - \frac{(2-\gamma)\rho_{\rm a}}{2P}\dot{R}^2\right). \tag{2.89}$$

In particular, it may be expressed in terms of quantities at the time $t_{\rm o}$. Depending on the sign of H, there are two different branches of solutions. By evaluating the kinetic energy of the shell and the thermal energy of the inner hot bubble respectively as:

$$E_{\rm kin} = \frac{4\pi R^3}{3}\frac{\rho_{\rm a}\dot{R}^2}{2}, \tag{2.90}$$

$$E_{\rm th} = \frac{4\pi R^3}{3}\frac{P}{\gamma-1}, \tag{2.91}$$

Eq. (2.89) shows that, in the two branches, the energy ratio $\kappa = E_{\rm kin}/E_{\rm th} = (\gamma - 1)\rho_{\rm a}\dot{R}^2/2P$ is respectively less (H-positive case) and greater (H-negative case) than $(\gamma-1)/(2-\gamma)$, and that time evolution does not change the sign of this inequality.

Let us label these two branches of solutions as "slow" and "fast", depending whether the kinetic energy is respectively less (H positive case) or greater (H negative case) than $(\gamma-1)E_{\rm th}/(2-\gamma)$; or, equivalently, less or greater than $(\gamma-1)E_{\rm tot}$ (where $E_{\rm tot} = E_{\rm kin} + E_{\rm th}$). The choice of the appropriate branch of solutions only depends on the initial conditions.

Although in the next subsection we shall see that the slow case is that physically relevant for the SNR evolution, let us discuss here both branches. When double signs are shown, in some of the following equations, the convention used is that the upper sign refers to the slow branch, while the lower sign to the fast branch. Once defined space and time scale units as

$$\tilde{R} = (\pm H)^{1/3(2-\gamma)}; \tag{2.92}$$

$$\tilde{t} = (\pm H)^{(2+3\gamma)/6(2-\gamma)} K^{-1/2}, \tag{2.93}$$

and introduced the dimensionless space and time coordinates $r = R/\tilde{R}$, $\tau = t/\tilde{t}$, the evolution in size follows the equation:

$$\frac{dr}{d\tau} = \sqrt{r^{-3\gamma} \mp r^{-6}}, \tag{2.94}$$

that can be integrated to give $\tau(r)$. The dimensional velocity is obtained multiplying $dr/d\tau$ by the velocity scale $\tilde{V} = \tilde{R}/\tilde{t}$. It is evident that, while fast solutions extend to all positive values of r, solutions in the slow branch are real only for $r \geq 1$.

For a general value of γ, the solution involves hypergeometric functions (F), and can be written as:

$$\begin{aligned} \tau_{\rm F}(r) = & \frac{r^4}{4} F\left(\frac{1}{2}, \frac{4}{3(2-\gamma)}, 1 + \frac{4}{3(2-\gamma)}; -r^{3(2-\gamma)}\right) \\ & -\frac{1}{4} F\left(\frac{1}{2}, \frac{4}{3(2-\gamma)}, 1 + \frac{4}{3(2-\gamma)}; -1\right) + C \end{aligned} \tag{2.95}$$

for the fast branch, and as:

$$\begin{aligned} \tau_{\rm S}(r) = & \frac{ir^4}{4} F\left(\frac{1}{2}, \frac{4}{3(2-\gamma)}, 1 + \frac{4}{3(2-\gamma)}; r^{3(2-\gamma)}\right) \\ & -\frac{i}{4} F\left(\frac{1}{2}, \frac{4}{3(2-\gamma)}, 1 + \frac{4}{3(2-\gamma)}; 1\right) + C \end{aligned} \tag{2.96}$$

for the slow branch. The time evolution of the SNR radius is obtained by inverting the above equations. Note that individual terms in Eq. (2.96) are complex, but when $r \geq 1$ their imaginary parts cancel out. Eqs. (2.95) and (2.96) contain an arbitrary constant, C; both equations have been written here in such a way that $C = \tau(1)$.

A quantity useful to describe the evolution is the deceleration parameter m. The general formula for this quantity is rather complex, but its asymptotic behaviour at

large values of r may be evaluated as:

$$m(r) = \frac{2}{2+3\gamma} \pm \frac{6(2-\gamma)}{(9\gamma-10)(2+3\gamma)} r^{-3(2-\gamma)} + \mathcal{O}\left(r^{-6(2-\gamma)}\right). \tag{2.97}$$

This power expansion is valid in the range $10/9 < \gamma < 2$. Note that the limit $2/(2+3\gamma)$ is the same found by Ostriker and McKee [266].

In terms of the dimensionless quantity r, the ratio of kinetic and thermal energies is:

$$\kappa = \frac{\gamma-1}{2-\gamma}\left(1 \mp r^{-3(2-\gamma)}\right). \tag{2.98}$$

Therefore at late times the asymptotic value of this ratio is $\kappa_{\rm as} = (\gamma-1)/(2-\gamma)$ for both branches.

The ratio between internal and shock pressure is:

$$\frac{P}{P_{\rm s}} = \frac{(\gamma-1)(\gamma+1)}{4\kappa} = \frac{(2-\gamma)(\gamma+1)}{4(1 \mp r^{-3(2-\gamma)})}, \tag{2.99}$$

then leading to the asymptotic value $(2-\gamma)(\gamma+1)/4$.

The total energy follows the evolutive law:

$$E_{\rm tot} = \tilde{E} r^3 \left(\frac{r^{-3\gamma}}{\gamma-1} \mp r^{-6}\right). \tag{2.100}$$

where $\tilde{E} = 2\pi\rho_{\rm a}\tilde{V}^2\tilde{R}^3/3$. It is easy to show that, in the range of validity of the solutions, $dE_{\rm tot}/dr$ is always negative, as expected for a radiative solution.

Finally, it can be shown that the original Oort [263] solution, $R \propto t^{1/4}$, is just a special case of the fast-branch solution. Neglecting the pressure effect leads the right side of Eq. (2.85) to vanish. Since $P = 0$ implies the energy ratio κ to diverge (and therefore to be larger than $(\gamma-1)/(2-\gamma)$), the solution must belong to the fast branch. From Eq. (2.88) it is apparent that K is required to vanish, while $H \to -\infty$, in such a way that the product $-KH$ be equal to $R^6\dot{R}^2$ (being this a constant, it can be then evaluated in terms of $R_{\rm o}$ and $\dot{R}_{\rm o}$). Using Eqs. (2.92) and (2.93), it can be shown that both $\tilde{R}$ and $\tilde{t}$ diverge, so that this solution must be limited to vanishingly small r and τ values. Therefore Eq. (2.94) simplifies into $dr/d\tau = r^{-3}$, which admits the solution $\tau(r) = r^4/4 - 1/4 + C$, where we have defined $C = \tau(1)$ for consistency with the formulation given in Eq. (2.95). For $C = 1/4$, which means

$\tau(0) = 0$, we simply have $\tau(r) = r^4/4$ that, when inverted, gives the Oort's law $r \propto t^{1/4}$. The same result can be extracted from the general solution, Eq. (2.95), by using the fact that $F(a, b, c; x) \to 1$ when $x \to 0$.

2.4.2. The slow branch of solutions for gamma=5/3. In the standard case $\gamma = 5/3$, Eqs. (2.95) and (2.96) get a much simpler functional dependence, respectively:

$$\tau_{\rm F}(r) = \frac{2}{35}\sqrt{r+1}(5r^3 - 6r^2 + 8r - 16) + \frac{18\sqrt{2}}{35} + C, \tag{2.101}$$

$$\tau_{\rm S}(r) = \frac{2}{35}\sqrt{r-1}(5r^3 + 6r^2 + 8r + 16) + C, \tag{2.102}$$

where again we use $C = \tau(1)$.

The deceleration parameter m, for the two branches, evaluates:

$$m_{\rm F}(r) = \frac{2}{35}\frac{r+1}{r^4}(5r^3 - 6r^2 + 8r - 16) + \frac{\sqrt{r+1}}{r^4}\left(C + \frac{18}{35}\sqrt{2}\right), \tag{2.103}$$

$$m_{\rm S}(r) = \frac{2}{35}\frac{r-1}{r^4}(5r^3 + 6r^2 + 8r + 16) + \frac{\sqrt{r-1}}{r^4}C. \tag{2.104}$$

The asymptotic behaviour at large values of r is:

$$m(r) = \frac{2}{7} \pm \frac{2}{35r} + \mathcal{O}\left(\frac{1}{r^2}\right) \tag{2.105}$$

(which is consistent with the more general Eq. (2.97)). Therefore, for r approaching to infinity, in both branches m tends to the value 2/7, namely to the asymptotic solution given by McKee and Ostriker [247]. However, an analysis of Eqs. (2.103) and (2.104) show different properties for the two branches. In particular, only in the slow branch $m(r)$ shows a local maximum. In a given solution, the position of the maximum and the value reached by m are related by:

$$m_{\rm max} = \frac{2(r_{\rm max} - 1)}{7r_{\rm max} - 8}, \tag{2.106}$$

valid for $r_{\rm max} > 8/7$. Therefore, $m_{\rm max}$ is always larger than 2/7 for any solution in the slow branch, and it can be considerably larger than 2/7, if $r_{\rm max}$ gets close to 8/7. Furthermore, if during its evolution $m(r)$ is larger than 2/7 and still increasing

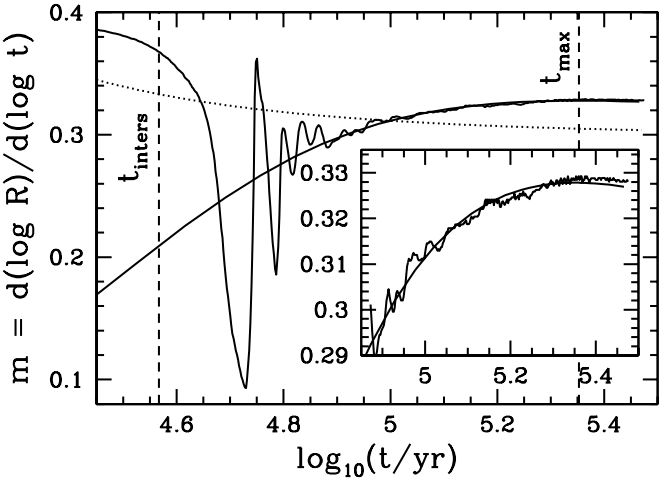

Figure 2.13. Our best fit solution (slow branch, $C = -0.248$, $\tilde{t} = 3.64 \times 10^4\,\mathrm{yr}$) compared with numerical data from [90]. The small frame shows just the data used for the fit. With the exception of strong oscillations in the early transient, the analytic solution closely describes also the evolution at earlier times. Dashed lines indicate the positions of $t_{\max}$ and t_{inters}, while the dotted line is obtained by using the analytic fit by Cioffi et al. [114].

with r, it must reach a maximum before approaching the asymptotic value $2/7$, and then it must belong to the slow branch. This is what shown by Blondin et al. [90] (their Fig. 3, actually limited to the increasing part): therefore in the following we shall consider only the slow branch of solutions.

2.4.3. Most appropriate initial conditions. Let us use the numerical results from [90] to determine the most appropriate parameters for our analytic solution. For the fit we use the evolution of m (Fig. 3 in [90]), excluding the oscillatory transient: the numerical data fitted are for times ranging from 7.4×10^4 till $3.0 \times 10^5\,\mathrm{yr}$. The best (least-square) fit is obtained for $C = -0.248 \pm 0.006$; while the time scale inferred from this fit allows us to fix $\tilde{t} = (3.64 \pm 0.05) \times 10^4\,\mathrm{yr}$ (for all best fit quantities, here we also indicate their 1-σ error). In Fig. 2.13, the best fit curve is shown against the numerical data. The best fit curve reaches its maximum value ($m_{\max} = 0.328$) at $r_{\max} = 2.11$ (i.e. at $\tau_{\max} = 6.18$). Moreover, using Fig. 8 (velocity evolution) from the [90], we derive $\tilde{R} = 17.6 \pm 0.1\,\mathrm{pc}$. From these quantities, the dimensional scaling for energy is $\tilde{E} = (1.51 \pm 0.07) \times 10^{51}\,\mathrm{erg}$.

The numerical simulation we refer to corresponds to the following basic physical parameters: energy of the explosion, $E_{51} = 1$ (in units of $10^{51}\,\mathrm{erg}$); and hydrogen ambient density, $n_{\mathrm{a}} = 0.84\,\mathrm{cm}^{-3}$. Adopting the same definitions of Blondin et al. [90]

for the transition time, and corresponding SNR radius

$$t_{\rm tran} \approx 2.9 \times 10^4 E_{51}^{4/17} n_{\rm a}^{-9/17} \, {\rm yr}, \tag{2.107}$$

$$R_{\rm tran} \approx 19.1 E_{51}^{5/17} n_{\rm a}^{-7/17} \, {\rm pc}, \tag{2.108}$$

we determine the dimensionless quantities $\tilde{t}/t_{\rm tran} = 1.14$ and $\tilde{R}/R_{\rm tran} = 0.85$. All these quantities, although obtained after the comparison with a specific numerical simulation, can be taken of general validity, for a SNR expanding in a homogeneous medium, because the analytic solutions allow scaling.

Fig. 2.13 shows also (dotted curve) the analytic fit as derived from Cioffi et al. [114]. Cioffi et al. [114] use a different cooling function from that of Blondin et al. [90], whose simulation is shown in Fig. 2.13. Therefore in Cioffi et al. [114] the functional dependence of time and length scales on parameters of a model are different from those given in Eqs. (2.107) and (2.108). In order to compare our results with Cioffi et al. [114] analytic fit, we have evaluated the scaling time $t_{\rm tran}$ (labelled as $t_{\rm PDS}$ in their Eqs. (3.10) and (3.11)), using $E_{51} = 1$ and $n_{\rm a} = 0.84 \, {\rm cm}^{-3}$ (with solar abundances), obtaining $t_{\rm tran} = 14670 \, {\rm yr}$. The formula used for the deceleration parameter is $m = 0.3/(1 - t_{\rm tran}/4t)$, as derived from Eqs. (3.32) and (3.33) in that paper. It is apparent, from Fig. 2.13, that Cioffi et al. [114] fit does not trace the evolution of the deceleration parameter m.

Since the evolution of the SNR radius is a continuous function of time, let us compute the time at which the radiative solution intersects the Sedov one. With the parameters given above, it happens at $t_{\rm inters} = 1.16 t_{\rm tran}$ (when $R_{\rm inters} = 1.06 R_{\rm tran}$), namely, using our dimensionless variables, at $\tau_{\rm inters} = 1.01$ (with $r_{\rm inters} = 1.24$). At this time, the SNR kinetic, Eq. (2.90), and thermal, Eq. (2.91), energies are respectively $E_{\rm kin} = 0.191 \times 10^{51} \, {\rm erg}$ and $E_{\rm th} = 0.489 \times 10^{51} \, {\rm erg}$, equivalent to a total energy $E_{\rm tot} = 0.680 \times 10^{51} \, {\rm erg}$, and to an energy ratio $\kappa = 0.390$.

Nicely, although fortuitously, at $t_{\rm inters}$ the value of τ is very close to unity, while that of κ is very close to the Sedov value ($\kappa_{\rm Sed} = 0.394$). We could then use $\tau_{\rm o} = 1$ and $\kappa_{\rm o} = \kappa_{\rm Sed}$ as an approximate criterion, from which to derive, analytically, that: 1) the solution must belong to the slow branch, since $\kappa_{\rm o} < \kappa_{\rm as}$; 2) $r_{\rm o}$ and $m_{\rm o}$,

evaluated using the relatioships:

$$r_{\rm o} = 2/(2-\kappa_{\rm o}), \tag{2.109}$$

$$m_{\rm o} = \tau_{\rm o}(2-\kappa_{\rm o})^{7/2}\kappa_{\rm o}^{1/2}/16, \tag{2.110}$$

are respectively $r_{\rm o} \simeq 1.245$ and $m_{\rm o} \simeq 0.206$; 3) C, evaluated using Eq. (2.102), is $\simeq -0.272$ (to be compared with the best fit value -0.248).

2.4.4. Comparison with previous results. Using a thin-shell approach, we have developed the analytic treatment for the evolution of a shock front in SNR in the radiative phase, and we have also obtained a series of interesting relations. The main findings of the present work are the following.

The discrepancy between the analytic prediction of the asymptotic value of the deceleration parameter ($m = 2/7$ [247]) and that derived numerically ($m = 0.33$, [90]) is only apparent. This discrepancy has been attributed to the presence of a reverse shock moving towards the center. We show, instead, that a thin-shell model, that by definition does not contain any information on inner structure details, closely fits the SNR evolution as derived numerically.

We confirm that 2/7 is the correct asymptotic value, even though the convergence towards this value is expected to be slow. We believe that, if Blondin et al. [90] numerical simulation had been runned until later stages of the SNR evolution, it would have shown that m does not keep constant to 0.33, but eventually decreases. This has been already pointed out by Chevalier [109] and can be seen in Fig. 5 of Cioffi et al. [114], in Fig. 3 of Falle [148], and in Fig. 4b of Mansfield & Salpeter [241]. However, the convergence to the asymptotic value may need times longer than the SNR lifetime.

It might be expected that the evolution will eventually change from a "pressure-driven snowplow" ($m = 2/7$, McKee and Ostriker [247]) to a "momentum-conserving snowplow" ($m = 1/4$, Oort [263]), as a consequence that the right side of Eq. (2.85) vanishes when $R \to \infty$. However, Cioffi et al. [114] have noted that, even at very late times ($\sim 10^2 t_{\rm tran}$), the deceleration parameter m is still closer to 2/7 than to 1/4. We have shown that such evolutive transition may in fact not occur, because

the two kinds of evolution are associated with two different branches of solutions, corresponding to different initial conditions. In other words, for a deceleration parameter smaller than 2/7, the right side of Eq. (2.85) (with $\gamma = 5/3$) vanishes more slowly than the left side. Therefore, unless the pressure term is negligible from the beginning, or part of the internal energy of the hot interior is lost by other channels (e.g. by electron conduction, or radiative processes), pressure effects must play an important role in the evolution at any time, until the SNR merges with the ambient medium.

Some of the conclusions we have presented here could have been reached long before. In fact, Blinnikov et al. [89] as well as Pasko and Silich [269] have obtained a solution equivalent to our Eq. (2.102). However, they have not discussed the properties of this solution to larger extend.

2.5. Approximate analytical method for description of the flow downstream of the radiative shock

In our previous works [7, 195], a new approximate analytical method for description of the *adiabatic* flow behind the shock from the strong point explosion in a medium with arbitrary large-scale density gradient was developed. In Sect. 2.3, it was extended to the *post-adiabatic* phase in evolution of such shock. In the present section, the method is generalized to the *radiative* stage.

2.5.1. Equations for the radiative hydrodynamics. System of equations for radiative hydrodynamics are following [12]:

$$\frac{\partial \rho}{\partial t} + \frac{1}{r^N}\frac{\partial}{\partial r}(r^N \rho u) = 0, \tag{2.111}$$

$$\frac{\partial u}{\partial t} + u\frac{\partial u}{\partial r} + \frac{1}{\rho}\frac{\partial P}{\partial r} = 0, \tag{2.112}$$

$$\frac{\partial E}{\partial t} + u\frac{\partial E}{\partial r} - \frac{P}{\rho^2}\left(\frac{\partial \rho}{\partial t} + u\frac{\partial \rho}{\partial r}\right) = \Gamma(\rho, T) - \Lambda(\rho, T)/\rho, \tag{2.113}$$

where unknown functions – density of gas ρ, pressure P, temperature T, internal energy (in terms of unit mass) E and velocity u – depend on time t and spatial coordinate r, $N = 0, 1, 2$ for plane, cylindrical and spherical flows respectively, functions $\Gamma(\rho, T)$ and $\Lambda(\rho, T)$ describe respectively heating and cooling of gas. The role of energy losses due to radiation (function Λ) is the main factor which affects model presented in this subsection. Three equations (2.111)-(2.113) are completed with equation of state for ideal gas $P = \rho AT$ where $A = R_g/\mu$, R_g the universal constant, μ the molar mass, and with equation for energy $E = (\gamma - 1)^{-1} P/\rho$ where γ is the adiabatic index.

We also use Lagrangian form of the system (2.111)-(2.113), where thermodynamic functions and coordinate of the gas element depend on time t and initial coordinate a: $r = r(a, t)$, $\rho = \rho(a, t)$, $P = P(a, t)$, $T = T(a, t)$, $E = E(a, t)$ and

$$\frac{\partial \rho}{\partial t} + \frac{\rho^2}{\rho^o} \left(\frac{r}{a}\right)^N \frac{\partial u}{\partial a} + \frac{N u \rho}{r} = 0, \tag{2.114}$$

$$\frac{\partial u}{\partial t} + \frac{1}{\rho^o} \left(\frac{r}{a}\right)^N \frac{\partial P}{\partial a} = 0, \tag{2.115}$$

$$\frac{\partial E}{\partial t} - \frac{P}{\rho^2} \left(\frac{\partial \rho}{\partial t}\right) = \Gamma - \Lambda/\rho, \tag{2.116}$$

$$\frac{\partial r}{\partial t} - u = 0. \tag{2.117}$$

Here $\rho^o = \rho^o(a)$ is the ambient density distribution. We consider spherical shocks (i.e. $N = 2$) thereafter.

Thin shell is formed since $t_{\rm sf}$; its motion is forced by the pressure of hot gas inside. All approximate methods are based on "thin-layer" approximation, where the thickness of the shell is negligible, and pressure is considered to be uniform inside the shell ([11,85] and references therein); distribution of parameters – density, pressure, gas velocity – are not calculated. Let us consider a method which gives fill description of plasma flow on radiative stage. It consists of two parts: calculations of the shock dynamics and distribution of parameters downstream.

2.5.2. Dynamics of the radiative shock in nonuniform media. Let us describe the shell by average values: velocity $V_{\rm sh}$, density $\rho_{\rm sh}$, mass $M_{\rm sh}$. Hot gas

inside the region $0 < a < R_{\rm sf}$ pushes the thin (with thickness $\Delta_{\rm sh} \ll R$) cooled due to radiative losses shell, with coordinates $a > R_o$. Gas in the shell quickly cools down till the temperature $T_{\rm sh} \sim 10^4$ K, the shock velocity and radius become approximately equal to velocity and radius of the shell. Average pressure in the hot region is calculated as

$$P_{\rm hot} = \overline{P}(r,t) = \frac{\varepsilon(t)(\gamma-1)}{4\pi R(t)^3/3}, \tag{2.118}$$

where $\varepsilon(t)$ is the full (kinetic plus thermal) energy of the hot gas at time t, it is smaller than initial explosion energy E_o on the value of work done for moving the shell $\int P_{\rm hot} dV$.

In the assumed approximation, equations for the shell dynamics in nonuniform medium with 1-D density distribution $\rho(\vec{r}) = \rho(r)$ may be obtained from (2.82)-(2.84) substituting constant $\rho_{\rm a}$ with $\rho_{\rm o}(r)$.

In case of uniform ambient medium, the dynamics of the shell is given by the analytical solution of this system (Sect. 2.4), in case of nonuniform medium with the power-law density distribution by the solution we derived in [15] (cf. [269]).

2.5.3. The cold gas of the shell. Known shell dynamics allows us to find average parameters of gas inside the shell in a way similar to the post-adiabatic stage (Sect. 2.3). Pressure in the shell is determined by the equality of the thermal pressure $P_{\rm sh}$ and dynamical pressure of incoming gas:

$$P_{\rm sh} = \rho_o(R_{\rm sh}) V_{\rm sh}^2. \tag{2.119}$$

Temperature in the shell is of order of the temperature of the unperturbed gas $T_{\rm sh} = 10^4$ K. Density in the shell may be found from $P = \rho A T$:

$$\rho_{\rm sh} = \frac{\mu P_{\rm sh}}{R_g T_{\rm sh}} = \frac{\mu V_{\rm sh}^2}{R_g T_{\rm sh}} \rho_o(R_{\rm sh}) = \frac{V_{\rm sh}^2}{c_{\rm iso}^2} \rho_o(R_{\rm sh}) = \mathcal{M}^2 \rho_o(R_{\rm sh}). \tag{2.120}$$

Thickness of the shell $\Delta_{\rm sh}$ may be determined from known shell mass $M_{\rm sh}$

$$\Delta_{\rm sh} = \frac{M_{\rm sh}}{4\pi R_{\rm sh}^2 \rho_{\rm sh}}. \tag{2.121}$$

2.5.4. The hot gas inside the shell. The hot gas flow parameters cannot be found in the traditional thin-layer approximation (except for the volume-average

pressure $P_{\rm in}$). At the same time, our approach (which is based on the simultaneous use of the Lagrangian and Eulerian descriptions) is applicable for estimating the flow parameters at the radiative stage. Since the hot-gas velocity is zero at the SNR center and is equal to the shell velocity $V_{\rm sh}(t)$ at the outer boundary of the remnant, we can assume that the hot-gas velocity depends linearly on distance:

$$v(r,t) = V_{\rm sh}(t)(r/R_{\rm sh}(t)), 0 < r < R_{\rm sh} \tag{2.122}$$

We operated with the similar relation in the case of the transition stage (Sect. 2.3.3), but the velocity amplitude was larger. A decrease in the velocity amplitude is caused by the transformation of the kinetic energy into the thermal energy in the backward shock. Linear relation (2.122) describes the homological expansion of the hot gas, as in the case of the transition stage. Expressions for the flow parameters are derived in the same way as formulas (2.65)-(2.68):

$$r(a,t) = r(a,t_{\rm sf})\left(\frac{R_{\rm sh}(t)}{R_{\rm sf}}\right) \tag{2.123}$$

$$\rho(a,t) = \rho(a,t_{\rm sf})\left(\frac{R_{\rm sf}}{R_{\rm sh}(t)}\right)^3 \tag{2.124}$$

$$P(a,t) = P(a,t_{\rm sf})\left(\frac{R_{\rm sf}}{R_{\rm sh}(t)}\right)^{3\gamma} \tag{2.125}$$

$$T(a,t) = T(a,t_{\rm sf})\left(\frac{R_{\rm sf}}{R_{\rm sh}(t)}\right)^{3(\gamma-1)} \tag{2.126}$$

Equations (2.122)-(2.126) give full description of the hot gas inside the thin cold shell; it is determined in any time $t > t_{\rm sf}$ by the initial state of the system at the time $t_{\rm sf}$ and by motion law for the shell $R_{\rm sh}(t)$.

Full description of the radiative stage includes also equations (2.82)-(2.84), with $\rho_{\rm o}(r)$ instead constant $\rho_{\rm a}$, for shell dynamics $R_{\rm sh}(t)$ and equations (2.119)-(2.121) for parameters inside the shell.

2.5.5. Accuracy of the method. Let us consider accuracy of the proposed method comparing it with numerical calculations for case of uniform ISM. Accuracy of our description of the shell dynamics is demonstrated in Sect. 2.4 where an analytical solution is compared with detailed calculations. Approximate distributions of

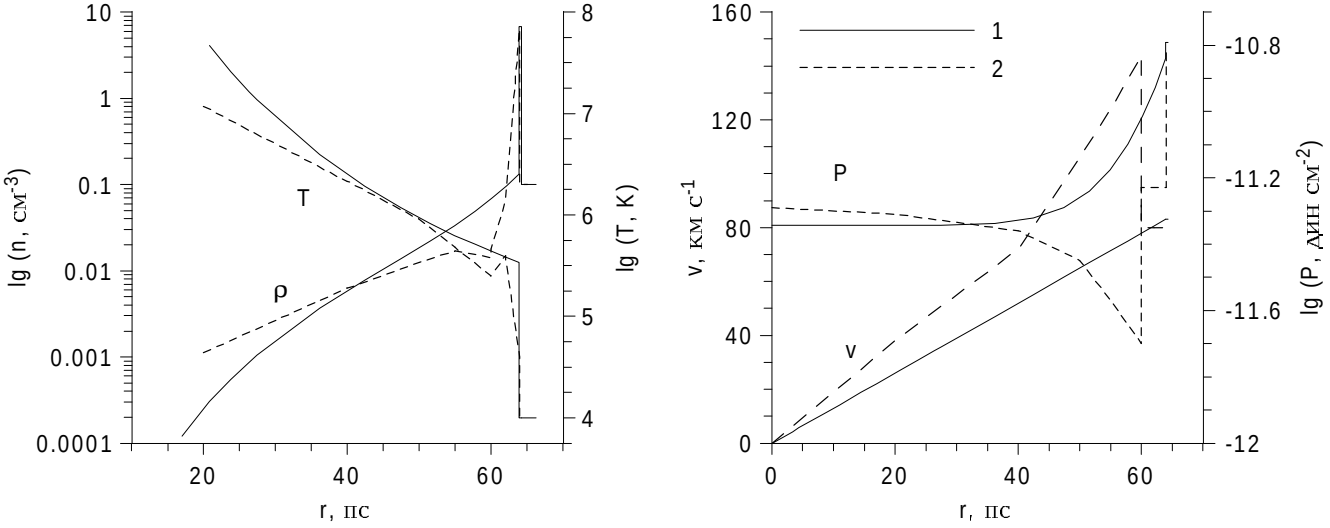

Figure 2.14. Distribution of gas parameters downstream of the shock. Method (lines marked with 1), numerical calculations [114] (lines marked with 2). Spherical explosion, $\gamma = 5/3$, $E_o = 0.931 \cdot 10^{51}$ erg, $n_o = 0,1$ cm^{-3}, $t = 2.5 \cdot 10^5$ yr $= 3.3 t_{\rm sf}$.

characteristics of the hot gas are compared with the numerical simulations from [114] on Fig. 2.14. Figure demonstrate high enough accuracy of the method that allows one to use it for modeling the real objects.

2.6. Conclusions

Chapter 2 is devoted to hydrodynamic description of flows with strong nonrelativistic shocks, in particular, approximate analytical methods for description of the shock front and plasma flow are developed. They may be used in cases of uniform and nonuniform ISM, after the time when deviation from the condition of adiabaticity becomes to be effective. In addition, a new model for morphological class of SNRs, namely, the thermal X-ray composites, is presented. It bases on an idea about the motion of adiabatic shock in ISM with strong gradient of density.

1. Considering 2-D or 3-D models of SNRs it is necessary to take into account the effects of projection. Once projected onto the plane of the sky, such an object changes its appearance depending on the actual density contrast across the remnant and on the angle between the density gradient and the direction towards the observer. A new possibility to explain the nature of thermal X-ray composites, i.e. a class of

SNRs with a thermal X-ray centrally-filled morphology within a radio shell, as a projection effect of the 2- or 3-dimensional shell-like SNR evolved in a nonuniform medium with scale-height $\leq 10\,\mathrm{pc}$ is proposed. Theoretical properties of a shell-like SNR evolved at the edge of a molecular cloud correspond to the observed properties of TXCs if the gradient of the ambient density does not lie in the projection plane and the magnetic field is nearly aligned with the line of sight. So, at least a part of objects from the class may be interpreted within the framework of the considered effect.

2. Different reference times which appear in the description of transition of a strong adiabatic shock into the radiative era are reviewed. The need for consideration of an additional transition phase in between the end of the adiabatic era and the beginning of the radiative "pressure-driven snowplow" stage for a shock running in the uniform or nonuniform medium is emphasized. This could be of importance in particular for studying of the interaction of supernova remnants with molecular clouds and therefore for understanding the processes of the cosmic ray production in such systems. The duration of this subphase – about 70% of SNR age at its beginning – is almost independent of the density gradient for media with increasing density and is longer for higher supernova explosion energy and for smaller density in the place of explosion: $t_{\mathrm{tr}} \propto E_{\mathrm{SN}}^{a(\omega)} A^{-b(\omega)}$ with $a > 0$ and $b > 0$ for shock in a medium with $\rho_{\mathrm{o}} \propto A R^{-\omega}$. It is shown as well that if the density of the ambient medium decreases then the cooling processes could differ from the commonly accepted scenario of the "thin dense radiative shell" formation. This property should be studied in the future because it is important for models of nonspherical SNRs which could be only partially radiative.

3. An approximate analytical method of hydrodynamical description of the transition of SNR from the adiabatic stage of their evolution to the radiative one are developed. It allows one to model the dynamics of the shook, formation of the thin cold shell as well as distribution of parameters inside the shell and the internal hot region. The model fits the results of the numerical simulations from [90, 114, 331] with sufficient accuracy.

4. The general analytic solution for the evolution of radiative SNRs in a uniform interstellar medium, under thin-shell approximation, is presented. This approximation is shown to be very accurate approach to this task. For a given set of parameters, our solution closely matches the results of numerical models, showing a transient in which the deceleration parameter reaches a maximum value of 0.33, followed by a slow convergence to the asymptotic value 2/7. Oort [263] and McKee and Ostriker [247] analytic solutions are discussed, as special cases of the general solution we have found. Approach developed is extended to the case of a non-uniform ISM with power-low density distribution in [15] and to motion of shock under a force from gas with non-zero mass in [16].

5. An approximate analytical method for hydrodynamical modeling of the flow downstream of the radiative shock from the spherical point explosion in a nonuniform isotropic medium is presented. Comparison of the method with few known results of the numerical calculations [114] shows that the accuracy of the method is high enough to use it in physical applications.

CHAPTER 3

KINETICS AND RADIATION OF COSMIC RAYS IN SNRS

Conclusions about CRs accelerated by shocks in SNRs may be inferred from observations. Relativistic electrons emit in radio, X-rays through synchrotron mechanism and in γ-rays via inverse-Compton effect (non-thermal bremsstrahlung is also possible, but its contribution is dominated by the inverse-Compton emission). Accelerated protons after interaction with protons with much smaller energy produce neutral pions which decay in γ-photons [1, 2, 326].

Radio emission is observed from SNRs of different ages [172, 368], as well as thermal and synchrotron X-rays [112, 330]; some SNRs emit also in γ-rays with energies 0.1-100 GeV [152, 181] and 0.1-100 TeV [186, 346].

There are few components in model of CRs emission in SNR: 1) dynamics of the shock and plasma downstream of the shock, 2) kinetics of charged particles in vicinity of the shock an their evolution downstream after leaving region of acceleration and 3) emission processes of CRs, 4) synthesis of emission from SNR (e.g. images). Many aspects of particle acceleration are known [86,128,202,240], as well as main processes which are responsible for nonthermal emission of SNRs [67,97]. However, it is almost unknown how particles start acceleration (i.e. how they are "injected").

In the next chapters of the thesis, we consider emission of leptonic component of CRs. In Sect 3.1, a model of injection is described and factors which influence this process are determined. Evolution of the energy spectrum of relativistic electrons inside the volume of SNRs are described in Sect 3.2, in cases of the shock motion in uniform and nonuniform ISM and ISMF. Known methodology of simulation of inverse-Compton emission [326] requires calculations of many enclosed integrals in each point within SNR, that, together with necessity of calculations of magneto-hydro dynamics and evolution of CRs in three dimensions, requires incred-

ible CPU resources. Therefore, we developed an analytical approximation for IC emission (Sect 3.3) which allows us, for the first time, to synthesize images of SNRs in γ-rays.

To make the proton-origin γ-rays surely dominating in an SNR model, we need a high number density of target nuclei $\gtrsim 10^2$ cm^{-3}. Therefore, π^o decay γ-rays are naturaly expected from SNRs which interact with molecular clouds. Our model for TXCs (Sect. 2.1) strongly suggests to consider members of this class as prospective sources of hadronic γ-emission. Respective estimations have been done in Sect 3.4.

Results presented in this chapter are published in [17, 18, 72, 264, 265, 275, 278–280, 285].

3.1. Influence of thermalisation on electron injection in SNR shocks

3.1.1. Injection problem and the individual particle approach. The standard theory of diffusive acceleration, in test-particle approximation (see e.g. the review of Jones & Ellison [202]), shows that a power-law distribution develops at high energies. The spectral index of this high-energy population depends on the shock compression ratio, while it does not depend at all on the original energy distribution of the injected particles. In fact, a simplified way to describe the overall particle evolution, from nearly thermal to very high velocities, is to treat particle *injection* and *acceleration* as two separate problems. The *injection* problem consists in finding out the initial momentum distribution of the fraction of (originally thermal) particles that can enter the acceleration process, i.e. which make at least one acceleration cycle. The *acceleration* problem, instead, consists in following the evolution of the distribution of these particles along all next acceleration cycles.

In order to keep the number of free parameters low, while modelling more effectively the emission in all observed spectral ranges, one needs to introduce a physically self-consistent scenario for the thermal and nonthermal populations. For instance, the standard model of particle acceleration constrains the slope of the electron distri-

bution at high velocities, but does not predict its normalization: in other terms, the injection efficiency (i.e. the fraction of particles that enter the acceleration process) is poorly known, because this process is sensitive to physical details not included in the standard model of Fermi acceleration. The level of electron-ion equilibration or, alternatively, the electron temperature is another key quantity hard to determine "a priori" in collisionless shocks. While in models of SNR shocks injection and equilibration efficiencies are taken as independent free parameters, in the reality both depend on the physical conditions within the shock transition, and therefore they are not independent. Goal of this section is in fact to investigate, in nonrelativistic SNR shocks, a possible connection between electron injection and thermal equilibration.

A self-consistent treatment of injection and acceleration must include a microphysical model of particle-wave interactions in the plasma. We approach the problem in a simplified way. We assume the presence of scattering centres, without concentrating on their nature, but simply assuming that they match the following requirements: i) the interaction with these scattering centres generates a nearly isotropic, Maxwellian velocity distribution of particles on timescales not longer than one collision time; ii) the timescales for (wave-mediated) isotropization and energy exchange between electrons are both smaller than the (wave-mediated) electron-ion equilibration time; iii) the scattering centres play at the same time the role of thermalising, within the shock, the incoming particle population to the post-shock temperature and that of driving the process of diffusive acceleration. When we will need to use more specific properties of the wave-particle interaction, we will refer to the results of Bykov & Uvarov [96] on the electron kinetics.

There are in general three ways to calculate the post-shock momentum distribution of particles: either by solving the kinetic equations, or by making a hybrid simulation (which is however unable to model the momentum distribution of electrons because electrons are treated as a fluid), or finally by extending the individual particle approach of Bell [69]. He has estimated the probability for a particle to *return* to the shock from downstream and has shown that in this way one obtains a power-law distribution for the accelerated particles with velocities $v \gg V$ (where

V is the shock velocity).

In the present section we propose to extend the Bell approach to the problem of injection by introducing the probability to *recross* the shock from downstream to upstream. This probability is connected to the process of thermalisation of the incoming flow within the shock. This fact has been shown by Malkov [239] in the case of protons. Namely, the idea that ions are prevented from backstreaming by the self-generated waves (which also participate in thermalisation of ions) has allowed Malkov to obtain an analytic solution of the injection problem for protons. The main point in his thermal leakage theory is that only those protons that can "leak" upstream are injected into the Fermi process.

We use the same idea in our approach to electrons, even though we are not tight to any specific kind of interaction. We consider only the case of parallel shocks, namely when the ambient magnetic field is parallel to the shock normal.

3.1.2. Injection efficiency and distributions of electrons.

Efficiency of electron injection. Let us assume that all electrons are injected into the acceleration process from the downstream thermal population, i.e. we do not invoke seed particles with velocities already much higher than the thermal velocity. Their distribution is then well approximated by $n_{\rm es} f_{\rm M}$, where

$$f_{\rm M}(y) = \frac{4}{\sqrt{\pi}} y^2 \exp(-y^2) \tag{3.1}$$

is a normalized Maxwellian, isotropic in the fluid comoving frame. We have introduced the reduced momentum $y = p/p_{\rm th}$, which is also equal to the reduced velocity $v/v_{\rm th}$, as long as non-relativistic particles are considered, as it is the case at injection. Thermal momentum and velocity are defined by $p_{\rm th} = m_{\rm e} v_{\rm th} = \sqrt{2 m_{\rm e} k T_{\rm es}}$, where $T_{\rm es}$ is the post-shock electron temperature. We consider a fully ionized H+He gas (with $n_{\rm He} = 0.1 n_{\rm H}$, for a mean mass per particle $\mu = 0.609$), and a strong, unmodified shock. For an adiabatic index $\gamma = 5/3$, the shock compression ratio is $\sigma = 4$ but, for the sake of generality, in the following formulae we shall allow for a

general σ. Therefore, the ratio of the electron thermal velocity, $v_{\rm th}$, to V is

$$\frac{v_{\rm th}}{V} = \sqrt{\frac{2(\sigma-1)}{\sigma^2}\frac{\chi_{\rm s}}{\chi_{\rm o}}}, \tag{3.2}$$

where $\chi_{\rm o} = m_{\rm e}/(\mu m_{\rm p}) \simeq 8.94 \times 10^{-4}$. The factor $\chi_{\rm s} = T_{\rm es}/T_{\rm s}$, where $T_{\rm s}$ is the mean shock temperature, accounts for the thermal equilibration level between electrons and ions immediately after the shock, and ranges from $\chi_{\rm o}$ (no equilibration) to 1 (full equilibration).

Introducing the simple-minded assumption that only particles in the high-velocity tail of the Maxwellian distribution can be accelerated, it is easy to link the minimum momentum of this tail, $p_{\rm tail} = y_{\rm tail} p_{\rm th}$, to the injection efficiency ς (i.e. the fraction of accelerated particles). One has just to solve the equation $\int_{y_{\rm tail}}^{\infty} f_{\rm M}(y) = \varsigma$, which gives for instance $y_{\rm tail} = 2.85$ for $\varsigma = 10^{-3}$ and $y_{\rm tail} = 3.91$ for $\varsigma = 10^{-6}$. It is worth noticing that, for reasonable values of ς, this integral is dominated by particles with $y \sim y_{\rm tail}$, with $y_{\rm tail}$ of order of unity: it is apparent from this example that injection involves mostly particles with velocities of the order of the thermal one, and not only those with $v \gg V$.

In the above estimation, we have assumed that all particles with $y > y_{\rm tail}$, and only them, are accelerated. In order to find out the injection efficiency in a more general case, we introduce the probability $\mathcal{P}(y)$ for a particle with velocity $v = y v_{\rm th}$ to be accelerated, i.e. to recross the shock from downstream to upstream at least once. This probability yields the fraction of particles, with a given velocity, which can be accelerated; while the Maxwellian distribution in turn gives the number density of particles with that velocity. Thus, for an isotropic velocity distribution, the fraction of accelerated particles (injection efficiency) is given by the integral

$$\varsigma = \int_0^{\infty} \mathcal{P}(y) f_{\rm M}(y)\, dy. \tag{3.3}$$

In other terms, the distribution of particles injected into the acceleration process is

$$f_{\rm inj}(y) = \mathcal{P}(y) f_{\rm M}(y). \tag{3.4}$$

The probability $\mathcal{P}(y)$ in turn can be estimated as the product of the probability, $P_{\rm r}$, that a particle returns to the shock from downstream, times the probability, $P_{\rm c}$, that this particle crosses the shock moving upstream. The next two subsections will be devoted to estimate these two probabilities.

We wish to point out that a common misconception lies underneath the Fermi acceleration approach, namely that the electrons must enter this process having already a velocity much higher than V. This is usually obtained, by requiring either i) that the electron temperature is close to equipartition, or ii) that only electrons in the high-energy tail of the Maxwellian distribution enter into the acceleration process, or finally iii) that some unknown pre-acceleration mechanism takes place to accelerate electrons to the required velocity regime. The condition $v \gg V$ is in fact very useful to simplify the mathematical treatment of the process, but in our belief is not strictly required by physical arguments. In the present section we will show instead i) that electrons may be injected efficiently also when their temperatures is far from equipartition, ii) that, in order to have reasonably high injection efficiencies, $\chi_{\rm s}$ has to be considerably less than unity; in other words, the velocities of the majority of the injected electrons must not be not too far from the thermal velocity and the minimum injection momentum can even be much smaller than thermal one, and finally iii) that there is no physical need for an independent pre-acceleration process, if the treatment of the acceleration is modified in order to account also for relatively low particle velocities (this can be done by introducing the probability of crossing the shock).

Probability of returning to the shock. In the case of isotropic velocity distribution in the downstream flow, the probability for particles with velocity v to return to the shock from downstream is given by the ratio of the upstream and downstream fluxes [202]:

$$P_{\rm r}(v) = \frac{\left| \int\limits_{-v}^{-u_2} (u_2 + v_x)\, dv_x \right|}{\int\limits_{-u_2}^{v} (u_2 + v_x)\, dv_x} = {\rm H}(v - u_2) \left(\frac{1 - u_2/v}{1 + u_2/v} \right)^2 , \tag{3.5}$$

where: $u_2 = V/\sigma$ is the velocity of the downstream flow, in the shock reference frame; v is the velocity, in the downstream flow reference frame, of the particle that has just reached the shock; $\mathrm{H}(v - u_2)$ is the Heaviside step function (meaning that u_2 is the minimum value of v that allows a particle to return to the shock). In this section, we label quantities refering to upstream with "1" and quantities refering to downstream with "2". Coordinates are defined in such a way that, in the reference frame of the shock, the flow moves along the x-axis in the positive direction.

It is useful to re-write Eq. (3.2) to fix a lower boundary to the reduced momenta of the injected particles

$$y_{\mathrm{min}} = \frac{u_2}{v_{\mathrm{th}}} = \left(\frac{\chi_{\mathrm{o}}}{2(\sigma - 1)\chi_{\mathrm{s}}} \right)^{1/2} . \tag{3.6}$$

The quantity y_{min} is always less than $(2(\sigma-1))^{-1/2}$ (i.e. $p_{\mathrm{min}} < 0.4 p_{\mathrm{th}}$ for $\sigma = 4$) and can be much smaller than that if $\chi_{\mathrm{s}} \sim 1$ (which means $v_{\mathrm{th}} \gg V$). This means that, the higher the level of electron-ion equilibration, the higher the electron thermal velocity compared to V, and thus the higher the fraction of electrons able to *return* to the shock from downstream.

Probability of crossing the shock. The standard theory of diffusive acceleration [69] implicitely assumes $P_{\mathrm{c}} \simeq 1$, which means that the particle mean free path λ is longer than the thickness, Δx, of the shock transition region. This condition applies only for particles with high enough velocity ($v \gg V$).

On the contrary, the evolution of particles with lower velocities is affected by scatterings within the shock transition. In fact, the mere existence of a shock implies that the incoming ambient plasma must be thermalised, within the shock transition region, by some kind of scatterings centres. Also particles that enter the shock transition region from downstream, as long as they have velocities similar to thermal particles, must experience a similar rate of scatterings. Thus, also for them $\lambda < \Delta x$.

In the presence of scatterings, only a fraction of these particles will succeed crossing the shock and finally reaching the upstream region. In general, modelling this process is very complex. Here we will present a simplified treatment, based on some approximations. The first of them is diffusive approximation, which requires that

mean free paths are smaller than the shock thickness, and that the velocity distribution is nearly isotropic.

However, this assumption is invalid near the downstream boundary of the shock layer. In fact, the original distribution of downstream particles which return to the shock is highly anisotropic, since all particles entering the shock have, in the shock reference frame, an x-component opposite to the flow velocity. The above assumption is anyway valid over most of the volume, provided that isotropization processes within the shock are very efficient. Namely, we require that the length scale for isotropization is of the order of one mean free path (similarly to what happens for Coulomb collisions between similar particles).

The estimation of $P_{\rm c}(v)$ is generally very complex. Here we use a crude approximation (based on the so-called "modulation" equation, see e.g. [202]) and write

$$P_{\rm c} = \exp(-\langle u\rangle \Delta x/\varkappa). \tag{3.7}$$

where $\langle u\rangle \approx (u_1+u_2)/2 = u_2(\sigma+1)/2$ and $\varkappa$ is the diffusion coefficient.

We want to point out that probability of crossing is closely related to the thermalization level $\chi_{\rm s}$. The thickness Δx may be derived from the condition that the temperature of the incoming fluid increases to the post-shock value $T_{\rm es} = \chi_{\rm s} T_{\rm s}$ while the fluid moves through the shock transition from upstream to downstream. In this way, the two problems – injection and thermalisation – become closely connected. This can be seen by rewriting

$$\Delta x = \langle u\rangle \Delta t_{12} = \langle u\rangle \int\limits_0^{\chi_{\rm s}} \left(\frac{d\chi}{dt}\right)^{-1} d\chi \tag{3.8}$$

where Δt_{12} is the time it takes to a fluid element to cross the shock, moving from its upstream boundary to the downstream one. In general, it is necessary to introduce a microphysical model of thermalisation in order to obtain explicitely the functional dependence of the rate of thermalization $d\chi/dt$.

For the diffusion coefficient we use the standard formula $\varkappa = \lambda' v'/3$, where v' is the velocity of a particle in the local reference frame of the flow and λ' is the particle mean free path with respect to scatterings within the shock transition. A

further assumption behind this formula is that the scattering centres are frozen into the fluid. This is, for instance, the case in the Bykov & Uvarov [96] model for the electron kinetics in a strong shock. In this model, particles are scattered by the ion-generated Alfvénic waves, and the Alfvénic speed is much lower than the shock velocity. In case of electron diffusion in presence of magnetic field turbulence, it is common to parametrize the mean free path as $\lambda' = \eta r_{\rm g}$, where $r_{\rm g} = p'c/eB$ is the gyroradius and η accounts for the level of turbulence. We concentrate here on particles with velocities not much larger than V, and therefore we will use the nonrelativistic formula for λ'. For such parameterization of the mean free path, λ' may be written as $\lambda' = \tau_{\rm D} v'$ where $\tau_{\rm D}$ is the average deflection time defined as $\tau_{\rm D} = \eta m_{\rm e} c (eB)^{-1}$.

In order to compute a probability $P_{\rm c}(v)$ for particles having a given velocity v in the downstream reference frame, we need to average over all v' velocities corresponding to a a given v downstream. In the reference frame of the average flow within the shock transition, velocities v' corresponding to the same v are different in different directions, namely $\vec{v'} = \vec{v} - (\langle\vec{u}\rangle - \vec{u_2})$. The angle-averaged value of $\overline{v'^2}$ for these particles is given by

$$\begin{aligned} \overline{v'^2} &= \int_{-v}^{-u_2} \left((v_x - u_2(\sigma-1)/2)^2 + v_\perp^2\right) dv_x \Big/ \int_{-v}^{-u_2} dv_x \\ &= v^2 + \frac{\sigma-1}{2} v u_2 + \frac{\sigma^2-1}{4} u_2^2. \end{aligned} \tag{3.9}$$

Let us assume that, on the average, electrons in the incoming flow are thermalised to the level $\chi_{\rm s}$ in $N_{\rm c}$ collisionless interactions. For the sake of illustration, let us calculate the number of scatterings, $N_{\rm c}$, which yield a given injection efficiency. The involved time is approximately $\Delta t_{12} = N_{\rm c}\tau_{\rm D}$ and therefore

$$\frac{\langle u\rangle \Delta x}{\varkappa} = \frac{3\langle u\rangle^2}{v'^2}\frac{\Delta t_{12}}{\tau_{\rm D}} = \frac{3\langle u\rangle^2}{v'^2} N_{\rm c}, \tag{3.10}$$

so that the probability (3.7) becomes

$$P_{\rm c}(v') = \exp\left(-\frac{3(\sigma+1)^2}{4}\left(\frac{u_2}{v'}\right)^2 N_{\rm c}\right). \tag{3.11}$$

Eq. (3.3), together with probabilities (3.5), (3.11) and Eqs.(3.6), (3.9), shows that, in order to get an injection efficiency $\varsigma = 10^{-3}$, $N_{\rm c}$ must be equal to 9 for $\chi_{\rm s} = 0.001$, and to 770 for $\chi_{\rm s} = 0.1$.

It is interesting to note that our expression for $P_{\rm c}$ behaves like the "leakage probability" $\nu_{\rm esc}$ of Malkov [239], calculated for protons. Namely, the probability for protons to leak across the shock from downstream is approximately $\nu_{\rm esc}(y) \propto \exp\left(-\text{const } (y')^{-2}\right)$ [167].

Finally, we want to stress that the introduction of the probability $P_{\rm c}$ does not affect the slope of the accelerated spectrum at relativistic energies. Following standard test-particle approach to Fermi acceleration [69], a power-law momentum distribution of relativistic particles is generated, with an index $\alpha = -(2-\sigma)/(\sigma-1)$ that depends only on the shock compression ratio. This index is obtained by combining the term for the momentum increment per cycle ($\Delta p/p$) with that for the difference $(1-P_{\rm r})$ per cycle, in the high-velocity limit. The asymptotic behaviour of both terms is $\propto v^{-1}$; while Eq. (3.7) is such that $(1-P_{\rm c}) \propto v^{-2}$. Therefore, in the high velocity limit $P_{\rm c}$ gives negligible contribution to the formation of the particle spectrum in comparison to $P_{\rm r}$, and does not affect the formula for α.

3.1.3. Thermalisation of electrons and injection. In the shock-front reference frame, if upstream electrons and ions enter the leading edge of the shock transition with the same velocity then the electron energy is lower than that of protons by a factor $m_{\rm e}/m_{\rm p}$. Therefore, if the velocities of electrons and ions are randomized independently within the shock front, we obtain $T_{\rm es} = (m_{\rm e}/\mu m_{\rm p})T_{\rm s} \ll T_{\rm s}$ (i.e. $\chi_{\rm s} = \chi_{\rm o} \ll 1$ in our notation), while the ionic temperatures are about $(n_{\rm e}+n_{\rm i})T_{\rm s}/n_{\rm i}$ (where "i" denotes ions), namely much closer to $T_{\rm s}$.

The temperatures of electrons and ions may get closer, if there is a process within the shock which allows energy exchanges between the two species. In collisional shocks, the equilibration process is Coulomb scattering between ions and electrons, while, in the collisionless case (like it generally occurs in SNRs), turbulence plays the dominant role.

Results from observations. Since longtime, it has been suggested that plasma instabilities could lead to prominent heating of electrons within the shock (e.g. [245]). Some observations and theoretical results put forward the possibility that collisionless processes within the shock of SNRs could heat electrons up to the level $\chi_{\rm s} \simeq 0.4$ ([94] and references therein). Results on SNR DEM L71 in LMC [297] and on RCW86 [169] also suggest $\chi_{\rm s} \sim 0.3$. Analysis of Chandra data on Tycho SNR indicates that $\chi_{\rm s} \lesssim 0.1$ [169, 199]. Other recent observations (SN1006, Tycho, 1E 0102.2–7219) favour a considerably lower thermalisation level, namely $\chi_{\rm s} \lesssim 0.03 \div 0.07$ [170, 197, 214, 221, 222, 356]).

It is important to know how does the level $\chi_{\rm s}$ depend on the properties of the shock. Observational estimations of the shocks with Mach number $\mathcal{M}$ up to ~ 400 suggest that stronger shocks (namely with higher $V_{\rm s}$) could equilibrate species less effectively. Namely, Schwartz et al. [327] present results of measurements of $T_{\rm es}/T_{\rm s}$ for interplanetary shocks and planetary bow shocks ($\mathcal{M} \lesssim 25$) and find strong evidence that this ratio depends on the Mach number as $\mathcal{M}^{-1}$. Ghavamian et al. [169] estimations for a number of SNRs seem to extend this trend to stronger shocks, with $25 \lesssim \mathcal{M} \lesssim 200$. Rakowski [298] summarises the observational methods and estimations of $\chi_{\rm s}$ in SNRs shocks and confirms the inverse dependence in the range $25 \lesssim \mathcal{M} \lesssim 400$.

Results from Bykov and Uvarov (1999). Interactions of electrons with ion- or self-generated waves could be responsible for both accelerating and heating of electrons (see [98, 240] for a review).

Bykov & Uvarov [96] have considered the interactions of electrons with ion-generated electro-magnetic fluctuations and have developed a kinetic model that accounts at the same time for electron injection, acceleration and thermalisation in quasiparallel shocks. Their model is applicable for shocks with local Mach number $\mathcal{M}$ less than $\sim \sqrt{m_{\rm p}/m_{\rm e}}$. They have introduced the effective electron temperature $T_{\rm eff}$ (measured in units of the upstream temperature $T_{\rm o}$), which may be related to

our $\chi_{\rm s}$ by

$$\chi_{\rm s} = T_{\rm eff}\frac{T_{\rm o}}{T_{\rm s}} = T_{\rm eff}\frac{\sigma^2}{(\sigma+1)\mathcal{M}^2}, \tag{3.12}$$

and have shown that it depends on the Mach number. This dependence can be approximately described by a power law: $T_{\rm eff} \propto \mathcal{M}^a$, with index $0 < a \lesssim 2$ depending on which model of wave-particle interaction is considered. Therefore, the level of thermalisation depends on the velocity of the shock: $\chi_{\rm s} \propto \mathcal{M}^{a-2}$ for strong shocks, namely the higher the velocity the smaller the thermalisation level.

If λ' is momentum independent (transport of electrons is due to large-scale magnetic field fluctuations that provide effective heating) then $a \approx 2$, and the level of equilibration $\chi_{\rm s}$ does not depend on the Mach number. This means that $T_{\rm es} \propto V^2$, but with a factor that may be higher than that inferred from Rankine-Hugoniot equations for the electron population [246]. The opposite case is when electron heating in the shock transition region is effectively suppressed by a developed small-scale vortex turbulence, giving $a \approx 0$. In such a situation the postshock electron temperature is $T_{\rm es} \approx T_{\rm o}$, independently of the Mach number. Another interesting model of wave-particle interactions is Bohm-like diffusion, for which $\lambda' \propto p$ and $a = 1$. In the present section we consider only the Bohm-like diffusion case since it seems to be in agreement with observations (namely $\chi_{\rm s} \propto \mathcal{M}^{-1}$, see Sect. 3.1.3).

Bykov & Uvarov [96] also introduce the dimensionless parameter $\Gamma = u_1\Delta x/v'\lambda'$ (calculated for electrons with $v = v_{\rm th}$), and in their Fig. 4 they show its dependence on $T_{\rm eff}$, for different models of wave-particle interactions (Fig. 4a for diffusion boundary conditions and Fig. 4b for free escape boundary conditions). In particular, their curve 4 represents result for Bohm-like diffusion.

Application of Bykov & Uvarov results to our model. We have approximated Bykov & Uvarov [96] numerical results by using $\Gamma = T_{\rm eff}^{1/a}/\xi - 1$ where ξ is a constant. This, together with (3.12), gives

$$\Gamma = \left(\frac{(\sigma+1)\mathcal{M}^2\chi_{\rm s}}{\sigma^2}\right)^{1/a}\frac{1}{\xi} - 1. \tag{3.13}$$

In a Bohm-like case, i.e. with $a = 1$, $\xi = 1.25$ corresponds to the diffusive boundary conditions and $\xi = 0.75$ to free escape boundary conditions. The parameter Γ is proportional to the combination $\langle u \rangle \Delta x / \varkappa$ in the exponent of the transition probability. This allows us to write

$$P_{\rm c}(y, \chi_{\rm s}, \mathcal{M}) = \exp\left(-\frac{3(\sigma+1)}{2\sigma} \frac{\Gamma(\chi_{\rm s}, \mathcal{M})}{y'^2} \right) \tag{3.14}$$

for nonrelativistic electrons and $\lambda' \propto p$.

By using (3.13) for Γ in (3.14), the dependence of the fraction of injected particles ς on the level of electron thermalisation $\chi_{\rm s}$ may be obtained (Fig. 3.1). By comparing (3.14) with (3.11), using (3.6) for $y_{\rm min}$, we finally obtain a relation between Γ and $N_{\rm c}$:

$$N_{\rm c} = \frac{4(\sigma-1)\chi_{\rm s}\Gamma(\chi_{\rm s})}{(\sigma+1)\sigma\chi_{\rm o}}. \tag{3.15}$$

The calculated dependence of the injection efficiency on the Mach number and on the thermalisation level is shown in Fig. 3.1 for the Bohm-like diffusion. The range of values plotted in this figure corresponds to a range from 2 to 20 for Γ in Fig. 4 of Bykov & Uvarov [96], with the minimum Γ corresponding to the maximum ς. The curves in Fig. 3.1 are essentially the same curve, with different horizontal offsets. Namely, the formula for the injection efficiency $\varsigma(\mathcal{M}, \chi_{\rm s})$ is very well approximated by a function of $\mathcal{M}^2\chi_{\rm s}$. The reason of this can be found in Eq. (3.3), together with the explicit definitions of $P_{\rm r}$ and $P_{\rm c}$ (respectively, Eqs. (3.5) and (3.7)): for standard parameter ranges, the most effective term is the argument in the exponential of $P_{\rm c}$, which is proportional to Γ. In turn, Eq. (3.13) shows that the dependence of Γ from $\mathcal{M}$ and $\chi_{\rm s}$ is only through the combination $\mathcal{M}^2\chi_{\rm s}$. In this sense, we may say that Γ is a function of a single parameter (not considering, of course, the dependence on the assumed diffusion type and on the boundary conditions, which can be accounted for by using parameters a and ξ). For instance, in a Bohm-like case a power-law approximation of the curves shown in Fig. 3.1 is $\varsigma \simeq 2 \times 10^5 \mathcal{M}^{-10} \chi_{\rm s}^{-5}$ (this approximation is represented in the figure by dashed lines). Since in this case $\chi_{\rm s} \propto \mathcal{M}^{-1}$, the overall dependence of the injection efficiency on the Mach number in a Bohm-like case is as strong as $\varsigma \propto \mathcal{M}^{-5}$.

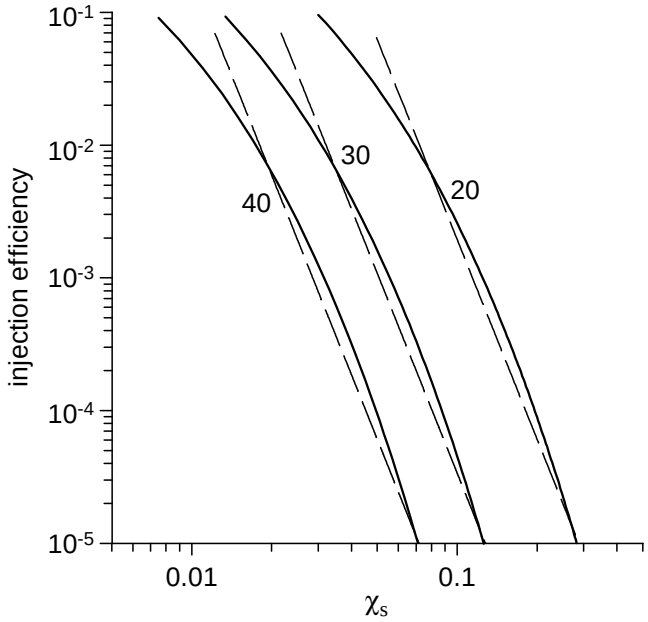

Figure 3.1. Injection efficiency ς versus post-shock ratio $\chi_{\rm s}$ for a model of Bykov & Uvarov [96] for Bohm-like diffusion and diffusion boundary conditions. Curves are labelled by their respective Mach number. The approximation $\varsigma = 2 \times 10^5 \left(\mathcal{M}^2 \chi_{\rm s}\right)^{-5}$ is shown by dashed lines.

In order to allow for different types of diffusion, as well as for different electron-wave interactions etc., one could consider a more general case, in which: i) $\chi_{\rm s} \propto \mathcal{M}^{-m}$; and, ii) $\varsigma \propto \mathcal{M}^{-2q} \chi_{\rm s}^{-q}$ (where we expect q to be always positive). We then obtain $\varsigma \propto \mathcal{M}^{-b}$ with $b = q(2-m)$. In other words, in the case of a decelerating SNR shock $\chi_{\rm s}$ always increases, while ς increases if $m < 2$, and decreases if $m > 2$.

3.1.4. Discussion. The electron injection and thermalisation are not independent processes. This is clearly outlined by Fig. 3.2 where the probabilities $P_{\rm r}$ and $P_{\rm c}$ as a function of reduced momentum are shown for two values of $\chi_{\rm s}$ together with the initial distribution (3.4) of injected particles. The hybrid electron distribution $n_{\rm es} f_{\rm H}(y) dy$, Maxwellian up to $y_{\rm b}$ and power-law above [291], is also shown on the figure to see the differences. The break momentum $y_{\rm b}$ is given by the assumption that all injected particles obtain momenta higher than $y_{\rm b}$ after acceleration i.e. is defined by $\varsigma = \int_{y_{\rm b}}^{\infty} f_{\rm H}(y) dy$.

It is a common believe that only particles from the energetic tail of Maxwellian distribution are capable to be accelerated. On the contrary, the distribution $f_{\rm inj}$ shows that thermal particles with velocities $v > v_{\rm min}$ have the possibility to participate in acceleration process, although with different probability. The minimum

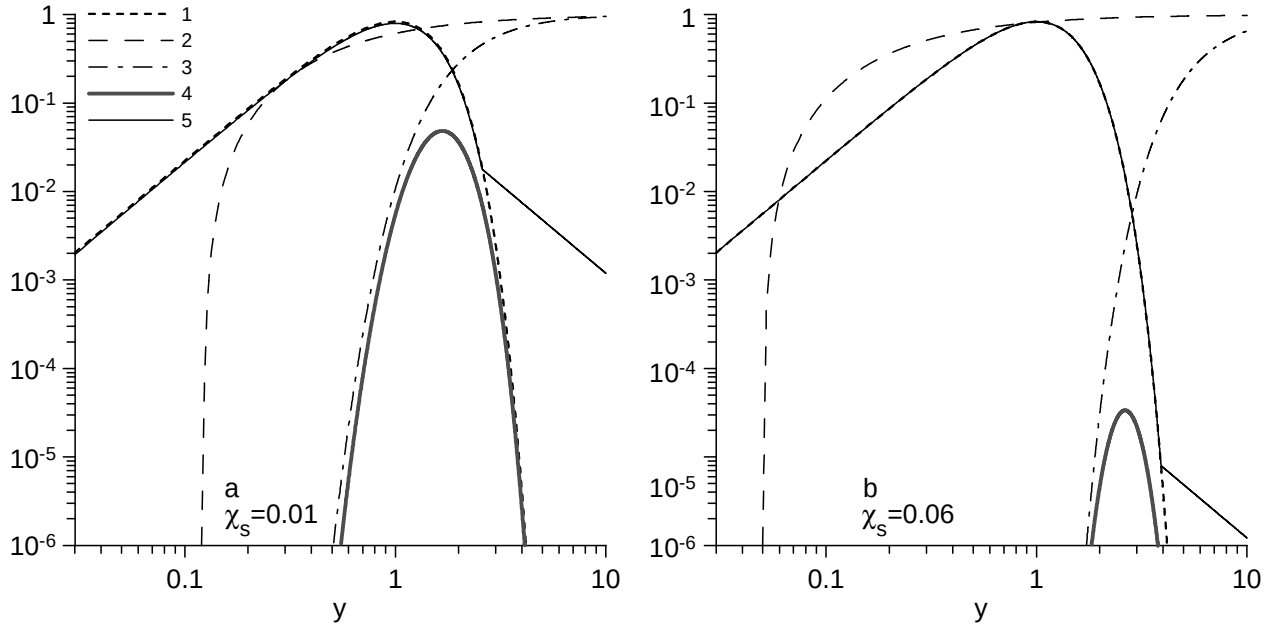

Figure 3.2. Electron distribution functions and probabilities calculated for two different values of χ_s. 1 – Maxwellian distribution, 2 – probability to return to the shock P_r, 3 – probability to cross the shock P_c, 4 – initial distribution f_{inj} of electrons injected into acceleration process, 5 – final hybrid electron distribution ($\alpha = 2$). Plots are calculated for the model of electron-wave interaction developed by Bykov & Uvarov [96] (case of Bohm-like diffusion with diffusive boundary conditions), $\mathcal{M} = 40$. a) $\chi_s = 0.01$, in this case $y_{min} = 0.12$, $y_b = 2.6$, $\varsigma = 0.048$, $N_c = 20$; b) $\chi_s = 0.06$, in this case $y_{min} = 0.05$, $y_b = 3.9$, $\varsigma = 3.1 \times 10^{-5}$, $N_c = 930$.

velocity $v_{min} = 0.07\,(\chi_s/0.03)^{-1/2}\,v_{th}$ may be considerably less than the thermal velocity (see Eq. (3.6)). The most probable velocity v_* at which the maximum of the distribution f_{inj} occurs is $v_* \approx (2 \div 3)v_{th}$ for a wide range of injection fractions $\varsigma = 10^{-3} \div 10^{-6}$ (Fig. 3.3 and compare with Fig. 3.1). In other words, most of the electrons are injected with velocities $v_* \simeq 50\chi_s^{1/2}V$.

The injection efficiency ς of electrons in a collisionless shock is associated to the process of electron heating within the shock, through the competition of two effects. On one side, the higher the post-shock electron temperature, the higher the energy of thermal electrons and the higher the fraction of those which are ready to cross the shock from downstream to upstream (this is given by the probability P_r, lines 2 on Fig 3.2a,b). On the other side, however, the higher the temperature, the higher the number of scattering centers. Electrons traversing the shock from downstream to upstream also interact with these sites and the more such interactions the less electrons are able to cross the shock and to enter into the Fermi acceleration loop (see probability P_c, lines 3 on Fig 3.2a,b). In this section we show that, for a given

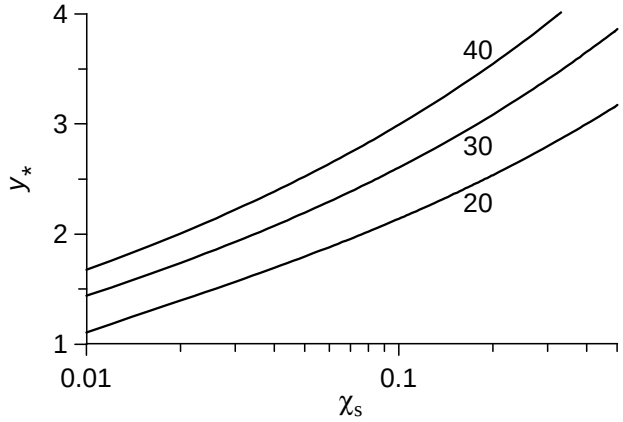

Figure 3.3. Velocity corresponding to the maximum of the distribution function $f_{\rm inj}$ versus $\chi_{\rm s}$ for a few choices of the shock Mach number (see curve labels). Model of electron kinetics is the same as in the previous figure.

$\mathcal{M}$, the combined effect of these two processes is that the quantity ς decreases with increasing of $\chi_{\rm s}$ (Fig. 3.1).

Both injection and thermalisation are sensitive to the Mach number. It is shown (see Sect. 3.1.3) that, for a standard range of parameters, $\varsigma(\chi_{\rm s}, \mathcal{M})$ is a decreasing function of a single argument $\varsigma = \varsigma(\mathcal{M}^2\chi_{\rm s})$. Theoretical models show that in high-velocity shocks the energy of the shock is transferred to the thermal electrons less efficiently, so that $\chi_{\rm s} \propto \mathcal{M}^{-m}$ with $0 \leq m \leq 2$ (Bykov & Uvarov [96]). Observations favour a dependence $\chi_{\rm s} \propto \mathcal{M}^{-1}$, suggesting a Bohm-like type of diffusion. Our calculations show that the level of electron-ion equilibration is expected to depend on the injection fraction as well, so that the approximate relation between these three parameters is $\chi_{\rm s} \propto \mathcal{M}^{-2}\varsigma^{-1/q}$ (Sect. 3.1.3). The smaller the Mach number, the higher the level of electron-ion equilibration for a given injection efficiency. On the other hand, for a given thermalisation level, the stronger the shock the less particles can be injected.

To conclude, we would like to review the assumptions used in the present section.

Our approach is in test-particle approximation. Actually, it is known that, in young SNRs, shocks could be strongly modified; and the inclusion of nonlinear effects could change our results significantly. The usage of a test-particle approach in the present section is however consistent with what done by Bykov & Uvarov [96], and the results of their analysis are valid at least for shocks with Alfvén Mach number

less than $\simeq 43$. Thus our results should be applicable at least to SNRs either in the late adiabatic phase or beyond. Our opinion is that, together with using nonlinear treatments, it is valuable investigating what happens in the linear (test-particle) approximation, also in consideration that a nonlinear theory has anyway to give, as limit case, the linear results.

Eqs. (3.1) and (3.5) assume nearly isotropic distribution of particles. In general, this is not fully true for the thermal population right after the shock. In order to overcome this difficulty, in numerical calculations these formulae are assumed to apply a few mean free paths downstream, in order to insure that the distribution is isotropic in the local frame (e.g. [138]). Within our approach, this implies some restrictions on the underlying physics. Our assumptions about properties of the scattering centers in our model (see Introduction) require that the timescale for isotropisation is not larger than the timescale for one interaction. This means that, in order to assume isotropy of particles velocities, we would in principle need to increase the number of interactions $N_{\rm c}$ at least by one (see Eq. (3.11)). Since already $N_{\rm c} \gg 1$ for, say, $\chi_{\rm s} > 10^{-3}$ (see estimations after Eq. (3.11)), this increment would not change much our results, in the case of shocks producing an electron population thermalised up to the level $\chi_{\rm s}$ higher than 10^{-3}. Since $\chi_{\rm s} \propto \mathcal{M}^{-1}$, our models are limited again to the shocks with moderate Mach numbers.

3.2. Electron energy spectrum and its evolution downstream of the adiabatic shock

3.2.1. Energy spectrum of electrons. Let us assume that the synchrotron X-ray or IC γ-ray radiation is due to relativistic electrons distributed with an energy spectrum $N(E) = KE^{-s}\exp(-E/E_{\rm max})$ electrons cm^{-3} erg^{-1}, where E is the electron energy, $N(E)$ is the number of electrons per unit volume with arbitrary directions of motion and with energies in the interval $[E, E+dE]$, K is the normalization of the electron distribution, s the power-law index and $E_{\rm max}$ the maximum

energy of electrons accelerated by the shock. The distribution of the radio-emitting electrons $N(E)$ simplifies to $N(E) = KE^{-s}$. In general, the spectral index s may depend on E, e.g. $s(E) = s + \delta s(E)$ like it would be in case of the nonlinear acceleration. Unless otherwise stated, the value $s = 2$ is used, as it appears in the test-particle acceleration theory, $s = (2 + \sigma)/(\sigma - 1)$, where $\sigma = (\gamma + 1)/(\gamma - 1)$ the shock compression ratio (defined as $\sigma = n_{\rm s}/n_{\rm o}$), which is 4 for adiabatic index $\gamma = 5/3$.

Some observations suggest that the cut-off could be broader than pure exponent (at least in SN 1006 and G347.3-0.5 [140, 141, 223, 352]). We have shown [278], that this broadening should be attributed to the physics of acceleration rather than to an artifact of observations (i.e. superposition of spectra in different conditions along the line of sight as suggested by [302]). Therefore we assume that the energy spectrum of accelerated electrons is given by

$$N(E) = KE^{-s} \exp\left[-\left(\frac{E}{E_{\rm max}}\right)^{\alpha}\right] , \tag{3.16}$$

where $\alpha \leq 1$ is the parameter regulating the broadening/narrowing of the high-energy end of electron spectrum. It could be that $\alpha = 0.5 - 0.6$ ([140] and references therein). Also the larger values of the parameter, $\alpha = 1 \div 2$, appear in recent theoretical works [208, 334, 375] suggesting that the end may be narrower than the pure exponent.

Injection efficiency and normalization of the spectrum. The normalization of the electron distribution $K_{\rm s}$ depends on the injection efficiency (the fraction of electrons that move into the cosmic-ray pool). On theoretical grounds, $K_{\rm s}$ is expected to vary with the shock velocity $V(t)$ and, in case of inhomogeneous ISM, with the immediately post-shock value of mass density, $\rho_{\rm s}$; let us assume that approximately $K_{\rm s} \propto \rho_{\rm s} V(t)^{-b}$. Reynolds [303] considered three empirical alternatives for b as a free parameter, namely, $b = 0, -1, -2$. In Sect. 3.1, we showed that one can expect $b > 0$. Negative b reflects an expectation that *injection* efficiency may behave in a way similar to *acceleration* efficiency: stronger shocks might inject particles more effectively. In contrast, positive b represents a different point of

view: efficiencies of injection and acceleration may have opposite dependencies on the shock velocity. Stronger shock produces higher turbulence which is expected to prevent more thermal particles to recross the shock from downstream to upstream and to be, therefore, injected. Since the picture of injection is quite unclear from both theoretical and observational points of view, we do not pay attention to the physical motivations of the value of b. Instead, our goal is to see how different trends in evolution of injection efficiency may affect the visible morphology of SNRs. Such understanding could be useful for future observational tests on the value of b.

The electron injection efficiency may also vary with the obliquity angle between the external magnetic field and the shock normal, $\phi_{\rm o}$. There are numerical simulations which suggest that injection efficiency is larger for parallel shocks, i.e. where the magnetic field is parallel to the shock speed (obliquity angle close to zero; [137]). However, it has been shown [157] that models with injection strongly favoring parallel shocks produce SNR maps that do not resemble any known objects (it is also claimed that injection is more efficient where the magnetic field is perpendicular to the shock speed; [200]). In such an unclear situation, we consider, in particular, the three cases: quasi-parallel, quasi-perpendicular, and isotropic injection models. In practise, the obliquity variation of $K_{\rm s}$ is given by $K_{\rm s}(\Theta_{\rm o}) = K_{\rm s\parallel}\mathcal{F}_{\rm K}(\Theta_{\rm o})$ with $\mathcal{F}_{\rm K}(\Theta_{\rm o})$ independent of time. Typically, one considers three models for injection [225, 303]: quasi-parallel ($\mathcal{F}_{\rm K}(\Theta_{\rm o}) = \cos^2\Theta_{\rm s}$), isotropic ($\mathcal{F}_{\rm K}(\Theta_{\rm o}) = 1$) and quasi-perpendicular ($\mathcal{F}_{\rm K}(\Theta_{\rm o}) = \sin^2\Theta_{\rm s}$) where $\Theta_{\rm s}$ is the angle between the post-shock magnetic field and the shock normal; the obliquity angle between the external magnetic field and the shock normal, $\Theta_{\rm o}$, is related to $\Theta_{\rm s}$ by $\sin^2\Theta_{\rm o} = (\cot^2\Theta_{\rm s}/\sigma^2 + 1)^{-1}$ or $\cos\Theta_{\rm s} = \sigma_{\rm B}^{-1}\cos\Theta_{\rm o}$ (e.g. [157]). Since $K_{\rm s} \propto \rho_{\rm s}V(t)^{-b}$, the surface variation of $K_{\rm s}$, in case of the nonuniform ISM, is given by

$$K_{\rm s} = K_{\rm s\parallel}\mathcal{F}_{\rm K}(\Theta_{\rm o})\mathcal{R}_{\rm s}\mathcal{V}^{-b} \tag{3.17}$$

where $\mathcal{R}_{\rm s} = \rho_{\rm s}/\rho_{\rm s\parallel}$, $\mathcal{V} = V/V_{\parallel}$.

Maximum energy of electrons. We follow the approach of Reynolds [303] for the description of time evolution and surface variation of $E_{\rm max}$, generalizing his ap-

proach to cases of non-uniform ISM and/or non-uniform ISMF. He [303] considered three alternatives for time and spatial dependence of $E_{\rm max}$. Namely, the maximum accelerated energy maybe determined: 1) by the electron radiative losses (due to synchrotron and IC processes), 2) by the limited time of acceleration (if age of SNR is smaller than characteristic time for losses) and 3) by properties of micro-physics when the scattering of electrons with $E > E_{\rm max}$ becomes less efficient and the electrons freely escape from the region of acceleration[1].

The obliquity variation of the maximum energy is $E_{\rm max} = E_{\rm max,\parallel}\mathcal{F}_{\rm E}(\Theta_{\rm o})$ with $\mathcal{F}_{\rm E}(\Theta_{\rm o})$ independent of time. Shocks of different strength are able to accelerate electrons to different $E_{\rm max}$; this is reflected by $E_{\rm max} \propto V^q$.

In case of the nonuniform ISM/ISMF, the maximum energy should account for the surface variation of shock velocity V and magnetic field B:

$$E_{{\rm max},\xi} \propto \mathcal{F}_{{\rm E},\xi}(\Theta_{\rm o})\, V^{q_\xi}\, B_{\rm o}^{\lambda_\xi}\ , \tag{3.18}$$

where $\xi = 1, 2, 3$ corresponds respectively to loss-limited, time-limited and escape-limited models of $E_{\rm max}$. The values of q and λ are: $q_1 = 1$, $q_2 = q_3 = 0$, and $\lambda_1 = -1/2$, $\lambda_2 = \lambda_3 = 1$ [303]. Note that we assume $q_2 = 0$ because $E_{\rm max}$ rises quite slowly with time when it is determined by the finite time of acceleration [303], even in the nonuniform ISM, and most of emission rises therefore from downstream regions close to the shock. From Eq. (3.18), we express the surface variation of $E_{\rm max}$ as

$$E_{{\rm max},\xi} = E_{{\rm max},\xi,\parallel}\ \mathcal{F}_{{\rm E},\xi}(\Theta_{\rm o})\ \mathcal{V}^{q_\xi}\ \mathcal{B}_{\rm o}^{\lambda_\xi}\ , \tag{3.19}$$

where $E_{{\rm max},\xi,\parallel}$ is a free parameter, representing the maximum energy in a point p on the SNR surface where the ISMF is parallel to the shock normal, $\mathcal{B}_{\rm o} = B_{\rm o}/B_{\rm o,\parallel}$.

[1]For the escape case, it is commonly assumed that MHD waves responsible for the scattering are much weaker above some wavelength, $\lambda_{\rm max}$, and $E_{\rm max}$ is approximately the energy of particles with that gyroradius (e.g. [303]).

The obliquity dependence of $E_{\rm max}$ is [303]

$$f_{\rm E,1}(\Theta_{\rm o}) = \sqrt{\frac{G(\Theta_{\rm o})}{G(0)R_{\rm j}(\Theta_{\rm o})}} \ ,$$

$$f_{\rm E,2}(\Theta_{\rm o}) = \frac{1}{R_{\rm j}(\Theta_{\rm o})} \ , \tag{3.20}$$

$$f_{\rm E,3}(\Theta_{\rm o}) = 1 \ ,$$

where

$$G(\Theta_{\rm o}) = \frac{\sigma_{\rm B} Z(\Theta_{\rm o}) + \sigma}{\sigma_{\rm B} Z(\Theta_{\rm o})(1+d^2) + \sigma(\sigma_{\rm B}^2 + d^2)} \ ,$$

$$Z(\Theta_{\rm o}) = \sigma_{\rm B}^2 \frac{1+\eta^2+\tan^2\Theta_{\rm o}}{1+\eta^2+\sigma^2\tan^2\Theta_{\rm o}} \ ,$$

$$\sigma_{\rm B}^2(\Theta_{\rm o}) = \frac{1+\sigma^2\tan^2\Theta_{\rm o}}{1+\tan^2\Theta_{\rm o}} \ ,$$

$$R_{\rm j}(\Theta_{\rm o}) = \frac{\sigma_{\rm B}}{\sigma_{\rm B}+\sigma}\left[\left(\cos^2\Theta_{\rm o} + \frac{\sin^2\Theta_{\rm o}}{1+\eta^2}\right) + \frac{\sigma}{\sigma_{\rm B}}\left(\cos^2\Theta_{\rm s} + \frac{\sin^2\Theta_{\rm s}}{1+\eta^2}\right)\right]$$

$d = B_{\rm CMB}/B_{\rm o}$, $B_{\rm CMB} = 3.27$ μG is the magnetic field strength with energy density equal to that in the CMB, $\eta = \lambda_{\parallel}/r_{\rm g}$ is the "gyrofactor", i.e. the ratio between the mean free path, $\lambda_{\parallel}$, along the magnetic field and the gyroradius, $r_{\rm g}$ (see [303]). In general it is expected that the mean free path can be no less than $r_{\rm g}$, so that $\eta \geq 1$; the equality corresponds to the Bohm limit, i.e. a level of turbulence leading to wave amplitudes comparable to the stationary magnetic field strength. Figure 3.4 shows the obliquity dependence of $E_{\rm max}$ in the time-limited and loss-limited models for different η and $\gamma = 5/3$, assuming the remnant expanding through uniform ISM and ISMF.

3.2.2. Electrons with radiative losses downstream of the shock in uniform media. Relativistic electrons leaving the region of acceleration and evolving downstream of the shock suffer from adiabatic expansion and radiative losses due to synchrotron and IC processes. Electrons are considered to be confined to the fluid element which removed them from the acceleration cite [303]. Let the fluid element

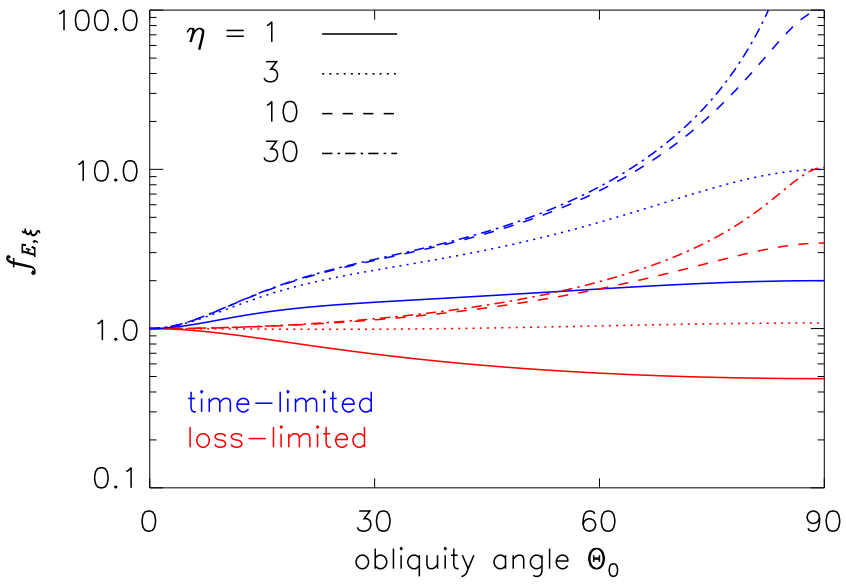

Figure 3.4. Obliquity dependence of $E_{\max}$ (see Eq. 3.20) in the time-limited (blue) and loss-limited (red) model, for the labeled values of the gyrofactor η, assuming $\gamma = 5/3$.

with Lagrangian coordinate a was shocked at time $t_{\rm i}$. If energy of electrons was $E_{\rm i}$ at $t_{\rm i}$, it becomes at present time t [303]

$$E = \frac{E_{\rm i}}{\bar{n}(\bar{a})^{-1/3} + \mathcal{I}(\bar{a}) E_{\rm i}/E_{\rm f\|}} \tag{3.21}$$

where the first summand in the denominator reflects adiabatic losses, the second one is due to radiative losses, overline means that the parameter is normalized to its value immediately post-shock, e.g. $\bar{n} = n/n_{\rm s}$, $\bar{a} = a/R(t)$, the fiducial energy for the parallel shock is defined as $E_{\rm f\|} = 637/(B^2_{\rm eff,s\|} t)$ cgs (it is the energy an initially infinitely energetic electron would have after radiating for a time t in a constant magnetic field of strength $B_{\rm eff,s\|}$). The effective magnetic field is $B^2_{\rm eff} = B^2 + B^2_{\rm CMB}$; $B_{\rm CMB}$ is introduced in order to account for the IC losses [303], therefore it is constant everywhere. The synchrotron channel dominates IC losses if $B_{\rm s} \gg B_{\rm CMB}$.

The dimensionless function $\mathcal{I}$ accounts for evolution of fluid during time from $t_{\rm i}$ to t; it was initially defined as integral over time [303]. In case of Sedov shock, $\mathcal{I}$ may be written in terms of spatial coordinate that is more convenient for simulations than original representation in terms of time. Namely, one can show that for uniform ISM:

$$\mathcal{I}(\bar{a}, \Theta_{\rm o}, d) = \frac{5\sigma_{\rm B}^2}{2\bar{n}(\bar{a})^{1/3}} \int_{\bar{a}}^{1} x^{3/2} \bar{B}_{\rm eff} \left(\frac{\bar{a}}{x}\right)^2 \bar{n} \left(\frac{\bar{a}}{x}\right)^{1/3} dx. \tag{3.22}$$

Eq. (3.21) results in relations

$$E_{\rm i} = \frac{E}{\mathcal{E}_{\rm ad}\mathcal{E}_{\rm rad}}, \qquad dE_{\rm i} = \frac{dE}{\mathcal{E}_{\rm ad}\mathcal{E}_{\rm rad}^2} \tag{3.23}$$

where the adiabatic and radiative losses are represented by

$$\mathcal{E}_{\rm ad} = \bar{n}(\bar{a})^{1/3}, \qquad \mathcal{E}_{\rm rad} = 1 - \mathcal{I}(\bar{a}, \Theta_{\rm o})E/E_{\rm f}. \tag{3.24}$$

If shock accelerates electrons to $E_{\rm max}$ at present time t, then, at some previous time $t_{\rm i}$ when fluid element $a \equiv R(t_{\rm i})$ was shocked, the shock was able to accelerate electrons to

$$E_{\rm max}(t_{\rm i}) = E_{\rm max}\left(\frac{V(t_{\rm i})}{V(t)}\right)^q = E_{\rm max}\bar{a}^{-3q/2}. \tag{3.25}$$

Let us assume that, at time $t_{\rm i}$, an electron distribution has been produced at the shock

$$N(E_{\rm i}, t_{\rm i}) = K_{\rm s}(t_{\rm i})E_{\rm i}^{-s}\exp\left[-\left(\frac{E_{\rm i}}{E_{\rm max}(t_{\rm i})}\right)^{\alpha}\right]. \tag{3.26}$$

Conservation equation

$$N(E, a, t) = N(E_{\rm i}, a, t_{\rm i})\frac{a^2 da dE_{\rm i}}{\sigma r^2 dr dE} \tag{3.27}$$

and continuity equation $n_{\rm o}(a)a^2da = n(a,t)r^2dr$, where r is the Eulerian coordinate, shows that downstream

$$\begin{aligned} N(E, a, t) &= K(a, t, \Theta_{\rm o})\ E^{-s}\ \mathcal{E}_{\rm rad}(\bar{a}, E, \Theta_{\rm o})^{s-2} \\ &\times \exp\left[-\left(\frac{E\ \bar{a}^{\,3q/2}}{E_{\rm max\|}(t)\ \mathcal{E}_{\rm ad}(\bar{a})\ \mathcal{E}_{\rm rad}(\bar{a}, E)\ \mathcal{F}_{\rm E}(\Theta_{\rm o})}\right)^{\alpha}\right] \end{aligned} \tag{3.28}$$

with $K(a,t) = K_{\rm s}(t_{\rm i})\bar{n}\mathcal{E}_{\rm ad}^{s-1}$. If $K_{\rm s} \propto V^{-b}$, then evolution of K is self-similar downstream

$$\bar{K}(\bar{a}) = K(a,t)/K_{\rm s}(t) = \bar{a}^{\,3b/2}\ \bar{n}(\bar{a})^{(2+s)/3}. \tag{3.29}$$

Therefore, in general,

$$K(a, t, \Theta_{\rm o}) = K_{\rm s\|}(t)\mathcal{F}_{\rm K}(\Theta_{\rm o})\bar{K}(\bar{a}) \tag{3.30}$$

where the profile $\bar{K}(\bar{a})$ is independent of obliquity. Note, that $K(a, t, \Theta_{\rm o})$ is not affected by the radiative losses, therefore it behaves in the same way also for the

radio emitting electrons. Once s is close to 2, the radiative losses influence the shape of $N(E)$ mostly through the exponential term in Eq. (3.28). In other words, they are effective only around the high-energy end of the electron spectrum as it is shown in [303].

Note that no specific value of the adiabatic index γ is assumed here. It influences the downstream evolution of relativistic electrons through $\bar{n}(\bar{a})$ which depends on γ (Sedov [21]).

3.2.3. Radio-emitting electrons downstream of the shock in non-uniform ISM and ISMF. The approach of the previous subsection is extended here to the possibility to deal with non-uniform ISM. At time $t_{\rm i}$, the electron distribution on the shock was

$$N(E_{\rm i}, t_{\rm i}) = K_{\rm s}(t_{\rm i}) E_{\rm i}^{-s}. \tag{3.31}$$

Since we are interested in radio emission, we have to account for only energy losses of electrons due to the adiabatic expansion [303]:

$$\frac{dE}{dt} = \frac{E}{3\rho}\frac{d\rho}{dt}, \tag{3.32}$$

where ρ is the mass density, so, the energy varies as

$$E = E_{\rm i}\mathcal{E}_{\rm ad} \tag{3.33}$$

where

$$\mathcal{E}_{\rm ad}(a,t) = \left(\frac{\rho(a,t)}{\rho_{\rm s}(t_{\rm i})}\right)^{1/3} = \left(\frac{\rho(a,t)}{\rho_{\rm s}(t)}\right)^{1/3}\left(\frac{\rho_{\rm o}(R)}{\rho_{\rm o}(a)}\right)^{1/3}. \tag{3.34}$$

The conservation law for the number of particles per unit volume per unit energy interval

$$N(E,a,t) = N(E_{\rm i},a,t_{\rm i})\frac{a^2\,da\,dE_{\rm i}}{\sigma r^2\,dr\,dE}, \tag{3.35}$$

together with the continuity equation $\rho_{\rm o}(a)a^2da = \rho(a,t)r^2dr$ and the derivative

$$\frac{dE_{\rm i}}{dE} = \mathcal{E}_{\rm ad}^{-1}, \tag{3.36}$$

implies that downstream

$$N(E,a,t) = K_{\rm s}(a,t_{\rm i})E^{-s}\left(\frac{\rho(a,t)}{\rho_{\rm s}(a,t_{\rm i})}\right)^{(2+s)/3}. \tag{3.37}$$

Assuming that $K_{\rm s} \propto \rho_{\rm s} V(t)^{-b}$,

$$K_{\rm s}(a, t_{\rm i}) = K_{\rm s}(R, t) \left(\frac{\rho_{\rm o}(a)}{\rho_{\rm o}(R)}\right) \left(\frac{V(t)}{V(t_{\rm i})}\right)^{b}. \tag{3.38}$$

Therefore, the distribution of relativistic electrons follows

$$\frac{K(a,t)}{K_{\rm s}(R,t)} = \frac{N(E,a,t)}{N(E,R,t)} = \left(\frac{\rho_{\rm o}(a)}{\rho_{\rm o}(R)}\right) \left(\frac{V(t)}{V(t_{\rm i})}\right)^{b} \left(\frac{\rho(a,t)}{\rho_{\rm s}(a,t_{\rm i})}\right)^{(2+s)/3}. \tag{3.39}$$

Now we can substitute Eq. (3.39) with the ratio of the shock velocities [195]

$$\frac{V(t_{\rm i})}{V(t)} = \left(\frac{P(a,t)}{P_{\rm s}(t)}\right)^{1/2} \left(\frac{\rho_{\rm o}(a)}{\rho_{\rm o}(R)}\right)^{(\gamma-1)/2} \left(\frac{\rho(a,t)}{\rho_{\rm s}(t)}\right)^{-\gamma/2}. \tag{3.40}$$

Thus, the downstream variation of $K(a,t)$ is described by the relation

$$\begin{aligned} \frac{K(a,t)}{K_{\rm s}(R,t)} = &\left(\frac{P(a,t)}{P_{\rm s}(R,t)}\right)^{-b/2} \\ &\times \left(\frac{\rho_{\rm o}(a)}{\rho_{\rm o}(R)}\right)^{-b(\gamma-1)/2-(s-1)/3} \left(\frac{\rho(a,t)}{\rho_{\rm s}(R,t)}\right)^{b\gamma/2+(s+2)/3}. \end{aligned} \tag{3.41}$$

This formula may easily be used to calculate the profile of $K(a)$ for known $P(a)$ and $\rho(a)$ in the case of the radial flow of fluid. In the case when mixing is allowed, the position $\vec{R}$ should correspond to the same part of the shock which was at $\vec{a}$ at time $t_{\rm i}$. It is important to note that this formula accounts for variation of injection efficiency caused by the non-uniformity of ISM.

3.2.4. Shock in non-uniform ISM and ISMF: electrons with radiative losses.

At variance with Sect. 3.2.3, we are interested here in synchrotron X-ray and γ-ray emitting electrons. In this case, the evolution of the evolution of the energy distribution of electrons has to account for energy losses of electrons due to both adiabatic expansion and radiative losses caused by synchrotron and IC processes. At time $t_{\rm i}$, the energy of the electron confined in the fluid element with Lagrangian coordinates $\vec{a} \equiv \vec{R}(t_{\rm i})$ was $E_{\rm i} = E/\mathcal{E}_{\rm ad}\mathcal{E}_{\rm rad}$ where $\mathcal{E}_{\rm ad}$ is given by (3.34), $\mathcal{E}_{\rm rad}$ is a term accounting for the radiative losses of electrons; it is similar to (3.24):

$$\mathcal{E}_{\rm rad}(E,a,t) = 1 - \mathcal{I}(a,t)\frac{E}{E_{\rm f\|}} \tag{3.42}$$

where $\mathcal{I}(a,t)$ is an integral independent of E which is calculated in case of nonuniform medium and field with the approach described in Appendix D. The electron

energy losses in a given fluid element are mainly due to radiative losses if $E_{\rm f} < E_{\rm max}$ and to adiabatic expansion if $E_{\rm f} \gtrsim E_{\rm max}$.

At time $t_{\rm i}$, the shock was able to accelerate electrons to $E_{\rm max}(t_{\rm i})$. From Eq. (3.18), we derive that

$$\frac{E_{\rm max}(t_{\rm i})}{E_{\rm max}(t)} = \left(\frac{V(t_{\rm i})}{V(t)}\right)^{q} \left(\frac{B_{\rm o}(a)}{B_{\rm o}(R)}\right)^{\lambda} \equiv \mathcal{F}(a,R) \ . \tag{3.43}$$

Again, the ratio, $V(t_{\rm i})/V(t)$, may be expressed through pressure and density; the conservation law (3.35) together with the continuity equation and the derivative $dE_{\rm i}/dE = 1/\mathcal{E}_{\rm ad}\mathcal{E}_{\rm rad}^2$, implies that downstream

$$N(E,a,t,\Theta_{\rm o}) = K(a,t,\Theta_{\rm o}) E^{-s} \mathcal{E}_{\rm rad}^{s-2} \times \exp\left[-\left(\frac{E}{E_{\rm max}(t,\Theta_{\rm o})\,\mathcal{F}(a,R)\,\mathcal{E}_{\rm ad}\mathcal{E}_{\rm rad}}\right)^{\alpha}\right] \ , \tag{3.44}$$

with $E_{\rm max}(t,\Theta_{\rm o})$ is given by Eq. (3.19); $K(a,t) = K_{\rm s}(t_{\rm i})\,\mathcal{E}_{\rm ad}^{s+2}$, the downstream variation of $K(a,t)$ is described by (3.41).

Radiative losses of electrons $\dot{E} \propto E^2$ are mostly effective in modification of the distribution $N(E,a,t)$ around $E \sim E_{\rm max}$ [303]. This may be noted in Eq. (3.44). The variation of the energy distribution $N(E,a,t)$ of electrons with energy $E \ll E_{\rm max}$ (in this case also $E \ll E_{\rm f}$, leading to $\mathcal{E}_{\rm rad} \to 1$), i.e. electrons with negligible radiative losses, is given by $N(E,a,t)/N_{\rm s}(E,R,t) = K(a,t)/K_{\rm s}(R,t)$, where $N_{\rm s}(E,R,t)$ is the energy distribution of electrons immediately after the shock. This expression does not depend on energy E and, in fact, we will use this expression for investigation of properties of the radio surface brightness distribution of SNR. In contrast, the modification of the distribution $N(E,a,t)$ due to effective electron radiation is given by the two last multipliers in Eq. (3.44). The radiative losses of electrons therefore are important for the surface brightness distribution of SNR in X-ray and γ-rays.

3.3. Approximation of the radiation power of electrons due to the inverse-Compton process in the black-body photon field

A common approach to calculate IC emission is to deal with IC emissivity for a given energy of the initial field photons (e.g. [91, 201]) with assumption of a given a priori shape of the electron spectrum, power law as a common choice. The resulting IC photon spectrum is then given by the integration over the energy distribution of the field photons. Such an approach is essential for special cases of the energy distribution of the field photons.

It is known, however, that the conditions when the IC gamma-ray photons are produced by relativistic electrons propagating in the isotropic blackbody radiation field are often met in astrophysical sources. In particular, for SNRs under typical conditions, one may just consider black-body photons, with a few different temperatures representing CMB/IR/optical radiation. Even more, in SNRs not assosiated with IR emission, the contribution from CMB photons takes over the role of infrared and optical photons (see discussion in Appendix in [223]). The IR/optical photon fields may typically contribute 10%-15% of the IC flux in such SNRs [67,162]. Similar situations are found in other astrophysical environments, too.

On the other hand, the shape of the electron spectrum at energies that are important for IC gamma-ray emission may differ considerably from a power law, especially, if one considers the emission of electrons with energy E around maximum possible values (e.g. contribution from electrons accelerated by the SNR shock to $E_{\rm max} \sim 30 - 300$ TeV is important for interpreting the HESS observations of shell SNRs).

We present an approximation for IC emissivity that may be applied to IC emission originating from the isotropic black-body photon field with temperature T. Our approximation is given in terms of an energy of incident electrons rather than in the commonly used terms of the field photon energy. Such an approach gives the possibility of accurately modeling IC emission of electrons with energy spectra different

from power law, a situation often appearing in astrophysical objects.

Since the temperature of the initial photons T is a parameter in our approach, our approximation may be used for calculating IC radiation from different photon fields (CMB, IR, optical). The target radiation field in some circumstances (e.g. around Galactic center) may not be black-body and/or the contribution from IR/optical photons may dominate CMB there [191,292]. In cases where the different components of the target radiation field may be approached by a superposition of multiple Planck distributions with different T, our approximation may be used in a similar fashion. The overall IC emission will be the weighted sum of single approximations, each with a different value for the temperature. In cases where the initial radiation field may not be approximately described by a sum of black-body distributions, our formulae do not apply.

Another assumption is the isotropy of the electron and photon fields. A thorough treatment of anisotropic IC scattering from cosmic-ray electrons is done in [259].

3.3.1. Overview of known formulae. The spectral distribution of the volume emissivity of (isotropically distributed) electrons due to the IC process is [91, 201, 326]

$$P\left(E_\gamma\right) = cE_\gamma \int d\gamma N(\gamma) \int d\epsilon n_{\rm ph}(\epsilon) \sigma_{\rm KN}\left(E_\gamma, \epsilon; \gamma\right) \tag{3.45}$$

where γ is the Lorenz factor of the electron, $N(\gamma)$ the spectral distribution of electrons, ϵ and E_γ are the energies of photon before and after interaction, $n_{\rm ph}(\epsilon)$ is the (isotropic) initial photon energy distribution,

$$\sigma_{\rm KN}\left(E_\gamma, \epsilon; \gamma\right) = \frac{3\sigma_{\rm T}}{4\epsilon\gamma^2} G\left(q, \eta\right) \tag{3.46}$$

is the angle-integrated IC cross-section, $\sigma_{\rm T}$ the Thomson cross-section,

$$G\left(q, \eta\right) = 2q \ln q + (1 + 2q)(1 - q) + 2\eta q(1 - q), \tag{3.47}$$

and

$$q = \frac{E_\gamma}{\Gamma(\gamma m_{\rm e} c^2 - E_\gamma)}, \qquad \Gamma = \frac{4\epsilon\gamma}{m_{\rm e} c^2}, \qquad \eta = \frac{\epsilon E_\gamma}{(m_{\rm e} c^2)^2}. \tag{3.48}$$

Kinematic requirements result in $(4\gamma^2)^{-1} \leq q \leq 1$ [91]. Setting q to its minimum and maximum values limits energies of up-scattered photons:

$$E_{\gamma,\min} = \frac{\gamma m_e c^2 \Gamma}{4\gamma^2 + \Gamma}, \tag{3.49}$$

$$E_{\gamma,\max} = \frac{\gamma m_e c^2 \Gamma}{1 + \Gamma} \tag{3.50}$$

that simplifies to

$$E_{\gamma,\min} = \epsilon, \qquad E_{\gamma,\max} = 4\gamma^2 \epsilon \tag{3.51}$$

in Thomson limit ($\Gamma \ll 1$) and to

$$E_{\gamma,\min} = \epsilon \text{ (if } \Gamma \ll 4\gamma^2), \qquad E_{\gamma,\max} = \gamma m_e c^2 \tag{3.52}$$

in extreme Klein-Nishina limit ($\Gamma \gg 1$). The condition $q \leq 1$ sets the minimum Lorentz factor

$$\gamma_{\min} = \frac{E_\gamma}{2 m_e c^2} \left[1 + \left(1 + \frac{(m_e c^2)^2}{\epsilon E_\gamma} \right)^{1/2} \right] \tag{3.53}$$

electron should have in order to scatter photon with energy ϵ to energy E_γ. The function $\gamma_{\min}(E_\gamma)$ may approximately be split into two parts

$$\gamma_{\min} = \begin{cases} E_\gamma^{1/2} / \left(2\epsilon^{1/2} \right), & \text{for} \quad \eta \ll 1 \\ E_\gamma / \left(m_e c^2 \right), & \text{for} \quad \eta \gg 1 \end{cases} . \tag{3.54}$$

(The Klein-Nishina decline is negligible for $\eta \ll 1$, Eq. 3.47.) The point where one could approximately switch from $\gamma_{\min} \propto E_\gamma^{1/2}$ to $\gamma_{\min} \propto E_\gamma$ is

$$E_{\gamma,*} = \frac{\left(m_e c^2 \right)^2}{4\epsilon}. \tag{3.55}$$

3.3.2. Method of approximation. In some astrophysical environments, the initial photon field may well be represented by the isotropic black-body radiation

$$n_{\rm ph}(\epsilon) = \frac{1}{\pi^2 \hbar^3 c^3} \frac{\epsilon^2}{\exp\left(\epsilon/\epsilon_{\rm c}\right) - 1} \tag{3.56}$$

with $\epsilon_{\rm c} = kT$.

Let us re-write Eq. (3.45) in the form

$$P\left(E_\gamma\right) = \int d\gamma N(\gamma) p(\gamma, E_\gamma) \tag{3.57}$$

where the spectral distribution of IC radiation power of a 'single' electron with Lorenz factor γ is

$$p(\gamma, E_\gamma) = \frac{3\sigma_{\rm T} m_{\rm e}^2 c^2 \epsilon_{\rm c}}{4\pi^2 \hbar^3} \gamma^{-2} \mathcal{I}(\eta_{\rm c}, \eta_{\rm o}) = \frac{2e^4 \epsilon_{\rm c}}{\pi \hbar^3 c^2} \gamma^{-2} \mathcal{I}(\eta_{\rm c}, \eta_{\rm o}) \tag{3.58}$$

with the function $\mathcal{I}(\eta_{\rm c}(E_\gamma), \eta_{\rm o}(\gamma, E_\gamma))$

$$\mathcal{I}(\eta_{\rm c}, \eta_{\rm o}) = \int \frac{(\eta/\eta_{\rm c}) G(\eta_{\rm o}/\eta, \eta)}{\exp(\eta/\eta_{\rm c}) - 1} d\eta, \tag{3.59}$$

$$\eta_{\rm c} = \frac{\epsilon_{\rm c} E_\gamma}{(m_{\rm e} c^2)^2}, \qquad \eta_{\rm o} \equiv q\eta = \frac{E_\gamma^2}{4\gamma m_{\rm e} c^2 (\gamma m_{\rm e} c^2 - E_\gamma)}. \tag{3.60}$$

Let us introduce

$$G_1(q) = 2q \ln q + (1+2q)(1-q), \tag{3.61}$$

$$G_2(q, \eta_{\rm o}) = 2\eta_{\rm o}(1-q). \tag{3.62}$$

In the limit $\eta \to \infty$, $G_1,\ G_2,\ G$ asymptotically approach the values

$$G_{1,\rm as} = 1, \qquad G_{2,\rm as} = 2\eta_{\rm o}, \qquad G_{\rm as} = 1 + 2\eta_{\rm o}. \tag{3.63}$$

The minimum value of η, namely $\eta_{\rm min} = \eta_{\rm o}$, is given by the condition $G(\eta_{\rm o}/\eta, \eta_{\rm o}) = 0$. Relation $\eta_{\rm min} = \eta_{\rm o}$ with definition of η, Eq. (3.48), yield the formula for the minimum energy of the photon $\epsilon_{\rm min}$, which may be up-scattered to the energy E_γ by the electron with Lorentz factor γ:

$$\epsilon_{\rm min} = \frac{E_\gamma m_{\rm e} c^2}{4\gamma (\gamma m_{\rm e} c^2 - E_\gamma)}. \tag{3.64}$$

In the limit $\eta_{\rm o} \ll \eta_{\rm c}$, which is equivalent to the Thomson limit $\Gamma(\epsilon_{\rm c}) \ll 1$, the integral (3.59) may be found analytically

$$\mathcal{I}_{\rm T}(\eta_{\rm c}, \eta_{\rm o}) = \eta_{\rm c} \int_0^\infty \frac{\eta' d\eta'}{\exp(\eta') - 1} = \frac{\pi^2 \eta_{\rm c}}{6}. \tag{3.65}$$

With decreasing η, G falls rather rapidly from $G_{\rm as}$ to zero. Let $G(\eta_{\rm o}/\eta, \eta)$ be approximated by Heavicide step function

$$G(\eta_{\rm o}/\eta, \eta) \approx (1 + 2\eta_{\rm o}) H(\eta - \eta_{\rm o}). \tag{3.66}$$

The integral $\mathcal{I}$ may then be approximately found as $\mathcal{I}(\eta_c, \eta_o) \approx \mathcal{I}_H(\eta_c, \eta_o)$:

$$\begin{aligned}\mathcal{I}_H(\eta_c, \eta_o) &= (1+2\eta_o)\int\limits_{\eta_o}^{\infty} \frac{\eta/\eta_c}{\exp(\eta/\eta_c)-1}d\eta \\ &= (1+2\eta_o)\eta_c\left(\frac{\pi^2}{6} + \mathrm{Li}_2(\exp(\eta_o/\eta_c)) + \frac{(\eta_o/\eta_c)^2}{2}\right),\end{aligned} \tag{3.67}$$

where the dilogarithm function

$$\mathrm{Li}_2(x) = -\int\limits_{x}^{1} \frac{\ln(t)}{1-t}dt. \tag{3.68}$$

An accurate approximation of (3.67) is

$$\mathcal{I}_H(\eta_c, \eta_o) \approx \frac{\pi^2}{6}\eta_c(1+2\eta_o)\exp\left(-\frac{2\eta_o}{3\eta_c}\right). \tag{3.69}$$

This expression restores $\mathcal{I}$ almost exactly for $\eta_o/\eta_c \lesssim 10^{-2}$ and $\eta_o/\eta_c \gtrsim 1$. However, $\mathcal{I}_H(\eta_c, \eta_o)$ overestimates $\mathcal{I}(\eta_c, \eta_o)$ up to 2 times for $10^{-2} \lesssim \eta_o/\eta_c \lesssim 1$. This is because the deviation of G from the Heavicide step function is important in this range.

The original integral $\mathcal{I}$ has an important property, because it may be split as $\mathcal{I} = \mathcal{I}_1 + \mathcal{I}_2$ with

$$\mathcal{I}_1(\eta_c, \eta_o) = \int \frac{(\eta/\eta_c)G_1(\eta_o/\eta)}{\exp(\eta/\eta_c)-1}d\eta = \eta_c\int \frac{xG_1(x_o/x)}{\exp(x)-1}dx, \tag{3.70}$$

$$\begin{aligned}\mathcal{I}_2(\eta_c, \eta_o) &= \eta_o\int \frac{(\eta/\eta_c)G_{2*}(\eta_o/\eta)}{\exp(\eta/\eta_c)-1}d\eta \\ &= \eta_c\eta_o\int \frac{xG_{2*}(x_o/x)}{\exp(x)-1}dx,\end{aligned} \tag{3.71}$$

where $x_o = \eta_o/\eta_c$ and $G_{2*} = G_2/\eta_o$. As one can see, these integrals may be scaled:

$$\mathcal{I}_1(a\eta_c, a\eta_o) = a\mathcal{I}_1(\eta_c, \eta_o), \quad \mathcal{I}_2(a\eta_c, a\eta_o) = a^2\mathcal{I}_2(\eta_c, \eta_o). \tag{3.72}$$

The possibility of scaling these integrands (integral $\mathcal{I}$ may not be universally scaled) is an important property that allows us to obtain an analytic approximation. It is also the reason for the approximation accuracy over the wide range of parameters.

Using $a = \eta_c^{-1}$ in the scale laws (3.72), one has

$$\mathcal{I}_1(\eta_c, \eta_o) = \eta_c\mathcal{I}_1(1, \eta_o/\eta_c), \quad \mathcal{I}_2(\eta_c, \eta_o) = \eta_c^2\mathcal{I}_2(1, \eta_o/\eta_c). \tag{3.73}$$

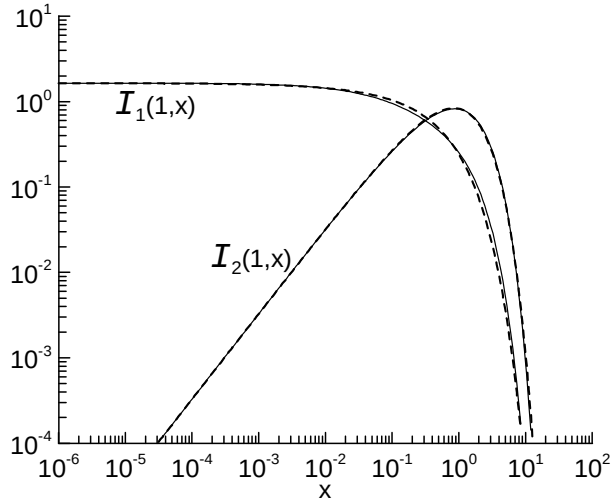

Figure 3.5. The accuracy of the approximation (3.76) as the sum $\mathcal{I}_1 + \mathcal{I}_2$. Integrals $\mathcal{I}_1(1,x)$, $\mathcal{I}_2(1,x)$ (solid lines) are compared here with their approximations (3.74) and (3.75) (dotted lines).

This means that it is enough to check how accurate approximate expressions will be in approximation of just $\mathcal{I}_1(1,x)$ and $\mathcal{I}_2(1,x)$, and we will know how accurate these approximations will be for any η_c and η_o.

Let us slightly correct exponential part in each terms of (3.69) by introducing into the exponents the second terms of the form $c_1(\eta_o/\eta_c)^{c_2}$ where c_1 and c_2 are constant. These terms make (3.69) more accurate in the representation of $\mathcal{I}_1$ and $\mathcal{I}_2$. It is important that the terms are also scaled with (3.72). With these corrections, we come to approximations

$$\mathcal{I}_1 \approx \frac{\pi^2}{6}\eta_c \exp\left[-\frac{2\eta_o}{3\eta_c} - \frac{5}{4}\left(\frac{\eta_o}{\eta_c}\right)^{1/2}\right], \tag{3.74}$$

$$\mathcal{I}_2 \approx \frac{\pi^2}{3}\eta_c\eta_o \exp\left[-\frac{2\eta_o}{3\eta_c} - \frac{5}{7}\left(\frac{\eta_o}{\eta_c}\right)^{0.7}\right]. \tag{3.75}$$

The values of c_1 and c_2 are obtained by fitting the exact $\mathcal{I}_1(1,x)$ and $\mathcal{I}_2(1,x)$. The approximations are compared with the exact dependences in Fig. 3.5 which reveals good accuracy of obtained approximate formulae.

The scaling property is a reason that the sum of approximations (3.74) and (3.75)

$$\begin{aligned}\mathcal{I}(\eta_c,\eta_o) \;\approx \frac{\pi^2}{6}\eta_c \Bigg(&\exp\left[-\frac{5}{4}\left(\frac{\eta_o}{\eta_c}\right)^{1/2}\right] \\ &+2\eta_o \exp\left[-\frac{5}{7}\left(\frac{\eta_o}{\eta_c}\right)^{0.7}\right]\Bigg)\exp\left[-\frac{2\eta_o}{3\eta_c}\right]\end{aligned} \tag{3.76}$$

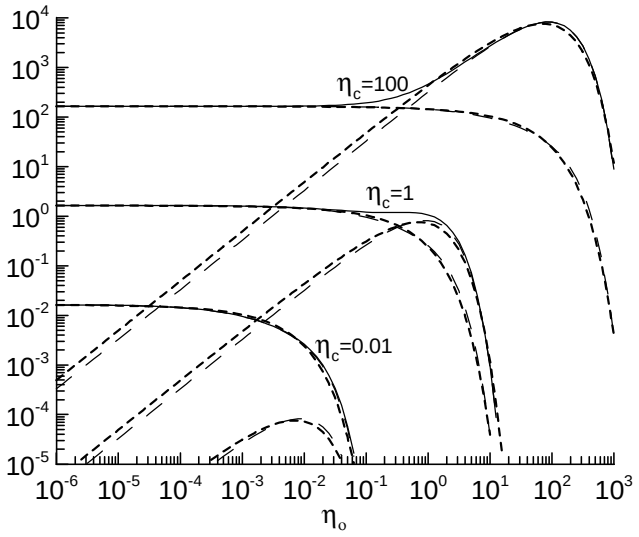

Figure 3.6. Accuracy of approximation (3.77). Integrals $\mathcal{I}$ (3.59) (solid lines), $\mathcal{I}_1$ and $\mathcal{I}_2$ (3.70), (3.71) (dashed lines), and respective terms of approximation (3.77) (dotted lines) versus η_o for a number of $\eta_c = 0.01, 1, 100$ (from below).

is accurate to represent $\mathcal{I}$ in any regime, from Thomson to extreme Klein-Nishina.

Equation (3.76) is good for any η_c. We may suggest two simpler approximations for different ranges of η_c. If mostly interested in $\eta_c \lesssim 100$ (e.g. the case of IC emission of electrons accelerated by the forward shock in SNRs), then one can use an expression

$$\mathcal{I}(\eta_c, \eta_o) \approx \frac{\pi^2}{6}\eta_c\,(1+3\eta_o)\exp\left[-\frac{2\eta_o}{3\eta_c} - \frac{5}{4}\left(\frac{\eta_o}{\eta_c}\right)^{1/2}\right]. \qquad (3.77)$$

Figure 3.6 shows that the second term here (the one proportional to $3\eta_o$) overestimates $\mathcal{I}_2$ in its power-law part. Nevertheless, this error is negligible for $\eta_c \leq 100$ (Fig. 3.6). If $\eta_c \gtrsim 10$ is of interest, then one may neglect accuracy in exponential part of approximation of $\mathcal{I}_1$ and use the approximation (Fig. 3.7)

$$\mathcal{I}(\eta_c, \eta_o) \approx \frac{\pi^2}{6}\eta_c\,(1+2\eta_o)\exp\left[-\frac{2\eta_o}{3\eta_c} - \frac{5}{7}\left(\frac{\eta_o}{\eta_c}\right)^{0.7}\right]. \qquad (3.78)$$

Figure 3.8 shows the accuracy of Eq.(3.77) in approximation of emission power (3.58) for electrons with energies $10^{12} \div 10^{16}$ eV.

3.3.3. 'Delta-function' approximation. Figure 3.8 demonstrates that a 'single' electron with Lorentz factor γ – being scattered by all black-body photons – emits most of its IC radiation at photons with some characteristic energy $E_{\gamma m}$.

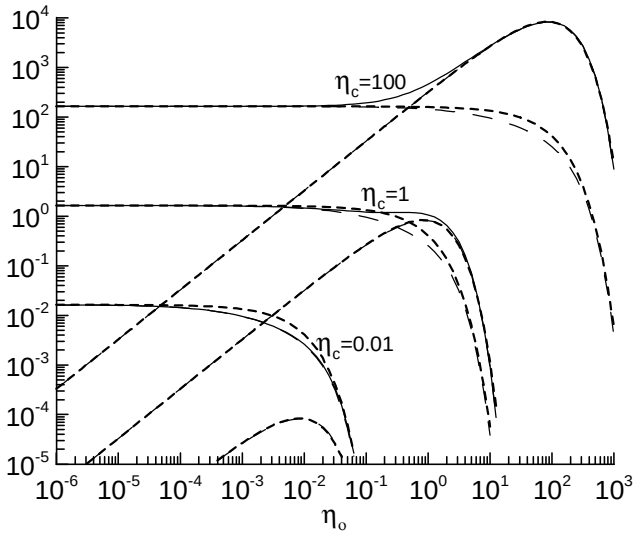

Figure 3.7. Accuracy of approximation (3.78). Integrals $\mathcal{I}$ (3.59) (solid lines), $\mathcal{I}_1$ and $\mathcal{I}_2$ (3.70), (3.71) (dashed lines), and respective summands of approximation (3.78) (dotted lines) versus η_o for a number of $\eta_c = 0.01, 1, 100$ (from below).

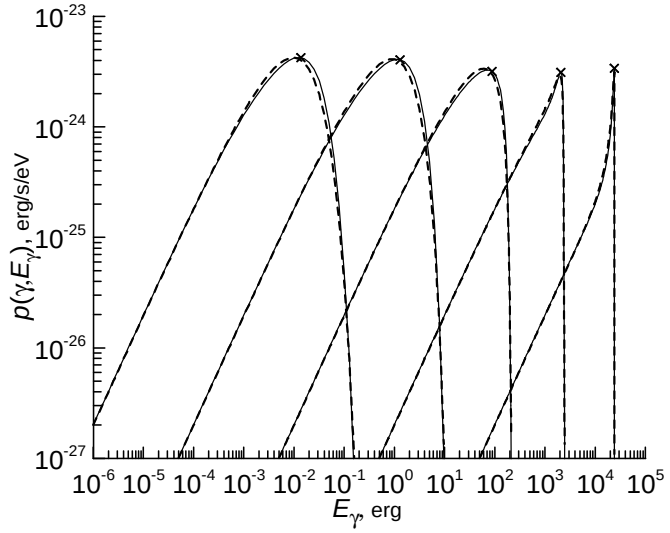

Figure 3.8. The spectrum $p(E_\gamma)$ (3.58) calculated with integral $\mathcal{I}$ (solid lines) and with its approximation (3.77) (dashed lines) for energies of electrons $E = 1.5 \cdot (10^{12}, 10^{13}, 10^{14}, 10^{15}, 10^{16})$ eV. Crosses correspond to position of $E_{\gamma,\max}(\gamma, \epsilon_c)$. The temperature of the black-body radiation is $T = 2.75\,\mathrm{K}$.

One can introduce a 'delta-function approximation', in addition to the classical 'monochromatic approximation' where the electron is scattered by the photons with a fixed energy ϵ_o (e.g. [326]). One can namely assume that a 'single' electron (scattered by all black-body photons) emits all of its IC power at photons with $E_{\gamma m}$:

$$p(\gamma, E_\gamma) \approx p_m(\gamma)\delta(E_\gamma - E_{\gamma m}) \tag{3.79}$$

where

$$p_m(\gamma) = \int_0^\infty p(\gamma, E_\gamma) dE_\gamma. \tag{3.80}$$

There are well known approximations for the total IC energy loss $p_{\rm m}$ of electron in the Thomson (see (3.85) below) and extreme Klein-Nishina limits (e.g. Sect. 4.2.3 in [326]).

Our numerical calculations show (Fig. 3.8) that $E_{\gamma{\rm m}}$ may be approximated by

$$E_{\gamma{\rm m}}(\gamma) \approx E_{\gamma,{\rm max}}(\gamma, \epsilon_{\rm c}) \tag{3.81}$$

where $E_{\gamma,{\rm max}}(\gamma, \epsilon)$ is given by (3.50). In the Thomson limit, this is

$$E_{\gamma{\rm m}}(\gamma) \approx 4\epsilon_{\rm c}\gamma^2. \tag{3.82}$$

In the classical 'monochromatic approximation' (e.g. [326]), the average $\langle E_\gamma \rangle = (4/3)\epsilon_{\rm o}\gamma^2$ is used to estimate the energy of 'monochromatic' IC photons emitted by electron.

3.3.4. Thomson limit. The use of (3.65) in (3.58) allows us to write down the expression for IC emissivity in the Thomson limit $\eta_{\rm o} \ll \eta_{\rm c}$. The spectral distribution of IC radiation power of a 'single' electron with energy $E = \gamma m_{\rm e}c^2$ is

$$p_{\rm T}(\gamma, E_\gamma) = \frac{\sigma_{\rm T}\epsilon_{\rm c}^2}{8\hbar^3c^2}\frac{E_\gamma}{\gamma^2} = \frac{\pi e^4\epsilon_{\rm c}^2}{3\hbar^3c^2}\frac{E_\gamma}{E^2}, \qquad E_\gamma \le E_{\gamma,{\rm lim}} \tag{3.83}$$

where $E_{\gamma,{\rm lim}}$ is the characteristic maximum energy defined below. This expression represents integration over all possible energies ϵ of the seed black-body photons.

The power $p_{\rm T}(\gamma, E_\gamma)$ is the increasing function of E_γ, while $p(\gamma, E_\gamma)$ decreases rather rapidly after the maximum (Fig. 3.8). We define an energy $E_{\gamma,{\rm lim}}$ by the condition

$$\int\limits_0^{E_{\gamma,{\rm lim}}} p_{\rm T}(\gamma, E_\gamma) dE_\gamma = p_{\rm mT}(\gamma) \tag{3.84}$$

where

$$p_{\rm mT}(\gamma) = (4/3)c\sigma_{\rm T}\omega\gamma^2 \tag{3.85}$$

is the total energy loss of electron due to IC in the Thomson limit, and $\omega = \int \epsilon n_{\rm ph}(\epsilon) d\epsilon$ is the energy density of all initial photons. The definition (3.84) results in

$$E_{\gamma,{\rm lim}} = \frac{4}{\pi}\epsilon_{\rm c}\gamma^2 \left[\frac{2}{3}\int\limits_0^\infty \frac{z^3 dz}{\exp(z)-1}\right]^{1/2} = 2.65\epsilon_{\rm c}\gamma^2. \tag{3.86}$$

Note that $E_{\gamma,\mathrm{lim}}$ differs only a little from $E_{\gamma,\mathrm{max}}(\epsilon_\mathrm{c}) = 4\epsilon_\mathrm{c}\gamma^2$.

The volume emissivity of electrons distributed as

$$N(\gamma) = N_\mathrm{o}\gamma^{-s} \quad \text{for} \quad \gamma_\mathrm{min} < \gamma < \gamma_\mathrm{max}, \quad \gamma_\mathrm{min} \ll \gamma_\mathrm{max} \tag{3.87}$$

is

$$P\left(E_\gamma\right) = \frac{\sigma_\mathrm{T}\epsilon_\mathrm{c}^2}{8\hbar^3c^2(s+1)} N_\mathrm{o} E_\gamma \gamma_\mathrm{min}^{-(s+1)}. \tag{3.88}$$

For $E_\gamma \lesssim E_{\gamma,*}$, the minimum Lorentz factor is $\gamma_\mathrm{min} = E_\gamma^{1/2}/(2\epsilon_*^{1/2})$, Eq. (3.54), and we approximate the (3.57) in the Thomson limit

$$P\left(E_\gamma\right) = \frac{2^{s-2}\sigma_\mathrm{T}\epsilon_\mathrm{c}^2\epsilon_*^{(s+1)/2}}{\hbar^3c^2(s+1)} N_\mathrm{o} E_\gamma^{-(s-1)/2}, \tag{3.89}$$

with the known slope $P\left(E_\gamma\right) \propto E_\gamma^{-(s-1)/2}$. The value of ϵ_* may be fixed by comparing (3.89) with e.g. expression (4.2.17) in [326]; i.e., $\epsilon_* = \mathcal{A}(s)\epsilon_\mathrm{c}$ with

$$\mathcal{A}(s) = \left[\frac{12}{\pi^2}\frac{(s^2+4s+11)}{(s+5)(s+3)^2}\int\limits_0^\infty \frac{z^{(s+3)/2}dz}{\exp(z)-1}\right]^{2/(s+1)}. \tag{3.90}$$

Numerically, $\mathcal{A}(1.8) = 0.665$, $\mathcal{A}(2) = 0.710$, $\mathcal{A}(2.2) = 0.755$.

3.4. Thermal X-ray composites as sources for hadronic γ-rays

Up to now, there is no clear observational confirmation that hadronic component of CRs is generated by SNRs. Gamma-rays from proton-proton collisions are mainly expected from the SNRs which are located near the dense interstellar material and reveal evidence about interaction with it.

To look for signatures of proton acceleration in SNR, it is interesting to consider a class of SNRs which is known as thermal X-ray composites (Sect. 2.1). It is interesting that most of these SNRs reveal observational evidence about the interaction with nearby molecular clouds. Thus, ambient media in the regions of their location are nonuniform and cause a nonsphericity of SNRs. Model of TXC described in Sect. 2.1 strongly suggests that the thermal X-ray peak inside the radio shell tells

us that one part of SNR shock has entered into a denser medium compared with other parts. This makes TXCs promising sites for γ-ray generation via π^o decays.

Let us consider this possibility in more details.

3.4.1. Estimations on the pion-decay γ-ray luminosity of SNR. Luminosity of an SNR in π^o decay γ-rays in $\varepsilon \geq \varepsilon_{\rm min}/6$ band is [194, 342]:

$$L_\gamma = \frac{c\overline{\sigma}_{pp}}{6} n_N W_{\rm cr}. \tag{3.91}$$

where $\varepsilon_{\rm min} \approx 600$ MeV is the minimal proton kinetic energy of the effective pion creation, cross section $\sigma_{pp}(\varepsilon)$ is close to the mean value $\overline{\sigma}_{pp} = 3 \cdot 10^{-26}$ cm^2, n_N is the mean number density of target nuclei and $W_{\rm cr}$ is the total energy of cosmic rays in the SNR with $\varepsilon \geq \varepsilon_{\rm min}$. There are different estimations of the efficiency ν of the flow's kinetic energy transformation into the energy of accelerated particles: $W_{\rm cr} = \nu E_o$. . Thus, in the first approach, the theoretical estimation on the π^o decay γ-luminosity of any SNR is

$$L_\gamma^{\geq 100} = 6.3 \cdot 10^{33} \overline{n}_o \nu_3 E_{51} \quad {\rm erg/s},$$

where $\nu_3 = \nu/0.03$, E_{51} is the energy of supernova explosion in the units of 10^{51} erg, $\overline{n}_o = \overline{n}_N^o/1.4$ is the average hydrogen number density within SNR which equals to average hydrogen number density of the ambient medium in the region of an SNR location, in cm^{-3}.

The real situation is more complicated. Often only a part of SNR (with volume $V_{\rm int}$) interacts with a denser ISM material. There are factors which increase CR energy density ω_{cr} [194]: 1) The CRs are not uniformly distributed inside an SNR; most of CRs are expected to be in a thin shell near the shock front where most of swept-up mass is concentrated. 2) The reverse shock from interaction with dense cloud also increases the energy density of CRs. These factors enhance ω_{cr} in the region of interaction as we have shown in [194]:

$$\omega_{\rm cr} \approx 1.7 \left(\frac{\gamma}{\gamma - 1} \right)^{3/2} \overline{\omega}_{\rm cr} \ , \tag{3.92}$$

where CR energy density in the region of interaction is $\omega_{\rm cr} = W_{\rm cr}/V_{\rm int}$ and $\overline{\omega}_{\rm cr} = W_{\rm cr}/V_{\rm snr}$. This gives $\omega_{\rm cr} \approx 6.6\ \overline{\omega}_{\rm cr}$ for $\gamma = 5/3$.

If we put $W_{\rm cr} = \omega_{\rm cr} V_{\rm int}$ into (3.91), we obtain with (3.92) that for any SNR

$$L_\gamma^{\geq 100} = 1.7 \cdot 10^{35} \eta n_o \nu_3 E_{51} \quad \text{erg/s} \tag{3.93}$$

where $\eta = V_{\rm int}/V_{\rm snr}$, n_o is the number density of the ambient medium before the shock wave in the region of interaction, $\gamma = 5/3$. We have to take into account that region of interaction is not extended to the region before the shock, since the energy density of CR should be considerably lower outside the SNR [1, 161, 194]. It is easy to estimate η following our consideration in [194]:

$$\eta = 0.18 \mu^2 \sqrt{\xi}, \qquad \mu \leq 0.2, \tag{3.94}$$

where $\xi = n_o/\overline{n}_o$, $\mu = R_{int}/\overline{R}$, R_{int} is the average radius of the surface of interaction, $\overline{R}$ is the average radius of SNR.

Thus, considering the hydrodynamic process of SNR-cloud interaction in details, it is possible to increase the expected π^o decay γ-ray flux by $26\eta\xi \simeq 0.2\xi^{3/2}$ times, i. e., up to few orders of magnitude.

3.4.2. Hadronic origin of γ-rays from MSH 11-61A. SNR G290.1-0.8 (MSH 11-61A) is located in the southern hemisphere. The distance to the remnant, 7 kpc, is obtained from the optical observations [320], but not yet confirmed by X-ray observations [337]. X-ray and radio morphologies [330,368] make the SNR a member of TXC class. In the direction to MSH 11-61A lies the γ-ray source 2EG 1103-6106 (3EG J1102-6103) [319, 343]. Is it possible to consider observed flux of the source directed toward the MSH 11-61A as π^o decay γ-ray emission?

The γ-flux from the source 3EG J1102-6103 in the EGRET band $\varepsilon_\gamma = 30 \div 2 \cdot 10^4$ MeV is approximated as [248]

$$S_\gamma = (1.1 \pm 0.2) \cdot 10^{-9} \left(\frac{\varepsilon_\gamma}{213 \text{ MeV}} \right)^{-2.3 \pm 0.2} \quad \frac{\text{photon}}{\text{cm}^2 \cdot \text{s} \cdot \text{MeV}} \, .$$

Thus, the luminosity of the source in $\varepsilon_\gamma \geq 100$ MeV band is respectively

$$L_{\gamma,\rm obs}^{\geq 100} = 4 \cdot 10^{34} \, d_{\rm kpc}^2 \quad \text{erg/s}.$$

The parameters of MSH 11-61A [337] are presented in Table 3.1 (different for different distance assumed). There are also values of ξ in the table which allow to

Table 3.1
Parameters of MSH 11-61A [337], luminosity $L_{\gamma,\rm obs}^{\geq 100}$ of 2EG 1103-6106 and estimations on the proton origin γ-luminosity of the SNR. Presented values of ξ allow us to satisfy condition $L_{\gamma,\rm obs} = L_\gamma$.

d, kpc	Age t, 10^4 yrs	$\overline{R}$, pc	E_{51}, 10^{51} erg	$\overline{n}_o$, cm^{-3}	$L_{\gamma,\rm obs}^{\geq 100}$, 10^{36} erg/s	$L_\gamma^{\geq 100}/\xi^{3/2}$, 10^{32} erg/s	ξ, 10^2
10	1.3	18	1	0.27	4	3.2	5
7	0.9	13	0.4	0.27	2	1.3	6

adjust the expected luminosity of MSH 11-61A in π^o decay γ-rays with observed flux from the source 3EG J1102-6103. We see that moderate number density $\sim$ 150 cm^{-3} of cloud located near the one region of the remnant is enough to explain the luminosity of 3EG J1102-6103, by protons accelerated on the shock front of MSH 11-61A. Note, if we take $\nu \simeq 0.1 - 0.2$ [47] instead of the value used here, $\nu = 0.03$, the density of cloud needs to be only $\sim 20 \div 40$ cm^{-3}.

The same consideration allows us to adjust also the γ-luminosity of the source 3EG J0617+2238 toward IC 443 with the luminosity of this SNR [194].

3.5. Conclusions

Some properties of relativistic charged particles which are accelerated by forward shocks in SNRs are investigated. In particular, electron injection, evolution of accelerated electrons downstream of the shock as well as its γ-ray emission due to inverse-Compton process and pp-interactions are considered.

1. Within a test-particle approach, an analytic treatment of the electron injection at parallel nonrelativistic shock is presented. The probability of a particle to be injected is estimated as that of going back to the upstream region at least once. This is the product of the probability of returning to the shock from downstream times that of recrossing the shock from downstream to upstream. The latter probability is expected to be sensitive to details of the process of electron thermalisation within the (collisionless) shock, a process that is poorly known. In order to include this effect,

results of a numerical study [96] are used. It becomes apparent that the injection efficiency is related to the post-shock electron temperature, and that it results from the balance between two competing effects: the higher the electron temperature, the higher the fraction of downstream electrons with enough velocity to return to the shock and thus to be ready to cross the shock from downstream to upstream; at the same time, however, the higher the turbulence, which would hinder the crossing.

2. Downstream evolution of the energy spectrum of relativistic electrons accelerated on the strong nonrelativistic shock is considered. It includes energy-dependent adiabatic and radiative losses due to synchrotron and IC emission. The description developed includes for the first time the possibility to account for the shock motion in the nonuniform ISM and/or nonuniform ISMF. It allows for a detailed modeling of the non-thermal leptonic emission of SNRs in radio, X-ray and gamma-ray bands.

3. An approximation is presented for the inverse-Compton radiation power of electrons in the isotropic black-body photon field. This approximation allows calculation of IC emissivity as an integral over the energies of incident electrons rather than over the field photon energies. Such an approach allows for accurate modeling of IC emission of electrons with energy spectra different from power law, in tasks where essential CPU resources are needed, e.g. in modeling the SNR emission. The main idea behind our approach is the possibility of splitting the initial integral into two parts that may be scaled, contrary to the original integral. This scaling is the reason for the high accuracy of the approximation over the wide range of parameters, from the Thomson to extreme Klein-Nishina regime. This approach also results in some new analytic expressions representing the known results in the Thomson limit.

4. A new model for the thermal X-ray composites strongly suggest that thermal X-ray peak inside the radio shell of SNR tells us that one part of SNR shock enters into a denser medium compared with other parts of the shell. This makes a TXCs promising sites for γ-ray generation via π^o-decays. Detailed consideration of SNR-cloud interaction allows one to increase an expected proton induced γ-ray flux from SNR at least on an order of magnitude, that is enough to adjust the theoretical π^o-decay γ-luminosities with observed fluxes in SNR MSH 11-61A and IC 443.

CHAPTER 4

SURFACE BRIGHTNESS DISTRIBUTION IN THE SHELL-TYPE SNRS

The current generation of large X-ray observatories (NASA's Chandra and ESA's XMM-Newton) together with improvements made in the field of gamma-ray experiments (HESS, Fermi etc.) allow us to investigate properties of SNRs which were unknown earlier. It has become clear that simple idealized models have been pushed to their limit; a comprehensive understanding requires the inclusion of physical effects which have been traditionally neglected (like, for instance: the dependence of the acceleration processes on the shock dynamics, as well as on the angle between the ambient magnetic field and the shock normal; deviations from e-p thermal equilibration). In addition, it is now a common belief that SNR models cannot ignore details like the configuration of the magnetized SNR environment, or the presence of molecular clouds (important for generation of the proton-origin gamma-rays), or any other small and/or large-scale gradients.

Current studies cover however only few directions of that complex picture. Namely, very important observational results are explored only partially: scientists make use almost exclusively the spectral characteristics of the sources. Spectral analysis gives valuable constraints on the parameter space. Nevertheless, the γ-ray part of the broad-band spectra of nonthermal emission from SNRs may be explained either as leptonic or as hadronic in origin. The analysis of the spatial distribution of nonthermal emission - one of the main goals of the present thesis - is an additional important channel of the experimental information which remains almost unexplored yet.

The present chapter is devoted to theoretical modeling of the nonthermal maps of adiabatic SNRs. We present models and synthesize the radio, synchrotron X-ray and IC γ-ray images of SNRs in uniform media in Sect. 4.1. Analytical approximations

which reveal the main factors affecting the azimuthal and radial profiles of surface brightness of Sedov SNRs due to emission of relativistic electrons are obtained in Sect. 4.2. The role of ISM/ISMF nonuniformity in radio, X-ray and gamma-ray maps of SNRs is explored in Sects. 4.3 and 4.4.

In order to clearly see the role of different factors (in particular, nonuniformities of ISM or ISMF) in determining the morphology of SNRs, we use some simplifying assumptions about electron kinetic and behavior of magnetic field in vicinity of the shock front. Our our studies of SNR maps assume classic MHD and test-particle theory of acceleration. Though they neglect effects of the back-reaction of the efficiently accelerated particles, they nevertheless are able to explain general properties of the distribution of the surface brightness in radio, X-rays and γ-rays. This is because the classic theory, in contrast to the non-linear one, is able to deal with oblique shocks, that is vital for synthesis of SNR images. Effects of non-linear acceleration on the radial profiles of brightness are considered in [104, 143, 224, 376]. In particular, the radial profiles of hard X-ray brightness were used for estimates of the post-shock magnetic field in some SNRs (e.g. [78]) and the radial structure of the X-ray emission from the shock precursor in SN 1006 was used to find evidence about efficient particle acceleration [258].

Approximations developed in Sect. 4.2 are able to account for non-linear effects. Future studies on SNR morphology should consider these effects in more details. Beside that, it is important to know the properties of the 'classic' images because they create the reference base for investigation of the efficiency of NLA effects in the surface brightness distribution of SNRs.

Results presented in this chapter are published in [264, 265, 271, 274, 276, 278, 281, 282, 285].

4.1. Radio, X-ray and gamma-ray maps of SNRs in uniform ISM and ISMF

There are some discussions emphasyzing that observed correlations of brightness in radio, X-rays and γ-rays may be considered to favor electrons to be responsible for TeV emission in RX J1713.7-3946, Vela Jr. and some other SNRs (e.g. [45, 287]). However, should the patterns of surface brightness in radio, X-rays and γ-rays realy correlate if the TeV γ-radiation originates from electrons? What should be the limitations for theory once observed patterns are really quite similar, especially in symmetrical bilateral SNRs, like in SN 1006 [28]?

An experimental investigation of SNR images have to be complemented with theoretical modelling of SNR maps in different energy domains. A detailed approach to modeling the synchrotron images of adiabatic SNRs in uniform ISMF and uniform ISM is developed by Reynolds [303]. He uses modeled synchrotron maps of SNRs to put constraints on some properties of accelerated particles [157, 303, 305]. We extend the approach of Reynolds [303] to investigate properties of the patterns of brightness distribution in SNR, factors which mostly affect them and to compare maps in different bands.

4.1.1. Synthesis of maps: model. Let us consider adiabatic SNR in uniform ISM and uniform ISMF. We use the Sedov solutions for dynamics of fluid [21] as well as description of the MF behavior downstream of the shock from Reynolds [303]. The use of analytical solutions allows us to reduce the computational time considerably. We improve the approach from [303] to calculation of the evolution of the distribution function $N(E)$ of relativistic electrons downstream of the shock in Sect. 3.2.2.

The ISMF orientation versus observer is described by the aspect angle $\phi_{\rm o}$, an angle between ISMF and the line of sight. The obliquity angle $\Theta_{\rm o}$ is the angle between ISMF and the normal $\vec{n}$ to the shock. The azimuth angle φ (in the projection plane) is measured from the direction of the component of ISMF in the plane of the sky (Fig. 4.1). The compression factor for ISMF $\sigma_{\rm B}$ increases from unity at parallel shock

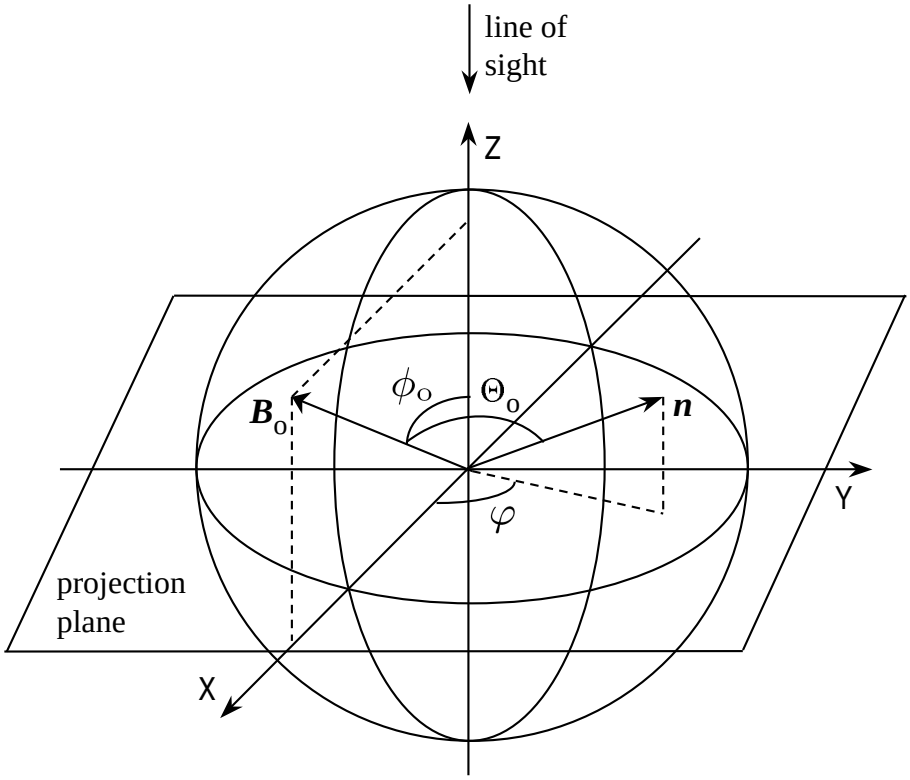

Figure 4.1. Geometry of the task. The obliquity angle Θ_o, the aspect angle ϕ_o and the azimuth angle φ are shown. For clarity, ISMF B_o is chosen to be parallel to the X0Z plane.

to σ at perpendicular one, in an agreement with [303].

An important point is the degree of ordering of magnetic field downstream of the shock. Radio polarization observation of a number of SNRs (e.g. Tycho [126], SN1006 [311]) show the low degree of polarization, 10-15% (in case of ordered magnetic field the value expected is about 70%; [157]), indicating highly disordered magnetic field. Thus we calculated the synchrotron images of SNR for two opposite cases. First, since our hydrodynamic code gives us the three components of magnetic field, we are able to calculate images with ordered magnetic field. Second, we introduce the procedure of the magnetic field disordering (with randomly oriented magnetic field vector with the same magnitude in each point) and then synthesize the radio maps. In models which have a disordered magnetic field, we use the post-shock magnetic field before disordering to calculate the angle Θ_s; as discussed by [157], this corresponds to assume that the disordering process takes place over a longer time-scale than the electron injection, occurring in the close proximity of the shock. Since we found that the asymmetries induced by gradients either of ambient plasma density or of ambient magnetic field strength are not significantly affected by the

degree of ordering of the magnetic field downstream of the shock, in the following we will focus on the models with disordered magnetic field.

It is common to consider three models for injection: quasi-parallel, isotropic and quasi-perpendicular. The pattern of the radio surface brightness distribution in the case of the quasi-perpendicular injection is quite similar to the isotropic injection case, though with different contrasts ([157] and Sect. 4.3). The numerical calculations of [137] show that the obliquity dependence of the injection efficiency ς (a fraction of accelereted electrons) may be either flatter or steeper than in the classic quasi-parallel case ($\varsigma \propto \cos^2 \Theta_\mathrm{o}$). Therefore, in order to be more general than Reynolds [303], in the Sects. 4.1.2 and 4.1.3, we allow also the injection efficiency to vary with obliquity angle with different 'sensitivity' which is given by the parameter Θ_K:

$$\varsigma(\Theta_\mathrm{o}) = \varsigma_\parallel \exp\left(-(\Theta_\mathrm{o}/\Theta_\mathrm{K})^2\right) \tag{4.1}$$

where $\varsigma_\parallel$ is the efficiency for the parallel shock. This expression restores approximately the results of Ellison et al. [137] with $\Theta_\mathrm{K} = \pi/9 \div \pi/4$. The classic quasi-parallel injection may be approximated with $\Theta_\mathrm{K} = \pi/6$. Isotropical injection assumes $\Theta_\mathrm{K} = \infty$, but the values $\Theta_\mathrm{K} \geq 2\pi$ produces almost the same images as $\Theta_\mathrm{K} = \infty$ because the range for obliquity angle is $0 \leq \Theta_\mathrm{o} \leq \pi/2$. The variation of the parameter Θ_K provide smooth transition from polar-cap ($\Theta_\mathrm{K} \leq \pi/6$) to barrel-like ($\Theta_\mathrm{K} \geq \pi$) models of SNR. We consider also quasi-perpendicular injection:

$$\varsigma(\Theta_\mathrm{o}) = \varsigma_\parallel \exp\left(-((\Theta_\mathrm{o} - \pi/2)/\Theta_\mathrm{K})^2\right). \tag{4.2}$$

The surface brightness is calculated integrating emissivities along the line of sight within SNR, assuming the source is optically thin. The emissivity of electrons is given by

$$q(\varepsilon) = \int_0^\infty N(E) p(E, \varepsilon) dE \tag{4.3}$$

where ε is the photon energy and p is the spectral distribution of synchrotron or inverse-Compton radiation power of electrons.

In the case of synchrotron emissivity, the spectral distribution of radiation power

of a single electron with energy E in the magnetic field $\vec{B}$ is

$$p(E,\varepsilon) = \frac{\sqrt{3}e^3\mu_\phi B}{m_{\rm e}c^2}\, F\left(\frac{\varepsilon}{\varepsilon_{\rm c}}\right) \ , \tag{4.4}$$

where $\varepsilon_{\rm c} = h\nu_{\rm c} = hc_1\mu_\phi BE^2$, h is the Plank constant, $\nu_{\rm c}$ is the critical frequency, ϕ the angle between the magnetic field and the LoS, μ_ϕ is either $\mu_\phi = \sin\phi$ for the case of ordered magnetic field or $\mu_\phi = \langle\sin\phi\rangle = \pi/4$ for disordered magnetic field, $c_1 = 3e/(4\pi m_{\rm e}^3c^5)$, e and $m_{\rm e}$ are the charge and mass of electron, respectively, c is the speed of light. The special function $F(w)$ can be approximated as (e.g. [325, 365]):

$$F(w) = \begin{cases} 2.15\, w^{1/3} & w < 0.01 \ , \\ \sqrt{\pi}\, w^{0.29}\exp(-w) & 0.01 \le w \le 5 \ , \\ \sqrt{\pi/2}\, w^{1/2}\exp(-w) & w > 5 \ . \end{cases} \tag{4.5}$$

We found the above approximation quite accurate with discrepancies $\lesssim 4\%$ from the exact value; in particular, $\int_0^\infty F d\varepsilon = 1.59$ while the exact value is $8\pi/9\sqrt{3} = 1.61$.

We synthesize the radio emission, assuming that it is only due to synchrotron radiation from relativistic electrons distributed with a power law spectrum $N(E) = KE^{-s}$. The radio emissivity can be expressed as [168]

$$q(\nu) = C_1 K (\mu_\phi B)^{\,\alpha+1}\nu^{\,-\alpha}, \tag{4.6}$$

where C_1 is a constant, ν is the frequency of the radiation, $\alpha = (s-1)/2$ is the synchrotron spectral index (assumed to be uniform everywhere as consequence of the fact that adiabatic losses are independent of E, therefore, the electron spectrum has the same power-law shape downstream of the shock).

In the case of γ-ray emissivity due to IC process, the spectral distribution of radiation power of a single electron in a black-body photon field in Eq. 4.3) is (e.g. [326])

$$p(E,\varepsilon) = \frac{2e^4\epsilon_{\rm c}}{\pi\hbar^3c^2}\Gamma^{-2}\mathcal{I}_{\rm ic}(\eta_{\rm c},\eta_0) \ , \tag{4.7}$$

where Γ is the Lorenz factor of electron, $\epsilon_{\rm c} = kT_{\rm CMBR}$, $T_{\rm CMBR}$ is the temperature of CMB (assumed to be $T_{\rm CMBR} = 2.75$ K), and the special function $\mathcal{I}_{\rm ic}(\eta_{\rm c},\eta_0)$ can be accurately approximated by our Eq. (3.76).

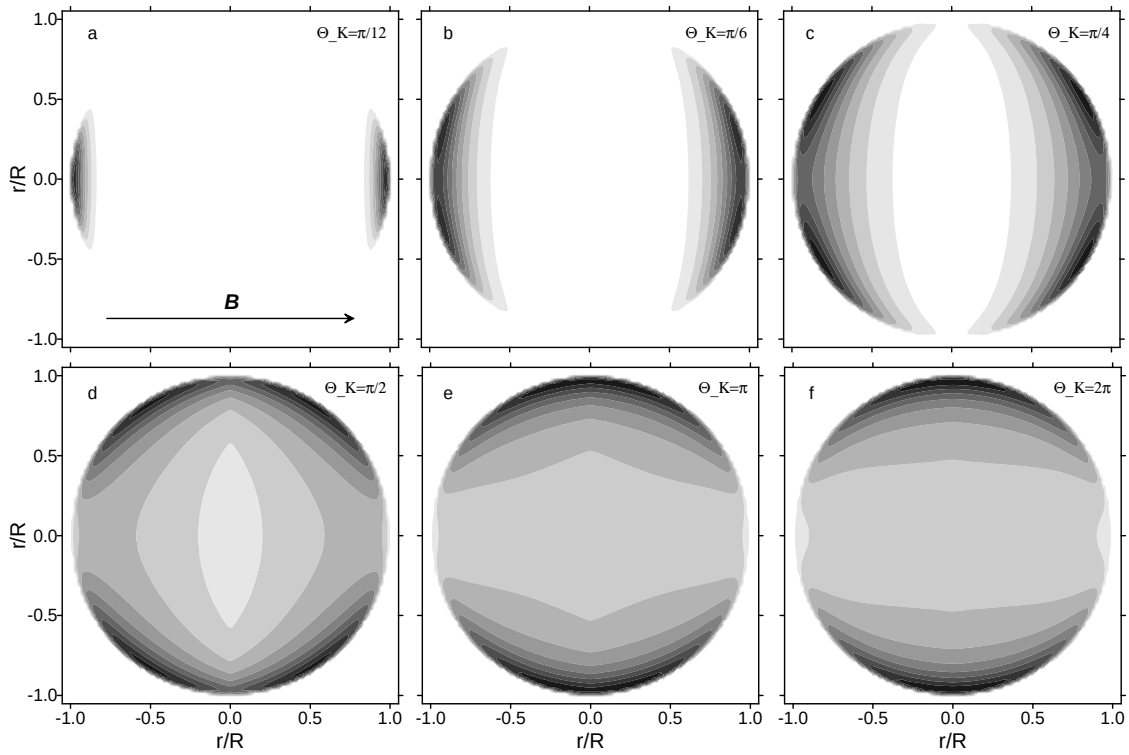

Figure 4.2. Radio images of SNR for an aspect angle $\phi_o = 90^o$ and different Θ_K: $\pi/12$ (a), $\pi/6$ (b), $\pi/4$ (c), $\pi/2$ (d), π (e), 2π (f). Ambient magnetic field is oriented along the horizontal axis. Hereafter, the increment in brightness is $\Delta S = 0.1 S_{\max}$.

4.1.2. Synchrotron radio images. In the present subsection, we assume that K is constant in time; eventual evolution of K affects the radial thickness of rims and does not modify the main features of the surface brightness pattern (Sect. 4.1.4).

Fig. 4.2 shows how Θ_K affects a radio image of SNR. We note that *smooth increase of* Θ_K *results in transition from the 3-D polar-cap model of SNR to the 3-D barrel-like one*. This is also visible on Fig. 4.3 where ISMF is directed toward observer. Namely, increase of Θ_K change the visual morphology from centrally-bright to shell-like.

There are three names for a class of SNRs which have two opposite bright limbs in the literature: 'barrel-shaped' [212], 'bipolar' [157] and 'bilateral' [159]. They were introduced on the base of 2-D visual morphology. It is interesting that the first two names reflects de facto the two different conceptions of SNRs in 3-D: either "barrel" or with two "caps".

Fig. 4.2 also shows that an assumption about orientation of ISMF leads to limi-

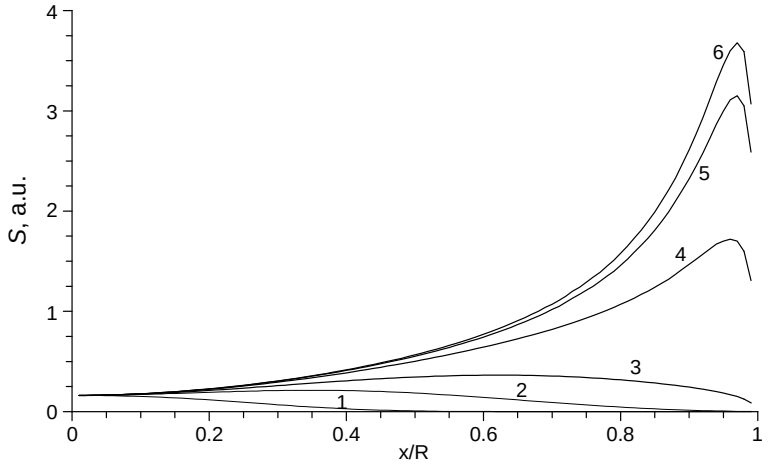

Figure 4.3. Profiles of the radio surface brightness for an aspect angle $\phi_o = 0^o$ (the radial profile of brightness is the same for any azimuth). Θ_K is $\pi/12$ (line 1), $\pi/6$ (line 2), $\pi/4$ (line 3), $\pi/2$ (line 4), π (line 5), 2π (line 6).

tation of possible injection model. Ambient magnetic field in all images on Fig. 4.2 is along horizontal axis. Thus, *if one consider the polar-cap scenario for bilateral SNR* (ISMF is along axis which crosses two limbs) *then one should consider the quasi-parallel injection model which strongly depends on the obliquity* ($\Theta_K \leq \pi/6$, Fig. 4.2a,b). Instead, *if the barrel is the preferable model* (ISMF is parallel to the symmetry axis between two limbs) *then the injection efficiency should be almost independent of obliquity* ($\Theta_o \geq \pi$, Fig. 4.2e,f), or prefer quasiperpendicular shocks.

The angle ψ between the symmetry axis in 17 'clearly' bilateral SNRs and the Galactic plane was measured in [159]. Axes are more or less aligned with the Galactic plane in 12 SNRs ($\psi < 30^o$), 2 SNRs have $\psi \approx 45^o$ and 3 SNRs is almost perpendicular ($\psi > 60^o$). If we assume that ISMF is parallel to the plane of Galaxy then most of bilateral SNRs should be 3-D barrels preffering thus isotropic (or quasiperpendicular) injection.

An interesting feature appears on images for $\Theta_K = \pi/4 \div \pi/2$ (Fig. 4.2c,d). Namely, SNR has 'quadrilateral' morphology. With increasing of obliquity, the injection efficiency decreases while the compression factor of ISMF icreases. The variation of injection $\varsigma(\Theta_o)$ dominates $\sigma_B(\Theta_o)$ for $\Theta_K \leq \pi/6$. If $\Theta_K \geq \pi$ (injection is almost isotropic) then $\sigma_B(\Theta_o)$ plays the main role in azimuthal variation of the radio surface brightness. In the intermediate range of Θ_K, the significance of the two variations are comparable leading therefore to azimuthal migration of the brightness maxima

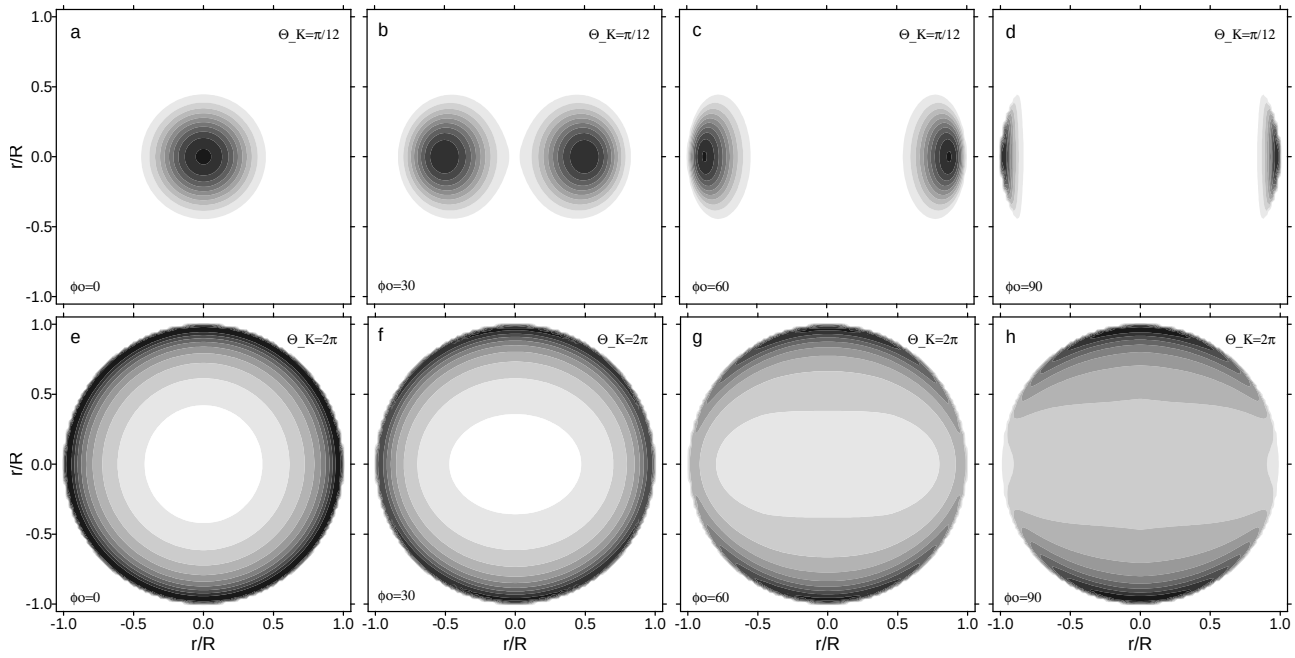

Figure 4.4. Radio images of SNR for different aspect angles ϕ_o: 0° (a,e), 30° (b,f), 60° (c,g), 90° (d,h). $\Theta_K = \pi/12$ (upper panel), $\Theta_K = 2\pi$ (lower panel). Component of the ambient magnetic field which is perpendicular to the line of sight, is oriented along the horizontal axis.

in the modelled images. There is no 'quadrilateral' SNR reported in the literature. If there is no such SNR at all, the range $\Theta_K \simeq \pi/4 \div \pi/2$ may be excluded. However, we stress that a complete statistical study of the morphology of radio SNRs would be needed to definitly asses the lack of quadrilateral SNRs[1].

The visual morphology of SNR is different for different aspect angles. Fig. 4.4 shows SNR images for quasi-parallel injection with $\Theta_K = \pi/12$ (upper panel) and for isotropic injection ($\Theta_K = 2\pi$, lower panel). We may expect that ISMF may have different orientation versus observer in various SNRs. If quasi-parallel injection is not a rare exception then the polar-cap SNRs should be projected in a different way and we may expect to observe not only 'bipolar' SNRs (Fig. 4.4c,d) but also SNRs with one or two radio eyes within thermal X-ray rim (Fig. 4.4a,b). Authors [157] developed statistically this thought and showed that the quasi-parallel injection model would be unlikely, but again, we would need a complete study to verify this statement[2]. Statistical arguments of [157] may be affected by the fact that centrally-bright radio SNRs (lines 1-2 on Fig. 4.3) are expected to be fainter than bilateral or circular SNRs with the same characteristics (lines 4-6 on Fig. 4.3): it could be that

[1] G338.3-0.0 could be an example of quadrilateral SNR

[2] G311.5-0.3 and G337.2-0.7 could be examples of SNRs with two radio 'eyes'

most of the centrally-peaked SNRs may not be observable.

4.1.3. IC γ-ray images. The fiducial energy at parallel shock $E_{\mathrm{f}\parallel}$, which is responsible for the 'sensitivity' of relativistic electrons to the radiative losses [303] and which is used in IC images is set to $E_{\max}$. Also we assume here that K is constant in time. Electrons emitting IC photons have energies $E \sim E_{\max}$. Like K, $E_{\max}$ is assumed to be constant in time. Its possible variation in time does not change the pattern of IC brightness and leads to effects similar to those originating from the time dependence of K. Namely, features in IC images have to be radially thicker if $E_{\max}$ decreases with time (i.e. increases with the shock velocity): since $E_{\max}$ was larger at previous times, there are more electrons in the SNR interior able to emit IC photons at the present time. If $E_{\max}$ increases with time (i.e. decreases with the shock velocity) then maxima in brightness are expected to be radially thinner.

In the most cases presented in this subsection, $E_{\max}$ is assumed to be constant over SNR surface; this choice allows us to clearly see the role of other parameters. [303] considered loss-limited, time-limited and escape-limited models for $E_{\max}$. In all cases, except of the loss-limited one with the level of turbulence comparable with the Bohm limit, $E_{\max}$ should grow with increase of Θ_{o} [303]. Later on (Fig. 4.9), we model the role of possible increase of $E_{\max}$ with obliquity with a simple parameterization

$$E_{\max}(\Theta_{\mathrm{o}}) = E_{\max\parallel} \exp\left(-((\Theta_{\mathrm{o}} - \pi/2)/\Theta_{\mathrm{E}})^2\right) \tag{4.8}$$

where Θ_{E} is a parameter, $E_{\max\parallel}$ the maximum energy at parallel shock. This formula, with different values of Θ_{E}, is able to restore approximately different cases considered by [303].

All IC images (except of that on Fig. 4.10) are calculated for the initial photon field with $T = 2.75$ K and for the γ-ray photon energy $\varepsilon = 0.1\varepsilon_{\max}(E_{\max})$ that is for example $\varepsilon = 0.3\,\mathrm{TeV}$ for $E_{\max} = 30\,\mathrm{TeV}$.

Synthesized IC γ-ray images of SNRs are presented on Fig. 4.5, for different aspect angles. These images assume almost *isotropic* injection ($\Theta_{\mathrm{K}} = 2\pi$) and should be compared with radio maps on the lower panel of Fig. 4.4. The component of ISMF which is perpendicular to the line of sight is along horizontal axis on all images.

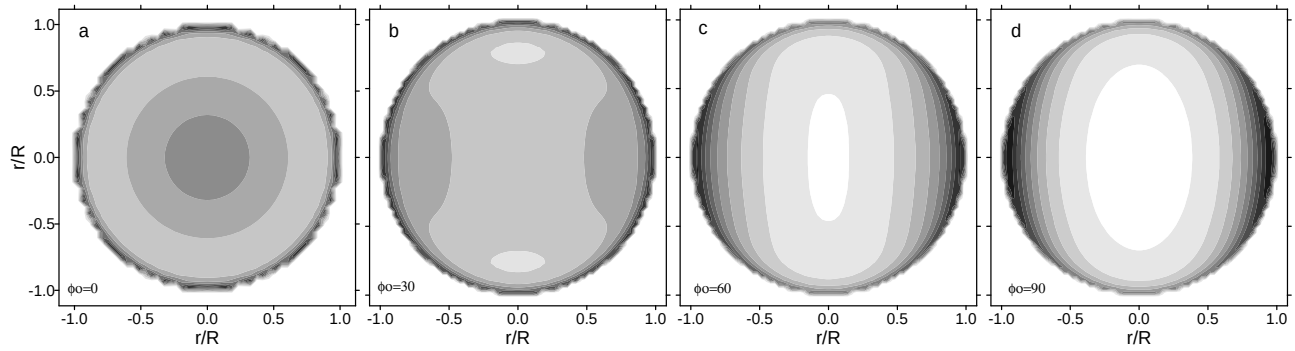

Figure 4.5. IC γ-ray images of SNR. Isotropic injection, $E_{\max}$ is constant over SNR surface. Aspect angles ϕ_o: 0° (a), 30° (b), 60° (c), 90° (d). Component of the ambient magnetic field which is perpendicular to the line of sight, is oriented along the horizontal axis.

An important difference is prominent from these two figures. Namely, the two lobes develop with increasing of ϕ_o in both radio and γ-rays. However, *their location in respect to ISMF is opposite*. The line conecting two maxima in radio is perpendicular to ISMF while it is parallel to ISMF on IC images (cf. Fig 4.5d and Fig 4.4h).

The reason of this effect is the following. For assumed isotropic injection, the azimuthal variation of the radio brightness is determined only by the dependence σ_B on obliquity (the azimuth angle equals to the obliquity angle for $\phi_o = \pi/2$). Electrons emitting TeV γ-rays have energies $E \sim E_{\max}$ and experience substantial radiative losses (this effect is negligible for radio emitting electrons). Magnetic field does not appear directly in the formulae for IC emission, but it affects the downstream distribution of relativistic electrons emitting IC γ-rays. The larger post-shock magnetic field the larger radiative losses. The downstream distribution of IC-emitting electrons is therefore steeper where magnetic field is stronger. This leads to lower IC brightness in SNR regions with larger magnetic field (while radio brightness increases there because of proportionality to $B^{3/2}$).

In TeV γ-ray image of SN 1006 [28], the two maxima coincide in location with limbs in radio and nonthermal X-rays. This fact, in view of the 'limb-inverse' property, could be considered as argument against the leptonic origin of γ-ray emission in SN 1006 (if injection is isotropic). However, these IC images are obtained under assumption that $E_{\max}$ does not vary over SNR surface. If $E_{\max}$ is high enough at regions with large magnetic field (at perpendicular shock), then the 'limb-inverse' effect may be less prominent or even might not be important (see below).

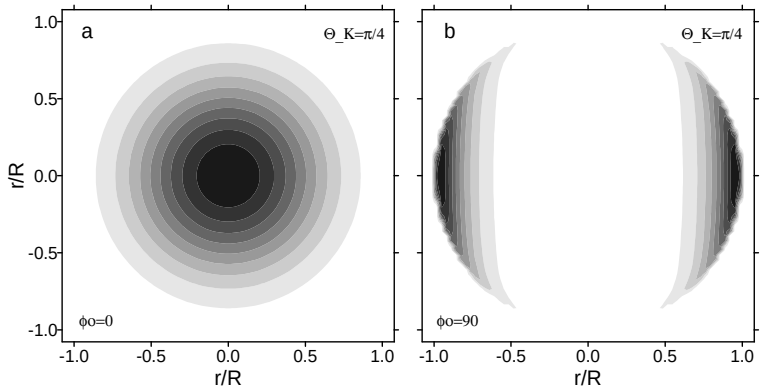

Figure 4.6. IC γ-ray images of SNR. Quasi-parallel injection (4.1) with $\Theta_{\rm K} = \pi/4$, $E_{\rm max}(\Theta_{\rm o}) =$ const. Aspect angles $\phi_{\rm o}$: 0$^{\rm o}$ (a), 90$^{\rm o}$ (b). In the latter, ISMF is along the horizontal axis.

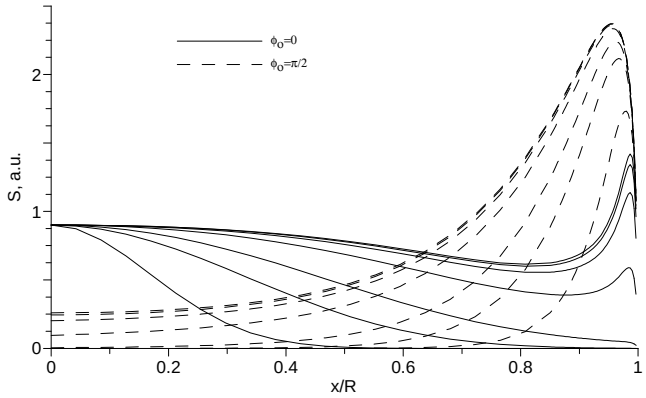

Figure 4.7. Profiles of the IC surface brightness along X-axis for the aspect angle $\phi_{\rm o} = 0^{\rm o}$ (the radial profile of brightness is the same for any azimuth; to be compared with Fig. 4.3) and $\phi_{\rm o} = 90^{\rm o}$ (ISMF is along the horizontal axis). Dependence of injection is given by (4.1) with $\Theta_{\rm K}$ (from below): $\pi/12$, $\pi/6$, $\pi/4$, $\pi/2$, π, 2π, ∞. $E_{\rm max}$ is constant over SNR surface.

In case if injection strongly prefers *parallel* shocks (limbs in SN 1006 are polar caps), the dependence $\varsigma(\Theta_{\rm o})$ might dominate $\sigma_{\rm B}(\Theta_{\rm o})$. The maxima of brightness in radio and IC γ-rays are therefore located at the same regions of SNR projection (Fig. 4.6, to be compared with Fig. 4.4a,d), in agreement with the Chandra and HESS observations of SN 1006.

The role of intermediate values $\Theta_{\rm K}$ for injection which prefers parallel shock, Eq. (4.1), on profiles of IC brightness is shown on Fig. 4.7. Increase of the sencitivity of injection to the obliquity leads to radially thinner and more contrast features.

If injection prefers *perpendicular* shock, Eq. (4.2), its increase in the regions of larger magnetic field may compensate the lack of γ-ray emitting electrons. In that case, the position of limbs coincide in radio and IC γ-rays if the dependence $\varsigma(\Theta_{\rm o})$ is strong enough (Fig. 4.8b,d). In the range of intermediate $\Theta_{\rm K}$, the quadrilateral

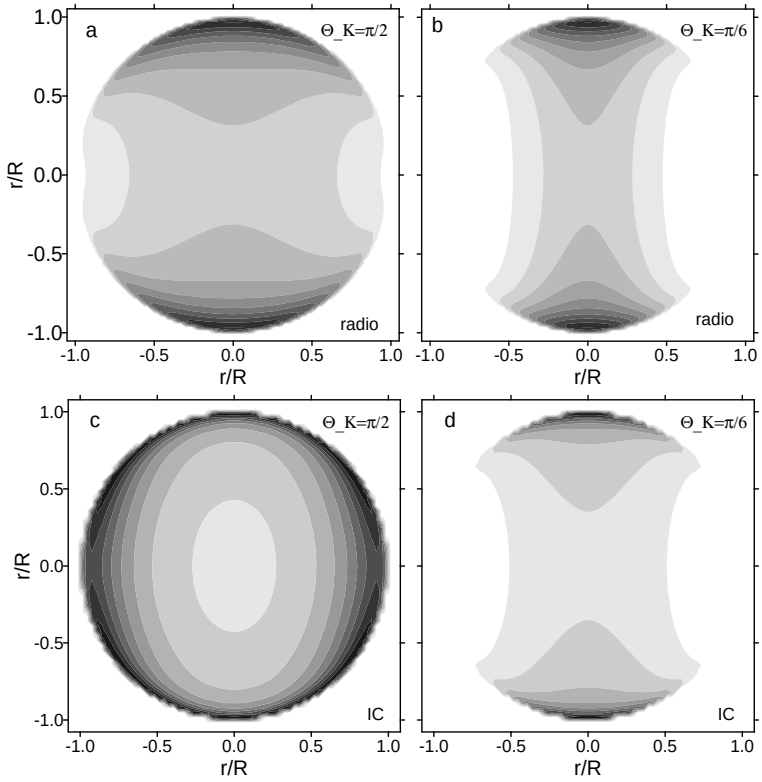

Figure 4.8. Radio (a,b) and IC γ-ray images (c,d) of SNR for $\phi_{\rm o} = 90^{\rm o}$. Quasi-perpendicular injection (4.2) with $\Theta_{\rm K} = \pi/2$ (a,c) and $\Theta_{\rm K} = \pi/6$ (b,d) (to be compared with Fig. 4.4d and Fig. 4.5d). $E_{\rm max}$ is constant over SNR surface.

morphology appears also in models of IC γ-rays (Fig. 4.8c), as an intermediate morphology between those on Fig. 4.5d and Fig. 4.8d. (The contrast of maxima in the image of quadrilateral SNR is so small that this feature may probably not be observable.)

Note that the quasi-perpendicular injection model leads to *radio* images similar to those in the isotropic injection case, cf. Fig. 4.8a,b and Fig. 4.2f (see also [264]), because magnetic field and injection efficiency increase at perpendicular shocks both leading to larger synchrotron emission. In contrast, there is a lack of IC radiating electrons around perpendicular shocks which may or may not (depending on $\Theta_{\rm K}$ in (4.2)) be compensated by injection. Thus *IC* images involving the quasi-perpendicular injection may radically differ from those with isotropic injection, cf. Fig. 4.8d and Fig. 4.5d.

The obliquity variation of the electron maximum energy is an additional factor affecting the IC γ-ray brightness in SNRs. Actually, [321] have shown that the cut-off frequency increases at radio limbs of SN 1006 that may (partially) be due to larger

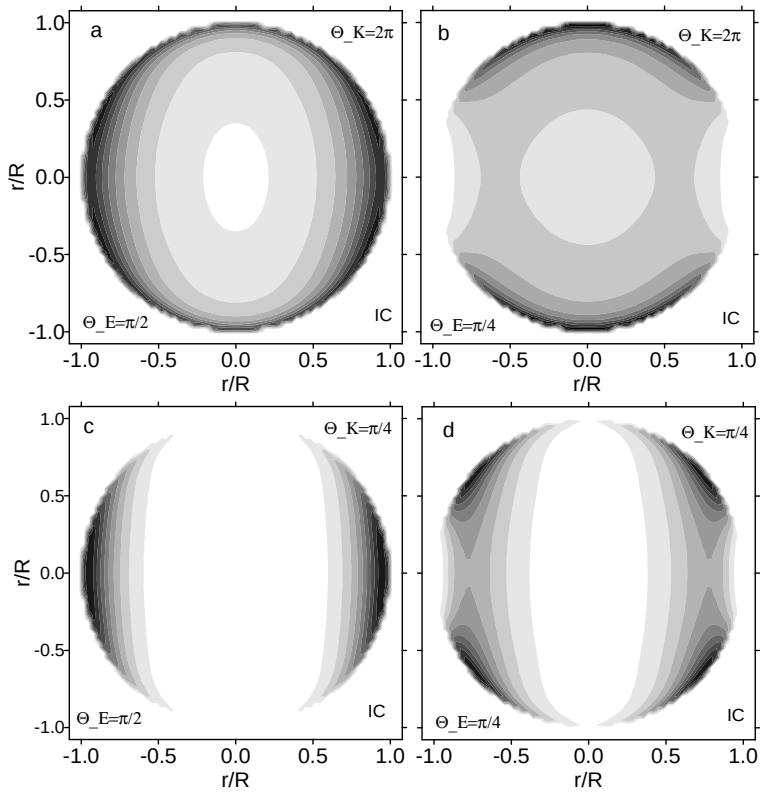

Figure 4.9. IC γ-ray images of SNR for $\phi_o = 90^o$ and E_{max} increasing with obliquity, with $\Theta_E = \pi/2$ (a,c) and $\Theta_E = \pi/4$ (b,d). Isotropic injection (a,b), to be compared with Fig. 4.5d; quasi-parallel injection with $\Theta_K = \pi/4$ (c,d), to be compared with Fig. 4.6b.

E_{max} there. Therefore E_{max} is expected to be largest in this SNR at the perpendicular shock (at equatorial belt) if injection is isotropic or quasi-perpendicular or at the parallel shock (at polar caps) if injection is quasi-parallel. In the latter case, the calculations of [303] suggest that the only possible model for E_{max} in SN 1006 should be loss-limited one in the Bohm limit.

The role of E_{max} increasing with obliquity, Eq. (4.8), is shown on Fig. 4.9. The 'limb-inverse' property may not be important and the limbs may coincide in radio, X-rays and IC γ-rays even for the isotropic injection if the maximum energy is large enough at perpendicular shocks to provide energetical electrons in despite of radiative losses (Fig. 4.9b, cf. with Fig. 4.4h and Fig. 4.5d). Note also that the limbs are thicker in this case, because of the more effective radiative losses at perpendicular shock (due to larger ISMF compression), comparing to limbs if they are at parallel shock.

The dependence of E_{max} on Θ_o may also cause splitting and rotation of IC limbs in case of the quasi-parallel injection (Fig. 4.9d, cf. with Fig. 4.6b) or the quasi-

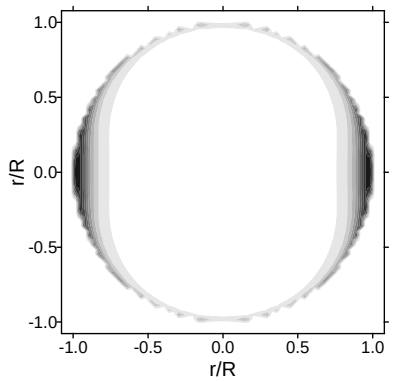

Figure 4.10. The same as Fig. 4.5d, for 10 times larger photon energy, $\varepsilon = \varepsilon_{\max}(E_{\max})$.

perpendicular one. There is a possibility for quadrilateral SNRs to appear in γ-rays due to the interplay between dependences $E_{\max}(\Theta_{\rm o})$, $\varsigma(\Theta_{\rm o})$ and $\sigma_{\rm B}(\Theta_{\rm o})$ (Fig. 4.9a,d).

All above IC images are calculated for the photon energy $\varepsilon = 0.1\varepsilon_{\max}(E_{\max})$. The pattern of the γ-ray surface brightness remain almost the same with increasing of the photon energy, though regions of maximum brightness become radially thinner and also contrasts change (Fig. 4.10). This is because electrons which contribute most of emission at larger photon energy experience higher radiative losses and therefore the downstream distribution of these electrons are steeper.

4.1.4. Synchrotron X-ray images. Now, in order to reduce the parameter space, we consider the only classical quasi-parellel, quasi-perpendicular and isotropic injection [303].

Azimuthal distribution. The pattern of synchrotron X-ray brightness of SNR is in general similar to radio one. In most cases, the bright X-ray limbs or other features are located in the same azimuth as in the radio images. The only differences appear due to radiative losses which modify downstream distribution of the electrons emitting in X-rays (thus the features of brightness are radially thinner) and due to variation of $E_{\max}$ over the SNR surface. In the radio (see figures in Sect 4.1.2) as also in the X-ray band, the remnant shows two symmetric bright lobes (for $\phi_{\rm o} = 90^{\rm o}$) in all the injection models with the maxima in surface brightness coincident in the two bands. The maxima are located at perpendicular shocks in the quasi-perpendicular and isotropic models (i.e. where B is higher), and at parallel shocks in the quasi-

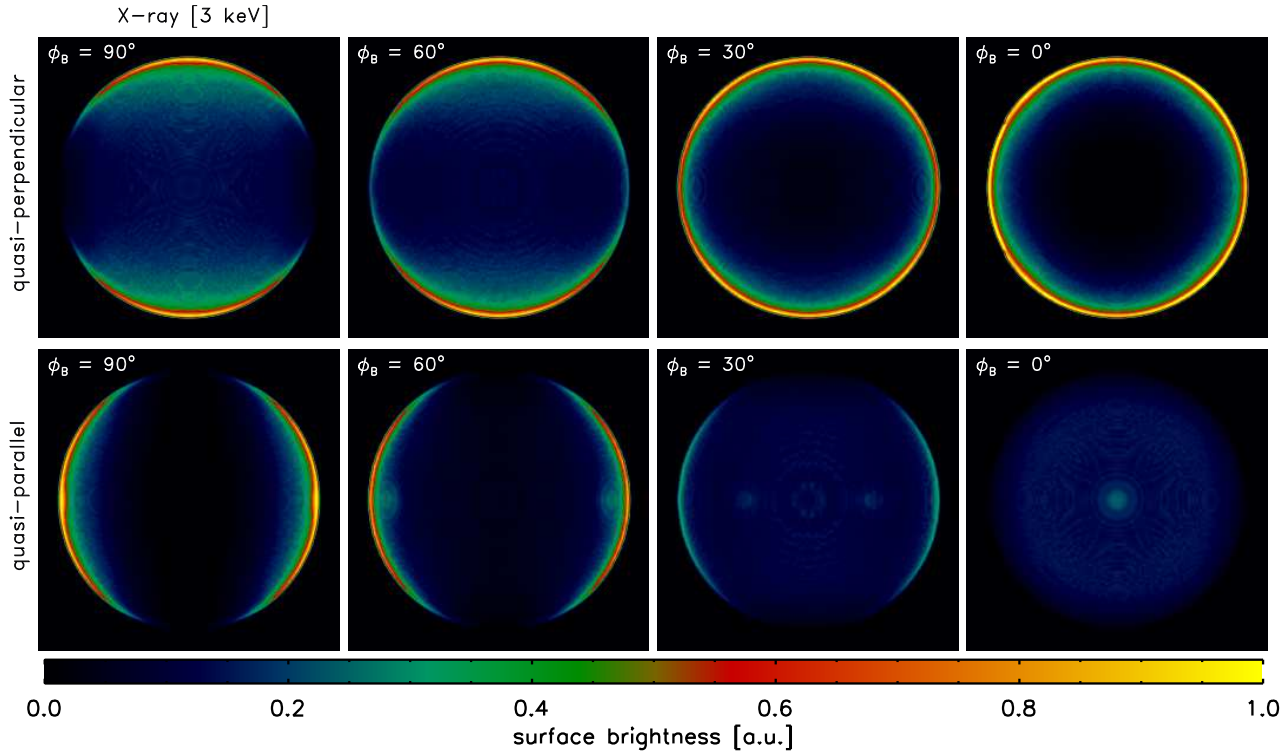

Figure 4.11. Maps of synchrotron X-ray surface brightness synthesized for different aspect angles (labeled in the upper left corner of each panel). The figure shows the quasi-perpendicular (top), and quasi-parallel (bottom) particle injection models. The model of $E_{\rm max}$ is time-limited with $\eta = 1$. Calculations are done for $E_{\rm max\|} = 26\,{\rm TeV}$, $B_{\rm o} = 30\,\mu{\rm G}$, $s = 2$, $\alpha = 0.5$, $b = -3/2$. The ambient magnetic field is along the horizontal axis.

parallel model (i.e. where emitting electrons are only presented). The lobes are much radially thinner in X-rays than in radio because of the large radiative losses at the highest energies that make the X-ray emission dominated by radii closest to the shock.

The X-ray morphology of SNR is different for different aspect angles (Fig. 4.11, cf. with radio and γ-ray images in Sects. 4.1.2 and 4.1.3). In the case of quasi-perpendicular injection, the morphology is bilateral (two lobes) for large aspect angles ($\phi_{\rm o} > 60^0$, i.e. the component of ISMF in the plane of the sky is larger than that along the line of sight) and almost ring-like for low aspect angles ($\phi_{\rm o} < 30^0$; see Fig. 4.11) with intermediate morphology between 30^0 and 60^0. In the case of quasi-parallel injection, the remnant morphology in the radio band is known to be bilateral for large aspect angles and characterized by one or two eyes for low aspect angles [157]. On the other hand, it is worth noting that the remnant morphology in X-rays is in general bilateral for aspect angles $\phi > 30^0$ and centrally bright

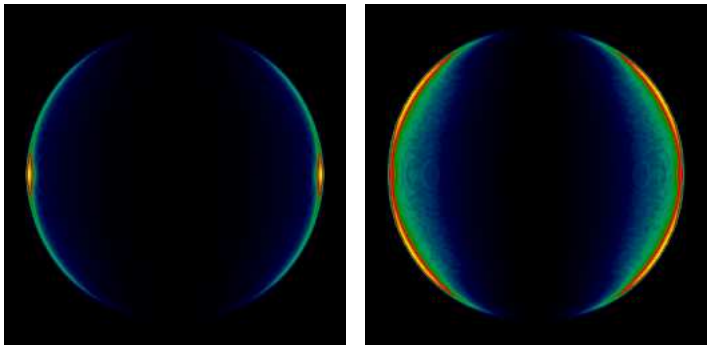

Figure 4.12. Maps of synchrotron X-ray surface brightness. The model of $E_{\rm max}$ is loss-limited with $\eta = 1$ (left) and $\eta = 50$ (right), to be compared with bottom left map on Fig. 4.11. Quasi-parallel injection, $\phi_{\rm o} = 90^{\rm o}$, $\alpha = 1$, other parameters are the same as on Fig. 4.11.

for very low angles, indeed a rather limited set of possible cases (lower panels in Fig. 4.11). This happens because the non-thermal X-ray emission originates from a very thin shell behind the shock making the effect of limb brightening in X-rays more important than in the radio band. In addition, we note that centrally bright X-ray (and radio) SNRs are expected to be much fainter than bilateral SNRs (see lower panels in Fig. 4.11) and consequently much more difficult to be observed. The above considerations may affect the statistical arguments generally invoked against the quasi-parallel injection (i.e. the fact that this model produces morphology which is not observed; e.g. [157, 264]).

Images on Fig. 4.11 are calculated for the time-limited model of $E_{\rm max}$ with $\eta = 1$, so $E_{\rm max}$ is quite similar for different obliquities, namely $E_{\rm max\perp}/E_{\rm max\parallel} = 1.3$. Larger $\eta > 1$ always provide $E_{\rm max\perp}/E_{\rm max\parallel} > 1$ thus the character of azimuthal variation of brightness would be similar. It would be more interesting to see the role of obliquity variation of the maximum energy in case of the loss-limited model. Fig. 4.12 shows two SNR maps for this case, for $\eta = 1$ ($E_{\rm max\perp}/E_{\rm max\parallel} = 0.49$) and $\eta = 50$ ($E_{\rm max\perp}/E_{\rm max\parallel} = 17$). Left one demonstrates decrease of the azimuthal width of the limb (emitting electrons dissapears quickly toward perpendicular shock). The increase of η influences the morphology of the remnant going in the direction to change the morphology type from polar-caps to barrel-like; however, even $\eta = 50$ does not provide rapid enough increase of number the emitting electrons to overcome the decreasing injection; therefore, an intermediate morphology (quadrilateral) is obtained.

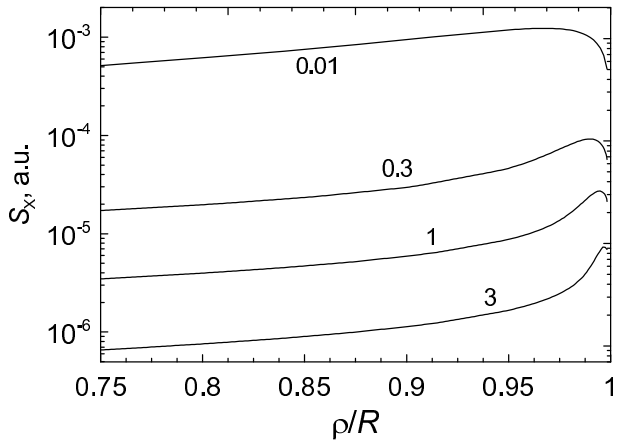

Figure 4.13. Radial profiles of X-ray surface brightness for different photon energies $\tilde{\varepsilon}$ (marked near respective lines). Calculations are done for $\phi_{\rm o} = 0$, $\varphi = 0$, $b = -3/2$, $\epsilon_{\rm f\parallel} = 1$.

The efficiency of variation of $E_{\rm max}$ with obliquity in modification of the azimuthal distribution of X-ray synchrotron brightness depends obviously on the photon energy: if the maximum contribution to the emission at given photon energy is from electrons with energy much less than $E_{\rm max}$ then this effect is negligible. It is useful to introduce the reduced photon energy, as $\tilde{\varepsilon} = \nu/\nu_{\rm c}(E_{\rm max\parallel}, B_{\rm o})$ where $\nu_{\rm c}(E, B) = c_1 \langle \sin\phi \rangle E^2 B$ is the synchrotron characteristic frequency, $c_1 = 6.26 \times 10^{18}$ cgs, or

$$\tilde{\varepsilon} = 19\ \varepsilon_{\rm keV} \left(\frac{E_{\rm max\parallel}}{10\,{\rm TeV}} \right)^{-2} \left(\frac{B_{\rm o}}{10\,\mu{\rm G}} \right)^{-1}, \qquad (4.9)$$

where $\varepsilon_{\rm keV}$ is the photon energy in keV. If $\tilde{\varepsilon} = 0.29$ then the most contribution to the synchrotron X-ray emission is from electrons with energy $E = E_{\rm max}$.[3] Figs. 4.11 and 4.12 are calculated for $\tilde{\varepsilon} = 2.8$, i.e. images shown are mainly due to emission of electrons with energy an order of magnitude higher than $E_{\rm max\parallel}$; the role of variation of $E_{\rm max}$ is therefore clealy visible in images.

Radial profiles. In the present subsection, $E_{\rm max}$ is assumed to be constant in time and the same for any obliquity; in addition, isotropic injection, $s = 2$ and $\alpha = 1$ are assumed.

The radial thickness of features in the X-ray images is sensitive to the photon energy: the larger the energy the thinner the limbs (Fig. 4.13). This is because

[3]For reference: the maximum contribution to synchrotron X-ray emission at 3 keV in MF 30 μG is from electrons with energies 72 TeV; the maximum contribution to IC γ-ray emission at 1 TeV is from electrons with energies 17 TeV.

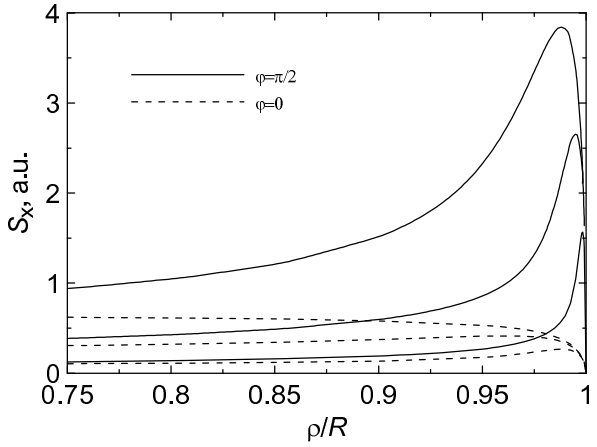

Figure 4.14. Effect of radiative losses (represented by $\epsilon_{\mathrm{f}\|}$) on the radial profiles of X-ray surface brightness, at two azimuth. The reduced fiducial energy $\epsilon_{\mathrm{f}\|} = 0.3, 1, 3$ (from below); $\phi_{\mathrm{o}} = \pi/2$, $\tilde{\varepsilon} = 1$, $b = 0$.

radiative losses $\dot{E}$ of electrons with energy E is efficient for more energetic electrons, $\dot{E} \propto E^2$. If $\tilde{\varepsilon} > 0.29$ then the most contribution to the synchrotron X-ray emission is from electrons with energies $E > E_{\max}$ where the radiative losses are of the main importance.

An important factor for emission of highly energetic electrons is the fiducial energy, which reflects the importance of radiative losses in modification of the electron distribution. It is defined as $\epsilon_{\mathrm{f}} = 637 \left(B_{\mathrm{s}}^2 t E_{\max}\right)^{-1}$ [303], or

$$\epsilon_{\mathrm{f}} = 13 \left(\frac{B_{\mathrm{s}}}{10\,\mu\mathrm{G}}\right)^{-2} \left(\frac{E_{\max}}{10\,\mathrm{TeV}}\right)^{-1} \left(\frac{t}{1000\,\mathrm{yrs}}\right)^{-1}. \qquad (4.10)$$

Radiative losses are important for $\epsilon_{\mathrm{f}} < 1$ and minor for $\epsilon_{\mathrm{f}} > 1$. Fig. 4.14 demonstrates how the value of ϵ_{f} affects the radial profiles of X-ray brightness: the smaller ϵ_{f} the thinner the rim.

Our model does not include consistently the effects on shock dynamics due to back-reaction of accelerated CRs. However, we may approach the effect of shock modification by considering different values of the adiabatic index γ which is expected to drop from the value of an ideal monoatomic gas. In particular, Fig. 4.15 considers the cases of $\gamma = 5/3$ (for an ideal monatomic gas), $\gamma = 4/3$ (for a gas dominated by relativistic particles), and $\gamma = 1.1$ (for large energy drain from the shock region due to the escape of high energy CRs). The shock modification results in more compressible plasma and, therefore, in the radially-thinner features of the

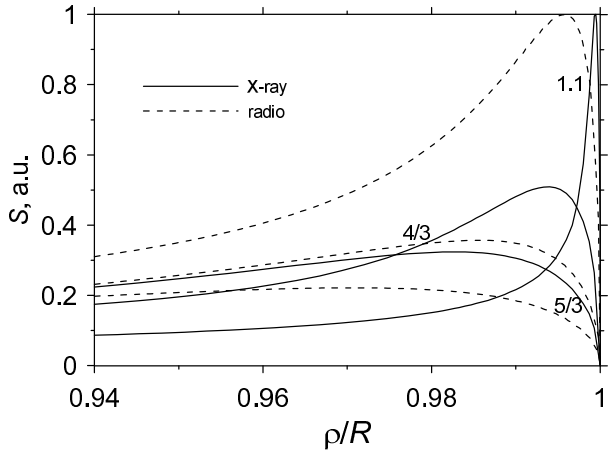

Figure 4.15. Radio (dashed lines) and X-ray (solid lines) radial profiles of surface brightness for the adiabatic index $\gamma = 5/3$, $4/3$ and 1.1. Calculations are done for $\phi_{\rm o} = 0$, $\varphi = 0$, $b = 0$, $\epsilon_{\rm f\|} = 3$, $\tilde{\varepsilon} = 0.3$.

nonthermal images of SNRs. A small distance between the forward shock and contact discontinuity [106, 250] could also be attributed to $\gamma < 5/3$. Effect of the index γ on the profiles of hydrodynamical parameters downstream of the adiabatic shock is widely studied [21]: smaller γ makes the shock compression factor higher,

$$\sigma = \begin{cases} 4 & \text{for } \gamma = 5/3, \\ 7 & \text{for } \gamma = 4/3, \\ 21 & \text{for } \gamma = 1.1, \end{cases} \tag{4.11}$$

and the gradient of density downstream stronger (e.g. Appendix B),

$$\bar{n}(\bar{r}) \approx \bar{r}^{\kappa_{\rm nr}}, \qquad \kappa_{\rm nr} = \begin{cases} 12 & \text{for } \gamma = 5/3, \\ 25 & \text{for } \gamma = 4/3, \\ 88 & \text{for } \gamma = 1.1, \end{cases} \tag{4.12}$$

($\bar{r} = r/R \leq 1$). In addition to that, the X-ray (and also TeV γ-ray) brightness is modified by increased radiative losses of emitting electrons. Really, the larger compression leads to the higher post-shock MF and thus to increased losses, $\dot{E} \propto B^2$, which results in turn in the thinner radial profiles of brightness.

It is unknown how the injection efficiency (the fraction of nonthermal particles) depends on the properties of the shock. We parameterized its evolution as $K_{\rm s} \propto V^{-b}$ where b is a constant. Effect of the parameter b on the radial profiles of the surface brightness is demonstrated on Fig. 4.16. The smaller b the thicker the profiles,

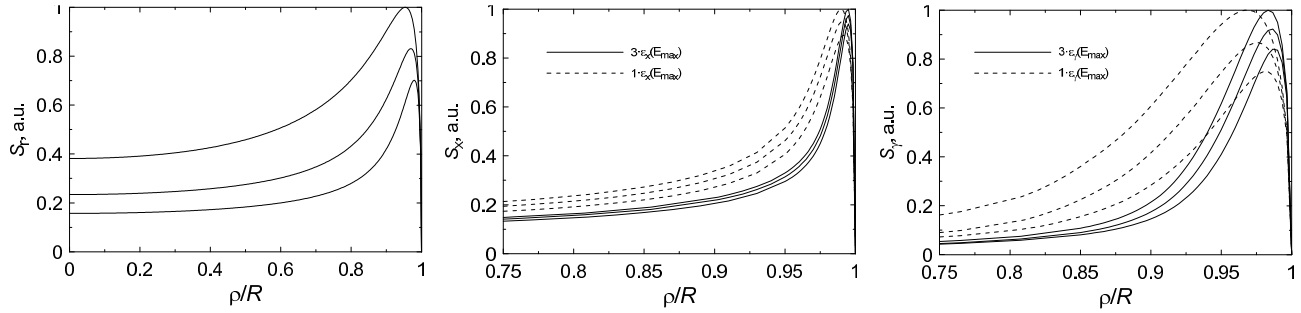

Figure 4.16. Evolution of injection efficiency (represented by b) and radial profiles of surface brightness in radio (left), X-rays (middle) and γ-rays (right). The parameter in relation $K_\mathrm{s} \propto V^{-b}$ is $b = -3/2, 0, 2$. Other parameters are $\phi_\mathrm{o} = \pi/2$, $\varphi = 0$ (for radio and X-rays) and $\varphi = \pi/2$ (for γ-rays), $\epsilon_{\mathrm{f}\parallel} = 1$. X-ray and γ-ray profiles are shown for two photon energies: where the most contribution is from electrons with $E = E_\mathrm{max}$ (dashed lines) and three times larger (solid lines); in case of X-rays, solid lines correspond to $\tilde{\varepsilon} = 1$.

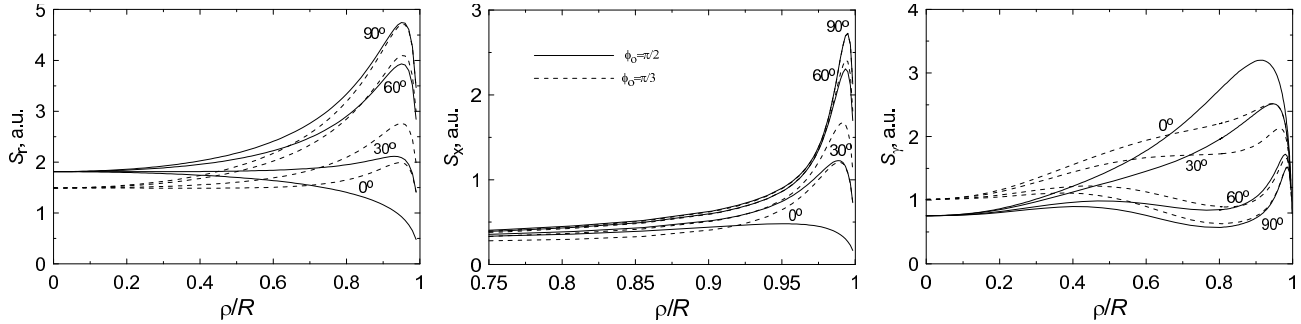

Figure 4.17. Radial profiles of the radio (left), X-ray (middle) and γ-ray (right) surface brightness of SNR for different azimuth: $0, \pi/6, \pi/3, \pi/2$ (marked near lines). The aspect angles are $\pi/2$ (solid lines) and $\pi/3$ (dashed lines); $b = -3/2$, $\epsilon_{\mathrm{f}\parallel} = 1$, $\tilde{\varepsilon} = 1$, γ-ray profiles are for photons with energy $0.1\varepsilon_\gamma(E_\mathrm{max})$.

because there are more emitting electrons in deeper layers, which were injected at previous times. This property affects the nonthermal emission in all bands. However, the effect is less prominent in X-rays (and in TeV γ-rays) if radiative losses are quite effective to dominate it (see Fig. 4.16, lines for different photon energies). Profiles of the radio brightness may be used to put limitations on the value of b.

In a similar fashion, the X-ray and γ-ray radial profiles are affected also by the time evolution of the maximum energy, $E_\mathrm{max} \propto V^q$. However, it seems impossible to determine q from such profiles because contribution of other factors is often dominant.

An interesting feature of the synchrotron images of SNRs is apparent from Fig. 4.17. The maxima of the radial profiles of brightness for different azimuth are located almost at the same distance ρ from the center of projection, for radio and X-rays.

Thus, the best way to analyze the azimuthal profiles of the surface brightness is to find the position ρ of the maximum for one azimuth and then to trace the azimuthal profile of brightness $S_\rho(\varphi)$ for fixed ρ.

4.2. Approximate formulae for azimuthal and radial variations of surface brightness in adiabatic SNRs

What are the main factors which determine the pattern of the nonthermal images of SNRs? Which of them are mostly responsible for the azimuthal variation of the surface brightness and which for the radial one? In order to understand how the properties of MF, electron injection and acceleration influence the brightness distribution, we developed analytic approximate formulae for the azimuthal and radial profiles of the surface brightness of adiabatic SNR in uniform ISM and uniform ISMF.

The analytical formulae are valid close to the shock only, but are adequate to describe azimuthal and radial variations of brightness around maxima which are located close to the edge of SNR shells.

4.2.1. Radio profiles. Let the evolution and obliquity variation of the electron injection efficiency be denoted as $V(t)^{-b}\varsigma(\Theta_\mathrm{o})$ and of the obliquity variation of MF compression as $\sigma_\mathrm{B}(\Theta_\mathrm{o})$. Properties of the azimuthal and radial profiles of the **radio** brightness is determined mostly by (Appendix C.2)

$$S_\mathrm{r}(\varphi,\bar{\varrho}) \propto \varsigma(\Theta_{\mathrm{o,eff}}\,(\varphi,\phi_\mathrm{o})\,)\sigma_\mathrm{B}(\Theta_{\mathrm{o,eff}}\,(\varphi,\phi_\mathrm{o})\,)^{(s+1)/2} I_\mathrm{r}(\bar{\varrho}) \tag{4.13}$$

where

$$I_\mathrm{r} = \frac{1}{\sqrt{1-\bar{\varrho}^2}} \frac{1-\bar{\varrho}^{\sigma(\kappa_\mathrm{r}+1)}}{\sigma(\kappa_\mathrm{r}+1)}, \tag{4.14}$$

$\bar{\varrho} = \rho/R$, σ is the shock compression ratio,

$$\kappa_\mathrm{r} = 3b/2 + (2+s)\kappa_\mathrm{ad} + 1/\sigma + s, \tag{4.15}$$

$\kappa_{\rm ad}$ is close to unity for $\gamma = 1.1 \div 5/3$ (Appendix B). The effective obliquity angle $\Theta_{\rm o,eff}$ is related to azimuth φ and aspect $\phi_{\rm o}$ as

$$\cos\Theta_{\rm o,eff}\left(\varphi,\phi_{\rm o}\right) = \cos\varphi\sin\phi_{\rm o}, \tag{4.16}$$

the azimuth angle is measured from the direction of ISMF in the plane of the sky.

Eq. (4.13) shows that the azimuthal variation of the radio surface brightness $S_\varrho(\varphi)$ at a fixed radius ϱ of projection, is mostly determined by the variations of the magnetic field compression (and amplification, if any) $\sigma_{\rm B}$ and by the variation of the electron injection efficiency ς. The radial profile $S_\varphi(\varrho) \propto I_{\rm r}(\varrho)$ is determined mostly by σ, b and s. Adiabatic index γ affects the radial and azimuthal profiles mostly through the compression factor $\sigma = (\gamma+1)/(\gamma-1)$ because $\kappa_{\rm ad}$ weakly depends on γ.

4.2.2. Synchrotron X-ray profiles. Let us assume that the maximum energy is expressed as $E_{\rm max}(\Theta_{\rm o},t) \propto V(t)^q\mathcal{F}(\Theta_{\rm o})$. The **synchrotron X-ray** brightness close to the forward shock is approximately (Appendix C.3)

$$S_{\rm x}(\varphi,\bar{\varrho}) \propto \varsigma(\varphi)\sigma_{\rm B}(\varphi)^{(s+1)/2}\exp\left[-\left(\frac{\epsilon_{\rm m}(\varphi)}{\mathcal{F}(\varphi)}\right)^{\alpha}\right] I_{\rm rx}(\varphi,\bar{\varrho}) \tag{4.17}$$

where

$$I_{\rm rx} = I_{\rm r}(\bar{\varrho})I_{\rm x}(\varphi,\bar{\varrho}) \tag{4.18}$$

with

$$I_{\rm x} = \left[1 - \frac{\epsilon_{\rm m}^{\alpha}(\psi+1)\alpha}{\mathcal{F}^{\alpha}}\left(1 - \frac{1-\bar{\varrho}^{\sigma(\kappa_{\rm r}+2)}}{1-\bar{\varrho}^{\sigma(\kappa_{\rm r}+1)}}\frac{\kappa_{\rm r}+1}{\kappa_{\rm r}+2}\right)\right]. \tag{4.19}$$

The parameter

$$\psi = \kappa_{\rm ad} + \frac{5\sigma_{\rm B}^2\epsilon_{\rm m}}{2\epsilon_{\rm f\|}} - \frac{3q}{2} \tag{4.20}$$

is responsible for the adiabatic (the first term) and radiative (the second term) losses of emitting electrons and the time evolution of $E_{\rm max}$ on the shock (the third term). The reduced electron energy which gives the maximum contribution to emission of photons with energy $\tilde{\varepsilon}$ is

$$\epsilon_{\rm m} = \left(\frac{\tilde{\varepsilon}}{0.29\sigma_{\rm B}}\right)^{1/2}, \tag{4.21}$$

it varies with obliquity (since MF varies; electrons with different energies contribute to the synchrotron emission at $\tilde{\varepsilon}$). Parameters ψ, $\epsilon_{\rm m}$, $\mathcal{F}$ depend on $\Theta_{\rm o,eff}$ and, therefore, on the aspect angle $\phi_{\rm o}$ and the azimuth angle φ.

If $\epsilon_{\rm m} \ll 1$ then Eq. (4.17) for the X-ray brightness transforms to Eq. (4.13) for the radio brightness.

The thickness of the hard X-ray radial profile is used to estimate the post-shock strength of MF in a number of SNRs [78]. The absolute value of MF is present in Eq. (4.17) through $\tilde{\varepsilon}$ and $\epsilon_{\rm f}$, Eqs. (4.9), (4.10) which appear in ψ and $\epsilon_{\rm m}$, Eqs. (4.20), (4.21). In both cases, $B_{\rm s}$ is in combination with $E_{\rm max}$ (thus, the value of the electron maximum energy may affect the estimations). The idea of the method bases on the increased role of losses in X-rays due to larger MF, i.e. on the role of the second term in ψ, Eq. (4.20). Really, the influence of $\kappa_{\rm r}$ (i.e. of s and b) is minor in X-rays (middle panel on Fig. 4.16), if radiative losses affect the electron evolution downstream of the shock (i.e. for $\tilde{\varepsilon} \gtrsim 0.29$, $\epsilon_{\rm f} \lesssim 1$). The role of the first and the third terms in ψ are also minor in most cases ($q = 0$ for the time-limited and escape-limited models and unity for the loss-limited one) because the second term $\gtrsim 10$. However, the adiabatic index makes an important effect on the thickness of the profile, mostly through σ which appears in $\sigma_{\rm B}$ and in $I_{\rm x}$. Being smaller than 5/3 (that is reasonable especially in the case of efficient acceleration, which is actually believed to be responsible for the large MF), the index may compete to some extend the role of losses, used in the method for estimation of MF (see e.g. Fig. 4.15) that might lead to smaller estimates of MF strength.

4.2.3. IC gamma-ray profiles. The **IC γ-ray** brightness may approximately be described as (Appendix C.4)

$$S_{\rm ic}(\varphi, \bar{\varrho}) \propto \varsigma(\varphi) \exp\left[-\left(\frac{\epsilon_{\rm m}}{\mathcal{F}(\varphi)}\right)^{\alpha}\right] I_{\rm ic}(\varphi, \bar{\varrho}) \tag{4.22}$$

where

$$I_{\rm ic}(\varphi,\bar{\varrho}) \approx \frac{1}{\sqrt{1-\bar{\varrho}^2}}\frac{1-\bar{\varrho}^{\sigma(\kappa_{\rm ic}+1)}}{\sigma(\kappa_{\rm ic}+1)} \tag{4.23}$$

$$\times\left[1-\frac{\epsilon_{\rm m}^{\alpha}\psi\alpha}{\mathcal{F}^{\alpha}}\left(1-\frac{1-\bar{\varrho}^{\sigma(\kappa_{\rm ic}+2)}}{1-\bar{\varrho}^{\sigma(\kappa_{\rm ic}+1)}}\frac{\kappa_{\rm ic}+1}{\kappa_{\rm ic}+2}\right)\right],$$

$$\kappa_{\rm ic} = 3b/2+(2+s)\kappa_{\rm ad}+1/\sigma-1. \tag{4.24}$$

The expression for ψ is the same as (4.20) but $\epsilon_{\rm m}$ is different:

$$\epsilon_{\rm m} = \frac{\varepsilon^{1/2}}{2(kT)^{1/2}\gamma_{\rm max\|}}, \tag{4.25}$$

where ε is the γ-ray photon energy, T the temperature of the seed photon field, $\gamma_{\rm max}$ the Lorentz factor of electrons with energy $E_{\rm max}$, or

$$\epsilon_{\rm m} = 1.66\left(\frac{E_{\rm max\|}}{10\,{\rm TeV}}\right)^{-1}\left(\frac{\varepsilon}{1\,{\rm TeV}}\right)^{1/2}\left(\frac{T}{2.75\,{\rm K}}\right)^{-1/2}. \tag{4.26}$$

The azimuthal variation of the IC γ-ray brightness depends mostly on the injection efficiency. The role of variation of $E_{\rm max}$ is prominent only if obliquity dependence of injection is not strong. Parameter α, being smaller than unity, results in smaller azimuthal contrasts of synchrotron X-ray or IC γ-ray brightness comparing to model with purely exponential cut-off in $N(E)$. The radial distribution of IC brightness is determined mostly by σ, $\epsilon_{\rm m}$, $\epsilon_{\rm f}$, b and, to the smaller extend, by s and q.

4.2.4. Accuracy of the formulae. The approximations presented above do not require long and complicate numerical simulations but restore all the properties of nonthermal images discussed in the previous sections, including dependence on the aspect angle. Therefore, they may be used as a simple diagnostic tool for nonthermal maps of SNRs.

The formulae are rather accurate in description of the brightness distribution close to the shock. They do not represent centrally-brightened SNRs. Instead, they may be used in SNR shells for those azimuth φ where $\epsilon_{\rm m} \lesssim 1$ and $\epsilon_{\rm f} \gtrsim 0.1$, in the range of $\bar{\varrho}$ from $(1-2\Delta\bar{\varrho}_{\rm m})$ to 1, where $\Delta\bar{\varrho}_{\rm m} = 1-\bar{\varrho}_{\rm m}$, $\bar{\varrho}_{\rm m}$ is the radius (close to the shock) where the maximum in the radial profile of brightness happens. Approximations are compared with numerical calculations in respective Appendices.

4.2.5. Properties of the non-thermal images. Analysis of azimuthal profiles of brightness in different bands allows one to put limitations on models of injection, MF, $E_{\max}$. In most cases, the best way to estimate the azimuthal variation $S_\rho(\varphi)$ of the surface brightness is following. An approximate radial profile $S_\varphi(\rho)$ of the brightness should be produced for azimuth where the largest losses occur (i.e. where $\epsilon_{\rm f} \propto \left(\mathcal{F}\sigma_{\rm B}^2\right)^{-1}$ is smaller; e.g. at $\varphi = 90^{\rm o}$). This allows us to find $\bar{\varrho}_{\rm m}$ which should be used in $S_\rho(\varphi)$ in order to estimate the azimuthal variation of brightness.

Energy of electrons evolve downstream of the shock as $E(\bar{a}) = E_{\rm i}\mathcal{E}_{\rm ad}\mathcal{E}_{\rm rad}$, where $E_{\rm i}$ is initial energy, $\bar{a} = a/R$, a the Lagrangian coordinate. Adiabatic and radiative losses of electrons in a given fluid element a are represented by functions $\mathcal{E}_{\rm ad}(\bar{a}) \leq 1$, $\mathcal{E}_{\rm rad}(\bar{a}) \leq 1$ respectively (Sect. 3.2.2). Close to the shock, they are approximately $\mathcal{E}_{\rm ad} \approx \bar{a}^{\kappa_{\rm ad}}$ ($\kappa_{\rm ad}$ depends on the adiabatic index γ only and is close to unity for $\gamma = 1.1 \div 5/3$), $\mathcal{E}_{\rm rad} \approx \bar{a}^{5\sigma_{\rm B}^2\epsilon_{\rm m}/(2\epsilon_{\rm f\|})}$ (Appendix B). The latter expression clearly shows that the fiducial energy $\epsilon_{\rm f}$ is important parameter reflecting the 'sensitivity' of the model to the radiative losses, as it shown by [303]: the larger the fiducial energy the smaller the radiative losses. In fact, $\mathcal{E}_{\rm rad} = 1$ means no radiative losses at all. Another fact directly visible from this approximation is that radiative losses are much more important at the perpendicular shock (where $\sigma_{\rm B} = \sigma$) than at the parallel one (where $\sigma_{\rm B} = 1$). In addition, the radiative losses depends rather strongly on the index γ: $\sigma_{\rm B}^2 = 16$ for $\gamma = 5/3$ but $\sigma_{\rm B}^2 = 49$ for $\gamma = 4/3$.

Our approximations reflects also the general 'rule' for IC emission: there is less IC emission where MF is stronger. Namely, the azimuthal variation is $I_{\rm ic}(\varphi) \propto 1 - {\rm const}\cdot\psi(\varphi)/\mathcal{F}(\varphi)^\alpha$ with $\psi \propto \sigma_{\rm B}(\varphi)^2$: emitting electrons disappears toward the shock with larger $\sigma_{\rm B}$ because MF strength is a reason of higher losses there. Similar dependence on $\sigma_{\rm B}$ is for X-rays, Eq. (4.19); it is however dominated by the increased term $S_{\rm x}(\varphi) \propto \sigma_{\rm B}(\varphi)^{3/2}$.

TeV γ-ray image of SN 1006 demonstrates good correlations with X-ray image smoothed to the HESS resolution [28]. We mean here both the location and sizes of the bright limbs. Let us consider the polar-caps model of SN 1006. The shock is

quasi-parallel around the limbs, MF azimuthally increases (in ≈ 4 times) and the injection efficiency decreases (in $> 10^{-3}$ times) out of the limbs. The number of electrons emitting in X-rays and TeV γ-rays is dramatically low at perpendicular shock comparing to the parallel, that is in agreement with no TeV emission at NW and SE regions of SN 1006. However, the azimuthal sizes of the limbs in X-rays and γ-rays have to be different, in the polar-caps model. They should be larger in X-rays. Really, $S_{\rm x} \propto \varsigma \sigma_{\rm B}^{3/2}$ while $S_{\rm ic} \propto \varsigma$. We hope that future observations allows us to see if there is a difference in azimuthal sizes of the limbs in various bands.

How back-reaction of accelerated particles may modify nonthermal images of SNRs? Our formulae can restore some of these effects. In our approximations, s, in general, is allowed to vary with E, e.g. to be $s(E) = s + \delta s(E)$. The index s reflects the 'local' slope of the electron spectrum around $\epsilon_{\rm m}$. Therefore, if $s(E) \neq$ const, the index s have to vary with azimuth because $\epsilon_{\rm m}$ varies, Eq. (4.21). Generally speaking, such approach allows one to estimate the role of the nonlinear 'concavity' of the electron spectrum in modification of the nonthermal images. However, we expect that this effect is almost negligible because $\delta s(E)$ is very slow function, at least within interval of electron energies contributing to images. Other effect of efficient acceleration consists in the adiabatic index γ smaller than 5/3. Our approximations are written for general γ. Namely, the index γ affects $S(\varphi, \bar{\varrho})$ through σ. Cosmic rays may also cause the amplification of the seed ISMF. In our formulae, $\sigma_{\rm B}(\Theta_{\rm o})$ represents the obliquity variation of the ratio of the downstream MF to ISMF strength, $B_{\rm s}/B_{\rm o}$. Therefore, it may account for both the compression and amplification of ISMF; for such purpose, $\sigma_{\rm B}$ should be expressed in a way to be unity at parallel shock.

4.3. Asymmetries in bilateral supernova remnants due to nonuniform ISM and nonuniform ISMF

The bilateral SNRs are characterized by two opposed radio-bright limbs separated by a region of low surface brightness. In general, the remnants appear asymmetric, distorted and elongated with respect to the shape and surface brightness of the two opposed limbs. In most (but not all) of the BSNRs the symmetry axis is parallel to the galactic plane, and this has been interpreted as a difficulty for "intrinsic" models, e.g. models based on SN jets, rather than for "extrinsic" models, e.g. models based on properties of the surrounding galactic medium [159].

In spite of the interest around BSNRs, a satisfactory and complete model which explains the observed morphology and the origin of the asymmetries does not exist. The galactic medium is supposed to be stratified along the lines of constant galactic latitude, and characterized by a large-scale ambient magnetic field with field lines probably mostly aligned with the galactic plane. The magnetic field plays a threefold role: first, a magnetic tension and a gradient of the magnetic field strength is present where the field is perpendicular to the shock velocity leading to a compression of the plasma; second, cosmic ray acceleration is most rapid where the field lines are perpendicular to the shock speed [200, 267]; third, the electron injection could depend on orientation of MF with respect to the shock speed. [159] notes that magnetic models (i.e. those considering uniform ISM and ordered magnetic field) cannot explain the asymmetric morphology of most BSNRs, and invokes a dynamical model based on pre-existing ISM inhomogeneities, e.g. large-scale density gradients, tunnels, cavities. Unfortunately, the predictions of these ad-hoc models have consisted so far of a qualitative estimate of the BSNRs morphology, with no real estimates of the ISM density interacting with the shock. Moreover, most likely also nonuniform ambient magnetic fields may cause asymmetries in BSNRs, without the need to assume ad-hoc density ISM structures. Two main aspects of the nature of BSNRs, therefore, remain unexplored: how and under which physical conditions

do the asymmetries originate in BSNRs? What is more effective in determining the morphology and the asymmetries of this class of SNRs, the ambient magnetic field or the non-uniform ISM?

Answering such questions at an adequate level requires detailed physical modeling, high-level numerical implementations and extensive simulations. Our purpose here is to investigate whether the morphology of BSNR observed in the radio band could be mainly determined by the propagation of the shock through a non-uniform ISM or, rather, across a non-uniform ambient magnetic field. To this end, we model the propagation of a shock generated by an SN explosion in the magnetized non-uniform ISM with detailed numerical MHD simulations, considering two complementary cases of shock propagation: 1) through a gradient of ambient density with a uniform ambient magnetic field; 2) through a homogeneous isothermal medium with a gradient of ambient magnetic field strength.

4.3.1. MHD modeling and numerical setup. In the case of the nonuniform media, the shock propagation is modeled by solving numerically the time-dependent ideal MHD equations of mass, momentum, and energy conservation in a 3-D cartesian coordinate system (x, y, z):

$$\frac{\partial \rho}{\partial t} + \nabla \cdot (\rho \mathbf{u}) = 0 \ , \tag{4.27}$$

$$\frac{\partial \rho \mathbf{u}}{\partial t} + \nabla \cdot (\rho \mathbf{u}\mathbf{u} - \mathbf{B}\mathbf{B}) + \nabla P_* = 0 \ , \tag{4.28}$$

$$\frac{\partial \rho E}{\partial t} + \nabla \cdot [\mathbf{u}(\rho E + P_*) - \mathbf{B}(\mathbf{u} \cdot \mathbf{B})] = 0 \ , \tag{4.29}$$

$$\frac{\partial \mathbf{B}}{\partial t} + \nabla \cdot (\mathbf{u}\mathbf{B} - \mathbf{B}\mathbf{u}) = 0 \ , \tag{4.30}$$

where

$$P_* = P + \frac{B^2}{2} \ , \qquad E = \epsilon + \frac{1}{2}|\mathbf{u}|^2 + \frac{1}{2}\frac{|\mathbf{B}|^2}{\rho} \ ,$$

are the total pressure (thermal pressure, P, and magnetic pressure) and the total gas energy (internal energy, ϵ, kinetic energy, and magnetic energy) respectively, t is the time, $\rho = \mu m_H n_{\rm H}$ is the mass density, $\mu = 1.3$ is the mean atomic mass (assuming cosmic abundances), m_H is the mass of the hydrogen atom, $n_{\rm H}$ is the hydrogen number density, $\mathbf{u}$ is the gas velocity, T is the temperature, and $\mathbf{B}$ is the magnetic field. We use the ideal gas law, $P = (\gamma - 1)\rho\epsilon$, where $\gamma = 5/3$ is the adiabatic index. The simulations are performed using the FLASH code [156], an adaptive mesh refinement multiphysics code for astrophysical plasmas.

As initial conditions, we adopted the model profiles of [350], assuming a spherical remnant with radius $r_{0\rm snr} = 4$ pc and with total energy $E_0 = 1.5 \times 10^{51}$ erg, originating from a progenitor star with mass of 15 $M_{\rm sun}$, and propagating through an unperturbed magnetohydrostatic medium. The initial total energy is partitioned so that 1/4 of the SN energy is contained in thermal energy, and the other 3/4 in kinetic energy. The explosion is at the center $(x, y, z) = (0, 0, 0)$ of the computational domain which extends between -30 and 30 pc in all directions. At the coarsest resolution, the adaptive mesh algorithm used in the FLASH code (PARAMESH; [237]) uniformly covers the 3-D computational domain with a mesh of 8^3 blocks, each with 8^3 cells. We allow for 3 levels of refinement, with resolution increasing twice at each refinement level. The refinement criterion adopted follows the changes in density and temperature. This grid configuration yields an effective resolution of ≈ 0.1 pc at the finest level, corresponding to an equivalent uniform mesh of 512^3 grid points. We assume zero-gradient conditions at all boundaries.

We follow the expansion of the remnant for 22 kyrs, considering two sets of simulations: 1) through a gradient of ambient density with a uniform ambient magnetic field; or 2) through a homogeneous isothermal medium with a gradient of ambient magnetic field strength. Table 4.1 summarizes the physical parameters characterizing the simulations.

In the first set of simulations, the ambient magnetic field is assumed uniform with strength $\mathbf{B} = 1$ μG and oriented parallel to the x axis. The ambient medium is modeled with an exponential density stratification along the x or the z direction

Table 4.1
Relevant initial parameters of the simulations: n_0 and n_i are particle number densities of the stratified unperturbed ISM (see text), h is the density scale length, and (x, y, z) are the coordinates of the magnetic dipole moment. The ambient medium is either uniform or with an exponential density stratification along the x or the z direction ($x-$strat. and $z-$strat., respectively); the ambient magnetic field is uniform or dipolar with the dipole oriented along the x axis and located at (x, y, z).

	ISM	n_0	n_i	h	**B**	(x, y, z)
	ISM	cm^{-3}	cm^{-3}	pc		pc
GZ1	$z-$strat.	0.05	0.2	25	uniform	-
GZ2	$z-$strat.	0.05	0.2	10	uniform	-
GX1	$x-$strat.	0.05	0.2	25	uniform	-
GX2	$x-$strat.	0.05	0.2	10	uniform	-
DZ1	uniform	0.25	-	-	$z-$strat.	$(0, 0, -100)$
DZ2	uniform	0.25	-	-	$z-$strat.	$(0, 0, -50)$
DX1	uniform	0.25	-	-	$x-$strat.	$(-100, 0, 0)$
DX2	uniform	0.25	-	-	$x-$strat.	$(-50, 0, 0)$

(i.e. parallel or perpendicular to the **B** field) of the form: $n(\xi) = n_0 + n_i \exp(-\xi/h)$ (where ξ is, respectively, x or z) with $n_0 = 0.05$ cm^{-3} and $n_i = 0.2$ cm^{-3}, and where h (set either to 25 pc or to 10 pc) is the density scale length. This configuration has been used in our work [195] to describe the SNR expansion in an environment with a molecular cloud. Our choice leads to a density variation of a factor ~ 6 or ~ 60, respectively, along the x or the z direction over the spatial domain considered (60 pc in total). The temperature of the unperturbed ISM is $T = 10^4$ K at $\xi = 0$ and is determined by pressure balance elsewhere. The adopted values of $T = 10^4$ K, $n = 0.25$ cm^{-3} and $B = 1$ μG at $\xi = 0$, outside the remnant, lead to $\beta \sim 17$ (where $\beta = P/(B^2/8\pi)$ is the ratio of thermal to magnetic pressure) a typical order of magnitude of β in the diffuse regions of the ISM [236].

In the second set of simulations, the unperturbed ambient medium is uniform with temperature $T = 10^4$ K and particle number density $n = 0.25$ cm^{-3}. The ambient magnetic field, **B** , is assumed to be dipolar. This idealized situation is adopted here mainly to ensure magnetostaticity of the non-uniform field. The dipole is oriented parallel to the x axis and located on the z axis ($x = y = 0$) either at

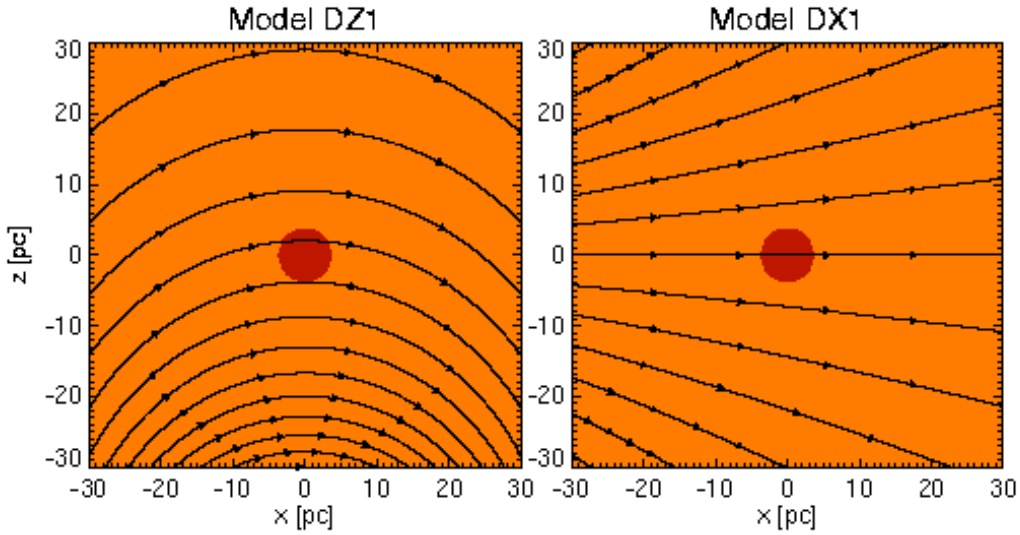

Figure 4.18. 2-D sections in the (x, z) plane of the initial mass density distribution and initial configuration of the unperturbed dipolar ambient magnetic field in two cases: dipole moment located on the z axis (DZ1, left panel), or on the x axis (DX1, right panel). The initial remnant is at the center of the domain. Black lines are magnetic field lines.

$z = -100$ pc or at $z = -50$ pc; alternatively the dipole is located on the x axis ($y = z = 0$) either at $x = -100$ pc or at $x = -50$ pc (as shown in Fig. 4.18). In both configurations, the field strength varies by a factor ~ 6 (z or $x = -100$ pc) or ~ 60 (z or $x = -50$ pc) over 60 pc: in the first case in the direction perpendicular to the average ambient field $\langle \mathbf{B} \rangle$, whereas in the second case parallel to $\langle \mathbf{B} \rangle$. In all the cases, the initial magnetic field strength is set to $B = 1$ μG at the center of the SN explosion ($x = y = z = 0$).

Note that the transition time from adiabatic to radiative phase for a SNR is (e.g. [90], Sect. 2.2)

$$t_{\rm tr} = 2.84 \times 10^4 \; E_{51}^{4/17} \; n_{\rm ism}^{-9/17} \; \text{yr} \; , \tag{4.31}$$

where $E_{51} = E_0/(10^{51}$ erg) and $n_{\rm ism}$ is the particle number density of the ISM. In our set of simulations, runs GZ2 and GX2 present the lowest values of the transition time, namely $t_{\rm tr} \approx 25$ kyr. Since we follow the expansion of the remnant for 22 kyrs, our modeled SNRs are in the adiabatic phase.

$K_{\rm s}$ is expected to vary with the shock velocity $V_{\rm sh}(t)$ and, in case of inhomogeneous ISM, with the immediately post-shock value of mass density, $\rho_{\rm s}$; let us assume that approximately $K_{\rm s} \propto \rho_{\rm s} V_{\rm sh}(t)^{-b}$.

We found, in Sect. 4.1 and 4.2, that the value of b does not affect the main features of the surface brightness distribution if SNR evolves in uniform ISM. Therefore we use the value $b = 0$ to produce the SNR images in models with uniform ISM (models DZ1, DZ2, DX1, and DX2). In cases where non-uniformity of ISM causes variation of the shock velocity in SNR (models GZ1, GZ2, GX1, and GX2), we calculate images for $b = -2, 0, 2$. The post-shock evolution of relativistic electrons is calculated as described in Sect. 3.2.3.

4.3.2. Effect of the environment on radio maps of SNRs. In all the models examined, we found the typical evolution of adiabatic SNRs expanding through an organized ambient magnetic field (see [62] and references therein): the fast expansion of the shock front with temperatures of few millions degrees, and the development of Richtmyer-Meshkov (R-M) instability, as the forward and reverse shocks progress through the ISM and ejecta, respectively (see [207]). As examples, Fig. 4.19 shows 2-D sections in the (x, z) plane of the distributions of mass density and of the module of the magnetic field for the models GZ2, DZ2, and DX2 at $t = 18$ kyrs. The inner shell is dominated by the R-M instability that causes the plasma mixing and the magnetic field amplification. In the inner shell, the magnetic field shows a turbulent structure with preferentially radial components around the R-M fingers (see Fig. 4.20). Note that, some authors have invoked the R-M instabilities to explain the dominant radial magnetic field observed in the inner shell of SNRs (e.g. [205]); however, in our simulations, the radial tendency is observed well inside the remnant and not immediately behind the shock as inferred from observations.

We found that, throughout the expansion, the shape of the remnant is not appreciably distorted by the ambient magnetic field because, for the values of explosion energy and ambient field strength (typical of SNRs) used in our simulations, the kinetic energy of the shock is many orders of magnitude larger than the energy density in the ambient $\mathbf{B}$ field (see also [254]). The shape of the remnant does not differ visually from a sphere also in the cases with density stratification of the ambient

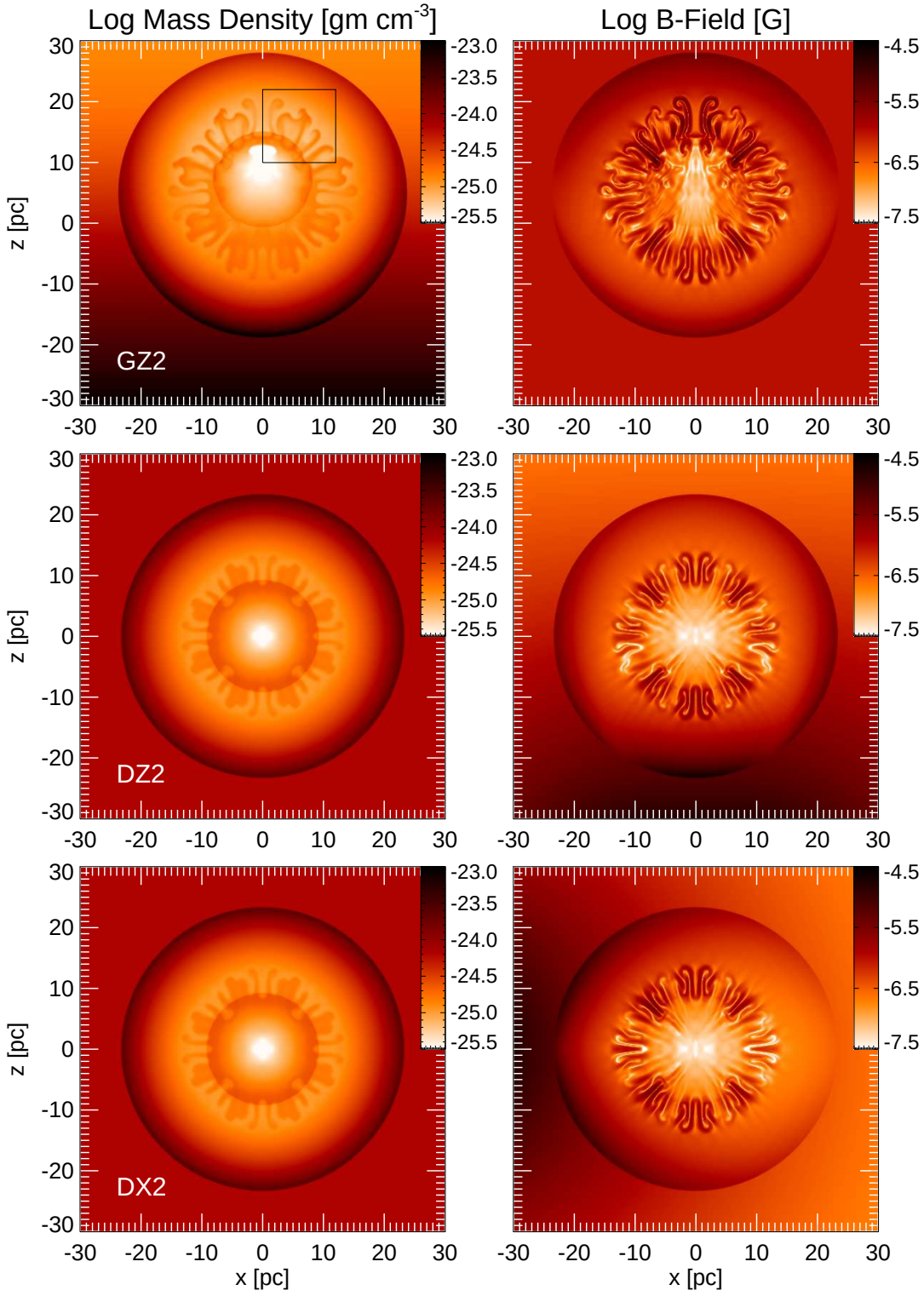

Figure 4.19. 2-D sections in the (x, z) plane of the mass density distribution (left panels), in log scale, and of the distribution of the magnetic-field strength (right panels), in log scale, in the simulations GZ2 (upper panels), DZ2 (middle panels), and DX2 (lower panels) at $t = 18$ kyrs. The box in the upper left panel marks the region shown in Fig. 4.20.

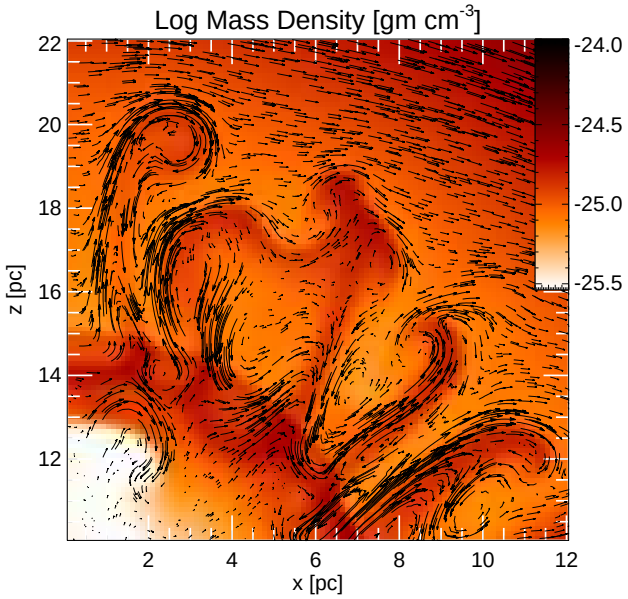

Figure 4.20. Close-up view of the region marked with a box in Fig. 4.19. The dark fingers mark the R-M instability. The magnetic field is described by the superimposed arrows the length of which is proportional to the magnitude of the field vector.

medium[4] as we have shown earlier [195].

The radio emission of the evolved remnants is characterized by an incomplete shell morphology when the viewing angle is not aligned with the direction of the average ambient magnetic field (cf. [157]); in general, the radio emission shows an axis of symmetry with low levels of emission along it, and two bright limbs (arcs) on either side (see also [159]). This morphology is very similar to that observed in bilateral SNRs.

Obliquity angle dependence. For each of the models listed in Table 4.1, we synthesized the synchrotron radio emission, considering each of the three cases of variation of electron injection efficiency with shock obliquity: quasi-parallel, quasi-perpendicular, and isotropic particle injection. As an example, Fig. 4.21 shows the synchrotron radio emission synthesized from the uniform ISM model DZ1 with randomized internal magnetic field at $t = 18$ kyrs in each of the three cases. We recall that for these uniform density cases, we have adopted an injection efficiency independent from the shock speed ($b = 0$). All images are maps of total intensity normalized to the maximum intensity of each map and have a resolution of 400

[4]In these cases, the remnant appears shifted toward the low density region; see upper panels in Fig. 4.19 (see also [127]).

beams per remnant diameter ($D_{\rm SNR}$). The images are derived when the LoS is parallel to the average direction of the unperturbed ambient magnetic field $\langle \mathbf{B} \rangle$ (LoS aligned with the x axis), or perpendicular both to $\langle \mathbf{B} \rangle$ and to the gradient of field strength (LoS along y), or parallel to gradient of field strength (LoS along z).

The different particle injection models produce images that can differ considerably in appearance. In particular, the quasi-parallel case leads to morphologies of the remnant not reproduced by the other two cases: a center-brightened SNR when the LoS is aligned with x (upper left panel in Fig. 4.21), a BSNR with two bright arcs slanted and converging on the side where $\mathbf{B}$ field strength is higher when the LoS is along y (upper middle panel), and a remnant with two symmetric bright spots located between the center and the border of the remnant when the LoS is along z (upper right panel). Neither the center-brightened remnant nor the double peak structure, showing no structure describable as a shell, seems to be observed in SNRs[5]. We found analogous morphologies in all the models listed in Table 4.1, considering the quasi-parallel case. As extensively discussed by [157] for models with uniform ambient magnetic field and $b = -2$, we also conclude that the quasi-parallel case leads to radio images unlike any observed SNR (see also [212]).

The isotropic case leads to remnant's morphologies similar to those produced in the quasi-perpendicular case although the latter case shows deeper minima in the radio emission than the first one. When the LoS is aligned with x (center and lower left panels in Fig. 4.21) or with y (center and lower middle panels), the remnants have one bright arc on the side where the $\mathbf{B}$ strength is higher. When the LoS is aligned with z (center and lower right panels), the remnants have two opposed arcs that appear perfectly symmetric. We found that the isotropic and quasi-perpendicular cases lead to morphologies of the remnants similar to those observed.

Non-uniform ISM: dependence from parameter b. For models describing the SNR expansion through a non-uniform ISM (models GZ1, GZ2, GX1, GX2), we derived the synthetic radio maps considering three alternatives for the dependence

[5]Excluding filled center and composite SNRs, but these are due to energy input from a central pulsar.

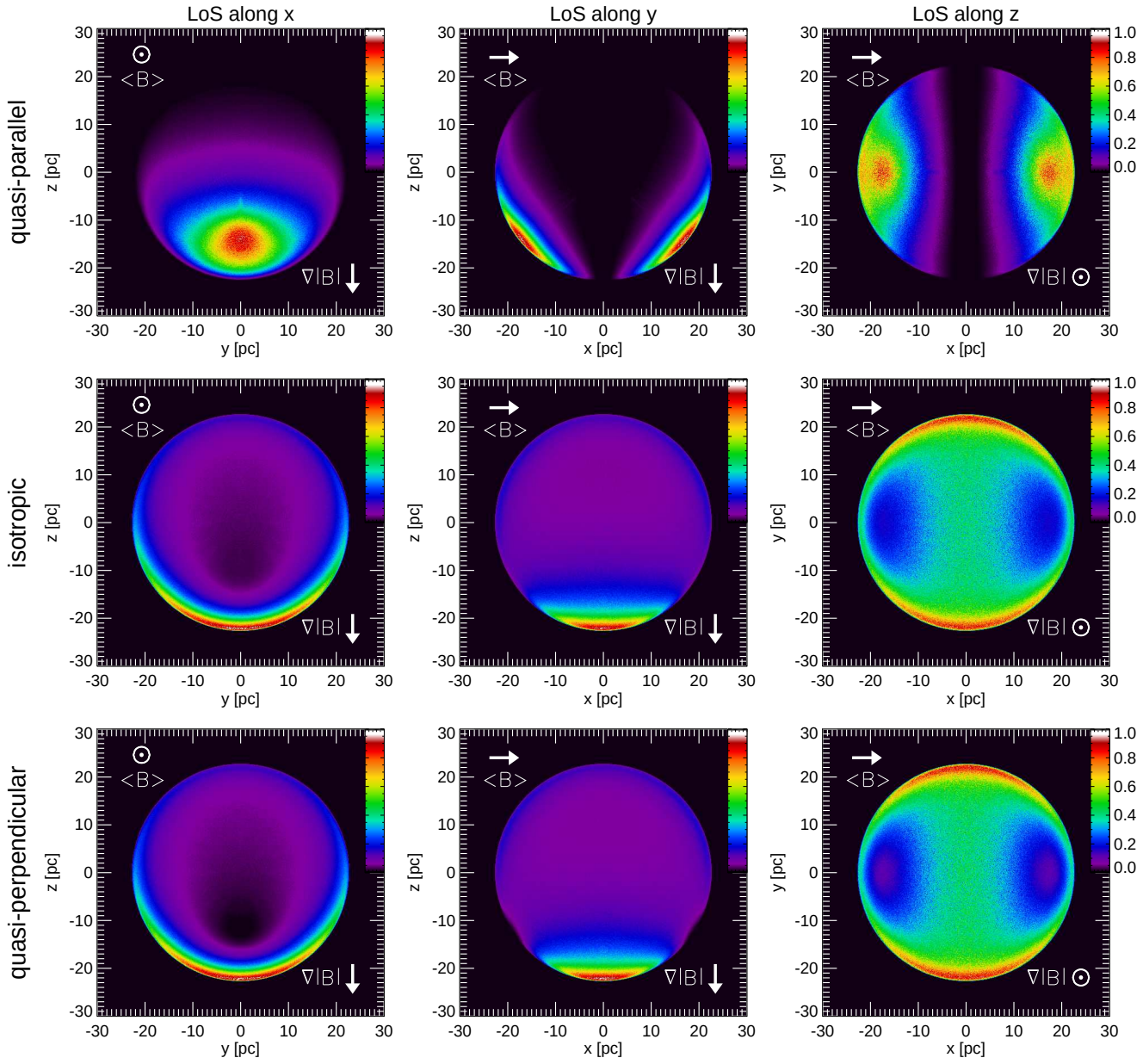

Figure 4.21. Synchrotron radio emission (normalized to the maximum of each panel), at $t = 18$ kyrs, synthesized from model DZ1 assuming $b = 0$ (see text) and randomized internal magnetic field, when the LoS is aligned with the x (left), y (center), or z (right) axis. The figure shows the quasi-parallel (top), isotropic (middle), and quasi-perpendicular (bottom) particle injection cases. The color scale is linear and is given by the bar on the right. The directions of the average unperturbed ambient magnetic field, $\langle \mathbf{B} \rangle$, and of the magnetic field gradient, $\nabla |\mathbf{B}|$, are shown in the upper left and lower right corners of each panel, respectively.

of the injection efficiency on the shock speed, namely $b = -2, 0, 2$. As an example, Fig. 4.22 shows the synthetic maps derived from model GZ1 with randomized internal magnetic field, assuming quasi-perpendicular particle injection, and considering $b = -2$ (top panels), $b = 0$ (middle) and $b = 2$ (bottom).

When the LoS is not aligned with the density gradient, the radio images show asymmetric morphologies of the remnants. In this case, the main effect of varying b is to change the degree of asymmetry observed in the radio maps. In the example shown in Fig. 4.22, the density gradient is aligned with the z axis and asymmetric morphologies are produced when the LoS is aligned with x (left panels) or with y (middle panels). In all the cases, the remnant is brighter where the mass density is higher. On the other hand, the degree of asymmetry increases with increasing value of b.

The reason of such behavior consists in the balance between the roles of the shock velocity and density in changing the injection efficiency. Consider, as an example, the top left panel in Fig. 4.22: the increase of the shock velocity on the north (due to fall of the ambient density) leads to an increase of the brightness there (due to rise of the injection efficiency) that partially balances the increase of the brightness on the south due to higher density of ISM. On the other hand, for the model shown in the bottom left panel in Fig. 4.22, the fraction of accelerated electrons increases on the south due to both the rise of density and the decrease of the shock velocity.

When the LoS is aligned with the density gradient, the radio images are symmetric. In the example shown in Fig. 4.22, this corresponds to the maps derived when the LoS is along z (right panels); the remnants are characterized by two opposed arcs with identical surface brightness.

Morphology. Fig. 4.23 shows the radio emission maps, at a time of 18 kyrs, synthesized from models with a gradient of ambient plasma density (panels A and D; assuming $b = 2$) and of ambient $\mathbf{B}$ field strength (panels B and E; assuming $b = 0$). All the models assume quasi-perpendicular particle injection (the isotropic case produces radio maps with similar morphologies and the quasi-parallel case

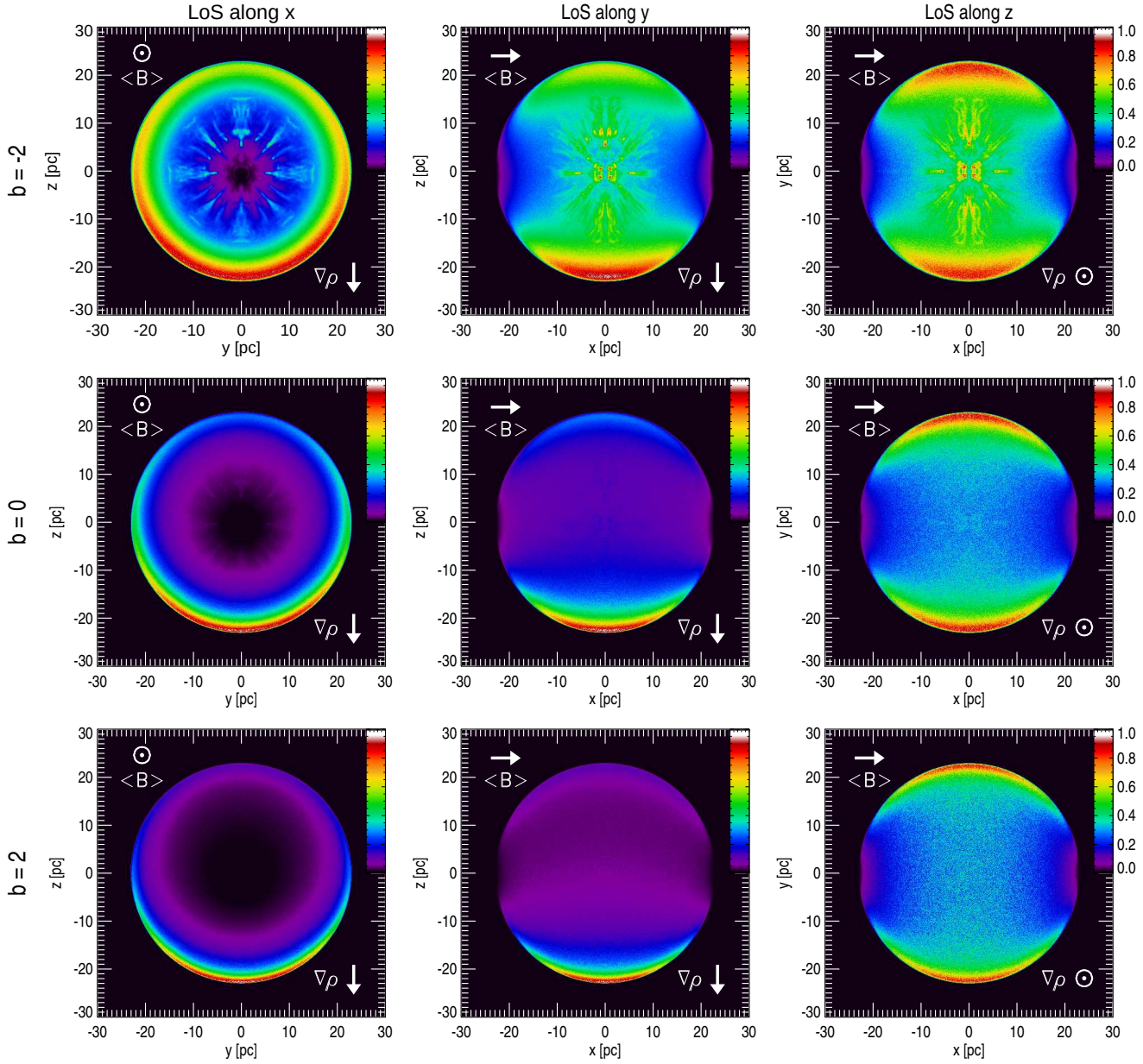

Figure 4.22. Presentation as in Fig. 4.21 for model GZ1 with randomized internal magnetic field, assuming quasi-perpendicular particle injection and $b = -2$ (top panels), $b = 0$ (middle) and $b = 2$ (bottom). The directions of the average unperturbed ambient magnetic field, $\langle \mathbf{B} \rangle$, and of the ambient plasma density gradient, $\nabla\rho$, are shown in the upper left and lower right corners of each panel, respectively.

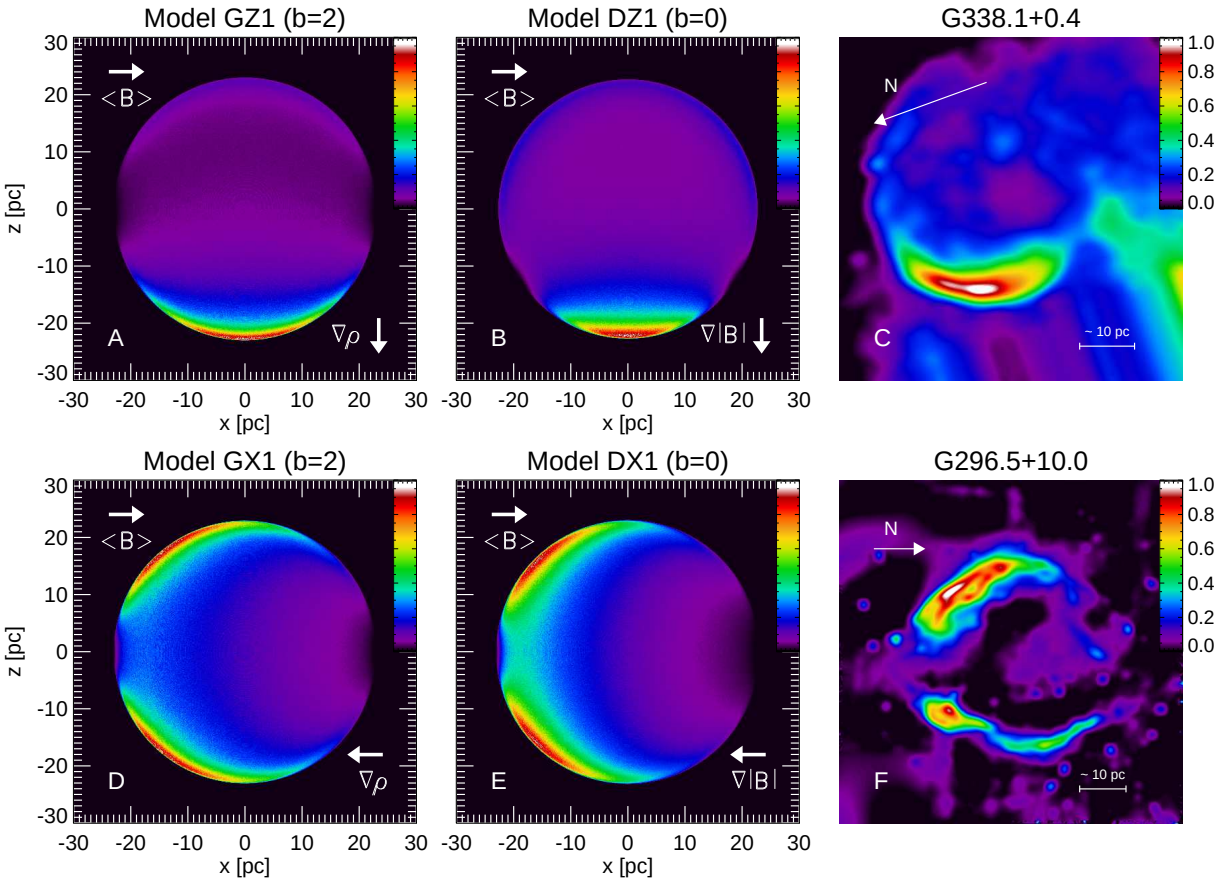

Figure 4.23. Synchrotron radio emission (normalized to the maximum of each panel), at $t = 18$ kyrs, synthesized from models assuming a gradient of ambient plasma density (panels A and D; with $b = 2$) or of ambient magnetic field strength (panels B and E; with $b = 0$) when the LoS is aligned with the y axis. All the models assume quasi-perpendicular particle injection. The directions of the average unperturbed ambient magnetic field, $\langle \mathbf{B} \rangle$, and of the plasma density or magnetic field strength gradient, are shown in the upper left and lower right corners of each panel, respectively. The right column shows two examples of radio maps (data adapted from [368] and [159]; the arrows point in the north direction) collected for the SNRs G338.1+0.4 (panel C) and G296.5+10.0 (panel F). The color scale is linear and is given by the bar on the right.

is discussed later) and randomized internal magnetic field. The viewing angle is perpendicular both to the average direction of the unperturbed ambient magnetic field $\langle \mathbf{B} \rangle$ (direct along the x axis) and to the gradients of density or field strength (direct either along z, panels A and B, or x, panels D and E). The right panels show, as examples, the radio maps of the SNRs G338.1+04 (panel C, data from [368]) and G296.5+10.0 (panel F, from [159]).

In the quasi-perpendicular case discussed here, the maximum synchrotron emissivity is reached where the magnetic field is strongly compressed. This configuration has been referred as "equatorial belt" (e.g. [321]); $\langle \mathbf{B} \rangle$ runs between the two opposed arcs (along the x axis). We found that, when the density or the magnetic

field strength gradient is perpendicular to the field itself, the morphology of the radio map strongly depends on the viewing angle. In these cases, the two opposed arcs appear perfectly symmetric when the LoS is aligned with the gradient (see, for instance, the right panels in Fig. 4.22), otherwise the two arcs can have very different radio brightness, leading to strongly asymmetric BSNRs (see panels A and B in Fig. 4.23). In the former case, the remnant is characterized by two axes of symmetry: one between the two symmetric arcs and the other perpendicular to the two. In models with strong magnetic field strength gradients (DZ2; $\mathbf{B}$ varies by a factor ~ 60 over 60 pc), we found that the radio images are center-brightened when the LoS is aligned with the gradient (figure not reported). The fact that center-brightened remnants are not observed suggests that the external $\mathbf{B}$ varies moderately in the neighborhood of the remnants.

In case of asymmetry, the gradient is always perpendicular to the arcs, and the brightest arc is located where either magnetic field strength or plasma density is higher (see panels A and B in Fig. 4.23), since the synchrotron emission depends on the plasma density, on the pressure, and on the field strength (see Eqs. 4.6 and 3.41); in this case, there is only one axis of symmetry oriented along the density or $\mathbf{B}$ gradient. When the LoS is parallel to $\langle\mathbf{B}\rangle$ (along x in our models), the radio maps show a shell structure with a maximum intensity located where magnetic field strength or plasma density is higher (see Fig. 4.21 for isotropic and quasi-perpendicular cases and Fig. 4.22). Our simulations show that, when the density or the magnetic field strength gradient is perpendicular to the field itself, remnants with a monopolar morphology can be observed at LoS not aligned with the gradient (see also [310]). Examples of observed monopolar remnants are G338.1+0.4 (see panel C in Fig. 4.23) or G327.4+1.0 or G341.9-0.3.

When the density or $\mathbf{B}$ field gradient is parallel to $\langle\mathbf{B}\rangle$ (panels D and E in Fig. 4.23) and the LoS lies in the plane perpendicular to $\langle\mathbf{B}\rangle$, the morphology of the radio map does not depend on the viewing angle and the two opposed arcs have the same radio brightness. In these cases, however, there is only one axis of symmetry and the two arcs appear slanted and converging on the side where field

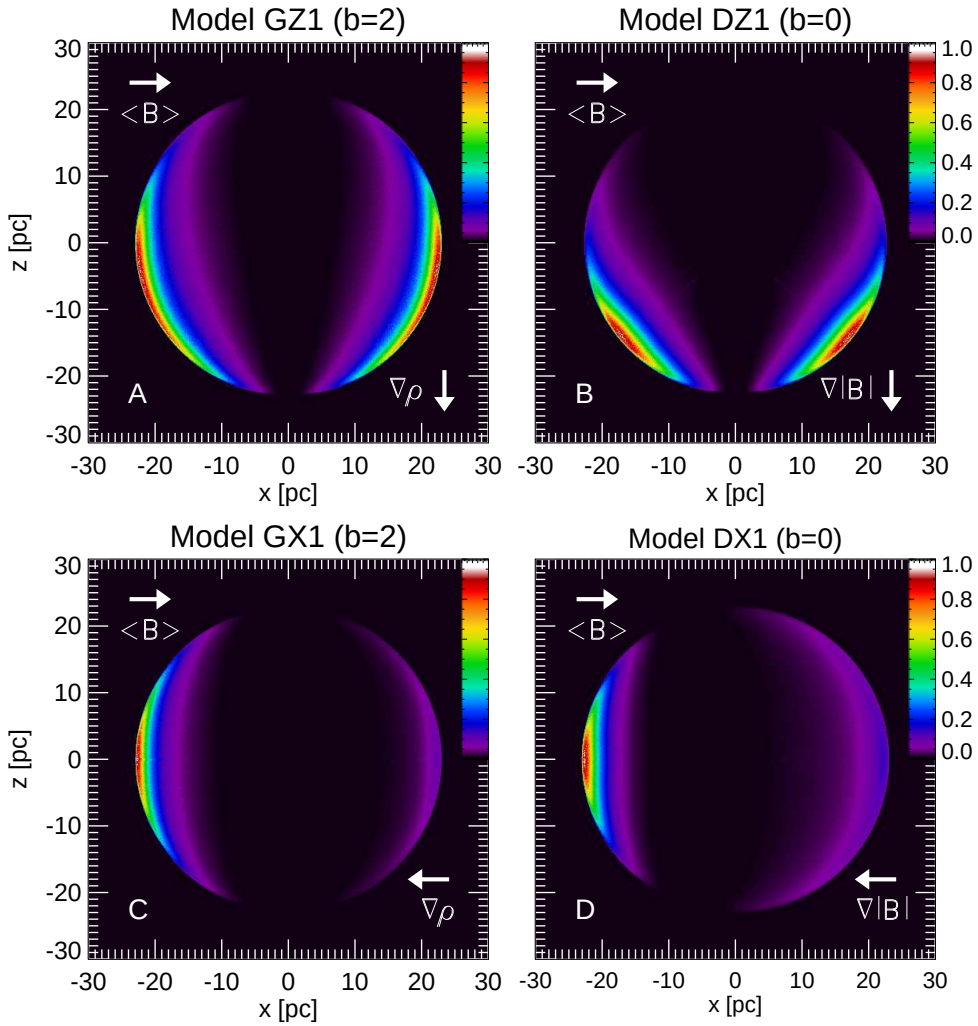

Figure 4.24. Presentation as in Fig. 4.23, assuming quasi-parallel instead of quasi-perpendicular particle injection.

strength or plasma density is higher; again, the symmetry axis is aligned with the density or **B** gradient. Examples of this kind of objects are G296.5+10.0 (see panel F in Fig. 4.23) or G332.4-004 or SN1006 (which is, however, much younger than the simulated SNRs). When the external magnetic field is parallel to the LoS, because the system is symmetric about the magnetic field, the remnant is axially symmetric and the radio maps show a complete radio shell at constant intensity.

In the quasi-parallel case, $\langle \mathbf{B} \rangle$ runs across the arcs. This configuration has been referred as "polar caps" and it has been invoked for the SN1006 remnant [321]. The quasi-parallel case, apart from the center-brightened morphology discussed in Sect. 4.3.2, can also produce remnant morphologies similar to those shown in Fig. 4.23. As examples, Fig. 4.24 shows the radio emission maps obtained in the cases discussed in

Fig. 4.23 but assuming quasi-parallel instead of quasi-perpendicular particle injection. Again, the viewing angle is perpendicular both to $\langle \mathbf{B} \rangle$ (direct along the x axis) and to the gradients of density or field strength (direct either along z, panels A and B, or x, panels C and D). In the quasi-parallel case, remnants with a bright radio limb are produced if the gradient of ambient density or of ambient $\mathbf{B}$ field strength is parallel to $\langle \mathbf{B} \rangle$ (instead of perpendicular to $\langle \mathbf{B} \rangle$ as in the quasi-perpendicular case), whereas slanting similar radio arcs are obtained if the gradient is perpendicular to $\langle \mathbf{B} \rangle$ (instead of parallel as in the quasi-perpendicular case).

4.3.3. Measuring the degree of asymmetry. Our simulations show that asymmetric BSNRs are explained if the ambient medium is characterized by gradients either of density or of ambient magnetic field strength: the two opposed arcs have different surface brightness if the gradient runs across the arcs (see panels A and B in Fig. 4.23, and panels C and D in Fig. 4.24), whereas the two arcs appear slanted and converging on one side if the gradient runs between them (see panels D and E in Fig. 4.23 and panels A and B in Fig. 4.24). In all the cases (including the three alternatives for the particle injection), the symmetry axis of the remnant is always aligned with the gradient.

Following [157], we quantify the degree of "bipolarity" of the remnants by using the so-called azimuthal intensity ratio A, i.e. the ratio of maximum to minimum intensity around the shell of emission as derived from the azimuthal intensity profiles[6]. In addition, we quantify the degree of asymmetry of the BSNRs by using a measure we call the azimuthal intensity ratio $R_{\max} \geq 1$, i.e. the ratio of the two maxima around the shell, and the azimuthal distance $\theta_{\rm D}$, i.e. the distance in deg of the two maxima. In the case of symmetric BSNRs, $R_{\max} = 1$ and $\theta_{\rm D} = 180^o$. As already noted by [157], the parameter A depends on the spatial resolution of the radio maps and on the aspect angle (i.e. the angle between the LoS and the unperturbed magnetic field); moreover we note that, in real observations, the measure

[6]To calculate one of these profiles from a model, we first find the point on the map where the intensity is maximum. Then the contour of points at the same radius as the point of maximum intensity defines the azimuthal radio intensity profile.

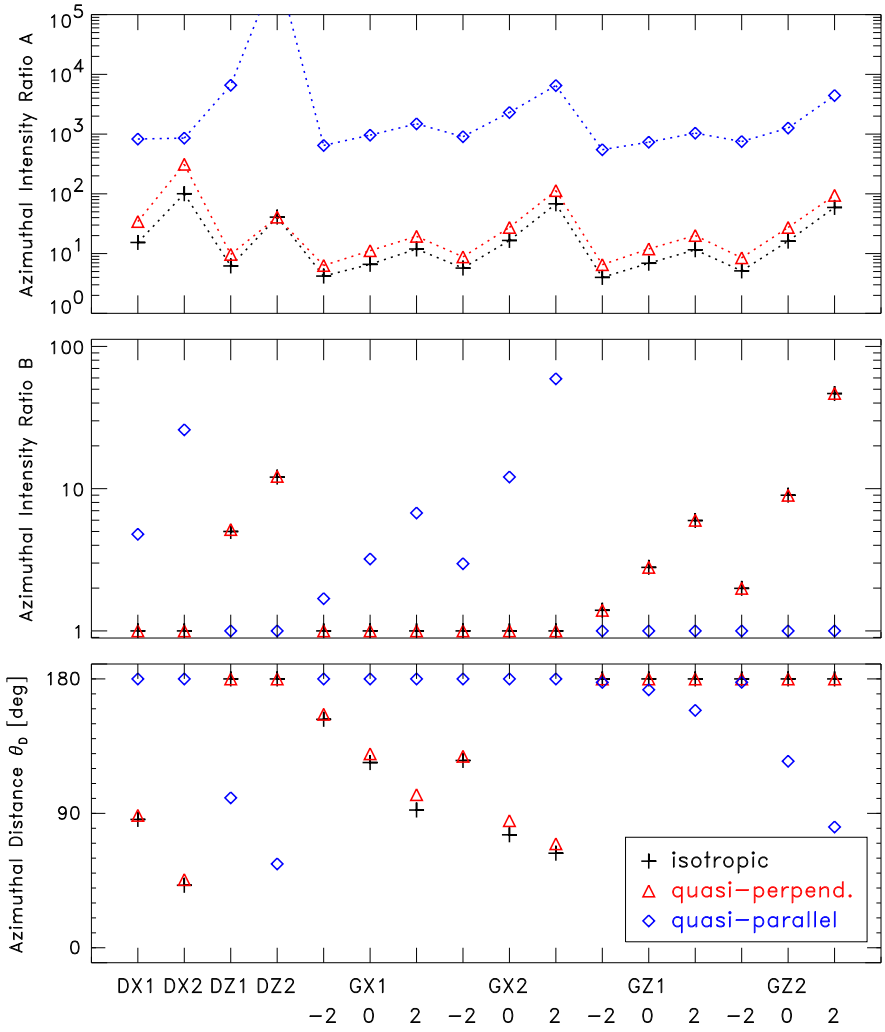

Figure 4.25. Azimuthal intensity ratio A (upper panel), azimuthal intensity ratio $R_{\rm max}$ (middle panel), and azimuthal distance $\theta_{\rm D}$ (lower panel) for all the cases examined, considering the LoS aligned with the y axis and a spatial resolution of 25 beams per remnant diameter, $D_{\rm SNR}$. Crosses: isotropic; triangles: quasi-perpendicular; diamonds: quasi-parallel.

of A gives a lower limit to its real value if the background is not accurately taken into account. On the other hand, the parameters $R_{\rm max}$ and $\theta_{\rm D}$ have a much less critical dependency on these factors and, therefore, they may provide a more robust diagnostic in the comparison between models and observations.

Fig. 4.25 shows the values of A, $R_{\rm max}$, and $\theta_{\rm D}$ derived for all the cases examined in this section, considering the LoS aligned with the y axis, and radio maps with a resolution of 25 beams per remnant diameter[7] ($D_{\rm SNR}$). Note that, our choice of the LoS aligned with y (aspect angle $\phi = 90^o$) implies that the values of A in Fig. 4.25 are upper limits, being A maximum at $\phi = 90^o$ and minimum at $\phi = 0^o$

[7]After the radio maps are calculated, they are convolved with a gaussian function with σ corresponding to the required resolution.

(see [157]). The three models of particle injection (isotropic, quasi-perpendicular and quasi-parallel) lead to different values of A. In the isotropic and quasi-perpendicular cases, most of the values of A range between 5 and 20 (for model DX2, A is even larger than 100); in the quasi-parallel case, the values of A are larger than 500.

We found that, in general, a gradient of the ambient magnetic field strength leads to remnant morphologies similar to those induced by a gradient of plasma density (compare, for instance, panel A with B and panel D with E in Fig. 4.23). On the other hand, if $b < 0$ in GX and GZ models, ambient $\mathbf{B}$ field gradients are more effective in determining the morphology of asymmetric BSNRs. This is seen in a more quantitative form in Fig. 4.25. DX and DZ models give $R_{\rm max}$ values higher and $\theta_{\rm D}$ values lower than GX and GZ models with $b < 0$: a modest gradient of the magnetic field (models DX1 and DZ1) gives a value of $R_{\rm max}$ higher or $\theta_{\rm D}$ lower than the two models with strong density gradients (models GX2 and GZ2) and $b < 0$.

Fig. 4.25 also shows that, in models with a density gradient, the degree of asymmetry of the remnant increases with increasing value of b; the GX and GZ models with $b > 0$ give values of $R_{\rm max}$ and $\theta_{\rm D}$ comparable with (or, in the case of $R_{\rm max}$, even larger of) those derived from DX and DZ models. In the case of quasi-parallel particle injection for remnants with converging similar arcs, it is necessary a strong gradient of density perpendicular to $\mathbf{B}$ and $b \geq 0$ (compare models GZ1 and GZ2 in the lower panel in Fig. 4.25) to give values of $\theta_{\rm D}$ comparable to those obtained with a moderate gradient of ambient $\mathbf{B}$ field strength perpendicular to $\mathbf{B}$ (see model DZ1 in Fig. 4.25).

In order to compare our model predictions with observations of real BSNRs, we have selected 11 SNR shells which show one or two clear lobes of emission in archive total intensity radio images, separated by a region of minima. We have discarded all those cases in which several point-like or extended sources appear superimposed to the bright limbs, or other cases in which the location of maximum or minimum emission around the shell is difficult to derive. Unlike other lists of BSNRs published in the literature (e.g. [157, 159, 212]), here we focus on a reliable measure of the parameters A, $R_{\rm max}$ and $\theta_{\rm D}$; we avoid, therefore, patchy and irregular limbs, as in

the case of G320.4-01.2 of [159]. Moreover, we are obviously not discarding remnants which have constraints on A, $R_{\rm max}$ or $\theta_{\rm D}$ (e.g. [157] considered only cases with $R_{\rm max} < 2$), and we are considering remnants observed with a resolution greater than 10 beams per remnant diameter. Since in our models we follow the remnant evolution during the adiabatic phase, we also need to discard objects that are clearly in the radiative phase. Unfortunately, for most of the objects selected, there is no indication of their evolutionary stage in literature. Assuming that the remnant expands in a medium with particle number density $n_{\rm ism} \lesssim 0.3$ cm^{-3}, the shock radius derived from the Sedov solution at time $t_{\rm tr}$ (i.e. at the transition time from the adiabatic to the radiative phase; see Eq. 4.31) is

$$r_{\rm tr} = 19\ E_{51}^{5/17}\ n_{\rm ism}^{-7/17} \lesssim 35\ {\rm pc}\ , \tag{4.32}$$

where we have assumed that $E_{51} = 1.5$. Therefore, we only considered remnants with radius $r_{\rm snr} < 35$ pc (i.e. with size < 70 pc) that are, most likely, in the adiabatic phase. Our list does not pretend to be complete or representative of the class, and it is compiled to derive the observed values of the parameters A, $R_{\rm max}$ and $\theta_{\rm D}$ with the lowest uncertainties. For this reason, we have considered remnants for which a total intensity radio image in digital format is available. Actually, in most of the cases, we have used the 843 MHz data of the MOST supernova remnant catalogue [368].

Our list is reported in Table 4.2. We have separated evolved and young SNRs. While the young SNRs listed in Table 4.2 have very reliable measurement of A, $R_{\rm max}$ and $\theta_{\rm D}$ and a good record of literature, making them very good candidate to test the diagnostic power of our model, we stress that we are focused on evolved SNRs. For each object in Table 4.2, we show the apparent size, the distance (from dedicated studies where possible, otherwise from the revised $\Sigma - D$ relation of [103], see their paper for caveats on usage of the $\Sigma - D$ relation to derive SNR distance), the real size, the resolution of the observation, and the parameters A, $R_{\rm max}$, and $\theta_{\rm D}$ we have introduced here.

Table 4.2 shows that most of the 11 remnants have $A \leq 10$, i.e. values consistent

Table 4.2
List of barrel-shaped SNR shells for which a measurement of A, B and $\theta_{\rm D}$ is presented for comparison with our models.

Remnant[a]	Flux Jy	size arcmin	d kpc	size pc	Res.[b] beams/$D_{\rm SNR}$	A	$R_{\rm max}$	$\theta_{\rm D}$ deg	Ref./ notes
Evolved Remnants									
G296.5+10.0	48	90×65	2.1	55×40	108	> 11	1.2	85	1
G299.6-0.5	1.1	13×13	18.1	68	18	6	2	160	2
G304.6+0.1	18	8×8	7.9	18	11	20	1.5	120	3
G327.4+1.0	2.1	14×13	13.9	56	19	> 10	> 10	ND	2,4
G332.0+0.2	8.9	12×12	< 20	< 70	17	5	1	145	2,7
G338.1+0.4	3.8	16×14	9.9	46×40	21	3	2	> 120	2
G341.9-0.3	2.7	7×7	14.0	28	10	8	3	170	2
G346.6-0.2	8.7	11×10	8.2	26×23	15	2	1.1	110	2,7
G351.7+0.8	11	18×14	6.7	35×27	22	2	1.6	130	2
Young Remnants									
G327.6+14.6	19	30×30	2.2	19×19	42	22	1	127	5
G332.4-0.4	34	11×10	3.1	10×9	15	7	1.6	98	6

References and notes. - (1) A.k.a. PKS 1209-51/52. Age: 3–20 kyrs, [318]. Distance from [166]. (2) Distance derived by [103] using a revised $\Sigma - D$ relation. (3) Distance from [108]. (4) This shell has only one limb ("monopolar" according to the definition of [157]). A and $R_{\rm max}$ are lower limits and no $\theta_{\rm D}$ is derived. (5) A.k.a. SN1006. Distance from [369]. (6) A.k.a. RCW103. Distance from [314]. (7) Two maxima have been found in one lobe. $\theta_{\rm D}$ is the average of the two.

[a] All the data are from the MOST supernova remnant catalogue [368], except where noted.
[b] Spatial resolution of the observation in beams per remnant diameter.

with those derived in Fig. 4.25 for the three alternatives for the particle injection (recall that the values shown in the figure have to be considered as upper limits). Four remnants show high values of A ($10 < A < 100$) that are difficult to explain in terms of the isotropic or the quasi-perpendicular injection models with $b < 0$ unless the remnant expands through a non-uniform ambient magnetic field (see models DX2, and DZ2 in Fig. 4.25). In the light of these considerations, we cannot exclude a priori any of the three alternative models for the particle injection.

Four of the 11 objects in Table 4.2 show values of $R_{\rm max} \geq 2$, pointing out that, in these objects, the bipolar morphology is asymmetric with the two radio limbs

differing significantly in intensity. An example of this kind of remnants is G338.1+0.4 (see panel C in Fig. 4.23). In the light of our results, its morphology can be explained if a gradient of ambient density or of ambient magnetic field strength is either perpendicular to the radio limb in the isotropic and quasi-perpendicular cases or parallel to the radio limb in the quasi-parallel case. It is worth noting that reveling such a gradient from the observations may be a powerful diagnostic to discriminate among the alternative particle injection models, producing real advances in the understanding of the nonthermal physics of strong shock waves.

An extreme example of a monopolar remnant with a bright radio limb is G327.4+1.0 whose value of $R_{\rm max}$ is larger than 10. Fig. 4.25 shows that high values of $R_{\rm max}$ can be easily explained as due to non-uniform ambient magnetic field strength or to non-uniform ambient density if $b > 0$. We suggest that the morphology of G327.4+1.0 may give some hints on the value of b (and, therefore, on the dependence of the injection efficiency on the shock velocity) if the observations show that the asymmetry is due to a non-uniform ambient medium through which the remnant expands.

In Table 4.2, six of the 11 remnants (including the two young remnants SN1006 and RCW103) have values of $\theta_{\rm D} < 140^o$, pointing out that, in these objects, the two bright radio limbs appear slanted and converging on one side. An example of this class of objects is G296.5+10.0 (a.k.a PKS 1209-51/52) shown in panel F in Fig. 4.23. In this case, the value of $\theta_{\rm D} \sim 85^o$ derived from the observations may be easily explained as due to a gradient of magnetic field strength either perpendicular to the radio limbs in the isotropic and quasi-perpendicular cases or parallel to the radio limbs in the quasi-parallel case. Models with a gradient of ambient density cannot explain the low values of $\theta_{\rm D}$ found for G296.5+10.0 unless the gradients are strong (the density should change by a factor 60 over 60 pc) and the dependence of the injection efficiency on the shock velocity gives $b \geq 2$.

4.3.4. Summary. Our findings have significant implications on the diagnostics and lead to several useful conclusions:

1. The three different particle injection models (namely, quasi-parallel, quasi-

perpendicular and isotropic dependence of injection efficiency from shock obliquity) can produce considerably different images (see Fig. 4.21). The isotropic and quasi-perpendicular cases lead to radio images similar to those observed. The parallel-case may produce radio images unlike any observed SNR (center-brightened or with a double-peak structure not describable as a shell). This is in agreement with the findings of [157].

2. In models with gradients of the ambient density, the dependence of the injection efficiency on the shock velocity (through the parameter b) affects the degree of asymmetry of the radio images: the asymmetry increases with increasing value of b.

3. Small variations of the ISMF lead to significant asymmetries in the morphology of BSNRs (see Figs. 4.23 and 4.24). Therefore, we conclude that the close similarity of the radio brightness of the opposed limbs of a BSNR (i.e. $R_{\rm max} \approx 1$ and $\theta_{\rm D} \approx 180^o$) is evidence of uniform ambient $\mathbf{B}$ field where the remnant expands.

4. Variations of the ambient density lead to asymmetries of the remnant with extent comparable to that caused by non-uniform ambient magnetic field if $b \geq 2$. We conclude that remnants with $R_{\rm max} \approx 1$ and $\theta_{\rm D} \approx 180^o$ are evidence of $b < 2$ if the remnant expands in a strongly non-uniform ISM.

5. Strongly asymmetric BSNRs (i.e. $R_{\rm max} \gg 1$ or $\theta_{\rm D} \ll 180^o$) imply either moderate variations of $\mathbf{B}$ or strong (moderate) variations of the ISM density if $b < 2$ ($b \geq 2$) as in the case, e.g., of interaction with a giant molecular cloud.

6. BSNRs with different intensities of the emission of the radio arcs (i.e. $R_{\rm max} > 1$) can be produced by models with a gradient of density or of MF perpendicular to the arc (upper panels in Fig. 4.23 and lower panels in Fig. 4.24), and the brightest arc is in the region of higher plasma density or higher magnetic field strength.

7. SNRs with two slanting similar arcs (i.e. $\theta_{\rm D} < 180^o$) can be produced by models with a gradient of density or of MF running centered between the two arcs (lower panels in Fig. 4.23 and upper panels in Fig. 4.24), and the region of convergence is where either the plasma density or the magnetic field strength is higher.

8. In all the cases examined, the symmetry axis of the remnant is always aligned with the gradient of density or of magnetic field.

We found that the degree of ordering of the magnetic field downstream of the shock does not affect significantly the asymmetries induced by gradients either of ambient plasma density or of ambient magnetic field strength; thus our conclusions, derived in the case of disordered magnetic field, do not change in the case of ordered magnetic field.

We defined useful model parameters to quantify the degree of asymmetry of the remnants. These parameters may provide a powerful diagnostic in the comparison between models and observations, as we have shown in a few cases drawn from a randomly selected sample of BSNRs presented in Table 4.2. For instance, if the density of the external medium is known by other means (e.g. thermal X-rays, HI and Co maps, etc.), BSNRs can be very useful to investigate the variation of the efficiency of electron injection with the angle between the shock normal and the ambient magnetic field (Sect. 5.3) or to investigate the dependence of the injection efficiency from the shock velocity (Sect. 5.4). Alternatively, BSNRs can be used as probes to trace the local configuration of the galactic magnetic field if the dependence of the injection efficiency from the obliquity is known or assumed.

It is worth emphasizing that our model follows the evolution of the remnant during the adiabatic phase and, therefore, their applicability is limited to this evolutionary stage. In the radiative phase, the high degree of compression suggested by radiative shocks leads to increase of the radio brightness due to compression of ambient magnetic field and electrons. Since our model neglects the radiative cooling it is limited to relatively small compression ratios and, therefore, it is not able to simulate this mechanism of limb brightening.

It will be interesting to expand the present study, considering the detailed comparison of model results with observations. This may lead to a major advance in the study of interactions between the magnetized ISM and the whole galactic SNR population (not only BSNRs), since the mechanisms at work in the BSNRs are also valid for SNRs of more complex morphology.

4.4. Effects of nonuniform ISMF on synchrotron X-ray and inverse-Compton gamma-ray morphology of SNRs

In a previous Sect. 4.3, we have investigated the origin of asymmetries in the radio morphology of BSNRs through a model of SNR expanding through either a non-uniform ISM or a non-uniform ISMF. In this section, we extend our analysis to the non-thermal X-ray and IC γ-ray emission. In particular, we develop a numerical code to synthesize the synchrotron radio, X-ray, and IC γ-ray emission from 3D MHD simulations; then we couple the synthesis code with the MHD model introduced in Sect. 4.3 and investigate the effects of a nonuniform ISMF on the morphology of the remnant in the hard X-ray and γ-ray bands.

4.4.1. Modeling and numerical setup. We adopt the MHD model introduced in Sect. 4.3, describing the propagation of a SNR shock through a magnetized ambient medium. The shock propagation is modeled by numerically solving the time-dependent ideal MHD equations of mass, momentum, and energy conservation in a 3D Cartesian coordinate system (x, y, z). The model does not include consistently the effects on shock dynamics due to back-reaction of accelerated CRs. However, we approach the effect of shock modification by considering different values of the adiabatic index γ which is expected to drop from the value of an ideal monoatomic gas; in particular, we consider here the cases of $\gamma = 5/3$ (for an ideal monatomic gas), $\gamma = 4/3$ (for a gas dominated by relativistic particles), and $\gamma = 1.1$ (for large energy drain from the shock region due to the escape of high energy CRs). The simulations are performed using the FLASH code ([156]), an adaptive mesh refinement multiphysics code for astrophysical plasmas.

As initial conditions, we adopt parameters appropriate to reproduce the SNR SN 1006 after 1000 yr of evolution: we assume an initial spherical remnant with radius $r_{0\mathrm{snr}} = 0.5$ pc, originating from a progenitor star with mass of 1.4 M_{sun}, and propagating through an unperturbed magneto-static medium. The initial total energy E_0 is set to a value leading to a remnant radius $r_{\mathrm{snr}} \approx 9$ pc at $t = 1000$ yr

($E_0 \approx 1.3-1.8\times10^{51}$ erg, depending on γ) and is partitioned so that most of the SN energy is kinetic energy. The remnant expands through an homogeneous isothermal medium with particle number density $n = 0.05$ cm^{-3} and temperature $T = 10^4$ K. We consider three different configurations of the unperturbed ambient magnetic field: 1) a uniform ambient magnetic field (runs Unif-g1, Unif-g2, and Unif-g3); 2) a gradient of ambient magnetic field strength perpendicular to the average magnetic field (runs Grad-BZ-g1, Grad-BZ-g2, and Grad-BZ-g3); and 3) a gradient of ambient magnetic field strength aligned with the average magnetic field (runs Grad-BX-g1, Grad-BX-g2, Grad-BX-g3).

In the case of a uniform ISMF, we assume that the field is oriented parallel to the x axis. In the other two cases, the ambient magnetic field is assumed to be dipolar[8]. The dipole is oriented parallel to the x axis and located either on the z axis ($x = y = 0$) at $z = -100$ pc (Grad-BZ-g1, Grad-BZ-g2, Grad-BZ-g3) or on the x axis ($y = z = 0$) at $x = -100$ pc (Grad-BX-g1, Grad-BX-g2, Grad-BX-g3). In all the cases, the initial magnetic field strength is set to $B_0 = 30$ μG at the center of the SN explosion ($x = y = z = 0$). In the configurations with nonuniform ISMF, the field strength varies by a factor ~ 6 over 60 pc: either in the direction perpendicular to the average ambient field $\langle\mathbf{B}\rangle$ (Grad-BZ-g1, Grad-BZ-g2, Grad-BZ-g3), or parallel to $\langle\mathbf{B}\rangle$ (Grad-BX-g1, Grad-BX-g2, Grad-BX-g3). We follow the expansion of the remnant for 1000 yr. Table 4.3 summarizes the physical parameters characterizing the simulations considered here.

The SN explosion is at the center $(x, y, z) = (0, 0, 0)$ of the computational domain which extends between -10 and 10 pc in all directions. At the coarsest resolution, the adaptive mesh algorithm used in the FLASH code (PARAMESH; [237]) uniformly covers the 3D computational domain with a mesh of 8^3 blocks, each with 8^3 cells. We allow for 5 additional nested levels of refinement during the first 100 yr of evolution with resolution increasing twice at each refinement level; then the number of nested levels progressively decreases down to 2 at $t = 1000$ yr as the remnant radius increases following the expansion of the remnant through the magnetized medium.

[8]This idealized situation is adopted here mainly to ensure magnetostaticity of the nonuniform field.

Table 4.3

Relevant initial parameters of the simulations.

	γ	E_{sn} [10^{51} erg]	magnetic field configuration	$(x, y, z)^a$ pc
Unif-g1	5/3	1.30	uniform	-
Unif-g2	4/3	1.54	uniform	-
Unif-g3	1.1	1.81	uniform	-
Grad-BZ-g1	5/3	1.30	$z-$strat.	$(0, 0, -100)$
Grad-BZ-g2	4/3	1.54	$z-$strat.	$(0, 0, -100)$
Grad-BZ-g3	1.1	1.81	$z-$strat.	$(0, 0, -100)$
Grad-BX-g1	5/3	1.30	$x-$strat.	$(-100, 0, 0)$
Grad-BX-g2	4/3	1.54	$x-$strat.	$(-100, 0, 0)$
Grad-BX-g3	1.1	1.81	$x-$strat.	$(-100, 0, 0)$

[a] Coordinates of the magnetic dipole moment.

The refinement criterion adopted follows the changes in density and temperature. This grid configuration yields an effective resolution of ≈ 0.0098 pc at the finest level during the first 100 yr of evolution (when the radius of the remnant was < 2 pc) and ≈ 0.078 pc at the end of the simulation, corresponding to an equivalent uniform mesh of 2048^3 and 256^3 grid points, respectively. We assume zero-gradient conditions at all boundaries.

Post-shock evolution of the electron distribution in nonuniform ISM and/or ISMF is modelled as described in Sect. 3.2.4.

From the model results, we synthesize synchrotron radio, X-ray, and IC γ-ray emission.

4.4.2. Synchrotron X-ray and IC γ-ray maps of SNRs in nonuniform ISMF. Figure 4.26 shows the 3D rendering of the mass density at $t = 1000$ yr in the three cases of γ considered for uniform ISMF. The main effect of γ on the shock dynamics is to change its compression ratio and the distance of the contact discontinuity from the blast wave position; no dependence on the obliquity angle is present, γ being uniform in each simulation. The value of γ is expected therefore to influence the absolute values of emission in the radio, X-ray and γ-ray bands but

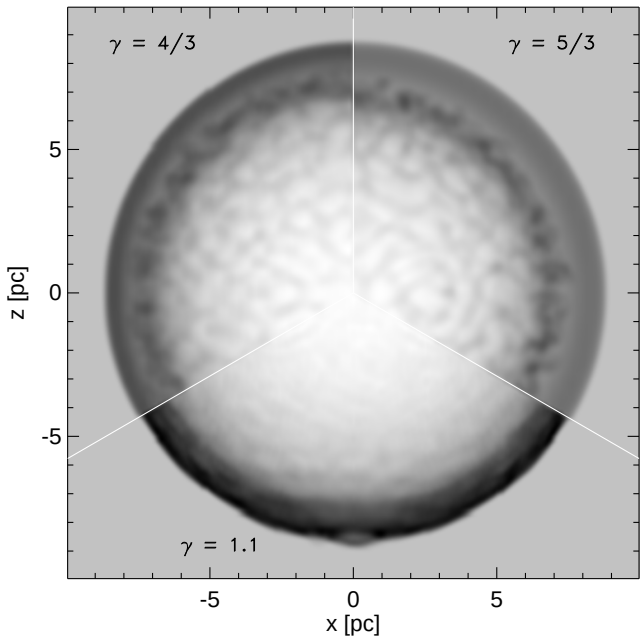

Figure 4.26. 3D rendering of the mass density at $t = 1000$ yr for a remnant expanding through a uniform ISMF and for three cases of $\gamma = 5/3$, 4/3, 1.1 (runs Unif-g1, Unif-g2, and Unif-g3, see Table 4.3).

not the large scale morphology of the remnant to which this section is focused on. In the following, we first discuss the effects of nonuniform ISMF on the synchrotron and IC emission adopting, as reference, the case with $\gamma = 5/3$, allowing the direct comparison of our results with those available in the literature; then in Sect. 4.4.2, we discuss the effect of γ on the morphology of the non-thermal emission.

In all the synthetic images presented below, we introduce the procedure of magnetic field disordering (with randomly oriented magnetic field vector in each point) downstream of the shock, according to observations showing a low degree of polarization (10-15%; e.g. Tycho [126], SN 1006 [311]).

In all the simulations, we assume the (average) unperturbed ISMF $\langle \mathbf{B} \rangle$ oriented along the x axis. In the two magnetic field configurations we explored, the gradient of ISMF strength is either normal (runs Grad-BZ-g1, Grad-BZ-g2, Grad-BZ-g3; $\nabla|\langle \mathbf{B} \rangle|$ along z) or aligned (runs Grad-BX-g1, Grad-BX-g2, Grad-BX-g3; $\nabla|\langle \mathbf{B} \rangle|$ along x) to $\langle \mathbf{B} \rangle$. Since we analyze the remnant morphology as it would be observed from different points of view, we define two angles to describe the orientation of $\langle \mathbf{B} \rangle$ and $\nabla|\langle \mathbf{B} \rangle|$ in the space (see Fig. 4.27): $\phi_{\rm B}$ is the angle between $\langle \mathbf{B} \rangle$ and the LoS, and $\phi_{\nabla \rm B}$ is the angle between $\nabla|\langle \mathbf{B} \rangle|$ and the normal to the ISMF in the

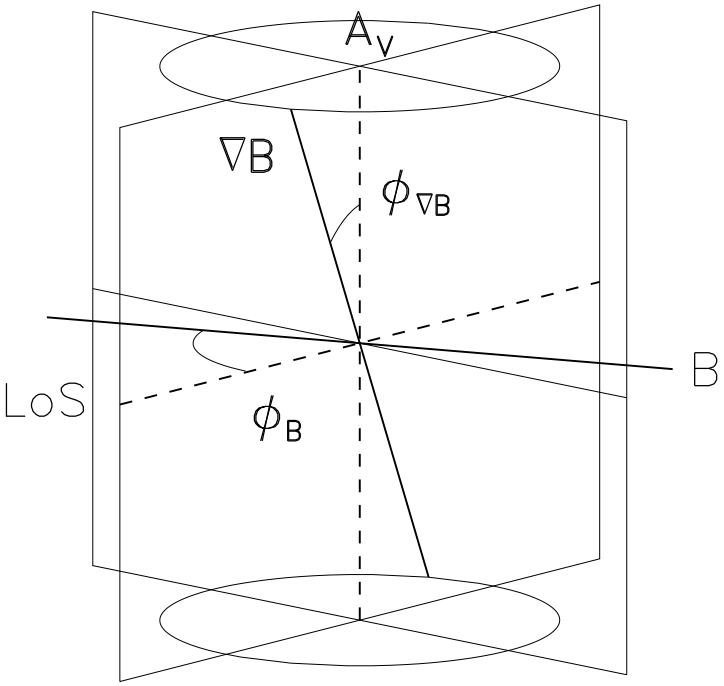

Figure 4.27. Relevant angles describing the orientation of the ISMF and of the gradient of ISMF strength with respect to the observer: $\phi_{\rm B}$ is the angle between the (average) unperturbed ISMF and the LoS, and $\phi_{\nabla \rm B}$ is the angle between the gradient of the ISMF strength and the vertical line passing through the center of the remnant $A_{\rm V}$.

plane of the sky (axis $A_{\rm v}$ in Fig. 4.27). The first angle is the aspect angle commonly used in the literature. The definition of the second angle allows us to explore the remnant morphology for various aspect angles and for fixed $\phi_{\nabla \rm B}$, $\nabla|\langle \mathbf{B} \rangle|$ lying on a cone with angle $\phi_{\nabla \rm B}$ (see Fig. 4.27). In cases in which the gradient ∇B is aligned with the average ISMF (runs Grad-BX-g1, Grad-BX-g2, Grad-BX-g3) $\phi_{\nabla \rm B} = 90^0$ by definition. In Grad-BZ models, the angle between $\langle \mathbf{B} \rangle$ and $\nabla|\langle \mathbf{B} \rangle|$ is always 90^0. In the following, the images are calculated for various values of the angles defined above and with a resolution of 256×256 pixels.

Parameter space. The prescriptions for the electron energy distribution at any point inside the remnant and for the synthesis of synchrotron and IC emission are characterized by several parameters regulating the energy spectrum of relativistic electrons, the injection efficiency, the time and spatial dependence of $E_{\rm max}$, etc. In the following, we limit the model parameter space through some assumptions that allow us to fix some of the parameters.

In particular, we assume that the high-energy end of the spectrum in Eq. (3.16)

is characterized by $\alpha = 0.5$. The maximum energy at parallel shock $E_{\mathrm{max},\xi,\parallel}$ is a free parameter in Eq. (3.19) that we assume to be $E_{\mathrm{max},\xi,\parallel} = 26$ TeV in all our calculations. Another important parameter for emission from high energy electrons is the fiducial energy E_{f} [303]; at parallel shock, $E_{\mathrm{f},\parallel} = 22$ TeV in models with uniform ISMF, $E_{\mathrm{f},\parallel} = 20$ TeV in Grad-BZ models and $E_{\mathrm{f},\parallel} = 10$ TeV in Grad-BX models[9]. In all the cases, therefore, $E_{\mathrm{f}} < E_{\mathrm{max}}$ for a significant portion of the remnant and the electron energy losses are mainly due to radiative losses (see discussion in Sect. 3.2.4).

Since no effect on the asymmetries induced by a nonuniform ISMF is expected, we assume $b = 0$ in all our calculations, this being the most neutral case.

To reduce further the number of model parameters, we focus here on remnant 1 kyr old, as in the case of SN 1006. Finally, radio, X-ray and γ-ray images are synthesized at 1 GHz, 3 keV, and 1 TeV, respectively. It is worth to emphasize that all the above parameters are not expected to influence the degree of the asymmetries induced by a nonuniform ISMF on which we are focused.

Asymmetries in the remnant morphology. In Sect. 4.3, we analyzed the asymmetries induced by a nonuniform ISMF in the radio morphology of the remnant. In particular, we found there that asymmetric BSNRs are produced if a gradient of the ambient magnetic field strength ∇B is not aligned with the LoS. In this section we extend our analysis to non-thermal X-rays and IC γ-rays. To this end, we synthesize the synchrotron and IC emission, considering each of the three cases of variation of electron injection efficiency with shock obliquity (quasi-perpendicular, isotropic, and quasi-parallel particle injection). In this section, the adiabatic index is assumed to be $\gamma = 5/3$; we explore only the time-limited model for E_{max} and assume to be in the Bohm limit (gyrofactor $\eta = 1$; see Sect. 3.2.1). The effects of γ, E_{max}, and η on the remnant morphology are explored in Sect. 4.4.2. As an example, Figs. 4.28 and 4.29 show the maps of synchrotron radio, X-ray, and IC γ-ray surface

[9]Note that $E_{\mathrm{f},\parallel}$ depends on the magnetic field strength at parallel shock which is different in the three configurations of unperturbed ISMF explored here due to the magnetic field gradient (in all the cases, we assume $B_0 = 30$ μG at the center of the SN explosion).

brightness at $t = 1$ kyr, in each of the three injection models. The aspect angle is $\phi_{\rm B} = 90^0$ in all images, i.e. the ambient magnetic field is perpendicular to the LoS; the angle $\phi_{\nabla \rm B}$ is 0^0 for run Grad-BZ-g1 and 90^0 for Grad-BX-g1.

The main factors affecting the azimuthal variations of surface brightness are the variations of: injection efficiency $\varsigma(\Theta_{\rm o})$ and magnetic field $B_{\rm s}(\Theta_{\rm o})$ in the radio band; $\varsigma(\Theta_{\rm o})$, $B_{\rm s}(\Theta_{\rm o})$ and maximum energy $E_{\rm max}(\Theta_{\rm o})$ in the X-ray band; $\varsigma(\Theta_{\rm o})$ and $E_{\rm max}(\Theta_{\rm o})$ in the IC γ-ray band. Therefore, the morphology of the remnant in the three bands can differ considerably in appearance. In the radio and in the X-ray band, the remnant shows two lobes located at perpendicular shocks in the quasi-perpendicular and isotropic models (i.e. where the magnetic field is larger), and at parallel shocks in the quasi-parallel model (i.e. where emitting electrons reside). The lobes are much thinner in X-rays than in radio because of the large radiative losses at the highest energies that make the X-ray emission dominated by radii closest to the shock. In the γ-ray band, the remnant morphology changes significantly in the three injection models: it is almost ring-like (with two faint minima at parallel shocks) when the injection is quasi-perpendicular; the morphology shows two lobes located at parallel shocks when the injection is isotropic, at variance with the lobes in radio and X-rays that are located at perpendicular-shocks (i.e. bright γ-ray lobes correspond to dark radio and X-ray areas); the morphology is characterized by two narrow bright lobes almost superimposed to those in radio and X-rays when the injection is quasi-parallel. A ring-like γ-ray morphology is compatible with those found by HESS in the SNRs RX J1713.7-3946 [45] and RX J0852.0-4622 (Vela Jr.; [38]) where γ-rays are detected virtually throughout the whole remnant and the emission is found to resemble a shell structure. On the other hand, the bipolar γ-ray morphology of SN 1006 revealed by HESS [28], with the bright lobes strongly correlated with non-thermal X-rays, may be easily reproduced in the polar-caps scenario (quasi-parallel injection).

The effects of the nonuniform ISMF on the remnant morphology in the X-ray band are similar to those discussed in Sect. 4.3 for the radio band: remnants with two non-thermal X-ray lobes of different brightness (upper left panel in Fig. 4.28

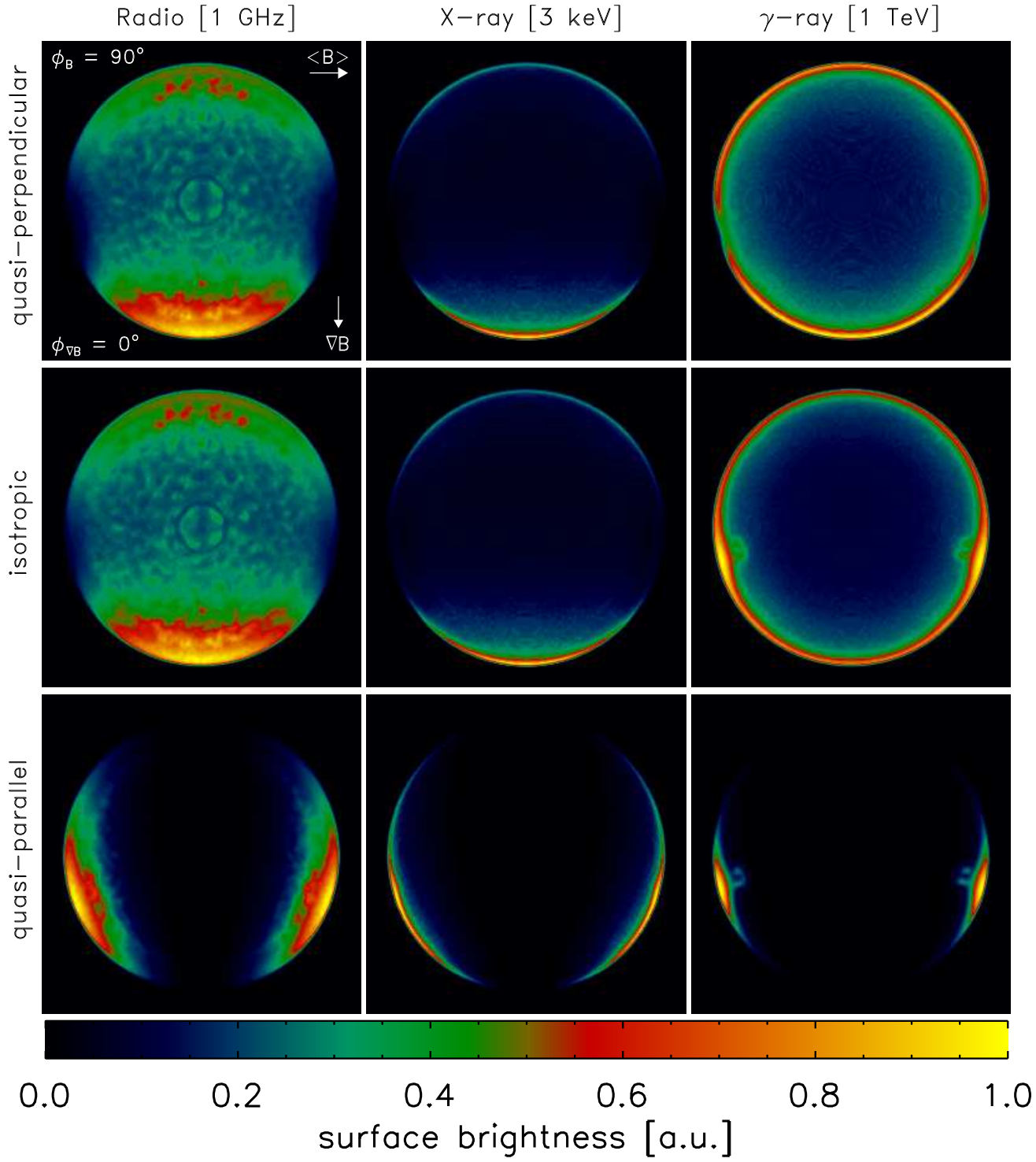

Figure 4.28. Maps of synchrotron radio (left), X-ray (center), and IC γ-ray (right) surface brightness (normalized to the maximum of each map) at $t = 1$ kyr synthesized from run Grad-BZ-g1, assuming randomized internal magnetic field. The relevant angles are $\phi_B = 90^0$ and $\phi_{\nabla B} = 0^0$. The figure shows the quasi-perpendicular (top), isotropic (middle), and quasi-parallel (bottom) particle injection models. The model of E_{max} is time-limited, the gyrofactor is $\eta = 1$ (Bohm limit) and the adiabatic index is $\gamma = 5/3$. The average ambient magnetic field is along the horizontal axis; the gradient of magnetic field strength is along the vertical axis.

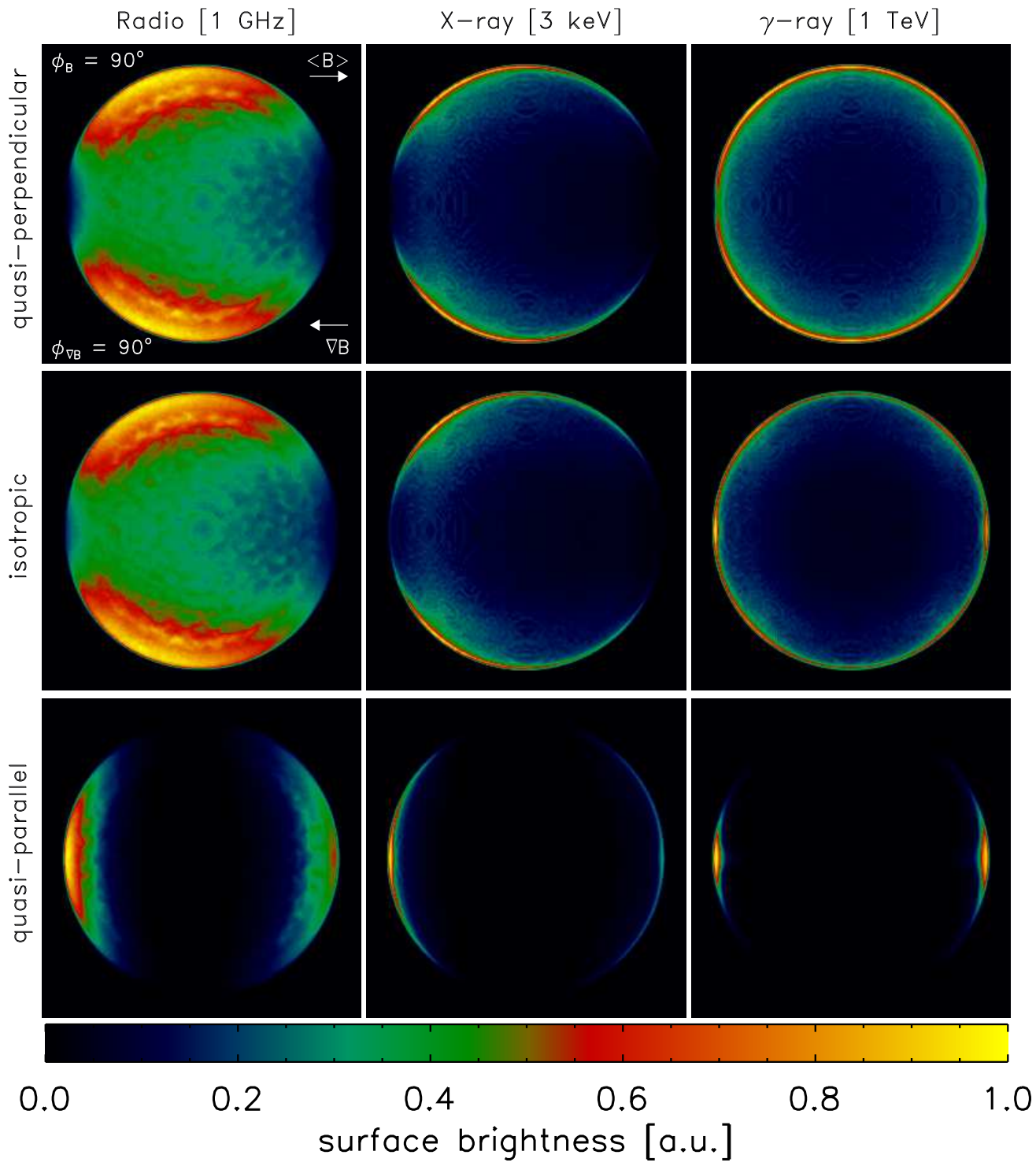

Figure 4.29. As in Fig. 4.28 for run Grad-BX-g1. Both the average ambient magnetic field and the gradient of magnetic field strength are along the horizontal axis. The relevant angles are $\phi_{\rm B} = 90^0$ and $\phi_{\nabla \rm B} = 90^0$.

and lower left panel in Fig. 4.29) are produced if a gradient of ambient magnetic field strength is perpendicular to the lobes; remnants with converging similar non-thermal X-ray lobes (lower left panel in Fig. 4.28 and upper right panel in Fig. 4.29) are produced if the gradient runs between the two lobes. Analogous asymmetries are found in the γ-ray morphology of the remnant although the degree of asymmetry is less evident. Note however that, in the case of isotropic injection, the γ-ray lobes are converging on one side when radio and X-ray lobes are characterized by different brightness (see Fig. 4.28). This is the consequence of the "limb-inverse" property in γ-rays (Sect. 4.1) In general, this property is valid not only in the case of isotropic injection; this type of injection is just the more prominent case. In fact, the critical quantities determining the "limb-inverse" property are the contrasts between electron injection, ISMF, and model of $E_{\rm max}$. For instance, in the case of uniform ISMF, the azimuthal contrast in IC γ-ray brightness is roughly

$$\begin{aligned} \frac{S_\parallel}{S_\perp} &\propto \frac{\text{injection}_\parallel}{\text{injection}_\perp} \exp\left[-E_{\rm m}\left(\frac{1}{E_{\rm max,\parallel}} - \frac{1}{E_{\rm max,\perp}}\right)\right] = \\ &= \frac{\text{injection}_\parallel}{\text{injection}_\perp} \exp\left[-\frac{E_{\rm m}}{E_{\rm max,\parallel}}\left(1 - \frac{E_{\rm max,\parallel}}{E_{\rm max,\perp}}\right)\right] \end{aligned} \tag{4.33}$$

where $E_{\rm m}$ is the electron energy which gives the maximum contribution to IC emission at a considered frequency and subscripts refer to positions along the limb where the ambient magnetic field is either parallel ($\parallel$) or perpendicular ($\perp$) to the shock normal. Even in the case of quasi-parallel injection ($\text{injection}_\parallel/\text{injection}_\perp > 1$), the contrast $S_\parallel/S_\perp$ depends on the contrast of $E_{\rm max}$: the ratio $E_{\rm max,\parallel}/E_{\rm max,\perp}$ may lead to an exponential term either > 1 or < 1, leading to $S_\parallel/S_\perp$ either > 1 or < 1.

Figure 4.30 shows the azimuthal profiles of the synchrotron radio, X-ray, and IC γ-ray surface brightness synthesized from runs Grad-BZ-g1 and Grad-BX-g1 for the three injection models when the relevant angles are $\phi_{\rm B} = 90^0$ and $\phi_{\nabla \rm B} = 0^0$ for run Grad-BZ-g1 and $\phi_{\nabla \rm B} = 90^0$ for Grad-BX-g1. Note the "limb-inverse" property in γ-rays for isotropic injection as discussed in Sect. 4.1. In general we find that the degree of asymmetry (whatever the pattern of asymmetry – either different brightness or

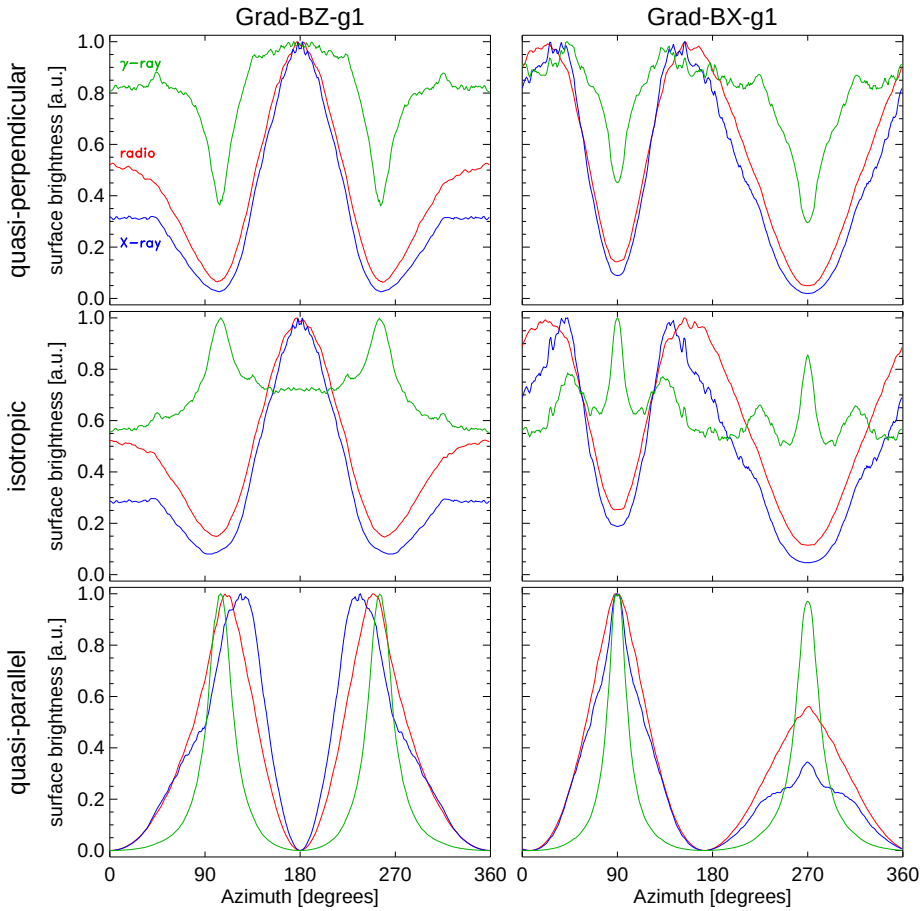

Figure 4.30. Azimuthal profiles of the synchrotron radio (red), X-ray (blue), and IC γ-ray (green) surface brightness synthesized from runs Grad-BZ-g1 (left; the relevant angles are $\phi_{\rm B} = 90^0$ and $\phi_{\nabla {\rm B}} = 0^0$) and Grad-BX-g1 (right; $\phi_{\rm B} = 90^0$ and $\phi_{\nabla {\rm B}} = 90^0$), assuming quasi-perpendicular (top), isotropic (middle), and quasi-parallel (bottom) injection models. The model of $E_{\rm max}$ is time-limited, the gyrofactor is $\eta = 1$ (Bohm limit) and the adiabatic index is $\gamma = 5/3$. The azimuth is measured from the north (see Figs 4.28 and 4.29).

convergence of the lobes – is) induced by ∇B in the remnant morphology is different in the three bands: the non-thermal X-ray (IC γ-ray) emission appears to be the most (less) sensitive to the gradient. This happens because the emissivity $q(\epsilon)$ depends directly on the magnetic field strength only in the synchrotron emission process (no in the IC process). Consequently, the IC γ-ray emission shows a weaker dependence on the ∇B. In fact, IC brightness depends on $\vec{B}$ indirectly, through radiative losses of electrons: larger $\vec{B}$ induces decrease of the number of electrons emitting IC γ-rays. Note that the sensitivity on ∇B depends also on the energy of photons, and on the reduced fiducial energy $E_{\rm f}$, which is the measure of efficiency of the role of radiative losses in modification of the downstream evolution of emitting electrons.

Useful parameters to quantify the degree of asymmetry of the remnant are those

defined in Sect. 4.3: the azimuthal intensity ratio $R_{\rm max} \geq 1$, i.e. the ratio of the maxima of intensity of the two lobes as derived from the azimuthal intensity profiles (a measure of different brightness of the lobes; $R_{\rm max} > 1$ in case of asymmetry), and the azimuthal distance $\theta_{\rm D}$, i.e. the distance in deg of the two maxima (a measure of the convergence of the lobes; $\theta_{\rm D} < 180^0$ in case of asymmetry). For instance, in the case of quasi-parallel injection in Fig. 4.30 (lower panels), we find that the azimuthal distance $\theta_{\rm D}$ ranges from 148^0 in γ-rays to 134^0 in radio to 98^0 in X-rays for run Grad-BZ-g1, and the azimuthal intensity ratio $R_{\rm max}$ ranges from 1.01 in γ-rays to 1.82 in radio to 2.86 in X-rays for run Grad-BX-g1.

Dependence on the adiabatic index. In Sect. 4.1, we analyzed the effect of γ on non-thermal images of SNR expanding through homogeneous ISM and uniform ISMF. They showed that reducing the value of γ, the synchrotron brightness of SNR is modified by increased radiative losses of emitting electrons, due to increased compression of $\vec{B}$, which results in thinner radial profiles of brightness. Figure 4.31 shows maps of synchrotron radio, X-ray, and IC γ-ray emission for the case of ISMF characterized by a gradient of field strength perpendicular to the average MF and different values of the adiabatic index γ (runs Grad-BZ-g1, Grad-BZ-g2, and Grad-BZ-g3). As expected, γ determines both the shock compression ratio σ and the distance of the contact discontinuity from the blast wave position $D_{\rm cd}$ (see also Fig 4.26 in the case of uniform ISMF): the smaller γ, the larger σ (and the larger the radiative losses of emitting electrons) and the shorter $D_{\rm cd}$. As shown in the figure, the main effect of smaller γ is to make thinner the lobes in the three bands. In particular, in the extreme case of $\gamma = 1.1$, the lobes are so thin that they are largely perturbed by the hydrodynamic instabilities forming at the contact discontinuity, the typical size of the instabilities being comparable with $D_{\rm cd}$. The adiabatic index slightly influences also the azimuthal thickness of the lobes, especially in the quasi-parallel case: the smaller γ, the narrower this thickness. Nevertheless, the adiabatic index does not change significantly neither the degree nor the pattern of asymmetry of the remnant morphology caused by the gradient of ambient MF.

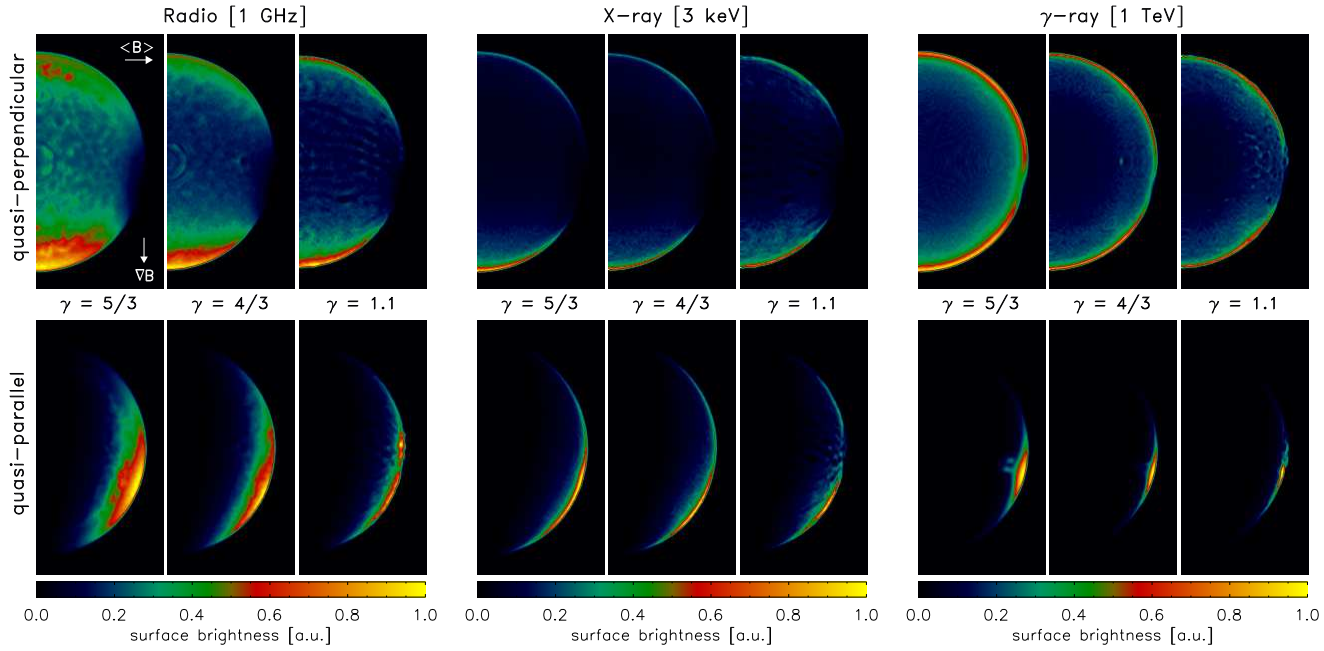

Figure 4.31. As in Fig. 4.28 for runs Grad-BZ-g1 ($\gamma = 5/3$), Grad-BZ-g2 ($\gamma = 4/3$), and Grad-BZ-g3 ($\gamma = 1.1$). The figure shows synchrotron radio (left panels), X-ray (center panels) and IC γ-ray (right panels), assuming either quasi-perpendicular (upper panels) or quasi-parallel (lower panels) injection models. Each panel shows only one half of the remnant which is symmetric with respect to the vertical axis.

Dependence on the maximum energy. The model of $E_{\rm max}$ may affect both the degree and the pattern of asymmetry of the remnant morphology due to the different dependencies of the three $E_{\rm max}$ models on the magnetic field strength. The largest differences can be found in the IC γ-ray band when the two lobes are characterized by different brightness (i.e. a gradient of magnetic field strength is perpendicular to the lobes). We found that the asymmetry between the two lobes can be reduced in the X-ray band or even inverted in the IC γ-ray band when the $E_{\rm max}$ model is loss-limited. As an example, Fig. 4.32 shows the azimuthal profiles of the IC γ-ray surface brightness synthesized from runs Grad-BZ-g1 and Grad-BX-g1 when the lobes have different brightness. In the loss-limited case, the brightest γ-ray lobe is located where both the radio and the X-ray lobes are fainter. This happens because, at variance with the other cases, $E_{\rm max}$ depends inversely on the pre-shock ambient magnetic field strength in the loss-limited case (see Eq. 3.19): $E_{\rm max}$ is the largest where the magnetic field strength is the lowest. In the case of the IC surface brightness, this determines the inversion of the asymmetry in the remnant morphology, as the IC emissivity weakly depends on $\vec{B}$. In the case of the

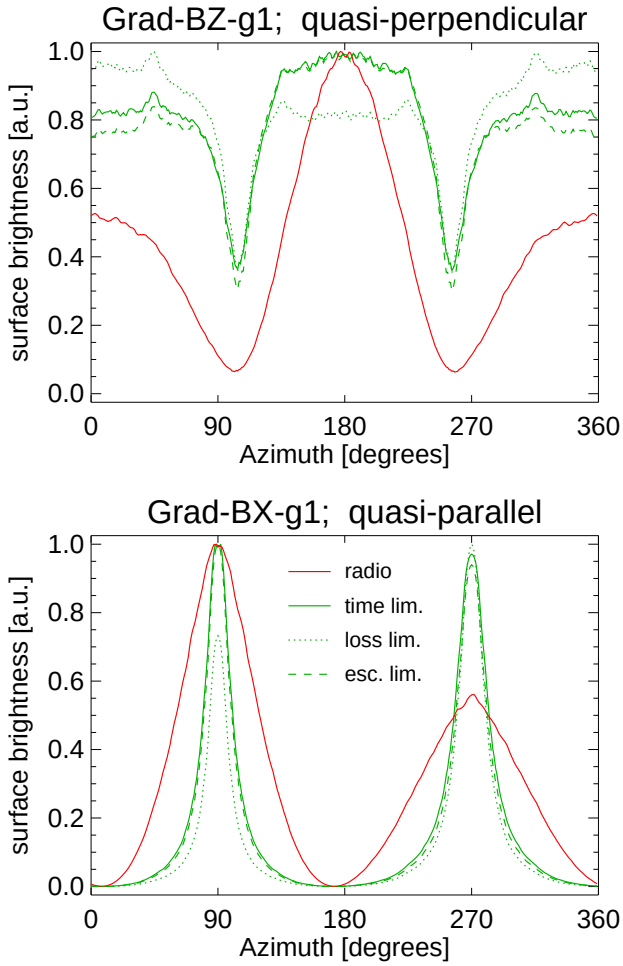

Figure 4.32. Azimuthal profiles of the synchrotron radio (red lines) and IC γ-ray surface brightness (green) synthesized from run Grad-BZ-g1 with quasi-perpendicular injection (top), and from run Grad-BX-g1 with quasi-parallel injection (bottom); the aspect angle is $\phi_{\rm B} = 90^0$. The figure shows the time-limited (solid), loss-limited (dotted), and escape-limited (dashed) $E_{\rm max}$ models. The gyrofactor is $\eta = 1$ (Bohm limit).

non-thermal X-ray surface brightness, the inverse dependence of $E_{\rm max}$ on $\vec{B}$ partially contrast the dependence of the non-thermal X-ray emissivity on $\vec{B}$, reducing the degree of asymmetry between the lobes. It is worth to note that, if $E_{\rm max}$ is high enough in regions with weak magnetic field, than the inversion of asymmetry may be present even in the X-ray band.

On the other hand, when the nonuniform ISMF leads to non-thermal lobes converging on one side (i.e. when a gradient of ISMF is running between the lobes) the model of $E_{\rm max}$ does not affect significantly the degree and the pattern of asymmetry of the remnant morphology.

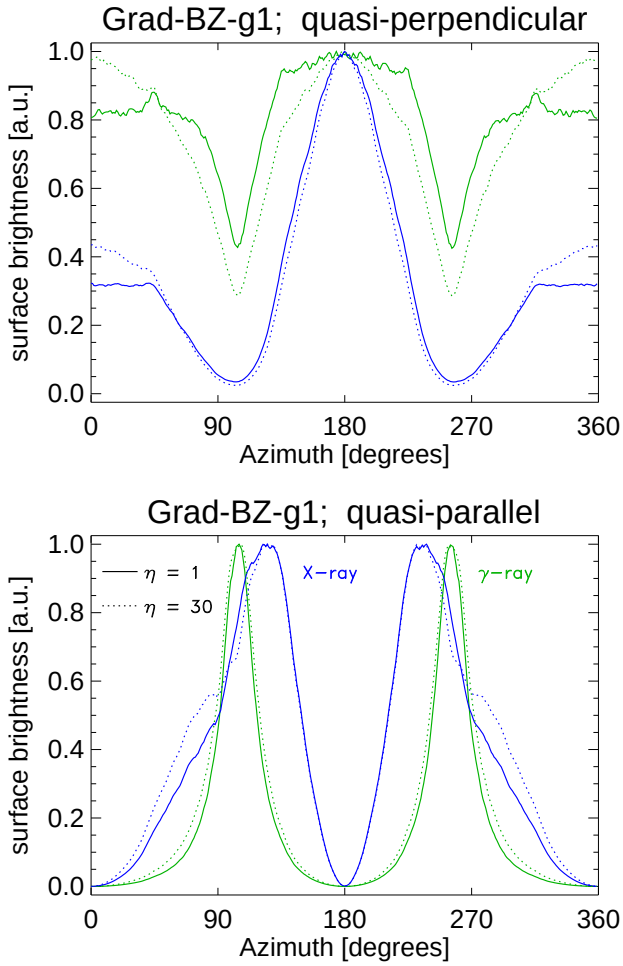

Figure 4.33. Azimuthal profiles of the synchrotron X-ray (blue lines) and IC γ-ray (green) surface brightness (for angles $\phi_{\rm B} = 90^0$ and $\phi_{\nabla \rm B} = 0^0$) synthesized from run Grad-BZ-g1 with quasi-perpendicular (top) and quasi-parallel (bottom) injection, and for $\eta = 1$ (solid) and $\eta = 30$ (dotted). The model of $E_{\rm max}$ is time-limited.

Dependence on the gyrofactor. In the case of synchrotron X-ray emission, Reynolds [303] has shown that the value of gyrofactor η determines the enlargement of the zone containing the most energetic particles and consequently of the emitting regions (see Fig. 3.4). We expect therefore that, in our model, η influences the azimuthal thickness of X-ray and IC γ-ray lobes but not the degree nor the pattern of asymmetry of the remnant morphology due to a nonuniform ISMF. This issue has been investigated by comparing simulations with different η. As an example, Fig. 4.33 shows the azimuthal profiles of both X-ray and IC γ-ray surface brightness synthesized from run Grad-BZ-g1 when the gyrofactor is either $\eta = 1$ or $\eta = 30$. For the parameters we explored, the gyrofactor slightly influences X-ray and γ-ray azimuthal profiles and has virtually no effect on the degree nor the pattern of

asymmetry of the remnant morphology, although the different brightness of the two lobes in the upper panel of Fig. 4.33 is reduced for higher values of η.

Dependence on the orientation of ISMF gradient. As expected, the degree of asymmetry of the remnant morphology depends on the orientation of ∇B with respect to the plane of the sky. In the case of run Grad-BZ-g1, Fig. 4.34 shows the azimuthal intensity ratio $R_{\rm max}$ and the azimuthal distance $\theta_{\rm D}$ vs. the angle $\phi_{\nabla \rm B}$, for an aspect angle $\phi_{\rm B} = 90^0$. The asymmetries are the largest when ∇B lies in the plane of the sky (i.e. $\phi_{\nabla \rm B} = 0^0$), whereas no asymmetries are present when ∇B is along the LoS (i.e. $\phi_{\nabla \rm B} = 90^0$). In all the intermediate cases, the degree of asymmetry is determined by the component of ∇B lying in the plane of the sky. Note that the remnant morphology shows only one kind of asymmetry when the injection is quasi-perpendicular or quasi-parallel and the aspect angle is $\phi_{\rm B} = 90^0$. On the other hand, the lobes have different brightness in radio and non-thermal X-rays and are converging in IC γ-rays when the injection is isotropic due to the "limb-inverse" property.

When the ∇B is not aligned with the average ambient magnetic field (for instance in the case of run Grad-BZ-g1), the projection of the ∇B in the plane of the sky has (for generic values of $\phi_{\rm B}$ and $\phi_{\nabla \rm B}$) a component perpendicular to the projected lobes and one running between them. In this case both kind of asymmetries (lobes converging on one side and with different brightness) are expected in the remnant morphology. As an example, Fig. 4.35 shows the synchrotron radio, X-ray, and IC γ-ray images synthesized from run Grad-BZ-g1, for different injection models, and assuming time-limited $E_{\rm max}$. The relevant angles are $\phi_{\rm B} = 45^0$ and $\phi_{\nabla \rm B} = 45^0$.

4.4.3. Summary. We developed a numerical code to synthesize the synchrotron radio, X-ray, and IC γ-ray emission from MHD simulations, in the general case of a remnant expanding through a nonuniform ISM and/or a nonuniform ISMF. As a first application of the code, we coupled the synthesis code to the MHD model discussed in Sect. 4.3 and investigated the effects of a nonuniform ISMF on the remnant morphology in the X-ray and γ-ray bands. Our findings lead to several conclusions:

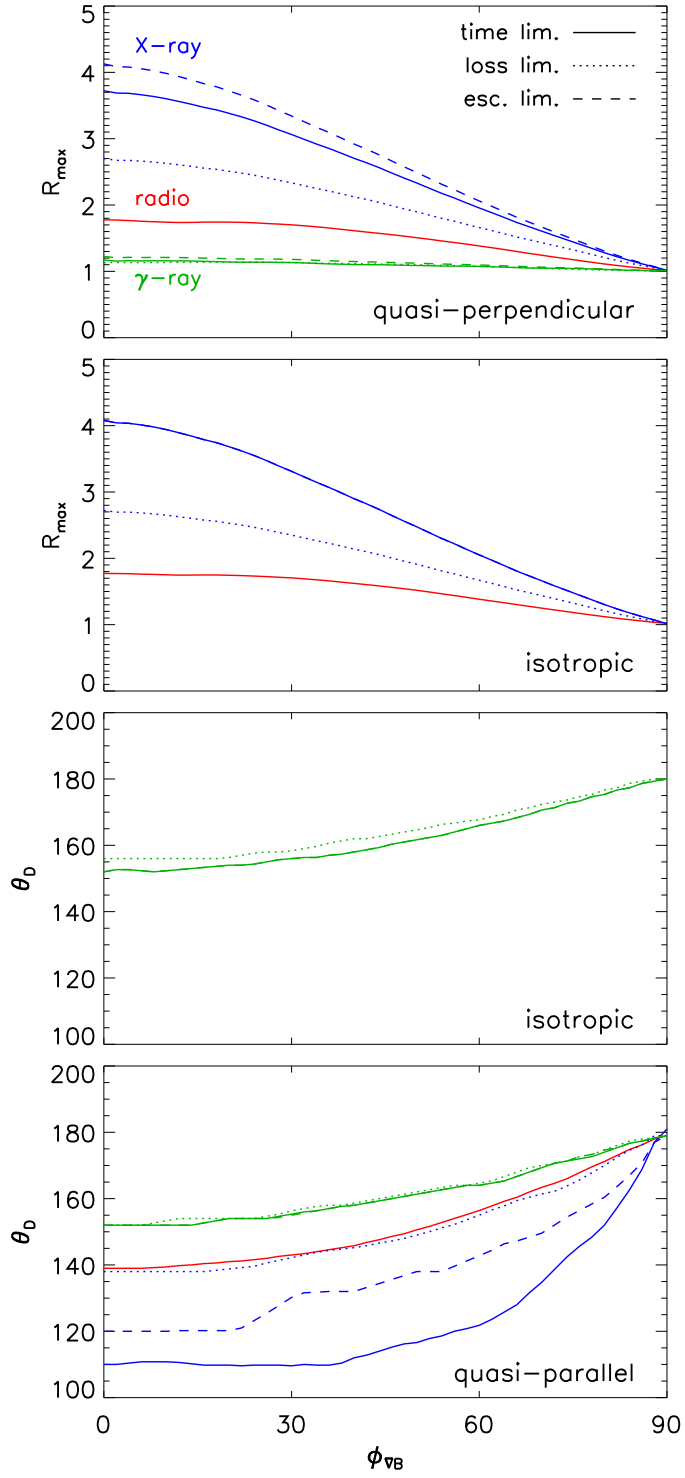

Figure 4.34. Azimuthal intensity ratio $R_{\rm max}$ (i.e. the ratio of the maxima of intensity of the two lobes around the shell) and azimuthal distance $\theta_{\rm D}$ (i.e. the distance in deg of the two maxima of intensity around the shell) vs. the angle between ∇B and the vertical line passing through the remnant center $\phi_{\nabla \rm B}$, for an aspect angle $\phi_{\rm B} = 90^0$. The run is Grad-BZ-g1.

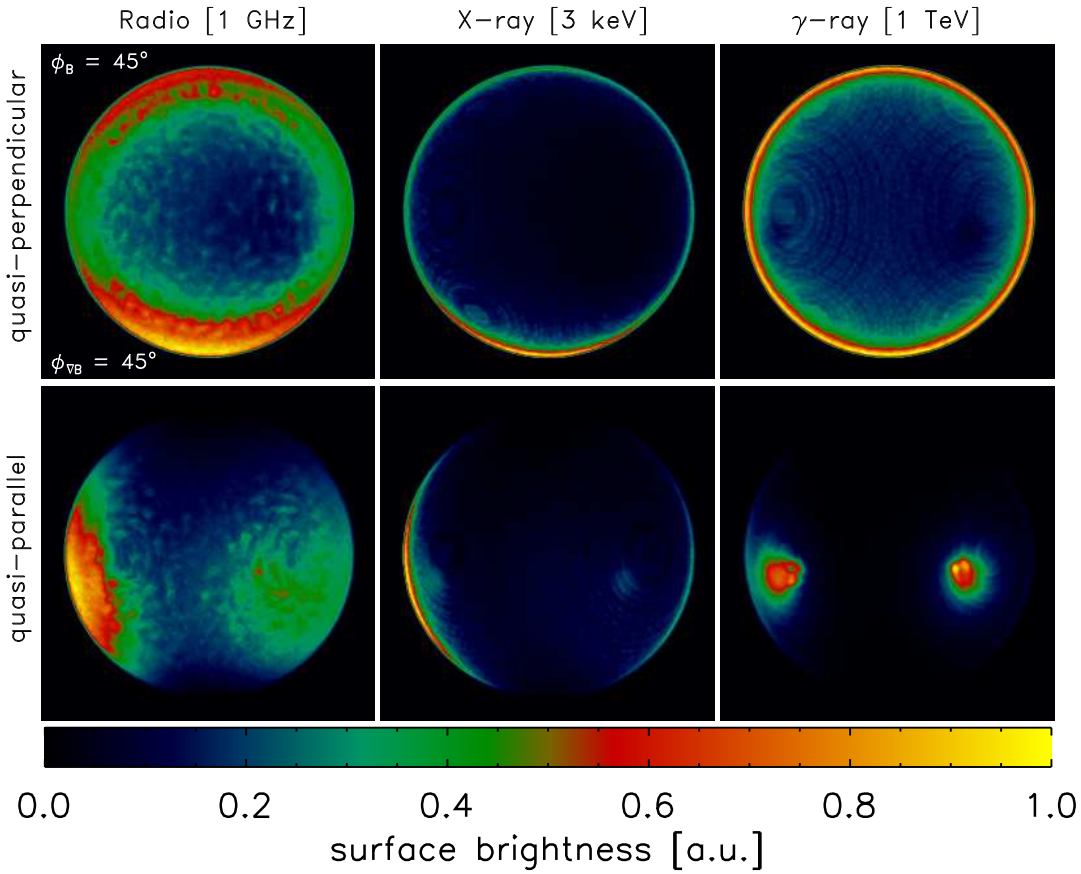

Figure 4.35. Maps of synchrotron radio (left), X-ray (center), and IC γ-ray (right) surface brightness synthesized from run Grad-BZ-g1, assuming quasi-perpendicular (top), and quasi-parallel (bottom) injection models. The model of $E_{\rm max}$ is time-limited and the gyrofactor is $\eta = 1$. The relevant angles are $\phi_{\rm B} = 45^0$ and $\phi_{\nabla \rm B} = 45^0$. The angle between $\langle \mathbf{B} \rangle$ and $\nabla |\langle \mathbf{B} \rangle|$ is 90^0.

– A gradient of ISMF strength induces asymmetries in both the X-ray and γ-ray morphology of the remnant if the gradient has a component perpendicular to the LoS. In general, the asymmetries are analogous to those found in Sect. 4.3 in the radio band, independently from the models of electron injection and of maximum energy of electrons accelerated by the shock. In the γ-ray band, the asymmetry in the remnant morphology is inverted with respect to those in the radio and X-ray bands if the model of $E_{\rm max}$ is loss-limited: the brightest γ-ray lobe is located where both the radio and the X-ray lobes are the faintest.

– The non-thermal lobes are characterized by different brightness when a gradient of ISMF strength is perpendicular to the lobes; they are converging on one side when a gradient of ISMF is running between them. In the general case of a gradient with components parallel and perpendicular to the lobes, both kinds of asymmetry may characterize the remnant morphology.

- The non-thermal X-ray emission is confined in very thin limbs because of the large radiative losses at high energy and is the most sensitive to nonuniform ISMF. In fact the remnant morphology in this band shows the highest degree of asymmetry among the images synthesized in the three bands of interest (i.e. radio, X-ray, and γ-ray).
- The IC γ-ray emission is weakly sensitive to the nonuniform ISMF, the degree of asymmetry being the lowest in the three bands considered. The remnant morphology is almost ring-like for quasi-perpendicular injection, shows the "limb-inverse" property discussed in Sect. 4.1 for isotropic injection (i.e. bright γ-ray lobes correspond to dark radio and X-ray areas), and is bilateral for quasi-parallel injection. The "limb-inverse" property implies, for instance, that γ-ray lobes are symmetric and converging on one side when radio and X-ray lobes have different brightness (see Fig. 4.28). Note that the γ-ray morphology of the SNRs RX J1713.7-3946 [45] and RX J0852.0-4622 [38] could be reproduced in the equatorial-belt scenario (the injection is either quasi-perpendicular or isotropic), whereas the morphology of SN 1006 [28] is compatible with that predicted in the polar-caps scenario (quasi-parallel injection).

We approach the effect of shock modification by considering different values of the adiabatic index γ (namely, 5/3, 4/3, 1.1). The main effect of γ is to change the compression ratio of the shock and the distance of the contact discontinuity from the blast wave position. In the simplest case considered here, namely the modification on γ is isotropic with no dependence on the obliquity angle, we found that the modified γ influences the absolute values of non-thermal emission but not the large scale morphology of the remnant and the pattern of asymmetries induced by a nonuniform ISMF. Conversely, we expect a significant effect of the modified γ on the remnant morphology if the shock modification depends on the obliquity. This issue deserves further investigation in future studies.

4.5. Conclusions

Section deals with modeling and analysis of surface brightness distribution in adiabatic SNRs resulting from leptonic component of accelerated CRs. Maps of SNRs produced by emission of CRs in radio, X-rays and γ-rays are synthesized. In order to understand the role of different factors on patterns of brightness, SNRs in uniform ISM and ISMF are modeled. Then, the influence of nonuniform ISM and/or nonuniform ISMF on SNR images are considered.

1. The synchrotron radio and X-ray as well as IC γ-ray maps of adiabatic SNRs in uniform ISM and ISMF are synthesized. The properties of images in these different wavelength bands are compared, with particular emphasis on the location of the bright limbs in bilateral SNRs. Nonthermal maps are synthesized for different assumptions about obliquity variations of the injection efficiency, MF and maximum energy of accelerated electrons.

a) The azimuthal variation of the synchrotron X-ray and IC γ-ray brightness is mostly determined by variations of ς, $\sigma_{\rm B}$ and $E_{\rm max}$, of the radio brightness by ς and $\sigma_{\rm B}$ only. In general, higher B increases X-ray and decreases IC γ-ray brightness. Really, higher MF is a reason of larger losses of emitting electrons (i.e. decrease of their number) and thus of the smaller brightness due to IC process. In contrast, X-rays are more efficient there because $S_{\rm x} \propto B^{3/2}$. The radial profiles of brightness in all three bands depend on a number of factors. They are quite sensitive to the adiabatic index: $\gamma < 5/3$ makes plasma more compressible. Therefore, the brightness profile is thinner due to larger compression factor, larger gradient of density and MF downstream of the shock and larger radiative losses. The radial profiles of synchrotron X-ray and IC γ-ray brightness (e.g. thickness of rim) depend on the photon energy. They are radially thinner at larger photon energies, as expected.

b) In case if $E_{\rm max}$ is constant over the SNR surface, we found an opposite behavior of azimuthal variation of surface brightness in radio and IC γ-rays, in case if injection is isotropic and the aspect angle is larger than $\simeq 60^{\rm o}$. Namely, the line crossing the

two limbs in radio are perpendicular to the ISMF while they are parallel in IC γ-rays. In particular, bright radio limbs correspond to dark IC areas, in disagreement with X-ray and HESS observations of SN 1006. This happens because IC image is affected by large radiative losses of emitting electrons behind perpendicular shock while the larger magnetic field increases the radio brightness there. Variation of $E_{\rm max}$ over SNR surface may (to some extent) hide this effect. The maximum energy should increase with obliquity in this case. In case of the polar-cap model of SNR (quasi-parallel injection), the maxima in surface brightness are expected to coincide in radio and IC γ-rays (in agreement with HESS observation of SN 1006), unless increase of $E_{\rm max}$ with obliquity will be very strong, which is unlikely in case of SN 1006 because the cut-off frequency is larger at limbs which are at parallel shock in this injection model.

c) The radio and IC γ-ray limbs may coincide in location if: i) injection is isotropic but the variation of the maximum energy of electrons is rather quick to compensate for differences in magnetic field; ii) obliquity dependence of injection (either quasi-parallel or quasi-perpendicular) and the electron maximum energy is strong enough to dominate magnetic field variation. In the latter case, the obliquity dependence of the injection and the maximum energy should not be opposite.

2. Approximate analytical formulae for the azimuthal and radial profiles of the synchrotron radio and X-ray as well as the inverse-Compton γ-ray brightness are derived. They reveal the main factors which influence the pattern of the surface brightness distribution due to leptonic emission processes in shells of adiabatic SNRs. They accurately represent numerical simulations close to the shock and are able to account for some non-linear effects of acceleration if necessary. These approximations provide observers and theorists with a set of simple diagnostic tools for quick analysis of the non-thermal maps of SNRs due to emission of accelerated electrons.

3. It is investigated whether the assymetrical morphology of bilateral supernova remnants observed in the radio band is determined mainly either by a nonuniform interstellar medium (ISM) or by a nonuniform ambient magnetic field. The 3-D MHD simulations of a spherical SNR shock propagating through a magnetized ISM

is performed. From the simulations, the synchrotron radio emission, making different assumptions about the details of acceleration and injection of relativistic electrons is synthesized. It is found that asymmetric BSNRs are produced if the line-of-sight is not aligned with the gradient of ambient plasma density or with the gradient of ambient magnetic field strength. Useful parameters to quantify the degree of asymmetry of the remnants are derived that may provide a powerful diagnostic of the microphysics of strong shock waves through the comparison between models and observations. BSNRs with two radio limbs of different brightness can be explained if a gradient of ambient density or, most likely, of ambient magnetic field strength is perpendicular to the radio limbs. BSNRs with converging similar radio arcs can be explained if the gradient runs between the two arcs.

4. Even a very small gradient of the ISMF can influence significantly the non-thermal remnant morphology. A gradient of the ambient magnetic field strength induces asymmetric morphologies in both X-ray and γ-ray bands independently from the model of electron injection if the gradient has a component perpendicular to the line-of-sight. The degree of asymmetry of the remnant morphology depends on the details of the electron injection and acceleration and is different in the radio, hard X-ray, and γ-ray bands. In general, the non-thermal X-ray morphology is the most sensitive to the gradient, showing the highest degree of asymmetry. The IC γ-ray emission is weakly sensitive to the nonuniform ISMF, the degree of asymmetry of the remnant morphology being the lowest in this band.

CHAPTER 5

EXPERIMENTAL CONSTRAINTS ON MODELS OF COSMIC RAYS IN SN 1006

Simulations of nonthermal emission from SNRs which is based on basic theoretical principles (previous Section) is a necessary step toward understanding behavior of CRs in vicinity of strong nonrelativistic shocks. Nevertheless, another direction in studies is also of importance. Namely, analysis of experimental data as well as model-independent methods for derivation of characteristics of SNRs and CRs from observations. Radio, X-ray and γ-ray observations keep unique information about processes in magnetized cosmic plasma, about motion and emissivity of CRs.

Therefore, next sections of the present thesis are devoted to experimental methods of exploration of CRs. Namely, a certain SNR, SN 1006, is investigated. In particular, Sect. 5.1 presents observations of SNR in radio and X-ray bands which we analyse; its γ-ray data are reported by the HESS collaboration in [28]. SN 1006 is one of the most interesting objects for studies of Galactic cosmic rays. The precise knowledge of its age, its quite symmetrical, rather simple bilateral (two opposed bright limbs characterized by non-thermal emission separated by a region of low surface brightness) morphology in radio (Sect. 5.1.1), nonthermal X-rays (Sect. 5.1.2) and TeV γ-rays [28]. Its prominent feature is the positional coincidence of the two bright nonthermal limbs in all these bands, including TeV γ-rays.

In the following, new methods for 1) prediction of the γ-ray image of SNR from its radio and X-ray maps (Sect. 5.2) and 2) determination of the three-dimensional orientation of ISMF from a radio map (Sect. 5.3) are presented; both methods are applied to SN 1006. In Sect. 5.4, radio, X-ray and γ-ray data are used to determine some properties of SN 1006 and accelerated CRs.

Results presented in this chapter are published in [250, 281, 283, 284].

5.1. Radio and X-ray observations of SN 1006

The X-ray thermal emission, compared to the non-thermal, is more uniformly distributed over the entire remnant [321]. Despite the importance of thermal X-rays to the study of shock acceleration processes, the physical origin of the thermal emission is still uncertain and the spatial distribution of its properties has not yet been studied. Several studies have shown that thermal X-rays in SN 1006 cannot be uniquely associated with solar-abundance shocked plasma (e. g. [134]). X-ray emitting ejecta have been observed in the north-western and south-eastern rims of the remnant [29] and even Fe K lines emission has been detected in the interior of the shell, where an iron overabundance has been revealed [373]. The presence of significant X-ray emission from the shocked ISM and the value of its temperature remain controversial. Authors of [29] modeled the X-ray emission of their spectral regions with one non-thermal component plus two thermal components (ejecta for the soft emission and ISM for the hard emission). However, they found that the shocked ISM component (with $kT_{ISM} \sim 1.5 - 2$ keV) is almost not needed from a statistical point of view, since the quality of the fits does not change by associating the thermal emission only with the ejecta. In [373], instead, authors used three thermal components to model the *SUZAKU* thermal emission of very large regions of SN 1006, by associating the soft component with the shocked ISM ($kT_{ISM} \sim 0.5$ keV), and the hot components with the ejecta. Nevertheless they could not exclude that the O line complexes, which dominate the soft component, originate in the ejecta.

Since a spatially resolved study of the emission at the rim of SN 1006 has not yet been performed, here we present our analysis of archive radio VLA and X-ray *XMM-Newton* observations of SN 1006. As to the γ-rays, SN 1006 was detected as a TeV γ-ray source by HESS; results of these observations, including spectrum in photons with energies 0.2-20 TeV, azimuthal and radial profiles of brightness as well as an image of SNR are published in [28].

We focus mostly on maps of SNR, on the rim of the remnant to study the azimuthal variations in radio, thermal and non-thermal X-ray emission immediately behind the main shock front. We aim to obtain detailed information about the nature of the X-ray and γ-ray emission and study its link with the shock acceleration processes. We also use an X-ray *Chandra* archive observation of the north-eastern limb of SN 1006 taking advantage of its larger spatial resolution to test our conclusions.

5.1.1. Radio data. A new radio image of SN 1006 at $\lambda \sim 20$ cm was produced on the basis of archival VLA[1] data obtained in October 1991, February 1992 and July 1992 in the hybrid AnB, BnC and CnD configurations, respectively. The observations in the AnB configuration were carried out at 1370 and 1376 MHz, while the observations in the BnC and CnD arrays were performed at 1370 and 1665 MHz. The data corresponding to the more compact configurations of the VLA, BnC and CnD, were published as a part of an expansion study of SN 1006 [257], but not the data from the AnB configuration, which provides the highest angular resolution of southern sources. The new interferometric image is produced on the basis of 4 hours per configuration (the maximum possible taking into account the elevation restrictions for this source when observed from the northern hemisphere) and recovers emission from all spatial structures with angular scales between a few arcsec and 15 arcmin.

All data were processed using the MIRIAD software package. To avoid the diffraction effects produced by point sources present in the field, for each of the brightest sources we imaged a small region around, and the clean components were Fourier transformed and subtracted from the visibilities. The residual visibilities, containing all the source structure except for the offending point sources were then imaged and the point sources were added back into the SN 1006 image in the image plane. To recover flux density contribution from structures on angular scales larger than 15 arcmin (which is important in this case since SN 1006 is $\sim$30 arcmin in diameter) we added single dish observations acquired in 2002 with the Parkes 64 m radiotele-

[1]The Very Large Array of the National Radio Astronomy Observatory, USA.

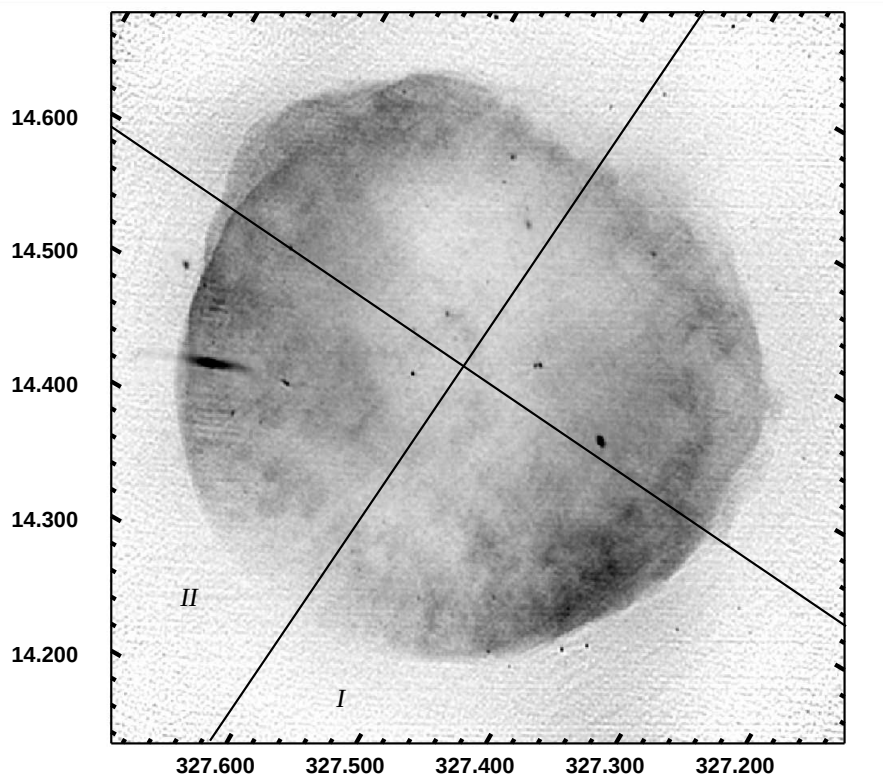

Figure 5.1. Radio image of SN 1006, in linear scale (galactic coordinates). Axes outline regions I and II used in our analysis.

scope placed in Australia. Also, since the primary beam of the VLA (the half-power beamwidth of a single VLA antenna) at $\lambda 20$ cm is 32 arcmin, comparable to the size of the source, a correction was applied to the interferometric data taking into account the attenuation introduced near the primary beam edge.

The final image has a synthesized beam of $7''.7 \times 4''.8$, position angle $8°.3$, and an rms noise of 1×10^{-4} Jy/beam. When combined with Parkes single-dish data, the total recovered flux is S=14.9 Jy, in excellent agreement with previous estimates from Green's catalogue of SNRs [172]. The new image is presented in Fig. 5.1.

5.1.2. X-ray data processing. We consider all the *XMM-Newton* EPIC archive observations of SN 1006 available. All the observations that we analyze were performed with the Medium filter by using the Full Frame Mode for the MOS cameras [351] and the Extended Full Frame Mode for the pn camera [341]. The relevant information about the *XMM-Newton* observations presented here are summarized in Table 5.1. We process the data by using the Science Analysis System (SAS).

Table 5.1

Relevant information about the data.

OBS_ID	Date	MOS-pn t_{exp} (ks)*	RA, J2000	DEC, J2000
0111090101	2000-08-20	7-3	$15^h03^m50^s$	$-41°47'00''$
0111090601	2001-08-08	7-3	$15^h03^m30^s$	$-42°01'00''$
0077340101	2001-08-10	30-21	$15^h01^m51^s$	$-41°49'00''$
0077340201	2001-08-10	24-19	$15^h04^m07^s$	$-41°52'32''$
0143980201	2003-08-14	16-11	$15^h03^m30^s$	$-41°48'12''$
0202590101	2004-02-10	26-17	$15^h02^m35^s$	$-42°04'37''$
0306660101	2005-08-21	11-4	$15^h03^m35^s$	$-42°04'20''$

* Unscreened/Screened exposure time.

We produced the images of the entire remnant by superimposing (using the *EMOSAIC* task) the MOS1, MOS2, and pn images of the pointings shown in Table 5.1. Spectral analysis was performed in the energy band $0.5 - 5$ keV using XSPEC, for each of the spectral regions presented in Sect. 5.1.3. To check the validity and the robustness of our result we adopted two different procedures for spectral extraction and background subtraction. Details are desribed in [250].

We here present the results obtained with method 1, since it allows us to use also the pn data. We verified that the results obtained are perfectly consistent with that produced with method 2.

We also used a *Chandra* archive observation of SN 1006 to perform the test described in Sect. 5.1.4. In particular, we used the observation of the NE limb of SN1006 with ID 732, taken on 7 Jul 2000, which has an exposure time of 69 ks.

5.1.3. X-ray data analysis.

Spatially resolved spectral analysis. Figure 5.2 shows the mosaiced EPIC images of SN 1006 in the $0.8 - 2$ keV band, $0.5 - 0.8$ keV band ("oxygen band", central panel), and in the $2 - 4.5$ keV band ("hard band", lower panel). Since we aim to study the effects of the acceleration process, we select our spectral regions at the border of the shell. The set of 30 regions selected for the spatially resolved spectral analysis is shown (in white) in the upper panel of Fig. 5.2. All the regions

cover the same area in the plane of the sky and they extend in the radial direction to 1.5′ (i. e., $\sim$ 10% of the SNR radius), corresponding to $\sim$ 1 pc at 2.2 kpc. Our approach is similar to that followed by [321], although we also focus on the thermal emission.

There are striking differences between the 30 spectra. Figure 5.3 shows the pn and MOS spectra extracted from region 29 (upper panel), where several emission line complexes are visible, and, for comparison, from region 23 (lower panel), located in the bright north-eastern non-thermal limb, where the emission is completely featureless. Despite these differences, we plan to describe all the spectra with a unified model, so as to explain the different spectral properties in terms of azimuthal variations in the best-fit parameters. We then use an isothermal model of optically thin plasma in non-equilibrium of ionization and with free abundances (VPSHOCK model in XSPEC, [93]) to describe the thermal component, plus a synchrotron emission from an electron power law with exponential cut-off (SRCUT model in XPSEC, [312]) to model the non-thermal component. We verify that the quality of the fit does not improve by adding another thermal component. Moreover, an additional thermal component introduces too many free parameters (considering the available statistics) and this generates entanglements between the best-fit values, thus determining large errors and useless results. We therefore consider only one thermal component. Our model of the thermal emission differs therefore from the two-temperatures model adopted by [29] for the north-eastern and south-western regions of the shell and it is simpler than the three-temperatures model used by [373], where much larger and less uniform extraction regions are considered. We fix the N_H parameter to 7×10^{20} cm^{-2}, in agreement with [132].

We constrain the normalization of the non-thermal component (i. e., its flux at 1 GHz) by extracting the radio flux from the same regions defined in the X-ray map. The spectral index α is free parameter in our analysis, at variance with [321], who fix $\alpha = 0.6$. The determination of the chemical abundances and other details of the spectral fitting may be found in [250]. The results of our spectral analysis are summarized in Fig. 5.4.

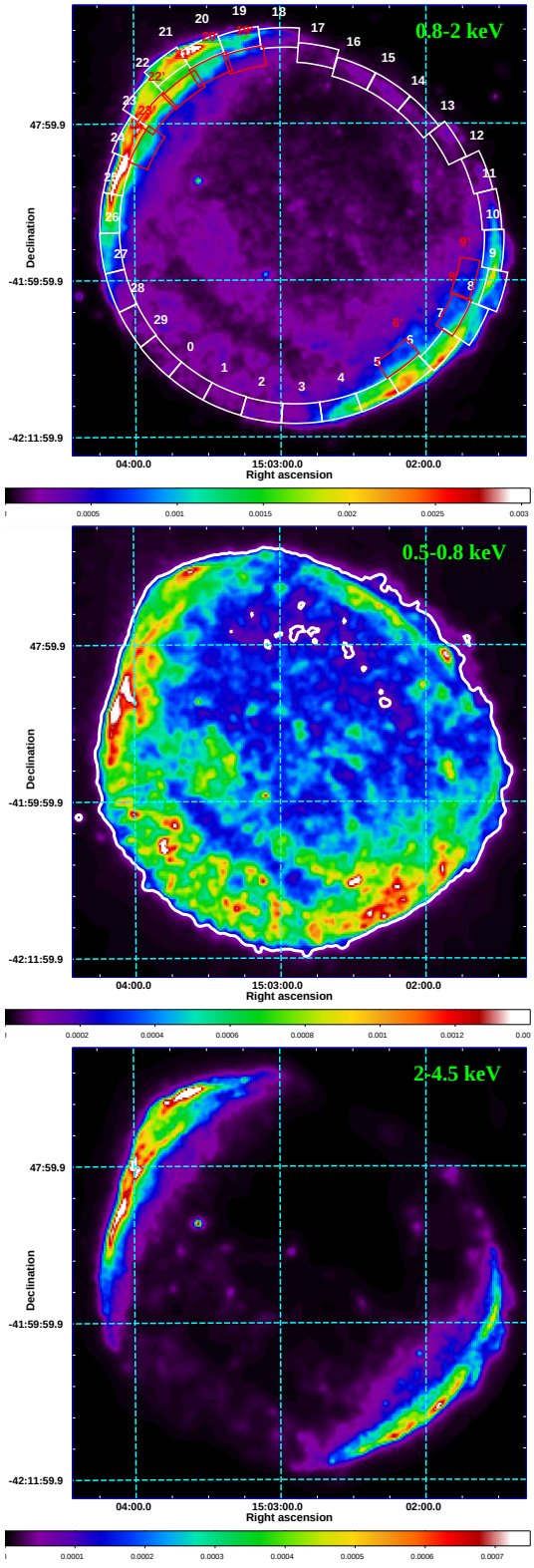

Figure 5.2. *Upper panel*: mosaiced count-rate images (counts per second per bin) of SN 1006 in the $0.8-2$ keV band. The bin size is $8''$ and the image is adaptively smoothed to a signal-to-noise ratio 10. The 30 regions selected for the spectral analysis of the rim (in white) and the 8 regions selected for the study of the ejecta emission measure (in red, see Sect. 5.1.4) are superimposed. *Central panel:* same as upper panel in the $0.5-0.8$ keV energy band. A contour level at 10% of the maximum is superimposed. *Lower panel*: same as upper panel in the $2-4.5$ keV energy band.

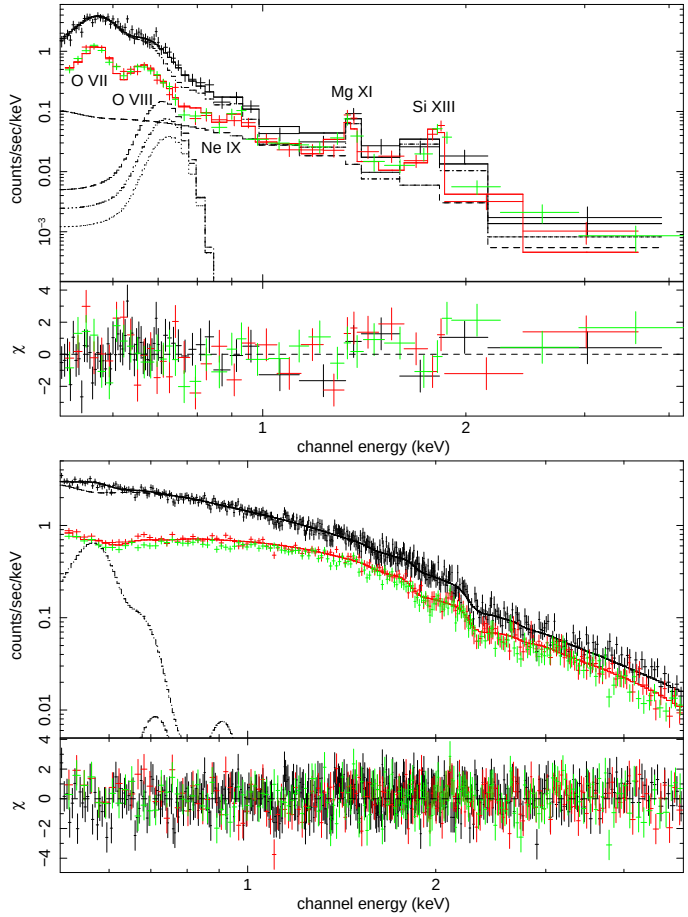

Figure 5.3. *Upper panel*: pn spectrum (upper, in black) and MOS1,2 (lower, in red and green) spectra of region 29 of Fig. 5.2 with the corresponding best-fit model and residuals. The best-fit thermal+non-thermal model described in Sect. 5.1.3 is shown as a continuous line, while individuals components are shown as dashed black lines for the pn spectrum only. Relevant emission lines are also indicated. *Lower panel*: same as upper panel for region 23.

Non-thermal emission. As shown in Fig. 5.4, the azimuthal profile of the synchrotron cut-off frequency ν_{break} presents a trend that is perfectly consistent with that derived by [321], the cut-off frequency increasing in the non-thermal limbs. However, our break frequencies are systematically lower than their ones (by a factor of $\sim$ 10). This discrepancy is due to the value of the radio spectral index α. In fact, we here derive $\alpha \sim 0.50 \pm 0.04$ from our spectral fittings in the non-thermal regions[2], while [321] do not measure α, and assume $\alpha = 0.6$. The lower values of the spectral index naturally imply lower cut-off frequencies. Notice that, as shown by the green points in Fig. 5.4, we obtain also $\alpha \sim 0.5$ by using the method 2 for the analysis of the background, as described in Sect. 5.1.2. Our best-fit value $\alpha \sim 0.5$ and our cut-off frequencies are in agreement with the results obtained by [54].

[2]In the thermal regions we therefore fix $\alpha = 0.5$, as shown in Fig. 5.4.

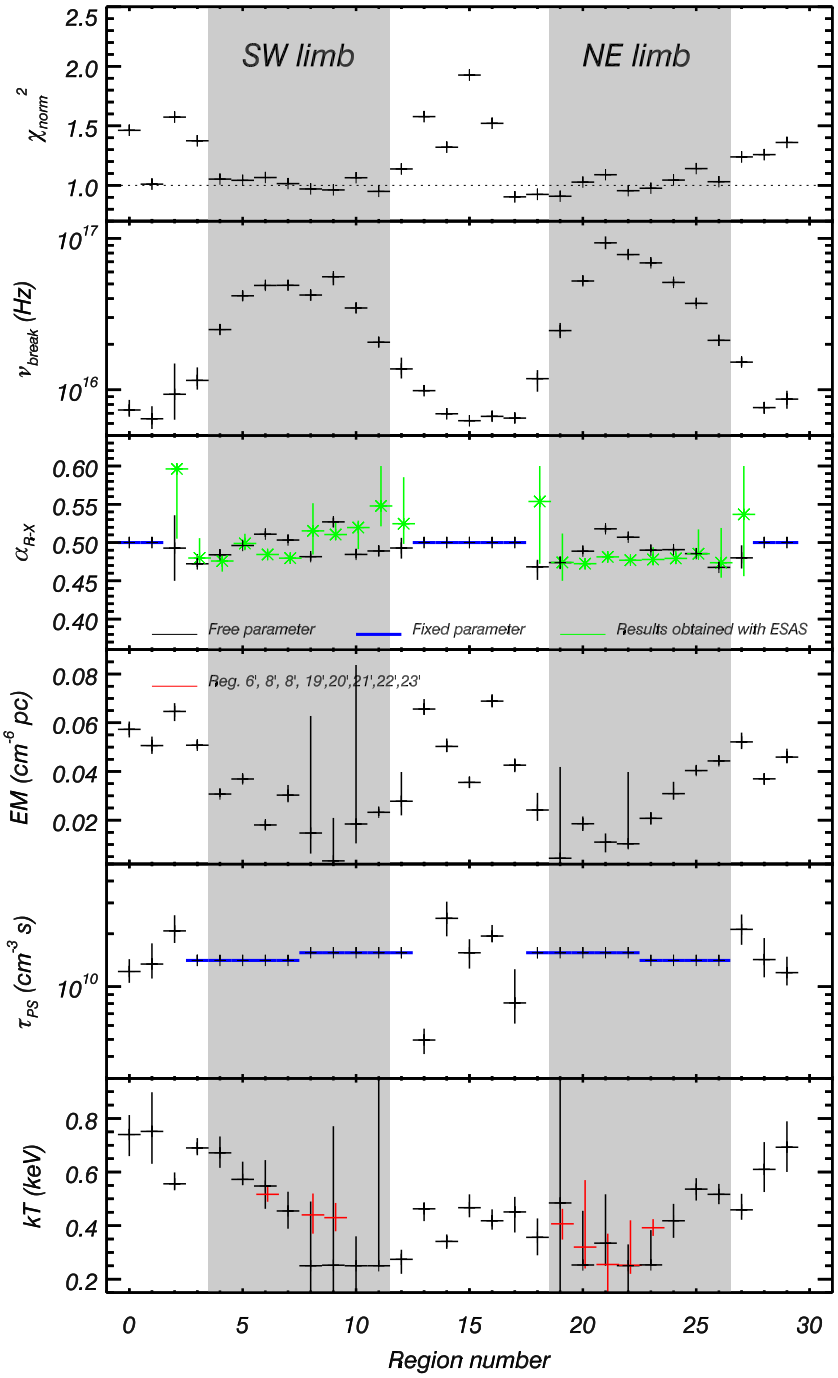

Figure 5.4. Best-fit parameters for the 30 regions shown in the upper panel of Fig. 5.2 (*in black*) and for the 8 regions of the upper panel of the same figure (*in red*). The model consists in a non-equilibrium of ionization isothermal component plus a synchrotron SRCUT model. The blue crosses indicate where the parameters are fixed. The errors are at 90% confidence level. The chemical abundances are tied to those of region NW, for regions $8-22$, and to those of region SE, for regions $23-7$. For comparison, the best-fit values of α obtained by using the method 2 for the analysis of the background (Sect. 5.1.2) are shown as *green* stars.

Thermal emission. Figure 5.4 clearly shows that the emission measure per unit area, EM, of the thermal component significantly decreases in the bright non-thermal limbs (we obtain the same trend by also analyzing the spectra with the ESAS method described in Sect. 5.1.2). In the North-East (regions 19-23) and at South-West (regions 6-10), in particular, EM is a factor of $\gtrsim 4$ lower than in the North-West or South-East, and in regions 9 and 19 it is consistent with being zero. This is quite surprising because one would expect EM to be large in the non-thermal limbs, where the particle acceleration is supposed to be more efficient.

The temperature of the ejecta is not uniform and in the north-western part of the rim, in particular (regions 13-18 in Fig. 5.4), the temperatures are clearly lower. Unfortunately, in the non-thermal limbs, the determination of temperature is affected by large errors, because of the low EM.

5.1.4. Procedure to extract the pure thermal image of SN 1006. Since the thermal emission is completely dominated by the shocked ejecta, it is interesting to study their spatial distribution and obtain an image of their X-ray emission. Authors of [63] suggested that there are differences in the spatial distribution of thermal and non-thermal emission in the north-eastern region of SN 1006. Cassam-Chenaï et al. [106] assumed that (in the south-eastern quarter of the shell) the X-ray emission in the "oxygen band" ($0.5 - 0.8$ keV) is completely associated with the ejecta. Indeed, even in this soft band, there is a non-negligible flux associated with the non-thermal component, especially in the non-thermal limbs (see Fig. 5.3). We use our results for the non-thermal component to estimate this contribution.

The spectral properties of the SRCUT component are very robust. They do not depend strongly on the model adopted for the thermal component, since the normalization of the synchrotron emission is derived from the radio data and the values of α and the azimuthal profile of the roll-off frequency are in good agreement with those reported in literature. Using our result, we calculate that in only one third of the rim (regions $28 - 2$ and $18 - 22$) the contribution of the thermal emission in the oxygen band is larger than 80% of the total flux, while in fifteen regions ($4 - 11$ and

$19-25$) it is $\leq 50\%$. This means that the $0.5-0.8$ keV map of SN 1006 shown in the central panel of Fig. 5.2 cannot be used as a proxy of the ejecta.

We developed the procedure to produce the image of the thermal emission in the $0.5-0.8$ keV band (we call this image TH). The scheme of the procedure consists of three steps: A) we assume the emission in the $2-4.5$ keV band to be completely associated with the non-thermal component; B) we extrapolate the $2-4.5$ keV image to produce an image of the non-thermal component in the $0.5-0.8$ keV band, (we call this image $NONTH$) by using the results of our spatially resolved spectral analysis; and C) we subtract $NONTH$ from the total image in the $0.5-0.8$ keV band, thus obtaining the thermal image.

Step A. We assume the thermal emission to be negligible in the $2-4.5$ keV band. The results of our spatially resolved spectral analysis show indeed that this assumption is strictly valid in the non-thermal limbs (where the non-thermal flux is $\gtrsim 99\%$ of the total), while it does not hold in the thermal regions (e.g. regions $28-2$), where about 50% of the flux in the $2-4.5$ keV is associated with the thermal component. Nevertheless, we can show that this problem does not generate significant effects. In fact, even if we overestimate the contribution of the synchrotron emission in the thermal region (by a factor of a few) this contribution remains small in the $0.5-0.8$ keV band: for example we verified (after step B) that it is $\sim 10\%$ and $\sim 6\%$ of the total flux in the oxygen band in region 0 and region 16, respectively. This means that, when we produce TH, the flux in the thermal regions is not significantly underestimated, while that in the non-thermal region is correct. In conclusion, we can say that our assumption holds where it is more necessary.

Step B. From the $2-4.5$ keV image, we can produce $NONTH$ by considering a given spectral shape of the synchrotron emission (i. e., a given value of α and a given value of the roll-off frequency ν_{break}) in each pixel. Since we found that in the entire rim the photon index is fairly uniform (see Fig. 5.4), we can assume that in each point of the image in the hard band the spectrum has a photon index $\alpha = 0.5$. As for ν_{break}, we found in Sect. 5.1.3 that it depends on the azimuthal angle θ at the rim. We then interpolate the values of ν_{break} shown in Fig. 5.4 by using a Fourier

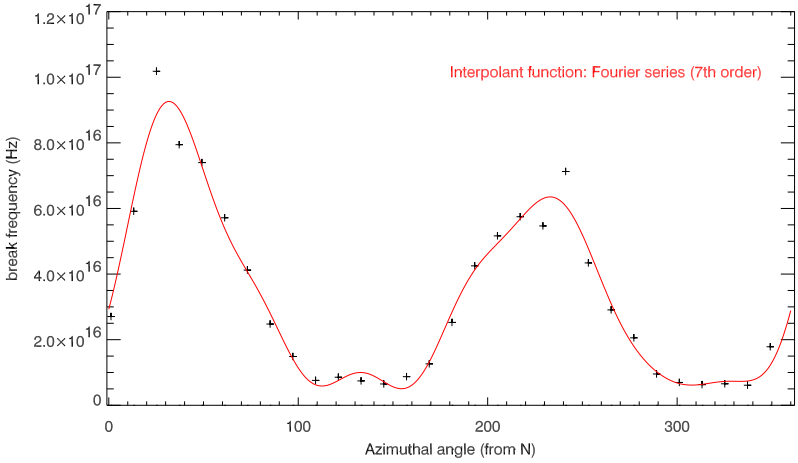

Figure 5.5. Break frequency $\nu_{\rm break}$ azimuthal profile.

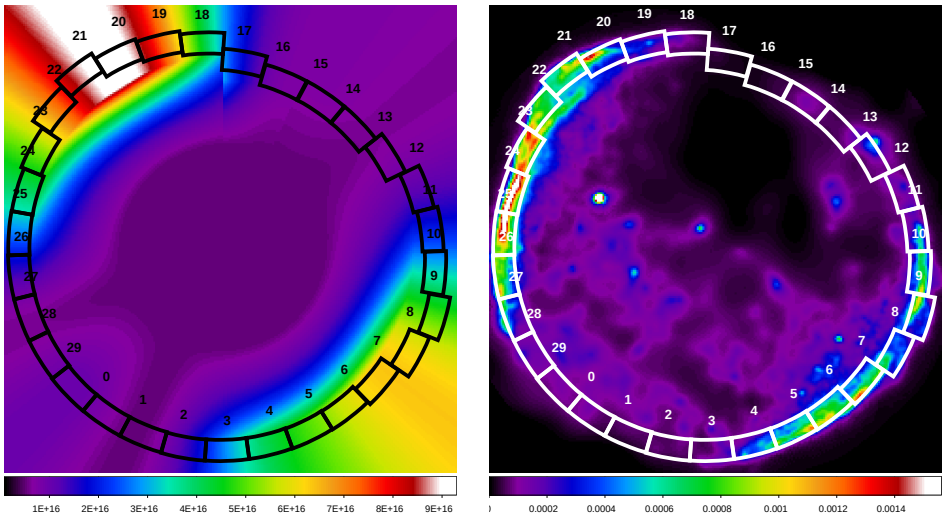

Figure 5.6. *Left panel:* map of the cut-off frequency derived according to the procedure described in Step B. The 30 regions selected for the spectral analysis of the rim are indicated in black. *Rigth panel:* image of the non-thermal emission in the $0.5-0.8$ keV band.

series (up to the 6th order) and we assume that the azimuthal trend of $\nu_{break}(\theta)$ at the rim is given by this interpolating function at angular distances from the center $R > R_{int}(\theta)$, where $R_{int}(\theta) = 11.7'$ for regions $13-17$ and $R_{int}(\theta) = 13.5'$ elsewhere (Fig. 5.5). As for the radial profile of $\nu_{break}(R)$ for $R < R_{int}(\theta)$, we follow [321] and assume that: i) in the center ($R < 7'$), the cut-off frequency is uniform and its value is equal to the minimum ν_{break} found in the rim and ii) for $7' < R < R_{int}(\theta)$, the cut-off frequency increases exponentially with R, going from its minimum value (at the center) to the corresponding value at the rim. In this way, we produce the map of ν_{break} shown in Fig. 5.6. Since we know the spectral shape of the synchrotron emission in each pixel of the $2-4.5$ keV image, we can produce the image of the

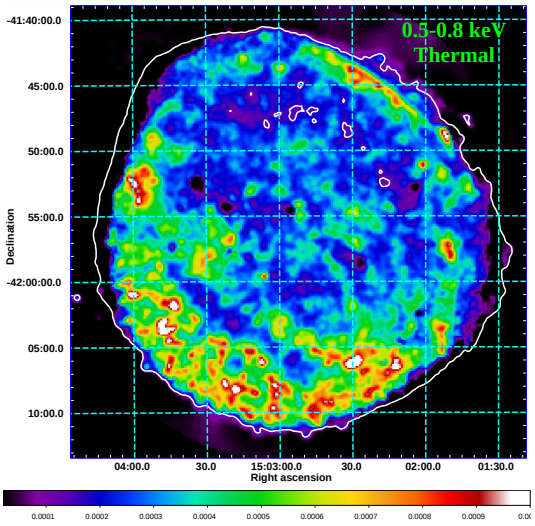

Figure 5.7. Pure thermal image (counts per second per bin) of SN 1006 in the $0.5 - 0.8$ keV band. The contribution of the non-thermal emission in the soft energy band has been subtracted. The bin size is $8''$ and the image is adaptively smoothed to a signal-to-noise ratio 10. The same contour level shown in the central panel of Fig. 5.2 is overimposed for comparison.

non-thermal emission in the $0.5 - 0.8$ keV band. This image is shown in the right panel of Fig. 5.6.

Step C. Once $NONTH$ has been produced, we simply subtract it from the total image in the oxygen band, thus obtaining the pure thermal image in the $0.5 - 0.8$ keV band shown in Fig. 5.7. The map shown in Fig. 5.7 presents striking differences from the total image in the same band (central panel of Fig. 5.2), especially in the non-thermal limbs, where the emission of the ejecta is negligible. This differences are important for procedure of determination of position of the contact discontinuity used in a number of papers (e.g. [106]) as an evidence about efficient CRs acceleration.

5.2. Model-independent method for synthesis of the gamma-ray image of SNR due to inverse Compton emission

Hadronic γ-rays arise at the location of the target protons. Rather large density of target protons – as e.g. in molecular clouds – is the condition for the effective hadronic emission in SNRs with high TeV γ-ray fluxes. The morphology of this type of emission in such SNRs is expected to follow the structures of regions of enhanced

density of target protons, not the structures in the SNRs where initial protons are accelerated. In SNRs which are bright in γ-rays, surface brightness distribution of proton-origin γ-ray emission may not therefore be expected to follow the radio and/or nonthermal X-ray images of SNRs, like it is observed in IC443, W28 or CTB 37B.

In contrast, the TeV γ-ray and hard X-ray morphologies are observed to be well correlated in the cases of RX J1713.7-3946, Vela Jr., SN 1006 and possibly RCW86. Thus it could be that TeV γ-rays reflect the same structures where the radio and nonthermal X-ray emission arise. In this scenario, electrons with energies of tens TeV may be responsible both for the (synchrotron) X-rays with energies of few keV and for the inverse-Compton γ-rays with energies of few TeV which are observable by HESS.

The HESS image of SN 1006 reported recently [28] reveals a very good correlation between X- and γ-ray maps (Fig. 1.8). Can the correlation between IC γ-ray and synchrotron X-ray images really be an argument for leptonic origin of TeV γ-ray emission? In the present section, we make use of the spatially resolved analysis of the radio and X-ray data of SN 1006 to generate images with the possible appearance that this SNR would acquire if the whole TeV γ-emission were due to leptonic IC process.

Since the purpose of the present analysis is to be as much model independent as possible, our work is mostly based on experimental results, without involving models of SNR dynamics, electron kinetics and evolution, etc., contrary to what has been carried out in previous approaches to the problem ([157, 303, 305] and Chapter 4). Radio and nonthermal X-ray emission contain information about the accelerated electrons, their distribution inside SNR, maximum energies, etc. The method we propose extracts most of the important properties, which are needed to synthesize an IC γ-ray image, from the radio and X-ray data. The major exception is the magnetic field (MF). In the absence of observational information about it, we consider three cases of possible MF configurations.

5.2.1. Description of the method. Let us assume that the energy spectrum of electrons holds the following relation

$$N(E) = KE^{-s}\exp(-E/E_{\max}). \tag{5.1}$$

where $N(E)$ is the number of electrons per unit volume with arbitrary directions of motion, E the electron energy, K the normalization of the electron distribution, s the power law index and $E_{\max}$ the maximum energy of electrons accelerated by the shock. This equation neglects small concave-up curvature of the spectrum predicted by efficient shock acceleration but allows us to be in the framework of the methodology of the X-ray spectral analysis (*srcut* model was used, Sect. 5.1.3). The concavity results in a small bump around $E_{\max}$ which leads mainly to some increase of the IC flux, which we are not interested in. It is not expected to affect the pattern of the gamma-ray brightness obtained with our method. Simpler spectrum $N(E) = KE^{-s}$ is valid for the radio emission. The emissivity due to synchrotron or IC emission is

$$q(\varepsilon) = \int dEN(E)p(E, \varepsilon, [B]) \tag{5.2}$$

where p is the radiation power of a single electron with energy E, ε is the photon energy. The strength of magnetic field B is involved only in the synchrotron emission process.

The simplest way to reach our goal is to use the delta-function approximation of the single-electron emissivities applied to spectrum Eq. (5.1). Namely, the special function F appeared in the theory of synchrotron radiation is substituted with

$$\mathcal{F}\left(\frac{\nu}{\nu_{\rm c}}\right) = \delta\left(\frac{\nu}{\nu_{\rm c}} - 0.29\right)\int\limits_0^\infty F(x)dx \tag{5.3}$$

where ν is the frequency, $\nu_{\rm c}(B, E) = c_1BE^2$ is the characteristic frequency, $c_1 = 6.26 \times 10^{18}$ cgs. This results in synchrotron radio and X-ray emissivities with the following dependencies:

$$q_{\rm r} \propto \nu_{\rm r}^{-(s-1)/2}KB^{(s+1)/2} \tag{5.4}$$

$$q_{\rm x} \propto \nu_{\rm x}^{-(s-1)/2}KB^{(s+1)/2}\exp\left[-\left(\frac{\nu_{\rm x}}{\nu_{\rm break}}\right)^{1/2}\right] \tag{5.5}$$

where $\nu_{\rm break}$ is

$$\nu_{\rm break} = \nu_{\rm c}(B, E_{\rm max}). \tag{5.6}$$

With Eq. (5.4) and Eq. (5.5), we approximate the relation between the radio and X-ray synchrotron emissivities:

$$q_{\rm x} = q_{\rm r} \left(\frac{\nu_{\rm x}}{\nu_{\rm r}}\right)^{-(s-1)/2} \exp\left[-\left(\frac{\nu_{\rm x}}{\nu_{\rm break}}\right)^{1/2}\right]. \tag{5.7}$$

However, exponentially cut off electron distribution Eq. (5.1) convolved with the δ-function approximation for the single-particle emissivity, Eq. (5.5), underestimates the synchrotron flux from the same electron distribution convolved with the full single-particle emissivity, Eq. (5.2), at frequencies $\nu > 30\nu_{\rm break}$ (see Fig. 3 in [303], $\nu_{\rm break}$ is marked as $\nu_{\rm m}$ there).

In this section, we use $\nu_{\rm x} = 2.4\,{\rm keV} = 5.8 \times 10^{17}\,{\rm Hz}$. The range of $\nu_{\rm break}$ in SN 1006 is found to be $(0.06 \div 1) \times 10^{17}\,{\rm Hz}$ (Sect. 5.1.3). Thus, we are working with $\nu_{\rm x} \approx (6 \div 100)\nu_{\rm break}$. Using Eq. (5.7) , we may therefore underestimate the real X-ray flux in ~ 10 times in regions where $\nu_{\rm break}$ is small. Thus, as it is pointed out by Reynolds [312], the approximate Eq. (5.7) is not robust at highest frequencies.

We suggest therefore an empirical approximation of the numerically integrated synchrotron emissivity Eq. (5.2), i.e. emissivity of the exponentially cut off electron distribution convolved with the full single-particle emissivity:

$$q_{\rm x} = q_{\rm r} \left(\frac{\nu_{\rm x}}{\nu_{\rm r}}\right)^{-(s-1)/2} \exp\left[-\beta_{\rm x}\left(\frac{\nu_{\rm x}}{\nu_{\rm break}}\right)^{0.364}\right] \tag{5.8}$$

where $\beta_{\rm x} = 1.46 + 0.15(2 - s)$. This approximation is quite accurate. Its errors are less than 18% for $s = 1.8 \div 2.5$ and $\nu_{\rm x} \leq 10^3\nu_{\rm break}$.

We assume that TeV γ-ray emission from SN 1006 is due to IC process in the black-body photon field of the cosmic microwave background. The convolution of the electron distribution Eq. (5.1) with the δ-function approximation for the single-particle IC emissivity is also inaccurate to describe the γ-ray radiation of electrons with energies around $E_{\rm max}$. Therefore, like in the case of the synchrotron radiation, we use an approximate formula for the IC emissivity, too.

Let us consider IC emission at 1 TeV. We developed an approximation for the numerically integrated IC emissivity (5.2) of electrons with the energy spectrum (5.1) at γ-ray energy 1 TeV:

$$q_{\rm ic@1} \propto K \exp\left(-\beta_{\rm ic} E_{\rm max}^{-0.75}\right) \tag{5.9}$$

where $\beta_{\rm ic} = 15$ for $2 \leq s \leq 2.5$ and $\beta_{\rm ic} = 15 + 2(2 - s)$ for $1.8 \leq s < 2$. The error of this approximation is less than 25% for $E_{\rm max} \geq 0.3$ TeV. This approximation accounts for the Klein-Nishina decline where necessary.

The maximum energy is related to $\nu_{\rm break}$ by Eq. (5.6) :

$$E_{\rm max} = C_1 \nu_{\rm break}^{1/2} B^{-1/2} \tag{5.10}$$

where $C_1 = c_1^{-1/2}$. Substitution of Eq. (5.9) with this $E_{\rm max}$ and K from Eq. (5.4) results in

$$q_{\rm ic@1} \propto q_{\rm r} B^{-(s+1)/2} \exp\left[-\beta_{\rm ic}\left(\frac{B^{1/2}}{C_1 \nu_{\rm break}^{1/2}}\right)^{0.75}\right]. \tag{5.11}$$

This expression relates the radio emissivity and the IC γ-ray emissivity at 1 TeV with only one unknown, B. It may be used in the same cases where the *srcut* model is applicable, that is, if the spectrum of electrons may be approximated by Eq. (5.1) with s assumed constant from the radio to X-ray emitting electrons.

The idea of our method is represented by Eq. (5.11). Namely, this expression may be used in a small region ("pixel") of a SNR projection in order to relate the surface brightness in radio band and IC γ-rays. Having this relation applied to all "pixels", we may predict the main features of the γ-ray morphology of SNR originated in an IC process. This procedure 'converts' the radio image to an IC one.

Another possibility is to start from the hard X-ray map and 'translate' it into the γ-ray image in a similar fashion. Namely, substitution Eq. (5.11) with $q_{\rm r}$ from Eq. (5.8) yields

$$q_{\rm ic@1} \propto q_{\rm x} B^{-(s+1)/2} \exp\left[-\beta_{\rm ic}\left(\frac{B^{1/2}}{C_1 \nu_{\rm break}^{1/2}}\right)^{0.75} + \beta_{\rm x}\left(\frac{\nu_{\rm x}}{\nu_{\rm break}}\right)^{0.364}\right]. \tag{5.12}$$

However, an X-ray image can be used only if it is dominated everywhere by the nonthermal emission.

Eqs. (5.11) and (5.12) relate emissivities of the uniform plasma. We use these equations to deal with surface brightnesses that are superpositions of the local emissivities along the line of sight. Strictly speaking, this may be done only for the thin rim around SNR edge where plasma is approximately uniform along the line of sight. However, this approach may also be extended to deeper regions of SNR projection (see Appendix C.1). Since X-ray limbs are (and γ-ray ones are expected to be) quite thin and close to the edge, our method is able to correctly determine the location of the bright limbs in the IC γ-ray image of SN 1006. In the interior of SNR projection, we consider B and $\nu_{\rm break}$ as 'effective' values for a given 'pixel'.

It is interesting to note that Eq. (5.11) [or Eq. (5.12)] may be solved for the value of B. In this way, the method proposed here may be used for deriving the effective (line-of-sight averaged) MF pattern in SNR from its radio [or synchrotron X-ray] and IC γ-ray maps. The distribution of $\nu_{\rm break}$ may be obtained from the radio ($q_{\rm r}$) and synchrotron X-ray ($q_{\rm x}$) images by solving Eq. (5.8), without the need of the spatially resolved X-ray analysis.

5.2.2. Application to SN 1006. Experimental data and models of magnetic field. In order to make use of Eq. (5.11) or Eq. (5.12), one needs: i) an initial image, i.e. the map of distribution of the synchrotron radio (or X-ray) surface brightness, ii) the distribution of $\nu_{\rm break}$ obtained from the spatially resolved spectral analysis of X-ray data and iii) the distribution of the effective magnetic field over the initial image.

We use the high resolution radio image of SN 1006 at $\lambda \sim 20$ cm (Fig. 5.8), produced on the basis of archival Very Large Array data combined with Parkes single-dish data presented in Sect. 5.1.1.

As for the X-ray image, we use the 2.0-4.5 keV XMM-Newton EPIC mosaic obtained in Sect 5.1.3, shown in Fig. 5.9. A contour plotted on the images delineates the boundary of SN 1006. It corresponds to the level of 10% of the maximum brightness in the soft ($0.5 - 0.8$ keV) X-ray map of SNR (see Fig. 5.2).

The image of the break frequency (Fig. 5.10) was derived on the basis of spatially

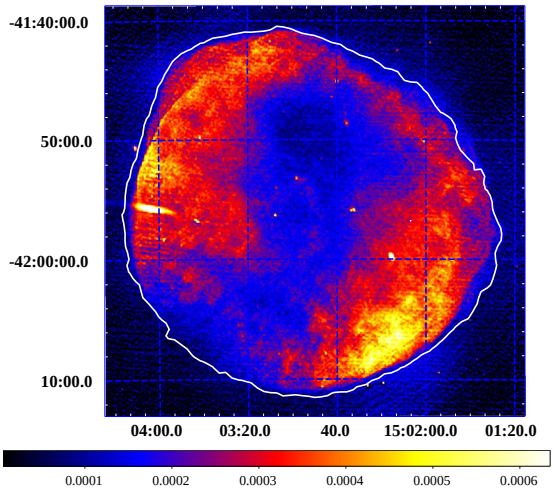

Figure 5.8. Radio image of SN 1006 at $\lambda \sim 20$ cm. The color scale is in units Jy beam^{-1}. The white contour denotes the boundary of SN 1006.

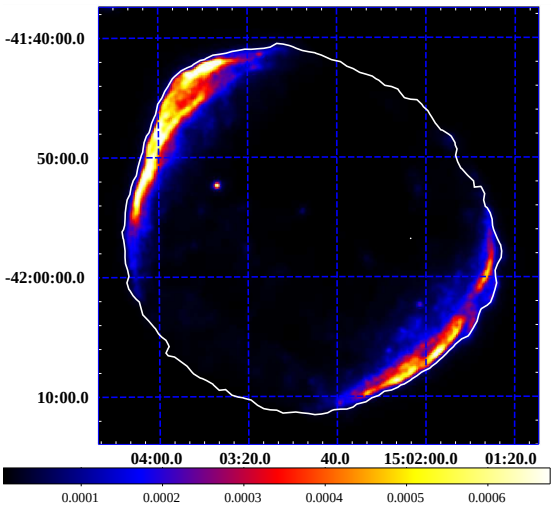

Figure 5.9. X-ray image of SN 1006 in $2-4.5$ keV. The pixel size is $8''$. The color scale is in units MOS1 counts s^{-1} pixel^{-1}.

resolved X-ray spectral fitting results (Sect. 5.1.4). The spectral fits show that α, the radio spectral index, is between 0.47 and 0.53 everywhere around the shock (Fig. 5.4). Therefore, we take $s = 2\alpha + 1 = 2$ to be constant in SN 1006.

We consider three models for magnetic field inside SNR. SN 1006 is rather symmetrical. In the procedure of MF map simulation, SNR is assumed to be spherical, with the radius equal to the average radius of SN 1006. For technical reasons, MF is fixed to the postshock value also outside the boundary of the spherical SNR (Fig. 5.11). This allows us to deal correctly also with regions of SN 1006 which are larger than the average radius.

Classical MHD description corresponds to the unmodified shock theory. It takes

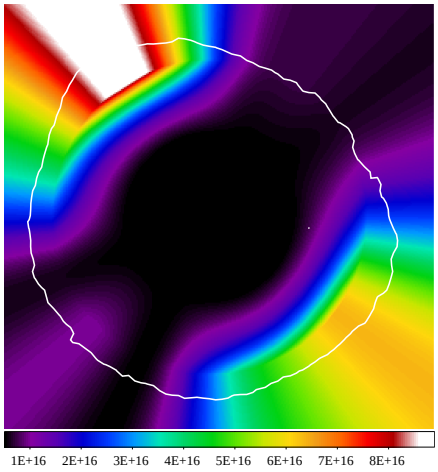

Figure 5.10. Break frequency $\nu_{\rm break}$ image (the color scale is in units of Hz).

into account the post-shock evolution of MF and the compression factor which increases with the shock obliquity. In this case, two possible orientations of ISMF are considered. Namely, NW-SE (Fig. 5.11) in model MF1 (equatorial, or barrel-like, model) and NE-SW in MF2 (polar caps model). ISMF is assumed to be constant around SN 1006 with the strength $B_{\rm o} = 10\,\mu$G. This value is choosen to give, in models MF1 and MF2, the postshock magnetic field $20 \div 40\ \mu G$, a value which follows from estimations for downstream MF strength [362] and reported γ-ray flux [28]. Such ISMF looks to be unrealistic at the position of SN 1006 far above the Galactic plane. A possibility to provide tens of μG upstream of the shock would be the magnetic field amplificaion as an effect of efficient cosmic ray acceleration, which is out of the scope of this study. It should be noted however that the absolute value of the upstream field plays no role for the purpose of this section. The aspect angle between ISMF and the line of sight is taken to be $70^{\rm o}$ for MF1 (Sect. 5.3) and, for simplicity, also for MF2 (we shall see below that the actual value of the aspect angle is not crucial for the purpose of the present section, because even different models of MF lead to quite similar γ-ray pattern).

The procedure of generation of the average MF maps for MF1 and MF2 models is as follows. First we calculated numerically MHD model of Sedov SNR [13,21,303]. This gives us three-dimensional distribution of MF inside SNR. An effective MF in a given 'pixel' of SNR projection is taken as a straight average for this 3-D MF distribution along the line of sight, accounting for the azimuthal orientation and

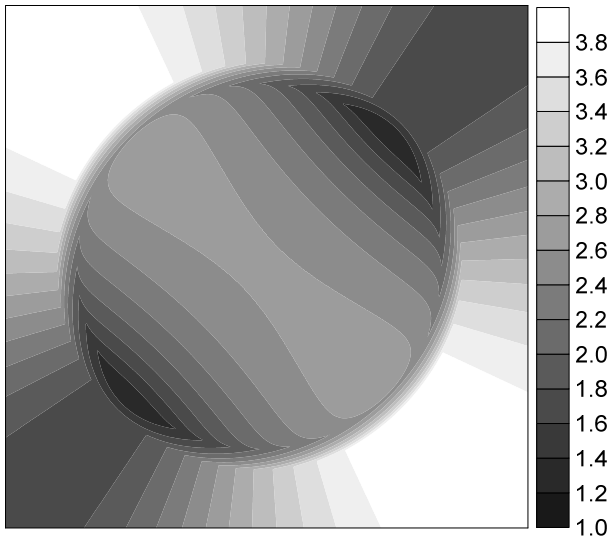

Figure 5.11. Map of effective MF used in calculations for the model MF1. $\zeta = 0.9$. This map is rotated on 90° for the other scenario, MF2. The color scale is in units of B_o.

an aspect angle of the ambient MF in respect to the observer as well as the fact that most of emission arise right after the shock. Really, in order to generate map of effective MF one should calculate the emissivity-weighted average. Such an approach requires however the knowledge of 3-D distribution of emitting electrons within SNR which is unknown until one makes the full modelling from basic theoretical principles. In contrast, the scope of the present section is to 'extract' the structure of radiating material from the observational data. Therefore, our procedure consists in approximate calculation of emissivity-weighted MF, without considering the 3-D distribution of relativistic electrons. In fact, most emission comes from a rather thin shell with thickness $\sim 10\%$ of SNR radius. Therefore, in calculations of the average magnetic field, we consider only this part of SNR interior, namely the integration along the line of sight is within regions from ζR to R, with $\zeta < 1$ (Fig. 5.11). A choice of ζ is rather arbitrary. It is apparent from calculations that contrasts between the outer regions and the interior of the IC image depend on this choice. The preference to the value of ζ does not alter, however, the main features of the predicted IC morphology of SNR. Note that the azimuthal variation of the brightness is not affected at all by ζ for radii of SNR projection $\geq \zeta R$. In other words, the position of the limbs on the synthesized IC γ-ray image may not be altered by the particular choice of ζ. Nevertheless, in order to determine the most appropriate value

of ζ, we made the full MHD simulations of Sedov SNR with model of evolution of the relativistic electrons in the SNR interior from [303]. Then the map of the emissivity-weighted average MF was produced from these simulations and compared with our maps of effective MF derived for different ζ. In this way, we found that the value $\zeta = 0.9$ provides the good correspondence between MF maps in these two approaches.

The third model of MF is relevant to the nonlinear acceleration theory with the time-dependent MF amplification and the high level of turbulence (Bohm limit; [361]). The quasi-parallel theory assumes in this case that the turbulence is produced ahead of the shock, not downstream. The compression of the (already turbulent) magnetic field then does not depend on the original obliquity [75, 363]. Rakowski et al. [299] argue that shocks of different initial obliquity subject to magnetic field amplification become perpendicular immediately upstream. ISMF is therefore assumed to increase on the shock by a large factor (due to compression and amplification), the same for any obliquity. In addition, in model MF3, we assume MF to be approximately uniform everywhere inside SNR [77], with the strength $150\,\mu$G [219].

Theoretical work on magnetic-field amplification starting with [70] focuses on shocks which are originally parallel far upstream, with some implications that the process is less effective for (initially) perpendicular shocks. In this scenario, obliquity dependence of the post-shock MF would be opposite to the classical one. Really, MF amplification is expected to follow acceleration efficiency which decrease with the obliquity. If so, limbs in SN 1006 should correspond to the largest post-shock MF. Such MF morphology is qualitatively represented by MF1 model (Fig. 5.11).

Some other notes to our methodology are in order. All initial maps were homogenized to the same size, orientation, resolution and pixel size. Eq. (5.11) is applied to each pixel of the initial images. The maximum brightness on images is fixed at the maximum value in the histogram distribution which has at least 10 pixels. The minimum is fixed at the level 1/100 of the maximum value. This is true for all the images, including the synthesized images, the observed X-ray and radio ones, and excluding the MF and $\nu_{\rm break}$ maps.

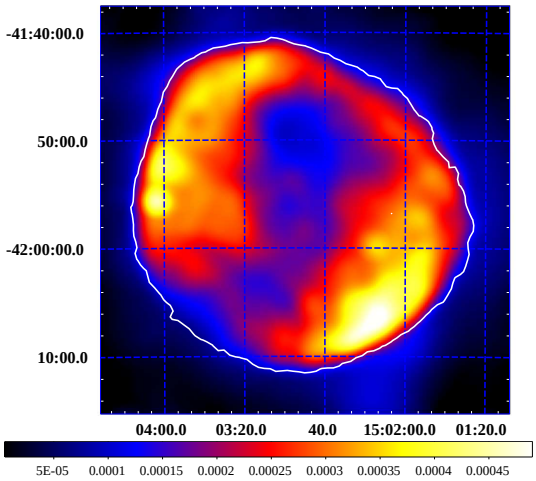

Figure 5.12. Radio image of SN 1006 at $\lambda \sim 20$ cm, from Fig. 5.8, smoothed with Gaussian with $2'$ sigma.

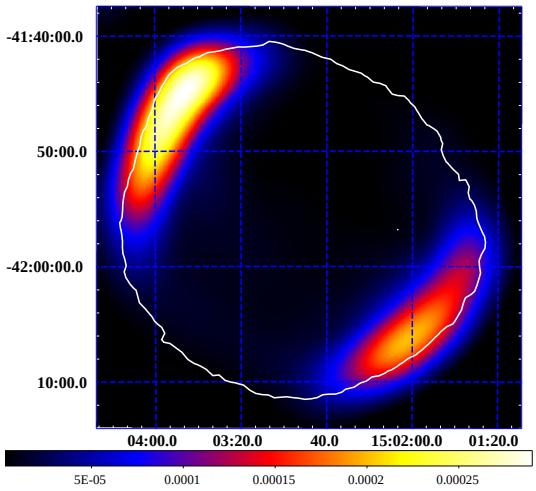

Figure 5.13. X-ray image of SN 1006 in 2-4.5 keV, from Fig. 5.9, smoothed with Gaussian with $2'$ sigma.

Some images are smoothed to fit the resolution of HESS. The resolution used is FWHM $= 4.75'$ [37], so the Gaussian sigma is $2'$. The role of smoothing is visible on Figs. 5.12, 5.13, to be compared with radio and X-ray images on Figs. 5.8, 5.9.

5.2.3. Synthesized images and HESS observations of SN 1006. To check our approach, we made use of Eq. (5.8) to generate the X-ray image of SN 1006 starting from the radio one. We stress that we do not need any assumption about MF configuration for this test, everything needed for radio to X-ray conversion may be taken from observations. Really, we need just the input radio image (Fig. 5.8), and the distribution of the break frequency (Fig. 5.10). The resulting image is presented on Fig. 5.14. It shows good correlation with the hard X-ray observations (Fig. 5.13),

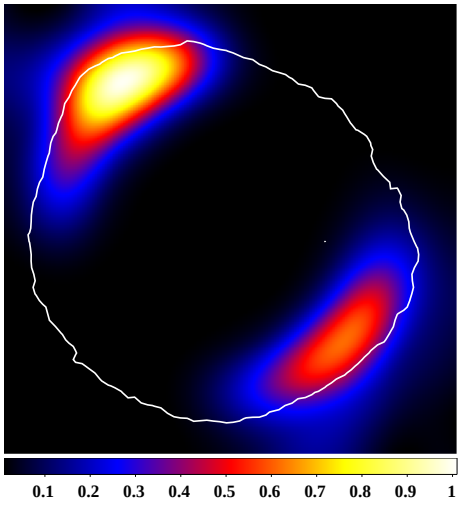

Figure 5.14. X-ray image of SN 1006 at 2.4 keV generated from the radio one (Fig. 5.8) with the use of Eq. (5.8) and smoothed to 2′ Gaussian sigma. The color scale is normalized to the maximum brightness.

confirming that the proposed method works well. It restores the main properties of the observed hard X-ray image: essential decrease of the thickness of the two bright synchrotron limbs in X-rays comparing to the radio band (Fig. 5.12), correct position of the limbs and negligible emission from the interior. Therefore, the method is reliable to be used for simulation of the γ-ray images of SNRs[3].

Synthesized TeV γ-ray images of SN 1006 due to IC process are presented on Fig. 5.15 (model MF1, barrel-like SNR in classical MHD or polar caps in non-linear approach), Fig. 5.16 (MF2, polar-caps in classical MHD) and Fig. 5.17 (MF3, uniform MF in the SNR interior for Berezhko et al. [75] non-linear model). Images presented on the left panels were obtained from the radio map as initial model, while those shown in the right panels have the hard X-ray map as the starting point. Middle panels represent 'radio-origin' γ-images of the left panels smoothed to the resolution of HESS.

Let us first consider the γ-ray morphologies obtained from the radio image. Two arcs dominate in all three MF configurations. Their locations correspond to limbs in

[3]The agreement between the observational and the synthesized X-ray maps is not perfect because the 'effective' resolution of the synthesized X-ray image cannot be better than the 'resolution' of the image of $\nu_{\rm break}$. The effective resolution of $\nu_{\rm break}$ image is defined by the size of 30 rim regions used for spectral analysis (see Fig. 5.2) that in turn is determined by the photon statistics. Namely, the *radial* resolution in the image of $\nu_{\rm break}$ is limited, since the radial profile of the cut-off frequency is assumed to be constant inside the rim regions. Note that the *azimuthal* 'resolution' is better than radial (see profile of $\nu_{\rm break}$ on Fig. 5.5).

radio and X-ray images. This confirms that correlation between TeV γ-ray and X-ray/radio morphologies may be considered as direct evidence that the γ-ray emission of SN 1006 observed by HESS is leptonic in origin.

Geometry of MF essentially different from those we considered might result in different predicted γ-ray images of SNR. Nevertheless, our results demonstrate that if MF strength varies within factor ~ 3 around the shock (Fig. 5.11), any configuration of MF results in double-limb IC γ-ray image of SN 1006. The reason, in accordance with Eq. (5.11), is the contrasts in (radio or X-ray) brightness and $\nu_{\rm break}$ which dominate any moderate azimuthal variation of MF. The use of the observed ratios of the radio surface brightness and the break frequency between NE and SE regions in Eq. (5.11) shows that a variation of MF $B_{\rm NE}/B_{\rm SE}$ larger than a factor of 4 may reverse the location of bright IC limbs.

For areas with the same radio surface brightness, higher MF implies lower IC γ-ray brightness, Eq. (5.11). We have therefore different azimuthal contrasts (i.e. the ratio of maximum to minimum brightness around the rim) in γ-ray images for different models of MF. In particular, in model MF1 the strength of the postshock MF is maximum in NE and SW regions (Fig. 5.11) where the radio brightness has maxima. At the same time, MF is smaller in faint NW and SE regions. This leads to small azimuthal contrast of brightness between bright and faint regions in γ-ray image (Fig. 5.15, left). In the opposite model MF2 the strength of the postshock MF is maximum in the faint NW and SE regions, that results in the largest brightness contrast (Fig. 5.16, left). Two arcs are therefore more pronounced in the γ-ray image for models MF2 and MF3.

The differences in γ-images for three models of MF are not so prominent after smoothing them to the resolution of HESS. In all three cases (Fig. 5.15-5.17, center panels), there are two bright limbs in the same locations corresponding to limbs on the smoothed X-ray map shown in Fig. 5.13. The synthesized images can be also directly compared to the HESS map of SN 1006, Fig. 1.8, [28]. Good correlation between the synthesized and the observed images allows us to prefer leptonic origin of TeV γ-ray emission of this SNR. The uncertainties introduced in our method by

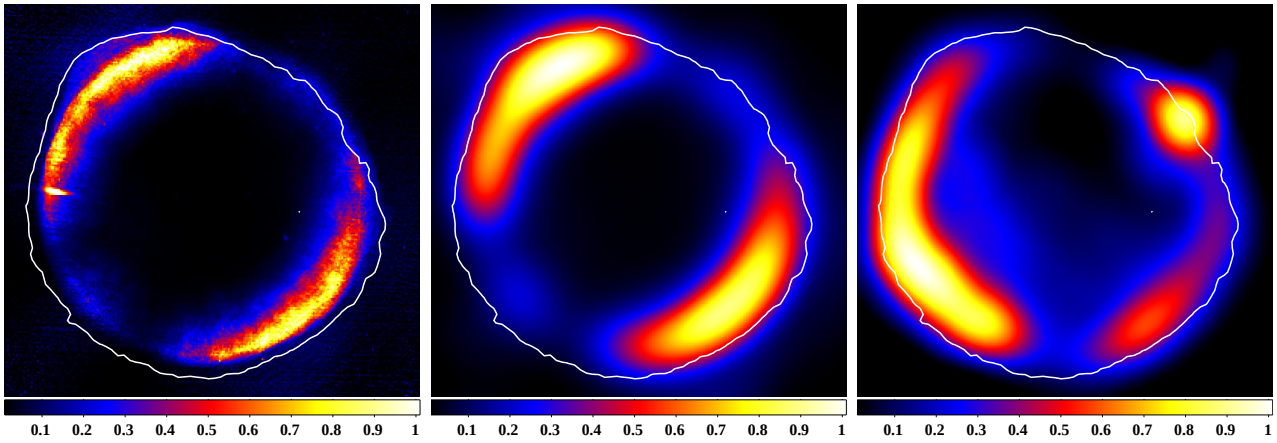

Figure 5.15. Predicted IC morphology of SN 1006 at photons with energy 1 TeV, for the model MF1. IC image generated from the radio map (left); the same smoothed to 2′ Gaussian sigma to fit the HESS resolution (centre); IC image generated from X-ray map and smoothed to 2′ Gaussian sigma (right). The color scales are normalized to the maximum brightness.

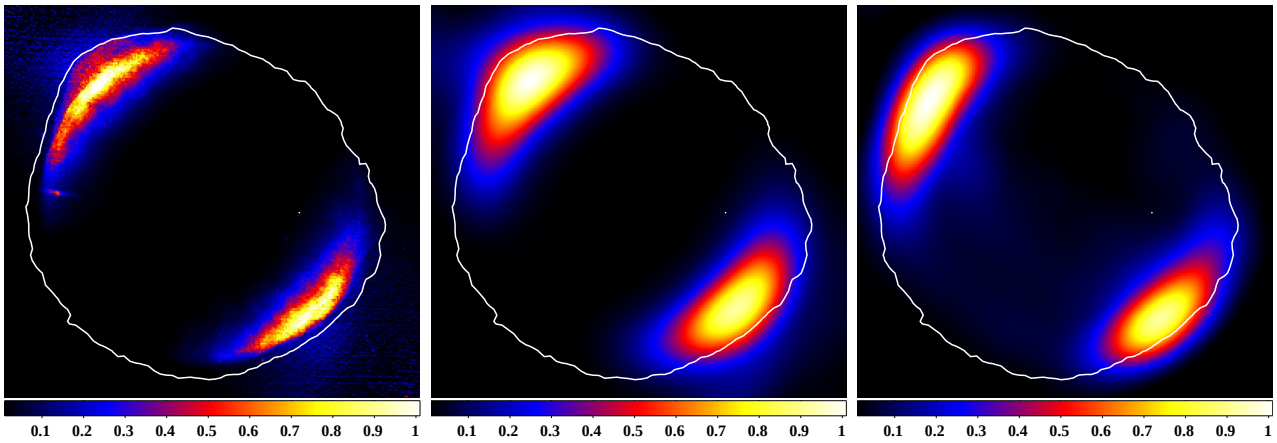

Figure 5.16. The same as on Fig. 5.15 for the model MF2.

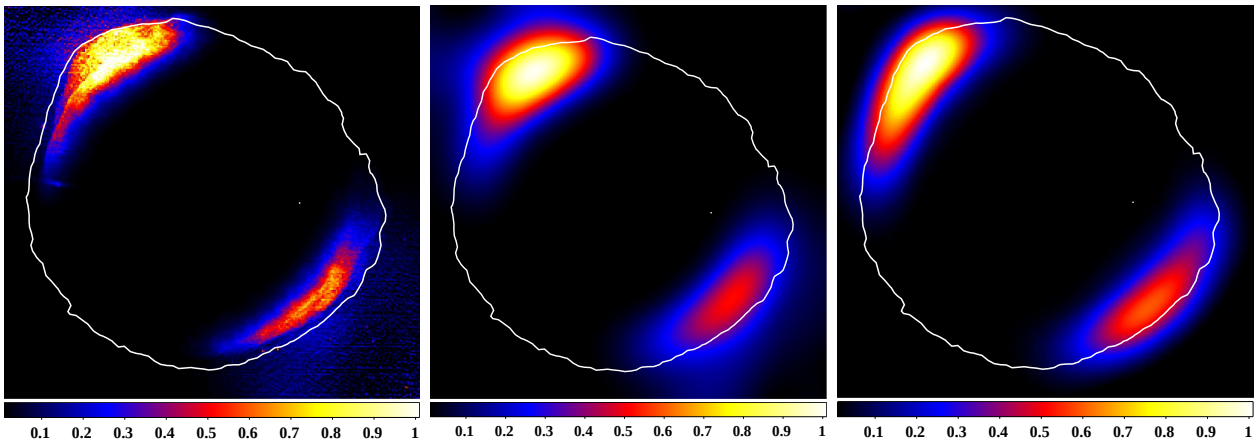

Figure 5.17. The same as on Fig. 5.15 for the model MF3.

the lack of knowledge of the real MF inside the remnant do not alter this correlation, as it is clearly seen from our synthesized images.

TeV γ-ray images obtained from the initial hard X-ray map (Fig. 5.15-5.17, right

panels) are quite similar to those from the initial radio map, except for the configuration MF1. This fact reinforce the goodness of our method. The reason of differences between the 'radio-origin' and the 'X-ray-origin' γ-ray images in the MF1 case (Fig. 5.15right) is the contribution of the thermal X-ray emission to the hard X-ray image which was used, in the SE and NW regions of SN 1006. Namely, our fitting show that the fraction of thermal emission in the overall 2-4.5 keV flux in the SE region is about 50% [250]. The prominent but localized NW bright spot is completely dominated by the thermal X-ray emission [356]. So, the γ-ray brightness in these regions is overestimated in our synthesized images. This effect is not prominent for MF2 and MF3 configurations because MF is large enough in SE region to visually decrease the brightness there. Thus, the X-ray map may be used as initial one in our method only if it is completely dominated everywhere by the nonthermal emission.

5.3. Injection model and orientation of ISMF in SN 1006

The interstellar magnetic field creates different obliquity angles with the shock normal in different places of the SNR surface. Efficiencies of injection and acceleration, compression and/or amplification of ISMF may depend on the shock obliquity. Therefore, in order to model non-thermal emission, it is important to make assumptions about ISMF orientation around these objects.

In many cases the ISMF, galactic in origin, may be assumed to be rather uniform on the scales of SNR sizes. Bilateral supernova remnants [159, 212]) with symmetric structure in radio images limit the orientation of the ISMF component in the plane of the sky. In the case of the BSNR archetype SN 1006, for instance, the ISMF may be parallel to the symmetry axis, spanning from SE to NW, or be perpendicular to it, running from NE to SW. The former corresponds to barrel-like (equatorial belt) structure and the latter to polar-cap structure [321]. However, in order to draw reliable conclusions about the shock obliquity, it is also necessary to consider the aspect angle – the angle between ISMF and the line of sight – which is still unknown.

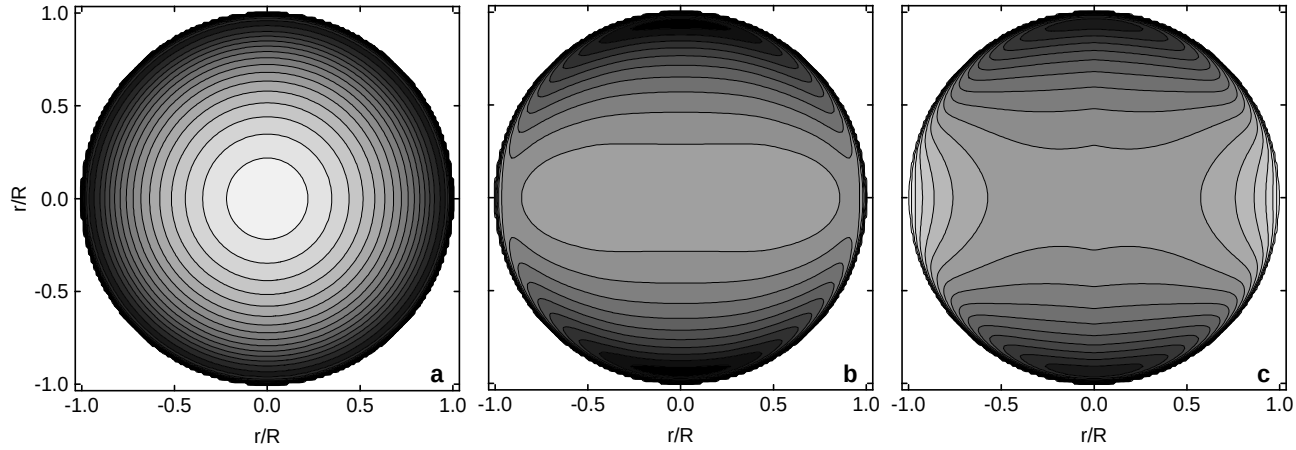

Figure 5.18. Surface brightness distributions (in linear scale) of the radio emission of adiabatic SNR for different aspect angles: $\phi_o = 0^o$ (**a**), 60^o (**b**), 90^o (**c**). Uniform ISM, uniform ISMF and isotropic injection are assumed. In cases (**b**) and (**c**), the component of ISMF in the plane of the sky is parallel to the horizontal axis. In all three plots, the levels of brightness are spaced in the same way.

In the present section, we propose a new method for determination of the aspect angle. We extract the azimuthal profiles of the synchrotron surface brightness distribution in a given SNR and compare the observed profiles with those synthesized from theoretical models, making different assumptions on the aspect angle and/or on the details of injection and acceleration of electrons. The "true" aspect angle is that of the best-fitting model. As a first application of the method, we analyzed SN 1006.

5.3.1. Aspect angle in bilateral SNRs: the method. The method to determine the aspect angle ϕ_o between ISMF and the line of sight on the basis of radio emission in SNRs, can be deduced from the simulated radio maps produced for a Sedov SNR expanding through a uniform ISM and ISMF, presented in Fig. 5.18. As shown in the figure, the *azimuthal* profile of the surface brightness is sensitive to the aspect angle: it is constant for $\phi_o = 0^o$ (Fig. 5.18a: ISMF is directed towards the observer) and it is steepest for $\phi_o = 90^o$ (Fig. 5.18c: ISMF is in the plane of the sky). Thus, comparison of an observed azimuthal profile with theoretical ones allows one to conclude about the aspect angle.

The radio surface brightness S at some 'point' of SNR image is

$$S \propto \int K B^{(s+1)/2} dl \tag{5.13}$$

where the integration is along the line of sight within the volume of SNR. The post-shock magnetic field is generally a subject of compression, and under conditions of efficient cosmic ray acceleration, amplification. The magnetic field can be expressed as $B_{\rm s} = A_{\rm B}(\Theta_{\rm o})B_{\rm o}$ where $A_{\rm B}$ is a product of the compression factor $\sigma_{\rm B}$ and an amplification factor. Since it is unknown whether magnetic field amplification depends on the shock obliquity, we assume it to be independent of $\Theta_{\rm o}$. In this case, the variation of the post-shock MF with obliquity is only determined by the compression [303], $B_{\rm s} \propto \sigma_{\rm B}(\Theta_{\rm o})B_{\rm o}$, where

$$\sigma_{\rm B}(\Theta_{\rm o}) = \left(\frac{1+\sigma^2\tan^2\Theta_{\rm o}}{1+\tan^2\Theta_{\rm o}}\right)^{1/2}, \tag{5.14}$$

$\sigma = 4$ is the shock compression ratio for unmodified shocks (changes in this prescription and our results due to the shock modification are discussed in Sect. 5.3.3).

At the shock, the normalization, $K_{\rm s} \propto \varsigma(\Theta_{\rm o})$ where ς is the injection efficiency defined as the fraction of accelerated electrons. There are three alternatives for dependence of injection efficiency ς on obliquity of the shock typically considered in the literature: isotropic injection (i.e. ς independent of $\Theta_{\rm o}$), quasi-parallel ($\varsigma \propto \cos^2\Theta_{\rm s}$) or quasi-perpendicular ($\varsigma \propto \sin^2\Theta_{\rm s}$) injection [157]. Therefore, the injection efficiency either decreases (quasi-parallel) or increases (quasi-perpendicular) with increasing obliquity, or it is independent of $\Theta_{\rm o}$. The MF compression factor increases with $\Theta_{\rm o}$.

There are theoretical expectations that injection is higher at parallel shocks [137, 363]. In contrast, observational evidence seems to argue for isotropic or quasi-perpendicular injection in SNRs [157, 264]. We consider all three possibilities.

In symmetric, bilateral SNRs (like SN 1006), the possible orientations of the ISMF *in the plane of the sky* are limited. Namely, ISMF may be parallel to the symmetry axis or perpendicular to it. For example, in SN 1006, if the injection is isotropic or quasi-perpendicular, the bright limbs correspond to the magnetic

"equator" (equatorial belt) and ISMF should be oriented in SE-NW direction. If injection prefers quasi-parallel shocks, the bright limbs of SN 1006 are two polar caps and MF should be oriented in the NE-SW direction. In other words, the model of injection determines the orientation of the plane-of-the-sky component of ISMF.

We synthesized a number of radio surface brightness maps of a Sedov SNR evolving in a uniform ISM and uniform ISMF.

Radio maps of the model SNR were calculated for a range of indices: s from 2 to 2.2, b from $-3/2$ to 2, β from 0 to 2. For each set of parameters, we produced a series of images by changing the aspect angle $\phi_{\rm o}$ from 0 to $\pi/2$. For the image with $\phi_{\rm o} = \pi/2$ in each series, we found the radius of projection $\varrho_{\rm Smax}$ which corresponds to the position of the maximum brightness $S_{\rm max} = S(\varrho_{\rm Smax}, \varphi_{\rm Smax})$ (by definition $\varphi_{\rm Smax} = \pi/2$ for this position)[4]. We then traced the surface brightness $S(\varrho_{\rm Smax}, \varphi)$ at this $\varrho_{\rm Smax}$ for azimuthal angles φ from 0 to $\pi/2$ and plotted these distributions normalized by the brightness $S(\varrho_{\rm Smax}, \varphi_{\rm Smax})$.

Fig. 5.19 shows the plots for different aspect angles, assuming $b = 0$, $\beta = 0$, $s = 2.2$, and considering the three models for obliquity dependence of injection efficiency. We found a reasonable result, namely that all the azimuthal profiles of surface brightness which we obtained are almost insensitive (within $10 - 20\%$) to the values of s, b and β (at least in the case of uniform ISM and uniform ISMF assumed here). That means the azimuthal profiles of radio brightness are almost independent of the shapes of the distributions of relativistic electrons and magnetic field downstream of the shock, in a full agreement with approximate formulae from Sect. 4.2. Such stability allows one to safely use the method proposed here for determination of the aspect angles from radio maps of SNRs if the ISM and ISMF in which SNR expands can be considered to be mostly uniform.

5.3.2. Application to SN 1006. The method is applicable to SNRs expanding in almost uniform ISM and ISMF. BSNRs, particularly SN 1006, are ideal candi-

[4]The radius $\varrho_{\rm Smax}$ is almost the same for any aspect angle, except for $\phi_{\rm o} < 30^{\rm o}$ in the quasiparallel model. In the case of quasiparallel injection, the angle $\phi_{\rm o} = 30^{\rm o}$ roughly separates cases with a centrally peaked morphology ($\phi_{\rm o} < 30^{\rm o}$) and a bilateral one ($\phi_{\rm o} > 30^{\rm o}$).

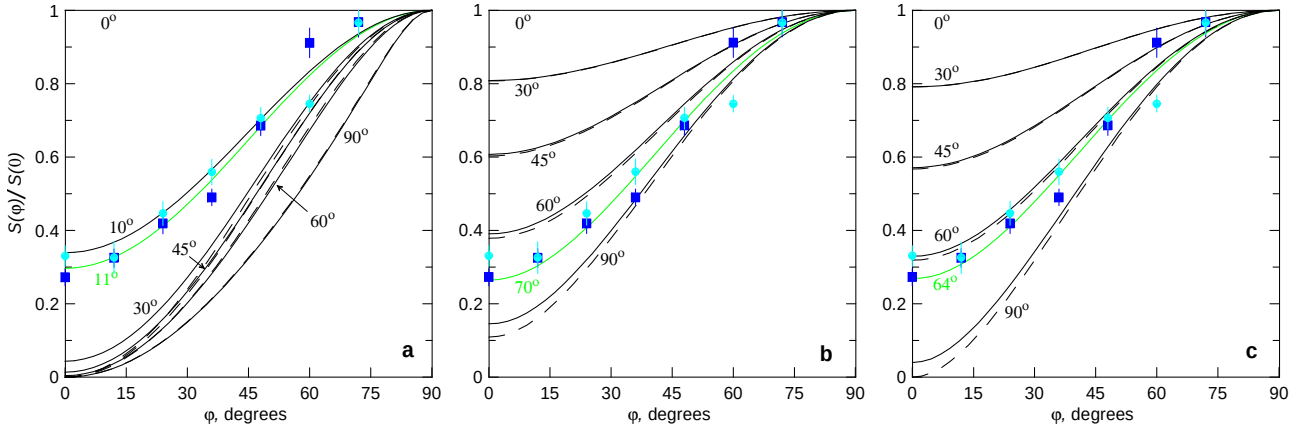

Figure 5.19. Azimuthal variation of the radio surface brightness $S(\varrho_{\rm Smax}, \varphi)$ for different aspect angles $\phi_{\rm o}$. Numerical results (solid lines) are normalized to $S(\varrho_{\rm Smax}, \pi/2)$. Calculations are done for $b = 0$, $\beta = 0$, $s = 2.2$; the plots however are almost the same for different values of b, β and s. The models of injection are quasi-parallel (**a**), isotropic (**b**) and quasi-perpendicular (**c**). $\bar{\varrho}_{\rm Smax} = 0.98$ (**a**) and $\bar{\varrho}_{\rm Smax} = 0.97$ (**b**, **c**). Experimental data for SN 1006 are shown for region I (dark) and II (light). They are measured at 1.5 GHz between 12 and 14 arcmin from the centre and are normalized to the maximum value of 1-σ errors. Azimuthal profiles given by the approximate formula (5.15) are shown by dashed lines.

date targets of this study. In this SNR, uniform conditions are likely to be achievable since SN 1006 is located over 500 pc above the galactic plane. In addition, the SE edge of the SNR exhibits a near-spherical shape, a good argument for expansion of the shock into a uniform ISM.

To determine the MF orientation we only considered the SE half of SN1006 (regions I and II on Fig. 5.1) because this part is quite spherical and therefore is more appropriate for comparison with the numerical results obtained in Sect. 5.3.1 for a SNR in uniform ISM. From the radio map of SN 1006, we extracted the radial brightness profiles (along radii of the SNR projection separated on $\Delta\varphi = 12$ degrees). The experimental radial distributions are subject to pixel-to-pixel variations. In order to lower the possibility of error due to fluctuations in observational data, we calculated the averages of brightness and 1-σ errors within 12 to 14 arcmin from the centre of SN 1006 (where the maximum in radial distribution of the surface brightness is located).

Experimental data are compared with the theoretical results on Fig. 5.19. The estimated aspect angle $\phi_{\rm o}$ differs much for the polar-cap and the equatorial-rim models of SN 1006. From the numerical simulations, the best-fitted aspect angle is $\phi_{\rm o} = 70^{\rm o} \pm 4.2^{\rm o}$ for isotropic injection, $\phi_{\rm o} = 64^{\rm o} \pm 2.8^{\rm o}$ for quasi-perpendicular

injection and $\phi_{\rm o} = 11^{\rm o} \pm 0.8^{\rm o}$ for quasi-parallel injection. Considering an isotropic injection and equatorial-rim model for SN 1006, Reynolds [302] found a similar aspect angle, $\phi_{\rm o} = 60^{\rm o}$.

5.3.3. Implications for model of injection. We found that the azimuthal profiles of the radio surface brightness of the Sedov SNR are almost independent of the shapes of the distributions of relativistic electrons and magnetic field downstream of the shock. Close to the shock, the azimuthal variations of the radio brightness of the SNR may be approximately described as (Appendix C.2):

$$S_\varrho(\varphi) \propto \varsigma(\Theta_{\rm o,eff}(\varphi,\phi_{\rm o}))\ A_{\rm B}(\Theta_{\rm o,eff}(\varphi,\phi_{\rm o}))^{(s+1)/2} \tag{5.15}$$

In order to compare the approximate azimuthal profiles given by this formula with the numerical results, we plotted them on Fig. 5.19 with dashed lines. This figure shows that (5.15) can be used as an approximation for the azimuthal distributions of the radio surface brightness in SNRs evolving in uniform medium and uniform magnetic field.

It is worth emphasizing that our analysis may have some implications for the model of injection efficiency.

Our argument against the quasi-parallel injection is the morphology of SN 1006 it should have in uniform ISM and uniform ISMF. Fig. 5.20 shows an image of SN 1006 in case of the quasi-parallel injection ($\varsigma \propto \cos^2\Theta_{\rm s}$) and aspect angle $\phi_{\rm o} = 11^{\rm o}$. Since the ambient magnetic field should be almost aligned with the line of sight and injections prefer parallel shocks ('polar caps' directed toward and away from observer), the brightness distribution of SN 1006 should be centrally brightened (with one or two radio 'eyes' within thermal X-ray rim), contrary to what is observed.

Our argument seems therefore to disagree with polar-cap morphology, and favour a NW-SE orientation of interstellar magnetic field around this SNR.

Rothenflug et al. [321] suggested a criterion, which is considered as an argument on behalf of the polar-cap model for SN 1006. Namely, if SN 1006 has an equatorial rim the observer should see some emission between the bright limbs. Numerically, the value of the parameter $R_{\pi/3}$ defined as a ratio between total power coming from

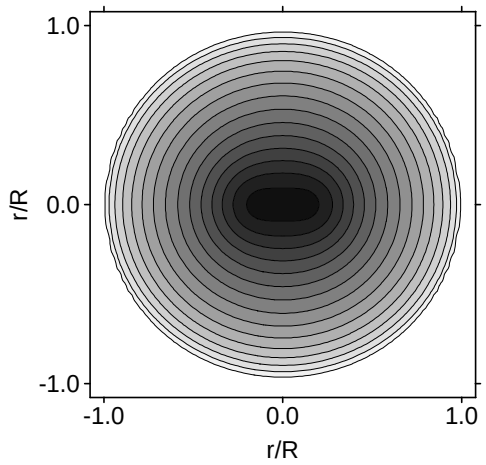

Figure 5.20. Surface brightness distribution (in linear scale) of SNR with the same parameters as on Fig. 5.19. The surface brightness distribution is calculated assuming the quasi-parallel model of injection and the aspect angle $\phi_o = 11^o$. The component of ISMF in the plane of the sky is parallel to the horizontal axis. The levels of brightness are spaced in the same way as on the Fig 5.18.

the interior and that from the limbs should be $R_{\pi/3} > 0.5$ if SN 1006 is a barrel. The most likely explanation for the smaller value of $R_{\pi/3}$ is that the visible limbs are polar caps [321]. The value of this ratio is $R_{\pi/3} \approx 0.7$ in radio [321]. Therefore, based on the $R_{\pi/3}$ criterion alone, the radio data itself cannot give preference neither to equatorial-rim nor to polar-cap model of SN 1006. However, $R_{\pi/3} \leq 0.3$ in X-rays [321], prefering therefore the latter model.

To this end, our argument against polar caps are in contradiction with $R_{\pi/3}$-criterion applied to X-ray data. Note, that the $R_{\pi/3}$-criterion is obtained for cylindrical source of isotropic emission. It would be interesting to see how deviations from this assumption may affect the criterion. Our models assume a uniform ISM and uniform ISMF. Could it be possible to reproduce the bilateral morphology (i.e. to obtain $\phi_o > 30^o$) with quasiparallel injection if one considers a gradient in the ISMF? Assuming the contrast of the ISMF between the NE and SE regions can be determined by the relationship $B_{SE}/B_{NE} \simeq (S_{SE}/S_{NE})^{2/3}$, a ratio of 4 for $\phi_o = 45^o$, and 20 for 60^o, could make the azimuthal profile of radio emission comparable to the observed one. Further investigation, including multi-dimensional modeling of SN 1006, as recent VHE γ-ray data could help us to understand the nature of morphology of this SNR.

5.4. Observational constraints on SN 1006

The question of the origin of TeV γ-rays is closely related to the problem of the presence and the role of non-linear effects of cosmic ray acceleration by the forward shock. One of the key parameter distinguishing these two possibilities is the strength (and thus the nature) of the post-shock magnetic field. Classical picture considers only compression of typical ISMF $B_{\rm o} \sim 3\,\mu$G to downstream values of order of tens micro Gauss. Model including non-linear acceleration (NLA) predicts ISMF to be first amplified upstream due to the back reaction of accelerated protons to $B_{\rm o} \sim 30\,\mu$G and then compressed above hundred micro Gauss. In the former case the IC emission of electrons would be responsible for the most of TeV γ-rays, in the latter case the proton-origin TeV γ-radiation is expected to be dominant.

The spectrum of SN 1006 may be explained in these two scenarios. One limiting possibility (we call it 'extreme NLA model'), namely the case of ISMF amplified and compressed to $B_{\rm s} \approx 150\,\mu$G is considered in details by Berezhko et al. [83]. The model successfully fits the broadband nonthermal spectrum from SN 1006 and the sharpest radial profile of the X-ray brightness. TeV γ-rays are shown to be produced in both the inverse-Compton mechanism and the pion-decay one, the latter is dominant.

We present a new way to compare model and observations, namely, our goal is to investigate the formation of the patterns of the nonthermal images in radio, X-rays and γ-rays. At present time, this may be done only with the use of the classic MHD and acceleration scenario. Therefore, the questions behind the present section are: may a classical model explain the radio to TeV γ-ray observations of SN 1006 and can one put observational constraints on some properties of particle kinetics and on MF?

In the present section, such 'classic' model of SN 1006 is described and we use the spatial distribution of the observational data to estimate some parameters of the model. The subsection order is determined by the order of parameters determi-

nation. Namely, the radio azimuthal and radial profiles are analysed in Sect. 5.4.1, variation of the break frequency in Sect. 5.4.2, the broadband spectrum of SN 1006 is calculated in Sect. 5.4.3 to check consistency of our model and to determine the average MF, X-ray and γ-ray brightness are subject to Sect. 5.4.4. Sect. 5.4.5 presents critical discussion about both our 'cassical' and NLA models of SN 1006.

5.4.1. Radio maps. Let us consider an SNR in uniform ISM and uniform ISMF, in the adiabatic stage of evolution. The Sedov solution is therefore applied for hydrodynamics. We consider ideal gas with the adiabatic index $\gamma = 5/3$. MF behaviour is classic, without amplification. Classic (unmodified) shock creates the energy spectrum of relativistic electrons in the form $N(E) = KE^{-s}\exp(-E/E_{\max})$.

Azimuthal profiles. Symmetrical bright limbs in SN 1006 limit possible orientations of ISMF in the plane of the sky (Sect. 5.3). Close to the shock, the azimuthal distribution of the radio surface brightness $S_{\rm r}$ is mostly determined by $S_{\rm r}(\varphi) \propto \varsigma(\varphi)\ \sigma_{\rm B}(\varphi)^{(s+1)/2}$. If injection is isotropic, $\varsigma(\Theta_{\rm o}) = {\rm const}$, $\Theta_{\rm o}$ the obliquity angle, (or prefers quasi-perpendicular shocks) then the bright radio limbs correspond to projection of the equatorial belt with NW-SE orientation of ISMF (BarMF or barrel-like model). If injection prefers quasi-parallel shocks, the bright limbs of SN 1006 are two polar caps and ISMF should be oriented in the NE-SW direction (model CapMF). ISMF creates an aspect angle $\phi_{\rm o}$ with the line of sight. The comparison of the experimental azimuthal profiles of the radio brightness with profiles from theoretically synthesized radio images allows us to determine an aspect angle. It is $\phi_{\rm o} = 70^{\rm o}$ for BarMF. For a sake of generality, in the next subsection, we explore also the CapMF model with $\phi_{\rm o} = 70^{\rm o}$ (in the polar caps morphology, the aspect angle larger than $\simeq 50^{\rm o}$ keeps the two radio limbs in the observed locations).

Radial profiles. The post-shock value of the normalization $K_{\rm s}$ is proportional to the injection efficiency ς (the fraction of accelerated electrons in the total post-shock electron density $n_{\rm es}$). Injection efficiency may vary with the shock strength. We assume that $K_{\rm s} \propto V^{-b}$ where V is the shock velocity, b is a parameter.

It may be shown (Appendix E.1) that the surface brightness distribution of Sedov SNR in the radio band is

$$S_{\rm r} = {\rm const}\ \mathcal{S}_{\rm r}(\bar{\rho}, \varphi; \phi_{\rm o}, b)\ \nu^{-(s-1)/2} K_{\rm s\parallel} B_{\rm o}^{(s+1)/2} R \tag{5.16}$$

where $\bar{\rho} = \rho/R$, ρ is the coordinate along radius of SNR. For fixed φ, $\mathcal{S}_{\rm r}(\bar{\rho})$ is a universal profile which, for a given dependence of $\varsigma(\Theta_{\rm o})$, aspect angle $\phi_{\rm o}$ and index s, depends only on the parameter b[5].

Let us use the experimental radio image of SN 1006 [281] for determination of b. We extract the radial profiles of the radio brightness along a number of the regions shown on Fig. 5.21. They are presented on Fig. 5.22 together with the theoretical profiles $\mathcal{S}_{\rm r}(\bar{\rho}; b)$ calculated numerically for three values of $b = -1, 0, 1$. Close to the shock front, the experimental profiles seems to be between theoretical ones calculated for $b = -1$ and $b = 0$.

However, Fig. 5.22 demonstrates that theoretical profiles of the radio brightness calculated for Sedov SNR in uniform ISM/ISMF do not follow the experimental data to larger extend, namely for $\rho < 0.94R$. The reason of such behavior could be nonuniformity of ISMF (or ISM). The radio profiles from SW limb support such scenario: they monotonically increase from the shock to $\simeq 0.85R$ (Fig. 5.21) while the maximum of the radio brightness in Sedov SNR should be located around $\simeq 0.97R$. In the present study, we adopt $b = 0$.

5.4.2. Obliquity dependence of the maximum energy. Dependence of $E_{\rm max}$ on obliquity angle $\Theta_{\rm o}$ is represented with $E_{\rm max}(\Theta_{\rm o}) = E_{\rm max\parallel} f_{\rm E}(\Theta_{\rm o})$. Sect. 5.1 consider 30 small regions around the whole forward shock of SN 1006. Spectral fitting of X-ray emission from these regions results in particular in azimuthal variation of $\nu_{\rm break}$, a parameter in *srcut* model of XSPEC which is related to the maximum energy of electrons as

$$E_{\rm max} = c_1^{-1/2} \nu_{\rm break}^{1/2} B_{\rm s}^{-1/2}. \tag{5.17}$$

[5]Eq. (5.16) shows also that the universal azimuthal profile of the radio brightness $\mathcal{S}_{\rm r}(\varphi)$ depends only on the aspect angle $\phi_{\rm o}$ because b is assumed to be independent of obliquity. This property allowed us to determine $\phi_{\rm o}$ from the radio map (Sect. 5.4.1)

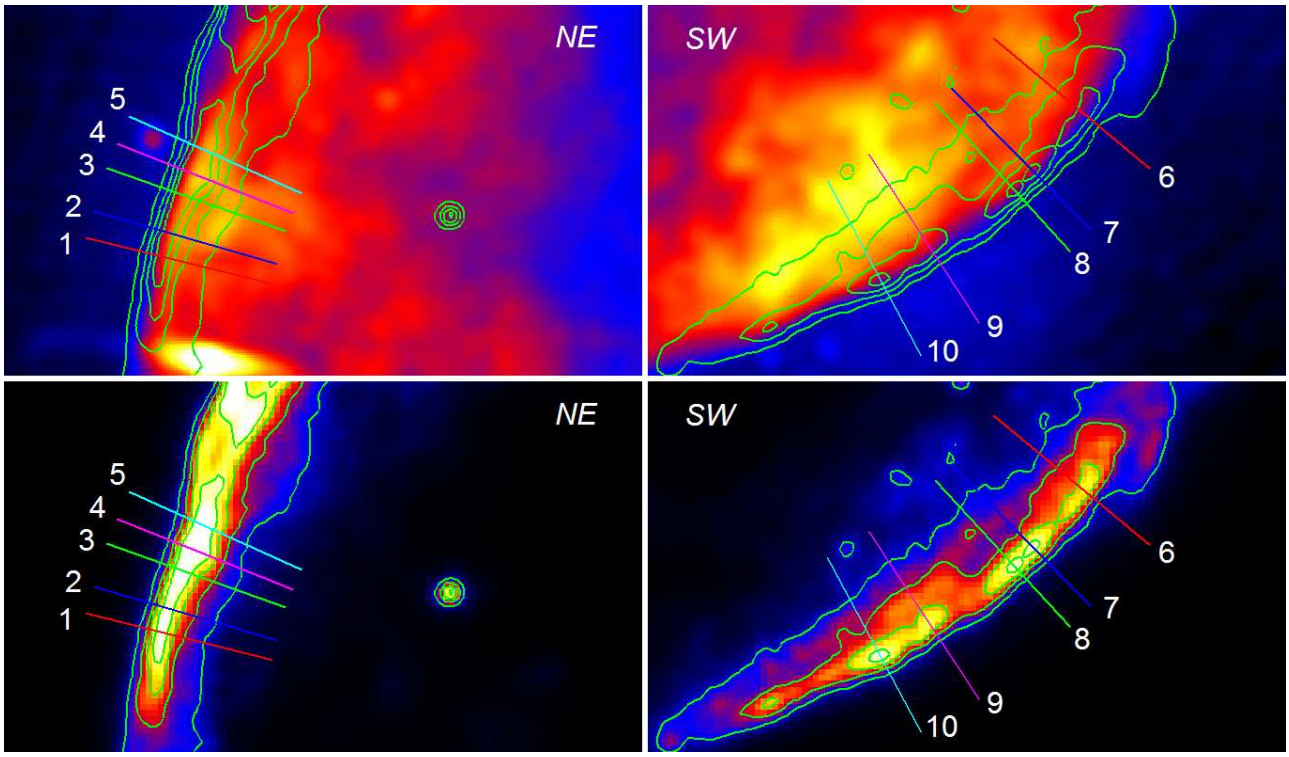

Figure 5.21. NE and SW limbs of SN 1006 in radio at $\lambda \sim 20\,\mathrm{cm}$ (top panels) and X-rays with energy 2-4.5 keV (bottom panels) [250, 281]. The maximum value of brightness is 100 times the minimum one, in the radio and X-ray images. Radio image is smoothed with Gaussian with $\sigma = 0.4'$ to lower fluctuations. Color straight lines mark the regions used for extraction of the radial profiles of brightness; length of regions shown is from $0.8R$ to $1.1R$. Green lines represent X-ray contours, linearly spaced.

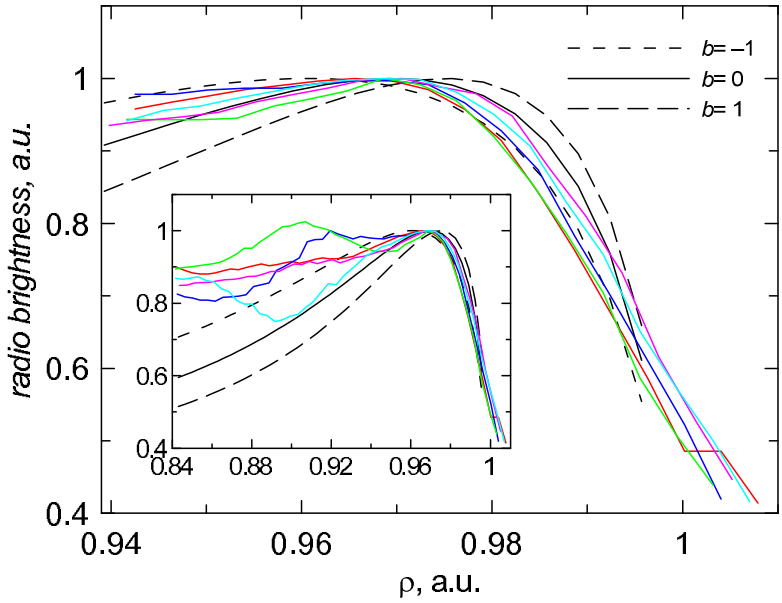

Figure 5.22. Radial profiles of the radio brightness in NE limb of SN 1006. Experimental profiles (from regions 1-5, Fig. 5.21) are in color. Theoretical profiles are in black, for $b = -1$ (dot), $b = 0$ (solid), $b = 1$ (dashed). They are calculated for $s = 2$, $\phi_o = 70^o$, isotropic injection and $\varphi = 70^o$ ($\varphi = 65^o - 75^o$ for the observational profiles).

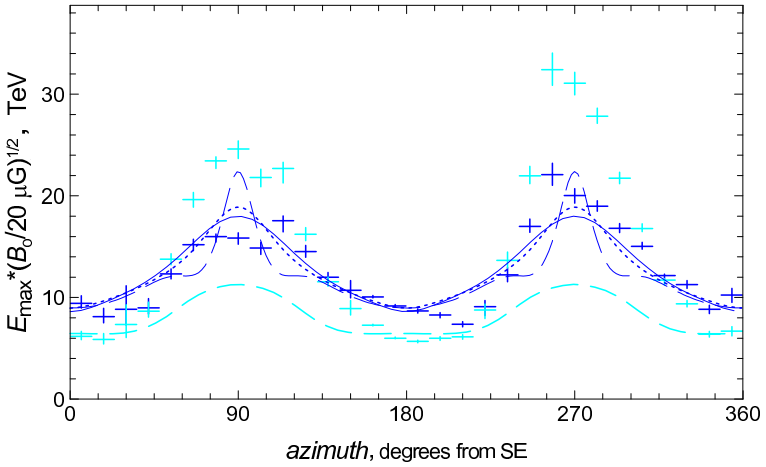

Figure 5.23. Variation of $E_{\max}$ (shown with vertical one-sigma errors) over the forward shock in SN 1006, obtained from experimental data on $\nu_{\rm break}$ and Eq. (5.17), for two models of ISMF: BarMF (dark crosses), CapMF (light crosses). Aspect angle $\phi_{\rm o} = 70^{\rm o}$. Dashed light line: the loss-limited model with $\eta = 1$ for CapMF. Solid dark line: the time-limited model with $\eta = 1.5$ for BarMF. Dashed dark line: the loss-limited model with $\eta = 7.6$ for BarMF. Dotted dark line: the loss-limited model with $\eta = 3.1$ for BarMF and IC radiative losses of electrons included, $B_{\rm o} = 0.65\,\mu$G.

where $B_{\rm s}$ is the strength of the post-shock MF. We use this relation together with the experimental data on $\nu_{\rm break}$ to determine the function $E_{\max}(\varphi)$.

The azimuthal profiles of $E_{\max}$ determined with (5.17) for two models of ISMF is shown on Fig. 5.23.

In the frame of the classical theory of acceleration, Reynolds [303] developed three different theoretical models for surface variation of $E_{\max}$. Namely, the maximum energy of accelerated electrons may be determined 1) by the electron radiative losses, 2) by the limited time of acceleration and 3) by escaping of particles from the region of acceleration. The third model results in constant $E_{\max}$ that contradicts to Fig. 5.23. We do not consider it. The rest two models depend on the level of turbulence reflected by the ratio $\eta \geq 1$ of the mean free path of particle to its Larmour radius.

Minimum of $\Theta_{\rm o}$ happens in SN1006 at azimuth $0^{\rm o}$ for BarMF and at azimuth $90^{\rm o}$ for CapMF. Therefore, $E_{\max}$ is expected to increase or decrease with obliquity for BarMF and CapMF respectively (Fig. 5.23). In the loss-limited model of $E_{\max}$, the function $f_{\rm E}(\Theta_{\rm o})$ increases with increasing obliquity for $\eta \geq 3$. In the time-limited model, the function $f_{\rm E}(\Theta_{\rm o})$ increases with obliquity for any η. In contrast, Fig. 5.23 shows decrease of $E_{\max}$ from $\varphi = 90^{\rm o}$ to $180^{\rm o}$ for CapMF (light crosses). Thus, the

time-limited model and loss-limited with $\eta \geq 3$ are not applicable if one considers polar-caps morphology of SN 1006. In the loss-limited case, the fastest decrease with obliquity is for $\eta = 1$ but it does not fit the experimental profile of $E_{\rm max}$ for model CapMF (light dashed line on Fig. 5.23). To the end, the NE-SW orientation of ISMF (CapMF, polar caps) is not able to explain observed azimuthal variation of $\nu_{\rm break}$, under assumptions of uniform ISMF/ISM and classic MHD/acceleration. We tried also other aspect angles, $\phi_{\rm o} > 50^{\rm o}$, with and without inclusion of IC radiative losses. However, the conclusion remains unchanged.

In case BarMF (dark crosses), the function $f_{\rm E}(\Theta_{\rm o})$ for SN 1006 may be determined by fitting experimental data with a model of [303]. The best-fit in the time-limited model is reached for $\eta = 1.5 \pm 0.02$ ($\chi^2/{\rm dof} = 12.7$, solid dark line on Fig. 5.23). The best-fit for the loss-limited model is for $\eta = 7.6 \pm 0.11$ ($\chi^2/{\rm dof} = 25.8$, dashed dark line) but the shape of the fit does not follow well the observed one. The last fit becomes better after inclusion of IC radiative losses of relativistic electrons: $\eta = 3.1 \pm 0.02$ ($\chi^2/{\rm dof} = 14.0$, dotted dark line). ISMF in this case is lower, $B_{\rm o} = 0.65\,\mu$G that results in $E_{\rm max}$ about 120 TeV in NE limb. Though so low pre-shock MF could be relevant for the location of SN 1006 far above the Galactic plane, it looks to be unreasonable to provide observed radially-thin X-ray limbs as well as synchrotron and inverse-Compton spectra.

Thus, the azimuthal variation of $\nu_{\rm break}$ may be explained in the frame of the classic MHD/acceleration theories. It limits ISMF orientation to only BarMF configuration, in agreement with the same conclusion obtained from azimuthal fits of the radio surface brightness (Sect 5.3). If so, the efficiency of injection should be quasi-isotropic (i.e. almost independent of obliquity) in the classical model of SN 1006. The time-limited model of [303] with $\eta = 1.5$ is the most appropriate for $E_{\rm max}(\Theta_{\rm o})$; we use it the present section. In this model, the maximum energy of accelerated electrons varies with time very slowly [303]. We assume therefore that $E_{\rm max}$ is independent of the shock velocity.

Solid dark line on Fig. 5.23 shows that $E_{\rm max} = 8.5(B_{\rm o}/20\,\mu{\rm G})^{-1/2}$ TeV at azimuth $\varphi = 0$. Because the aspect angle $\phi_{\rm o} = 70^{\rm o}$, this value of $E_{\rm max}$ corresponds therefore

to the obliquity $\Theta_{\rm o} = 20^{\rm o}$. It is smaller at the parallel shock, namely $E_{\max\parallel} = 0.644 E_{\max}$ for $\eta = 1.5$ [303]. Therefore,

$$E_{\max\parallel} = 5.4 \left(\frac{B_{\rm o}}{20\,\mu{\rm G}}\right)^{-1/2} \ {\rm TeV}. \tag{5.18}$$

The same time-limited model predicts $E_{\max\perp} = 3.25 E_{\max\parallel}$.

5.4.3. Total radio, X-ray and TeV gamma-ray spectrum. In calculations of the synchrotron spectrum, the self-similarity of Sedov solutions allows us to represent all the properties of the downstream evolution of the fluid elements, the magnetic field and the relativistic electrons in the SNR interior by a universal constant $\zeta_{\rm r}$ and modification factor $\eta_{\rm syn}$; the former convolves the volume distribution of the radio emissivity, the latter reflects the deviation of the X-ray spectrum from the power-law (for more details see Appendix F.1). Namely, in a broad band (from radio to X-rays), the synchrotron spectrum of the volume-integrated emission from the whole SNR may be represented by (Appendix F.1)

$$F_{\rm syn}(\nu) = C_{\rm r}\zeta_{\rm r}\nu^{-(s-1)/2}\eta_{\rm syn}(\tilde{\varepsilon};\epsilon_{\rm f\parallel})B_{\rm o}^{(s+1)/2}K_{\rm s\parallel}R^3 d^{-2} \tag{5.19}$$

where $C_{\rm r}$ is a constant, d the distance to SNR, R the SNR radius.

The constant $\zeta_{\rm r}$ is different for different models (Appendix F.1); it is $\zeta_{\rm r} = 2.68$ (for $s = 2.0$) or $\zeta_{\rm r} = 2.77$ (for $s = 2.1$) in our model of SN 1006, i.e. for the BarMF model of MF and the isotropic injection (Sect. 5.4.2) and $b = 0$ (Sect. 5.4.1).

Reduced photon energy is defined as $\tilde{\varepsilon} = \tilde{\nu} = \nu/\nu_{\rm c}(E_{\max\parallel}, B_{\rm o})$, $\nu_{\rm c}(E,B) = c_1 \langle\sin\phi\rangle E^2 B$ is the synchrotron characteristic frequency:

$$\tilde{\varepsilon} = 9.5\ \varepsilon_{\rm keV} \left(\frac{E_{\max\parallel}}{10\,{\rm TeV}}\right)^{-2} \left(\frac{B_{\rm o}}{20\,\mu{\rm G}}\right)^{-1}, \tag{5.20}$$

where $\varepsilon_{\rm keV}$ is the photon energy in keV. With Eq. (5.18), this becomes $\tilde{\varepsilon} = 32.6\varepsilon_{\rm keV}$.

The reduced fiducial energy $\epsilon_{\rm f} = 637\left(B_{\rm s}^2 t E_{\max}\right)^{-1}$ is one of the key parameter for modeling the X-ray and γ-ray emission [303]. The energy $\epsilon_{\rm f}$ is a measure of importance of radiative losses in modification of the high-energy end of electron spectrum and therefore of the X-ray and γ-ray spectra and images: radiative losses are essential for $\epsilon_{\rm f} < 1$; if $\epsilon_{\rm f} > 1$, adiabatic losses are dominant even for electrons

with $E \sim E_{\rm max}$ [303]. With Eq. (5.18) and the age $t = 1000\,$yrs,

$$\epsilon_{\rm f\parallel} = 5.8 \left(\frac{B_{\rm s\parallel}}{20\,\mu{\rm G}} \right)^{-3/2}, \tag{5.21}$$

$\epsilon_{\rm f\perp}$ is $\sigma_{\rm B}^2 E_{\rm max\,\perp}/E_{\rm max\,\parallel} = 52$ times smaller because both $B_{\rm s}$ and $E_{\rm max}$ are larger at the perpendicular shock.

The modification factor $\eta_{\rm syn}(\nu)$ shows how the synchrotron spectrum $F_{\rm syn}(\nu)$ deviates from the power-low dependence $\nu^{-(s-1)/2}$. The modification factor is defined to be $\eta_{\rm syn} = 1$ for the radio band; it is effective in the X-ray band and rather quickly approaches unity with ν decreasing below $\nu_{\rm c}(E_{\rm max}, B)$.

In a similar fashion, the spectral distribution of the IC emission from the whole SNR is (Appendix F.2)

$$F_{\rm ic}(\nu) = C_{\rm T}\zeta_{\rm T}\nu^{-(s-1)/2}\eta_{\rm ic}(\nu, \epsilon_{\rm f\parallel}, E_{\rm max\parallel})K_{\rm s\parallel}R^3 d^{-2}. \tag{5.22}$$

where $\eta_{\rm ic}$ is the modification factor and $\zeta_{\rm T}$ the universal constant for IC γ-rays (exact definitions are given in Appendix F.2). For our model of SN 1006 (isotropic injection, $b = 0$), $\zeta_{\rm T} = 0.81$ for $s = 2$ and $\zeta_{\rm T} = 0.79$ for $s = 2.1$.

Fit to the radio spectrum. One choice for the spectral index $\alpha = (s-1)/2$ of the synchrotron spectrum could be $\alpha = 0.5$; a value found during local fitting the broad-band synchrotron emission [250]. The joint fit of the X-ray spectrum and the radio flux was done for each of 30 small regions around the whole shock of SN 1006 where the most of the synchrotron emission arises. The value $\alpha = 0.5$ is almost within 1-σ error of the best-fit $\alpha = 0.6^{+0.08}_{-0.09}$ [54], obtained for the radio fluxes from SN 1006 at 8 different radio frequencies (most of the fluxes are from [252]). The best-fit ($\chi^2/{\rm dof} = 1.0$) for these radio data and fixed $\alpha = 0.5$ is

$$F_{\rm r,obs}(\nu) = 18.4\,(\nu/1\,{\rm GHz})^{-0.5}\ {\rm Jy}. \tag{5.23}$$

Another choice we consider is $\alpha = 0.55$ (i.e. $s = 2.1$), a value successfully used in the broad-band model of the synchrotron and IC spectrum of SN 1006 [28]. The best-fit ($\chi^2/{\rm dof} = 0.56$) for the same radio data and fixed $\alpha = 0.55$ is

$$F_{\rm r,obs}(\nu) = 18.1\,(\nu/1\,{\rm GHz})^{-0.55}\ {\rm Jy}. \tag{5.24}$$

Fit to the X-ray spectrum. The X-ray modification factor is compared with the observations on Fig. 5.24. The use of the modification factor allows us to avoid uncertainties in distance, SNR radius and density of emitting electrons. The experimental modification factor $\eta_{\rm x,obs}$ is calculated with the use of the SUZAKU X-ray spectrum $F_{\rm x,obs}$ from the whole SN 1006 (Fig. 6 in [64]) as a ratio of the observed X-ray spectrum to the extrapolation of the radio spectrum to X-rays

$$\eta_{\rm x,obs}(\nu) = \frac{F_{\rm x,obs}(\nu)}{F_{\rm r,obs}(\nu)}. \tag{5.25}$$

This definition and Eqs. (5.20) with (5.18) provides the modification factor $\eta_{\rm x,obs}(\tilde{\nu})$ to be essentially independent of MF. Theoretical $\eta_{\rm x}(\tilde{\varepsilon};\epsilon_{\rm f\parallel})$, for fixed s, b, $f_{\rm K}(\Theta_{\rm o})$ and $f_{\rm E}(\Theta_{\rm o})$, is a function of the reduced fiducial energy $\epsilon_{\rm f\parallel}$ only. This parameter reflects the efficiency of the radiative losses on the evolution of electrons with energies around $E_{\rm max}$ and therefore on the shape of the synchrotron X-ray spectrum. In SN 1006, it is related to $B_{\rm o}$ with Eq. (5.21).

The strength of ambient MF $B_{\rm o} = 25\,\mu$G together with $s = 2.0$ provide agreement between the X-ray modification factors in our model and observations (Fig. 5.24 blue line). Smaller MF, $B_{\rm o} = 12\,\mu$G fits SUZAKU spectrum if $s = 2.1$ (Fig. 5.24 green line). Thus, the radio and X-ray synchrotron spectrum from the whole SNR may be fitted with few sets of $B_{\rm o}$ and s.

The value $B_{\rm o} = 25\,\mu$G is close to that found in the extreme NLA model [83]. However, NLA model assumes that $B_{\rm o}$ is compressed by the shock to the level $B \approx 150\,\mu$G and such high strength is the same everywhere in the SNR volume. In contrast, our model allows for the large compressed MF only close to the perpendicular shock; an average MF in the classical model of SN 1006 is smaller than in the extreme NLA case.

Fit to the TeV γ-ray spectrum. Fig. 5.25 compares the modification factor $\eta_{\rm ic}$ for γ-rays with observations. The experimental modification factor $\eta_{\gamma,\rm obs}$ is calculated from TeV γ-ray spectrum $F_{\gamma,\rm obs}$ of SN 1006 [28]. It is evaluated as a ratio $\eta_{\gamma,\rm obs} =$

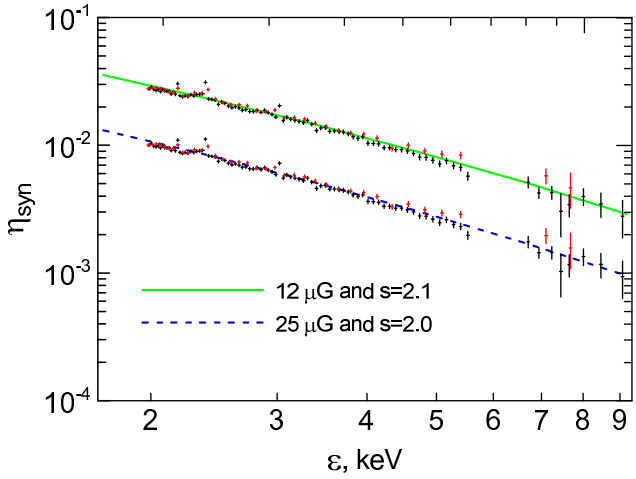

Figure 5.24. The modification factors $\eta_{\rm syn}$ in our model of SN 1006 for a set ($B_{\rm o} = 25\,\mu$G, $s = 2.0$) is shown by the blue line and for a set ($B_{\rm o} = 12\,\mu$G, $s = 2.1$) by the green line. The modification factors calculated from SUZAKU data [64] are also shown for cases $s = 2.0$ (lower) and $s = 2.1$ (upper).

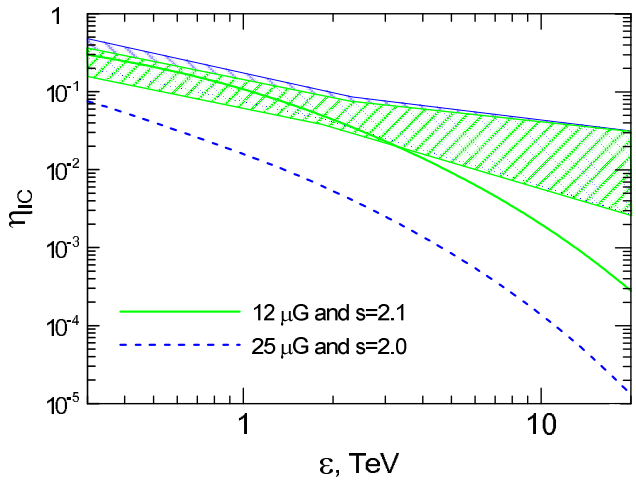

Figure 5.25. The modification factor $\eta_{\rm ic}$ for our model of SN 1006 (lines) and from the data of ([28] shaded regions) for the parameter sets ($B_{\rm o} = 12\,\mu$G, $s = 2.1$) and ($B_{\rm o} = 25\,\mu$G, $s = 2.0$).

$F_{\gamma,\rm obs}/F_{\rm T}$ of the observed γ-ray spectrum to the extrapolation of the Thomson IC spectrum to TeV γ-rays. The latter is found from the radio spectrum as $F_{\rm T} = (F_{\rm T}/F_{\rm r})_{\rm theor}\, F_{\rm r,obs}$ where the ratio $(F_{\rm T}/F_{\rm r})_{\rm theor}$ is calculated with Eqs. (5.19) and (5.22) for $\eta_{\rm syn} = \eta_{\rm ic} = 1$. Thus,

$$\eta_{\gamma,\rm obs} = \frac{F_{\gamma,\rm obs}}{F_{\rm r,obs}} \frac{C_{\rm r}\zeta_{\rm r}}{C_{\rm T}\zeta_{\rm T}} B_{\rm o}^{(s+1)/2}. \tag{5.26}$$

The transformation of the observational TeV spectrum $F_{\gamma,\rm obs}$ to the modification factor $\eta_{\gamma,\rm obs}$ depends directly on the magnetic field strength. Note that this is not a new way to estimate MF but just a different representation of the method used by Berezhko and Volk [362].

TeV γ-ray spectrum is almost restored by by the pure IC emission in the model with $B_{\rm o} = 12\,\mu$G and $s = 2.1$ (Fig. 5.25 green line). The model with $25\,\mu$G and $s = 2.0$ which is supported by the X-ray spectrum as well (Fig. 5.24) does not agree with the TeV spectrum (Fig. 5.25 blue line) if the only leptonic γ-ray emission is considered. Larger MF results in requirement of an additional component to fit TeV spectrum, as it is in NLA model of [83] or in a mixed or hadronic models of [28].

Further in the present section, we consider the pure leptonic model for the TeV γ-ray emission to see whether it satisfies other observational data on SN 1006; thus, we assume $B_{\rm o} = 12\,\mu$G. We would like to note the difference between the spectral index $s_{\rm tot} = 2.1$ for SN 1006 as a whole and the local indexes $s_{\rm loc} = 2.0$ representing small regions covering the SNR edge [250]. We shall analyse the azimuthal and radial profiles of the surface brightness extracted from regions located quite close to the shock and use $s = 2.0$ for this purpose, a value found during the fits of the local X-ray spectra around the shock. However, our calculations show that $s = 2.1$ results in almost the same profiles of brightness.

5.4.4. X-ray and gamma-ray maps.

X-ray azimuthal profiles. It may be shown (Appendix E.1) that the distribution of the surface brightness of Sedov SNR due to synchrotron emission may be represented by

$$S_{\rm x} = \text{const}\ \mathcal{S}_{\rm x}(\tilde{\nu}, \bar{\rho}, \varphi; \phi_{\rm o}, b, \epsilon_{\rm f\parallel})\ E_{\rm max}^{1-s} K_{\rm s\parallel} B_{\rm o} R. \tag{5.27}$$

The universal *shape* $\mathcal{S}_{\rm x}$ of the radial (for fixed φ) and azimuthal (for fixed $\bar{\rho}$) profiles is determined just by one parameter, $\epsilon_{\rm f\parallel}$, if s, $\phi_{\rm o}$, b as well as an obliquity dependence of the injection efficiency and a model for the maximum energy of electrons are fixed. In case $\epsilon_{\rm f\parallel} \gg 1$ and/or $\tilde{\nu} \ll 1$, the role of radiative losses on the downstream electron distribution is negligible and the profiles of the brightness is then independent of the fiducial energy:

$$S_{\rm x} = \text{const}\ \mathcal{S}_{\rm r}(\bar{\rho}, \varphi; \phi_{\rm o}, b)\ \tilde{\nu}^{-(s-1)/2} E_{\rm max}^{1-s} K_{\rm s\parallel} B_{\rm o} R, \tag{5.28}$$

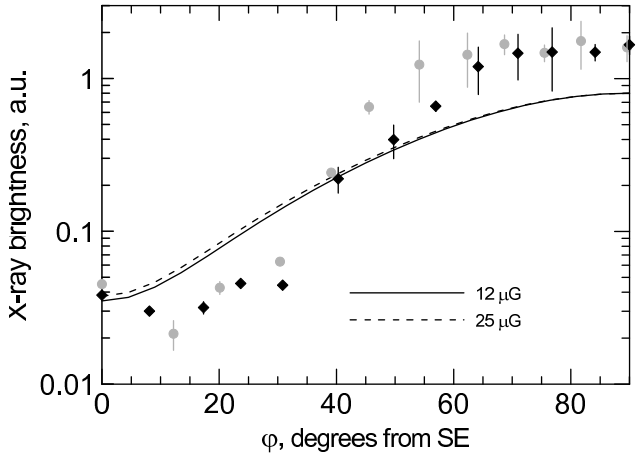

Figure 5.26. Azimuthal profile of the X-ray brightness at fixed $\bar{\rho}$ which corresponds to the maximum of the radial distribution of brightness at $\varphi = \pi/2$. Calculations are done for $B_0 = 12\,\mu$G (solid line) and $25\,\mu$G (dashed line); $s = 2$, $\varepsilon = 1.2\,$keV. Experimental data are taken from the hard X-ray image of SN 1006 (Sect. 5.1.3): profile from SE to SW is by circles, profile from SE to NE is by diamonds.

that is the same as Eq. (5.16) for the radio brightness. On the other hand, calculations show that the role of evolution of injection efficiency in time (which is represented by b) is less important for X-rays than for the radio because radiative losses (represented by $\epsilon_{\mathrm{f}\parallel}$) is dominant in determination of the downstream distribution of X-ray emitting electrons.

In our model of SN 1006, even $\epsilon_{\mathrm{f}\parallel}$ is not already free parameter, because it is determined through Eq. (5.21) by the strength of MF. Fig. 5.26 compares theoretical and experimental results. Experimental data are derived averaging X-ray brightness along radii within annuli centered on the remnant and covering maximum in limbs (from $13.8'$ to $14.8'$ off the center for SE-NE and from $14.4'$ to $15.2'$ for SE-SW profile). The hard X-ray image of SN 1006 (Sect. 5.1.3) was used. Synthesized azimuthal profiles of the X-ray brightness agree with the observations though the fit is not ideal. Simulations reveal that the strength of MF is not important for the azimuthal variation of X-ray brightness. In general, the azimuthal profile depends also on the model of $E_{\max}$ and, in particular, on the gyrofactor η. However, in our model they are already fixed (Sect. 5.4.2).

Another possibility to change the azimuthal variation of the synchrotron X-ray surface brightness in a model is to consider the broader end of the electron spectrum, e.g. $N(E) \propto \exp\left(-\left(E/E_{\max}\right)^{\alpha}\right)$ with $\alpha = 0.5$ [140]. However, such cut off makes

the fit even worse. Really, the azimuthal distribution of the brightness is roughly proportional to $\exp\left(-(E_{\rm m}(\varphi)/E_{\rm max}(\varphi))^{\alpha}\right)$ where $E_{\rm m}$ is the energy of electrons which give the largest contribution to emission at an observed frequency. Fig 5.26 assumes $\alpha = 1$; smaller α results in smaller contrasts between azimuth $\varphi = \pi/2$ and $\varphi = 0$ that is against of the observations.

The differences in the synthesized and observed profiles might be due to nonuniformity of ISMF and/or ISM.

X-ray radial profiles. The method for the MF strength estimation from the radial profile of the X-ray brightness is described by [61, 78]. Radiative losses of electrons with energy E is $\dot{E} \propto E^2 B^2$. These losses are less important for electrons emitting in radio but able to modify effectively the energy spectrum of electrons radiating X-rays. Therefore, comparing to radio, the synchrotron rim is thinner in X-rays (its maximum is located within few percents of the SNR radius from the shock). The idea of the method is that relativistic electrons experience larger radiative energy losses in the stronger magnetic field. This leads therefore to the rapid decrease of the spatial distribution of electrons behind the shock and therefore to thin maximum in the radial X-ray brightness profile. From the observational point of view, the thinner the rim in X-rays the stronger the magnetic field is expected to be.

Fig. 5.27 compares theoretical profiles $\mathcal{S}_{\rm x}(\bar{\rho})$ with data from XMM and Chandra. Simulated distribution with $B_{\rm o} = 12\,\mu$G satisfy XMM data. In our model, the MF compression factor is $\sigma_{\rm B} = 3.8$ at the azimuth $\varphi = 70^{\rm o}$. The post-shock MF is therefore $B_{\rm s} \simeq 45\,\mu$G in both NE and SW limbs. This value could be considered as an upper limit for an average MF within the limbs because some observed profiles are a bit thicker than the theoretical one shown by thick green line. Strength $B_{\rm o} = 25\,\mu$G (long-dashed blue line) does not fit XMM radial profiles of X-ray brightness.

However, the sharpest Chandra profile (Fig. 4A in [232]) may not be explained by $12\,\mu$g field. Our model fits this profile if the post-shock field is $B_{\rm s} \simeq 95\,\mu$G. The same filament was used by [76] to deduce MF $\simeq 130\,\mu$G. Our estimate for the

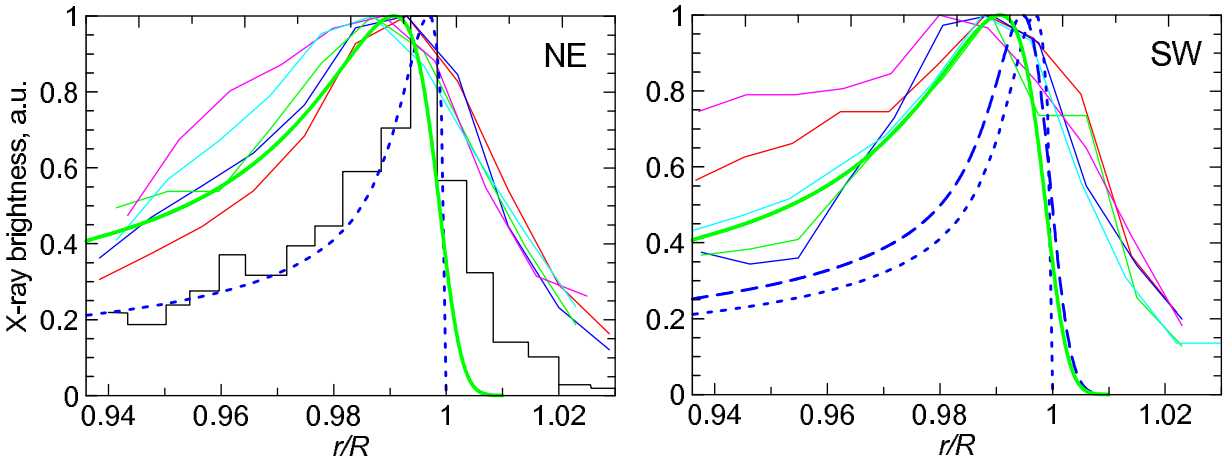

Figure 5.27. Radial profiles of the X-ray brightness in NE (left) and SW (right) limbs of SN 1006. Experimental XMM-Newton profiles (from regions 1-5 and 6-10 respectively, Fig. 5.21) for the photon energy range $2 \div 4.5$ keV are in color. The sharpest Chandra radial profile (from Fig. 4A in [232]) is shown by the histogram (photon energy is $1.2 \div 2$ keV). Theoretical profiles are shown by the thick blue dotted line (for $B_o = 25\,\mu$G, smoothed to the Chandra resolution by Gaussian with sigma $0.2''$), and by the thick green solid line (for $12\,\mu$G, smoothed to the XMM resolution by Gaussian with sigma $2.6''$). They are calculated at 1.2 keV photons, for azimuth $\varphi = 70^o$ in our model of SN 1006, $s = 2$. Theoretical profile for $B_o = 25\,\mu$G smoothed to the XMM-Newton resolution is shown by the long-dashed blue line.

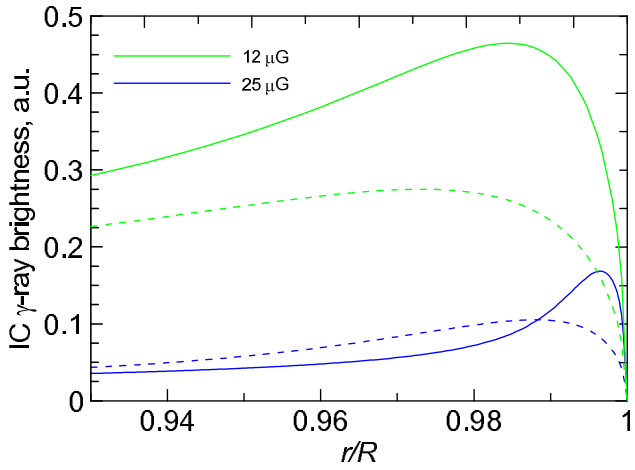

Figure 5.28. Radial profiles of the IC γ-ray brightness at 1 TeV in our model of SN 1006, for azimuth $\varphi = 0$ (dotted lines) and $\varphi = \pi/2$ (solid lines), for two values of B_o; $\phi_o = 70^o$, $s = 2$.

thinnest filament is comparable but lower than in the NLA model. The reasons of such discrepancy are in some differences between our and their models. Namely, in our model, MF decreases downstream of the shock while the extreme NLA model assumes uniform MF. In addition, we accept (following [303]) that accelerated electrons are confined in the fluid element while [76] include diffusion.

In general, MF estimated from the radial profile of X-ray brightness reflects the local conditions. The quite large strength of the downstream magnetic field, $B \simeq 130 - 150\,\mu$G, adopted in the extreme NLA model, was assumed to be the same

everywhere in the SN 1006 interior [83]. This value is reasonable for a thinnest NE filament (Fig. 4A in [232]) as it is apparent from fitting of the radial profile of X-ray brightness [76, 219]. However, the two close radial profiles are already thicker (Fig. 4B,C in [232]) suggesting therefore a smaller value of B even around the location of the original sharpest filament.

An effective MF inside SN 1006 (i.e. which may be used to represent SNR as a whole) is smaller. Our model yields $\langle B\rangle_{\rm v} = 1.06 B_{\rm o} = 12\,\mu$G (the volume average) or $\langle B\rangle_{\rm ev} = 2.7 B_{\rm o} = 32\,\mu$G (the radio-emissivity weighted volume average). The latter is well in agreement with the strength $30\,\mu$G in the leptonic model of [28] and with an estimation $\approx 30\,\mu$G obtained from Fig. 1 in [362] with the HESS spectrum.

A note on the gamma-ray brightness. The distribution of the IC brightness at γ-rays with TeV energies is given by (Appendix E.2)

$$S_{\rm ic} = \text{const}\ \mathcal{S}_{\rm ic}(\varepsilon, \bar{\rho}, \varphi; \phi_{\rm o}, b, \epsilon_{\rm f\|}, E_{\rm max})\ K_{\rm s\|} R. \tag{5.29}$$

This formula shows which factors affect the shape of the azimuthal and radial profiles and which determine their amplitudes. It is important that the strength of MF $B_{\rm o}$ is related to $E_{\rm max\|}$ with Eq. (5.18) and to $\epsilon_{\rm f\|}$ with Eq. (5.21). Therefore, once other parameters are fixed, the nonthermal X-ray and γ-ray images of SN 1006 (namely, the shapes $\mathcal{S}$ of the azimuthal and radial profiles in these bands) depend only on the value of $B_{\rm o}$.

SN 1006 is rather faint in TeV γ-rays to allow at present for the observational azimuthal and radial profiles of the quality comparable to radio or X-ray bands. However, we may check whether our model provide the observed location of the bright γ-ray limbs. Fig. 5.28 shows the radial profiles of the γ-ray surface brightness in our model of SN 1006. The bright limbs are located at the azimuth $\varphi = \pi/2$ in both cases, as observed. Note that such property is not universal; it depends on the parameters of the model. For example, if an aspect angle would be 90° then the observed location of the TeV γ-ray limbs may be possible only for ISMF strength larger than $\sim 100\,\mu$G.

5.4.5. Discussion. Magnetic field strength in SN 1006 is one of the key parameter in the model. Being related to $E_{\max\|}$ with Eq. (5.18) and to the the parameter $\epsilon_{\mathrm{f}\|}$ (which regulates efficiency of the radiative losses of relativistic electrons) with Eq. (5.21), it influences almost everything. It is demonstrated that it is important in formation of the broad-band spectrum from the whole SNR. Nonthermal images of SN 1006 is also affected by the value of B_{o}.

We consider a 'classic' model of SN 1006, i.e. model which is based on classic MHD and acceleration theories. Since they are better developed compared to NLA approach, they allow us to put observational constraints on the (test-particle) kinetics and MF, to compare the azimuthal variations of the electron maximum energy and the surface brightness in radio, hard X-rays and TeV γ-rays. At the present time, such comparison may not be done in the frame of the NLA theory. We demonstrate that the 'classic' model is in agreement with most of the observational data.

We try to fix free parameters of the model step-by-step, looking for observations which is mostly sensitive to some of them (Table 5.2). In addition to the commonly used broad-band spectrum, the properties of the nonthermal (radio, X-ray and TeV γ-ray) images of SNR as well as spatially resolved spectral fits are considered.

In particular, the morphology and azimuthal profiles of the radio brightness may determine the orientation of ISMF. Namely, the radio data may be fitted by the model with uniform ISMF which is oriented perpendicular to the Galactic plane under an angle 70^{o} to the line of sight. If so, the injection efficiency should be independent of obliquity. The radial distribution of the radio brightness depends now only on the way the injection efficiency varies with time ($K \propto V^{-b}$). The observations however may not definitively fix b. It is somewhere between -1 and 0 but accuracy of the data allow also for a bit wider range. Spatially resolved X-ray analysis of regions around the forward shock demonstrate that distribution of ν_{break} may be explained by the time-limited model of [303] with $\eta = 1.5$. The maximum energy of electrons at the parallel shock is found $E_{\max\|} = 7(B_{\mathrm{o}}/12\,\mu\mathrm{G})^{-1/2}\,\mathrm{TeV}$. It is 3.25 times higher at the perpendicular shock.

Table 5.2

Summary of the observables used for parameter determination and cross-check[a]

Observable	Parameter	Value
radio azumuthal profile[b]	aspect angle	$\phi_{\rm o} = 70^{\rm o} \pm 4.2^{\rm o}$
	injection type	isotropic
	orientation of ISMF and SNR morphology	SE-NW, barrel-like
radio radial profile	b in $K_{\rm s} \propto V^{-b}$	$-1 \lesssim b \lesssim 0$
local broad-band fits of spectra[c]	local index $s_{\rm loc}$ over shock	$s_{\rm loc} = 2.0$ over most of SNR rim
$\nu_{\rm break}$ azimuthal profile[c]	model of $E_{\rm max}$	time-limited
	ratio of the mean free path to Larmour radius	$\eta = 1.5$
	electron maximum energy at parallel shock	$E_{\rm max\parallel} = 7.0(B_{\rm o}/12\,\mu{\rm G})^{-1/2}\,{\rm TeV}$
	electron maximum energy at perpendicular shock	$E_{\rm max\perp} = 3.25 E_{\rm max\parallel}$
radio and hard X-ray spectrum	MF strength and index $s_{\rm tot}$ for the whole SNR	($B_{\rm o} = 25\,\mu$G and $s_{\rm tot} = 2.0$) or
		($B_{\rm o} = 12\,\mu$G and $s_{\rm tot} = 2.1$)
radio and TeV γ-ray spectrum	γ-ray emission model, MF strength and index $s_{\rm tot}$	IC with $B_{\rm o} = 12\,\mu$G and $s_{\rm tot} = 2.1$
X-ray radial profiles	post-shock MF strength in the limbs	$B_{\rm s\perp} \simeq 50\,\mu$G
X-ray azimuthal profile	MF strength	OK
	ISMF orientation and aspect angle	OK
	model of $E_{\rm max}$	OK
γ-ray limbs location	MF strength, aspect angle	OK
	γ-ray emission model	OK

[a] the model assumes uniform ISMF/ISM and $\gamma = 5/3$

[b] [281]

[c] [250]

We obtain expressions for the radio, X-ray and γ-ray spectra from the whole SNR in a form which clearly show which parameter of the model is responsible for the amplitude of the spectrum and which one for its shape. The modification factor of the synchrotron X-ray spectrum may well be explained by the classical model with ISMF strength $B_{\rm o} = 25\,\mu$G if $s = 2.0$ or with $B_{\rm o} = 12\,\mu$G if $s = 2.1$. At the same time, the TeV γ-ray modification factor prefers only the pair $B_{\rm o} = 12\,\mu$G, $s = 2.1$ to have the whole TeV emission be due to IC process. $B_{\rm o} = 25\,\mu$G requires an additional component in the TeV γ-ray spectrum, from pion decays, as it is in the model of [83]. Such scenario, requires however the proton injection to increase with obliquity, in order to fit the observed azimuthal profiles of TeV γ-ray brightness (in our model, ISMF is along the SE-NW symmetry axis). It is unclear if the electron and proton injections may have so different dependences on obliquity in the same SNR: isotropic for electrons and quasi-perpendicular for protons.

The extreme NLA approach [83] predicts $B_{\rm o} = 30\,\mu$G immediately before the forward shock and $B = 150\,\mu$G everywhere inside SNR. The radial profiles of X-ray brightness obtained from XMM image agree with our model with an ambient MF $B_{\rm o} = 12\,\mu$G. Around the quasi-perpendicular shock, where the profiles are extracted from, our model predicts the post-shock MF with strength $B_{\rm s\perp} \simeq 50\,\mu$G. However, in the classic model of SN 1006, this is the value for MF immediately post-shock; after then it rapidly decreases downstream. Therefore, an effective (emissivity weighted average) MF within SN 1006 is estimated to be $2.7 B_{\rm o} \approx 32\,\mu$G that is in agreement with estimates of [362] and [28]. MF in the sharpest Chandra profile is fitted in our model with $B_{\rm s} = 95\,\mu$G; it reflects the local conditions within this filament.

We found that the broad-band spectrum from the whole SN 1006 is better represented with the electron spectral index $s_{\rm tot} = 2.1$ while local radio-to-X-ray spectra over the SNR shock prefers $s_{\rm loc} = 2.0$ (Sect. 5.1.3). Difference between $s_{\rm tot}$ and $s_{\rm loc}$ are negligible for azimuthal and radial profiles of radio, X-ray and IC γ-ray brightness.

Azimuthal profiles of the X-ray brightness in our model also agree with the observations though the fit is not ideal. Simulations show that the actual MF strength is

not important for azimuthal variation of X-ray brightness in SN 1006. The differences in the synthesized and observed azimuthal profiles may be due to nonuniformity of ISMF and/or ISM.

'Classic' model has also few difficulties. It does not agree with the criterion of Rothenflug et al. [321]. Nevertheless, the polar-caps scenario, which is in agreement with this criterion (and is adopted by the NLA model), is unable to explain the observed azimuthal profiles of the break frequency $\nu_{\rm break}$, under assumptions that ISMF/ISM are uniform and the obliquity variation of amplified/compressed MF is similar to the classical one (i.e. increasing with obliquity). This conclusion is in agreement with Sect. 5.3 where the polar-caps morphology was excluded also on the base of the comparison of the observed azimuthal profiles of the radio brightness with model of SNR in uniform ISMF/ISM.

The observed radio surface brightness of the regions deeper than $0.94R$ is higher than in our synthesized images. This is also against of the 'polar caps within uniform ISMF' scenario because there should be luck of the relativistic electrons, and thus the luck of the radio emission, in the interior of the SNR projection. Could the nonuniform ISMF/ISM be responsible for this radio 'over-brightness'?

Another minor point of the classic model of SN 1006 is the rather large ambient MF, $B_{\rm o} = 12\,\mu$G, which is difficult to expect without MF amplification at the high location of SN 1006 above the Galactic plane.

Our model deals with ideal gas with the adiabatic index $\gamma = 5/3$ and cannot explain the small distance between the forward shock and the contact discontinuity [106, 250]. Instead, if acceleration is so efficient that relativistic particles affect hydrodynamics then the adiabatic index may be smaller than ours. The small distance observed may naturally be explained by such, more compressible, plasma with the index like $\gamma = 1.1$. The shock compression factor is $\sigma = 21$. If so, then typical ISMF of few μG may become quite large downstream even without amplification.

The two models, classical and extream NLA, are compared in Table 5.3. It is evident that none of them explain the whole set of the SN 1006 properties.

All results presented here are obtained under assumption that SN 1006 evolve

Table 5.3

Comparison of SN 1006 models

Properties of SN 1006	Classic model (with uniform ISMF)	Extream NLA model [83] (with uniform ISMF)
two-limbs in radio and hard X-ray image	YES SN 1006 is barrel ISMF direction: SE-NW	YES? SN 1006 has polar caps ISMF direction: SW-NE
location of TeV γ-ray limbs	YES	YES?
[321] criterion	NO	YES
radio spectrum	YES as power low	YES with concave shape
hard X-ray spectrum	YES with $\langle B \rangle_{\rm ev} = 32\,\mu$G	YES with $\langle B \rangle_{\rm v} \approx 150\,\mu$G
TeV γ-ray spectrum	YES IC with $\langle B \rangle_{\rm ev} \approx 32\,\mu$G	YES IC with $\langle B \rangle_{\rm v} \approx 150\,\mu$G and pp component
radio radial profile	YES	NO? (uniform B inside SNR)
sharpest X-ray radial profile	YES with $B_{\rm s} \approx 95\,\mu$G	YES with $B_{\rm s} \approx 150\,\mu$G
radio azimuthal profile	YES	?
hard X-ray azimuthal profile	YES	?
TeV γ-ray azimuthal and radial profiles	YES	?
$\nu_{\rm break}$ azimuthal profiles	YES	NO?
pre-shock MF strength $B_{\rm o} = 12\,\mu$G	NO (if ISMF around SN 1006 is $\sim 3\,\mu$G)	YES as result of amplification (if any)
very close forward shock and contact discontinuity	NO	YES (with $\gamma = 1.1$)
radio 'overbrightness' in the SNR interior	NO	NO?
slanted lobes	NO	NO
ratio of radio $\mathcal{R}_{\rm r} < 1$ and X-ray brightness $\mathcal{R}_{\rm x} > 1$	NO	NO
$\nu_{\rm break,NE}/\nu_{\rm break,SW} > 1$	NO	NO

in the uniform ISMF and uniform ISM. It is shown that the scenario of classic MHD/acceleration plus uniform ISMF/ISM strongly prefers the barell-like morphology of SN 1006. However, we also see that nonuniform ISMF/ISM could be an essential element in the model of SN 1006. In particular, slanted lobes, the inversion of the brightness ratio between NE and SW limbs from radio to X-ray band and the higher break frequency in NE limb may only be explained by presence of gradient of ISMF and/or ISM. We expect that the effect of the nonuniform ISMF might dominate the role of some nonlinear effects arising from efficient acceleration of cosmic rays by the forward shock in SN 1006.

5.5. Conclusions

Analysis of observations of SN 1006 is presented; the experimental data are used to put constraints on SNR and properties of magnetic field and leptonic component of cosmic rays accelerated in this SNR.

1. Experimental spectra and maps of the supernova remnant SN 1006 have been reported for radio, X-ray and TeV gamma-ray bands. *Radio band:* A new radio image of SN 1006 is produced on the basis of archival VLA and Parkes data. The image recovers emission from all spatial structures with angular scales from few arcseconds to 15 arcmin. *X-ray band:* A combined analysis of the XMM-Newton EPIC archive observations of SN 1006 is performed and its results are presented. The spatial distribution of the physical properties of the X-ray emitting plasma at the shock front are described. The contribution of thermal and non-thermal emission to the X-ray spectrum at the rim of the remnant is investigated in order to study how the acceleration processes affect the X-ray emitting plasma. The spatially resolved spectral analysis of a set of regions covering the entire rim of the shell are performed and the azimuthal variations of different parameters characterizing the thermal and non-thermal X-ray emission are obtained. The results are applied to produce a count-rate image of the "pure" thermal emission of SN 1006 in the 0.5-0.8 keV energy band

(subtracting the non-thermal contribution). This image differs significantly from the total image in the same band, especially close to the bright limbs.

2. We propose a model-independent method to synthesize the inverse-Compton gamma-ray image of a supernova remnant starting from the radio (or hard X-ray) map and using results of the spatially resolved X-ray spectral analysis. The method is based on the idea that the surface brightness distribution of the synchrotron radio and X-ray emission of SNRs contains information about the distribution and properties of accelerated electrons which are responsible for the γ-ray emission as well. The method is successfully applied to SN 1006. We found that synthesized IC gamma-ray images of SN 1006 show morphology in nice agreement with that reported by the HESS collaboration. The good correlation found between the observed very-high energy gamma-ray and X-ray/radio appearance can be considered as an evidence that the gamma-ray emission of SN 1006 observed by HESS is leptonic in origin. However the hadronic origin cannot be ruled out in view of the measured ISM densities, consistent with a hadronic scenario [219]. If this is the case, the observed TeV brightness map could reflect the distribution of protons with energies $> 2.4\,\mathrm{TeV}$ which interact with compressed ISM downstream of the shock.

3. A number of important processes taking place around strong shocks in supernova remnants (SNRs) depend on the shock obliquity. The measured synchrotron flux is a function of the aspect angle between interstellar magnetic field (ISMF) and the line of sight. Thus a model of non-thermal emission from SNRs should account for the orientation of the ambient magnetic field. We develop a new method for the estimation of the aspect angle, based on the comparison between observed and synthesized radio maps of SNRs, making different assumptions about the dependence of electron injection efficiency on the shock obliquity. We apply our method to a radio image of SN 1006. We explore different models of injection efficiency and find the following best-fitting values for the aspect angle of SN 1006: $\phi_{\rm o} = 70^{\rm o} \pm 4.2^{\rm o}$ if the injection is isotropic, $\phi_{\rm o} = 64^{\rm o} \pm 2.8^{\rm o}$ for quasi-perpendicular injection (SNR has an equatorial belt in both cases) and $\phi_{\rm o} = 11^{\rm o} \pm 0.8^{\rm o}$ for quasi-parallel injection (polar-cap model of SNR). In the last case, SN 1006 is expected to have a centrally-

peaked morphology contrary to what is observed. Therefore, our analysis provides some indication against the quasi-parallel injection model. Rejection of the quasi-parallel injection model in SN 1006 means that the initial ISMF is directed from SE to NW and SN 1006 has a barrel-shaped, rather than polar-cap, morphology.

4. A new way to compare model and observations, in order to get constraints on the modeling the remnant is presented. Namely, it is shown that a model based on classic MHD and acceleration theories allows one to analyze the spatially distributed characteristics of SN 1006 and to put observational constraints on the kinetics and MF, including for the first time the comparison of the azimuthal and radial profiles of the surface brightness in radio, hard X-rays and TeV γ-rays as well as azimuthal variations of the electron maximum energy. We obtain expressions for the radio, X-ray and γ-ray spectra from the whole SNR in a form which show which parameter of the model is responsible for the amplitude of the spectrum and which one for its shape. It is demonstrated that the model of SN1006 also provides fits for the broadband (radio-to-gamma-rays) spectrum. Presented model agrees with effective MF strength in SN 1006 of $32\,\mu$G, in a good agreement with the 'leptonic' model of the HESS Collaboration.

CHAPTER 6

STATISTICAL APPROACH TO RADIO EMISSION FROM THE SHELL-TYPE SNRS

Present chapter continues "experimental" part of the thesis. Here, in contrast to studies of an individual SNR done above, statistical methods are applied to samples of SNRs. Such an approach allows one to reveal common properties of CRs in most of SNRs.

Results presented in this chapter are published in [66].

6.1. $\Sigma - D$ relation for SNRs and its extension to the third dimension

Radio emission is a quite common property of the shell-type SNRs. The intensity of the (synchrotron) radio emission is related to the magnetic field strength and the amount of accelerated electrons. However, the mechanisms leading to both the magnetic field amplification and the electron injection at the SNR shock and their respective efficiencies remain poorly constrained. To investigate these processes observationally, there have been detailed studies, mostly in X-rays, of some selected SNRs (see e.g., [105,106] and references therein). Relevant, complementary information should also be extracted from a statistical analysis of SNR data samples.

On the observational side, a well-known (even though not widely accepted) statistical relation is the so-called "Σ–D relation", namely the empirical correlation discovered between the SNR size (D) and its radio surface brightness (Σ). Various authors (e.g., [103, 107, 115, 253, 354]) have investigated this correlation. Originally applied as a tool for estimating SNR distances, it has been found to be unreliable for this purpose. Some authors (e.g., [174, 354]) have also argued that this correlation

may be affected by selection effects. For Galactic SNRs, Green [174] highlighted the selection effects: (1) in the surface brightness, with a completeness limit of about $10^{-20}\,\mathrm{W\,m^{-2}Hz^{-1}sr^{-1}}$, while SNRs below this limit are predominantly in regions where the Galactic background is low; (2) in the angular size, so that young but distant SNRs may be missed. For SNRs in other galaxies, Urošević et al. [354] also showed that there may be a selection effect in the integrated flux (valid for unresolved or mildly resolved SNRs), with the effect of leading to an observed slope shallower than the intrinsic one.

Even though selection effects may affect this correlation to some level, we believe that the relation itself has a physical origin, and that one can therefore extract from it information about the processes involved in the SNR radio emission: therefore, understanding its origin could eventually contribute to constraining the efficiency of these processes. There have been several attempts (e.g., [211, 290, 333, 355], or more recently [77, 133]) to explain the Σ–D relation as the average evolutionary track of a "typical" SNR. In all of these cases, the slope of the correlation is assumed to correspond to that of the SNR evolutionary track on the Σ–D parameter plane.

However, there is clear evidence that this assumption is incorrect. Berkhuijsen [84] has found tight correlations of both Σ and D with the ambient density (n_o), in the sense that smaller (and brighter) SNRs are typically located in a denser medium (indeed, the correlation between n_o and D had already been known for several years; see e.g., Fig. 4 in [247]). The best-fit results given by Berkhuijsen are

$$D \simeq 15\, n_\mathrm{o}^{-0.39\pm0.04}\,\mathrm{pc} \tag{6.1}$$

$$\Sigma \simeq 6\times10^{-20} n_\mathrm{o}^{1.37\pm0.21}\,\mathrm{W\,m^{-2}Hz^{-1}sr^{-1}} \tag{6.2}$$

Berkhuijsen concluded that the Σ–D relation ($\Sigma \propto D^{\xi}$) is just a secondary effect, while the two primary relations are those of D and Σ with n_o.

Although this conclusion may appear rather extreme, it is quite obvious that the Σ–D relation contains SNRs that evolve in very different ambient conditions. We then assume that the correlations between Σ, D, and n_o do not directly reflect the evolution of a "typical" object, but are rather the combined effect of the evolution

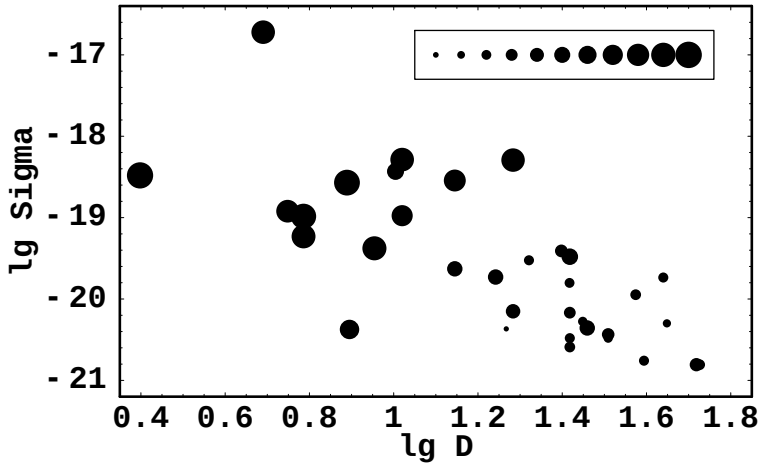

Figure 6.1. Distribution of SNRs from Berkhuijsen [84] sample in the $\lg D$–$\lg \Sigma$ parameter plane (D is measured in pc, while Σ is in $\mathrm{W\,m^{-2}Hz^{-1}sr^{-1}}$). The dot sizes are proportional to $\lg n_\mathrm{o}$ values, the legend showing in order sizes corresponding to $\lg n_\mathrm{o}$ from –1.5 to 1.0, in steps of 0.25 (n_o being measured in $\mathrm{cm^{-3}}$). It is apparent from this figure that smaller (and brighter) SNRs are typically located in a denser medium.

of different SNRs expanding in different ambient conditions. That the correlations with n_o are statistically so tight also suggests that D and Σ are more sensitive to the ambient conditions than to the SNR evolution. The combined effect of these correlations is that a clear trend of n_o across the Σ–D relation is observed (see Fig. 6.1), namely that smaller SNRs are preferentially located in higher-density environments.

In principle, correlations of Σ and D with n_o, accounting for at least qualitatively the trend of n_o across Σ–D relation, could also appear in the case of the evolution of an individual object, provided that it expands in a medium with a highly structured, fractal, density distribution. This would reflect that, during its life, a SNR always preferentially expands towards the direction in which the ambient density is lower. Therefore, at any time, the "effective" ambient density would be close to the "lowest" ambient density in the volume occupied by the SNR. In this way, one could explain why large SNRs typically seem to expand in a low-density medium.

However, it is hard to justify, in this scenario, the absence of small SNRs in low-density media (which would be the case, when the supernova itself is located in a low density region), as well as that low ambient density values are measured for all extended SNRs (which requires that such low density regions are ubiquitous in the Galaxy, on scales of tens of parsecs or even less). In addition, if the effects of the

fractal interstellar medium were dominant, virtually all SNRs should have a much brighter limb on one side, which is not observed. Therefore, for all these reasons, we conclude that the "fractal ambient density" hypothesis is implausible, and we do not consider it any longer.

One of our goals is to show that the best-fit line usually referred to as the "Σ–D relation" provides only a minor part of the information present in the data, while additional information could be extracted by analyzing in detail the distribution of points in the Σ–D–$n_{\rm o}$ parameter space. For this reason we propose a rather general (parametric) scenario, with the aim of constraining the physics of the electron injection and magnetic field behavior in SNR shocks and/or the SNR evolutionary phase in which they are most likely to be observed in radio.

6.2. Basic ideas, assumptions, and formulae

Our analysis is based on the fundamental criterion that the observed correlation in the Σ–D parameter plane originates from the combined effect of evolutionary tracks in very different ambient conditions. In this subsection, we implement this idea by adding some derived / secondary assumptions that will allow us to develop a more general scenario, on which our subsequent statistical analyses will be based.

6.2.1. When radio SNRs are preferentially seen. A preliminary consideration is that the conditions in which a given object is most likely observed, during its evolution, are those in which it spends most of its time. Since SNR expansion decelerates during most of their lifetime, it is statistically more likely to find them when their size is close to its final value. We are interested in finding SNRs that are visible in radio. Therefore, it is more important, in this case, to determine the evolutionary stage at which the processes responsible for enhancing magnetic fields and/or for producing high energy electrons are no longer efficient. In the following, we refer to this phase as the "final stage" of a radio SNR, but it should be clear that it is not the maximum size that a SNR can reach dynamically, before merging into

the ambient medium.

We parametrize the SNR expansion by a power law ($D \propto t^{1/a}$; $a > 1$) up to a maximum size (D_2) beyond which the SNR is no longer detectable in radio. During its evolution of a given SNR as a radio source, the probability of being observed with a given size D is proportional to dt/dD, namely

$$\mathcal{P}(D) = aD^{a-1}/D_2^a, \quad \text{where} \quad D < D_2, \tag{6.3}$$

(the initial diameter of this evolutionary phase, D_1, not being relevant provided that $(D_1/D_2)^{a-1} \ll 1$), so that the average value and standard deviation of the (decimal) logarithm of D are

$$\langle \lg D \rangle = \lg D_2 - \frac{1}{a \ln 10}, \tag{6.4}$$

$$\sigma_{\lg D} = \frac{1}{a \ln 10}. \tag{6.5}$$

For instance, during the adiabatic (Sedov) phase $a = 5/2$, so that $\langle \lg D \rangle = \lg D_2 - 0.17$ and $\sigma_{\lg D} = 0.17$, while, in the later radiative (pressure-driven snowplow) phase, $a = 7/2$, so that $\langle \lg D \rangle = \lg D_2 - 0.12$ and $\sigma_{\lg D} = 0.12$. This means that, on average, SNR diameters should be rather close to D_2, and that their dispersion should be rather small, i.e., an individual SNR, during its evolution, is seen to migrate only slightly in the Σ–D parameter plane. For this reason, we propose that selection effects, while important to determining the overall distribution of points across the Σ–D plane, should only have a marginal effect on the observed probability $\mathcal{P}(D)$.

6.2.2. The end of the radio phase. We consider, in particular, the end of the Sedov phase. According to Truelove & McKee [350], it should correspond to a size

$$D_B \sim 28 \left(E_{\rm SN}/10^{51}\,{\rm erg}\right)^{2/7} n_{\rm o}^{-3/7}\,{\rm pc}, \tag{6.6}$$

(where $E_{\rm SN}$ is the energy of the supernova explosion), while the dynamical end of the SNR, namely where it merges with the ambient medium, can be placed at much larger sizes. The above formula has been obtained by approximating the plasma

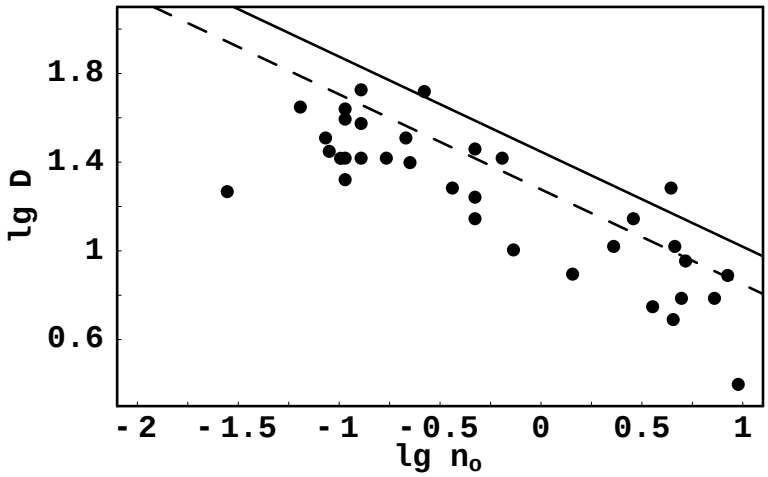

Figure 6.2. Distribution of SNRs (from Berkhuijsen [84] sample) in the $\lg n_{\rm o}$–$\lg D$ parameter plane. For comparison, the theoretical line corresponding to the end of the Sedov phase (as from Truelove & McKee [350]) is shown (solid line), as well as that of $\langle \lg D \rangle$, as from Eq. 6.4 (dashed line).

cooling function with a power law $\Lambda \propto T^{-1/2}$, where T is the gas temperature (while other papers use different power-law approximations; for instance, Blondin et al. [90] use $\Lambda \propto T^{-1}$). For a generic $\Lambda \propto T^{-\alpha}$ relation one may find that

$$D_B \propto E_{\rm SN}^{(3+2\alpha)/(11+6\alpha)} n_{\rm o}^{-(5+2\alpha)/(11+6\alpha)}. \tag{6.7}$$

For α changing from 1/2 to 1, the exponent of $n_{\rm o}$ in the above formula changes from 0.429 to 0.412: namely, the numerical value of that exponent is very weakly dependent on the power-law approximation used. In the following, we shall then use, without loss of generality, the formula (here Eq. 6.6) of Truelove & McKee [350].

The correlation found by Berkhuijsen between D and $n_{\rm o}$ (Eq. 6.1) is consistent with

$$D \simeq 0.54 \left(E_{\rm SN}/10^{51}\,{\rm erg}\right)^{-2/7} D_B, \tag{6.8}$$

namely with a D/D_B ratio that is independent of $n_{\rm o}$.

This can be also seen from Fig. 6.2, where the data points from Berkhuijsen [84] are displayed together with D_B, as evaluated for $E_{\rm SN} = 10^{51}\,{\rm erg}$ (solid line): we note that the line is not a fit, namely there are no free parameters to tune. This indicates that most of the known radio SNRs are observed close to the end of the Sedov phase, and that in general SNRs must extinguish their radio emission somewhere close to the end of their Sedov phase. It is then reasonable to use a Sedov law ($a = 5/2$) to

approximate the expansion law during the final phases of radio SNRs: therefore, in the following, whenever a numerical value for a is required, we shall use the Sedov value. For a Sedov expansion, the dashed line in Fig. 6.2 applies to the value of $\langle \lg D \rangle$, given by Eq. 6.4. The best-fit level (Eq. 6.8) is only 20% lower, providing a good argument for SNRs being (statistically) mostly visible around the end of their adiabatic stage.

It remains to be understood for which physical reason the end of the Sedov phase should roughly correspond to the switching off of the radio emission. There is also evidence that the extinguishing transient evolution must be rather rapid. Otherwise, we should also see SNRs with Σ values considerably lower than that derived from the Σ–D correlation for the same size; namely, in the Σ–D parameter plane, we should have points spread over the half-plane below the main correlation (of course, limited to the region of the Σ–D plane for which one expects SNRs to be detectable). This latter piece of observational evidence is also not easy to explain. The underlying problem is that the physical processes behind the injection of electrons are poorly understood in the general case, and are probably even harder to model for conditions near to marginal efficiency.

6.2.3. The "final-stage" approximation. We introduce in a parametric form a basic set of equations to describe the observed correlations and distributions, and eventually provide some constraints on future physical models of the injection of electrons in SNRs. That the Σ–D empirical relation is a power law suggests (even though it does not strictly imply) that all formulae of interest can be approximated by power laws, thus simplifying considerably the treatment.

As a starting point, we consider the extreme approximation that each of them is observed very close to its final stage as a radio SNR, namely that each individual evolutionary track in the Σ–D plane can be assimilated to just one point, corresponding to its final position (D_2, Σ_2). We also assume that the dependence of both quantities on the ambient density (n_o) can be approximated by the following power

laws:

$$D_2(n_\mathrm{o}) = K_1 n_\mathrm{o}^m, \tag{6.9}$$

$$\Sigma_2(n_\mathrm{o}) = K_2 n_\mathrm{o}^n. \tag{6.10}$$

In this limiting case, the slope of the Σ–D relation

$$\Sigma_2(D_2) = K_3 D_2^\xi, \tag{6.11}$$

would simply be $\xi = n/m$. In the above formulae, the functional dependence on other physical parameters is not given explicitely; however, other quantities may be involved. For instance, if SNRs really are efficient radio emitters only until the end of the Sedov phase (as suggested by Fig. 6.2), D_2 should also depend on the SN energy (see Eq. 6.7).

To describe the distribution of points along the correlation, one must also introduce the function $\tilde{\mathcal{P}}(n_\mathrm{o})$, giving the probability of finding a SNR in a region of a given density: this probability combines the density distribution of the interstellar medium, the dependence of the SN rate on the local density, and how the lifetime of a radio SNR depends on the ambient conditions. For the sake of simplicity, and in the absence of any observational evidence against it, we also approximate this function by a power law, namely

$$\tilde{\mathcal{P}}(n_\mathrm{o}) = K_4 n_\mathrm{o}^w. \tag{6.12}$$

This distribution is used in Sect. 6.5.1.

6.2.4. Introducing the SNR evolution. From this point on, we shall remove the "final-stage" approximation, introduced in the previous subsection. Nonetheless the evolution of individual SNRs will still be treated in a very simplified way, by assuming that SNR evolution in different ambient conditions differ only by a scaling law and, in practice, by only adopting power-law behaviors.

We introduce the SNR expansion in the following parametric form:

$$t(D, n_\mathrm{o}) = K_5 D^a n_\mathrm{o}^b \tag{6.13}$$

(for instance, in the Sedov case $a = 5/2$, $b = 1/2$, and $K_5 \propto E_{\rm SN}^{-1/2}$). As for the evolution in surface brightness, by assuming that a scaling law holds, the surface brightness could be expressed in a rather general form as

$$\Sigma(D, n_{\rm o}) = f(D/D_2(n_{\rm o}))\Sigma_2(n_{\rm o}), \tag{6.14}$$

where $f(x)$ must vanish at $x > 1$. We use a power-law approximation

$$\Sigma(D, n_{\rm o}) = \left(\frac{D}{D_2(n_{\rm o})}\right)^p \Sigma_2(n_{\rm o}) = K_6 D^p n_{\rm o}^q \quad \text{for} \quad D < D_2, \tag{6.15}$$

where $K_6 = K_2/K_1^p$ and $q = n - mp$. Parameters p and q in Eq. 6.15 can be derived independently. If the data sample is not heavily affected by selection effects, these parameters can be evaluated by simply applying a bilinear regression.

Determining the functional dependence of $\Sigma(D, n_{\rm o})$ would also allow one to derive the trajectory of individual SNRs in the parameter plane. They are simply given by the function $\Sigma(D)$ for a constant value of $n_{\rm o}$, which in principle differs from the $\Sigma(D)$ relation, as traditionally obtained, because the latter relation is obtained by combining cases with different $n_{\rm o}$ values. In the power-law case, the slope of the evolutionary track of an individual SNR is then given by the exponent p. In the following, we shall provide some evidence that the value of p is different from that of ξ: this means that evolutionary tracks in the Σ–D parameter plane have a different slope from that of the overall Σ–D relation.

Also m can be derived, by fitting Eq. 6.9 to the D–$n_{\rm o}$ data (provided that $\langle D \rangle$ is a constant fraction of D_2, as from Eq. 6.4). On the other hand, there is no way of deriving a and b (defined in Eq. 6.13) directly from the correlations between Σ, D, and $n_{\rm o}$. Coefficient a could be inferred, in principle, only by studying the distribution of points about the main correlation, while there is no way of estimatig the exponent b, because it would only affect the distribution of points with $n_{\rm o}$ along the correlations, a piece of information that is already included in the definition of the distribution $\tilde{\mathcal{P}}$ (Eq. 6.12).

In principle, a distribution of SN energies may also contribute; but, for the present analysis, we assume that SN energies are not correlated with any other quantity and

therefore that a distribution of energies would just produce an additional dispersion across the correlations, without affecting any of the above slopes. Some correlation could be possible, in principle, if different population stars have different distributions of their SN energies. However, to our knowledge no evidence in favour of this has been presented so far.

6.3. Data and statistical analysis

6.3.1. Data sample and best-fit parameters. We now apply the analysis outlined above to the data published by Berkhuijsen [84]. That paper presents a fundamental work on the subject and, although since then a great number of surveys of higher accuracy have been performed, it still contains the most extended data sample of SNRs in which, in addition to the SNR radio surface brightness and size, quantities derived by other spectral bands are also tabulated. We extracted from this data sample all SNRs with available data on Σ, D (radio), and $n_{\rm o}$ as well. We excluded SN 1006, because it is now known that the bulk of its X-ray emission is non-thermal. The total number of selected objects is 34: the original data sample is given in Table 6.1 (for two objects, Cas A and Tycho, in which two different values of $n_{\rm o}$ are given, we took their geometrical mean). Since distance estimates for Galactic SNRs have changed with time, in the last column of Table 6.1 we list the SNR sizes obtained from the most recent version of the Galactic SNR catalog, by Green [175]: they differ substantially from Berkhuijsen's values only for Kepler and Vela. The estimated distances of the Large Magellanic Cloud (LMC) and the Small Magellanic Cloud (SMC) have also slightly changed, from 55 kpc and 63 kpc (as in Berkhuijsen [84]), to 48 kpc and 61 kpc [187, 238], respectively. In our calculations, we used all of these new distances, and we revised accordingly the SNR linear size and density estimates (being $n_{\rm o} \propto d^{-1/2}$). The last two columns of Table 6.1 provide the D and $n_{\rm o}$ values that we used.

The average ambient density is estimated by Berkhuijsen [84] in a simple way,

Table 6.1

The data sample (extracted from [84])

	Object	$-\lg\Sigma$ (W m^{-2} Hz^{-1}sr^{-1})	D (as from Berkhuijsen) (pc)	n_o (as from Berkhuijsen) (cm^{-3})	D (after distance revision) (pc)	n_o (after distance revision) (cm^{-3})
GAL	W44	19.409	26.0	0.22	25.0	0.22
GAL	Cas A	16.721	4.1	4.94	4.9	4.52
GAL	Tycho	18.921	5.4	3.64	5.6	3.57
GAL	RCW103	19.377	9.6	5.04	9.0	5.21
GAL	Kepler	18.481	3.8	7.70	2.5	9.49
GAL	W49B	18.432	11.0	0.70	10.1	0.73
GAL	VelaXYZ	20.367	36.0	0.02	18.5	0.03
GAL	RCW86	20.276	35.0	0.08	28.1	0.09
LMC	0453–685	19.730	20.0	0.44	17.5	0.47
LMC	0454–665	19.629	16.0	0.44	14.0	0.47
LMC	0455–687	20.299	51.0	0.06	44.5	0.06
LMC	0500–702	20.590	30.0	0.12	26.2	0.13
LMC	0505–679	20.374	9.0	1.34	7.9	1.43
LMC	0506–680	18.976	12.0	2.14	10.5	2.29
LMC	0509–675	19.231	7.0	4.64	6.1	4.97
LMC	0519–697	19.524	24.0	0.10	20.9	0.11
LMC	0519–690	18.984	7.0	6.76	6.1	7.24
LMC	0520–694	20.435	37.0	0.20	32.3	0.21
LMC	0525–660	19.480	30.0	0.60	26.2	0.64
LMC	0525–696	18.293	22.0	4.12	19.2	4.41
LMC	0525–661	18.544	16.0	2.68	14.0	2.87
LMC	0527–658	20.807	61.0	0.12	53.2	0.13
LMC	0528–692	20.168	30.0	0.16	26.2	0.17
LMC	0532–710	19.947	43.0	0.12	37.5	0.13
LMC	0534–699	20.356	33.0	0.44	28.8	0.47
LMC	0534–705	20.481	37.0	0.08	32.3	0.09
LMC	0535–660	18.287	12.0	4.30	10.5	4.60
LMC	0536–706	20.481	30.0	0.10	26.2	0.11
LMC	0543–689	20.758	45.0	0.10	39.3	0.11
LMC	0547–697	19.736	50.0	0.10	43.6	0.11
LMC	0548–704	20.151	22.0	0.34	19.2	0.36
SMC	0045–734	19.802	27.0	0.10	26.1	0.10
SMC	0102–722	18.570	8.0	8.28	7.7	8.41
SMC	0103–726	20.807	54.0	0.26	52.3	0.26

using the following relation (derived from [230]):

$$n_{\rm o} = (6/\pi)^{1/2} \epsilon^{-1/2} f^{1/2} L_{\rm X}^{1/2} D^{-3/2}, \tag{6.16}$$

where ϵ (taken to be $3 \times 10^{-23}\,{\rm erg\,cm^{-3}\,s^{-1}}$) is the specific emissivity, f is the filling factor (taken to be close to unity), and $L_{\rm X}$ is the X-ray luminosity. While the exact values of ϵ and f are not important to our statistical analysis, it is crucial that these quantities remain constant, or at least independent of other parameters (such as size and surface brightness). In spite of its simplicity, this formula provides reasonably good results. Upper limits to the uncertainty in this $n_{\rm o}$ evaluation can be derived from the dispersion about the $\lg D$–$\lg n_{\rm o}$ regression. Based on the assumption that the measured dispersion depends only on the uncertainties in $n_{\rm o}$, one obtains $\sigma(\lg n_{\rm o}) = 0.42$; while also taking into account the dispersion in D, as modeled by Eq. 6.5 for the case of Sedov expansion, one derives a residual dispersion $\sigma(\lg n_{\rm o}) = 0.18$, namely a typical uncertainty in the density derived by Berkhuijsen of only about 50%.

By performing linear regressions between the logarithmic quantities (which is equivalent to assuming constant relative errors in the measurements), we obtain:

$$m = -0.37 \pm 0.04, \tag{6.17}$$

$$\xi = -2.06 \pm 0.34, \tag{6.18}$$

$$p = -0.89 \pm 0.57, \tag{6.19}$$

$$q = +0.62 \pm 0.25, \tag{6.20}$$

(where 1-σ uncertainties are indicated). It is apparent that, while m and ξ are found to have reasonably small uncertainties, the uncertainties of p and q are larger. The reason is that, in the data, there is a near-degeneracy between p and q, as is well shown by a plot of the confidence levels (Fig. 6.3). In this sense, a combined quantity that can be far more reliably determined is:

$$q - 0.39p = 0.97 \pm 0.14. \tag{6.21}$$

A potential problem of this sample, and of SNR samples in general, is the presence of selection effects. In the introduction, we mentioned the analyses of Green [174]

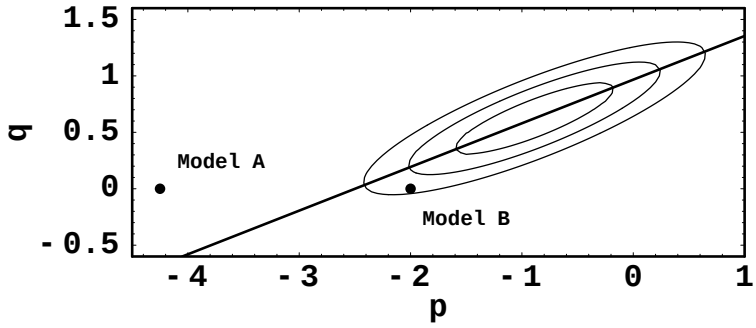

Figure 6.3. Plot of the confidence levels in the p-q parameter plane. The levels plotted correspond to 1, 2, and 3-σ confidence levels, while the line indicates the maximum spread direction (see Eq. 6.21). For comparison, two theoretical predictions are plotted: "Model A" $(-17/4, 0)$ indicates the case with constant efficiency in both particle acceleration and magnetic field compression plus amplification (Berezhko & Völk [77]); while "Model B" $(-2, 0)$ refers to the case in which particles are accelerated with constant efficiency but the magnetic field is constant (see text).

and Urošević et al. [354] on this subject. The points raised by Green [174] are more appropriate to our sample, which consists only of SNRs located in our Galaxy and the Magellanic Clouds.

Even though a detailed treatment of the selection effects is beyond the scope of this work, for the sake of illustration we repeated the computations that led to Fig. 6.3, but on subsamples containing, respectively, the 25 and 30 SNRs with the highest radio surface brightness with corresponding thresholds in $\lg \Sigma$ of -20.356 and -20.481 respectively (see Table 6.1). Figure 6.4 shows a comparison of the confidence levels (only 1-σ and 3–σ, for figure clarity) for the two subsamples, superimposed on those for the entire sample (as in Fig. 6.3). It is apparent that any additional selection in surface brightness does not generate any substantial difference in the results, apart from a slight terms of broadening compatible with the lower sample size being analyzed by statistics and a slight shift toward lower p and q values (the latter point will be discussed in the next subsection).

6.3.2. Testing the "constant efficiencies" model. Among the various theoretical attempts to model the radio emission from SNRs, one of the most recent and popular is that by Berezhko & Völk [77]. This paper assumes that the kinetic energy density entering the shock ($mn_{\rm o}V_{\rm sh}^2$, where m is the mean atomic mass) is converted with constant efficiencies into the energy densities of magnetic field and accelerated electrons (ϵ_B and ϵ_{CR}, respectively): this means, for instance, that the

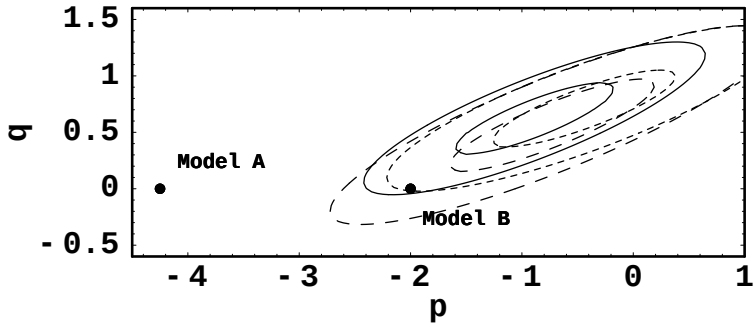

Figure 6.4. Plot of the 1-σ and 3–σ confidence levels in the p-q parameter plane, for the whole sample (solid lines), as well as for selections of the 25 and 30 SNRs with the highest surface brightness (short-dashed and long-dashed lines, respectively).

effective magnetic field in the synchrotron emitting region decreases with time, simply because the SNR shock is slowing down. For synchrotron emission with a power index -0.5 (namely the average index for radio SNRs), the surface brightness should scale as

$$\Sigma \propto K B^{3/2} D \propto \left(\epsilon_{CR} \epsilon_B^{3/4}\right) D \propto \left(n_{\rm o} V_{\rm sh}^2\right)^{7/4} D \tag{6.22}$$

A further assumption of this model is Sedov expansion, which implies that $m n_{\rm o} V_{\rm sh}^2 \sim E_{\rm SN}/D^3$, so that one finally obtains

$$\Sigma \propto E_{\rm SN}^{7/4} D^{-17/4}, \tag{6.23}$$

i.e., with $p = -4.25$, and $q = 0$ (labeled as "Model A" in Fig. 6.3). Namely, according to this model, individual SNR tracks in the Σ–D plane must be rather steep and "independent of the ambient density". Since Berezhko & Völk [77] state that the slope of the Σ–D relation should represent the slope of individual evolutionary tracks, they predict that $\xi = -4.25$ should be the slope of the Σ–D relation. However, neither their predicted value for ξ matches the data, nor does (and at an even higher significance level) their predicted (p, q) pair (see Fig. 6.3). It is unlikely that this mismatch is a mere consequence of a sample incompleteness in surface brightness. Figure 6.4 shows that for subsamples in which a further selection in surface brightness has been applied the barycenter of the confidence levels moves only mildly.

A more appropriate model (in the sense that it is "only" about 2-σ away from the best-fit model values) would be one in which electrons are accelerated with

constant efficiency ($\epsilon_{CR} \propto n_{\rm o} V_{\rm sh}^2$) but the magnetic field is taken to be constant, not only during the evolution of an individual SNR but also among different SNRs. This happens, for instance, if the post-shock field has been compressed only by the shock, i.e., is proportional to the ambient field, which in turn is roughly constant (see e.g., [123]), in near equipartition with the interstellar thermal pressure of the diffuse interstellar medium. This case does not exclude the presence of an extra field amplification, provided that it yields a constant factor. As in the previous case, but assuming B to be constant, one can now write

$$\Sigma \propto KD \propto \epsilon_{CR} D \propto \left(n_{\rm o} V_{\rm sh}^2\right) D \propto E_{\rm SN} D^{-2}, \tag{6.24}$$

namely $p = -2$ and $q = 0$ (which is labeled "Model B" in Fig. 6.3).

6.3.3. The results with a more "physical" flavour. We can approach the problem from the opposite direction, by trying to translate the information derived in terms of (p, q) into constraints on the physics that controls the magnetic and cosmic-ray efficiencies. We assume that

$$KB^{3/2} \propto n_{\rm o}^g V_{\rm sh}^h, \tag{6.25}$$

where g and h are free parameters. This is not the most general case, but it simply relates the efficiencies to primary local quantities encountered by the shock. Based on this assumption, and an expansion law $t \propto D^a$ passing through the endpoint of the Sedov phase (D_B, t_B), the equation for the surface brightness becomes

$$\Sigma \propto E_{\rm SN}^{(4a-3)/14} D^{1-(a-1)h} n_{\rm o}^{g-(3a-4)h/7}. \tag{6.26}$$

In the case of Sedov expansion, this equation simplifies into

$$\Sigma \propto E_{\rm SN}^{1/2} D^{1-3h/2} n_{\rm o}^{g-h/2}. \tag{6.27}$$

Figure 6.5 shows the confidence levels in this new pair of parameters. An advantage is that the direction of maximum dispersion is almost parallel to the h axis, which means that at least the best-fit value for g is well determined. We have

$$g = 1.25 \pm 0.14, \tag{6.28}$$

$$h = 1.26 \pm 0.38. \tag{6.29}$$

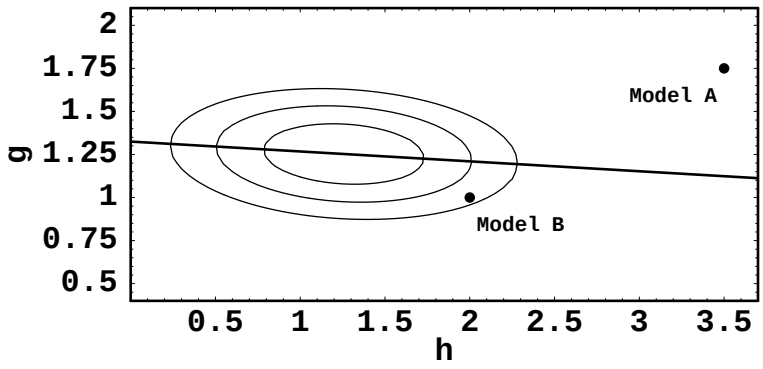

Figure 6.5. Same as Fig. 6.3, in the g-h parameter plane.

For comparison, the "constant efficiencies" model prescribes that $g = 1.75$ and $h = 3.5$, as can easily be derived from Eqs. 6.23 and 6.27. What we have found here is not different from the previous subsection, but is simply displayed in a more physical way.

To summarize, in most SNRs the constant efficiency assumption (namely for both field amplification and particle acceleration) does not hold. This may not be surprising, in the view that the statistically most common cases are those of SNRs close to their radio endpoint, namely when particle acceleration is close to being halted. Using observations to test these critical cases may indeed be important to obtaining a clearer understanding of the physical processes responsible for magnetic amplification and particle acceleration.

6.4. Results from an independent sample: M 33

As already mentioned in the introduction, SNR samples studied in other galaxies provide promising input to this kind of analysis. For mere comparison with what has already been obtained using the sample of Berkhuijsen, we present here the results for a M 33 SNR data sample, which is a sample completely independent from that used so far.

The sample was obtained by selecting SNRs for which radio fluxes are given by Gordon et al. [178], X-ray fluxes by Pietsch et al. [286] and (optical) diameters by Gordon et al. [177]. The X-ray survey of Plucinsky et al. [288], based on Chandra

data, was also used to solve some cases of uncertain identification. In this way, we selected 22 SNRs: the data sample is shown in Table 6.2. The first 3 columns report the SNR identification numbers in the various catalogs, respectively, [177] (labeled by "opt" in the Table), [178] (labeled by "rad"), and [286] (labeled by "xray"), while the next 3 columns show, respectively, the published linear (optical) diameters, 20 cm fluxes, and measured (i.e., absorbed) 0.2–4.5 keV fluxes.

To derive 1 GHz radio fluxes, we extrapolated the 20 cm fluxes tabulated by Gordon et al. [178], by assuming a spectral index of -0.5. For most SNRs, Gordon et al. [178] also estimate spectral indices, but the uncertainty in these estimates is rather large, and we therefore preferred to adopt a "standard" value for the spectral index. We evaluated the unabsorbed X-ray fluxes by taking a column density $N_H = 1.0 \times 10^{21}\,\mathrm{cm}^{-2}$ towards M 33 [288], and assuming for the average SNR spectrum a Raymond-Smith model with $kT = 0.3\,\mathrm{keV}$. Using WebPIMMS [1], a correction factor of ~ 1.94 is evaluated: the precise value of this factor is not very important for our purposes, provided that the X-ray SNR spectra are not too different among themselves. Finally, a M 33 distance of 817 kpc [155] is assumed here; since [177] use a distance of 840 kpc, for consistency we applied a small correction to their published SNR sizes.

Here are our results, to be compared with those presented above. The formulae equivalent to Eqs. 6.17–6.20, 6.28 and 6.29 are respectively

$$m = -0.34 \pm 0.07, \tag{6.30}$$

$$\xi = -2.20 \pm 0.46, \tag{6.31}$$

$$p = -1.37 \pm 0.64, \tag{6.32}$$

$$q = +0.52 \pm 0.30, \tag{6.33}$$

$$q - 0.37p = 1.04 \pm 0.20 \tag{6.34}$$

$$g = 1.31 \pm 0.20 \tag{6.35}$$

$$h = 1.58 \pm 0.42; \tag{6.36}$$

while Figs. 6.6, 6.7, 6.8 and 6.9 correspond, for M 33, to Figs. 6.1, 6.2, 6.3 and

[1] http://heasarc.gsfc.nasa.gov/Tools/w3pimms.html

Table 6.2

M 33 data sample

ID opt	ID rad	ID xray	D (pc)	S(20 cm) (mJy)	Flux(0.2–4.5) (erg cm^{-2}s^{-1})
9	11	93	18	0.7	4.29×10^{-15}
11	13	98	17	0.6	3.81×10^{-15}
15	20	106	27	0.6	2.79×10^{-15}
20	25	120	10	0.8	1.03×10^{-14}
21	29	121	28	0.9	1.41×10^{-13}
25	42	144	27	1.4	3.63×10^{-15}
27	47	153	23	1.2	2.99×10^{-15}
28	50	158	11	0.8	2.45×10^{-14}
29	52	161	20	0.5	1.73×10^{-14}
31	57	164	39	1.8	3.88×10^{-14}
35	64	179	32	3.5	1.01×10^{-14}
42	75	194	29	0.5	1.39×10^{-14}
47	90	207	36	0.2	7.05×10^{-15}
53	110	213	40	0.2	1.53×10^{-15}
54	111	214	16	1.3	2.08×10^{-15}
55	112	215	18	4.4	2.84×10^{-14}
57	114	220	21	0.4	1.87×10^{-15}
59	121	224	16	0.3	3.90×10^{-15}
62	125	225	29	0.4	4.87×10^{-15}
64	130	230	27	0.5	3.65×10^{-15}
73	148	250	17	0.5	1.41×10^{-14}
97	181	314	35	0.8	4.84×10^{-15}

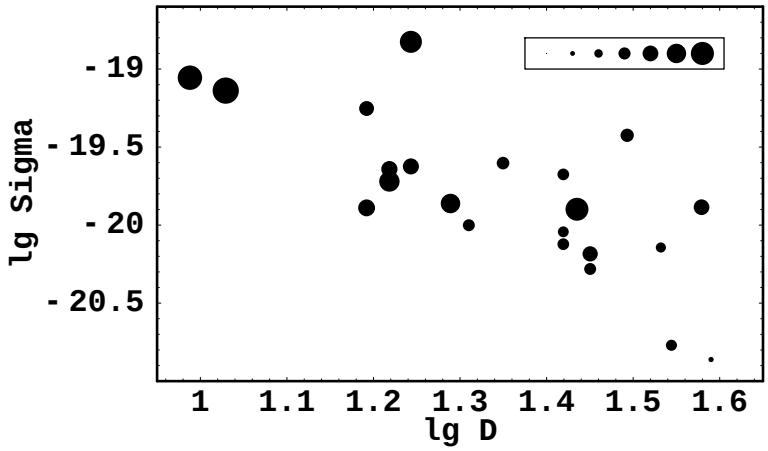

Figure 6.6. Distribution of the M 33 SNRs sample in the $\lg D$–$\lg \Sigma$ parameter plane (to be compared with Fig. 6.1). The dot sizes are proportional to $\lg n_{\rm o}$ values, the legend showing in order sizes corresponding to $\lg n_{\rm o}$ from –1.0 to 0.5, in steps of 0.25.

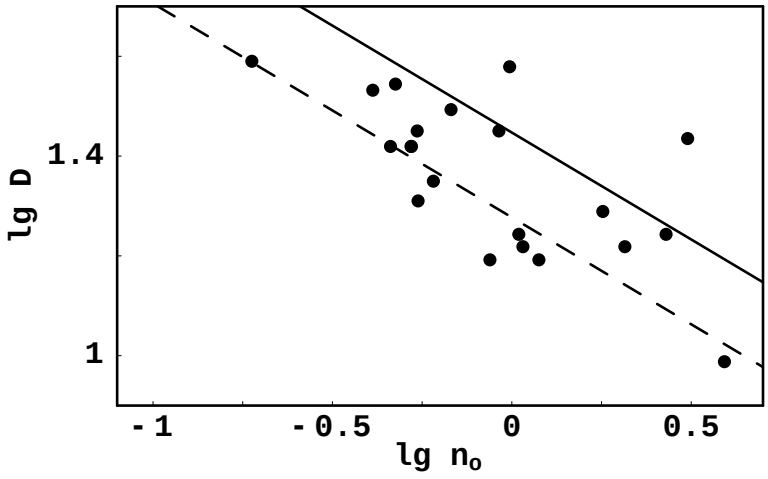

Figure 6.7. Distribution of M 33 SNRs in the $\lg n_{\rm o}$–$\lg D$ parameter plane (to be compared with Fig. 6.2).

6.5, respectively. It is apparent that all results from this further sample show close agreement, within the quoted errors, with what we found above using the data of Berkhuijsen. A comparison of the regression results for the two samples is given in Table 6.3.

6.5. The SNR cumulative distribution with size

6.5.1. The original paradox and how it can be solved. The cumulative distribution of the number of SNRs with sizes smaller than a given diameter (N–D relation) is another statistical distribution that has traditionally been studied.

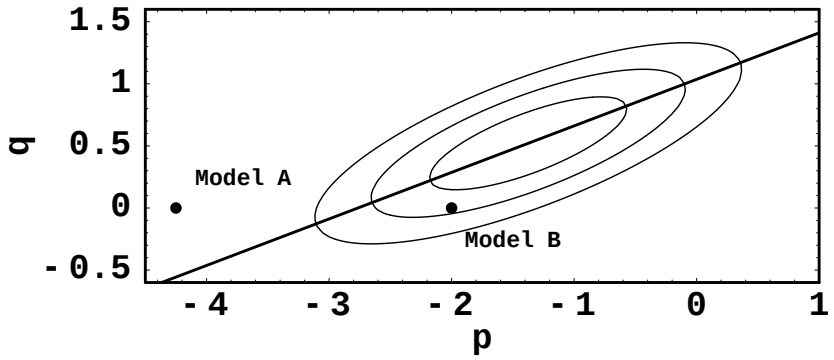

Figure 6.8. Plot, for M 33 SNRs, of the confidence levels in the p-q parameter plane (to be compared with Fig. 6.3).

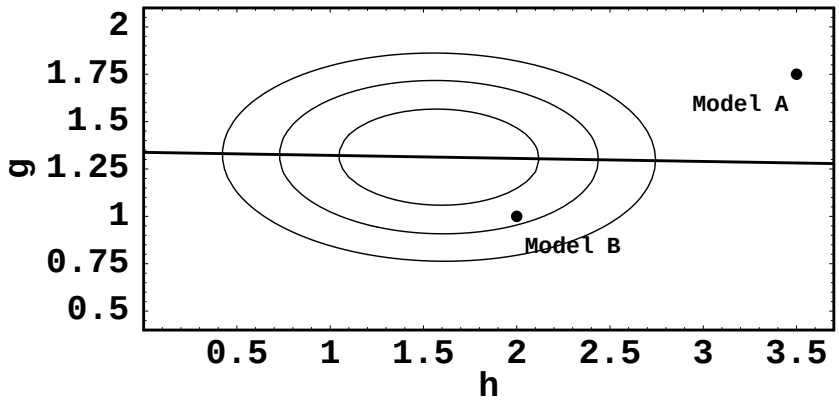

Figure 6.9. Plot, for M 33 SNRs, of the confidence levels in the g-h parameter plane (to be compared with Fig. 6.5).

Table 6.3

Synoptic table of the results of the regression analyses

Formula		Data Samples	
		Berkhuijsen	M 33
$D_2(n_\mathrm{o}) \propto n_\mathrm{o}^m$	$m =$	-0.37 ± 0.04	-0.34 ± 0.07
$\Sigma_2(D_2) \propto D_2^\xi$	$\xi =$	-2.06 ± 0.34	-2.20 ± 0.46
$\Sigma(D, n_\mathrm{o}) \propto D^p n_\mathrm{o}^q$	$p =$	-0.89 ± 0.57	-1.37 ± 0.64
	$q =$	$+0.62 \pm 0.25$	$+0.52 \pm 0.30$
$q - \lambda p = \mu$	$\lambda =$	$+0.39$	$+0.37$
	$\mu =$	$+0.97 \pm 0.14$	$+1.04 \pm 0.20$
$KB^{3/2} \propto n_\mathrm{o}^g V_\mathrm{sh}^h$	$g =$	$+1.25 \pm 0.14$	$+1.31 \pm 0.20$
	$h =$	$+1.26 \pm 0.38$	$+1.58 \pm 0.42$

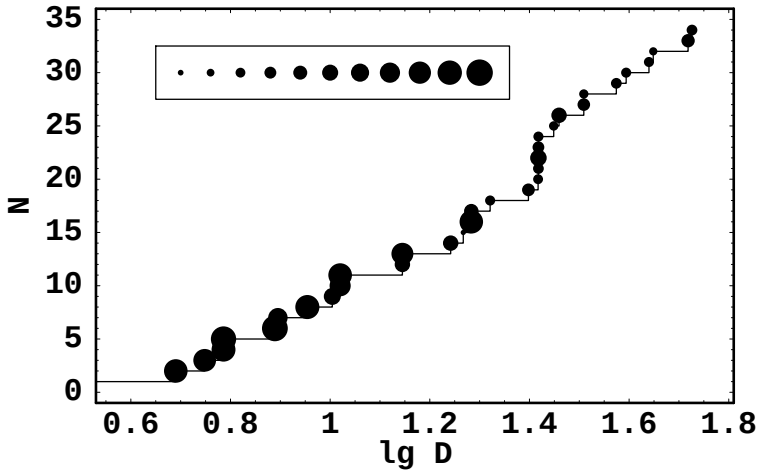

Figure 6.10. Cumulative distribution, for Berkhuijsen's sample, where the dot sizes are proportional to the $\lg n_{\rm o}$ value of the last SNR entering in the cumulative. The legenda uses for the dot sizes the same convention as in Fig. 6.1.

For the Magellanic Clouds, Mills at al. [251] derived an almost linear relation ($N \propto D^{1.2}$) up to sizes as large as 40 pc. They also argued that a similar relation should be present in our Galaxy. A linear cumulative distribution is usually taken as evidence that these SNRs are still in free expansion. However, when the SNR diameter is 40 pc, the swept-up mass is $\sim (1000/n_{\rm o})\,{\rm M}_\odot$. Therefore, except for cases of exceptionally low ambient density, at those sizes SNRs should already be in the Sedov phase, and therefore strongly decelerated.

Within our framework, the cumulative distribution with size is independent of the expansion law of individual SNRs, but is related instead to the statistical distribution of the ambient medium density, as defined by Eq. 6.12. Indeed

$$N(D) \propto \tilde{\mathcal{P}}(n_{\rm o}) n_{\rm o} \propto D^{(1+w)/m}. \tag{6.37}$$

In this sense, it is not even necessary to account for the sample incompleteness, as done by Green [173].

For the sake of illustration, Fig. 6.10 shows the $N(D)$ cumulative distribution of Berkhuijsen's sample. Here the close to linearity of the distribution is coincidental, since there is no reason to expect the sample of Berkhuijsen to be complete. Instead, the trend of dot sizes with SNR diameter (which is to some extent a different way of displaying the information contained in Fig. 6.2) clearly shows how, for increasing size, the cumulative is more populated by SNRs located in more tenuous ISM.

6.5.2. The case of M 82. Samples of SNRs in nearby galaxies have become increasingly available, and the close to linearity of the N–D relation is a rather standard property of these samples.

A particularly interesting case is that of M 82. In this nearby starburst galaxy, a number of radio sources have been detected [217], which may be SNRs that are much brighter and much smaller in size (a few parsec at most) than usual. Their positions on the Σ–D parameter plane are in all cases consistent with the extrapolation to lower sizes of the best-fit Σ–D relation for other galaxies. Chevalier & Fransson [113] proposed that these sources are SNRs expanding in a high-density ambient medium (with densities of order of $10^3\,\mathrm{cm}^{-3}$).

Kronberg et al. [218] also placed upper limits on the flux density variations in most of the radio sources: approximately 75% of these objects are very stable, with a lower limit of $\sim 10^3\,\mathrm{yr}$ to their characteristic radio-emitting lifetimes. Based on this upper limit, Seaquist & Stankovic [328] suggested that they may not be SNRs, but rather cluster wind-driven bubbles. Their main argument is that the lack of observed time variability is inconsistent with the estimated ages of these objects. That is, if they are SNRs in free expansion (with typical velocities of $\sim 10,000\,\mathrm{km\,s}^{-1}$), their ages should be a few hundred years at most, while to account for the lack of variability, velocities no greater than $\sim 500\,\mathrm{km\,s}^{-1}$ are required [113].

A crucial point in this reasoning is the expansion regime of these objects, if they are indeed SNRs. A linear expansion is argued in [150, 261] based on the cumulative distribution with size being almost linear. However, as we have explained above, a linear cumulative distribution does not imply a linear expansion, if it is caused by the combination of SNRs expanding in different ambient densities. Indeed, the data for SNRs in M 82 agree well with the extrapolation of the Σ–D relation derived for SNRs in other galaxies to smaller sizes. Thus, the arguments we have exposed should also be applied to SNRs in M 82.

Even though they have small sizes in the parsec range [261], they could be close to the end of their Sedov phase provided that the ambient densities are $\sim 10^3\,\mathrm{cm}^{-3}$,

with corresponding shock velocities of $\sim 10^3\,\mathrm{km\,s^{-1}}$ compared to $\sim 10^4\,\mathrm{km\,s^{-1}}$ as in the case of undecelerated expansion. These lower shock velocities infer characteristic times of $\sim 10^3\,\mathrm{yr}$, compatible with the average radio-emitting lifetime found by Kronberg et al. [218]. The only exceptions are a few fast-evolving radio sources that are probably radio SNe, namely young objects still evolving in their circumstellar medium. Although the detailed physical conditions and processes at such high densities may differ from those at densities typical of other galaxies, we are confident that the simple estimate presented above is adequate to justify the large measured characteristic times within our framework.

6.6. Conclusions

Studies of the statistical properties of SNR samples may provide insight into the physics of electron acceleration and the time evolution of SNRs. A new scenario is proposed, along the lines of previous work by Berkhuijsen [84], which interprets in a natural way the observed correlations between radio surface brightness Σ, size D, and ambient density n_o in a sample of SNRs. The main parameter of SNR evolution that enters into these correlations is the time at which a SNR ceases to behave as a radio source, and this endpoint is found to be located close to the end of the Sedov phase. It otherwise is found that the observed correlations mostly reflect that the sample consists of SNRs located in very different ambient conditions; while the evolution of individual SNRs plays a secondary role, and cannot be extracted by simply studying correlations between pair of quantities.

Within this framework, we present a new approach to analyzing the statistical data, based on a 2-dimensional fit to Σ as a function of D and n_o. We show that the slope of $\Sigma(D)$ at constant n_o should represent more closely the true evolutionary track of an individual SNR than the well known "Σ–D relation", which is obtained without including information about n_o.

As the first step, we have used data published by Berkhuijsen [84]. Although

this data sample is rather limited, our method of analysis applied to these data is already capable of discriminating to some level between different theoretical models. For instance, models prescribing constant efficiencies for both magnetic field (turbulent) amplification and electron acceleration (e.g., Berezhko & Völk [77]) are well outside the parameters region allowed by the data. On the other hand, models assuming a constant acceleration efficiency but a constant post-shock magnetic field are marginally (about 2-σ) consistent with the data.

We have also applied the same technique to a sample of SNRs in M 33. Although this sample could be affected by selection effects, it is completely independent from the sample of Berkhuijsen, and the parameters that we derive from the two samples are in close agreement, within the statistical errors. This may indicate again that our technique is robust and the assumptions at the basis of our statistical analysis are correct.

CONCLUSIONS

Present work summarizes studies on the acceleration and emission of CRs in SNRs. It contains both theoretical modeling and analysis of observations. In its structure, the thesis solves first a number of task on the shock dynamics and kinetics of charged particles, then it deals with modeling of the nonthermal emission of relativistic electrons. Theoretical models are compared with observations on example of SN 1006 and samples of SNRs in our and neighboring galaxies.

Thesis deals with a new direction of studies, namely analysis of the surface brightness distribution in SNRs. A number of methods to model dynamics of SNRs and emission of accelerated CRs are developed.

Main results are as follows.

1. Radio and X-ray data contain information about distribution of relativistic electrons and magnetic field in SNR. This allows us to develop a model-independent method for synthesis of the inverse-Compton γ-ray map of SNR from the radio (or hard X-ray) map and results of the spatially resolved X-ray spectral analysis. It is applied to SN 1006. It is found that synthesized IC gamma-ray image of SN 1006 is in agreement with HESS observations. This can be considered as an evidence that the TeV gamma-ray emission of SN 1006 is leptonic in origin.

2. The analysis of the spatial distribution of non-thermal emission in SNRs is important channel for theoretical and experimental exploration of CRs and MF in SNRs. Theoretical maps of surface brightness of SNR due to leptonic emission in radio, X-rays and γ-rays reveal that the main factors determining the azimuthal profile of brightness are the dependencies of the electron injection efficiency, the compression/amplification of ISMF and the electron maximum energy on the obliquity angle; radial distribution is mostly sensitive to the time evolution of injection efficiency, to the strength of MF and to the adiabatic constant.

3. Nonuniform ISM and/or nonuniform ISMF results in asymmetric surface bright-

ness distribution of SNR in radio, X-ray and γ-ray bands. SNRs with two limbs of different brightness can be explained if a gradient of ambient density or, most likely, of ambient magnetic field strength is perpendicular to the radio limbs. Converging arcs can be explained by the gradient running between the two arcs. The degree of asymmetry of the remnant morphology depends on the details of the electron injection and acceleration and is different in the radio, hard X-ray, and γ-ray bands. In general, the non-thermal X-ray morphology is the most sensitive to the gradient of ISMF, showing the highest degree of asymmetry. The IC γ-ray emission is weakly sensitive to the non-uniform ISMF, the degree of asymmetry of the remnant morphology being the lowest in this band.

4. Analysis of observation data on SNR should include not only analysis of the spectra but also the exploration of maps in different bands. Method to determine aspect angle of ISMF from the radio map of SNR is developed. It is applied to SN 1006; the aspect angle is $70^{\rm o}$. The model of electron injection should be isotropic in this SNR. Azimuthal variation of the break frequency obtained during the spatially resolved X-ray spectral analysis determines the model of the electron maximum energy; it is time-limited with the ratio of the mean free path of particle to its Larmour radius 1.5. The maximum energy of electrons at the parallel shock is found 7 TeV; it is 3.25 times higher at the perpendicular shock. The thickness of the radial profiles of X-ray brightness agree with the post-shock MF strength in the limbs $50\,\mu$G. The average MF strength in SN 1006 is found $32\,\mu$G, in a good agreement with the 'leptonic' model of the HESS collaboration.

5. In the common scenario of SNR evolution, it is necessary to consider an additional phase between the end of adiabatic and the beginning of radiative stages, because neither adiabatic nor radiative descriptions are applicable during this period. This post-adiabatic stage lasts about 70% of SNR age it has at the end of adiabatic stage and this number is almost independent of the density gradient for ISM with increasing density. The approximate analytical method for description of the shock dynamics and hydrodynamics of the flow downstream, at this evolutionary stage, is developed. The analytical solutions for the motion of the radiative shock

is found and the method for flow hydrodynamics at radiative stage is developed. Methods may be used to model SNRs in nonuniform ISM.

6. Thermal X-ray composites, a class of SNRs with a thermal X-ray centrally-filled morphology within a radio shell, may be explained as a projection of the 2- or 3-dimensional shell-like SNR evolved in a nonuniform medium with scale-height $\leq 10\,\mathrm{pc}$. Such conditions should happen in case of SNR-cloud interaction. TXCs are therefore promising candidates for observations of hadronic γ-ray emission.

7. The efficiency of electron injection (i.e. a fraction of accelerated particles) is related to the post-shock level of the electron-proton thermal equilibration. The efficiency results from the balance between two competing effects: the higher the electron temperature, the higher the fraction of downstream electrons with enough velocity to return to the shock and thus to be ready to cross the shock from downstream to upstream; at the same time, however, the higher the turbulence, which would hinder the crossing.

8. Shell-type supernova remnants exhibit correlations between radio surface brightness, SNR diameter, and ambient medium density, that between the first two quantities being the well known Σ–D relation. The observed correlations are the combined effect of SNRs evolving in a wide range of ambient conditions, rather than the evolutionary track of a "typical" SNR. Statistical analysis of the data samples demonstrates that SNRs cease to emit effectively in radio at a stage near the end of their Sedov evolution, and that models of synchrotron emission with constant efficiencies in particle acceleration and magnetic field amplification do not provide a close match to the data. The slope of the cumulative distribution of SNRs in size is not related to the expansion law of SNRs, as usually assumed, but only to the ambient density distribution.

BIBLIOGRAPHY

[1] Березинский В. Астрофизика космических лучей / Березинский В., Буланов С., Гинзбург В. и др. – Москва: Наука. – 1990. – 528 с.

[2] Гинзбург В. Происхождение космических лучей / Гинзбург В., Сыроватский С. – Москва: Изд. АН СССР. – 1963. – 384 с.

[3] Гинзбург В. Теоретическая физика и астрофизика. Дополнительные главы. – М.: Наука, 1987. – 488 с.

[4] Гинзбург В. Л. Астрофизика космических лучей (история и общий обзор) / Гинзбург В. Л. // Успехи физических наук. – 1996. – Т. 166, № 2. – С. 169-183.

[5] Гнатык Б.И. Сильные адиабатические ударные волны в произвольно неоднородных средах. Аналитический подход / Гнатык Б.И. // Астрофизика. – 1987. – Т. 26. – С. 113.

[6] Гнатык Б.И. Эволюция остатков вспышек сверновых звезд в межзвездной среде с крупномасштабным градиентом плотности / Гнатык Б.И. // Письма в Астрон. Журнал. – 1988. – Т. 14. – С. 725.

[7] Гнатик Б. Новий наближений аналітичний метод розрахунку точкового вибуху в неоднорідному середовищі та його застосування до моделювання рентґенівського випромінювання несферичних залишків наднових зір / Гнатик Б., Петрук, О. // Кінематика і фізика небесних тіл. – 1996. – Т. 12. – С. 44-64.

[8] Гнатик Б. Повний опис точкового вибуху в неоднорідному середовищі в рамках радіаційної газодинаміки / Гнатик Б., Петрук О. // Математичні методи та фізико-механічні поля. – 2002. – Т. 45, № 4. – С. 53-60.

[9] Гнатик Б. Перехід залишків Наднових з адіабатичної до радіаційної стадії еволюції. Аналітичний опис / Гнатик Б., Петрук О., Телєжинський І. // Кінематика і фізика небесних тіл. – 2007. – Т. 23, № 4. – С. 195-206.

[10] Зельдович Я.Б. Физика ударных волн и высокотемпературных гидродинамических явлений / Зельдович Я.Б., Райзер Ю.П. – Москва: Наука, 1966. – 686 с.

[11] Компанеец А.С. Точечный взрыв в неоднородной атмосфере / Компанеец А.С. // Докл. АН СССР. – 1960. – Т. 130. – С. 1001-1003.

[12] Коробейников В.П. Теория точечного взрыва / Коробейников В.П., Мельникова Н.С., Рязанов Е.В.. – Москва: Физматгиз. – 1961. – 332 с.

[13] Коробейников В. Задачи теории точечного взрыва / Коробейников В. – Москва: Наука, 1985. – 400 с.

[14] Лозинская Т. А. Сверхновые звезды и звездный ветер. Взаимодействие с газом Галактики / Лозинская Т. А. – Москва: Мир, 1986. – 304 с.

[15] Петрук О. Рух радіативної ударної хвилі в середовищі з неоднорідним розподілом густини / Петрук О. // Математичні проблеми механіки неоднорідних структур / Наук. збірник в 2 тт. – Т. 2. – Львів, 2006. – С. 142-144.

[16] Петрук О. Рух радіативної ударної хвилі під дією газу з ненульовою масою / Петрук О. // Сучасні проблеми механіки та математики / Наук. збірник в 3 тт. – Львів, 2008. – Т. 3. – С. 144-146.

[17] Петрук О. Синхротронне та теплове випромінювання залишків наднових зір в рентґенівському діапазоні. Слабкі радіаційні втрати електронів / Петрук О., Бешлей В. // Кінематика і фізика небесних тіл. – 2007. – Т. 23, № 1. – С. 25-39.

[18] Петрук О. Синхротронне випромінювання залишків наднових зір в рентґенівському діапазоні. Експоненційне обрізання спектру електронів / Петрук О., Бешлей В. // Кінематика і фізика небесних тіл. – 2008. – Т. 24, № 3. – С. 216-230.

[19] Птускин В. О происхождении галактических космических лучей / Птускин В. // Успехи физических наук. – 2007. – Т. 177, № 5 – С. 558-565

[20] Птускин В. Происхождение космических лучей / Птускин В. // Успехи физических наук. – 2010. – Т. 180, № 9 – С. 1000-1004

[21] Седов Л.И. Методы подобия и размерности в механике / Седов Л.И. – Москва: Наука. – 1977. – 438 с.

[22] Шкловский И. С. Сверхновые звезды / Шкловский И. С. – Москва: Наука, 1966. – 390 с.

[23] Abdo A. Fermi-LAT Discovery of Extended Gamma-ray Emission in the Direction of Supernova Remnant W51C / Abdo A., Ackermann M., Ajello M., Baldini L. et al. // Aph. J. – 2009. – V. 706. – P. L1-L6

[24] Abdo A. A. Fermi/Large area telescope bright gamma-ray source list / Abdo A. A., Ackermann M., Ajello M. et al. // Aph. J. Suppl. – 2009. – V. 183. – P. 46–66.

[25] Abraham J. Observation of the Suppression of the Flux of Cosmic Rays above 4×10^{19} eV / Abraham J., Abreu P., Aglietta M., Aguirre C. et al. // Physical Review Letters. – 2008. – V. 101. – id. 061101 (p.)

[26] Abraham J. Measurement of the Depth of Maximum of Extensive Air Showers above 10^{18} eV / Abraham J., Abreu P., Aglietta M., Ahn E. J. et al. // Phys. Rev. Let. – 2010. – V. 104. – id. 091101 (7 p.)

[27] Abreu P. Update on the correlation of the highest energy cosmic rays with nearby extragalactic matter Abreu P., Aglietta M., Ahn E. J., Allard D. et al. // Astropart. Phys. – 2010. – V. 34. – P. 314-326

[28] Acero F. First detection of VHE γ-rays from SN 1006 by HESS / Acero F., Aharonian F., Akhperjanian A. G. et al. // Astr. & Aph. – 2010. – V. 516. – id. A62 (7 p.).

[29] Acero F. The gas density around SN 1006 / Acero F., Ballet J., Decourchelle A. // Astr. & Aph. – 2007. – V. 475. – P. 883-890.

[30] Acero F. A joint spectro-imaging analysis of the XMM-Newton and HESS observations of the supernova remnant RX J1713.7-3946 / Acero F., Ballet J., Decourchelle A. et al. // Astr. & Aph. – 2009. – V. 505. – P. 157-167.

[31] Adriani O. An anomalous positron abundance in cosmic rays with energies 1.5-100 GeV / Adriani O., Barbarino G., Bazilevskaya G., Bellotti R. et al. // Nature. – 2009. – V. 458. P. 607-609

[32] Aharonian F. Very High Energy Cosmic Gamma Radiation / Aharonian F. – World Scientific, 2003. – 495 p.

[33] Aharonian F. High energy astrophysics with ground-based gamma ray detectors / Aharonian F., Buckley J., Kifune T., Sinnis G., // Rep. Prog. Phys. – 2008. – V. 71. – id. 096901 (56 p.)

[34] Aharonian F. Very high energy gamma rays from the composite SNR G 0.9+0.1 / Aharonian F., Akhperjanian A. G., Aye K.-M. et al. // Astr. & Aph. – 2005. – V. 432. – P. L25-L29.

[35] Aharonian F. Discovery of extended VHE gamma-ray emission from the asymmetric pulsar wind nebula in MSH 15-52 with HESS / Aharonian F., Akhperjanian A. G., Aye K.-M. et al. // Astr. & Aph. – 2005. – V. 435. – P. L17-L20.

[36] Aharonian F. Detection of TeV γ-ray emission from the shell-type supernova remnant RX J0852.0-4622 with HESS / Aharonian F., Akhperjanian A. G., Bazer-Bachi A. R. et al. // Astr. & Aph. – 2005. – V. 437. – P. L7-L10.

[37] Aharonian F. The H.E.S.S. Survey of the Inner Galaxy in Very High Energy Gamma Rays / Aharonian F., Akhperjanian A. G., Bazer-Bachi A. R. et al. // Aph. J. – 2005. – V. 636. – P. 777-797.

[38] Aharonian F. H.E.S.S. Observations of the Supernova Remnant RX J0852.0-4622: Shell-Type Morphology and Spectrum of a Widely Extended Very High Energy Gamma-Ray Source / Aharonian F., Akhperjanian A. G., Bazer-Bachi A. R. et al. // Aph. J. – 2007. – V. 661. – P. 236-249.

[39] Aharonian F. Discovery of very high energy gamma-ray emission coincident with molecular clouds in the W 28 (G6.4-0.1) field / Aharonian F., Akhperjanian A. G., Bazer-Bachi A. R. et al. // Astr. & Aph. – 2008. – V. 481. – P. 401-410.

[40] Aharonian F. Discovery of a VHE gamma-ray source coincident with the supernova remnant CTB 37A / Aharonian F., Akhperjanian A. G., Barres de Almeida U., Bazer-Bachi A. R. et al. // Astr. & Aph. – 2008. – V. 490. – P. 685–693

[41] Aharonian F. Chandra and HESS observations of the supernova remnant CTB 37B / Aharonian F., Akhperjanian A. G., Barres de Almeida U. et al. // Astr. & Aph. – 2008. – V. 486. – P. 829-836.

[42] Aharonian F. Discovery of Gamma-Ray Emission From the Shell-Type Supernova Remnant RCW 86 With HESS / Aharonian F. Akhperjania, A. G., Barres de Almeida U. et al. // Aph. J. – 2009. – V. 692. – P. 1500-1505.

[43] Aharonian F. Evidence for TeV gamma ray emission from Cassiopeia A / Aharonian F., Akhperjanian A., Barrio J. et al. // Astr. & Aph. – 2001. – V. 370. – P. 112-120.

[44] Aharonian F. High-energy particle acceleration in the shell of a supernova remnant / Aharonian F., Akhperjanian A. G., Aye K.-M., Bazer-Bachi A. R. et al. // Nature. – 2004. – V. 432. – P. 75-77

[45] Aharonian F. A detailed spectral and morphological study of the gamma-ray supernova remnant RX J1713.7-3946 with HESS / Aharonian F., Akhperjanian A. G., Bazer-Bachi A. R. et al. // Astr. & Aph. – 2006. – V. 449. – P. 223-242.

[46] Aharonian F. Primary particle acceleration above 100 TeV in the shell-type supernova remnant RX J1713.7-3946 with deep HESS observations / Aharonian F. Akhperjanian A. G., Bazer-Bachi A. R. et al. // Astr. & Aph. – 2007. – V. 464. – P. 235-243.

[47] Aharonian F. GeV/TeV gamma-ray emission from dense molecular clouds overtaken by supernova shells / Aharonian F., Drury L., Völk H. // Astr. & Aph. – 1994. – V. 285. – P. 645-647.

[48] Aharonian F. On the origin of TeV radiation of SN 1006 / Aharonian F., Atoyan A. // Astr. & Aph. – 1999. – V. 351. – P. 330-340.

[49] Aharonian F. High energy astrophysics with ground-based gamma ray detectors / Aharonian F., Buckley J., Kifune T., Sinnis G. // Rep. Prog. Phys. – 2008. – V. 71. – id. 096901 (56 p.).

[50] Albert J. Discovery of Very High Energy Gamma Radiation from IC 443 with the MAGIC Telescope / Albert J., Aliu E., Anderhub H. et al. // Aph. J. – 2007. – V. 664. – P. L87-L90.

[51] Albert J. Observation of VHE γ-rays from Cassiopeia A with the MAGIC telescope / Albert J., Aliu E., Anderhub H. et al. // Astr. & Aph. – 2007. – V. 474. – P. 937-940.

[52] Allen G. Evidence of X-Ray Synchrotron Emission from Electrons Accelerated to 40 TeV in the Supernova Remnant Cassiopeia A / Allen G., Keohane J., Gotthelf E. V. et al. // Aph. J. – 1997. – V. 487. – P. L97-L100.

[53] Allen G. X-ray synchrotron emission from 10-100 TeV cosmic-ray electrons in the supernova remnants SN 1006 / Allen G., Petre R., Gotthelf E. // Proc. 27th ICRC. – 2001. – V. 6. – P. 2440-2443

[54] Allen G. E. Evidence of a Curved Synchrotron Spectrum in the Supernova Remnant SN 1006 / Allen G. E., Houck J. C., Sturner S. J. // Aph. J. – 2008. – V. 683. – P. 773-785.

[55] Ammosov A. E. Synchrotron emission from type I supernova remnants / Ammosov A. E., Ksenofontov L. T., Nikolaev V. S., Petukhov S. I. // Astr. Let– 1994. – V. 20. – P. 157-162.

[56] Aschenbach B. Discovery of a young nearby supernova remnant / Aschenbach B. // Nature, 1998. – V. 396. – P. 141-142

[57] Aschenbach B. X-rays from Supernova Remnants / Aschenbach B. // Proceedings of the 270. WE-Heraeus Seminar on Neutron Stars, Pulsars, and Supernova Remnants. – Garching bei Munchen: Max-Plank-Institut fur extraterrestrische Physik, 2002. – P. 13-25.

[58] Baade W.Cosmic Rays from Super-novae / Baade W., Zwicky F. // Proc. of Nat. Acad of Sci. USA. – 1934. – V. 20. – P. 259

[59] Baade W. Remarks on Super-Novae and Cosmic Rays / Baade W., Zwicky F. // Phys. Rev. – 1934. – V. 46. – P. 76-77

[60] Ballet J. X-ray observations of Supernova Remnants / Ballet J. // ReV. Mex. AA (Serie de Conferencias). – 2003. – V. 15. – P. 237-242.

[61] Ballet J. X-ray synchrotron emission from supernova remnants / Ballet J. // Adv. Space Res. – 2006. – V. 37. – P. 1902-1908.

[62] Balsara D. The Evolution of Adiabatic Supernova Remnants in a Turbulent, Magnetized Medium / Balsara D., Benjamin R. A., Cox D. P. // Aph. J. – 2001. – V. 563. – P. 800-805.

[63] Bamba A. Oxygen line mapping of SN 1006 with Suzaku / Bamba A., Yamaguchi H., Koyama K. et al. // Adv. Space Res. – 2008. – V. 41. – P. 411-415.

[64] Bamba A. Suzaku Wide-Band Observations of SN1006 / Bamba A., Fukazawa Y., Hiraga J. et al. // Publ. Astr. Soc. Japan. – 2008. – V. 60. – P. S153-S162.

[65] Bandiera R. Analytic solutions for the evolution of radiative supernova remnants / Bandiera R., Petruk O. // Astr. & Aph. – 2004. – V. 419. – P. 419-423.

[66] Bandiera R. A statistical approach to radio emission from shell-type SNRs. I. Basic ideas, techniques, and first results / Bandiera R., Petruk O. // Astr. & Aph. – 2010. – V. 509. – id. A34 (9 p.).

[67] Baring M. Radio to Gamma-Ray Emission from Shell-Type Supernova Remnants: Predictions from Nonlinear Shock Acceleration Models / Baring M., Ellison D. C., Reynolds S. P. et al. // Aph. J. – 1999. – V. 513. – P. 311-338.

[68] Baring M. Topical Issues for Particle Acceleration Mechanisms in Astrophysical Shocks / Baring M. // Astrophysics and Space Science. – 2007. – V. 307. – P. 297-303.

[69] Bell A.R. The acceleration of cosmic rays in shock fronts. I / Bell A.R. // Mon. Not. Roy. Ast. Soc. – 1978. – V. 182. – P. 147-156.

[70] Bell A. R. Cosmic ray acceleration to very high energy through the non-linear amplification by cosmic rays of the seed magnetic field / Bell A. R., Lucek S. G. // Mon. Not. Roy. Ast. Soc. – 2001. – V. 321. – P. 433-438.

[71] Bell A. R. Turbulent amplification of magnetic field and diffusive shock acceleration of cosmic rays / Bell A. R. // Mon. Not. Roy. Ast. Soc. – 2004. – V. 353. – P. 550-558

[72] Berezinsky V. Specta of ultra high energy cosmic rays from astrophysical sources. Uniform extragalactic magnetic field / Berezinsky V., Grigorieva S., Petruk O. // Вісник Київського національного університету. Астрономія. – 2003. – Т. 40. – С. 60-63.

[73] Berezhko E. Maximum energy of cosmic rays accelerated by supernova shocks / Berezhko E. // Astropart. Phys. – 1996. – V. 5. – P. 367-378

[74] Berezhko E. A Simple Model of Nonlinear Diffusive Shock Acceleration / Berezhko E., Ellison D. // Aph. J. – 1999. – V. 526. – P. 385-399.

[75] Berezhko E. Emission of SN 1006 produced by accelerated cosmic rays / Berezhko E., Ksenofontov L., Völk H. // Astr. & Aph. – 2002. – V. 395. – P. 943-953.

[76] Berezhko E. G. Confirmation of strong magnetic field amplification and nuclear cosmic ray acceleration in SN 1006 / Berezhko E. G., Ksenofontov L. T., Völk H. J. // Astr. & Aph. – 2003. – V. 412. – P. L11-L14.

[77] Berezhko E. G. The theory of synchrotron emission from supernova remnants / Berezhko E. G., Völk H. J. // Astr. & Aph. – 2004. – V. 427. – P. 525-536.

[78] Berezhko E. G. Direct evidence of efficient cosmic ray acceleration and magnetic field amplification in Cassiopeia A / Berezhko E. G., Völk H. J. // Astr. & Aph. – 2004. – V. 419. – P. L27-L30.

[79] Berezhko E. G. Gamma-ray astronomy and cosmic ray origin problem / Berezhko E. G. // Adv. Space Res. – 2005. – V. 35. – P. 1031–1040.

[80] Berezhko E. G. Theory of cosmic ray production in the supernova remnant RX J1713.7-3946 / Berezhko E. G., Völk H. J. // Astr. & Aph. – 2006. – V. 451. – P. 981-990.

[81] Berezhko E. G. Spectrum of Cosmic Rays Produced in Supernova Remnants / Berezhko E. G., Völk H. J. // Aph. J. – 2007. – V. 661. – P. L175-L178.

[82] Berezhko E. G. Hadronic versus leptonic origin of the gamma-ray emission from supernova remnant RX J1713.7-3946 / Berezhko E. G., Völk H. J. // Astr. & Aph. – 2008. – V. 492. – P. 695-701.

[83] Berezhko E. G. Cosmic ray acceleration parameters from multi-wavelength observations. The case of SN 1006 / Berezhko E. G., Ksenofontov L. T., Völk H. J. // Astr. & Aph. – 2009. – V. 505. – P. 169-176.

[84] Berkhuijsen E. M. Properties of supernova remnants at kwnown distances I. Surface brightness and radio spectral index / Berkhuijsen E. M. // Astr. & Aph. – 1986. – V. 166. – P. 257-270.

[85] Bisnovatyi-Kogan G. Shock-wave propagation in the nonuniform interstellar medium / Bisnovatyi-Kogan G., Silich, S. // Rev. Mod. Phys. – 1995. – V. 67. – P. 661-712.

[86] Blandford R. Particle acceleration at astrophysical shocks: A theory of cosmic ray origin / Blandford R., Eichler D. // Phys. Rep. – 1987. – V. 154. – P. 1-75.

[87] Blasi P. A semi-analytical approach to non-linear shock acceleration / Blasi P. // Astroparticle Physics. – 2002. – V. 16. – P. 429-439.

[88] Blasi P. Cosmic Ray Acceleration in Supernova Remnants / Blasi P. [Електронний ресурс] // arXiv.org. – 2010. – http://arxiv.org/abs/1012.5005v1

[89] Blinnikov S. The Cygnus Superbubble as the remnant of a peculiar supernova / Blinnikov S., Imshennik V., Utrobin V. // Sov. Astr. Let. – 1982. – V. 8. – P. 361-365.

[90] Blondin J. Transition to the radiative phase in supernova remnants / Blondin J., Wright E., Borkowski K., Reynolds S. // Aph. J. – 1998. – V. 500. – P. 342-354.

[91] Blumenthal G. Bremsstrahlung, Synchrotron Radiation, and Compton Scattering of High-Energy Electrons Traversing Dilute Gases / Blumenthal G., Gould R. // Rev. Mod. Phys. – 1970. – V. 42. – P. 237-271.

[92] Bocchino F. High Resolution X-ray Observations of Supernova Remnants / Bocchino F. // Chin. J. Astr. Aph. Suppl. – 2003. – V. 3. – P. 329–340.

[93] Borkowski K. J. Supernova Remnants in the Sedov Expansion Phase: Thermal X-Ray Emission / Borkowski K. J., Lyerly W. J., Reynolds S. P. // Aph. J. – 2001. – V. 548. – P. 820-835.

[94] Borkowski K.J. On the X-ray spectrum of Kepler's supernova remnant / Borkowski K.J., Sarazin C.L., Blondin J.M. // Aph. J. – 1994. – V. 429. – P. 710-725.

[95] Brogan C. L. Discovery of a Radio Supernova Remnant and Nonthermal X-Rays Coincident with the TeV Source HESS J1813-178 / Brogan C. L., Gaensler B. M., Gelfand J. D., Lazendic J. S., et al. // Aph. J. – 2005. – V. 629. – P. L105–L108

[96] Bykov A. Electron kinetics in collisionless shock waves / Bykov A., Uvarov Yu. // J. Exper. and Theor. Phys. – 1999. – V. 88. – P. 465-475.

[97] Bykov A. M. Nonthermal Emission from a Supernova Remnant in a Molecular Cloud / Bykov A. M., Chevalier R. A., Ellison D. C., Uvarov Yu. A. // Aph. J. – 2000. – V. 538. – P. 203-216.

[98] Bykov A. M. Shocks and particle acceleration in SNRs: theoretical aspects / Bykov A. M. // Adv. Space Res. – 2004. – V. 33, No 4. – P. 366–375.

[99] Bykov A. M. Dots, Clumps, and Filaments: The Intermittent Images of Synchrotron Emission in Random Magnetic Fields of Young Supernova Remnants / Bykov A. M., Uvarov Y. A., Ellison D. C. // Aph. J. – 2008. – V. 689. – P. L133-L136

[100] Canizares C.R. Recent X-ray observations of supernova remnants / Canizares C.R. // Phil. Trans. Royal Soc. Lond. A. – 2002. – V. 360. – P. 1981-1989.

[101] Caprioli D. Non-linear diffusive acceleration of heavy nuclei in supernova remnant shocks / Caprioli D., Blasi P., Amato E. // Astropar. Phys. – 2011. – V. 34. – P. 447-456

[102] Catanese M. Very High Energy Gamma-Ray Astronomy / Catanese M., Weekes T. // Publ. Astr. Soc. Pasif. – 1999. – V. 111. – P. 1193-1222

[103] Case G. L. A New Sigma-D Relation and Its Application to the Galactic Supernova Remnant Distribution / Case G. L., Bhattacharya D. // Aph. J. – 1998. – V. 504. – P. 761-772.

[104] Cassam-Chenaï G. Morphology of synchrotron emission in young supernova remnants / Cassam-Chenaï G., Decourchelle A., Ballet J., Ellison D. C. // Astr. & Aph. – 2005. – V. 443. – P. 955-959.

[105] Cassam-ChenaïG. The blast wave of Tycho's supernova remnant / Cassam-ChenaïG., Hughes J. P., Ballet J., Decourchelle A. // Aph. J. – 2007. – V. 665. – P. 315-340.

[106] Cassam-Chenaï G. Morphological Evidence for Azimuthal Variations of the Cosmic-Ray Ion Acceleration at the Blast Wave of SN 1006 / Cassam-Chenaï G., Hughes J. P., Reynoso E. M., Badenes C., Moffett D. // Aph. J. – 2008. – V. 680. – P. 1180-1197.

[107] Caswell J. L. Galactic supernova remnants - Dependence of radio brightness on galactic height and its implications / Caswell J. L., Lerche I. // Mon. Not. Roy. Ast. Soc. – 1979. – V. 187. – P. 201-216.

[108] Caswell J. L. Neutral hydrogen absorption measurements yielding kinematic distances for 42 continuum sources in the galactic plane / Caswell J. L., Murray J. D., Roger R. S. et al. // Astr. & Aph. – 1975. – V. 45. – P. 239-258.

[109] Chevalier R. A. The Evolution of Supernova Remnants. Spherically Symmetric Models / Chevalier R. A. // Aph. J. – 1974. – V. 188. – P. 501-519.

[110] Chevalier R. A. Self-similar solutions for the interaction of stellar ejecta with an external medium / Chevalier R. A. // Aph. J. – 1982. – V. 258. – P. 790-797.

[111] Chandra X-ray Observatory Center [Електронний ресурс]. – http://chandra.harvard.edu/

[112] Chandra Supernova Remnant Catalogue [Електронний ресурс]. – http://hea-www.harvard.edu/ChandraSNR/

[113] Chevalier R. A. The nature of the compact supernova remnants in starburst galaxies / Chevalier R. A., Fransson C. // Aph. J. – 2001. – V. 558. – P. L27-L30.

[114] Cioffi D. F. Dynamics of radiative supernova remnants / Cioffi D. F., McKee C. F. Bertschinger E. // Aph. J. – 1988. – V. 334. – P. 252-265.

[115] Clark D. H. A study of galactic supernova remnants, based on Molonglo-Parkes observational data / Clark D. H., Caswell J. L. // Mon. Not. Roy. Ast. Soc. – 1976. – V. 174. – P. 267-305.

[116] Cohen E. Fluid Dynamics of Semiradiative Blast Waves / Cohen E., Piran T., Sari R. // Aph. J. – 1998. – V. 509. – P. 717-727.

[117] Cowsik R. A lower limit to the magnetic field in Cassiopeia-A / Cowsik R., Sarkar S. // Mon. Not. Roy. Ast. Soc. – 1980. – V. 191. – P. 855-861

[118] Cosmic ray // Wikipedia [Електронний ресурс]. – http://en.wikipedia.org /wiki/Cosmic_ray

[119] Cox D. P. Extended adiabatic blast waves and a model of the soft X-ray background / Cox D. P., Anderson P. R. // Aph. J. – 1982. – V. 253. – P. 268-289.

[120] Cox D. P. The terrain of evolution of isotropic adiabatic supernova remnants / Cox D. P. // Aph. J. – 1986. – V. 304. – P. 771-779.

[121] Cox D. P. Cooling and Evolution of a Supernova Remnant / Cox D. P. // Aph. J. – 1972. – V. 178. – P. 159-168.

[122] Cox D. Modeling W44 as a Supernova Remnant in a Density Gradient with a Partially Formed Dense Shell and Thermal Conduction in the Hot Interior. I. The Analytical Model / Cox D., Shelton R., Maciejewski W. et al. // Aph. J. – 1999. – V. 524. – P. 179-191.

[123] Crutcher R. Observations of Interstellar Magnetic Fields / Crutcher R., Heiles C., Troland T. // Lect. Notes in Phys. – 2003. – V. 614. – P. 155-181.

[124] Decourchelle A. Thermal X-Ray Emission and Cosmic-Ray Production in Young Supernova Remnants / Decourchelle A., Ellison D. C., Ballet J. // Aph. J. – 2000. – V. 543. – P. L57-L60.

[125] Decourchelle A. Elemental composition and distribution in SNRs: X-ray spectroscopy / Decourchelle A. // New Astronomy Rev. – 2004. – V. 48. – P. 75–79.

[126] Dickel J. R. Radio structure of the remnant of Tycho's supernova (SN 1572) / Dickel J. R., van Breugel W. J. M., Strom R. G. // Astr. J. – 1991. – V. 101. – P. 2151-2159.

[127] Dohm-Palmer R. C. Young Supernova Remnants in Nonuniform Media / Dohm-Palmer R. C., Jones T. W. // Aph. J. – 1996. – V. 471. – P. 279-291.

[128] Drury L.O'C. An introduction to the theory of diffusive shock acceleration of energetic particles in tenuous plasmas / Drury L.O'C. // Rep. Prog. Phys. – 1983. – V. 46. – P. 973-1027.

[129] Drury L. The gamma-ray visibility of supernova remnants. A test of cosmic ray origin / Drury L., Aharonian F., Völk H. // Astr. & Aph. – 1994. – V. 287. – P. 959-971.

[130] Drury L. O'C. Test of galactic cosmic-ray source models - Working Group Report / Drury L. O'C., Ellison D. E., Aharonian F. A. et al. // Space Sci. Rev. – 2001. – V. 99. – P. 329-352.

[131] Drury L. O'C. Current status of shock acceleration theory / Drury L. O'C. // J. Korean Astr. Society. – 2004. – V. 37. – P. 393-398.

[132] Dubner G. M. The neutral gas environment of the young supernova remnant SN 1006 (G327.6+14.6) / Dubner G. M., Giacani E. B., Goss W. M. et al. // Astr. & Aph. – 2002. – V. 387. – P. 1047-1056.

[133] Duric N. A theoretical interpretation of the Sigma-D relation for suprnova remnants / Duric N., Seaquist E. R. // Aph. J. – 1986. – V. 301. – P. 308-311.

[134] Dyer K. K. Separating Thermal and Nonthermal X-Rays in Supernova Remnants. II. Spatially Resolved Fits to SN 1006 AD / Dyer K. K., Reynolds S. P., Borkowski K. J. // Aph. J. – 2004. – V. 600. – P. 752-768.

[135] Early History of Cosmic Ray Studies / Eds Y. Sekido, H. Elliot. – Dordrecht: D. Reidel Publ. Co., 1985. – 460 p.

[136] Ellison D. C. Supernova remnants and the physics of strong shock waves / Ellison D. C., Reynolds S. P., Borkowski K. et al. // Publ. Astr. Soc. Pasif. – 1994. – V. 106. – P. 780-797.

[137] Ellison D. C. Acceleration Rates and Injection Efficiencies in Oblique Shocks / Ellison D. C., Baring M. G., Jones F. C. // Aph. J. – 1995. – V. 453. – P. 873-882.

[138] Ellison D.C. First-order Fermi particle acceleration by relativistic shocks / Ellison D.C., Reynolds S. P., Jones F. C. // Aph. J. – 1990. – V. 360. – P. 702-714.

[139] Ellison D. C. Galactic Cosmic Rays from Supernova Remnants. II. Shock Acceleration of Gas and Dust / Ellison D. C., Drury L. O., Meyer J.-P. // Aph. J. – 1997. – V. 487. – P. 197-217

[140] Ellison D. C. Nonlinear Shock Acceleration and Photon Emission in Supernova Remnants / Ellison D. C., Berezhko E. G., Baring M. G. // Aph. J. – 2000. – V. 540. – P. 292-307.

[141] Ellison D. C. Broadband Observations and Modeling of the Shell-Type Supernova Remnant G347.3-0.5 / Ellison D. C., Slane P. , Gaensler B. M. // Aph. J. – 2001. – V. 563. – P. 191-201.

[142] Ellison D. C. Hydrodynamic simulation of supernova remnants including efficient particle acceleration / Ellison D. C., Decourchelle A., Ballet J. // Astr. & Aph. – 2004. – V. 413. – P. 189-201.

[143] Ellison D. Radio and X-Ray Profiles in Supernova Remnants Undergoing Efficient Cosmic-Ray Production / Ellison D., Cassam-Chenaï G. // Aph. J. – 2005. – V. 632. – P. 920-931.

[144] Enomoto R. The acceleration of cosmic-ray protons in the supernova remnant RX J1713.7-3946 / Enomoto R., Tanimori T., Naito T. et al. // Nature. – 2002. – V. 416. – P. 823-826.

[145] Enomoto R. CANGAROO III Observations of the Supernova Remnant RX J0852.0-4622 / Enomoto R., Watanabe S., Tanimori T. et al. // Aph. J. – 2006. – V. 652. – P. 1268-1276.

[146] Erlykin A. D. Supernova remnants and the origin of the cosmic radiation: the electron component / Erlykin A. D., Wolfendale A. W. // J. Phys. G: Nuclear and Particle Physics. – 2002. – V. 28. – P. 359-378

[147] Falle S. A. E. G. Numerical calculation of thin shell formation in supernova remnants / Falle S. A. E. G. // Mon. Not. Roy. Ast. Soc. – 1975. – V. 172. – P. 55-84.

[148] Falle S. A. E. G., Catastrophic cooling in supernova remnants / Falle S. A. E. G. // Mon. Not. Roy. Ast. Soc. – 1981. – V. 195. – P. 1011-1028.

[149] Feenberg E. Interaction of Cosmic-Ray Primaries with Sunlight and Starlight / Feenberg E., Primakoff H. // Phys. Rev. – 1948. – V. 73. – P. 449-469

[150] Fenech D. M. Deep MERLIN 5 GHz radio imaging of supernova remnants in the M82 starburst / Fenech D. M., Muxlow T. W. B., Beswick R. J. et al. // Mon. Not. Roy. Ast. Soc. – 2008. – V. 391. – P. 1384-1402.

[151] Fermi Gamma-ray Space Telescope [Електронний ресурс]. – http://fermi.gsfc.nasa.gov/

[152] Fermi LAT 1-year Point Source Catalog [Електронний ресурс]. – http://fermi.gsfc.nasa.gov/ssc/data/access/lat/1yr_catalog/

[153] Ferrand G. 3D simulations of supernova remnants evolution including non-linear particle acceleration / Ferrand G., Decourchelle A., Ballet J. et al. // Astr. & Aph. – 2010. – V. 509. – id. L10 (4 p.).

[154] Franco J. Thin shell formation in radiative shocks. 1: Supernova remnants in low-density media / Franco J., Miller W.W., Arthur S.J. et al. // Aph. J. – 1994. – V. 435. – P. 805-814.

[155] Freedman W. L. Final results from the Hubble ST Key Project to Measure the Hubble Constant / Freedman W. L., Madore B. F., Gibson B. K. et al. // Aph. J. – 2001. – V. 553. – P. 47-72.

[156] Fryxell B. FLASH: An Adaptive Mesh Hydrodynamics Code for Modeling Astrophysical Thermonuclear Flashes / Fryxell B., Olson K., Ricker P. et al. // Aph. J. Suppl. – 2000. – V. 131. – P. 273-334.

[157] Fulbright M. S. Bipolar supernova remnants and the obliquity dependence of shock acceleration / Fulbright M. S., Reynolds S. P. // Aph. J. – 1990. – V. 357. – P. 591-601.

[158] Funk S. VHE Gamma-ray supernova remnants / Funk S. // Adv. Space Res. – 2008. – V. 41. – P. 464–472.

[159] Gaensler B. M. The Nature of Bilateral Supernova Remnants / Gaensler B. M. // Aph. J. – 1998. – V. 493. – P. 781-792.

[160] Gaffet B. Semianalytical treatment of the hydrodynamics of supernova remnants during the snowplow phase / Gaffet B. // Aph. J. – 1983. – V. 273. – P. 267-279.

[161] Gaisser T. K. Cosmic rays and particle physics / Gaisser T. K. – Cambridge: Cambridge University Press, 1990. – 279 p.

[162] Gaisser T. K. Gamma-Ray Production in Supernova Remnants / Gaisser T. K., Protheroe R. J., Stanev T. // Aph. J. – 1998. – V. 492. – P. 219-227.

[163] Gaiser T. Cosmic Rays at the Knee / Gaiser T. [Електронний ресурс] // arXiv.org. – 2006. – http://arxiv.org/abs/astro-ph/0608553v1

[164] Gerardy C. L., Fesen R. A. Near-Infrared Spectroscopy of the Cassiopeia A and Kepler Supernova Remnants / Gerardy C. L., Fesen R. A. // Astr. J. – V. 121. – P.2781-2791

[165] Giacalone J. Magnetic Field Amplification by Shocks in Turbulent Fluids / Giacalone J., Jokipii J. R. // Aph. J. – 2007. – V. 663. – P. L41-L44.

[166] Giacani E. B. The Interstellar Matter in the Direction of the Supernova Remnant G296.5+10.0 and the Central X-Ray Source 1E 1207.4-5209 / Giacani E. B., Dubner G. M., Green A. J., Goss W. M., Gaensler B. M. // Astr. J. – 2000. – V. 119. – P. 281-291.

[167] Gieseler U.D.J. Time dependent cosmic-ray shock acceleration with self-consistent injection / Gieseler U.D.J., Jones T.W., Kang H. // Astr. & Aph. – 2000. – V. 364. – P. 911-922.

[168] Ginzburg V. L. Cosmic Magnetobremsstrahlung (synchrotron Radiation) / Ginzburg V. L., Syrovatskii S. I. // Ann. Rev. Astr. Aph. – 1965. – V. 3. – P. 297-350.

[169] Ghavamian P. Balmer-dominated Spectra of Nonradiative Shocks in the Cygnus Loop, RCW 86, and Tycho Supernova Remnants / Ghavamian P., Raymond J.C., Smith R.C., Hartigan P. // Aph. J. – 2001. – V. 547. – P. 995-1009.

[170] Ghavamian P. The Optical Spectrum of the SN 1006 Supernova Remnant Revisited / Ghavamian P., Winkler P., Raymond J.C., Long K. // Aph. J. – 2002. – V. 572. – P. 888-896.

[171] Goodman A. A. Optical polarization maps of star-forming regions in Perseus, Taurus, and Ophiuchus / Goodman A. A., Bastien P., Menard F., Myers P. C. // Aph. J. – 1990. – V. 359. – P. 363-377.

[172] Green D.A. A Catalogue of Galactic Supernova Remnants / Green D.A. [Електронний ресурс]. – Cambridge: Mullard Radio Astronomy Observatory. – 2009. – `http://www.mrao.cam.ac.uk/surveys/snrs/`.

[173] Green D. A. Statistical studies of supernova remnants / Green D. A. // Mon. Not. Roy. Ast. Soc. – 1984. – V. 209. – P. 449-478.

[174] Green D. A. Some statistics of Galactic SNRs / Green D. A. // Memorie della Societa Astronomica Italiana. – 2005. – V. 76. – P. 534-541.

[175] Green D. A. A revised Galactic supernova remnant catalogue / Green D. A. // Bull. Astr. Soc. of India. – 2009. – V. 37. – P. 45-61.

[176] Greisen K. End to the Cosmic-Ray Spectrum? / Greisen K. // Phys. Rev. Let. – 1966. – V. 16. – P. 748-750

[177] Gordon S. M. A new optical sample of supernova remnants in M33 / Gordon S. M., Kirshner R. P., Long K. S. et al. // Aph. J. Suppl. – 1998. – V. 117. – P. 89-133.

[178] Gordon S. M. A new sample of radio-selected and optically confirmed SNRs in M33 / Gordon S. M., Duric N., Kirshner R. P. et al. // Aph. J. Suppl. – 1999. – V. 120. – P. 247-264.

[179] Halzen F. The Search for the Sources of the Cosmic Rays One Century after their Discovery / Halzen F. [Електронний ресурс] // arXiv.org. – 2010. – http://arxiv.org/abs/1010.0235

[180] Hamilton A. J. S. X-ray line emission from supernova remnants. I - Models for adiabatic remnants / Hamilton A. J. S., Sarazin C. L., Chevalier R. A. // Aph. J. Suppl. – 1983. – V. 51. – P. 115-147.

[181] Hartman R. The Third EGRET Catalog of High-Energy Gamma-Ray Sources / Hartman R., Bertsch D., Bloom S. D. et al. // Aph. J. Suppl. – 1999. – V. 123. – P. 79-202.

[182] Hayakawa S. Propagation of the Cosmic Radiation through Intersteller Space / Hayakawa S. // Prog. Theor. Phys. – 1952. – V. 8. – P. 571-572

[183] Helder E. A. Measuring the Cosmic-Ray Acceleration Efficiency of a Supernova Remnant / Helder E. A., Vink J., Bassa C. G., Bamba A. et al. // Science. – 2009. – 325. – P. 719-722

[184] Hendrick S. P. Maximum Energies of Shock-accelerated Electrons in Large Magellanic Cloud Supernova Remnants / Hendrick S. P., Reynolds S. P. // Aph. J. – 2001. – V. 559. – P. 903-908.

[185] The High Energy Stereoscopic System [Електронний ресурс]. – http://www.mpi-hd.mpg.de/hfm/HESS/

[186] The H.E.S.S. Source Catalog [Електронний ресурс]. – http://www.mpi-hd.mpg.de/hfm/HESS/pages/home/sources/

[187] Hilditch R. W. Forty eclipsing binaries in the Small Magellanic Cloud: fundamental parameters and Cloud distance / Hilditch R. W., Howarth I. D., Harries T. J. // Mon. Not. Roy. Ast. Soc. – 2005. – V. 357. – P. 304-324.

[188] Hillas A. M. Ground-based gamma-ray astronomy / Hillas A. M. // Proc. 24th International Cosmic Ray Conference / Eds. Iucci N., Lamanna E. – Bologna: Societa Italiana di Fisica, 1995. – P. 701.

[189] Hillas A. M. Can diffusive shock acceleration in supernova remnants account for high-energy galactic cosmic rays? / Hillas A. M. // J. Phys. G: Nucl. Part. Phys. – 2005. – V. 31. – P. R95–R131.

[190] Hillas A. M. Cosmic Rays: Recent Progress and some Current Questions / Hillas A. M. [Електронний ресурс] // arXiv.org. – 2006. – http://arxiv.org/abs/astro-ph/0607109v2

[191] Hinton J. A. Inverse Compton Scenarios for the TeV Gamma-Ray Emission of the Galactic Center / Hinton J. A., Aharonian F. A. // Aph. J. – 2007. – V. 657. – P. 302-307.

[192] Hinton J. A. Teraelectronvolt Astronomy / Hinton J. A., Hofmann W. // Ann. Rev. Astr. Aph. – 2009. – V. 47. – P. 523–65.

[193] Hnatyk B. I. Strong Adiabatic Shock Waves in Arbitrary Nonuniform Media - Analytic Approach / Hnatyk B. I. // Astrofizika. – 1987. – V. 26. – P. 113-128.

[194] Hnatyk B. Supernova Remnants as Cosmic Ray Accelerators / Hnatyk B., Petruk O. // Condensed Matter Physics. – 1998. – V. 1. – P. 655-667.

[195] Hnatyk B. Evolution of supernova remnants in the interstellar medium with a large-scale density gradient. I. General properties of the morphological evolution and X-ray emission / Hnatyk B., Petruk O. // Astr. & Aph. – 1999. – V. 344. – P. 295-309.

[196] Hoppe S. H.E.S.S. observations of the supernovae remnant RCW 86 / Hoppe S., Lemoine-Goumard M. // Proc. 30th International Cosmic Ray Conference / Eds. Caballero R., D'Olivo J. C. et al. – Mexico, 2008. – V. 2. – P. 585–588.

[197] Hughes J. Electron Heating and Cosmic Rays at a Supernova Shock from Chandra X-Ray Observations of 1E 0102.2-7219 / Hughes J., Rakowski C., Decourchelle A. // Aph. J. – 2000. – V. 543. – P. L61-L65.

[198] Hutchinson G. W. On the possible relation of galactic radio noise to cosmic rays / Hutchinson G. W. // Philosophical Magazine Series 7. – 1952. – V. 43. – P. 847–852

[199] Hwang U. Thermal and Nonthermal X-Ray Emission from the Forward Shock in Tycho's Supernova Remnant / Hwang U., Decourchelle A., Holt S. S., Petre R. // Aph. J. – 2002. – V. 581. – P. 1101-1115.

[200] Jokipii J. R. Rate of energy gain and maximum energy in diffusive shock acceleration / Jokipii J. R. // Aph. J. – 1987. – V. 313. – P. 842-846.

[201] Jones F. Calculated Spectrum of Inverse-Compton-Scattered Photons / Jones F. // Phys. Rev. – 1968. – V. 167. – P. 1159-1169.

[202] Jones F.C. The plasma physics of shock acceleration / Jones F.C., Ellison D.C. // Space Sci. Rev. – 1991. – V. 58. – P. 259-346.

[203] Jones T. W. 10^{51} Ergs: The Evolution of Shell Supernova Remnants / Jones T. W., Rudnick L., Jun Byung-Il. et al. // Publ. Astr. Soc. Pasif. – 1998. – V. 110, No 744. – P. 125–151.

[204] Jones T. The Identification of Infrared Synchrotron Radiation from Cassiopeia A / Jones T., Rudnick L., DeLaney T., Bowden J. // Aph. J. – 2003. – V. 587. – P. 227-234

[205] Jun B.-I. On the Origin of Radial Magnetic Fields in Young Supernova Remnants / Jun B.-I., Norman M. L. // Aph. J. – 1996. – V. 472. – P. 245-256.

[206] Kahn F.D. The temperature in very old supernova remnants / Kahn F.D. // Astr. & Aph. – 1976. – V. 50. – P. 145-148.

[207] Kane J. An Evaluation of the Richtmyer-Meshkov Instability in Supernova Remnant Formation / Kane J., Drake R. P., Remington B. A. // Aph. J. – 1999. – V. 511. – P. 335-340.

[208] Kang H. Diffusive Shock Acceleration in Test-particle Regime / Kang H., Ryu D. // Aph. J. – 2010. – V. 721. – P. 886-892

[209] Katagiri H. Detection of Gamma Rays around 1 TeV from RX J0852.0-4622 by CANGAROO-II / Katagiri H., Enomoto R., Ksenofontov L. T. et al. // Aph. J. – 2005. – V. 619. – P. L163-L166.

[210] Keohane J. A Possible Site of Cosmic Ray Acceleration in the Supernova Remnant IC 443 / Keohane J., Petre R., Gotthelf E. V. et al. // Aph. J. – 1997. – V. 484. – P. 350-359.

[211] Kesteven M. J. L. Supernova remnants as radio sources / Kesteven M. J. L. // Australian J. of Physics. – 1968. – V. 21. – P. 739-754.

[212] Kesteven M. J. Barrel-shaped supernova remnants / Kesteven M. J., Caswell J. L. // Astr. & Aph. – 1987. – V. 183. – P. 118-128.

[213] Korobeinikov V. / Korobeinikov V., Karlikov V. // Doklady Akademii Nauk SSSR. – 1960. – V. 133. – P. 764.

[214] Korreck K.E. Far Ultraviolet Spectroscopic Explorer Observation of the Non-radiative Collisionless Shock in the Remnant of SN 1006 / Korreck K.E., Raymond J.C., Zurbuchen T.H., Ghavamian P. // Aph. J. – 2004. – V. 615. – P. 280-285.

[215] Koyama K. Evidence for Shock Acceleration of High-Energy Electrons in the Supernova Remnant SN 1006 / Koyama K., Petre R., Hwang U. et al. // Nature. – 1995. – V. 378. – P. 255-258.

[216] Koyama K. Discovery of Non-Thermal X-Rays from the Northwest Shell of the New SNR RX J1713.7-3946: The Second SN 1006? / Koyama K., Kinugasa K., Pye J. P., Stewart G. C. // Publ. Astr. Soc. Japan. – 1997. – V. 49. – P. L7-L11.

[217] Kronberg P. K. The nucleus of M82 at radio and X-ray bands: discovery of a new radio population of supernova candidates / Kronberg P. K., Biermann P., Schwab F. R. // Aph. J. – 1985. – V. 291. – P. 693-707.

[218] Kronberg P. K. A search for flux density variations in 24 compact radio sources in M82 / Kronberg P. K., Sramek R. A., Birk G. T. et al. // Aph. J. – 2000. – V. 535. – P. 706-711.

[219] Ksenofontov L. T. Dependence of the gamma-ray emission from SN 1006 on the astronomical parameters / Ksenofontov L. T., Berezhko E. G., Völk H. J. // Astr. & Aph. – 2005. – V. 443. – P. 973-980.

[220] Lagage P. O. The maximum energy of cosmic rays accelerated by supernova shocks / Lagage P. O., Cesarsky C. J. // Astr. & Aph. – 1983. – V. 125. – P. 249

[221] Laming J.M. Electron Heating at SNR Collisionless Shocks / Laming J.M. // Aph. J. Suppl. – 2000. – V. 127. – P. 409-413.

[222] Laming J.M. Electron-Ion Equilibration in Nonradiative Shocks Associated with SN 1006 / Laming J.M., Raymond J.C., McLaughlin B.M., Blair W.P. // Aph. J. – 1996. – V. 472. – P. 267-274.

[223] Lazendic J. S. A High-Resolution Study of Nonthermal Radio and X-Ray Emission from Supernova Remnant G347.3-0.5 / Lazendic J. S., Slane P. O., Gaensler B. M. et al. // Aph. J. – 2004. – V. 602. – P. 271-285.

[224] Lee S.-H. Three-dimensional Model of Broadband Emission from Supernova Remnants Undergoing Nonlinear Diffusive Shock Acceleration / Lee S.-H., Kamae T., Ellison D. C. // Aph. J. – 2008. – V. 686. – P. 325-336.

[225] Leckband J. A. On evidence for quasi-parallel and quasi-perpendicular acceleration in supernova remnants / Leckband J. A., Spangler S. R., Cairns I. H. // Aph. J. – 1989. – V. 338. – P. 963-971.

[226] Lembege B. Selected problems in collisionless-shock physics / Lembege B., Giacalone J., Scholer M. et al. // Space Sci. Rev. – 2004. – V. 110. – P. 161–226.

[227] Leroy M. M. The structure of perpendicular bow shocks / Leroy M. M., Winske D., Goodrich C. C., Wu C. S., Papadopoulos K. // J. Geoph. Res. – 1982. – V. 87. – P. 5081-5094.

[228] Levinson A. Electron injection in collisionless shocks / Levinson A. // Aph. J. – 1992. – V. 401. – P. 73-80.

[229] Liang E. An Analytic Approximation to Radiative Blast Wave Evolution / Liang E., Keilty K. // Aph. J. – 2000. – V. 533. – P. 890-892.

[230] Long K. S. The X-ray properties of Suopernova Remnants in the Large Magellanic Cloud / Long K. S. // SNRs and their X-ray emission / Eds. Danziger J., Gorenstein P. – Dordrecht: Reidel Publishing, 1983. – P. 525-533.

[231] Long K. W28 and 3C 400.2 - Two shell-like radio supernova remnants with centrally peaked X-ray morphologies / Long K., Blair W., White R., Matsui Y. // Aph. J. – 1991. – V. 373. – P. 567-578.

[232] Long K. S. Chandra CCD Imagery of the Northeast and Northwest Limbs of SN 1006 / Long K. S., Reynolds S. P., Raymond J. C. et al. // Aph. J. – 2003. – V. 586. – P. 1162-1178.

[233] Longair M. S. High Energy Astrophysics / Longair M. S. – Vol. 1. – Cambridge: Cambridge University Press, 1992. – 440 p.

[234] Lucek S. G. Non-linear amplification of a magnetic field driven by cosmic ray streaming / Lucek S. G., Bell A. R. // Mon. Not. Roy. Ast. Soc. – 2000. – V. 314. – P. 65-74.

[235] Maciejewski W. Supernova Remnant in a Stratified Medium: Explicit, Analytical Approximations for Adiabatic Expansion and Radiative Cooling / Maciejewski W., Cox D.P. // Aph. J. – 1999. – V. 511. – P. 792-797.

[236] Mac Low M.-M. Control of star formation by supersonic turbulence / Mac Low M.-M., Klessen R. S. // Rev. Mod. Phys. – 2004. – V. 76. – P. 125-194.

[237] MacNeice P. PARAMESH: A parallel adaptive mesh refinement community toolkit / MacNeice P., Olson K. M., Mobarry C. et al. // Comp. Phys. Comm. – 2000. – V. 126. – P. 330-354.

[238] Macri L. M. A New Cepheid Distance to the Maser-host Galaxy NGC 4258 and its implication for the Hubble constant / Macri L. M., Stanek K. Z., Bersier D. et al. // Aph. J. – 2006. – V. 652. – P. 1133-1149.

[239] Malkov M. A. Ion leakage from quasiparallel collisionless shocks: Implications for injection and shock dissipation / Malkov M. A. // Phys. Rev. E. – 1998. – V. 58. – P. 4911-4928.

[240] Malkov M. A. Nonlinear theory of diffusive acceleration of particles by shock waves / Malkov M. A., Drury L.O'C. // Rep. Prog. Phys. – 2001. – V. 64. – P. 429-481.

[241] Mansfield V. N. Numerical Models for Supernova Remnants / Mansfield V. N., Salpeter E. E. // Aph. J. – 1974. – V. 190. – P. 305-314.

[242] Marcowith A. Turbulence and particle acceleration in collisionless supernovae remnant shocks. II. Cosmic-ray transport / Marcowith A., Lemoine A., Pelletier G. // Astr. & Aph. – 2006. – V. 453. – P. 193-202

[243] Matthews B. Magnetic Fields in Star-forming Molecular Clouds. I. The First Polarimetry of OMC-3 in Orion A / Matthews B., Wilson C. // Aph. J. – 2000. – V. 531. – P. 868-872.

[244] Mathewson D. S. Supernova remnants in the Magellanic clouds / Mathewson D. S., Ford V. L., Dopita M. A. et al. // Aph. J. Suppl. – 1984. – V. 55. – P. 189-210.

[245] McKee C. E. X-Ray Emission from an Inward-Propagating Shock in Young Supernova Remnants / McKee C. E. // Aph. J. – 1974. – V. 188. – P. 335-340.

[246] McKee C. F. Interstellar shock waves / McKee C. F., Hollenbach D. J. // Ann. Rev. Astr. Aph. – 1980. – V. 18. – P. 219-262.

[247] McKee C. F. A theory of the interstellar medium - Three components regulated by supernova explosions in an inhomogeneous substrate / McKee C. F., Ostriker J. P. // Aph. J. – 1977. – V. 218. – P. 148-169.

[248] Merck M. Study of the spectral characteristics of unidentified galactic EGRET sources. Are they pulsar-like? / Merck M., Bertsch D. L., Dingus B. L. et al. // Astr. & Aph. Suppl. – 1996. – V. 120. – P. 465-469.

[249] Messinger D. Interstellar Polarization in the Taurus Dark Clouds: Wavelength-dependent Position Angles and Cloud Structure near TMC-1 / Messinger D., Whittet D., Roberge W. // Aph. J. – 1997. – V. 487. – P. 314-319.

[250] Miceli M. Thermal emission, shock modification, and X-ray emitting ejecta in SN 1006 / Miceli M., Bocchino F., Iakubovskyi D. et al. // Astr. & Aph. – 2009. – V. 501. – P. 239-249.

[251] Mills B. Y. A new look at radio supernova remnants / Mills B. Y., Turtle A. J., Little A. G., Durdin J. M. // Australian J. Phys. – 1984. – V. 37. – P. 321-357.

[252] Milne D. K. The supernova of 1006 A. D. / Milne D. K. // Australian J. Phys. – 1971. – V. 24. – P. 757-767.

[253] Milne D. K. A new catalogue of galactic SNRs corrected for distance form the galactic plane / Milne D. K. // Australian J. Phys. – 1979. – V. 32. – P. 83-92.

[254] Mineshige S. Magnetic model for asymmetric supernova remnants / Mineshige S., Shibata K. // Aph. J. – 1990. – V. 355. – P. L47-L50.

[255] Moderski R. Klein-Nishina effects in the spectra of non-thermal sources immersed in external radiation fields / Moderski R., Sikora M., Coppi P. S., Aharonian F. // Mon. Not. Roy. Ast. Soc. – 2005. – V. 363. – P. 954-966.

[256] Moderski R. The Klein-Nishina Effects in Blazar Jets / Moderski R., Sikora M. // Astrophysics and Space Science. – 2005. – V. 297. – P. 369-376.

[257] Moffett D. A. The expansion of the radio remnant of the supernova of 1006 AD / Moffett D. A., Goss W. M., Reynolds S. P. // Astr. J. – 1993. – V. 106. – P. 1566-1572.

[258] Morlino G. Spatial structure of X-ray filaments in SN 1006 / Morlino G., Amato E., Blasi P., Caprioli D. // Mon. Not. Roy. Ast. Soc. – 2010. – V. 405. – P. L21-L25.

[259] Moskalenko I. V. Anisotropic Inverse Compton Scattering in the Galaxy / Moskalenko I.V., Strong A. W. // Aph. J. – 2000. – V. 528. – P. 357-367.

[260] Muraishi H. Evidence for TeV gamma-ray emission from the shell type SNR RX J1713.7-3946 / Muraishi H., Tanimori T., Yanagita S. et al. // Astr. & Aph. – 2000. – V. 354. – P. L57-L61.

[261] Muxlow T. W. B. The structure of young supernova remnants in M82 / Muxlow T. W. B., Pedlar A., Wilkinson P. N. et al. // Mon. Not. Roy. Ast. Soc. – 1994. – V. 266. – P. 455-467.

[262] Nagano M. Observations and implications of the ultrahigh-energy cosmic rays / Nagano M., Watson A. A. // Rev. Mod. Phys. – 2000. – V. 72. – P. 689-732

[263] Oort J. H. Problems in Cosmical Aerodynamics / Oort J. H. – Dayton: Central Air Documents Office, 1951. – 324 p.

[264] Orlando S. On the origin of asymmetries in bilateral supernova remnants / Orlando S., Bocchino F., Reale F., Peres G., Petruk O. // Astr. & Aph. – 2007. – V. 470. – P. 927-939.

[265] Orlando S. Effects of non-uniform interstellar magnetic field on synchrotron X-ray and inverse-Compton gamma-ray morphology of SNRs / Orlando S., Petruk O., Bocchino F., Miceli M. // Astr. & Aph. – 2011. – V. 526. – id. A129 (15 p.)

[266] Ostriker J. P. Astrophysical blastwaves / Ostriker J. P., McKee C. F. // Rev. Mod. Phys. – 1988. – V. 60. – P. 1-68.

[267] Ostrowski M. Acceleration of relativistic particles in shocks with oblique magnetic fields / Ostrowski M. // Mon. Not. Roy. Ast. Soc. – 1988. – V. 233. – P. 257-264.

[268] Parizot E. Observational constraints on energetic particle diffusion in young supernovae remnants: amplified magnetic field and maximum energy / Parizot E., Marcowith A., Ballet J., Gallant Y. A. // Astr. & Aph. – 2006. – V. 453. – P. 387-395

[269] Pasko V. On the theory of the propagation of intense shock waves in inhomogeneous gravitating media. II - Radiative cooling phase / Pasko V., Silich S. // Kinem. and Phys. of Celestial Bodies. – 1986. – V. 2. – P. 15-21.

[270] Patnaude D.J. Small-Scale X-Ray Variability in the Cassiopeia A Supernova Remnant / Patnaude D.J., Fesen R.A. // Astr. J. – 2007. – V. 133. P. 147-153

[271] Petruk O. X-ray emission of the remnants of an aspherical Supernova explosions / Petruk O. // Kinematics and Physics of Celestial Bodies, Suppl. – 2000. – No. 3. – P. 132-135.

[272] Petruk O. Approximations of the self-similar solution for a blastwave in a medium with power-law density variation / Petruk O. // Astr. & Aph. – 2000. – V. 357. – P. 686-696.

[273] Petruk O. Thermal X-ray composites as an effect of projection / Petruk O. // Astr. & Aph. – 2001. – V. 371. – P. 267-273.

[274] Petruk O. X-rays from Supernova Remnants in 3-D: Models and Effects / Petruk O. // Astr. Soc. of Pacific Conf. Proc. – 2001. – V. 251. – P. 266-267.

[275] Petruk O. A New Model for the Thermal X-ray Composites and the Neutral Pion Decay Gamma-Rays from Supernova Remnants / Petruk O. // Astrophysical Sources of High Energy Particles and Radiation / Eds. Wefel J., Shapiro M., Stanev T. – Kluwer Academic Publishers, 2001. – P. 93-100.

[276] Petruk O. Model for Synchrotron X-rays from Shell Supernova Remnants in Nonuniform Interstellar Medium and Nonuniform Magnetic Field / Petruk O. // J. Physical Studies. – 2002. – V. 6, No. 4. – P. 455-461.

[277] Petruk O. On the Transition of the Adiabatic Supernova Remnant to the Radiative Stage in a Nonuniform Interstellar Medium / Petruk O. // J. Physical Studies. – 2005. – V. 9, No. 4. – P. 364–373.

[278] Petruk O. The artificial broadening of the high-energy end of electron spectrum in supernova remnants / Petruk O. // Astr. & Aph. – 2006. – V. 460. – P. 375-379.

[279] Petruk O. Influence of Thermalisation on Electron Injection in Supernova Remnant Shocks / Petruk O., Bandiera R. // J. Physical Studies. – 2006. – V. 10. – P. 66-73.

[280] Petruk O. Approximation of the radiation power of electrons due to the inverse-Compton process in the black-body photon field / Petruk O., Bandiera R. // Astr. & Aph. – 2008. – V. 499. – P. 643-648.

[281] Petruk O. Aspect angle for interstellar magnetic field in SN 1006 / Petruk O., Dubner G., Castelletti G. et al. // Mon. Not. Roy. Ast. Soc. – 2009. – V. 393. – P. 1034-1040.

[282] Petruk O. Some properties of synchrotron radio and inverse-Compton gamma-ray images of supernova remnants / Petruk O., Beshley V., Bocchino F., Orlando S. // Mon. Not. Roy. Ast. Soc. – 2009. – V. 395. – P. 1467-1475.

[283] Petruk O. Predicted γ-ray image of SN 1006 due to inverse Compton emission / Petruk O., Bocchino F., Miceli M. et al. // Mon. Not. Roy. Ast. Soc. – 2009. – V. 399. – P. 157-165.

[284] Petruk O. Observational constraints on the modeling of SN1006 [Електронний ресурс] / Petruk O., Beshley V., Bocchino F., Miceli M., Orlando S. // Mon. Not. Roy. Ast. Soc. – 2010. – accepted. – http://adsabs.harvard.edu/abs/2010arXiv1012.4586P

[285] Petruk O. Radio, X-ray and gamma-ray surface brightness profiles as powerful diagnostic tools for non-thermal SNR shells [Електронний ресурс] / Petruk

O., Orlando S., Beshley V., Bocchino F. // Mon. Not. Roy. Ast. Soc. – 2010. – accepted. – http://adsabs.harvard.edu/abs/2010arXiv 1012.4579P

[286] Pietsch W. XMM-Newton survey of the Local Group galaxy M 33 // Pietsch W., Misanovic Z., Haberl F. et al. // Astr. & Aph. – 2004. – V. 426. – P. 11-24.

[287] Plaga R. Arguments against a dominantly hadronic origin of the VHE radiation from the supernova remnant RX J1713-3946 / Plaga R. // New Astronomy. – 2008. – V. 13. – P. 73-76.

[288] Plucinsky P. P. Chandra ACIS survey of M33 (ChASeM33): a first look / Plucinsky P. P., Williams B., Long K. S. et al. // Aph. J. Suppl. – 2008. – V. 174. – P. 366-378.

[289] Pohl M. Magnetically Limited X-Ray Filaments in Young Supernova Remnants / Pohl M., Yan H., Lazarian A. // Aph. J. – 2005. – V. 626. – P. L101-L104

[290] Poveda A. Supernovae and Supernova Remnants / Poveda A., Woltjer L. // Astr. J. – 1968. – V. 73. – P. 65-74.

[291] Porquet D. Impacts of a power-law non-thermal electron tail on the ionization and recombination rates / Porquet D., Arnaud M., Decourchelle A. // Astr. & Aph. – 2001. – V. 373. – P. 1110-1124.

[292] Porter T. A. Inverse Compton Emission from Galactic Supernova Remnants: Effect of the Interstellar Radiation Field / Porter T. A., Moskalenko I. V., Strong A. W. // Aph. J. – 2006. – V. 648. – P. L29-L32.

[293] Ptuskin V. S. On the spectrum of high-energy cosmic rays produced by supernova remnants in the presence of strong cosmic-ray streaming instability and wave dissipation / Ptuskin V. S., Zirakashvili V. N. // Astr. & Aph. – 2005. – V. 429. – P. 755-765

[294] Ptuskin V. S. Dissipation of Magnetohydrodynamic Waves on Energetic Particles: Impact on Interstellar Turbulence and Cosmic-Ray Transport / Ptuskin V. S. Moskalenko I. V., Jones F. C., Strong A. W., Zirakashvili V. N. // Aph. J. – 2006. – V. 642. – P. 902-916

[295] Ptuskin V. S. Nonlinear processes in cosmic-ray precursor of strong supernova shock: Maximum energy and average energy spectrum of accelerated particles / Ptuskin V. S., Zirakashvili V. N. // Adv. Space Res. – 2006. – V. 37. – P. 1898-1901

[296] Ptuskin V. Spectrum of Galactic Cosmic Rays Accelerated in Supernova Remnants / Ptuskin V., Zirakashvili V., Seo E.-S. // Aph. J. – 2010. – V. 718. – P. 31-36

[297] Rakowski C. The Physics of Supernova Remnant Blast Waves. II. Electron-Ion Equilibration in DEM L71 in the Large Magellanic Cloud / Rakowski C., Ghavamian P., Hughes J., Williams T. // Aph. J. – 2003. – V. 590. – P. 846-857.

[298] Rakowski C. Electron ion temperature equilibration at collisionless shocks in supernova remnants / Rakowski C. // Adv. Space Res. – 2005. – V. 35. – P. 1017-1026.

[299] Rakowski C. The Heating of Thermal Electrons in Fast Collisionless Shocks: The Integral Role of Cosmic Rays / Rakowski C., Laming J., Ghavamian P. // Aph. J. – 2008. – V. 684. – P. 348-357.

[300] Raymond J.C. Radiative cooling of a low-density plasma / Raymond J.C., Cox D.P., Smith B.W. // Aph. J. – 1976. – V. 204. – P. 290-292.

[301] Raymond J. Soft X-ray spectrum of a hot plasma / Raymond J., Smith B. // Aph. J. Suppl. – 1977. – V. 35. – P. 419-439.

[302] Reynolds S. Synchrotron Models for X-Rays from the Supernova Remnant SN 1006 / Reynolds S. // Aph. J. – 1996. – V. 459. – P. L13-.

[303] Reynolds S. Models of Synchrotron X-Rays from Shell Supernova Remnants / Reynolds S. // Aph. J. – 1998. – V. 493. – P. 375-396.

[304] Reynolds S. Dynamics and Nonthermal Emission of Shell Supernova Remnants / Reynolds S. // X-Ray and Radio Connections / Eds. Sjouwerman L.O., Dyer K.K. – Santa Fe, 2004. – id. E4.01 (15 p.)

[305] Reynolds S. P. Microphysics of shock acceleration from observations of X-ray synchrotron emission from supernova remnants / Reynolds S. P. // Adv. Space Res. – 2004. – V. 33. – P. 461-465.

[306] Reynolds S. Supernova Remnants at High Energy / Reynolds S. P. // Ann. Rev. Astr. Aph. – 2008. – V. 46. – P. 89–126.

[307] Reynolds S. Particle acceleration in supernova-remnant shocks / Reynolds S. [Електронний ресурс] // arXiv.org. – 2010. – http://arxiv.org/abs/1012.1306v1

[308] Reynolds S. Nonthermal Radiation from Supernova Remnants in the Adiabatic Stage of Evolution / Reynolds S., Chevalier R. // Aph. J. – 1981. – V. 245. – P. 912-919.

[309] Reynolds S.P. Electron acceleration in Tycho's and Kepler's supernova remnants - Spectral evidence of Fermi shock acceleration / Reynolds S.P., Ellison D.C. // ApJ. – 1992. – V. 399. – P. L75-L78

[310] Reynolds P. S. Electron Acceleration in Young Supernova Remnants: Inferences Drawn From Model Images / Reynolds P. S., Fulbright S. M. // Proc. 21st International Cosmic Ray Conference. – 1990. – V. 4. – P. 72-75.

[311] Reynolds S. P. Radio observations of the remnant of the supernova of AD 1006. II - Polarization observations / Reynolds S. P., Gilmore D. M. // Astr. J. – 1993. – V. 106. – P. 272-283.

[312] Reynolds S. P. Maximum Energies of Shock-accelerated Electrons in Young Shell Supernova Remnants / Reynolds S. P., Keohane J. W. // Aph. J. – 1999. – V. 525. – P. 368-374.

[313] Reynolds S. The Youngest Galactic Supernova Remnant: G1.9+0.3 / Reynolds S., Borkowski K. J., Green D. A., Hwang U., Harrus I., Petre R. // Aph. J. – 2008. – V. 680. – P. L41-L44

[314] Reynoso E. M. Influence of the Neutron Star 1E 161348-5055 in RCW 103 on the Surrounding Medium / Reynoso E. M., Green A. J., Johnston S. et al. // Publ. Astron. Soc. Australia. – 2004. – V. 21. – P. 82-88.

[315] Rho J. Mixed-Morphology Supernova Remnants / Rho J., Petre R. // Aph. J. – 1996. – V. 467. – P. 698.

[316] Rho J. Mixed-Morphology Supernova Remnants / Rho J., Petre R. // Aph. J. – 1998. – V. 503. – P. L167-L170.

[317] Rho J. An X-ray and optical study of the supernova remnant W44 / Rho J., Petre R., Schlegel E. // Aph. J. – 1994. – V. 430. – P. 757-773.

[318] Roger R. S. Symmetry of the radio emission from two high-latitude supernova remnants, G296.5 + 10.0 and G327.6 + 14.6 (SN 1006) / Roger R. S., Milne D. K., Kesteven M. J. et al. // Aph. J. – 1988. – V. 332. – P. 940-953.

[319] Romero G. Unidentified 3EG gamma-ray sources at low galactic latitudes / Romero G., Benaglia P., Torres D. // Astr. & Aph. – 1999. – V. 348. – P. 868-876.

[320] Rosado M. Kinematics of the galactic supernova remnants RCW 86, MSH 15-56 and MSH 11-61A / Rosado M., Ambrocio-Cruz P., Le Coarer E., Marcelin M. // Astr. & Aph. – 1996. – V. 315. – P. 243-252.

[321] Rothenflug R. Geometry of the non-thermal emission in SN 1006. Azimuthal variations of cosmic-ray acceleration / Rothenflug R., Ballet J., Dubner G., Giacani E., Decourchelle A., Ferrando P. // Astr. & Aph. – 2004. – V. 425. – P. 121-131.

[322] Rowell G. Observations of the supernova remnant W28 at TeV energies / Rowell G., Naito T., Dazeley S. A. et al. // Astr. & Aph. – 2000. – V. 359. – P. 337-346.

[323] Rowell G.P. H.E.S.S. Observations of Shell Type SNR / Rowell G.P., D. Berge, J.A. Hinton // Proc. 29th International Cosmic Ray Conference / Eds. Acharya B. S., Gupta S. et al. – Mumbai, 2005. – V. 4. – P. 155-158.

[324] Rowell G. Galactic TeV Gamma-Ray Sources: A Summary of H.E.S.S. Observations / Rowell G. // Journal of Physics: Conf. Series. – 2006. – V. 47. – P. 21–30.

[325] Rybicki G. B. Radiative processes in astrophysics / Rybicki G. B., Lightman A. P. – Wiley, 2004. – 382 p.

[326] Schlickeiser R. Cosmic Ray Astrophysics / Schlickeiser R. – Springer, 2002. – 519 p.

[327] Schwartz S. J. Electron heating and the potential jump across fast mode shocks / Schwartz S. J., Thomsen M. F., Bame S. J., Stansberry J. // J. Geoph. Research. – 1988. – V. 93. – P. 12923-12931.

[328] Seaquist E. R. Could the compact radio sources in M82 be cluster wind-driven bubbles? / Seaquist E. R., Stankovic M. // Aph. J. – 2007. – V. 659. – P. 347-358.

[329] Seward F. Supernova remnants containing neutron stars / Seward F. // Comments on Astrophysics. – 1985. – V. 11, No 1. – P. 15-51.

[330] Seward F. Einstein Observations of Galactic supernova remnants / Seward F. // Aph. J. Suppl. – 1990. – V. 73. – P. 781-819.

[331] Shelton R. Modeling W44 as a Supernova Remnant in a Density Gradient with a Partially Formed Dense Shell and Thermal Conduction in the Hot Interior. II. The Hydrodynamic Models / Shelton R., Cox D., Maciejewski W. et al. // Aph. J. – 1999. – V. 524. – P. 192-212.

[332] Shklovskii I. S. On the origin of cosmic rays / Shklovskii I. S. // Dokl. Akad. Nauk SSSR. – 1953. – V. 91. – P. 475–478

[333] Shklovsky I. S. Secular variation of the flux and intensity of radio emission from discrete sources / Shklovsky I. S. // Sov. Astr. – 1960. – V. 4. – P. 243-249.

[334] Schure K. M., Achterberg A., Keppens R., Vink J. Time-dependent particle acceleration in supernova remnants in different environments / Schure K. M., Achterberg A., Keppens R., Vink J. // Mon. Not. Roy. Ast. Soc. – 2010. – V. 406. – P. 2633-2649

[335] Slane P. Nonthermal X-Ray Emission from the Shell-Type Supernova Remnant G347.3-0.5 / Slane P., Gaensler B., Dame T. M. et al. // Aph. J. – 1999. – V. 525. – P. 357-367.

[336] Slane P. RXJ 0852.0-0462: Another Nonthermal Shell-Type SNR (G266.2-1.2) / Slane P., Huges J., Edgar R. et al. // Aph. J. – 2001. – V. 548. – P. 814-819.

[337] Slane P. An X-Ray Study of the Supernova Remnant G290.1-0.8 / Slane P., Smith R., Hughes J., Petre R. // Aph. J. – 2002. – V. 564. – P. 284-290.

[338] Smith R. K. Time-dependent Cooling and Grain Destruction in Hot Dusty Plasmas: A Simplified Model and Principal Results / Smith R. K., Krzewina L. G., Cox D. et al. // Aph. J. – 1996. – V. 473. – P. 864-872.

[339] Status and Perspective of Astroparticle Physics in Europe [Електронний ресурс] / Astroparticle Physics European Coordination, Peer Review Committee. – 2008. – 145 pp. – www.aspera-eu.com/images/stories/files/Roadmap.pdf

[340] Stephenson F. Historical Supernovae / Stephenson F. // Astr. Soc. Pasific Conf. Series. – 2005. – V. 342. – P. 63-70

[341] Strüder L. The European Photon Imaging Camera on XMM-Newton: The pn-CCD camera / Strüder L., Briel U., Dennerl K. et al. // Astr. & Aph. – 2001. – V. 365. – P. L18-L16.

[342] Sturner S. Association of unidentified, low latitude EGRET sources with supernova remnants / Sturner S., Dermer C. // Astr. & Aph. – 1995. – V. 293. – P. L17-L20.

[343] Sturner S. J. Are supernova remnants sources of $>$ 100 MeV γ-rays? / Sturner S. J., Dermer C. D., Mattox J. R. // Astr. & Aph. Suppl. – 1996. – V. 120. – P. 445-448.

[344] Sun M. X-Ray Observation and Analysis of the Composite Supernova Remnant G327.1-1.1 / Sun M., Wang Z., Chen Y. // Aph. J. – 1999. – V. 511. – P. 274-281.

[345] Sutherland R.S. Cooling functions for low-density astrophysical plasmas / Sutherland R.S., Dopita M.A. // Aph. J. Suppl. – 1993. – V. 88. – P. 253-327.

[346] "TeVCat", an online Gamma-ray Catalogue [Електронний ресурс]. – http://tevcat.uchicago.edu/

[347] Torres D. F. Supernova remnants and γ-ray sources / Torres D. F., Romero G. E., Dame, T. M. et al. // Phys. Rep. – 2003. – V. 382. – P. 303–380.

[348] Treumann R. A. Fundamentals of collisionless shocks for astrophysical application. – 1. Non-relativistic shocks / Treumann R. A. // Astr. & AphReviews. – 2009. – V. 17. – P. 409–535.

[349] Troland T. The Magnetic Fields in the Ophiuchus and Taurus Molecular Clouds / Troland T., Crutcher R., Goodman A. et al. // Aph. J. – 1996. – V. 471. – P. 302-307.

[350] Truelove J. K. Evolution of Nonradiative Supernova Remnants / Truelove J. K., McKee C. F. // Aph. J. Suppl. – 1999. – V. 120. – P. 299-326.

[351] Turner M. J. L. The European Photon Imaging Camera on XMM-Newton: The MOS cameras : The MOS cameras / Turner M. J. L., Abbey A., Arnaud M. et al. // Astr. & Aph. – 2001. – V. 365. – P. L27-L35.

[352] Uchiyama Y. Fine-structure in the nonthermal X-ray emission of SNR RX J1713.7-3946 revealed by Chandra / Uchiyama Y., Aharonian F. A., Takahashi T. // Astr. & Aph. – 2003. – V. 400. – P. 567-574.

[353] Uchiyama Y. Extremely fast acceleration of cosmic rays in a supernova remnant / Uchiyama Y., Aharonian F. A., Tanaka T., Takahashi T., Maeda Y. // Nature. – 2007. – V. 449. – P. 576-578

[354] Urošević D. The Sigma-D relation for supernova remnants in nearby galaxies / Urošević D., Pannuti T. G., Duric N., Theodorou A. // Astr. & Aph. – 2005. – V. 435. – P. 437-447.

[355] van der Laan H. Expanding supernova remnants and galactic radio sources / van der Laan H. // Mon. Not. Roy. Ast. Soc. – 1962. – V. 124. – P. 125-145.

[356] Vink J. The Slow Temperature Equilibration behind the Shock Front of SN 1006 / Vink J., Laming J. M., Gu M. F., Rasmussen A., Kaastra J. S. // Aph. J. – 2003. – V. 587. – P. L31-L34.

[357] Vink J. A Review of X-ray Observations of Supernova Remnants / Vink J. // Nucl. Phys. B (Proc. Suppl.). – 2004. – V. 132. – P. 21–30.

[358] Vink J. Shocks and particle acceleration in supernova remnants: observational features / Vink J. // Adv. Space Res. – 2004. – V. 33, No 4. – P. 356–365.

[359] Vink J. X-ray high resolution and imaging spectroscopy of supernova remnants / Vink J. [Електронний ресурс]. – 2006. – (Препринт astro-ph/0601131). – http://arxiv.org/abs/astro-ph/0601131

[360] Völк H. Shell-type Supernova Remnants / Völк H. // Towards a Network of Atmospheric Cherenkov Detectors / Eds. Degrange B., Fontaine G. – 2006. – P. 233-245

[361] Völк H. J. The theory of synchrotron emission from supernova remnants / Völк H. J., Ksenofontov L., Berezhko E. G. // Astr. & Aph. – 2004. – V. 427. – P. 525-536.

[362] Völк H. J. Inverse Compton gamma-ray models for remnants of Galactic type Ia supernovae? / Völк H. J., Ksenofontov L., Berezhko E. G. // Astr. & Aph. – 2008. – V. 490. – P. 515-519.

[363] Völк H. Variation of cosmic ray injection across supernova shocks / Völк H., Berezhko E., Ksenofontov L. // Astr. & Aph. – 2003. – V. 409. – P. 563-571.

[364] Völк H. J. Imaging very high energy gamma-ray telescopes / Völк H. J., Bernlöhr K. // Exp. Astr. – 2009. – V. 25. – P. 173–191.

[365] Wallis G. The determination of the energy distribution of relativistic electrons by the frequency distribution of their "synchrotron radiation" / Wallis G. // Paris Symposium on Radio Astronomy (IAU Symposium 9), (Ed. R. N. Bracewell). – Stanford: University Press, 1959. – P. 595-597.

[366] Weiler K. Radio emission from supernovae and gamma-ray bursters / Weiler K. // Ann. Rev. Astr. Aph. – 2002. – V. 40. – P. 387–438

[367] Weisskopf M. C. Six Years of Chandra Observations of Supernova Remnants / Weisskopf M. C., Hughes J. P. // Astrophysics Update 2 / Ed. J. W. Mason. – Heidelberg: Springer Verlag. – 2006. – P. 55-75 [препринт astro-ph/0511327].

[368] Whiteoak J.B. The MOST supernova remnant catalogue / Whiteoak J.B., Green A. // Astr. & Aph. Suppl. – 1996. – V. 118. – P. 329-380.

[369] Winkler P. F. The SN 1006 Remnant: Optical Proper Motions, Deep Imaging, Distance, and Brightness at Maximum / Winkler P. F., Gupta G., Long K. S. // Aph. J. – 2003. – V. 585. – P. 324-335.

[370] Woltjer L. Supernova Remnants / Woltjer L. // Ann. Rev. Astr. Aph. – 1972. – V. 10. – P. 129-158.

[371] Warren J. Cosmic-ray acceleration at the forward shock in Tycho's supernova remnant: evidence from Chandra X-ray observations / Warren J., Hughes J., Badenes C., Ghavamian P. et al. // Aph. J. – 2005. – V. 634. – P. 376-389

[372] XMM-Newton Science Operations Centre [Електронний ресурс]. – http://xmm.esac.esa.int/

[373] Yamaguchi H. X-Ray Spectroscopy of SN 1006 with Suzaku / Yamaguchi H., Koyama K., Katsuda S. et al. // Publ. Astr. Soc. Japan. – 2008. – V. 60. – P. S141-S152.

[374] Zatsepin G. T. Upper Limit of the Spectrum of Cosmic Rays / Zatsepin G. T., Kuz'min V. A. // J. Exper. Theor. Phys. Let. – 1966. – V. 4. – P. 78

[375] Zirakashvili V. Analytical solutions for energy spectra of electrons accelerated by nonrelativistic shock-waves in shell type supernova remnants / Zirakashvili V., Aharonian F. // Astr. & Aph. – 2007. – V. 465. – P. 695-702

[376] Zirakashvili V. Nonthermal Radiation of Young Supernova Remnants: The Case of RX J1713.7-3946 / Zirakashvili V., Aharonian F. // Aph. J. – 2010. – V. 708. – P. 965-980.

APPENDICES

Appendix A

Approximation of the temperature evolution behind the adiabatic shock in medium with power-low density variation

In order to simplify the estimation of $t_{\rm sag}$ and $t_{\rm dyn}$, let us approximate the distribution $\bar{T}(\bar{a}) = T(a,t)/T_{\rm s}(t)$ downstream close to the strong adiabatic shock; here a is Lagrangian coordinate, $\bar{T} = T/T_{\rm s}$ and $\bar{a} = a/R$. Note, that hereafter in this Appendix we use the normalized parameters, i.e. divided on their values on the shock front; thus we skip the overlines in the notations. We are interested in the approximation in the form

$$T(a) \approx a^{-\kappa(\gamma,\omega)}. \tag{A.1}$$

The value of κ is given by

$$\kappa = \left(-\frac{\partial \ln T(a)}{\partial \ln a} \right)_{a=1} \tag{A.2}$$

where $T(a)$ is the profile from Sedov [21] solutions. The equation of the mass conservation and the equation of the adiabaticity applied for the case of the shock motion in the medium with the power-law density distribution give the distribution of temperature $T(a) = P(a)/\rho(a)$ [272]

$$T(a) = \left(\frac{\gamma-1}{\gamma+1} \right)^{\gamma-1} a^{2\gamma-5+\omega} \left(r(a)^2 r_{\rm a}(a) \right)^{-\gamma+1} \tag{A.3}$$

where r is Eulier coordinate and $r_{\rm a} = \partial r/\partial a$. Instead of Sedov profiles for $r(a)$ – which is quite complex – we use the approximation

$$r(a) = a^{(\gamma-1)/\gamma} \exp\left(\alpha(a^\beta - 1)\right) \tag{A.4}$$

where α, β are constants; this approximation gives correct values of r and its derivatives in respect to a up to the second order on the shock [272]. Substitution (A.2)

with (A.3), (A.4) and with expressions for α, β from [272] yields

$$\kappa = \frac{2(8 - (\gamma + \omega)(\gamma + 1))}{(\gamma + 1)^2}. \tag{A.5}$$

For $\gamma = 5/3$, $\kappa = 1 - 3\omega/4$.

The approximation (A.1) underestimate Sedov temperature. The smaller a the larger difference. It is about 20% at $a \approx 0.5$ (that corresponds to $r \approx 0.8$).

Appendix B

Approximations for distributions of some parameters behind the adiabatic shock

Let us find approximations for dependence of some parameter $\bar{\mathcal{X}} \equiv X/X(R)$ on the Lagrangian coordinate $\bar{a} \equiv a/R$ downstream close to the adiabatic shock. We are interested in approximations of the form

$$\bar{\mathcal{X}}(\bar{a}) \approx \bar{a}^{\,\kappa} \tag{B.1}$$

where, by definition,

$$\kappa = \left[-\frac{a}{\mathcal{X}_*(a)}\frac{\partial \mathcal{X}_*(a)}{\partial a}\right]_{a=R} = \left[-\frac{\partial \ln \mathcal{X}_*(a)}{\partial \ln a}\right]_{a=R} \tag{B.2}$$

and star marks the dependence given by the Sedov solution.

This approach yields for density

$$\bar{n}(\bar{a}) \approx \bar{a}^{\kappa_{\rm na}}, \qquad \kappa_{\rm na} = \frac{5\gamma+13}{(\gamma+1)^2}, \tag{B.3}$$

for the relation between Eulerian and Lagrangian coordinates

$$\bar{r} \approx \bar{a}^{1/\sigma}, \qquad \bar{r}_{\bar{\rm a}} \approx (1/\sigma)\bar{a}^{(1/\sigma)-1} \tag{B.4}$$

where the shock compression factor is

$$\sigma = \frac{\gamma+1}{\gamma-1}. \tag{B.5}$$

Note that the density distribution in Eulerian coordinates is much more sensitive to γ (Table B.1):

$$\bar{n}(\bar{r}) \approx \bar{r}^{\kappa_{\rm nr}}, \qquad \kappa_{\rm nr} = \sigma\kappa_{\rm na} = \frac{5\gamma+13}{(\gamma+1)(\gamma-1)}. \tag{B.6}$$

Magnetic field is approximately

$$\bar{B} \approx \bar{a}^{\beta(\Theta_{\rm o,eff})}, \tag{B.7}$$

$$\beta(\Theta_{\rm o,eff}) = \frac{\beta_\parallel \cos^2\Theta_{\rm o} + \beta_\perp \sigma^2 \sin^2\Theta_{\rm o}}{\cos^2\Theta_{\rm o} + \sigma^2\sin^2\Theta_{\rm o}}, \tag{B.8}$$

$$\beta_{\parallel} = \frac{4}{\gamma+1}, \qquad \beta_{\perp} = \frac{3\gamma+11}{(\gamma+1)^2}. \tag{B.9}$$

Approximation for normalization K follows from the definition (Sect. 3.2.2)

$$\bar{K} = \bar{a}^{3b/2}\bar{n}^{(2+s)/3} \tag{B.10}$$

and approximation for $\bar{n}$.

Adiabatic losses are accounted with $\mathcal{E}_{\rm ad}(a)$ which is defined by (3.24). Its approximation is therefore

$$\mathcal{E}_{\rm ad}(\bar{a}) \approx \bar{a}^{\kappa_{\rm ad}}, \qquad \kappa_{\rm ad} = \frac{5\gamma+13}{3(\gamma+1)^2}, \tag{B.11}$$

it is valid for $\bar{r} > 0.8$ with error less than few per cent. The value of $\kappa_{\rm ad}$ is close to unity for $\gamma = 1.1 \div 5/3$ (Table B.1).

In order to approximate $\mathcal{E}_{\rm rad}$ defined by (3.24), we substitute (3.22) with approximations for $\bar{n}$ and $\bar{B}$. Then we use the property

$$\lim_{a\to 1}\left(\frac{a}{f(a)}\frac{df}{da}\right) = cy \tag{B.12}$$

for function of the form $f(a) = 1 - ca^x(1-a^y)$. In this way,

$$\mathcal{E}_{\rm rad}(\bar{a}, E) \approx \bar{a}^{\kappa_{\rm rad}}, \qquad \kappa_{\rm rad} = \frac{5\sigma_{\rm B}^2(\Theta_{\rm o})E}{2E_{\rm f\parallel}}. \tag{B.13}$$

This expression is good for $\bar{r} > 0.94$, with error of few per cent. It depends on γ through σ in $\sigma_{\rm B}$ which is [303]

$$\sigma_{\rm B} = \left(\frac{1+\sigma^2\tan^2\Theta_{\rm o}}{1+\tan^2\Theta_{\rm o}}\right)^{1/2}. \tag{B.14}$$

Table B.1

Parameters in approximations

Expression	$\gamma = 5/3$	$\gamma = 4/3$	$\gamma = 1.1$
$\kappa_{\rm na} = \dfrac{5\gamma+13}{(\gamma+1)^2}$	3	3.6	4.2
$\kappa_{\rm nr} = \dfrac{5\gamma+13}{(\gamma+1)(\gamma-1)}$	12	25	88
$\sigma = \dfrac{\gamma+1}{\gamma-1}$	4	7	21
$\beta_{\parallel} = \dfrac{4}{\gamma+1}$	1.5	1.7	1.9
$\beta_{\perp} = \dfrac{3\gamma+11}{(\gamma+1)^2}$	2.2	2.8	3.2
$\kappa_{\rm ad} = \kappa_{\rm na}/3$	1	1.2	1.4

Note that dependence on the absolute value of the magnetic field strength $B_{\mathrm{s}\parallel}$ is present in (B.13): $E_{\mathrm{f}\parallel} \propto B_{\mathrm{s}\parallel}^{-2}$.

The values of parameters in approximations for different adiabatic index γ are presented in Table B.1.

Appendix C

Approximate formulae for profiles of brightness in Sedov SNR

C.1. Approximate description of surface brightness. The surface brightness of a spherical SNR projection at distance ϱ from the center and at azimuth φ is

$$S(\varrho,\varphi) = 2\int_{a(\varrho)}^{R} q(a,\Theta_{\rm o})\frac{r r_{\rm a} da}{\sqrt{r^2-\varrho^2}}. \tag{C.1}$$

where q is emissivity, $\Theta_{\rm o} = \Theta_{\rm o}(\varphi, r/\varrho, \phi_{\rm o})$ is the shock obliquity, $\phi_{\rm o}$ an aspect angle, r and a are Eulerian and Lagrangian coordinates, $r_{\rm a}$ the derivative of $r(a)$ in respect to a. The emissivity in synchrotron or IC process is

$$q = \int dE N(E) p(E,\nu). \tag{C.2}$$

In the δ-function approximation of the single-electron emissivity $p(E,\nu)$, we may write that

$$q \propto N(E_{\rm m}) B^{\rm x} \tag{C.3}$$

where $E_{\rm m}$ is an energy of electron which gives maximum contribution to radiation at a given frequency ν, $\mathrm{x} = 1/2$ for synchrotron and $\mathrm{x} = 0$ for IC emission.

Energy spectrum of electrons $N(E)$ evolves in a different way downstream of the shocks with different obliquity, i.e. $N(E_{\rm m}) = N(E_{\rm m}; a, \Theta_{\rm o})$. In Sedov SNR, this evolution may approximately be expressed by the two independent terms (for details see below)

$$N(E_{\rm m}; a, \Theta_{\rm o}) \approx N_{\rm a}(a) N_{\Theta}(\varrho, \Theta_{\rm eff}) \tag{C.4}$$

where $\Theta_{\rm eff} = \Theta_{\rm o}(\varphi, 1, \phi_{\rm o})$. The similar relation holds for MF: $B(a,\Theta_{\rm o}) \approx B_{\rm s}(\Theta_{\rm o}) B_{\rm a}(a)$ where $B_{\rm s}$ is the immediately post-shock value. This allows Eq. (C.1) to be written as

$$\begin{aligned} S(\varrho,\varphi) \;\; &\propto N_{\Theta}(\varrho,\Theta_{\rm eff}) B_{\rm s}(\Theta_{\rm eff})^{\rm x} \\ &\times \int_{a(\varrho)}^{R} N_{\rm a}(a) B_{\rm a}(a)^{\rm x} \frac{r r_{\rm a} da}{\sqrt{r^2-\varrho^2}}. \end{aligned} \tag{C.5}$$

where integral depends on ϱ only. In other notations,

$$S(\varrho, \varphi) \approx q_{\rm eff}(\varrho, \varphi) \cdot \mathcal{I}(\varrho) \tag{C.6}$$

where $\mathcal{I}$ is an integral in (C.5) divided by $N_{\rm a}(\varrho)$. The accuracy of this approximate formula increases toward the edge of SNR projection where the bright limbs we are interested in are located.

It is important that the factor $\mathcal{I}$ is almost independent of $E_{\rm m}$, but only on the coordinate in the projection. This means that $\mathcal{I}$ differs just on a constant in a given position for the radio, X- and γ-ray images and we may use Eqs. (5.8), (5.11) and (5.12) written for emissivities in order to relate surface brightnesses in each 'pixel'. The factor $\mathcal{I}$ slightly dependent of φ (see below). Therefore, the azimuthal variations of the surface brightness S at a given ϱ may approximately be represented by the azimuthal variations of the effective emissivities. This provides justification for discussion in Sect. 5.2.1. However, the radial contrasts in brightness should account for the radial changes in $\mathcal{I}$ which is unknown until one considers detailed 3-D MHD model of SNR.

C.2. Radio brightness. Here we derive an approximate formula for azimuthal variation of the radio surface brightness. This formula allows one to avoid detailed numerical simulations and may be useful in situations where the approximate estimation of the aspect angle is reasonable. In addition, the formula allows us to have deeper insight in the main factors determining the azimuthal variation of the radio surface brightness in SNRs.

The downstream distributions of K and B in a Sedov SNR in uniform ISM and uniform ISMF are

$$K \propto \varsigma(\Theta_{\rm o})\bar{K}(\bar{r}), \quad B \propto \sigma_{\rm B}(\Theta_{\rm o})\bar{B}(\bar{r}, \Theta_{\rm o}). \tag{C.7}$$

If one neglects the small differences in downstream distributions of the parallel and perpendicular components of B (Fig. 1 in [303]), then

$$\bar{B}(\bar{r}, \Theta_{\rm o}) \approx \bar{B}(\bar{r}). \tag{C.8}$$

The obliquity angle $\Theta_{\rm o}$ is different for each radial sector of 3-D object. It is determined, for any position within SNR, by the set $(\varphi, \bar{r}/\bar{\varrho}, \phi_{\rm o})$. Integration along the line of sight gathers information from different radial sectors, with different obliquities. Let us determine the 'effective' obliquity angle by the relation

$$\Theta_{\rm o,eff}(\varphi, \phi_{\rm o}) = \Theta_{\rm o}(\varphi, 1, \phi_{\rm o}). \tag{C.9}$$

Actually, $\Theta_{\rm o,eff}$ for a given azimuth equals to the obliquity angle for a sector with the same azimuth lying in the plane of the sky (i.e. in the plane being perpendicular to the line of sight and containing the center of SNR). $\Theta_{\rm o}$ varies around $\Theta_{\rm o,eff}$ during integration along the line of sight. The closer ϱ to the edge of SNR projection the smaller the range for variation of $\Theta_{\rm o}$ and more accurate is our approximation. (Actually, we used ϱ corresponding to maximum in radial brightness distribution which happens rather close to the shock.)

The relation between the azimuthal angle φ, the obliquity angle $\Theta_{\rm o,eff}$ and the aspect angle $\phi_{\rm o}$ is as simple as

$$\cos\Theta_{\rm o,eff}\,(\varphi, \phi_{\rm o}) = \cos\varphi \sin\phi_{\rm o} \tag{C.10}$$

for the azimuth angle φ measured from the direction of ISMF in the plane of the sky.

Let us consider the azimuthal profile of the radio brightness S_ϱ at a given radius ϱ from the center of the SNR projection.

With the use of $\Theta_{\rm o,eff}$, the azimuthal and radial variation of the radio brightness for fixed ϱ may approximately be written from (5.13) as

$$S_{\rm r} \propto \varsigma(\Theta_{\rm o,eff})\sigma_{\rm B}(\Theta_{\rm o,eff})^{(s+1)/2}\int_{\bar{\varrho}}^{1} \frac{\bar{K}(\bar{r})\bar{B}(\bar{r})^{(s+1)/2}\bar{r}d\bar{r}}{\sqrt{\bar{r}^2-\bar{\varrho}^2}}. \tag{C.11}$$

The integral in (C.11) is the same for any azimuthal angle φ. The variation of the radio brightness is therefore approximately determined by

$$S_{\rm r}(\varphi) \propto \varsigma(\Theta_{\rm o,eff}(\varphi, \phi_{\rm o}))\ \sigma_{\rm B}(\Theta_{\rm o,eff}(\varphi, \phi_{\rm o}))^{(s+1)/2} I_{\rm r}(\bar{\varrho}). \tag{C.12}$$

where $I_{\rm r}$ is the same as for the X-ray approximation (C.30). Accuracy of this approximation for the radial profile of brightness is demonstrated on Fig. C.1 and on

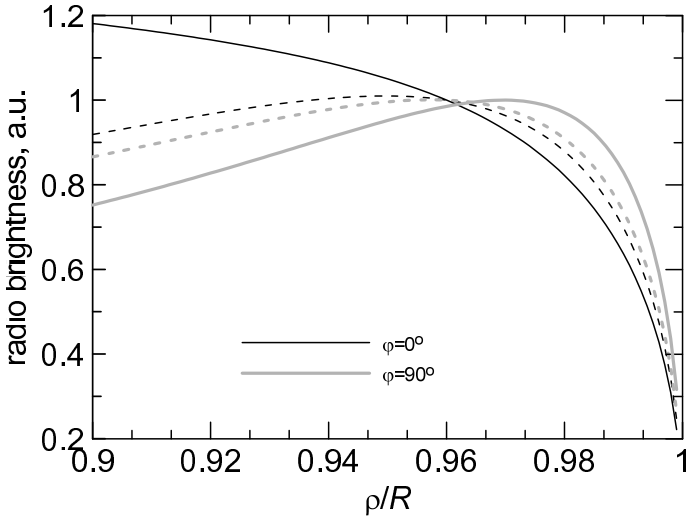

Figure C.1. Radial profile of the radio brightness S_ϱ (solid lines) and its approximation (C.31) (dashed lines) for azimuth $\varphi = 0^\circ$ (black lines) and $\varphi = 90^\circ$ (gray lines), $\phi_\mathrm{o} = 90^\circ$. For smaller aspects, $\phi_\mathrm{o} < 90^\circ$, the approximation agree better with the numerical profiles.

Fig. 5.19 for the azimuthal profiles. I_r varies with azimuth less than 10% (cf. e.g. black and blue dashed lines on Fig. C.1). This variation is due only to $\beta(\Theta_\mathrm{o})$. Thus, β may be taken constant with a good choice $\beta/2 = 1$ (see also Appendix C.3).

The smaller ϕ_o, the smaller differences between the radial profiles for azimuth $\varphi = 0^\circ$ and 90° (black and blue solid lines approach one another with decrease of the aspect angle).

The azimuthal profiles is sensitive to ϱ in quasi-parallel case for aspect angles less than about 30°, i.e. for SNR with centrally-brightened radio morphology ($\varsigma \propto \cos^2\Theta_\mathrm{o}$ and, for small aspect angles, $\Theta_\mathrm{o} \to \pi/2$ on the perifery of SNR and thus $\varsigma \to 0$ there). Therefore, the formula (C.12) does not give correct profiles in the case of quasi-parallel injection for $\phi_\mathrm{o} < 30^\circ$, unless $\bar{\varrho} \to 1$.

C.3. Synchrotron X-ray brightness. A formula obtained here may be useful in situations when an approximate quantitative estimation for the azimuthal variation of the synchrotron X-ray surface brightness is sufficient.

1. The emissivity due to synchrotron emission is

$$q(\varepsilon) = \int N(E) p(E, \varepsilon) dE \qquad \text{(C.13)}$$

Spectral distribution of the synchrotron radiation power of electrons with energy E in magnetic field of the strength B is

$$p(E,\nu) = \frac{\sqrt{3}e^3 B \sin\phi}{m_{\rm e}c^2} F\left(\frac{\nu}{\nu_{\rm c}}\right), \tag{C.14}$$

where ν is frequency, $\nu_{\rm c} = c_1 B E^2$ the characteristic frequency. Most of this radiation is in photons with energy $\varepsilon_{\rm p} = 0.29 h\nu_{\rm c}$. In the 'delta-function approximation', the special function F is substituted with

$$F\left(\frac{\nu}{\nu_{\rm c}}\right) = \delta\left(\frac{\nu}{\nu_{\rm c}} - 0.29\right) \int\limits_0^\infty F(x)dx \tag{C.15}$$

where

$$\int\limits_0^\infty F(x)dx = \frac{8\pi}{9\sqrt{3}}. \tag{C.16}$$

With this approximation, (C.13) becomes

$$q(\varepsilon) = \frac{4\pi e^3 \sin\phi\ \varepsilon^{1/2} B^{1/2}}{9 m_{\rm e}c^2\ 0.29 c_1^{1/2} h^{1/2}} N(E_{\rm m}) \tag{C.17}$$

where $E_{\rm m}$ is the energy of electrons which give maximum contribution to synchrotron emission at photons with energy ε: $E_{\rm m} = \varepsilon^{1/2} \left(0.29 h c_1 B\right)^{-1/2}$.

2. Let the energy of relativistic electrons is E in a given fluid element at present time. Their energy was $E_{\rm i}$ at the time this element was shocked. These two energies are related as

$$E = E_{\rm i} \mathcal{E}_{\rm ad} \mathcal{E}_{\rm rad} \tag{C.18}$$

where $\mathcal{E}_{\rm ad}$ accounts for the adiabatic losses and $\mathcal{E}_{\rm rad}$ for the radiative losses (Appendix 3.2.2). There are approximations valid close to the shock (Appendix B):

$$\mathcal{E}_{\rm ad} \approx \bar{a}^{\kappa_{\rm ad}}, \qquad \mathcal{E}_{\rm rad} \approx \bar{a}^{5\sigma_{\rm B}^2 E/2E_{\rm f,\parallel}} \tag{C.19}$$

where $\bar{a} = a/R$, a is Lagrangian coordinate of the fluid element, $E_{\rm f,\parallel}$ is the fiducial energy for parallel shock, $\kappa_{\rm ad}$ depends on γ and is given by (B.11); $\kappa_{\rm ad} = 1$ for $\gamma = 5/3$ (for other γ see Table B.1). The factor $\sigma_{\rm B}$ represents compression in the classical MHD [303] but may be interpreted also as amplification-plus-compression factor. In the latter case, it should be written in a way to be unity at parallel shock.

The downstream evolution of K in a Sedov SNR is (Appendix 3.2.2)

$$K \propto \varsigma(\Theta_{\rm o})\bar{K}(\bar{a}) \tag{C.20}$$

where ς is injection efficiency. With the approximations (C.19) and s close to 2, the distribution $N(E)$ may be written from (3.28) as

$$N(E,\Theta_{\rm o}) \propto \varsigma(\Theta_{\rm o})\bar{K}(\bar{a})E^{-s}\exp\left[-\left(\frac{E\bar{a}^{-\psi(E,\Theta_{\rm o})}}{E_{\rm max,\parallel}\mathcal{F}(\Theta_{\rm o})}\right)^{\alpha}\right] \tag{C.21}$$

where

$$\psi(E,\Theta_{\rm o}) = \kappa_{\rm ad} + \frac{5\sigma_{\rm B}(\Theta_{\rm o})^2 E}{2E_{\rm f,\parallel}} - \frac{3q}{2} \tag{C.22}$$

and s is allowed to vary with E.

3. Let us consider the azimuthal profile of the synchrotron X-ray brightness S_ϱ at a given radius ϱ from the center of the SNR projection.

Like in Paper II, we consider the 'effective' obliquity angle $\Theta_{\rm o,eff}$ which, for a given azimuth, equals to the obliquity angle for a sector with the same azimuth in the plane of the sky (see details in Paper II). The relation between the azimuthal angle φ, the obliquity angle $\Theta_{\rm o,eff}$ and the aspect angle $\phi_{\rm o}$ is as simple as

$$\cos\Theta_{\rm o,eff}\,(\varphi,\phi_{\rm o}) = \cos\varphi\sin\phi_{\rm o} \tag{C.23}$$

for the azimuth angle φ measured from the direction of ISMF in the plane of the sky.

The surface brightness of SNR projection at distance ϱ from the center and at azimuth φ is

$$S(\bar{\varrho},\varphi) = 2\int_{\bar{a}(\bar{\varrho})}^{1} q(\bar{a})\frac{\bar{r}\bar{r}_{\bar{\rm a}}d\bar{a}}{\sqrt{\bar{r}^2-\bar{\varrho}^2}}. \tag{C.24}$$

where $\bar{r}_{\bar{\rm a}}$ is the derivative of $\bar{r}(\bar{a})$ in respect to $\bar{a}$. The azimuthal variation of the synchrotron X-ray brightness is approximately

$$\begin{aligned} S_{\rm x} \;&\propto \varsigma(\Theta_{\rm o,eff})\sigma_{\rm B}(\Theta_{\rm o,eff})^{(s+1)/2} I_{\rm rx}(\Theta_{\rm o,eff},\bar{\varrho}) \\ &\times \exp\left[-\left(\frac{E_{\rm ms}(\varepsilon,\Theta_{\rm o,eff})}{E_{\rm max,\parallel}\mathcal{F}(\Theta_{\rm o,eff})}\right)^{\alpha}\right] \end{aligned} \tag{C.25}$$

where

$$I_{\rm rx} = \int_{\bar{a}(\bar{\varrho})}^{1} \frac{\bar{K}\bar{B}^{(s+1)/2}\bar{r}\bar{r}_{\bar{\rm a}}}{\sqrt{\bar{r}^2-\bar{\varrho}^2}} \times \exp\left[-\left(\frac{E_{\rm ms}}{E_{\rm max,\|}\mathcal{F}}\right)^{\alpha}\left(\bar{a}^{-\alpha\psi(E_{\rm m})}\bar{B}^{-\alpha/2}-1\right)\right] d\bar{a}, \tag{C.26}$$

reflects the dependence on ρ, $E_{\rm ms}$ is $E_{\rm m}$ for $\bar{B}=1$:

$$E_{\rm ms}(\varepsilon,\Theta_{\rm o,eff}) = \left(\frac{\varepsilon}{0.29hc_1B_{\rm o}\sigma_{\rm B}(\Theta_{\rm o,eff})}\right)^{1/2}. \tag{C.27}$$

Note, that $E_{\rm ms} \propto \varepsilon^{1/2}$, i.e. S_ϱ depends in our approximation on the energy ε of observed X-ray photons.

4. Let us approximate $I_{\rm rx}$. First, we use the approximations $\bar{a} \approx \bar{r}^{\sigma}$, $\bar{K}\bar{B}^{(s+1)/2}\bar{r}_{\bar{\rm a}} \approx \bar{a}^{\kappa_{\rm r}}/\sigma$, which are valid close to the shock (Appendix B), σ is the shock compression ratio. Next, we expand $\bar{r}/\sqrt{\bar{r}^2-\bar{\varrho}^2}$ in powers of the small parameter $(r-1)$ and consider the only first term of the decomposition:

$$\frac{\bar{r}}{\sqrt{\bar{r}^2-\bar{\varrho}^2}} \approx \frac{1}{\sqrt{1-\bar{\varrho}^2}}. \tag{C.28}$$

The exponential term in the integral expands in powers of the small parameter $(1-a)$:

$$\exp\left(-x_1(a^{-x_2}-1)\right) \approx 1 - x_1x_2(1-a). \tag{C.29}$$

In addition, $E_{\rm ms}$ is used instead of $E_{\rm m}$.

Close to the shock, the integral of interest is therefore

$$I_{\rm rx}(\varphi,\bar{\varrho}) \approx I_{\rm r}(\bar{\rho})I_{\rm x}(\varphi,\bar{\varrho}) \tag{C.30}$$

where

$$I_{\rm r} = \frac{1}{\sigma\sqrt{1-\bar{\varrho}^2}}\frac{1-\bar{\varrho}^{\sigma(\kappa_{\rm r}+1)}}{\kappa_{\rm r}+1}, \tag{C.31}$$

$$I_{\rm x} = \left[1 - \frac{\epsilon_{\rm m}^{\alpha}(\psi+\beta/2)\alpha}{\mathcal{F}^{\alpha}}\left(1-\frac{1-\bar{\varrho}^{\sigma(\kappa_{\rm r}+2)}}{1-\bar{\varrho}^{\sigma(\kappa_{\rm r}+1)}}\frac{\kappa_{\rm r}+1}{\kappa_{\rm r}+2}\right)\right]. \tag{C.32}$$

The parameter

$$\psi = \kappa_{\rm ad} + \frac{5\sigma_{\rm B}^2\epsilon_{\rm m}}{2\epsilon_{\rm f\|}} - \frac{3q}{2} \tag{C.33}$$

is responsible for the losses of emitting electrons and the time evolution of $E_{\max}$ on the shock. The value of $\kappa_{\rm ad}$ is rather close to unity for $\gamma = 1.1 \div 5/3$ (Table B.1); unless radiative losses (the second term in ψ) are negligible, one may use $\kappa_{\rm ad} \approx 1$ for any γ. Other parameters are

$$\epsilon_{\rm m} = \frac{E_{\rm ms}}{E_{\rm max,\parallel}} = \left(\frac{\tilde{\varepsilon}}{0.29\sigma_{\rm B}}\right)^{1/2}, \tag{C.34}$$

β is given by Eq. (B.8),

$$\kappa_{\rm r} = \frac{3b}{2} + \frac{2+s}{3}\kappa_{\rm na} + \frac{s+1}{2}\beta + \frac{1}{\sigma} - 1. \tag{C.35}$$

Parameters ψ, $\epsilon_{\rm m}$, $\sigma_{\rm B}$, $\mathcal{F}$ and β depend on $\Theta_{\rm o,eff}$ and therefore on the aspect angle $\phi_{\rm o}$ and the azimuth angle φ.

The parameter β reflects differences between MF distribution downstream the shock of the different obliquity. It varies from $\beta_\parallel$ at parallel shock to $\beta_\perp$ at perpendicular one, Eq. (B.8). In the approximate formulae, it appears in the combination $\beta/2$; the role of $\beta \in [\beta_\parallel; \beta_\perp]$ is minor in modification of the approximate azimuthal and radial profiles. Therefore, in order to simplify the approximation, we may take $\beta/2 \approx 1$.

The index s in (C.21), in general, is allowed to vary with E, e.g. to be $s(E) = s + \delta s(E)$. In our approximation, due to (C.15), s reflects the 'local' slope of the electron spectrum appropriate to $\epsilon_{\rm m}$. Therefore, if one assumes $s(E) \neq$ const, the index $s(\epsilon_{\rm m})$ may vary with azimuth because $\epsilon_{\rm m}$ varies, Eq. (C.34).

5. The final formula is

$$S_{\rm x}(\varphi, \bar{\varrho}) \propto \varsigma(\varphi)\sigma_{\rm B}(\varphi)^{(s+1)/2} \exp\left[-\left(\frac{\epsilon_{\rm m}(\varphi)}{\mathcal{F}(\varphi)}\right)^{\alpha}\right] I_{\rm rx}(\varphi, \bar{\varrho}; \epsilon_{\rm f\parallel}) \tag{C.36}$$

where only $I_{\rm x}$ depends on $\bar{\varrho}$ and $\epsilon_{\rm f\parallel}$.

The formula Eq. (C.36) gives us the possibility to approximate both the azimuthal and the radial brightness profiles of X-ray brightness for $\bar{\varrho}$ close to unity. It may be used (with a bit larger errors compared to the case of IC emission; Fig. C.2, cf. Fig. C.3), for those azimuth φ where $\epsilon_{\rm m} \lesssim 1$ and $\epsilon_{\rm f} \gtrsim 0.1$, in the range of $\bar{\varrho}$ from $1 - 2\Delta\bar{\varrho}_{\rm m}$ to 1, where $\Delta\bar{\varrho}_{\rm m} = 1 - \bar{\varrho}_{\rm m}$, $\bar{\varrho}_{\rm m}$ is the radius where the maximum in the

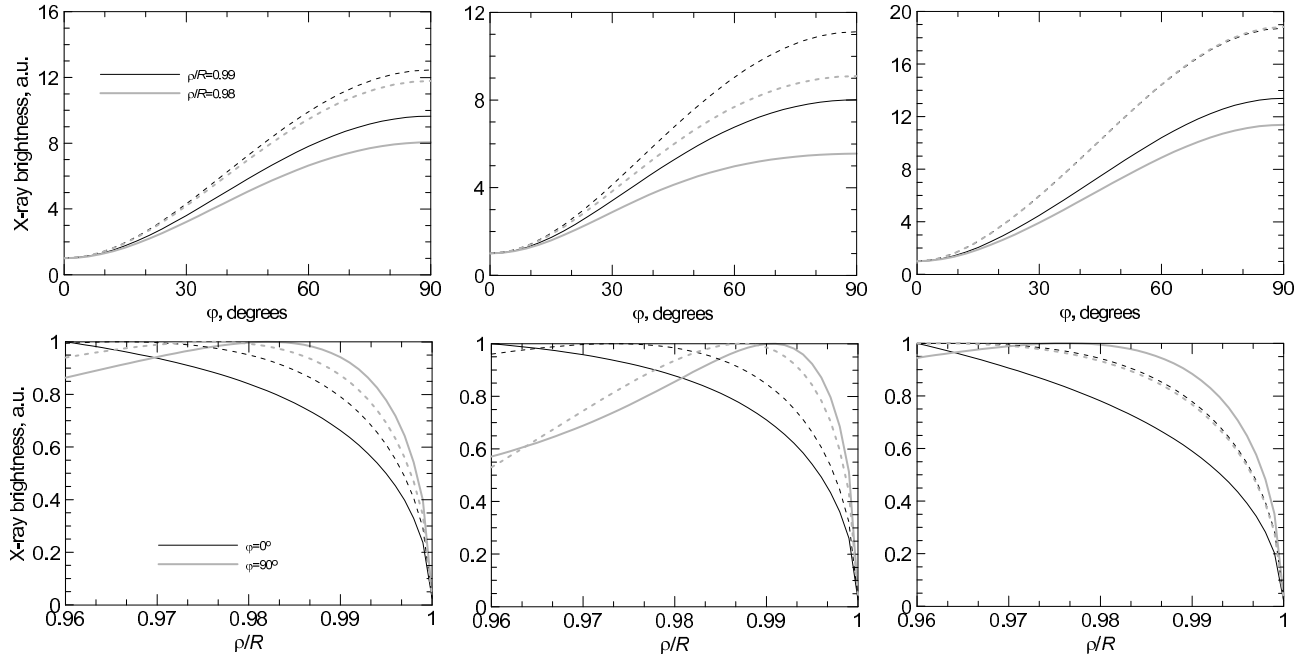

Figure C.2. Azimuthal (upper panels) and radial (lower panels) profiles of the X-ray surface brightness $S_{\rm x}$ (solid lines) and its approximations (C.36) (dashed lines). Calculations are done for $\phi_{\rm o} = 90^{\rm o}$, $b = 0$, isotropic injection, $\gamma = 5/3$, $s = 2$, $\alpha = 1$. Models of $E_{\rm max}$: $\mathcal{F} = {\rm const}$ (left and middle panels) and time-limited one with $\eta = 1.5$ (right panels). The reduced electron energy is $\epsilon_{\rm m} = 1$ and the reduced fiducial energy is $\epsilon_{\rm f\|} = 3$ (left), $\epsilon_{\rm f\|} = 1$ (middle), $\epsilon_{\rm f\|} = 5$ (right panels).

radial profile of brightness happens. We have in mind the maximum which is close to the shock, say $\bar{\varrho}_{\rm m} > 0.95$; therefore, in order to determine $\bar{\varrho}_{\rm m}$, one should look for the azimuth with the largest radiative losses. This is discussed in details on example of the IC emission in Sect. C.4.

Adiabatic index γ affects the approximation through σ, $\kappa_{\rm r}$, $\kappa_{\rm ad}$.

C.4. IC γ-ray brightness. Electrons with Lorentz factor γ emit most of their IC radiation in photons with energy $\varepsilon_{\rm m}$. Let us use the 'delta-function approximation' [280]:

$$p_{\rm ic}(\gamma,\varepsilon) \approx p_{\rm m}(\gamma)\delta(\varepsilon-\varepsilon_{\rm m}), \quad p_{\rm m}(\gamma) = \int\limits_0^\infty p_{\rm ic}(\gamma,\varepsilon)d\varepsilon. \tag{C.37}$$

In the Thomson limit, which is valid for SNRs in most cases, $\varepsilon_{\rm m}(\gamma) \approx 4kT\gamma^2$ [280] and $p_{\rm m}(\gamma) = (4/3)c\sigma_{\rm T}\omega\gamma^2$ [326], T and ω are the temperature and the energy density of initial black-body photons, $\sigma_{\rm T}$ is the Thomson cross-section.

Substitution (3.57) with (C.37) yields

$$q_{\rm ic} = \frac{c\sigma_{\rm T}\omega m_{\rm e}c^2\varepsilon^{1/2}}{12\epsilon_{\rm c}^{3/2}} N(E_{\rm m}) \tag{C.38}$$

where

$$E_{\rm m} = \frac{m_{\rm e}c^2\varepsilon^{1/2}}{2(kT)^{1/2}} \tag{C.39}$$

is the energy of electrons which give maximum contribution to IC emission at photons with energy ε.

Adopting the approach from the Appendix C.3 to IC emission, we come to the approximation

$$S_{\rm ic}(\varphi) \propto \varsigma(\Theta_{\rm o,eff}) \exp\left[-\left(\frac{E_{\rm m}(\varepsilon)}{E_{\rm max,\parallel}\mathcal{F}(\Theta_{\rm o,eff})}\right)^{\alpha}\right] I_{\rm ic}(\Theta_{\rm o,eff}, \bar{\rho}). \tag{C.40}$$

The factor

$$I_{\rm ic} = \int_{\bar{a}(\bar{\varrho})}^{1} \frac{\bar{K}\bar{r}\bar{r}_{\bar{\rm a}} d\bar{a}}{\sqrt{\bar{r}^2 - \bar{\varrho}^2}} \exp\left[-\left(\frac{E_{\rm m}}{E_{\rm max,\parallel}\mathcal{F}}\right)^{\alpha}\left(\bar{a}^{-\alpha\psi} - 1\right)\right] \tag{C.41}$$

is approximately

$$\begin{aligned} I_{\rm ic}(\varphi, \bar{\varrho}) &\approx \frac{1}{\sigma\sqrt{1-\bar{\varrho}^2}} \frac{1 - \bar{\varrho}^{\sigma(\kappa_{\rm ic}+1)}}{\kappa_{\rm ic}+1} \\ &\times \left[1 - \frac{\epsilon_{\rm m}^{\alpha}\psi\alpha}{\mathcal{F}^{\alpha}}\left(1 - \frac{1-\bar{\varrho}^{\sigma(\kappa_{\rm ic}+2)}}{1-\bar{\varrho}^{\sigma(\kappa_{\rm ic}+1)}}\frac{\kappa_{\rm ic}+1}{\kappa_{\rm ic}+2}\right)\right]. \end{aligned} \tag{C.42}$$

where $\kappa_{\rm ic}$ and σ comes from the approximations $\bar{a} \approx \bar{r}^{\sigma}$, $\bar{K}\bar{r}_{\bar{\rm a}} \approx \bar{a}^{\kappa_{\rm ic}}/\sigma$,

$$\psi = \kappa_{\rm ad} + \frac{5\sigma_{\rm B}^2\epsilon_{\rm m}}{2\epsilon_{\rm f\parallel}} - \frac{3q}{2}, \tag{C.43}$$

$$\epsilon_{\rm m} = \frac{E_{\rm m}}{E_{\rm max,\parallel}} = \frac{\varepsilon^{1/2}}{2(kT)^{1/2}\gamma_{\rm max\parallel}}, \tag{C.44}$$

$$\kappa_{\rm ic} = \frac{3b}{2} + \frac{2+s}{3}\kappa_{\rm na} + \frac{1}{\sigma} - 1. \tag{C.45}$$

The final formula is

$$S_{\rm ic}(\varphi, \bar{\varrho}) \propto \varsigma(\varphi) \exp\left[-\left(\frac{\epsilon_{\rm m}}{\mathcal{F}(\varphi)}\right)^{\alpha}\right] I_{\rm ic}(\varphi, \bar{\varrho}; \epsilon_{\rm f\parallel}) \tag{C.46}$$

It gives us the possibility to approximate both the azimuthal and the radial brightness profiles for $\bar{\varrho}$ close to unity.

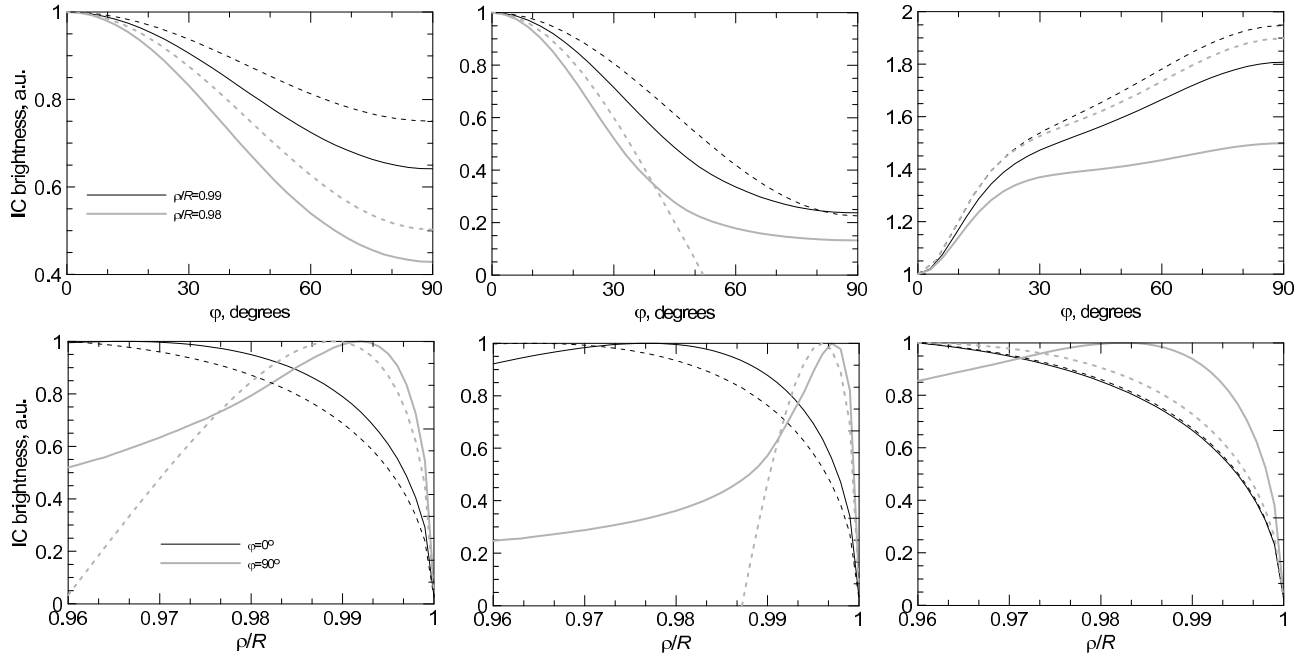

Figure C.3. Azimuthal (upper panels) and radial (lower panels) profiles of the IC surface brightness $S_{\rm ic}$ (solid lines) and its approximations (C.46) (dahsed lines). Calculations are done for $\phi_{\rm o} = 90^{\rm o}$, $b = 0$, isotropic injection, $\gamma = 5/3$, $s = 2$, $\alpha = 1$. Models of $E_{\rm max}$: $\mathcal{F} = {\rm const}$ (left and middle panels) and time-limited one with $\eta = 1.5$ (right panels). The reduced electron energy is $\epsilon_{\rm m} = 1$ and the reduced fiducial energy is $\epsilon_{\rm f\parallel} = 3$ (left), $\epsilon_{\rm f\parallel} = 1$ (middle), $\epsilon_{\rm f\parallel} = 5$ (right panels).

Accuracy of the approximation. Fig. C.3 demonstrates accuracy of the approximation (C.46) (left and middle panels show in fact the variation of $I_{\rm ic}$ because both ς and $\mathcal{F}$ are constant there). Our calculations may be summarized as follows: this approximation may be used, with errors less than $\sim 30\%$, for those azimuth φ where $\epsilon_{\rm m} \lesssim 1$ and $\epsilon_{\rm f} \gtrsim 0.1$, in the range of $\bar{\varrho}$ from $1-2\Delta\bar{\varrho}_{\rm m}$ to 1, where $\Delta\bar{\varrho}_{\rm m} = 1-\bar{\varrho}_{\rm m}$, $\bar{\varrho}_{\rm m}$ is the radius (close to the shock) where the maximum in the radial profile of brightness happens; in addition, approximation may not be used for $\bar{\varrho} \lesssim 0.9$. If for some azimuth, the above conditions on $\epsilon_{\rm m}$ and $\epsilon_{\rm f}$ do not hold, the accuracy of approximation gradually decreases because the role of the exponent in $N(E)$ and of the radiative losses may not be described by the first terms in the decompositions used for derivation of the formula.

Let's consider Fig. C.3. The photon energy $\epsilon_{\rm m}$ does not change with azimuth for IC process. On the left panels, the reduced fiducial energy $\epsilon_{\rm f}(\varphi) = \epsilon_{\rm f\parallel}/(\mathcal{F}\sigma_{\rm B}^2) \gtrsim 0.1$ for any azimuth: $\epsilon_{\rm f\parallel} = 3$ at the parallel shock and $\epsilon_{\rm f\perp} = 0.19$ at the perpendicular shock. The approximation is accurate for any azimuth, for $0.98 \lesssim \bar{\varrho} \leq 1$ at $\varphi = 90^{\rm o}$ and for a wider range of ϱ at $\varphi = 0^{\rm o}$. Middle panels on Fig. C.3 show the same

case except of $\epsilon_{\mathrm{f}\parallel} = 1$. At parallel shock (i.e. $\varphi = 90^{\mathrm{o}}$), the range for $\bar{\varrho}$ is smaller, $0.99 \lesssim \bar{\varrho} \leq 1$ (lower panel). Therefore, the approximation of the azimuthal profile for $\bar{\varrho} = 0.98$ is inaccurate (upper panel, blue line), especially for $\varphi > 45^{\mathrm{o}}$ where ϵ_{f} decreases; it is $\epsilon_{\mathrm{f}\perp} = 0.06$. The azimuthal profile is however accurate for $\bar{\varrho} = 0.99$ (black line). Similar situation is for variable E_{max} (right panels on Fig. C.3). $E_{\mathrm{max}\perp}/E_{\mathrm{max}\parallel} = 3.25$ for considered model, therefore $\epsilon_{\mathrm{f}\parallel}/\epsilon_{\mathrm{f}\perp} = 52$. Therefore, in order to obtain a representative approximation, the lowest possible $\epsilon_{\mathrm{f}\parallel}$ should be about $0.1 \times 52 = 5.2$. We see from the figure that accuracy decreases toward smaller ϵ_{f} (i.e. where the role of radiative losses are very efficient in modification of the electron distribution) and for smaller $\bar{\varrho}$.

In general, the accuracy of the approximation is better for larger ϵ_{f} and smaller ϵ_{m}. With decreasing of the aspect angle ϕ_{o}, the accuracy of the approximations for the azimuthal profile increases at the beginning (because contrasts in σ_{B}, ϵ_{f} and $\mathcal{F}$ are lower) and then decreases again, for the case of the quasi-parallel injection, because SNR becomes centrally-brightened while our approximation is developed for regions close to the edge of SNR.

Appendix D

Calculation of integral in Eq. (3.42)

The function $\mathcal{I}(a,t)$ in Eq. (3.42) is expressed as [303]

$$\mathcal{I}(a,t) = \sigma_{\rm B}^2 \int_{t_{\rm i}}^{t} \frac{B_{\rm eff}(a,t')^2}{B_{\rm eff,s}(t)^2} \left(\frac{\rho(a,t')}{\rho(a,t)}\right)^{1/3} \frac{dt'}{t} \ , \tag{D.1}$$

where $B_{\rm eff}^2 = B^2 + B_{\rm CMB}^2$ is the "effective" magnetic field introduced to account for the energy losses of electrons due to IC scatterings on the photons of CMB.

The integral (D.1) is rather CPU consuming because it requires to know, with high enough time resolution, the history of each parsel of gas inside the SNR since its shocking time. To reduce the computational cost, we calculate it approximately, changing integration on dt' to $dR' = V_{\rm sh}(t')dt'$, where R and $V_{\rm sh}$ are the shock position and velocity, respectively, and using some MHD properties of the fluid.

We calculate $\mathcal{I}(a,t)$ using an analytic description of mass density and magnetic field evolution inside the SNR which expands through a non-uniform ISM and/or ISMF. The continuity equation $\rho_{\rm o}(a)a^2da = \rho(a)r^2dr$ results in

$$\rho(a,t) = \rho_{\rm o}(a) \left(\frac{a}{r(a,t)}\right)^2 r_{\rm a}(a,t)^{-1} \tag{D.2}$$

where $r_{\rm a}(a,t)$ is the derivative of $r(a,t)$ with respect to a; the density term in Eq. (D.1) is

$$\frac{\rho(a,t')}{\rho(a,t)} = \frac{r(a,t)^2}{r(a,t')^2} \frac{r_{\rm a}(a,t)}{r_{\rm a}(a,t')} \ . \tag{D.3}$$

The magnetic field in Eq. (D.1) can be expressed as $B(a,t)^2 = B_{\parallel}(a,t)^2 + B_{\perp}(a,t)^2$, where $B_{\parallel}$ and $B_{\perp}$ are the components of magnetic field parallel and perpendicular to the shock normal, respectively. These two components follow the magnetic flux conservation $B_{\parallel}d\sigma_{\rm S} = const$, where $d\sigma_{\rm S}$ ia a surface element, and the flux-frozen condition $B_{\perp}(r)rdr = const$:

$$B_{\parallel}(a,t) = B_{\parallel,o}(a) \frac{a^2}{r(a,t)^2} \ , \tag{D.4}$$

$$B_\perp(a,t) = B_{\perp,o}(a)\frac{r(a,t)}{a}\frac{\rho(a,t)}{\rho_{\rm o}(a)} = B_{\perp,o}(a)\frac{a}{r(a,t)r_{\rm a}(a,t)} \ . \tag{D.5}$$

Thus, the magnetic field and the mass density in Eq. (D.1) can be expressed through the relation $r(a,t)$ between Eulerian and Lagrangian coordinates of a parcel of gas and its derivative, $r_{\rm a}(a,t)$. Considering that $r(a,t)$ and $r_{\rm a}(a,t)$ can be expressed in terms of the dynamical characteristics of the shock (i.e. as $r(a,R)$ and $r_{\rm a}(a,R)$), the integral (D.1) may be calculated as follows:

$$\mathcal{I}(a,t) = \frac{\sigma_{\rm B}^2}{t}\int_{R_{\rm i}}^{R}\frac{B(a,R')^2}{B_{\rm s}(R)^2}\left(\frac{r(a,R)^2 r_{\rm a}(a,R)}{r(a,R')^2 r_{\rm a}(a,R')}\right)^{1/3}\frac{dR'}{V_{\rm sh}(R')} \ . \tag{D.6}$$

Now, the relation $r(a,R)$ is approximated[2], using the method described in [195]:

$$\frac{r(a,R)}{R} = \left(\frac{a}{R}\right)^{\psi}(1 + a_1\upsilon + a_2\upsilon^2 + a_3\upsilon^3 + a_4\upsilon^4) \tag{D.7}$$

where $\upsilon = (R-a)/R$ and $\psi = (\gamma-1)/\gamma$. The parameters a_1, a_2, a_3, and a_4 are expressed as:

$$a_1 = -r_{\rm a,s} + \psi \ , \tag{D.8}$$

$$a_2 = \frac{1}{2}\left(Rr_{\rm aa,s} - 2\psi r_{\rm a,s} + \psi(\psi+1)\right) \ , \tag{D.9}$$

$$a_3 = \frac{1}{6}\left(-R^2 r_{\rm aaa,s} + 3\psi R r_{\rm aa,s} - 3\psi(\psi+1)r_{\rm a,s} + \psi(\psi+1)(\psi+2)\right) \ , \tag{D.10}$$

$$a_4 = \mathcal{C} - (1 + a_1 + a_2 + a_3) \ , \tag{D.11}$$

where $\mathcal{C}$ reflects the variation of $r(a)$ around the center of the SNR. We adopt $\mathcal{C} = \mathcal{C}_{\rm A}$ where $\mathcal{C}_{\rm A}$ is given by the self-similar Sedov solution for a spherical shock (for details see Appendix in [272] and references therein):

$$\mathcal{C}_{\rm A} = \left[\frac{\gamma}{\gamma+1}\bar{P}(0)^{-1/\gamma}\right]^{1/3} \ , \tag{D.12}$$

$\bar{P}(0)$ is the plasma pressure at the center of the remnant divided by its post-shock value

$$\bar{P}(0) = \left(\frac{1}{2}\right)^{6/5}\left(\frac{\gamma+1}{\gamma}\right)^{6/5-\gamma/(2-\gamma)}\left(\frac{(2\gamma+1)(\gamma+1)}{\gamma(7-\gamma)}\right)^{(-2+5/(2-\gamma))\cdot\zeta} \ , \tag{D.13}$$

[2]The approximation (D.7) is developed to give exact values of derivatives up to the third order at the shock and to the first order at the center.

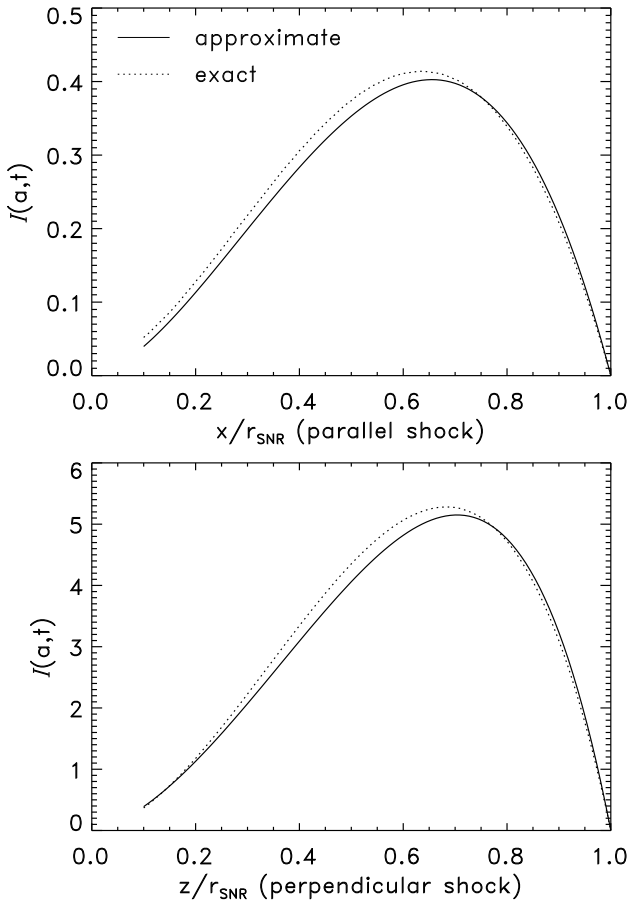

Figure D.1. Self-similar approximate and exact radial profiles of the integral $\mathcal{I}(a)$ when the ambient magnetic field is either parallel (upper panel) or perpendicular (lower panel) to the shock normal, and $\gamma = 5/3$.

$$\zeta = \frac{\gamma+1}{3(\gamma-1)+2} - \frac{2}{5} + \frac{\gamma-1}{2\gamma+1} \ . \tag{D.14}$$

Thus, we derive $\mathcal{C}_{\rm A}(\gamma = 5/3) = 1.083$, $\mathcal{C}_{\rm A}(\gamma = 4/3) = 1.055$ and $\mathcal{C}_{\rm A}(\gamma = 1.1) = 1.021$. The expressions for the derivatives $r_{\rm a,s}$, $r_{\rm aa,s}$, $r_{\rm aaa,s}$ in Eqs. (D.8)-(D.10) as functions of R, $\dot{R}$, $\ddot{R}$ and $R^{(3)}$ are given in Appendix A2 of [195].

Finally, we calculate $V_{\rm sh}(R)$ in Eq. (D.1) as well as $\ddot{R}$ and $R^{(3)}$, using the Hnatyk [193] approximate analytical formula for the strong shock in a non-uniform medium (see also Sect. 2.1 in [195]).

Integral $\mathcal{I}(a,t)$ can be calculated rather simply in the case of a SNR expanding through uniform ISM and ISMF. We therefore test our calculation of $\mathcal{I}(a,t)$ by comparing the approximate values derived from Eq. (D.6) with the exact ones derived from the Sedov solution in the case of $\gamma = 5/3$. Figure D.1 compares the exact and approximate values of $\mathcal{I}(a,t)$ in the limits of parallel and perpendicular shocks.

Appendix E

Surface brightness of Sedov SNR

Surface brightness of a spherical SNR is an integral of volume emissivity q along the line of sight

$$S_{\rm syn} = 2\int\limits_0^R qdl = 2R\int\limits_{\bar{a}(\bar{\rho})}^1 q\frac{\bar{r}\bar{r}_{\bar{a}}d\bar{a}}{\sqrt{\bar{r}^2-\bar{\rho}^2}}, \tag{E.1}$$

where ρ is distance from the center of projection, $\bar{r} = r/R$, a Lagrangian coordinate, $r_a = dr/da$,

$$q = \int N(E)p(E,\varepsilon)dE, \tag{E.2}$$

where E and ε are the electron and photon energies, p the radiation power of a single electron. In case of Sedov SNR in uniform medium the electron energy distribution downstream of the shock is (Sect. 3.2)

$$N(E) = KE^{-s}\mathcal{E}_{\rm rad}^{s-2}\exp\left(-\frac{E}{E_{\max\|}\mathcal{E}_{\rm ad}\mathcal{E}_{\rm rad}f_{\rm E}}\right), \tag{E.3}$$

the normalization $K = K_{\rm s\|}(t)f_{\rm K}(\Theta_{\rm o})\bar{K}(\bar{a})$, the magnetic field $B = B_{\rm s\|}(t)\sigma_{\rm B}(\Theta_{\rm o})\bar{B}(\bar{a})$ and the electron maximum energy $E_{\max} = E_{\max\|}f_{\rm E}(\Theta_{\rm o})$.

E.1. Synchrotron emission. The synchrotron radiation power is

$$p = \frac{\sqrt{3}e^3\left\langle\sin\phi\right\rangle}{m_{\rm e}c^2}BF_{\rm syn}\left(\frac{\nu}{\nu_{\rm c}}\right), \tag{E.4}$$

where all notations have their common meaning. The synchrotron surface brightness of Sedov SNR is therefore

$$S_{\rm syn} = \frac{2\sqrt{3}e^3\left\langle\sin\phi\right\rangle}{m_{\rm e}c^2}\mathcal{S}_{\rm syn}(\tilde{\nu},\bar{\rho},\varphi;\phi_{\rm o},b,\epsilon_{\rm f\|})\ E_{\max}^{1-s}K_{\rm s\|}B_{\rm o}R. \tag{E.5}$$

where $\mathcal{S}_{\rm syn}(\tilde{\nu},\bar{\rho},\varphi)$ is a universal dimensionless function

$$\mathcal{S}_{\rm syn}=\int\limits_{\bar{a}(\bar{\rho})}^{1}\left[\int\limits_{0}^{\infty}F_{\rm syn}\left(\frac{\tilde{\nu}}{\epsilon^2\sigma_{\rm B}\bar{B}}\right)\epsilon^{-s}\mathcal{E}_{\rm rad}^{s-2}\exp\left(-\frac{\epsilon}{\mathcal{E}_{\rm ad}\mathcal{E}_{\rm rad}f_{\rm E}}\right)d\epsilon\right] \times\sigma_{\rm B}\bar{B}f_{\rm K}\bar{K}\frac{\bar{r}\bar{r}_{\bar{a}}d\bar{a}}{\sqrt{\bar{r}^2-\bar{\rho}^2}}, \tag{E.6}$$

where $\epsilon=E/E_{\rm max\|}$. It depends on the dimensionless models of obliquity variations of K, B and $E_{\rm max}$ (i.e. on $f_{\rm K}$, $\sigma_{\rm B}$, $f_{\rm E}$) but is independent of the actual values of $E_{\rm max}$, $K_{\rm s}$, $B_{\rm o}$ and R.

In the limit $\epsilon_{\rm f\|}\gg 1$ and/or $\tilde{\nu}\ll 1$, Eq. (E.5) transforms to

$$S_{\rm syn}=\frac{2\sqrt{3}e^3\left\langle\sin\phi\right\rangle\mathcal{A}(s)}{m_{\rm e}c^2}\,\mathcal{S}_{\rm r}(\bar{\rho},\varphi;\phi_{\rm o},b)\tilde{\nu}^{-(s-1)/2}E_{\rm max}^{1-s}K_{\rm s\|}B_{\rm o}R. \tag{E.7}$$

where

$$\mathcal{S}_{\rm r}=\int\limits_{\bar{a}(\bar{\rho})}^{1}\left(\sigma_{\rm B}\bar{B}\right)^{(s+1)/2}f_{\rm K}\bar{K}\frac{\bar{r}\bar{r}_{\bar{a}}d\bar{a}}{\sqrt{\bar{r}^2-\bar{\rho}^2}}, \tag{E.8}$$

or, in other form,

$$S_{\rm r}=\frac{2\sqrt{3}e^3\left\langle\sin\phi\right\rangle\mathcal{A}(s)}{m_{\rm e}c^2}\,\mathcal{S}_{\rm r}(\bar{\rho},\varphi;\phi_{\rm o},b)\left(\nu/c_1\right)^{-(s-1)/2}K_{\rm s\|}B_{\rm o}^{(s+1)/2}R. \tag{E.9}$$

E.2. IC emission. The IC radiation power is

$$p=\frac{2e^4m_{\rm e}^2c^2kT}{\pi\hbar^3}E^{-2}\mathcal{I}(E,\varepsilon), \tag{E.10}$$

where all notations have their common meaning, $\mathcal{I}$ is a special integral [280]. The IC brightness is therefore

$$S_{\rm ic}=\frac{4e^4m_{\rm e}^2c^2kT}{\pi\hbar^3}\,\mathcal{S}_{\rm ic}(\varepsilon,\bar{\rho},\varphi;\phi_{\rm o},b,\epsilon_{\rm f\|},E_{\rm max})\,K_{\rm s\|}R. \tag{E.11}$$

The function $\mathcal{S}_{\rm ic}(\bar{\rho},\varphi)$ is not so universal as in case of the synchrotron emission; it depends on the absolute values of the photon energy and the maximum electron energy; we do not present it here.

Appendix F

Nonthermal spectrum of Sedov SNR

Flux is defined as

$$F(\nu) = \left(4\pi d^2\right)^{-1} \int P(\nu) dV \tag{F.1}$$

where V is the volume of SNR and P the volume emissivity. We assume that the energy spectrum of electrons in the form

$$N(E)dE = KE^{-s} \exp(-E/E_{\max})dE \tag{F.2}$$

are created at the shock. The volume emissivity is

$$P(\nu) = \int N(E)p(E,\nu)dE \tag{F.3}$$

where p is the spectral distribution of radiation power of 'single' electron with energy E. Let us consider adiabatic SNR in uniform ISM and uniform ISMF.

In general, the efficiency of injection may depend on the shock obliquity angle $\Theta_{\rm o}$. If particles are injected easier at quasiparallel shocks then $K_{\rm s}(\Theta_{\rm o})$ is decreasing function of $\Theta_{\rm o}$ with decrement rate dependent on the level of turbulence, shock strength etc. [137]. Let us consider parametric representation $K_{\rm s} = K_{\rm s\parallel} f_{\rm K}(\Theta_{\rm o})$ with approximation $f_{\rm K} = \exp\left(-\left(\Theta_{\rm o}/\Theta_{\rm K}\right)^2\right)$ where $K_{\rm s\parallel}$ the normalization for region immediately after the parallel shock, $\Theta_{\rm K}$ the parameter. $\Theta_{\rm K} = \pi/6$ approximates the classical quasiparallel dependence, $\varsigma \propto \cos^2(\Theta_{\rm o})$. In case of the isotropic injection, $\Theta_{\rm K} = \infty$.

F.1. Synchrotron emission. The radio flux (F.1) from Sedov SNR may be written as (for details, see [17])

$$F_{\rm r}(\nu) = C\nu^{-(s-1)/2} \zeta(b, \Theta_{\rm K}) K_{\rm s\parallel} B_{\rm o}^{(s+1)/2} R^3 d^{-2} \tag{F.4}$$

where

$$C = (4\pi)^{-1} \mathcal{A}(s) c_2 \mu_\phi c_1^{(s-1)/2}, \tag{F.5}$$

$c_1 = 3e/(4\pi m_\mathrm{e}^3 c^5)$, $c_2 = \sqrt{3}e^3/(m_\mathrm{e}c^2)$,

$$\mathcal{A}(s) = \frac{2^{(s-1)/2}}{s+1}\Gamma\left(\frac{3s+19}{12}\right)\Gamma\left(\frac{3s-1}{12}\right), \tag{F.6}$$

$\mu_\phi = \left\langle \sin(\varphi)^{(s+1)/2} \right\rangle$, ($C = 3.493 \times 10^{-14}$ cgs in case $s = 2$), φ the angle between MF and the line of sight,

$$\zeta(b, \Theta_\mathrm{K}) = \int\limits_0^{2\pi} d\varphi \int\limits_0^{\pi} d\theta \sin\theta f_\mathrm{K} \int\limits_0^1 d\bar{a}\bar{r}^2 \bar{r}_{\bar{\mathrm{a}}} \bar{K} \left(\sigma_\mathrm{B}\bar{B}\right)^{(s+1)/2}, \tag{F.7}$$

$\sigma_\mathrm{B}(\Theta_\mathrm{o})$ is the compression factor for MF, r and a are Eulerian and Lagrangian coordinates respectively, $r_\mathrm{a} = dr/da$, bar represents parameter divided by its post-shock value, (φ, θ) spherical coordinates. Thanks to the self-similarity, the constant ζ 'compactifies' the whole downstream evolution of fluid elements [21], magnetic field and relativistic electrons [303].

In a similar fasion, the X-ray flux is [18]

$$F_\mathrm{x}(\tilde{\nu}) = C_2 \zeta_\mathrm{x}(\tilde{\nu}; b, \Theta_\mathrm{K}, \epsilon_{\mathrm{f}\parallel}) K_{\mathrm{s}\parallel} B_\mathrm{o} E_{\mathrm{max}\parallel}^{1-s} R^3 d^{-2} \tag{F.8}$$

where $\tilde{\nu} = \nu/\nu_\mathrm{c}(E_{\mathrm{max}\parallel}, B_\mathrm{o})$, $\nu_\mathrm{c}(E, B) \propto E^2 B$ is the synchrotron characteristic frequency, $C_2 = c_2 \langle \sin\varphi \rangle / (4\pi)$ a constant, $\epsilon_{\mathrm{f}\parallel} = 637 \left(B_{\mathrm{s}\parallel}^2 t E_{\mathrm{max}\parallel}\right)^{-1}$ is the reduced fiducial energy. The energy ϵ_f is a measure of importance of radiative losses in modification of the electron spectrum [303]. The function

$$\zeta_\mathrm{x}(\tilde{\nu}; b, \Theta_\mathrm{K}, \epsilon_{\mathrm{f}\parallel}) = \int\limits_0^{2\pi} d\varphi \int\limits_0^{\pi} d\theta \sin\theta f_\mathrm{K} \int\limits_0^1 d\bar{a}\bar{r}^2 \bar{r}_{\bar{\mathrm{a}}} \bar{K} \sigma_\mathrm{B} \bar{B} \tag{F.9}$$

$$\times \int\limits_0^\infty d\epsilon \epsilon^{-s} \mathcal{E}_\mathrm{rad}^{s-2} \exp\left(-\frac{\epsilon}{\mathcal{E}_\mathrm{ad}\mathcal{E}_\mathrm{rad} f_\mathrm{E}}\right) F_\mathrm{syn}\left(\frac{\tilde{\nu}}{\epsilon^2 \sigma_\mathrm{B} \bar{B}}\right),$$

where $\mathcal{E}_\mathrm{ad}(a)$, $\mathcal{E}_\mathrm{rad}(a; \epsilon_{\mathrm{f}\parallel}, \Theta_\mathrm{o})$ represent adiabatic and radiative losses of relativistic electrons (Sect. 3.2), F_syn the function known in the theory of synchrotron radiation, $\epsilon = E/E_{\mathrm{max}\parallel}$.

With $\tilde{\nu}$, the radio flux (F.4) may be written in a form similar to (F.8):

$$F_\mathrm{r}(\tilde{\nu}) = C_2 \mathcal{A}(s) \tilde{\nu}^{-(s-1)/2} \zeta(b, \Theta_\mathrm{K}) K_{\mathrm{s}\parallel} B_\mathrm{o} E_{\mathrm{max}\parallel}^{1-s} R^3 d^{-2}. \tag{F.10}$$

Comparison of (F.8) and (F.10) demonstrates that, for ν much smaller than X-ray frequencies, $\zeta_{\rm x}$ transforms to ζ, as expected:

$$\zeta_{\rm x}(\tilde{\nu}) = \mathcal{A}(s)\ \tilde{\nu}^{-(s-1)/2}\zeta. \tag{F.11}$$

This transition may also be shown analytically from (F.9), in the limit $E \ll E_{\rm max}$ and $E \ll \epsilon_{\rm f} E_{\rm max}$ [18].

Let us introduce the modification factor for the synchrotron spectrum

$$\eta(\tilde{\nu}, \epsilon_{\rm f\|}) = \frac{\zeta_{\rm x}(\tilde{\nu}, \epsilon_{\rm f\|})\tilde{\nu}^{(s-1)/2}}{\mathcal{A}(s)\zeta}. \tag{F.12}$$

It is defined to be $\eta \leq 1$ and ensure $\eta \to 1$ for $\nu \ll \nu_{\rm c}(E_{\rm max\|}, B_{\rm o})$, as it is given by (F.11). In terms of $\tilde{\nu}$, the modification factor is almost universal (i.e. allows for scaling with frequency).

With the modification factor, the expression (F.8) which describes the broad-band (radio-to-X-ray) synchrotron spectrum from Sedov SNR becomes

$$F(\nu) = C\nu^{-(s-1)/2}\zeta(b, \Theta_{\rm K})\eta(\tilde{\nu}; \epsilon_{\rm f\|})K_{\rm s\|}B_{\rm o}^{(s+1)/2}R^3 d^{-2}. \tag{F.13}$$

The values of ζ are shown on Fig. F.1. The parameter ζ is important in normalization of synchrotron spectrum: it varies in about 8 times over the parameter space. If injection is considerably larger at parallel shocks ($\Theta_{\rm K} \leq \pi/3$), the value of b is almost unimportant for amplitude of the synchrotron spectrum, but rather small changes in $\Theta_{\rm K}$ may cause differences in ζ in few times. In contrast, if injection tends to be isotropic ($\Theta_{\rm K} \geq 2\pi/3$), b plays the dominant role.

In order to explore the parameter space, we made several runs to calculate the modification factors for different sets of parameters. Results are shown on Fig. F.2 where we also plot the experimental data in order to demonstrate relevance of the parameters for SN 1006. The modification factor depends on $\epsilon_{\rm f\|}$, b, $\Theta_{\rm K}$ and s as well as on the function $f_{\rm E}(\Theta_{\rm o})$.

F.2. IC emission. The inverse-Compton flux (F.1) from electrons in a black-body photon field with temperature $T_{\rm CMB}$, at photon energies far below TeV (i.e. when the Thomson regime and power-law electron distribution are assumed, see

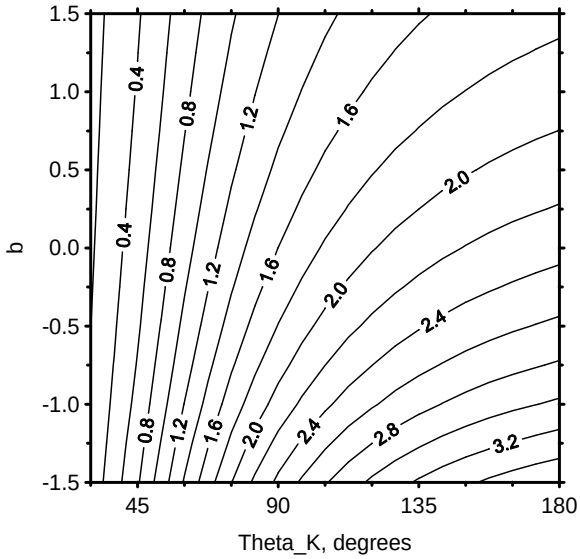

Figure F.1. ζ for different values of parameters b and $\Theta_{\rm K}$. $s = 2$

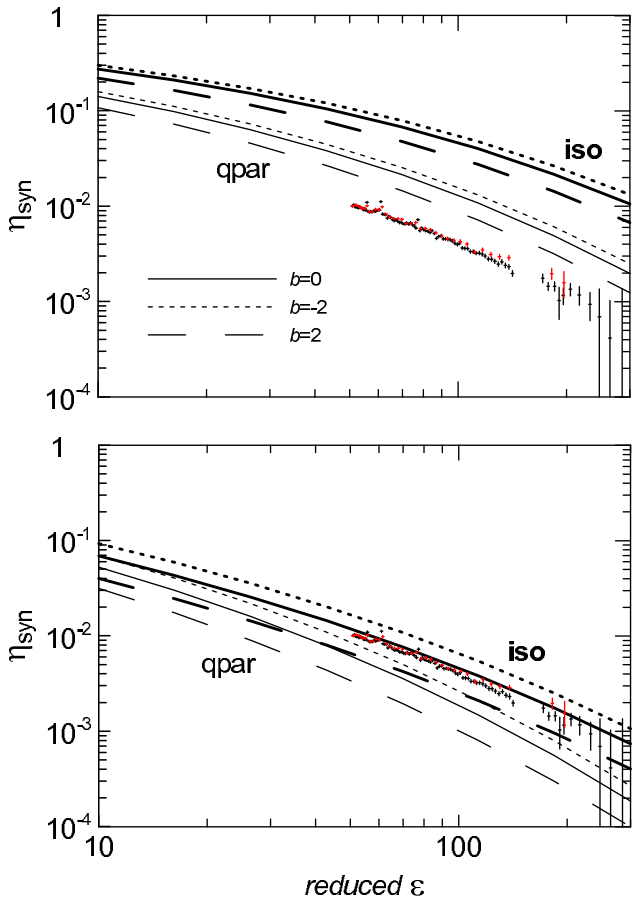

Figure F.2. Modification factor $\eta_{\rm syn}$. Calculations are done for $s = 2$, the time-limited model of $E_{\rm max}$ with $\eta = 1.5$, isotropic injection (thick lines) and quasiparallel injection (thin lines), three values of b, $\epsilon_{\rm f\parallel} = 100$ (upper panel) and $\epsilon_{\rm f\parallel} = 3.2$ (lower panel). Experimental modification factor for SN 1006 are shown for comparison. It is obtained from the SUZAKU spectrum (Fig. 6 [64]) for photon energies $\geq 2\,$keV, with the use of Eq. (5.25). MF strength is given by Eq. (5.21): $B_{\rm o} = 3\,\mu$G (upper panel) and $B_{\rm o} = 30\,\mu$G (lower panel).

Sect. 3.3 for details), is

$$F_{\rm T}(\varepsilon) = C_{\rm T}\varepsilon^{-(s-1)/2}\zeta_{\rm T}(b,\Theta_{\rm K})K_{\rm s\|}R^3 d^{-2} \tag{F.14}$$

where ε is the photon energy,

$$\zeta_{\rm T}(b,\Theta_{\rm K}) = \int\limits_0^{2\pi} d\varphi \int\limits_0^{\pi} d\theta \sin\theta f_{\rm K} \int\limits_0^1 d\bar{a}\bar{r}^2\bar{r}_{\bar{\rm a}}\bar{K}, \tag{F.15}$$

reflects the evolution of relativistic electrons downstream and

$$C_{\rm T} = \frac{2^{s-1}\pi^2\sigma_{\rm T}m_{\rm e}\mathcal{A}_{\rm T}(s)^{(s+1)/2}\left(kT_{\rm CMB}\right)^{(s+5)/2}}{(s+1)h^3(m_{\rm e}c^2)^s} \tag{F.16}$$

where $\sigma_{\rm T}$ is the Thomson cross-section,

$$\mathcal{A}_{\rm T}(s) = \left[\frac{12}{\pi^2}\frac{(s^2+4s+11)}{(s+5)(s+3)^2}\int\limits_0^{\infty}\frac{z^{(s+3)/2}dz}{\exp(z)-1}\right]^{2/(s+1)}. \tag{F.17}$$

The contribution from electrons with energies around $E_{\rm max}$ may be important for TeV γ-photons. The full expression for IC process is

$$F_{\rm ic}(\varepsilon) = C_{\rm ic}\zeta_{\rm ic}(\varepsilon; b, \Theta_{\rm K}, \epsilon_{\rm f\|}, E_{\rm max\|})K_{\rm s\|}R^3 d^{-2} \tag{F.18}$$

where

$$C_{\rm ic} = \frac{3\sigma_{\rm T}kT_{\rm CMB}(m_{\rm e}c^2)^{3-s}}{2h^3c^2}, \tag{F.19}$$

$$\begin{aligned}\zeta_{\rm ic}(\varepsilon; b, \Theta_{\rm K}, \epsilon_{\rm f\|}, E_{\rm max\|}) = \int\limits_0^{2\pi} d\varphi \int\limits_0^{\pi} d\theta \sin\theta f_{\rm K} \int\limits_0^1 d\bar{a}\bar{r}^2\bar{r}_{\bar{\rm a}}\bar{K} \\ \times \int\limits_{\gamma_{\rm min}(\varepsilon)}^{\infty} d\gamma\gamma^{-2-s}\mathcal{E}_{\rm rad}^{s-2}\exp\left(-\frac{\gamma}{\gamma_{\rm max\|}\mathcal{E}_{\rm ad}\mathcal{E}_{\rm rad}f_{\rm E}}\right)\mathcal{I}(\varepsilon, E),\end{aligned} \tag{F.20}$$

where γ is the electron Lorentz factor, $\mathcal{I}$ is an integral appearing in the theory of inverse-Compton process (Sect. 3.3); it accounts for the KN decline where nesessary.

In case $s = 2$ and $T_{\rm CMB} = 2.75$, $\mathcal{A}_{\rm T} = 0.710$ and $C_{\rm T} = 1.304 \times 10^{-14}$ cgs, $C_{\rm ic} = 1.186 \times 10^{12}$ cgs.

In the limit $E \ll E_{\rm max}$ and $E \ll \epsilon_{\rm f} E_{\rm max}$, one has $\mathcal{E}_{\rm rad} = 1$ and $\mathcal{I} \propto \varepsilon$, $E_{\rm min} \propto \varepsilon^{1/2}$ (Sect. 3.3) and (F.18) transforms to (F.14). Therefore

$$\zeta_{\rm ic}(\varepsilon) = c_{\rm o} \varepsilon^{-(s-1)/2} \zeta_{\rm T} \tag{F.21}$$

in this limit; $c_{\rm o} = C_{\rm T}/C_{\rm ic}$.

Let us introduce the modification factor for IC spectrum:

$$\eta_{\rm ic}(\varepsilon, \epsilon_{\rm f\parallel}, E_{\rm max\parallel}) = \frac{\zeta_{\rm ic}(\varepsilon, \epsilon_{\rm f\parallel}, E_{\rm max\parallel}) \varepsilon^{(s-1)/2}}{c_{\rm o} \zeta_{\rm T}}. \tag{F.22}$$

It is also defined to be $\eta_{\rm ic} \leq 1$ and ensure $\eta_{\rm ic} \to 1$ well below TeV energies. However, it is not so universal as for the synchrotron emission, Eq. (F.12): it does not scaled with the frequency and it depends on the absolute value of $E_{\rm max}$. The expression for the broadband IC spectrum is

$$F_{\rm ic}(\varepsilon) = C_{\rm T} \varepsilon^{-(s-1)/2} \zeta_{\rm T}(b, \Theta_{\rm K}) \eta_{\rm ic}(\varepsilon, \epsilon_{\rm f\parallel}, E_{\rm max\parallel}) K_{\rm s\parallel} R^3 d^{-2}. \tag{F.23}$$

The parameter $\zeta_{\rm T}$ behaves like ζ (Fig. F.3): it mostly depends on $\Theta_{\rm K}$ for quasi-parallel injection and on b for isotropic injection. However, the role of $\zeta_{\rm T}$ is less important for normalization of IC spectrum because it varies in about 4 times over the parameter space.

The modification factor of the IC specrum $\eta_{\rm ic}$ is shown on Fig. F.4, in comparison with the observational data for SN 1006. It depends on $\epsilon_{\rm f\parallel}$, b, $\Theta_{\rm K}$, s and $E_{\rm max}$ as well as on the function $f_{\rm E}(\Theta_{\rm o})$.

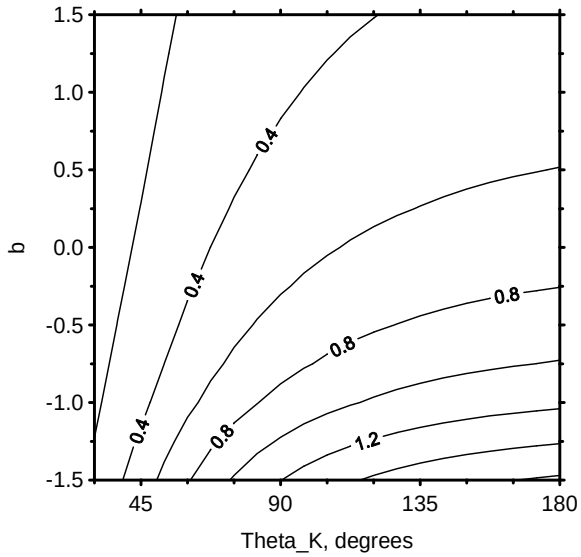

Figure F.3. $\zeta_{\rm T}$ for different values of parameters b and $\Theta_{\rm K}$. $s = 2$

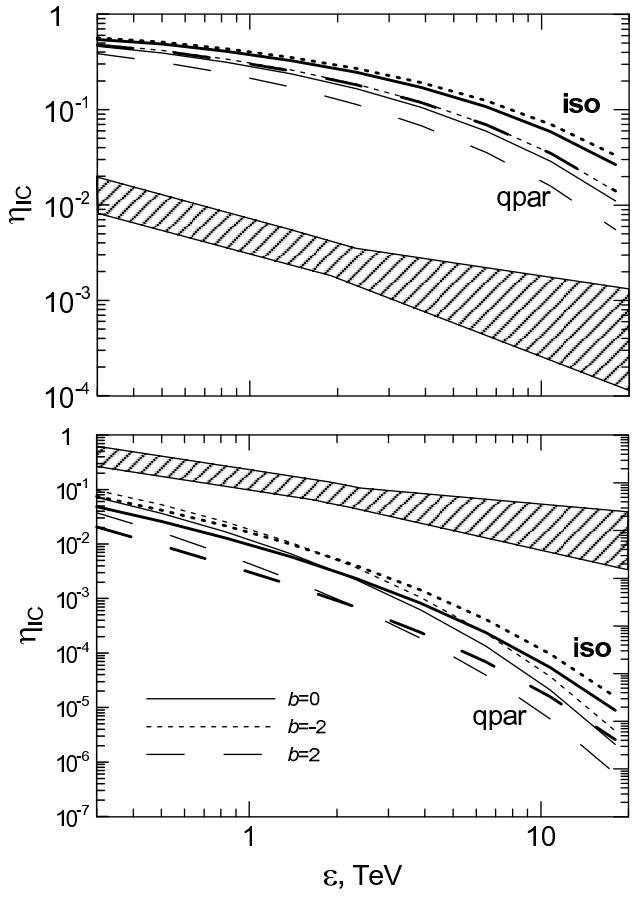

Figure F.4. Modification factor $\eta_{\rm ic}$. Lines are the same as on Fig. F.2. Experimental modification factor for SN 1006 are shown for comparison. It is obtained from the HESS data [28] with the use of Eq. (5.26) and MF strength $B_{\rm o} = 3\,\mu$G (upper panel) and $B_{\rm o} = 30\,\mu$G (lower panel).